Springer Proceedings in Physics 222

Olena Fesenko
Leonid Yatsenko *Editors*

Nanophotonics, Nanooptics, Nanobiotechnology, and Their Applications

Selected Proceedings of the 6th International Conference Nanotechnology and Nanomaterials (NANO2018), August 27-30, 2018, Kyiv, Ukraine

Springer

Springer Proceedings in Physics

Volume 222

The series Springer Proceedings in Physics, founded in 1984, is devoted to timely reports of state-of-the-art developments in physics and related sciences. Typically based on material presented at conferences, workshops and similar scientific meetings, volumes published in this series will constitute a comprehensive up-to-date source of reference on a field or subfield of relevance in contemporary physics. Proposals must include the following:

- name, place and date of the scientific meeting
- a link to the committees (local organization, international advisors etc.)
- scientific description of the meeting
- list of invited/plenary speakers
- an estimate of the planned proceedings book parameters (number of pages/ articles, requested number of bulk copies, submission deadline).

More information about this series at http://www.springer.com/series/361

Olena Fesenko • Leonid Yatsenko
Editors

Nanophotonics, Nanooptics, Nanobiotechnology, and Their Applications

Selected Proceedings of the 6th International Conference Nanotechnology and Nanomaterials (NANO2018), August 27-30, 2018, Kyiv, Ukraine

Springer

Editors
Olena Fesenko
National Academy of Sciences of Ukraine
Institute of Physics
Kyiv, Ukraine

Leonid Yatsenko
National Academy of Sciences of Ukraine
Institute of Physics
Kyiv, Ukraine

ISSN 0930-8989 ISSN 1867-4941 (electronic)
Springer Proceedings in Physics
ISBN 978-3-030-17754-6 ISBN 978-3-030-17755-3 (eBook)
https://doi.org/10.1007/978-3-030-17755-3

© Springer Nature Switzerland AG 2019
This work is subject to copyright. All rights are reserved by the Publisher, whether the whole or part of the material is concerned, specifically the rights of translation, reprinting, reuse of illustrations, recitation, broadcasting, reproduction on microfilms or in any other physical way, and transmission or information storage and retrieval, electronic adaptation, computer software, or by similar or dissimilar methodology now known or hereafter developed.
The use of general descriptive names, registered names, trademarks, service marks, etc. in this publication does not imply, even in the absence of a specific statement, that such names are exempt from the relevant protective laws and regulations and therefore free for general use.
The publisher, the authors, and the editors are safe to assume that the advice and information in this book are believed to be true and accurate at the date of publication. Neither the publisher nor the authors or the editors give a warranty, express or implied, with respect to the material contained herein or for any errors or omissions that may have been made. The publisher remains neutral with regard to jurisdictional claims in published maps and institutional affiliations.

This Springer imprint is published by the registered company Springer Nature Switzerland AG.
The registered company address is: Gewerbestrasse 11, 6330 Cham, Switzerland

Preface

This book highlights the most recent advances in nanoscience from leading researchers in Ukraine, Europe, and beyond. It features contributions from participants of the 6th International Research and Practice Conference "Nanotechnology and Nanomaterials" (NANO-2018), held in Kyiv, Ukraine, on August 27–30, 2018. This event was organized jointly by the Institute of Physics of the National Academy of Sciences of Ukraine, Taras Shevchenko National University of Kyiv (Ukraine), University of Tartu (Estonia), University of Turin (Italy), and Pierre and Marie Curie University (France). Internationally recognized experts from a wide range of universities and research institutes shared their knowledge and key results in the areas of nanocomposites and nanomaterials, nanostructured surfaces, microscopy of nano-objects, nanooptics and nanophotonics, nanoplasmonics, nanochemistry, nanobiotechnology, and surface-enhanced spectroscopy.

Today nanotechnology is becoming one of the most actively developing and promising fields of science. Numerous nanotechnology investigations are already producing practical results that can be applied in various areas of human life from science and technology to medicine and pharmacology. The aim of these books is to highlight the latest investigations from different areas of nanoscience and to stimulate new interest in this field. Volume II of this two-volume work covers such important topics as nanooptics, nanochemistry, nanobiotechnology, and enhanced nanoplasmonics.

This book is divided into three sections: Part I, *Nanophotonics and Nanooptics;* Part II, *Nanobiotechnology; and Part III, Applications.* Sections covering Nanocomposites and Nanostructures and Applications can be found in Volume I: Nanocomposites, Nanostructures, and Their Applications.

The papers published in these five sections fall under the broad categories of nanomaterial preparation and characterization, nanobiotechnology, nanodevices and quantum structures, and spectroscopy and nanooptics. We hope that both volumes will be equally useful and interesting for young scientists or PhD students and mature scientists alike.

Kyiv, Ukraine — Olena Fesenko
Kyiv, Ukraine — Leonid Yatsenko

Contents

Part I Nanophotonics and Nanooptics

1 SiO_2 /*n*-Si Template for Copper Nanostructure Formation 3
Egor Kaniukov, Dzmitry Yakimchuk, Victoria Bundyukova, Alexander Petrov, Evgenii Belonogov, and Sergey Demyanov

2 Synthesis, Morphology, Structure, and Luminescence Properties of Bi-Containing Phosphates: Review and Detailed Consideration on the Example of Pr^{3+}-doped $BiPO_4$ Nanopowders 19
V. Chornii, V. Boyko, S. G. Nedilko, M. Slobodyanik, and K. Terebilenko

3 Anomalous Change of Refractive Index for Au Sols Under Laser Illumination 53
Yuliia Harahuts, Valeriy Pavlov, Elena Mokrinskaya, Irina Davidenko, Nikolay Davidenko, Nataliya Kutsevol, Ihor Pampukha, and Victor Martynyuk

4 Development of the Waveguide Photonic Crystal Structures Formed by Distribution of Nanoparticles in Polymer Matrix 73
V. Hryn, O. Sakhno, A. Bendziak, V. Fito, P. Yezhov, and T. Smirnova

5 Optical Phenomena in Nanoscale Tin Dioxide Films Obtained by Means of Polymers 87
L. Filevska, A. Chebanenko, M. Klochkov, V. Grinevich, and V. Smyntyna

6 Optical Properties of Polytetrafluoroethylene –Carbon Nanotube Composite in the Light Spectrum Range 320 –1000 nm ... 95
I. Ye. Galstyan, M. M. Nishenko, M. M. Yakimchuk, and G. P. Prikhodko

7 Based on Pneumatic Photonic Structures, High-Accuracy Measurement Procedure for the Universal Gas Constant 103
E. Ya. Glushko

8 Nanoscale Photocatalytic Layers with Titania on Stainless Steel Foil 121
V. Honcharov, V. Zazhigalov, O. Sanzhak, F. Azimov, D. Brazhnyk, M. Parlinska-Wojtan, and E. Drzymala

9 New Methacrylic Polymers with Heterocyclic Analogs of Stilbene in Side Chain – Promising Materials for Optoelectronics 131
O. Krupka, O. Kharchenko, V. Smokal, A. Kysil, and A. Kolendo

10 The Effect of Ultraviolet Irradiation on the Electro-transport Properties of Carbon Nanotubes 145
Oleh D. Marinin, Iryna V. Ovsiienko, Tatiana A. Len, Lyudmila Yu. Matzui, Yuriy I. Prylutskyy, Dina D. Naumova, and Uwe Ritter

11 New Method for Rapid Digital Hologram Processing 165
Yu. M. Kotsiuba, H. A. Petrovska, V. M. Fitio, and Ya. V. Bobitski

12 Theory of Exciton States in Nanosystems Containing Dielectric Quantum Dots 173
Sergey I. Pokutnyi

Part II Nanobiotechnology

13 Magnetic Resonance Nanotherapy for Malignant Tumors 197
V. Orel, A. Shevchenko, T. Golovko, O. Ganich, O. Rihalsky, I. Orel, A. Burlaka, S. Lukin, V. Kotovsky, V. Dunaevsky, and S. Nazarchuk

14 Nanoporous Biochar for Removal of Toxic Organic Compounds from Water 209
Yuliya S. Dzyazko, Olexii V. Palchik, Vladimir M. Ogenko, Leon Y. Shtemberg, Valerii I. Bogomaz, Sergii A. Protsenko, Vladimir G. Khomenko, Irina S. Makeeva, Oxana V. Chernysh, and Olexander G. Dzyazko

15 The Regularities of Sorption of Substances of Different Nature by pH-Sensitive Acrylic Hydrogels for Plant Nanofertilizer Formation 225
K. V. Kalinichenko, G. N. Nikovskaya, V. O. Oliinyk, Yu. M. Samchenko, and Z. R. Ulberg

16 Effect of Porosity on Ion Transport Through Polymers and Polymer-Based Composites Containing Inorganic Nanoparticles (Review) 235
Yuliya Dzyazko, Yurii Volfkovich, Olga Perlova, Ludmila Ponomaryova, Nataliia Perlova, and Evgen Kolomiets

17 Features of the Influence of UFS/Raffinose Nanocomposites on In Vitro Cultivation of Gametes of Swine 255
O. V. Shcherbak, A. B. Zyuzyun, A. O. Sverhunov, and A. O. Sverhunova

18 The Infrared and Raman Spectra of Acetaminophen –Cholesterol Complex: DFT Study 263
A. Dawid and Z. Gburski

19 Change in Functional State of Bone Marrow-Derived Mesenchymal Stem Cells After Incubation with Silver Nanoparticles 273
N. A. Volkova, M. S. Yukhta, E. V. Pavlovich, and A. N. Goltsev

Part III Applications

20 Challenges in Studying the Incorporation of Nanomaterials to Building Materials on Microbiological Models 285
Adrian Augustyniak, Pawel Sikora, Krzysztof Cendrowski, Paweł Nawrotek, Ewa Mijowska, and Dietmar Stephan

21 Computational Studies of Adsorption of Toxic Molecules and Anions on the Surface of Doped and Functionalized Carbon Nanotubes 305
V. Borysiuk, S. G. Nedilko, Yu. Hizhnyi, and A. Shyichuk

22 Single-Molecule Conductance Theory Using Different Orbitals for Different Spins: Applications to π-Electrons in Graphene Molecules 341
Anatoliy V. Luzanov

23 Nanostructure Complexes in Water from the Position of SPE-Effect and from the Theory of Water, Created by J. Preparata 359
Ludmila Stepanovna Martseniuk and Aleksandr Stepanovich Martseniuk

24 Nanocomposite Hydrogels Containing Silver Nanoparticles as Materials for Wound Dressings 375
O. Nadtoka, N. Kutsevol, O. Linnik, and M. Nikiforov

25 Green Synthesis of Magnetic Spinel Nanoparticles 389
Mariia Liaskovska, Tetiana Tatarchuk, Mohamed Bououdina, and Ivan Mironyuk

26 Properties of Ultrathin Lipid Layers Surrounding Boron Nitride Nanotube: Computer Simulation Study 399
Przemyslaw Raczynski

27 Properties of n-Cyanobiphenyl Nematogene Phases Formed Between Carbon Nanotube Arrays: Computer Simulation Study 409
Violetta Raczyńska, Krzysztof Górny, Przemyslaw Raczynski, and Zbigniew Dendzik

28 Tryptophan-Stabilized Plasmonic Fe_3O_4/Ag Nanoparticles 417
Ie. V. Pylypchuk, Iu. P. Mukha, N. V. Vityuk, K. Szczepanowicz, L. P. Storozhuk, A. M. Eremenko, P. Warszyński, and P. P. Gorbyk

29 Influence of Mg Content on Structural and Magnetic Properties of Green-Synthesized $Li_{0.5-0.5x}Mg_xFe_{2.5-0.5x}O_4$ ($0.0 \leq x \leq 0.8$) Nanoferrites 431
P. Tiwari, S. N. Kane, R. Verma, T. Tatarchuk, and F. Mazaleyrat

30 Current State of Fuel Cell Research 443
Iryna Ivanenko, Yurii Fedenko, Anastasiia Ruda, and Mitchenko Tetiana

31 Synthesis and Study of Methacrylic Monomers and Polymers on the Basis of Aurones 457
Nataliia Iukhymenko, Anton Martynes-Harsiia, Oksana Kharchenko, Vitaliy Smokal, Oksana Krupka, and Aleksiy Kolendo

Index 469

Contributors

Adrian Augustyniak Department of Immunology, Microbiology and Physiological Chemistry, Faculty of Biotechnology and Animal Husbandry, West Pomeranian University of Technology, Szczecin, Poland

Building Materials and Construction Chemistry, Technische Universität Berlin, Berlin, Germany

F. Azimov Institute for Sorption and Problems of Endoecology, National Academy of Sciences of Ukraine, Kyiv, Ukraine

Evgenii Belonogov Voronezh State University, Voronezh, Russian Federation

Ya. V. Bobitski Department of Photonics Lviv Polytechnic National University, Lviv, Ukraine

Faculty of Mathematics and Natural Sciences University of Rzeszow, Rzeszow, Poland

Valerii I. Bogomaz "Ukravit" Agro LTD, Kyiv, Ukraine

V. Borysiuk Taras Shevchenko National University of Kyiv, Kyiv, Ukraine

Mohamed Bououdina Department of Physics, College of Science, University of Bahrain, Zallaq, Kingdom of Bahrain

V. Boyko National University of Life and Environmental Sciences of Ukraine, Kyiv, Ukraine

D. Brazhnyk Institute for Sorption and Problems of Endoecology, National Academy of Sciences of Ukraine, Kyiv, Ukraine

Victoria Bundyukova Scientific-Practical Materials Research Centre, NAS of Belarus, Minsk, Belarus

A. Burlaka R.E. Kavetsky Institute of Experimental Pathology, Oncology and Radiobiology, Academy of Science of Ukraine, Kyiv, Ukraine

Krzysztof Cendrowski Nanomaterials Physicochemistry Department, Faculty of Chemical Technology and Engineering, West Pomeranian University of Technology, Szczecin, Poland

A. Chebanenko Odessa I.I. Mechnikov National University, Odessa, Ukraine

Oxana V. Chernysh Kyiv National University of Technologies and Design, Kyiv, Ukraine

V. Chornii National University of Life and Environmental Sciences of Ukraine, Kyiv, Ukraine

Taras Shevchenko National University of Kyiv, Kyiv, Ukraine

Irina Davidenko Taras Shevchenko National University of Kyiv, Kyiv, Ukraine

Nikolay Davidenko Taras Shevchenko National University of Kyiv, Kyiv, Ukraine

A. Dawid Department of Computer Science, WSB University, Dąbrowa Górnicza, Poland

Sergey Demyanov Scientific-Practical Materials Research Centre, NAS of Belarus, Minsk, Belarus

Zbigniew Dendzik Institute of Physics, University of Silesia, Chorzów, Poland

Silesian Center for Education and Interdisciplinary Research, University of Silesia, Chorzów, Poland

E. Drzymala Institute of Nuclear Physics, PAS, Krakow, Poland

V. Dunaevsky V.Ye. Lashkaryov Institute of Semiconductor Physics, National Academy of Science of Ukraine, Kyiv, Ukraine

Olexander G. Dzyazko Taras Shevchenko Natiional University of Kyiv, Kyiv, Ukraine

Yuliya S. Dzyazko VI Vernadskii Institute of General and Inorganic Chemistry of the National Academy of Science of Ukraine, Kyiv, Ukraine

A. M. Eremenko Chuiko Institute of Surface Chemistry, NAS of Ukraine, Kyiv, Ukraine

Yurii Fedenko Department of Inorganic Substances Technology, Water Treatment and General Chemical Engineering of National Technical University of Ukraine "Igor Sikorsky Kyiv Polytechnic Institute", Kyiv, Ukraine

L. Filevska Odessa I.I. Mechnikov National University, Odessa, Ukraine

V. M. Fitio Department of Photonics Lviv Polytechnic National University, Lviv, Ukraine

I. Ye. Galstyan G. V. Kurdyumov Institute for Metal Physics of the N.A.S. of Ukraine, Kiev, Ukraine

O. Ganich National Cancer Institute, Kyiv, Ukraine

Z. Gburski Katowice Institute of Information Technologies, Katowice, Poland

Institute of Physics, University of Silesia in Katowice, Chorzów, Poland

V. Grinevich Odessa I.I. Mechnikov National University, Odessa, Ukraine

E. Ya. Glushko Institute of Semiconductor Physics, Kyiv, Ukraine

T. Golovko National Cancer Institute, Kyiv, Ukraine

A. N. Goltsev Institute for Problems of Cryobiology and Cryomedicine of the National Academy of Sciences of Ukraine, Kharkov, Ukraine

P. P. Gorbyk Chuiko Institute of Surface Chemistry, NAS of Ukraine, Kyiv, Ukraine

Krzysztof Górny Institute of Physics, University of Silesia, Chorzów, Poland

Silesian Center for Education and Interdisciplinary Research, University of Silesia, Chorzów, Poland

Yuliia Harahuts Taras Shevchenko National University of Kyiv, Kyiv, Ukraine

Yu. Hizhnyi Taras Shevchenko National University of Kyiv, Kyiv, Ukraine

V. Honcharov State Establishment "Lugansk State Medical University", Rubizhne, Ukraine

Nataliia Iukhymenko Department of Chemistry, Taras Shevchenko National University of Kyiv, Kyiv, Ukraine

Faculty of Chemistry, Macromolecular Chemistry Department, Taras Shevchenko National University of Kyiv, Kyiv, Ukraine

Iryna Ivanenko Department of Inorganic Substances Technology, Water Treatment and General Chemical Engineering of National Technical University of Ukraine "Igor Sikorsky Kyiv Polytechnic Institute", Kyiv, Ukraine

K. V. Kalinichenko Colloidal Technologies of the Natural Systems Department, F.D. Ovcharenko Institute of Biocolloidal Chemistry, National Academy of Sciences of Ukraine, Kiev, Ukraine

S. N. Kane Magnetic Materials Laboratory, School of Physics, D. A. University, Indore, India

Egor Kaniukov Scientific-Practical Materials Research Centre, NAS of Belarus, Minsk, Belarus

Oksana Kharchenko Department of Chemistry, Taras Shevchenko National University of Kyiv, Kyiv, Ukraine

Vladimir G. Khomenko Kyiv National University of Technologies and Design, Kyiv, Ukraine

M. Klochkov Odessa I.I. Mechnikov National University, Odessa, Ukraine

Aleksiy Kolendo Department of Chemistry, Taras Shevchenko National University of Kyiv, Kyiv, Ukraine

Evgen Kolomiets VI Vernadskii Institute of General and Inorganic Chemistry of the National Academy of Science of Ukraine, Kyiv, Ukraine

V. Kotovsky National Technical University of Ukraine "Igor Sikorsky Kyiv Polytechnic Institute", Kyiv, Ukraine

Yu. M. Kotsiuba Department of Photonics Lviv Polytechnic National University, Lviv, Ukraine

Oksana Krupka Department of Chemistry, Taras Shevchenko National University of Kyiv, Kyiv, Ukraine

Nataliya Kutsevol Taras Shevchenko National University of Kyiv, Kyiv, Ukraine

A. Kysil Taras Shevchenko National University of Kyiv, Kyiv, Ukraine

Tatiana A. Len Departments of Physics, Taras Shevchenko National University of Kyiv, Kyiv, Ukraine

Mariia Liaskovska Department of Chemistry, Vasyl Stefanyk Precarpathian National University, Ivano-Frankivsk, Ukraine

Department of Biological and Medical Chemistry named after academician Babenko H.O., Ivano-Frankivsk National Medical University, Ivano-Frankivsk, Ukraine

O. Linnik Chuiko Institute of Surface Chemistry, National Academy of Science of Ukraine, Kyiv, Ukraine

S. Lukin R.E. Kavetsky Institute of Experimental Pathology, Oncology and Radiobiology, National Academy of Science of Ukraine, Kyiv, Ukraine

V.Ye. Lashkaryov Institute of Semiconductor Physics, National Academy of Science of Ukraine, Kyiv, Ukraine

Anatoliy V. Luzanov SSI "Institute of Single Crystals", NAS of Ukraine, Kharkiv, Ukraine

Irina S. Makeeva Kyiv National University of Technologies and Design, Kyiv, Ukraine

Oleh D. Marinin Departments of Physics, Taras Shevchenko National University of Kyiv, Kyiv, Ukraine

Aleksandr Stepanovich Martseniuk National University of Food Technology, Kiev, Ukraine

Ludmila Stepanovna Martseniuk Institute of Nuclear Researches NAS Ukraine, Kiev, Ukraine

Anton Martynes-Harsiia Department of Chemistry, Taras Shevchenko National University of Kyiv, Kyiv, Ukraine

Victor Martynyuk Taras Shevchenko National University of Kyiv, Kyiv, Ukraine

Lyudmila Yu. Matzui Departments of Physics, Taras Shevchenko National University of Kyiv, Kyiv, Ukraine

F. Mazaleyrat SATIE, ENS Cachan, CNRS 8029, Universite Paris-Saclay, Cachan, France

Ewa Mijowska Nanomaterials Physicochemistry Department, Faculty of Chemical Technology and Engineering, West Pomeranian University of Technology, Szczecin, Poland

Ivan Mironyuk Department of Chemistry, Vasyl Stefanyk Precarpathian National University, Ivano-Frankivsk, Ukraine

Elena Mokrinskaya Taras Shevchenko National University of Kyiv, Kyiv, Ukraine

Iu. P. Mukha Chuiko Institute of Surface Chemistry, NAS of Ukraine, Kyiv, Ukraine

O. Nadtoka Taras Shevchenko National University of Kyiv, Kyiv, Ukraine

Dina D. Naumova Department of Chemistry, Taras Shevchenko National University of Kyiv, Kyiv, Ukraine

Paweł Nawrotek Department of Immunology, Microbiology and Physiological Chemistry, Faculty of Biotechnology and Animal Husbandry, West Pomeranian University of Technology, Szczecin, Poland

S. Nazarchuk National Technical University of Ukraine “Igor Sikorsky Kyiv Polytechnic Institute”, Kyiv, Ukraine

S. G. Nedilko Taras Shevchenko National University of Kyiv, Kyiv, Ukraine

M. Nikiforov Military Institute of Taras Shevchenko National University of Kyiv, Kyiv, Ukraine

G. N. Nikovskaya Colloidal Technologies of the Natural Systems Department, F.D. Ovcharenko Institute of Biocolloidal Chemistry, National Academy of Sciences of Ukraine, Kiev, Ukraine

M. M. Nishenko G. V. Kurdyumov Institute for Metal Physics of the N.A.S. of Ukraine, Kiev, Ukraine

Vladimir M. Ogenko VI Vernadskii Institute of General and Inorganic Chemistry of the National Academy of Science of Ukraine, Kyiv, Ukraine

V. O. Oliinyk Department of Physical and Chemical Geomechanics, F. D. Ovcharenko Institute of Biocolloidal Chemistry, National Academy of Sciences of Ukraine, Kiev, Ukraine

I. Orel National Cancer Institute, Kyiv, Ukraine

V. Orel National Cancer Institute, Kyiv, Ukraine

National Technical University of Ukraine "Igor Sikorsky Kyiv Polytechnic Institute", Kyiv, Ukraine

Iryna V. Ovsiienko Departments of Physics, Taras Shevchenko National University of Kyiv, Kyiv, Ukraine

Olexii V. Palchik VI Vernadskii Institute of General and Inorganic Chemistry of the National Academy of Science of Ukraine, Kyiv, Ukraine

Ihor Pampukha Taras Shevchenko National University of Kyiv, Kyiv, Ukraine

M. Parlinska-Wojtan Institute of Nuclear Physics, PAS, Krakow, Poland

E. V. Pavlovich Institute for Problems of Cryobiology and Cryomedicine of the National Academy of Sciences of Ukraine, Kharkov, Ukraine

Valeriy Pavlov Taras Shevchenko National University of Kyiv, Kyiv, Ukraine

Nataliia Perlova Odessa II Mechnikov National University, Odessa, Ukraine

Olga Perlova Odessa II Mechnikov National University, Odessa, Ukraine

Alexander Petrov Scientific-Practical Materials Research Centre, NAS of Belarus, Minsk, Belarus

H. A. Petrovska Department of Photonics Lviv Polytechnic National University, Lviv, Ukraine

Sergey I. Pokutnyi Chuiko Institute of Surface Chemistry of National Academy of Sciences of Ukraine, Kyiv, Ukraine

Ludmila Ponomaryova Sumy National University, Sumy, Ukraine

G. P. Prikhodko Chuiko Institute of Surface Chemistry of the N.A.S. of Ukraine, Kiev, Ukraine

Sergii A. Protsenko Crop Care Institute, Cherkasy, Ukraine

Yuriy I. Prylutskyy Department of Biophysics, Taras Shevchenko National University of Kyiv, Kyiv, Ukraine

Ie. V. Pylypchuk Chuiko Institute of Surface Chemistry, NAS of Ukraine, Kyiv, Ukraine

Violetta Raczyńska Institute of Physics, University of Silesia, Chorzów, Poland

Przemyslaw Raczynski Institute of Physics, University of Silesia, Katowice, Poland

Silesian Centre of Education & Interdisciplinary Research, Chorzów, Poland

O. Rihalsky National Cancer Institute, Kyiv, Ukraine

Uwe Ritter Technical University of Ilmenau, Ilmenau, Germany

Anastasiia Ruda Department of Inorganic Substances Technology, Water Treatment and General Chemical Engineering of National Technical University of Ukraine "Igor Sikorsky Kyiv Polytechnic Institute", Kyiv, Ukraine

Yu. M. Samchenko Department of Functional Hydrogel, F.D. Ovcharenko Institute of Biocolloidal Chemistry, National Academy of Sciences of Ukraine, Kiev, Ukraine

O. Sanzhak Institute for Sorption and Problems of Endoecology, National Academy of Sciences of Ukraine, Kyiv, Ukraine

O. V. Shcherbak Institute of Animal Breeding and Genetics nd.a. M.V. Zubets, National Academy of Agrarian Science of Ukraine, Kiev, Ukraine

A. Shevchenko G. V. Kurdyumov Institute for Metal Physics, National Academy of Science of Ukraine, Kyiv, Ukraine

Leon Y. Shtemberg Crop Care Institute, Cherkasy, Ukraine

A. Shyichuk Department of Rare Earth, Faculty of Chemistry, Adam Mickiewicz University, Poznań, Poland

Pawel Sikora Building Materials and Construction Chemistry, Technische Universität Berlin, Berlin, Germany

Faculty of Civil Engineering and Architecture, West Pomeranian University of Technology, Szczecin, Poland

M. Slobodyanik Taras Shevchenko National University of Kyiv, Kyiv, Ukraine

Vitaliy Smokal Department of Chemistry, Taras Shevchenko National University of Kyiv, Kyiv, Ukraine

V. Smyntyna Odessa I.I. Mechnikov National University, Odessa, Ukraine

Dietmar Stephan Building Materials and Construction Chemistry, Technische Universität Berlin, Berlin, Germany

L. P. Storozhuk Chuiko Institute of Surface Chemistry, NAS of Ukraine, Kyiv, Ukraine

A. O. Sverhunov Kharkiv State Zooveterinarian Academy, Kharkiv, Ukraine

A. O. Sverhunova Kharkiv National Medical University, Kharkiv, Ukraine

K. Szczepanowicz Jerzy Haber Institute of Catalysis and Surface Chemistry, Polish Academy of Sciences, Krakow, Poland

Tetiana Tatarchuk Department of Chemistry, Vasyl Stefanyk Precarpathian National University, Ivano-Frankivsk, Ukraine

Educational and Scientific Center of Materials Science and Nanotechnology, Vasyl Stefanyk Precarpathian National University, Ivano-Frankivsk, Ukraine

K. Terebilenko Taras Shevchenko National University of Kyiv, Kyiv, Ukraine

Mitchenko Tetiana Department of Inorganic Substances Technology, Water Treatment and General Chemical Engineering of National Technical University of Ukraine "Igor Sikorsky Kyiv Polytechnic Institute", Kyiv, Ukraine

P. Tiwari Magnetic Materials Laboratory, School of Physics, D. A. University, Indore, India

Department of Physics, Prestige Institute of Engineering Management and Research, Indore, India

Z. R. Ulberg Colloidal Technologies of the Natural Systems Department, F.D. Ovcharenko Institute of Biocolloidal Chemistry, National Academy of Sciences of Ukraine, Kiev, Ukraine

R. Verma Magnetic Materials Laboratory, School of Physics, D. A. University, Indore, India

N. V. Vityuk Chuiko Institute of Surface Chemistry, NAS of Ukraine, Kyiv, Ukraine

Yurii Volfkovich AN Frumkin Institute of Physical Chemistry and Electrochemistry of the RAS, Moscow, Russia

N. A. Volkova Institute for Problems of Cryobiology and Cryomedicine of the National Academy of Sciences of Ukraine, Kharkov, Ukraine

P. Warszyński Jerzy Haber Institute of Catalysis and Surface Chemistry, Polish Academy of Sciences, Krakow, Poland

Dzmitry Yakimchuk Scientific-Practical Materials Research Centre, NAS of Belarus, Minsk, Belarus

M. M. Yakimchuk G. V. Kurdyumov Institute for Metal Physics of the N.A.S. of Ukraine, Kiev, Ukraine

M. S. Yukhta Institute for Problems of Cryobiology and Cryomedicine of the National Academy of Sciences of Ukraine, Kharkov, Ukraine

V. Zazhigalov Institute for Sorption and Problems of Endoecology, National Academy of Sciences of Ukraine, Kyiv, Ukraine

A. B. Zyuzyun Institute of Animal Breeding and Genetics nd.a. M.V. Zubets, National Academy of Agrarian Science of Ukraine, Kiev, Ukraine

Part I
Nanophotonics and Nanooptics

Chapter 1
SiO_2 /*n*-Si Template for Copper Nanostructure Formation

Egor Kaniukov, Dzmitry Yakimchuk, Victoria Bundyukova, Alexander Petrov, Evgenii Belonogov, and Sergey Demyanov

Nowadays, nanostructures (NSs) attract great interest due to their unique magnetic, electronic, and optical properties [1, 2]. From the point of view of practical applications, interesting plasmonic metals for the creation of NSs are silver, gold, and copper. To create plasmonic NSs, various approaches are implemented [3–6] that make it possible to obtain crystallites with a certain shape [7–10]. However, in a number of cases, more branched structures consisting of nanocrystal-oriented (dendrites) in a certain way are of interest. Such hierarchical structures have a high specific surface and have practical application in various fields, in particular, in sensorics [11], in power engineering [12], in the creation of superhydrophobic surfaces [13], and as an alternative to standard graphite electrodes in Li-ion batteries [14]. The highly branched structure of dendrites is especially important when processes based on surface effects are involved, such as catalysis [15] or surface-enhanced Raman scattering (SERS) [16].

Given the broad prospects for the use of dendrites, a reliable method is needed that allows manageable creation of branched structures. At present, electrochemical [17–19] and chemical deposition [20], hydrothermal synthesis [21], and reduction of copper precursors [22] are used. Due to the simplicity, the high degree of control, and the scalability of the process, electrochemical deposition is the most suitable method for obtaining dendrites. When it is used, it is possible to control the shape [23] and to influence growth processes and crystallization mechanisms, by specifying grain sizes and the morphology of NSs [24].

One of the most important parameters influencing the efficiency of using is the relative positioning of dendrites on the substrate. The close arrangement of the

E. Kaniukov (✉) · D. Yakimchuk · V. Bundyukova · A. Petrov · S. Demyanov
Scientific-Practical Materials Research Centre, NAS of Belarus, Minsk, Belarus

E. Belonogov
Voronezh State University, Voronezh, Russian Federation

© Springer Nature Switzerland AG 2019

O. Fesenko, L. Yatsenko (eds.), *Nanophotonics, Nanooptics, Nanobiotechnology, and Their Applications*, Springer Proceedings in Physics 222,
https://doi.org/10.1007/978-3-030-17755-3_1

nanostructures could have both a positive (in catalytic reactions, when a high density of NSs is important) and negative effect (due to screening when interacting with electromagnetic radiation, e.g., in SERS).

Taking into account the gaps in the technique of creating spatially separated dendritic structures, in this work, we propose a simple procedure for obtaining them through template synthesis. Using this approach, various structures can be formed by self-organization of various materials in the pores [25–30]. For most applications, the use of silicon substrates is of greatest interest [31–33]. Depending on the requirements, it is possible to obtain templates with different pore parameters (diameter, aspect ratio, and density). The swift heavy ion-track technology allows creating templates with controlled pore density, shape, and size in the range from several tens of nanometers to several micrometers [34].

In this work, we consider the preparation and investigation of porous SiO_2/*n*-Si templates. Electrochemical synthesis of plasmonic copper NSs is presented, and the factors that affect the structural and morphological features of copper NSs in the pores of the SiO_2/*n*-Si template are analyzed. Optical properties of spatially separated Cu dendrites are studied to assess the possibility of their use as SERS-active substrates.

1.1 Methods

In the present experiment, single-crystal *n*-type silicon plates (100) were used. They had a resistance of 4.5 Ohm cm with an amorphous SiO_2 layer thickness of 700 nm. Irradiation of the samples was carried out at a facility in the GSI-Darmstadt accelerator center on the "UNILAC" linear accelerator. The samples were irradiated at a normal incidence of ^{197}Au ions with an energy of up to 2200 MeV at fluences of 10^7–10^9 cm^2.

Samples were etched in 1.4% aqueous hydrofluoric acid (HF) at the room temperature. Etching conditions were selected in such a way as to ensure the creation of a conical shape with an area of contact with Si sufficient to initiate the deposition of NSs. The NS deposition in the pores of the SiO_2 layer on the *n*-Si substrate has been carried out by the electrochemical technique in the three-electrode two-chamber cell (20 cm^3) with an optical quality window, platinum counter electrode, and the Ag, AgCl|$KCl_{(sat.)}$ reference electrode (+0.220 V as compared with the SHE). All the potentials in the work are given relative to this reference electrode. Potentials have been controlled by the Autolab potentiostat. Metallic electrodeposition has been carried out in the 0.01 M $CuSO_4$ + 0.5 M H_3BO_3 solution.

The morphology of the *n*-SiO_2(Cu)/Si sample surface was characterized by the field emission scanning electron microscopy (FESEM) by means of the JEOL JSM-7000F setup. A further investigations of the texture and morphology of the metallic phase were carried out by the transmission electron microscopy (TEM) on the PSEM-200 setup and by the selected area electrons diffraction (SAED) on the

EG-100 M electron diffractometer using carbon replicas with the "shadowing" and the "extraction." The replica with the shadowing is a carbon thin film, which was taken from the sample surface, and it is repeating the relief of its surface. The replica with the "extraction" is the extraction of the metallic deposit for its further peekaboo investigation by means of the TEM and SAED methods.

Investigations on the amplification of the Raman signals were carried out by means of the CARS (coherent anti-Stokes Raman scattering) microscope ("SOLAR-TII" company, Minsk, Belarus). The experiment was performed using the red light laser with the wavelength of 633 nm and power of 4 mW at the exposition time of 0.5 s. The use of the "100×" objective having the numerical aperture $N_A = 0.95$ has made it possible to achieve 2000-multiple amplification. The diameter of the focused laser beam was $\sim$ 500 nm, which is comparable to the dimensions of the copper deposit considered in the present work.

1.2 Characteristic Properties of the Formation of the Ion-Track Templates on the Base of SiO_2/Si

A formation of elongated regions with diameters up to 50 nm takes place during a passage of swift heavy ions in solids. These regions are characterized by a modified density and deformed chemical bonds. The radiation damage regions at the chemical etching are dominating from the point of view of the etch rate. This preconditions the possibility of a selective transformation of the latent ion tracks in the SiO_2 layers on silicon in pores, by means of the etching process [35–37].

The thermal spike model provides good results for a description of the latent ion-tracks formation process in the silicon oxide [38]. This model supposes a thermalization of the electron subsystem of a solid during the time, not exceeding 10^{-14} s. During the subsequent several picoseconds, the electron-phonon interaction leads to a rapid heating of an area along the swift heavy ion trajectory. A number of microscopic defects which are formed as a result of ion irradiation depend on the energy of the incident ion. This energy is transferred to the substrate as a result of the elastic (nuclear) or inelastic (electronic) interactions (Fig. 1.1). The elastic energy loss practically does not influence the process of chemical transformation of ion tracks to the pores, by means of the wasting of the nuclear retarding process just on the formation of the constant point defects [39].

Correspondingly, the etching process of the latent ion tracks is determined by the inelastic component $(dE/dx)_e$, which has a threshold character. In this way, the electron loss energy with value less than 1.5 keV·nm^{-1} is a threshold of the latent ion-tracks formation, below which it is impossible to obtain pores by means of the chemical etching. Small spherical highly defect areas with radii up to 1.5 nm appear at $(dE/dx)_e \sim 1.5 \pm 0.5$ keV·nm^{-1} (point A in Fig. 1.1). With an increase of $(dE/dx)_e$ up to $\sim$ 4 keV * nm^{-1} (point B in Fig. 1.1), the elongation of defect areas takes place, with a simultaneous increase of their radii up to 3 nm and a

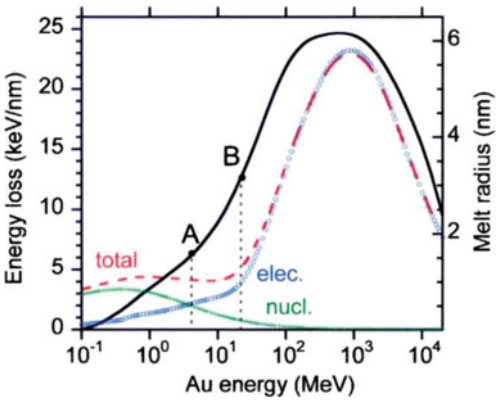

Fig. 1.1 Dependence of the energy loss on electronic, nuclear, and complete ones and the molten regions radii in SiO_2 on the irradiating Au ions [40]

subsequent formation of a simultaneous highly defect region [41]. The chemical etching is possible in the range $(dE/dx)_e \sim 1.5$–4 keV·nm^{-1}, but still the obtained pores are characterized with various diameters and etching cone angles, as well as the pore etching efficiency less than 100% (i.e., not all the ion tracks are transformed to pores). The energy larger than 4 keV·nm^{-1} is characterized by a formation of continuous highly defect areas, which are the necessary condition for obtaining by chemical etching of the pores with a homogeneous distribution by form and dimension with the etching efficiency of about 100% [41].

The hydrofluoric acid has been used for the etching of irradiated silicon oxide. The SiO_2 etching in the HF aqueous solutions takes place as a result of the following reaction:

$$SiO_2 + 6\,HF \rightarrow H_2SiF_6 + 2\,H_2O.$$

A selectability of the process of etching out of highly defect areas in the irradiated SiO_2 is determined by different rates of the bulk etching process V_B (solution of the unperturbed material) and the track etching V_T. The process of the etching pit formation near the latent ion-track base is accompanied by a decrease of the oxide layer thickness, as a simultaneous etching of the damaged and non-damaged material takes place. With that, the very form of the formed etching pit is close to the conical one, since the etching time of the pore intake opening is larger than that in the pore depth. After the approaching of the silicon surface, due to the fact that silicon does not interact with the HF, the pores obtain the form of a truncated cone. The knowledge of V_T and V_B value makes it possible to determine the main pore parameters (such as the diameter on the surface D, height in l, and the half-angle of the etching cone θ) at any given moment of time [42].

The dependence of pore parameters on the etching time has been investigated by the SEM studies of samples on the etching time up to 90 min. Results of these investigations are shown in Fig. 1.2a–f.

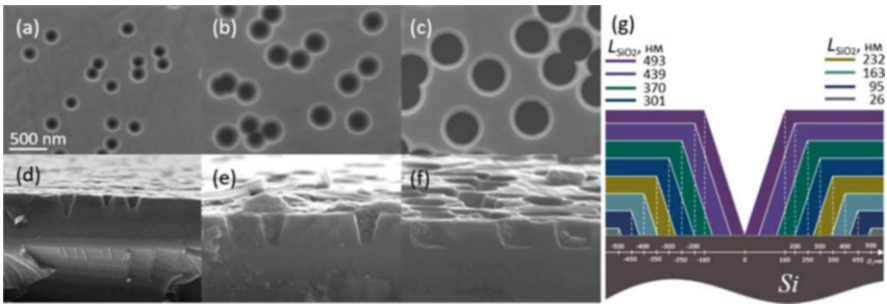

Fig. 1.2 SEM images of the surfaces (**a**–**c**) and cross sections (**d**–**f**) of the SiO_2 porous layer after the ^{197}Au ion irradiation with fluence of 5×10^8 cm^{-2} on different stages of etching in the HF solution with concentration of 1.4%; the time evolution of a pore profile (**g**)

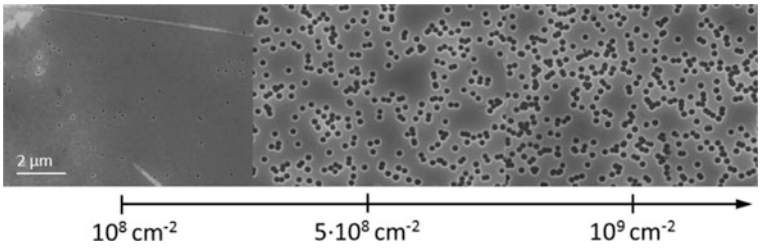

Fig. 1.3 SEM images of pores in the SiO_2 layer after irradiation by ^{197}Au ions with fluence of 10^8–10^9 cm^{-2}

On the base of an estimation of the quantitative characteristics of the pore parameters, their time dependences are constructed. The fact that all the dependences have got a linear character makes it possible to determine the etching rates with a high accuracy: $V_T = 21.0 \pm 0.5$ nm/min, $V_B = 5.8 \pm 0.1$ nm/min, $V = 3.6 \pm 0.2$ nm/min, and the angle $\theta = 16.0° \pm 0.5°$. The knowledge of the etching rate values has made it possible to specify the values of the time of pore opening (23 min) and etch removal of the SiO_2 layer (106 min). A change of the pore profiles with time is shown in Fig. 1.2g.

The constancy of V_T, V_B, V, and θ values makes it possible to obtain the comprehensive information on the characteristic pore sizes in any given moment of time. With the account of the fact that the half-angle of the etching cone value is in the area $18° \pm 2°$ for the most swift heavy ions [40], the knowledge of just one rate V_B value (which is not complicated to determine by means of the measurement of the SiO_2 thickness) makes it possible to forecast the parameters of obtained pores.

A dependence of the pore parameters on the irradiation fluence in the range of 10^8–5×10^9 cm^{-2} was studied on irradiated samples at the same etching time (36 min). The results are shown in Fig. 1.3.

One can see in Fig. 1.3 that the pores surface density in the SiO_2 layer has a direct dependence on the irradiation fluence. In this way, at the low fluence (10^8 cm^{-2}), an

average distance between pores is more than 1 μm. An increase of the fluence up to 5×10^8 cm^{-2} leads to a decrease of the distance between pores ~ 500 nm, with the appearance of an overlap between individual pores. Continuous strips containing of pores through the entire sample surface are registered in the SiO_2 layer at the fluence of 10^9 cm^{-2}. At the further increase of the irradiation dose up to 5×10^9 cm^{-2}, only individual SiO_2 islands remain on the silicon surface.

1.3 Characteristic Features of the Copper NSs in the Pores of SiO_2/Si Templates

A filling of the pores of the SiO_2/*n*-Si templates by copper has been carried out by the electrochemical deposition technique. With that, the working electrode was the single-crystalline *n*-silicon (100) substrate. With the account of the fact that the electrodeposition potential strongly influences the NS morphology, a selection of the potential value was performed with the account of the realization of the highly developed (dendrite) structure. The potentiodynamic current-voltage curves of the *n*-Si electrode without the oxide layer in the stationary electrolyte 0.01 $MCuSO_4$ + 0.5 MH_3BO_3 were obtained at the scanning rate 0.02 V/s. Results of the experiment are shown in Fig. 1.4.

Cathode currents are registered on the potentiodynamic current–voltage curve of the copper deposition are registered only at potentials being more negative than −0.3 V. The absence of Cu^{2+} cations recovery processes on the cathode in the

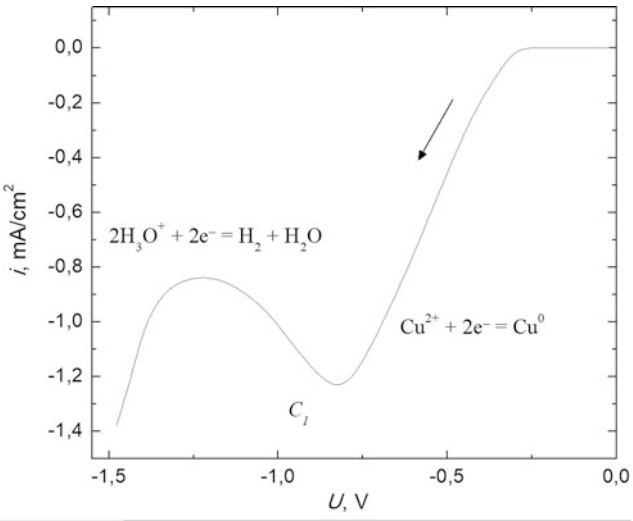

Fig. 1.4 A cathode potentiodynamic current-voltage curve of the *n*-Si electrode in the electrolyte on the base of the boric acid (0.5 MH_3BO_3) and the copper sulfate (0.01 $MCuSO_4$) [43]

voltage range of 0–0.3 V is concerned with a formation of the space-charge region on the border with the electrolyte. This is concerned with a low concentration of e^- in the barrier layer in silicon with the electron conductivity type. In the potential values range from −0.3 to −0.6 V, a cathode current growth and Cu^{2+} recovery with a formation of its local extremum are indicated as C_1 in Fig. 1.4. The cathode current maximum is alternated by a monotonic decrease of the absolute value i down to the potential −1.2 V. A decrease of the cathode current is a result of diffusive-limited character of the copper deposition on the silicon substrate. At potentials being more negative than −1.2 V, i value growth starts again, which most probably is concerned with a recovery reaction of the hydroxonium ions. With the account of the stated above facts, one can conclude that for the controlled acquisition of the copper NSs on the n-Si substrate, the electrodeposition potential should be in the range from −0.3 to −1.2 V.

Potentials corresponding to the sections with different slope of the potentiodynamic current-voltage curve have been selected from the determined range of working voltages. The potential of −0.5 V corresponded to the area of the normal recovery of copper on the n-Si substrate, and the potential of −1.0 V to the area of diffusive-limited processes. The experimentally determined output of metal by the current from the selected electrolyte was 91 ± 3% at the deposition potential of −0.5 V and 73 ± 3% at −1.0 V. The copper deposition time at different solution potentials with the predetermined copper ions concentration, which was calculated with the account of the current output, was 25 s (−0.5 V) and 16 s (−1.0 V). This corresponded to the charge 46 ± 2 μCoulomb/cm^2 passing though the electrochemical cell and should guarantee the complete filling of pores.

The estimation of the quality of the SiO_2 templates surface after the copper electrochemical deposition has been carried by the SEM technique. A general view of the SiO_2(Cu)/Si surface, shown in Fig. 1.5a, indicates that with the use of the electrochemical technique, the copper phase formation takes place exclusively on the conducting sections of the templates, i.e., in the pores, where the dielectric oxide layer is absent. A comparison of the amplified fragments of the surface of the SiO_2(Cu)/Si samples obtained at different deposition potentials (Fig. 1.5b, c) makes it possible to reveal the difference in the copper deposit morphology.

The use of potential of −0.5 V leads to a formation of the compact deposit with a smooth metallic surface (Fig. 1.5b). Shift of the deposition potential to the area of diffusive-limited processes (up to −1.0 V) leads to a formation of a more particulate deposit, with a realization of the preferential growth of individual crystallites, growing from pores perpendicular to the SiO_2 surface (Fig. 1.5c). With that, the pores localized on a large distance from the neighbors have a more branched structure of the copper deposit and somewhat larger degree of the pore filling, as compared to the pores placed more closely.

A detailed analysis of the copper deposit morphology, as well as determination of its size, form, and structure, was carried out in the process of the TEM investigations of the replicas with the “shadowing” and the “extraction,” as well as at the study of microdiffraction images of the distinguished area of the extraction fragments (Fig. 1.6).

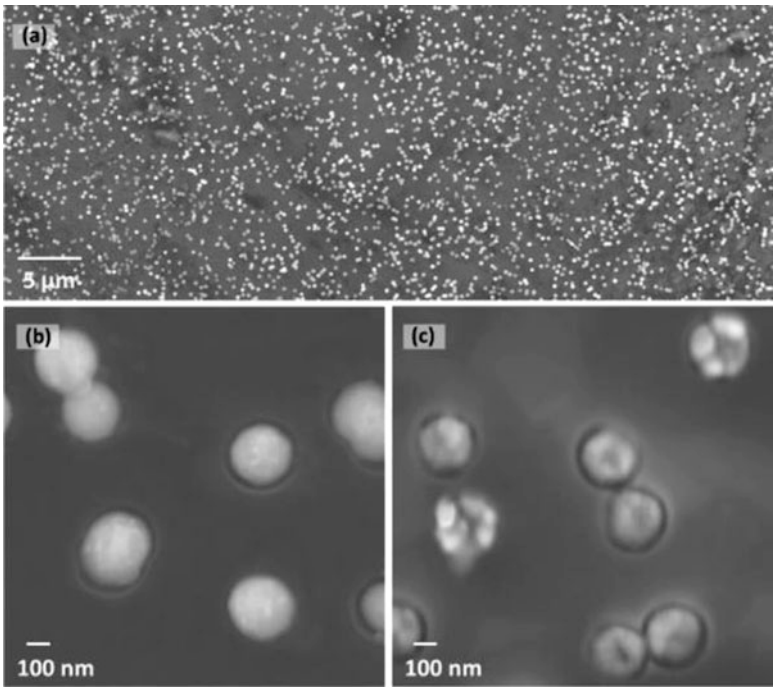

Fig. 1.5 SEM images of the SiO_2(Cu)/Si surface (**a**) and the amplified fragments of the copper deposit inside pores at deposition potentials of −0.5 V (**b**) and −1.0 V (**c**) [43]

A replica with the "extraction" (Fig. 1.6a), taken from the surface of the SiO_2(Cu)/Si structure, obtained at potential of −0.5 V confirms the formation of the compact deposit in this given deposition mode. This deposit minimally stands out over the SiO_2 surface in the pore center. A TEM image of the replica with the "extraction" (Fig. 1.6b), in which the metallic deposit is placed which was extracted from pores of the SiO_2 template, provides an impression on the copper growth morphology inside a pore: the deposit has a conical form, which exactly repeats the pore form.

The electrons diffraction on fragments of the metal, extracted from pores (Fig. 1.6c), indicates a formation of the face-centered cubic (fcc) lattice. All the most characteristic reflexes (110), (111), and (200) are registered on the electron-diffraction pattern, which evidences the absence of the copper deposit growth texture. Only point reflexes, which are present on the electron-diffraction pattern, evidence the dimensions of individual crystallites, which values are in the range of 40–70 nm. The analysis of diffraction peaks of the electron-diffraction pattern also makes it possible to reveal the presence of Cu_2O crystallites in the part of copper agglomerates.

The analysis of replicas with the "shadowing" for the metallic deposit, obtained at more negative deposition potentials (−1.0 V), indicates a high dispersivity of

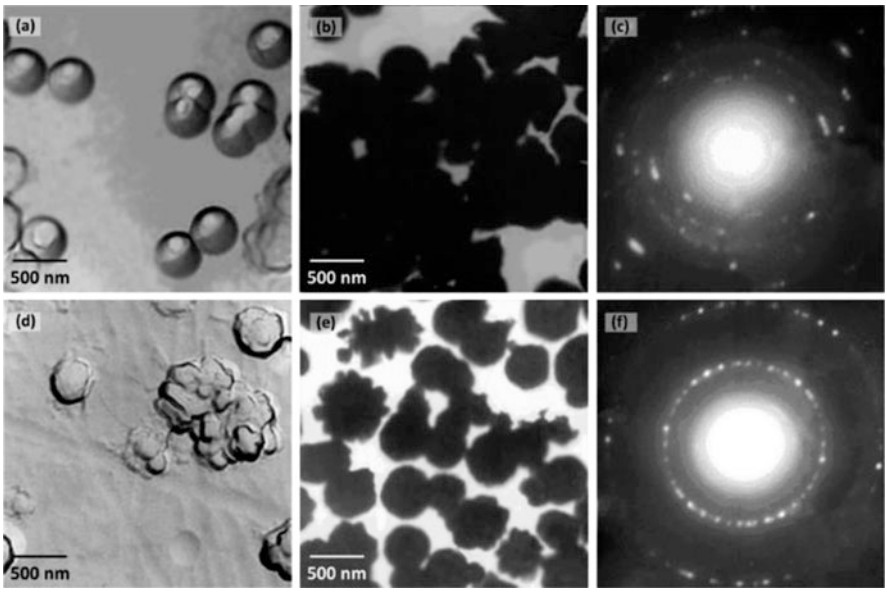

Fig. 1.6 Morphological features of the copper NSs obtained at deposition potentials of −0.5 V (**a**–**c**) and −1.0 V (**d**–**f**). TEM images of the replicas with the "shadowing" (**a**, **d**) and with the "extraction" (**b**, **e**), as well as microdiffraction images of the distinguished area with the extraction fragments (**c**, **f**) [43]

elements, forming a structure of the metallic cluster (Fig. 1.6d). A replica with the "extraction" indicates that the metal deposits in pores in the form of metallic particles contacting with each other. With that, being in a pore, the metallic deposit takes its form, and coming beyond the pore limits, the copper clusters overgrow with a tendency of the formation of agglomerates with a dendrite form (Fig. 1.6e).

The electron-diffraction pattern is a confirmation of the polycrystalline structure of the investigated extractions. A calculation from the radial broadening of a diffraction ring of a medium size of individual copper crystallites, which are a part of the agglomerate, has shown that the crystallite sizes are in the region of 30–50 nm. The analysis of diffraction peaks of the electron-diffraction pattern in Fig. 1.6f makes it possible to register part of agglomerates of the Cu_2O copper phase.

It should be noted that earlier in the work [44], we have shown that the nucleation of copper on the Si (100) surface in the studied potentials region takes place according to the progressive mechanism. With that, large voltage values increase the nucleation centers density per unit of electrode surface. Taking into account that a formation of the compact deposit takes place in the pores of SiO_2 at the potential of −0.5 V, one could suppose that individual nucleation centers are formed on initial stages of the process. With the passage of time, the nucleation centers are growing, filling all the pore-free volume. At the higher potential (−1.0 V), a

formation of several nuclei are competing among each other in the electrosynthesis process. The transfer of copper ions Cu^{2+}, being limited by a diffusion, leads to a development of morphological imbalance of the phase boundary and a passage to the dendrite morphology (Fig. 1.6). That is, the interaction of concentration fields of the neighboring growth centers leads to the alternating growth of one type crystallites and an amplification of the development of other type crystallites with a formation of a dendrite from the copper deposit.

The fact that we do not observe highly developed three-dimensional hierarchical structure (Fig 1.6b, c) at the selected deposition modes is a consequence of the fact that a limited pore volume hinders the dendrite formation inside it. This means that even at conditions of a simultaneous formation of a several nucleation centers, a development of individual crystallites does not take place due to their unification to an agglomerate. Correspondingly, in order to obtain the spatially separated dendrites, one should increase the NS volume being available for the development. This could be done either increasing the pore volume or increasing the deposition time, and when coming out beyond the SiO_2 surface, the metallic deposit would have a sufficient space for the development of three-dimensional dendrites. An influence of the pore volume on a form of the created deposit on the example of silver, which is deposited by the electroless technique in SiO_2/Si templates, has been shown in the work [45–47].

For a realization of the formation of spatially separated copper dendrites, the electrodeposition of copper was deposited at the increased of process duration time: 40 s for $U = -0.5$ V and 25 s for $U = -1.0$ V. SEM images of the obtained NSs are shown in Fig.1.7.

Images of SiO_2(Cu)/Si surface at the low magnification (Fig. 1.7a, b) evidence that the spatially separated NSs are homogeneously distributed on the surface area at the selected deposition parameters. With that at the deposition potential $U = -0.5$ V, corresponding to the area of the normal recovery of copper on the n-Si substrate ($j(U)$ curve, shown in Fig. 1.4), a compact deposit formation is realized (Fig.1.7c), and at $U = -1.0$ V (the region of the diffusive-limited processes), the three-dimensional dendrite-like structures are realized (Fig 1.7d, e).

At the low value of the deposition potential, the obtained NSs have dimensions ~500 nm with a minimal divergence by the value (Fig 1.7a, c). The more negative U leads to a formation of NSs with different lateral dimensions in the range from ~500 nm to ~1000 nm (Fig. 1.7b, d, e). With that, the smaller dimensions are inherent for the closely spaced NSs (Fig. 1.7d), and maximal dimensions are inherent for the separate NSs (Fig. 1.7e). The difference in NS sizes is concerned with the fact that at the larger cathode voltages, the overlap of the fronts of metal ions diffusion to the growing structures leads to a different rates of the dendrites growth. It is much more complicated to win the competition for the individual copper ion taking part in the structure formation for the NSs being on a small distance between each other than for the NSs being far away from the neighbors.

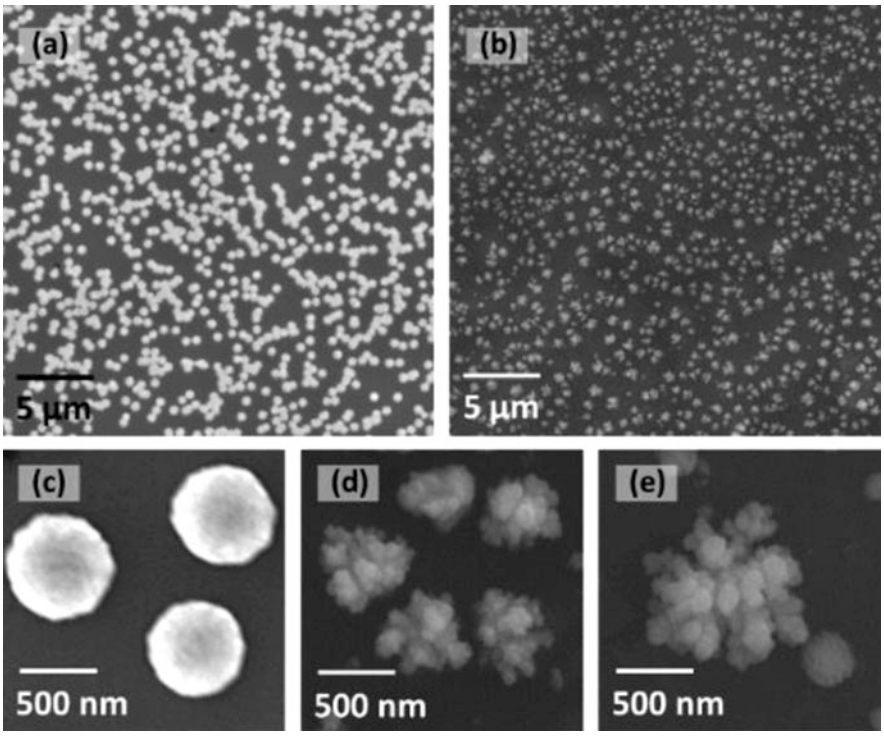

Fig. 1.7 SEM images of SiO_2/Si templates surface with copper NSs obtained at $U = -0.5$ V and $t = 40$ s (**a**, **c**) and also at $U = -0$ V and $t = 25$ s (**b**, **d**, **e**) [43]

1.4 Prospects of the Use of Plasmonic Nanostructures, Synthesized in the Pores of Swift Heavy Ion-Track Templates on the Base of SiO_2/Si

Investigations of the Raman spectra were carried out on the SiO_2(Cu)/Si structures obtained at $U = -1.0$ V and $t = 25$ s, in which SEM images are shown in Fig. 1.7b, d, e. The studies of the efficiency of the amplification of the Raman effect were realized on the base of a comparison of the reference signal of water solution of the Rhodamine 6G dye (R6G) with the 10^{-2} M concentration, placed on a special glass substrate, having a weak luminescence, and a signal from SiO_2(Cu)/Si structure surface at the R6G concentration of 10^{-6} M. The choice of the red light laser for the investigations was realized on the base on the position of the plasmonic resonance band for the copper dendrites, localized in the area of 630 nm [48]. Characteristic Raman spectra of R6G on the reference substrate and on the SiO_2(Cu)/Si structure surface are shown in Fig. 1.8.

The main line of 519 cm^{-1} is clearly distinguished on the spectrum from the SiO_2(Cu)/Si surface, corresponding to silicon, as well as characteristic lines of

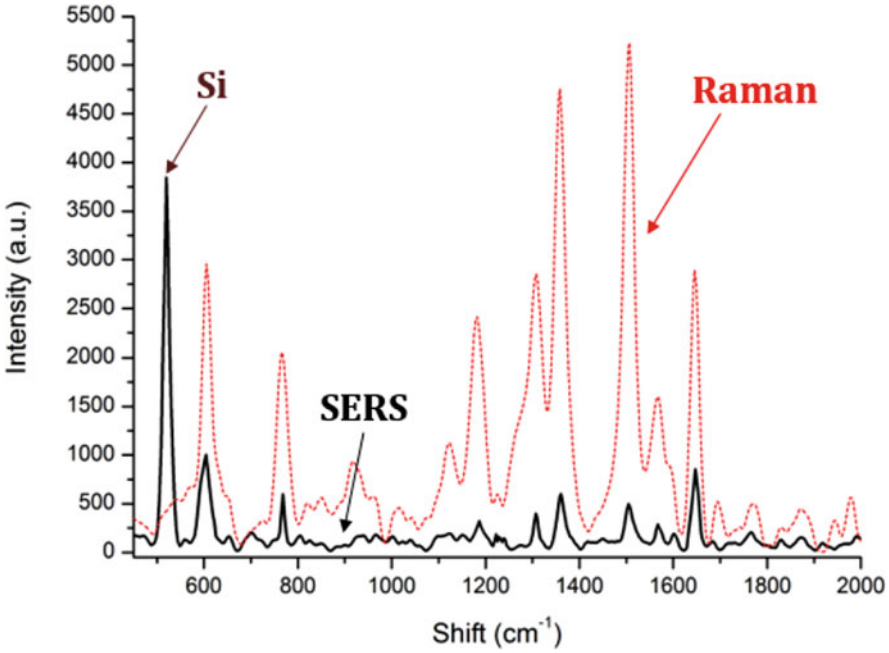

Fig. 1.8 Raman spectrum of the water solution of the Rhodamine 6G dye with concentration of 10^{-6} M, deposited on the SiO_2/Si substrates surfaces, containing copper dendrite nanostructures in the pores of silicon dioxide (black continuous line), with 10^{-2} M concentration, deposited on the surface of weakly luminescent glass substrates (red dashed line)

Rhodamine 6G. The enhancement factor (EF) for the signal for Cu dendrites was calculated relative to the reference signal according to the expression [49]:

$$\mathrm{EF} = (I_{\mathrm{SERS}}/C_{\mathrm{SERS}})\,(C_{\mathrm{Rs}}/I_{\mathrm{Rs}})\,,$$

where I_{SERS} corresponds to the intensity of the Raman scattering, obtained on the SERS substrate at a certain concentration on C_{SERS}, and I_{RS} corresponds to the intensity of the Raman scattering, obtained as a result of investigation at C_{RS} concentration on R6G analyte. EF on the entire investigation range is in the area of 10^3 with the amplification maximum of $3.4{\cdot}10^3$ for the line of 1650 cm^{-1}. A relatively small amplification coefficient is probably concerned with a formation of copper oxides on the dendrites surface, which could be created both at the oxidation of the air and at the performance of spectroscopic investigations in water solutions.

Taking into account a possibility of degradation of copper nanostructures, it is rather complicated to use the SiO_2(Cu)/Si structures directly as substrates for the Raman signal amplification. The covering of copper dendrites with a silver layer [50] or a gold layer [51] should make it possible not only to reliably protect the surface from a corrosion but also to provide a possibility to considerably increase the amplification coefficient [52].

1.5 Conclusion

SiO_2 templates on *n*-Si are formed using the swift heavy ion-track technology. Dependences of the pores characteristic dimensions (height, half-angle of the etching cone, and upper and lower diameters) on irradiation fluence and the etching time are investigated. The pore parameters have a linear dependence, which makes it possible to predict the pores quantity and their forms and dimensions.

Copper NSs in the pores of SiO_2/Si are formed by the electrochemical deposition technique. The studies of potentiodynamic current-voltage curves have made it possible to determine the characteristic features of copper deposition on *n*-Si substrate from an electrolyte, containing 0.5 M boric acid and 0.01 M copper sulfate, as well as to select the Cu deposition modes in the porous SiO_2 template, which has made it possible to form a compact copper deposit (with the potential of -0.5 V) or a branched one (with potential of -1.0 V). It was determined on the base of investigations of morphology of Cu NSs by SEM, TEM, and electronic diffraction techniques that at the electrochemical deposition, a selective filling of pores of the silicon dioxide by copper with a formation of crystallites with the face-centered cubic structure takes place without a manifestation of any preferential crystallographic orientation. The presence of the Cu_2O phase was revealed in the copper deposit, in which formation takes place due to the copper oxidation by the oxygen from air.

The SiO_2(Cu)/Si structures, obtained at $U = -1.0$ V, possess a branched copper deposit. It has been shown that several nuclei are formed on the pore bottom, at the initial deposition stages, which during the electrochemical process are competing for the Cu^{2+} ions which take part in the copper deposit formation. An overlap of the fronts of the growth of the copper individual crystallites does not enable one to obtain a developed form of a deposit before the metal comes out beyond the SiO_2 surface, due to the realization of the synthesis process in a limited pore volume. The overcoming of the pore volume removes restrictions on the NS development, which at the diffusion-limitation process leads to the unequal development of the individual crystallites with a formation of dendrites. The overlap of concentration fields of the neighboring pores leads to a dampened growth of closely placed dendrites and to the accelerated growth of separately placed dendrites, and this causes the formation of NSs with different sizes and forms on the same substrate.

An analysis of the efficiency of the surface-enhanced Raman spectroscopy (SERS) using the water solution of the Rhodamine 6G dye has made it possible to determine that for the entire studied frequency range, the amplification coefficient of the corresponding signal is in the area of 10^3, with a maximum ($3.4 \cdot 10^3$) for the line of 1650 cm^{-1}.

It is supposed that a covering of the copper dendrites by silver or golden films should make it possible not only to reliably protect the surface from a corrosion but also to considerably increase the amplification coefficient. This makes prospective use of the SiO_2(Cu)/Si structure with a spatially distributed copper dendrites as a plasmonic-active surfaces for a giant amplification of the Raman signal for an identification of substances in super low amounts.

References

1. Sanchez F, Sobolev K (2010) Nanotechnology in concrete – a review. Constr Build Mater 24(11):2060–2071
2. Manukyan A, Gyulasaryan H, Ginoyan A, Kaniukov E, Petrov A, Yakimchuk D, Shashov S, Nurijanyan M, Mirzakhanyan A (2016) Structural, morphological and magnetic properties of nickel-carbon nanocomposites prepared by solid-phase pyrolysis of Ni Phthalocyanine. Fundam Appl Nano-Electromagnetics 1:273–290
3. Lisiecki I, Pileni MP (1993) Synthesis of copper metallic clusters using reverse micelles as microreactors. J Am Chem Soc 115(10):3887–3896
4. Shao Q, Que R, Shao M, Cheng L, Lee S-T (2012) Copper nanoparticles grafted on a silicon wafer and their excellent surface-enhanced Raman scattering. Adv Funct Mater 22(10):2067–2070
5. Prunier H, Ricolleau C, Nelayah J, Wang G, Alloyeau D (2014) Original anisotropic growth mode of copper nanorods by vapor phase deposition. Cryst Growth Des 14(12):6350–6356
6. Kaniukov EY, Kozlovsky AL, Shlimas DI, Zdorovets MV, Yakimchuk DV, Shumskaya EE, Kadyrzhanov KK (2017) Electrochemically deposited copper nanotubes. J Surf Invest: X-Ray, Synchrotron Neutron Tech 11(1):270–275
7. Filankembo A, Giorgio S, Lisiecki I, Pileni MP (2003) Is the anion the major parameter in the shape control of nanocrystals? J Phys Chem B 107(30):7492–7500
8. Gou L, Murphy CJ (2003) Solution-phase synthesis of Cu2O nanocubes. Nano Lett 3(2):231–234
9. Zheng G, Patolsky F, Cui Y, Wang WU, Lieber CM (2005) Multiplexed electrical detection of cancer markers with nanowire sensor arrays. Nat Biotechnol 23:1294–1301
10. Kaniukov E, Kozlovsky A, Shlimas D, Yakimchuk D, Zdorovets M, Kadyrzhanov K (2016) Tunable synthesis of copper nanotubes. IOP Conf Series: Mater Sci Eng 110:012013
11. Qiu R, Cha HG, Noh HB, Shim YB, Zhang XL, Qiao R, Zhang D, Kim YI, Pal U, Kang YS (2009) Preparation of dendritic copper nanostructures and their characterization for electroreduction. J Phys Chem C 113(36):15891–15896
12. Li Y, Fu Z-Y, Su B-L (2012) Hierarchically structured porous materials for energy conversion and storage. Adv Funct Mater 22(22):4634–4667
13. He Z, He J, Zhang Z (2015) Selective growth of metallic nanostructures on microstructured copper substrate in solution. CrystEngComm 17(38):7262–7269
14. Plowman BJ, Jones LA, Bhargava SK (2015) Building with bubbles: the formation of high surface area honeycomb-like films via hydrogen bubble templated electrodeposition. Chem Commun 51(21):4331–4346
15. Rashid MH, Mandal TK (2007) Synthesis and catalytic application of nanostructured silver dendrites. J Phys Chem C 111(45):16750–16760
16. Fei Chan Y, Xing Zhang C, Long Wu Z, Mei Zhao D, Wang W, Jun Xu H, Sun XM (2013) Ag dendritic nanostructures as ultrastable substrates for surface-enhanced Raman scattering. Appl Phys Lett 102(18):183118
17. Trukhanov AV, Grabchikov SS, Vasiliev AN, Sharko SA, Mukhurov NI, Gasenkova IV (2014) Specific features of formation and growth mechanism of multilayered quasi-one-dimensional (Co-Ni-Fe)/Cu systems in pores of anodic alumina matrices. Crystallogr Rep 59(5):744–748
18. Kozlovskiy A, Meirimova T, Mashentseva A, Zdorovets M, Kanyukov E, Yakimchuk D, Petrov A, Kadyrzhanov K (2015) Electrochemical synthesis and crystal structure of ordered arrays of Co – nanotubes. Chem Bull Kazakh National University 30(3):72–80
19. Kozlovskiy AL, Korolkov IV, Kalkabay G, Ibragimova MA, Ibrayeva AD, Zdorovets MV, Mikulich VS, Yakimchuk DV, Shumskaya AE, Kaniukov EY (2017) Comprehensive study of Ni nanotubes for bioapplications: from synthesis to payloads attaching. J Nanomater 2017:1–9
20. Djokić S, Nikolić N, Živković P, Popov K, Djokić N (2011) Electrodeposition and electroless deposition of metallic powders: a comparison. In: Nano, vol 33, pp 7–31

21. Zhang X, Wang G, Liu X, Wu H (2008) Copper dendrites: synthesis, mechanism discussion, and application in determination of L-tyrosine. Cryst Growth Des 8(4):1430–1434
22. Ravi Kumar DV, Woo K, Moon J (2015) Promising wet chemical strategies to synthesize Cu nanowires for emerging electronic applications. Nanoscale 7(41):17195–17210
23. Tian N, Zhou Z-Y, Sun S-G, Ding Y, Wang ZL (2007) Synthesis of tetrahexahedral platinum nanocrystals with high-index facets and high electro-oxidation activity. Science 316(5825):732–735
24. Gurrappa I, Binder L (2008) Electrodeposition of nanostructured coatings and their characterization—a review. Sci Technol Adv Mater 9(4):043001
25. Martin CR (1994) Nanomaterials: a membrane-based synthetic approach. Science (New York, NY) 266(5193):1961–1966
26. Kaniukov EY, Shumskaya EE, Yakimchuk DV, Kozlovskiy AL, Ibragimova MA, Zdorovets MV (2017) Evolution of the polyethylene terephthalate track membranes parameters at the etching process. J Contemp Phys (Armenian Acad Sci) 52(2):155–160
27. Kaniukov E, Shumskaya A, Yakimchuk D, Kozlovskiy A, Ibrayeva A, Zdorovets M (2017) Characterization of pet track membrane parameters. In: Fesenko O, Yatsenko L (eds) Nanophysics, nanomaterials, interface studies, and applications: Selected Proceedings of the 4th International Conference Nanotechnology and Nanomaterials (NANO2016), August 24–27, 2016, Lviv, Ukraine. Springer International Publishing, Cham, pp 79–91
28. Kaniukov E, Shumskaya A, Yakimchuk D, Kozlovskiy A, Korolkov I, Ibragimova M, Zdorovets M, Kadyrzhanov K, Rusakov V, Fadeev M, Lobko E, Saunina K and Nikolaevich L (2018) FeNi nanotubes: perspective tool for targeted delivery. Appl Nanosci 1–10
29. Kaniukov EY, Shumskaya AE, Kutuzau MD, Bundyukova VD, Yakimchuk DV, Borgekov DB, Ibragimova MA, Korolkov IV, Giniyatova S, Kozlovskiy AL, Zdorovets MV (2019) Degradation mechanism and way of surface protection of nickel nanostructures. Mater Chem Phys 223:88–97
30. Kozlovskiy A, Zdorovets M, Kadyrzhanov K, Korolkov I, Rusakov V, Nikolaevich L, Fesenko O, Budnyk O, Yakimchuk D, Shumskaya A and Kaniukov E. (2018) FeCo nanotubes: possible tool for targeted delivery of drugs and proteins. Appl Nanosci 1–9
31. Lee K-L, Huang J-B, Chang J-W, Wu S-H, Wei P-K (2015) Ultrasensitive biosensors using enhanced Fano resonances in capped gold nanoslit arrays. Sci Rep 5:8547. -1-8547-8549
32. Yakimchuk D, Kaniukov E, Bundyukova V, Osminkina L, Teichert S, Demyanov S, Sivakov V (2018) Silver nanostructures evolution in porous SiO_2/p-Si matrices for wide wavelength surface-enhanced Raman scattering applications. MRS Commun 8(1):95–99
33. Kaniukov EY, Yakimchuk DV, Bundyukova VD, Shumskaya AE, Amirov AA, Demyanov SE (2018) Peculiarities of charge transfer in SiO_2(Ni)/Si nanosystems. Adv Condens Matter Phys 2018:8
34. Fink D (2004) Fundamentals of ion-irradiated polymers: fundamentals and applications. V. 1. Springer, Berlin–Heidelberg
35. Bergamini F, Bianconi M, Cristiani S, Gallerani L, Nubile A, Petrini S, Sugliani S (2008) Ion track formation in low temperature silicon dioxide. Nucl Inst Methods Phys Res B 266(10):2475–2478
36. Komarov FF, Vlasukova LA, Kuchinskyi PV, Didyk AY, Skuratov VA, Voronova NA (2009) Etched track morphology in SiO_2 irradiated with swift heavy ions. Lith J Phys 49(1):111–115
37. Yakimchuk D, Bundyukova V, Smirnov A, Kaniukov E (2018) Express method of estimation of etched ion track parameters in silicon dioxide template. Phys Status Solidi B Basic Research 256:1800316
38. Toulemonde M, Dufour C, Meftah A, Paumier E (2000) Transient thermal processes in heavy ion irradiation of crystalline inorganic insulators. Nucl Inst Methods Phys Res B 166:903–912
39. Devine RAB (1994) Macroscopic and microscopic effects of radiation in amorphous SiO_2. Nucl Instrum Methods Phys Res, Sect B 91:378–390
40. Dallanora A, Marcondes TL, Bermudez GG, Fichtner PFP, Trautmann C, Toulemonde M, Papaléo RM (2008) Nanoporous SiO_2/Si thin layers produced by ion track etching: dependence on the ion energy and criterion for etchability. J Appl Phys 104(2):024307. -1–024307-8

41. Toulemonde M, Enault N, Fan JY, Studer F (1990) Does continuous trail of damage appear at the change in the electronic stopping power damage rate? J Appl Phys 68(4):1545–1549
42. Kaniukov EY, Ustarroz J, Yakimchuk DV, Petrova M, Terryn H, Sivakov V, Petrov AV (2016) Tunable nanoporous silicon oxide templates by swift heavy ion tracks technology. Nanotechnology 27(11):115305
43. Kaniukov E, Yakimchuk D, Arzumanyan G, Terryn H, Baert K, Kozlovskiy A, Zdorovets M, Belonogov E, Demyanov S (2017) Growth mechanisms of spatially separated copper dendrites in pores of a SiO_2 template. Philos Mag 97(26):2268–2283
44. Ivanova YA, Ivanou DK, Fedotov AK, Streltsov EA, Demyanov SE, Petrov AV, Kaniukov EY, Fink D (2007) Electrochemical deposition of Ni and Cu onto monocrystalline n-Si(100) wafers and into nanopores in Si/SiO_2 template. J Mater Sci 42(22):9163–9169
45. Sivakov V, Kaniukov EY, Petrov AV, Korolik OV, Mazanik AV, Bochmann A, Teichert S, Hidi IJ, Schleusener A, Cialla D, Eugenia Toimil-Molares M, Trautmann C, Popp J, Demyanov SE (2014) Silver nanostructures formation in porous Si/SiO_2 matrix. J Cryst Growth 400:21–26
46. Yakimchuk DV, Kaniukov EY, Demyanov SE, Bundyukova VD, Dzeinak AV, Makoed II, Arzumanyan GM, Doroshkevich NV, Mamatkulov KZ, Sivakov V (2017) Dependence of the surface-enhanced Raman scattering signal on the shape of silver nanostructures grown in the SiO_2/n-Si porous template. Devices Methods Meas 8(3):228–235
47. Yakimchuk DV, Kaniukov EY, Demyanov SE, Arzumanyan GM, Sivakov V (2017) SERS activity of silver nanostructures with different shape in pores of SiO_2 template on n-Si. Physics, Chemistry and Application of Nanostructures: Reviews and Short Notes to Nanomeeting-2017. pp 216–219
48. Haas I, Shanmugam S, Gedanken A (2008) Synthesis of copper dendrite nanostructures by a sonoelectrochemical method. Chem Eur J 14:4696–4703
49. Le Ru EC, Blackie EJ, Meyer M, Etchegoin PG (2007) Surface enhanced Raman scattering enhancement factors: a comprehensive study. J Phys Chem C 111(37):13794–13803
50. Zhang R, Lin W, Lawrence K, Wong CP (2010) Highly reliable, low cost, isotropically conductive adhesives filled with Ag-coated Cu flakes for electronic packaging applications. Int J Adhes Adhes 30(6):403–407
51. Chen Y, Xu Q, Hu B, Xu J, Weng J (2016) Unconventional synthesis of Cu–Au dendritic nanowires with enhanced electrochemical activity. RSC Adv 6(3):2464–2469
52. Lee J-P, Chen D, Li X, Yoo S, Bottomley LA, El-Sayed MA, Park S, Liu M (2013) Well-organized raspberry-like Ag-Cu bimetal nanoparticles for highly reliable and reproducible surface-enhanced Raman scattering. Nanoscale 5:11620–11624

Chapter 2
Synthesis, Morphology, Structure, and Luminescence Properties of Bi-Containing Phosphates: Review and Detailed Consideration on the Example of Pr^{3+}-doped $BiPO_4$ Nanopowders

V. Chornii, V. Boyko, S. G. Nedilko, M. Slobodyanik, and K. Terebilenko

2.1 Introduction

Modern technologies are focused on using of environment-friendly and cost- and energy-effective materials in various devices. In particular, great attention has been paid to materials that can be used as luminophores in phosphor-converting/shifting white light-emitting diodes (pc/ps-WLED). The later ones are energy-effective devices for indoor and outdoor lighting based on semiconductor chip (source of UV/blue light) covered by luminescent material that adjusts the spectrum of emission. There are some issues related to deterioration of emission properties of pc/ps-WLED because of continued action of high luminous fluxes and relative high temperatures. In case of outdoor lighting, influence of humidity also can lead to worse emission properties. Thus, materials used in pc/ps-LED should have intensive photoluminescence (PL), good thermal stability, and high resistivity to action of intensive light fluxes and humidity. Phosphates as class of oxide materials satisfy almost all abovementioned requirements, and only luminescence of pure phosphates usually reveals low intensity. Due to their perfect physicochemical properties, such materials were proposed to be used not only as phosphors but

V. Chornii
National University of Life and Environmental Sciences of Ukraine, Kyiv, Ukraine

Taras Shevchenko National University of Kyiv, Kyiv, Ukraine

V. Boyko
National University of Life and Environmental Sciences of Ukraine, Kyiv, Ukraine

S. G. Nedilko (✉) · M. Slobodyanik · K. Terebilenko
Taras Shevchenko National University of Kyiv, Kyiv, Ukraine
e-mail: snedilko@univ.kiev.ua

© Springer Nature Switzerland AG 2019

O. Fesenko, L. Yatsenko (eds.), *Nanophotonics, Nanooptics, Nanobiotechnology, and Their Applications*, Springer Proceedings in Physics 222,
https://doi.org/10.1007/978-3-030-17755-3_2

also as photocatalysts [1, 2], supercapacitor [3], nuclear waste confinement [4], and some other applications [5, 6]. It should be noted that all the phosphates contain PO_4 tetrahedra which are either isolated or connected to each other by sharing oxygen atoms (e.g., pyrophosphates and metaphosphates). In this work, under the term phosphates, we mean both simple (with isolated phosphate groups) and polyphosphates.

This study is devoted to optical properties of Pr^{3+}-doped bismuth orthophosphate ($BiPO_4$) nanopowders as one of the poorly described in literature. It is worth noting that luminescence of various compounds usually depends on synthesis procedures, sizes, and morphology of particles, crystal, and electronic structures. Thus, a small review of literature data on the abovementioned factors will precede our finding in every part of this work.

2.2 Optical Properties of Phosphates

Before doing analysis of the Pr^{3+}-doped $BiPO_4$ nanopowders properties, it is expedient to analyze optical properties of phosphate compounds, in particular, those containing bismuth. Photoluminescence of un-doped phosphate compounds (so-called intrinsic luminescence) has been observed in different spectral regions from ultraviolet to near infrared (see Fig. 2.1 as example). Usually this luminescence consists of several components (PL bands) with intensity, maxima positions, and width, depending on cations constituent in their composition [7–12]. The PL components were ascribed to different luminescence centers. In particular, UV bands were related to decay of excitons or with charge transfer from cations to oxygen atoms [7–9]. Visible the PL bands were related to either intrinsic (if the Ti, Zr, or Hf cations are in the content of materials) or extrinsic (various luminescent ions) crystal defects. For the former case, luminescence was ascribed to abovementioned tetravalent cations that occupy regular crystal site in their unusual valence state +3 [4]. It was also shown in our work [13] that visible and near-IR PL bands of ZrP_2O_7 and $KZr_2(PO_4)_3$ crystals can be utilized for estimation of absorbed dose of γ-radiation. These bands were related to defects of crystal structures and content of the defects (e.g., vacancies of O and Zr) changing under action of ionizing radiation. This conclusion was confirmed by electronic band structure calculations made for some phosphates with oxygen vacancies [14].

In the case of Zr-containing phosphates, the main PL band is located at UV spectral region. Its maxima is at 289 nm for ZrP_2O_7 and 295 nm for $KZr_2(PO_4)_2$ crystals under excitation with $h\nu > E_g$ [7, 10]. Most long-wavelength bands of excitation spectra of this UV luminescence are generally ascribed in both compounds to charge transfer of electron from O^{2-} to Zr^{4+}. Thus, the reverse charge transfer from zirconium to oxygen is responsible for the UV PL band. According to the work [9], asymmetric PL band of $KHf_{2(1-x)}Zr_{2x}(PO)_3$ compound with maxima at 310 nm is determined by processes in $Zr(PO_4)_6$ structural complexes. However, analysis of spectroscopic properties of the $NaZr_2(PO_4)_3$ and some Zr-containing silicates indicates that major role in PL processes played not by $Zr(PO_4)_6$

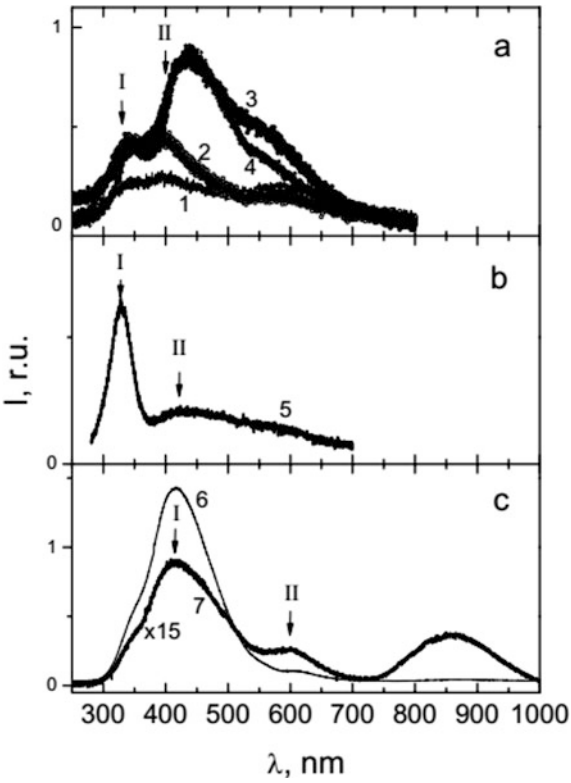

Fig. 2.1 Emission of $KAlP_2O_7$ (**a**), $CsAlP_2O_7$ (**b**), and $NaInP_2O_7$ (**c**) obtained under synchrotron excitation with $E_{exc} = 9.84$ (1), 7.08 (2), 5.87 (3), 5.23 (4), 6.52 (5), 7.04 (6), and 6.60 (7) eV at 10 (1–6) and 300 (7) K (Reproduced from Ref. [15])

complexes, but only by closest surrounding of Zr, or in the other words the processes in ZrO_x polyhedra are the most important and namely Zr-Zr and Zr-O distances determine the PL characteristics [7]. It was found that changes of cations type lead to significant changes of luminescence properties of Zr-containing phosphates, but luminescence mechanisms are the same for these compounds.

Optical properties of solids are greatly connected with structure of valence and conduction band, especially in the regions of band edges. In case of phosphates that have no luminescent cations in crystal structure (e.g., Bi^{3+}, rare-earth or transition metal ions), band gap edges are formed by the states of phosphate groups and sometimes by *d* states of cations. The typical electronic structure of such phosphates appears as shown in Fig. 2.2. It is seen that changes of cationic composition lead to changes in crystal band gap as well as in changes of bottom part of conduction band (CB). At the same time, the top part of valence band is formed by oxygen states for all compounds shown in the figure. Such situation is typical for most phosphates that have no luminescent ions in crystal lattice.

The band gap value, E_g, is an important characteristic in analysis of optical properties of various materials. From the viewpoint of E_g, the phosphates belong to dielectrics or to wide-gap semiconductors with typical values in 4.5–9.0 eV of E_g value. In particular, the band gap values are 4.6 eV for $LiInP_2O_7$, 6.7 eV for ZrP_2O_7,

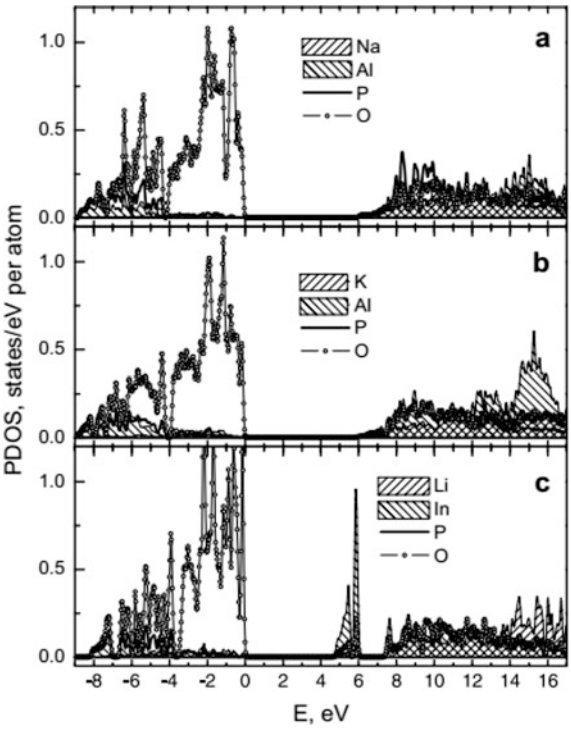

Fig. 2.2 Calculated PDOS of $NaAlP_2O_7$ (**a**), $KAlP_2O_7$ (**b**), and $LiInP_2O_7$ (**c**) phosphates. (Reproduced from Ref. [16])

6.6 eV for $K_2Zr(PO_4)_2$, and 8.0 eV for $LaPO_4$ [10, 16, 17]. The E_g value determines the lowest possible photon energy for band-to-band electronic transitions, allowing easy separation of defect-related absorption/excitation spectral bands.

The presence of various defects leads to decreasing of band gap value. In particular, the absorption transitions $2t_2 \rightarrow 2a,3\ t_2$ of molecular groups PO_4^{2-} for Bi-doped $LaPO_4$ were observed for 7.75 eV (160 nm), while the band nearly 5.0 eV was ascribed to absorption of Bi^{3+} ions in oxygen surrounding [18]. The Bi^{3+} ions belong to so-called mercury-like ions, and they were actively studied as luminescent ones. The scheme describing absorption and emission of Bi^{3+} ions is shown in Fig. 2.3. A similar scheme of energy levels consists of ground level $^1S_0$, one metastable level $^3P_0$ and two sub-levels $^3P_1{}^{(1)}$ and $^3P_1{}^{(2)}$ [19]. The photoluminescence characteristics of Bi-doped La_2O_3, Y_2O_3, $CaSb_2O_6$, $SrSb_2O_6$, and Y_2LuSbO_7 oxide materials can be explained by this scheme. It is worth noting that such energy-level scheme works better in case of free Bi^{3+} ions, but also it is frequently used in the case of Bi^{3+} ion that interacts with host.

The Bi^{3+}-containing phosphate compounds luminescence properties are poorly studied in the case when bismuth is a regular element of crystal lattice. However, there are some reports on luminescence properties of Bi-doped phosphates, namely, $LaPO_4$/Bi and $LiLaP_4O_{12}$/Bi [18, 20]. These compounds are interesting because their doping leads to isoelectronic substitution of La by Bi atoms, resulting in

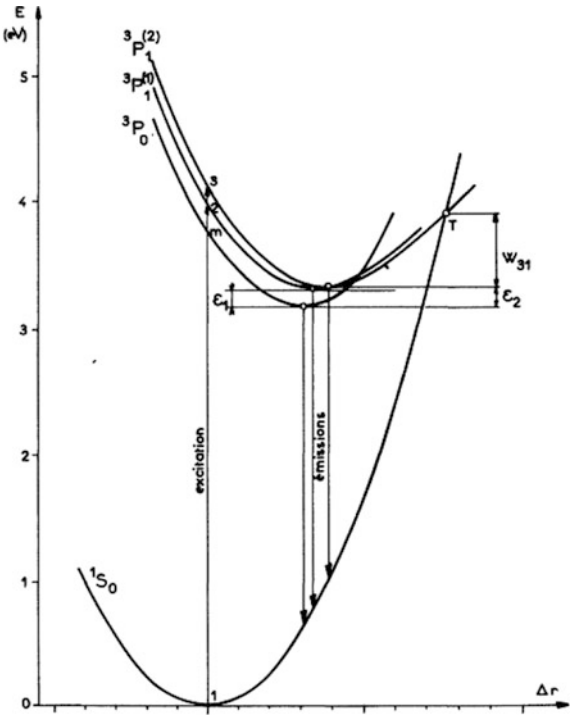

Fig. 2.3 Energy curves for Bi^{3+} ions. (Reproduced from Ref. [19])

insignificant changes in crystal structure. Bismuth ions actively interact with PO_4 groups, thus luminescence properties of Bi^{3+} cannot be treated as a case of free mercury-like ions [18]. Under excitation at 240 nm, one PL band with maxima nearly 450 nm is observed for $LaPO_4$/Bi. The studied temperature characteristics in the range from 0.2 to 74 K had shown the presence of at least two PL components. Increasing the temperature also leads to changes in the PL excitation spectra, namely, to broadening of bands in both short- and long-wavelength regions of the excitation spectra. Dependencies of the PL kinetics on temperature for $LaPO_4$/Bi are typical for Bi-containing compounds when total intensity is changed with increase of temperature in a similar way to that for other oxide materials doped with Bi^{3+} [19]. The PL band of Bi-doped $LiLaP_4O_{12}$ crystals consists of at least two well-distinguished bands [20]. The PL excitation spectra consist of complex band with two maxima at 230 and 250 nm, respectively. Large Stokes shift results in weak temperature quenching for $LiLaP_4O_{12}/Bi^{3+}$. The PL emission band ascribed to so-called A_X transitions in Bi^{3+} ions and two minima on the excited state curve was stated (as in case of Tl^+ ions in the alkaline-halides). The presence of two minima on curve of excitation state was confirmed by the PL kinetics studies which had showed non-exponential characters of quenching for both $LiLaP_4O_{12}$/Bi and $LaPO_4$/Bi compounds.

As was noted above, the cationic composition has significant influence on the PL properties of phosphate. Fig. 2.4 clearly demonstrates how the PL emission and

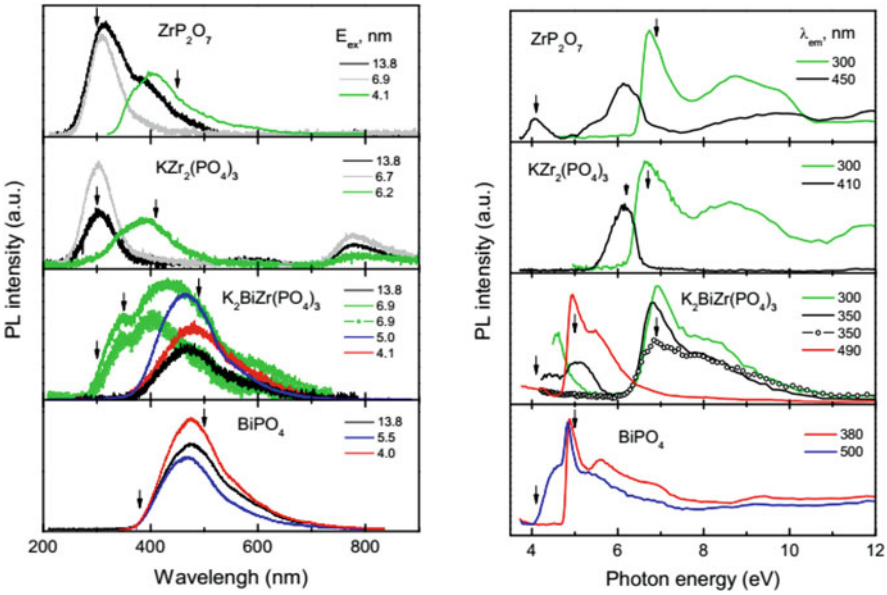

Fig. 2.4 PL emission (left) and excitation (right) spectra for ZrP_2O_7, $KZr_2(PO_4)_3$, $K_2BiZr(PO_4)_3$, and $BiPO_4$ compounds obtained at the temperatures 8 K (solid lines) and 300 K (lines with circles). (Reproduced from Ref. [21])

excitation spectra change with substitution of cations in the phosphate lattice. It is seen that incorporation of alkali metal (potassium in our case) in compounds leads to only little changes in the PL emission and excitation spectra of Zr-containing phosphates. At the same time, addition of bismuth completely alters the PL emission spectra, while peculiarities of PL excitation for UV bands are almost the same for compounds ZrP_2O_7, $KZr_2(PO_4)_3$, and $K_2BiZr(PO_4)_3$. All of these Zr-containing phosphates contain ZrO_6 polyhedra, and this is the reason for such similarity in PL excitation spectra.

The visible PL emission and its excitation spectra of the $K_2BiZr(PO_4)_3$ crystals greatly differ from those of ZrP_2O_7 and $KZr_2(PO_4)_3$ crystals. At the same time, the visible PL bands of $K_2BiZr(PO_4)_3$ crystals are very similar to those of the $BiPO_4$ crystals. It is seen from Fig. 2.4 that the visible PL band positions and shapes are similar for $K_2BiZr(PO_4)_3$ and $BiPO_4$ crystals for excitations at 13.8 and 4.1 eV at low temperatures. The PL excitation spectra for visible luminescence of these two compounds also have many similar peculiarities. Thus visible luminescence of $K_2BiZr(PO_4)_3$ with maxima nearly 480 nm (~ 2.6 eV) is likely to be related to Bi ions in oxygen surrounding.

Electronic band structure of this compound is shown in Fig. 2.5. The calculated PDOS distributions confirm the possible participation of the electronic states of both Zr and Bi ions in the processes associated with the intrinsic luminescence in $K_2BiZr(PO_4)_3$. The top of the valence band of this crystal is formed mainly by Bi

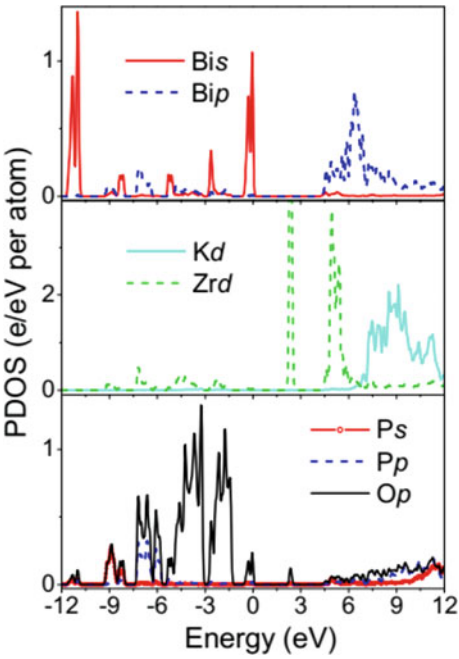

Fig. 2.5 Calculated PDOS for $K_2BiZr(PO_4)_3$ crystals. (Reproduced from Ref. [24])

6*s* states, while Zr 4*d* states dominate at the bottom of the conduction band. The presence of Bi *s* and Bi *p* states in the vicinity of the band is an inherent property Bi-containing crystals in which the intrinsic luminescence is related to Bi^{3+} ions [22, 23].

Analysis of luminescence processes in $BiPO_4$ is helpful in understanding luminescence properties of various Bi-containing phosphates. The $BiPO_4$ compound is among the simplest phosphates together with YPO_4 and $LaPO_4$. It can be found in the literature that the abovementioned compounds reveal visible luminescence under excitation at the vacuum ultraviolet and ultraviolet spectral regions [25–28]. In the cases of un-doped YPO_4 and $LaPO_4$ compounds, this luminescence is characterized by low intensity and associated with defect-related luminescence centers [25, 26]. Only in the case of $BiPO_4$, a presence of active in luminescence Bi^{3+} ions leads to significant intrinsic luminescence in UV-blue spectral region at low temperatures [22]. Intrinsic luminescence of bismuth phosphate was reported in recent years for the nano-sized samples of $BiPO_4$ [27, 28]. In particular, it was found that nano-sized particles of the monoclinic phase of $BiPO_4$ reveal at room temperature a two-component PL band with the main component peaking in the blue spectral region (at 460 nm or 2.7 eV) and with less intensive component peaking in the violet (405 nm or 3.1 eV) [27]. The un-doped $BiPO_4$ polycrystalline samples with grain sizes in the range of 0.1–1 mm reveal a broad multicomponent band with main peak nearly 2.7 eV (460 nm) for PL excitation at 300 nm (4.13 eV) and $T = 8$ K [22]. This band consists of three components peaking in the violet, blue, and red

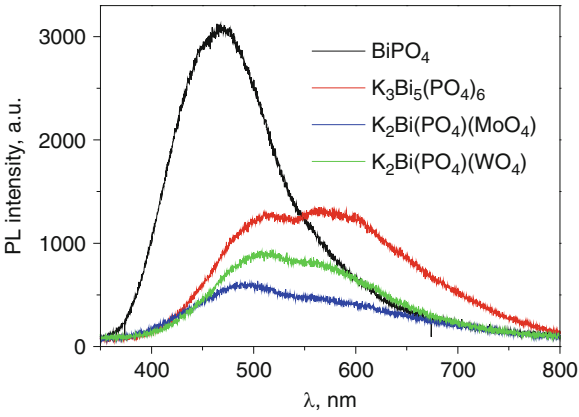

Fig. 2.6 PL emission spectra of Bi-containing compounds, $\lambda_{ex} = 240$ nm, $T = 8$ K

spectral regions ($h\nu_{max} = 2.9$, 2.6, and 2.05 eV, respectively). It was shown that the violet and blue components of $BiPO_4$ luminescence undergo thermal quenching after $T > 130$ K. Violet component was ascribed to transitions in Bi^{3+} ions, while blue and red components correspond to luminescence centers formed on the base of Bi^{3+} ions located near defects (e.g., oxygen vacancies).

The pattern of the $BiPO_4$ is a good starting point for studies of other Bi-containing materials. In particular, $K_3Bi_5(PO_4)_6$ phosphate has many peculiarities in structure and optical properties inherent to bismuth orthophosphate. An interesting case is Bi-containing mixed-anionic-group compounds like $K_2Bi(PO_4)(MoO_4)$, $K_2Bi(PO_4)(WO_4)$, and $K_{6.5}Bi_{2.5}W_4P_6O_{34}$ which can be treated as genealogically connected with $BiPO_4$. Figure 2.6 shows the luminescence spectra of some of the abovementioned compounds measured at low temperature for the case of the PL excitation corresponding to band-to-band transitions ($h\nu_{ex} = 5.17$ eV). For all of compounds presented in Fig. 2.6, the Bi in regular sites is surrounded by eight oxygen atoms with average distances Bi-O nearly 2.50 Å for phosphates and 2.44 Å for mixed-anionic-group compounds. The short-wavelength components of luminescence were recently ascribed for all these compounds to Bi^{3+}-related centers on the basis of comparative analysis of calculated PDOS, PL emission and excitation spectra, decay kinetics, and their dependencies on temperature [22].

The red PL component of $BiPO_4$ and $K_3Bi_5(PO_4)_6$ was ascribed to luminescence centers created on the base of Bi^{3+} ions located near structure defects.

In the case of $K_2Bi(PO_4)(MoO_4)$ and $K_2Bi(PO_4)(WO_4)$, the red luminescence band was related to $(MoO_4)^{2-}$ molecular anionic groups which are in these crystals as regular elements of the crystals or as formed due to the presence of uncontrolled impurity Mo for phosphate-molybdate and phosphate-tungstate compounds, respectively. Thus, bismuth either regular element or as impurity actively participates in luminescence processes in phosphate materials. This situation is due to the presence of Bi *s* and *p* states near valence and conduction band edges.

It is worth noting that particle sizes and morphology of samples have significant impact on luminescence properties of oxide materials. It was shown in the paper

[29] that the submicron particles of Y_2O_3/Eu^{3+} prepared by spray pyrolysis consist of crystallite and amorphous parts. The luminescence properties, namely, luminescence intensity of $^5D_0 \rightarrow {}^7F_2$ electronic transitions, increase with an increase in both particle and crystallites sizes. The optimum size of particles was estimated to be about 500 nm and crystallite size nearly 40 nm [29]. The dependence of the PL properties on particle sizes was studied also for Pr^{3+} (1 mole %)-doped lutetium aluminum garnet prepared by Pechini method [30]. The Rietveld analysis and TEM studies have shown that the studied samples consist of particles in sizes of 10–45 nm. Authors of a study [30] reported that absorption increases with an increase in the grain sizes, but the intensity of *f-d* transition decreased in PL excitation spectra. The main peak in the emission spectra was shifted toward red wavelengths with an increase in the grain size of the nanocrystalline powders. It was found that the change of size from 12 to 31 nm caused an important shift in the emitted light from bright violet to dark violet at room temperature. It was found that quantum efficiency increased with an increase in the grain size of the nanocrystalline powders. Quantum efficiency decrease with lowering particle sizes was explained by an increase in the surface defects quantity. The size effect on luminescence properties of lanthanide ions in nanoparticles was reported in a short review [31]. Attention was paid mostly to PL kinetics of oxide materials doped with Eu^{3+} ions. Authors of the abovementioned work stated that an increase in the surface-to-volume ratio in tripositive lanthanide-doped nanomaterials will produce a large number of surface defect states, which may act as nonradiative relaxation channels (traps or killer). In very small nanoparticles, the energy transfer is restricted based on the fact that the hopping length and the transfer probability are restricted for a donor to find a matching acceptor in the neighborhood of the nanoparticle. The $LaPO_4$/Ce, Tb phosphate nanoparticles were studied in work [32]. These nanoparticles can have high luminescence quantum yields despite their small size of about 6 nm. In case of PL of Eu^{3+}-doped $BiPO_4$ micro-/nanoparticles, an intensity greatly increased with an increase in the particle size from 150 nm to 0.5–1 μ [33]. It was reported that luminescence of Eu^{3+}-doped $BiPO_4$ highly depends on polymorph of host material. The impacts of polymorphs on luminescence properties were also clearly indicated by the changes in decay time, quantum efficiency, and nonradiative transition rates, in which several structural factors, such as the symmetric environment of Eu^{3+}, lattice water, and the dipole moment of Bi(Eu)-O polyhedra, contribute to the polymorph-sensitive luminescence properties, leading to a superior luminescence for low-temperature monoclinic polymorph [34].

Extensive studies have shown that Bi-containing phosphates are excellent hosts for luminescent RE ions, especially $BiPO_4$ one [33–39]. There are studies of luminescence of $BiPO_4$ compounds doped with various RE, but, at the same time, a few reports on Pr^{3+}-doped $BiPO_4$ and $PrPO_4$ crystals luminescence have been published so far [40, 41], in spite of the fact that Pr^{3+}-doped oxide compounds are regarded as perspective red luminophores [42–45]. The detailed analyses of synthesis methods, crystal and electronic structures, as well as luminescence properties of $Bi_{1-x}Pr_xPO_4$ ($x = 0$–1) nanopowders are given below.

2.3 Synthesis and Properties of Bismuth Orthophosphate

2.3.1 Synthesis Methods and Morphology of $BiPO_4$

Due to perspectives of $BiPO_4$ application as luminescent materials and photocatalyst, numerous methods have been applied in order to produce this compound in the form of both single crystals and polycrystalline samples.

The crystallinity, crystal structure, size, phase, and shape of materials based on bismuth phosphate play significant roles in properties, luminescent ones as well. Thus, the development of facile and efficient synthesis strategies in a highly controlled manner is essential for tailoring chemical and optical properties. Generally, the conventional methods used to synthesize highly crystalline, well-defined, and pure-phase or doped $BiPO_4$ can be divided into three categories: (i) molten salt crystallization, (ii) solvothermal/hydrothermal method, and (iii) co-precipitation method. Single crystals of bismuth-containing phosphates are generally obtained by high-temperature growth from a melt or a flux.

Commonly, bismuth oxide [46–49], carbonate [50], or nitrate [51] are used as sources of bismuth (III) in a reaction medium. Due to the presence of numerous non-stoichiometric bismuth phosphates in Bi_2O_3-P_2O_5 molten system [52, 53], addition of fluxes has been shown to be a successful approach in crystalline $BiPO_4$ preparation. Taking into consideration alkali metals' phosphates, different types of polyhedral condensation may occur, including PO_4^{3-}, $P_2O_7^{4-}$, $P_3O_{10}^{5-}$, and others. Mainly, the level of polyhedral condensation is frequently shown by molar ratios, for instance, the ratio K/P = 1 is achieved by melting and decomposition of pure KH_2PO_4, while K/Mo = 2 corresponds to the mixture of $K_2CO_3 \times MoO_3$. The calculated amounts of initial components are usually thoroughly mixed and melted in a suitable crucible such as platinum, alumina, or silica depending on the melting temperature and the nature of the molten solution prepared. The heating and cooling process is usually performed in electrically heated furnace which allows to control the heating temperature exposition and cooling rate. It is worth noting that the initial ratios and cooling rate are critically important for the quality and composition of the crystals prepared. Thus, for pure $BiPO_4$ crystal growth, 0.8 KPO_3-0.2 $K_2Mo_2O_7$ molten salts containing 10 mol % Bi_2O_3 should be cooled down to 500 °C, while application of higher K/P ratio leads to additional phosphates and mixed compound crystallization [46].

Frequently, bismuth oxide itself influences significantly the properties of the melt. One of the most important disadvantages of crystallization of bismuth-containing melts is high tendency to glass formation and high volatility of Bi_2O_3 at elevated temperatures [46, 54]. Among the advantages of bismuth oxide application in high-temperature growth is low melting point of Bi_2O_3 and its high solubility [47]. The content of some fluxes used for bismuth phosphate growth is given in Table 2.1.

To overcome the vitreous trend of bismuth-containing melts, additional salts treated as inert components are generally used. For example, $BiPO_4$ can be easily

Table 2.1 Synthesis methods used to prepare $BiPO_4$

Methods	Optimized conditions	Phase	Morphology/mean size	References
Flux growth	0.8 KPO_3-0.2 $K_2Mo_2O_7$ molten salts containing 10 mol % Bi_2O_3, cooling from 1000 to 550 °C	HTMP	Prismatic single crystals in size up to 5 mm long	[46]
	The ratio K/(P+V) = 0.7 for the molten salts K-Bi-V-P-O containing 25 mol % Bi_2O_3 cooling from 1000 to 550 °C	HTMP	Prismatic single crystals in size up to 2 mm long	[3]
	Slow cooling of a mixture 45 PbO-45 Bi_2O_3 -5 B_2O_3-5 P_2O_5 from 1050 to 300 °C	HTMP	Nanocrystals, 9 nm	[51]
Solvothermal/ hydrothermal synthesis	The mixture of $Bi(NO_3)_3{\cdot}5\ H_2O$ and $NH_4H_2PO_4$ in water at pH = 0.5–1, heating at 180 °C	HTMP	Shuttle-like crystals with size of 0.5–2 μm	[52]
	The water solution of $Bi(NO_3)_3 \times 5\ H_2O$ and equal molar $Na_3PO_4 \times 12\ H_2O$ at pH = 1, heating at 180 °C	HTMP	Nanocrystals, 80 ± 20 nm	[55]
	The solution of $Bi(NO_3)_3 \times 5\ H_2O$ in ethylene glycerol with $Na_3PO_4{\cdot}12\ H_2O$, heating at 160 °C, 6 h	LTMP	Roundish pellet-like particles, 100–200 nm	[56]
	The mixture of $Bi(NO_3)_3 \times 5\ H_2O$ and $NaH_2PO_4\ 2\ H_2O$ in glycerol/distilled water, kept at 200 °C for 3 h	HP and LTMP	Nano-cocoons, 100–150 nm	[28]
	The mixture of $Bi(NO_3)_3 \times 5\ H_2O$ and $NaH_2PO_4\ 2\ H_2O$ and Er^{3+}, Yb^{3+} admixtures in glycerol/distilled water, kept at 200 °C for 3 h	HP and LTMP	Nanorods, 50–85 nm	[57]
Co-precipitation method	The mixture of $Bi(NO_3)_3 \times 5\ H_2O$ and $NH_4H_2PO_4$ at 80 °C 48 h	HP	Hollow spindle-shaped, 0.5–2 μm	[58]
	The mixture of $Bi(NO_3)_3 \times 5\ H_2O$ and bis(2-ethylhexyl) phosphate in dissolved in oleic acid, heated at 180 °C in N_2 atmosphere.	LTMP	Nanocrystals, 9, 25, and 100 nm	[1]

(continued)

Table 2.1 (continued)

Methods	Optimized conditions	Phase	Morphology/mean size	References
Ball-milling	A mixture of $BiPO_4$ and ethanol was ball-milled in the presence of agate balls, and the product was dried and calcinated at 600 °C	HTMP	Powder, 0.5–2 μm	[59]
Bismuth anodization	Bi electrolysis in HF/H_3PO_4 electrolytes	HP	Nanorods 50 nm	[60]
Microwave synthesis	The mixture of $Bi(NO_3)_3 \times 5\ H_2O$ and $NaH_2PO_4\ 2\ H_2O$ in glycerol/distilled water, heated by an 800 W for 15 min	HP	Particles with an average size of 100 nm	[61]
Solid-state synthesis	Calcination in air of stoichiometric mixture of $Bi(NO_3)_3 \times 5\ H_2O$ and $NH_4H_2PO_4$ at 800 °C for 4 h	HTMP	Particles with an average size of 100 nm	[57]

crystallized from molten phosphates containing MoO_3 [46] or V_2O_5 [48] oxides. Their addition usually provokes depolymerization of phosphate media, lowering the melt viscosity, and, consequently, leads to widening of the crystallization area of the desired compound. Surprisingly, the opposite influence of WO_3 on K_2O-Bi_2O_3-P_2O_5 system has been shown indicating the absence of $BiPO_4$ area at alln49].

Polycrystalline ceramics based on $BiPO_4$ can be prepared by several synthetic methods. Conventional methods such as precipitation and solid-state reaction have been used for long and are widely applied for laboratory scale and industrial processes. Since the first fabrication of polycrystalline ceramic-containing bismuth, several methods have been reported for the preparation, such as a solid-state reaction, a sol-gel method, a hydrothermal method, co-precipitation, metalorganic decomposition, etc.

The hydrothermal/solvothermal method refers to a chemical synthesis procedure within a sealed environment under high pressure and temperature (often above the critical point of the solvent). In this method, bismuth salt precursors (nitrates or chlorides) and orthophosphate ($NH_4H_2PO_4$ [52, 55], Na_3PO_4 [56], or H_3PO_4) are mixed with glycerol, surfactants, and water, and then the mixture is placed in a Teflon-lined autoclave and then sealed and heated. Generally, these factors such as the type and concentration of bismuth ions, hydrothermal temperature and time, as well as value of pH have effects on the growth of the $BiPO_4$ crystals. Employing the modified hydrothermal method, a variety of doped with different ions, crystal phases, sizes, and morphologies were prepared by tuning the reaction at the interfaces of the different phases. Up to now, there are known at ordinary pressure three types of $BiPO_4$ structures: hexagonal, low-, and high-temperature monoclinic. The morphology of $BiPO_4$ prepared by hydrothermal methods at low temperatures in most cases is a nanorod shape with a mean diameter of 50–90 nm and a length ranging from 300 to 1000 nm, giving rise to a hexagonal phase. On the contrary, application of hydrothermal synthesis at higher temperatures without capping agents leads to formation of $BiPO_4$ particles of micron size [52]. More dispersed powders have been obtained in a media of ethylene glycerol [28, 56, 57]. To increase the surface area, $BiPO_4$ nanocrystals were also synthesized using a co-precipitation, ball-milling, bismuth anodization, and microwave methods as reported by [1, 57–61] (see Table 2.1). Compared with the two methods described above, the co-precipitation method shows more promise in industrial applications for synthesizing RE-doped $BiPO_4$ nanoparticles, due to its higher yield, lower cost, and more environment-friendly and convenient synthesis process.

The experimental process of co-precipitation method has five steps: (1) mixed the precipitator and cationic (Bi^{3+}) salts such as $Bi(NO_3)_3$ and $BiCl_3$ in a high boiling point solvent like oleic acid, (2) nucleation and growth, (3) precipitation, (4) filtration, and (5) calcination. Generally, a post-heat treatment of annealing is typically required to promote high crystallinity. However, micro- and nanoparticles obtained from co-precipitation method generally show irregular morphology and wider size distribution in comparison to that from other methods.

Currently, bismuth phosphate doped with rare-earth metals has been paid much attention due to potential applications in displays, artificial lights, photoelectronic

devices, lasers, and so on [61]. Moreover, it has been shown that the polymorphism, as well as morphology of the particles, has considerable influence on luminescence properties of the phosphors prepared [62]. Moreover, rare-earth ions can be taken as the probe ions for uncovering the microstructures of polymorphs and their impacts on the properties of $BiPO_4$.

Generally, all available methods for pure bismuth phosphate synthesis are convenient for preparation of a doped one. Thus, a widely applied hydrothermal approach in a presence of RE-containing salts, mainly nitrates, depending on the synthetic conditions, gives rise to all three polymorph stabilizations [27].

Taking into consideration one of the most studied doping agent, Eu^{3+}, one can admit the influence of synthesis on crystal structure and morphology change of bismuth phosphate as a host. Thus, in case of solvothermal approach, applied hexagonal phase (HP) of BiPO4/Eu^{3+} with a rodlike morphology was obtained in water and hydrophobic organic solvents such as arenes and cyclohexane, while low-temperature monoclinic phase (LTMP) in the form of tight agglomerates was prepared in hydrophilic alcohols [63]. Low-temperature phase of europium-containing bismuth phosphate, but in the form of prismatic nanoparticles, has been also obtained by co-precipitation technique from a hexagonal one. It is found that a hexagonal phase (HP) was formed at room temperature, which transformed to a low-temperature monoclinic phase (LTMP) and then a high-temperature monoclinic phase (HTMP) when the treatment temperature was increased to 500 and 700 °C, respectively [64]. With the phase transformation, the morphology changed from homogeneous rodlike shape to nearly spherical-like shape, which was followed by a change in the local environment of the lattice sites for Eu^{3+} and moreover the luminescence properties.

Importantly, a high-temperature phase of $BiPO_4$ requires annealing at elevated temperatures (700–900 °C) and can be easily prepared by a simple solid-state route [65]. The relationships described above are schematically shown in Fig. 2.7.

Among the synthetic pathways described, a solid-state approach for a RE-doped bismuth phosphate has been shown to meet most requirements for luminescent material preparation. Among the disadvantages of solid-state technique are multi-phase formation, the need for X-ray powder diffraction for phase conformation, and influence of the annealing time and temperature on completeness of phase formation and grain size.

More importantly, two kinds of substitution (i.e., iso- and aliovalent) could either complete the structure into exact crystallographical sites or provide extra defects. These controlled admixtures are then available as luminescent centers or sensitizers, which is essential to improve emitting properties of the material. Nevertheless, the crystal structural changes caused by substitution or small doping are not intrinsic, which hinder the applications of doped nanocrystalline materials. Therefore, the matching of the host and doped impurities is crucially important and lies at the heart of this technology.

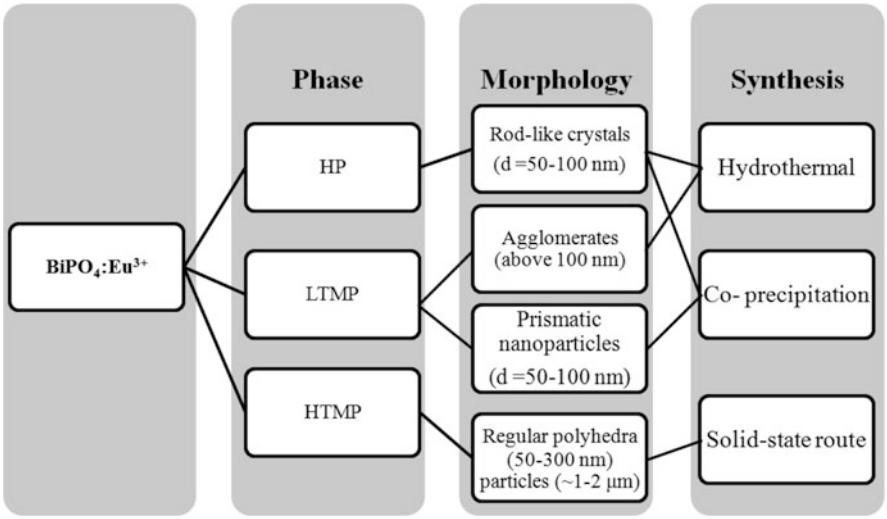

Fig. 2.7 Relationships between crystal structure, morphology, and applied synthetic route for $BiPO_4/Eu^{3+}$ preparation

In this work, a series of the $Bi_{1-x}Pr_xPO_4$ ($x = 0.001–0.1$) and $PrPO_4$ compounds were synthesized by a high-temperature solid-state reaction method. The initial materials, Bi_2O_3 (99.99%), $(NH_4)_2HPO_4$ (99.999%), and Pr_6O_{11} (99.999%), were weighted in stoichiometry and then thoroughly mixed and milled in agate mortar for more than 30 min till they were uniformly distributed. The obtained mixtures were heated at 450, 500, and 600 °C for 6 h at each temperature with intermediate regrinding in porcelain crucibles along with an atmosphere agent and then were naturally cooled to room temperature.

Variations in morphologies and particle sizes that accompany the doping process for $BiPO_4$ were examined. As indicated by the SEM images in Fig. 2.8, the sample with the low Pr^{3+} content almost entirely consists of prism-shaped particles. The particle sizes are in the range from about 50 nm up to 0.5 μ and the smaller particles observed on general view of samples in the case of lower concentrations of Pr. Increasing of RE ions content lead to the increase of quantity of rodlike particles, and these particles form agglomerates. As was said before for oxide compounds, a very low particle sizes could lead to significant quenching of luminescence. The particle size of our samples is close to that reported in [29] for Y_2O_3/Eu nanoparticles with the best luminescence efficiency, so we expect that the studied $Bi_{1-x}Pr_xPO_4$ nanopowders must possess intensive photoluminescence. Moreover, the PL intensity may increase with dopant concentration increasing due to size effects (in other words, through decreasing of surface-to-volume ratio, the concentration of surface defects which acts as quenching centers should decrease).

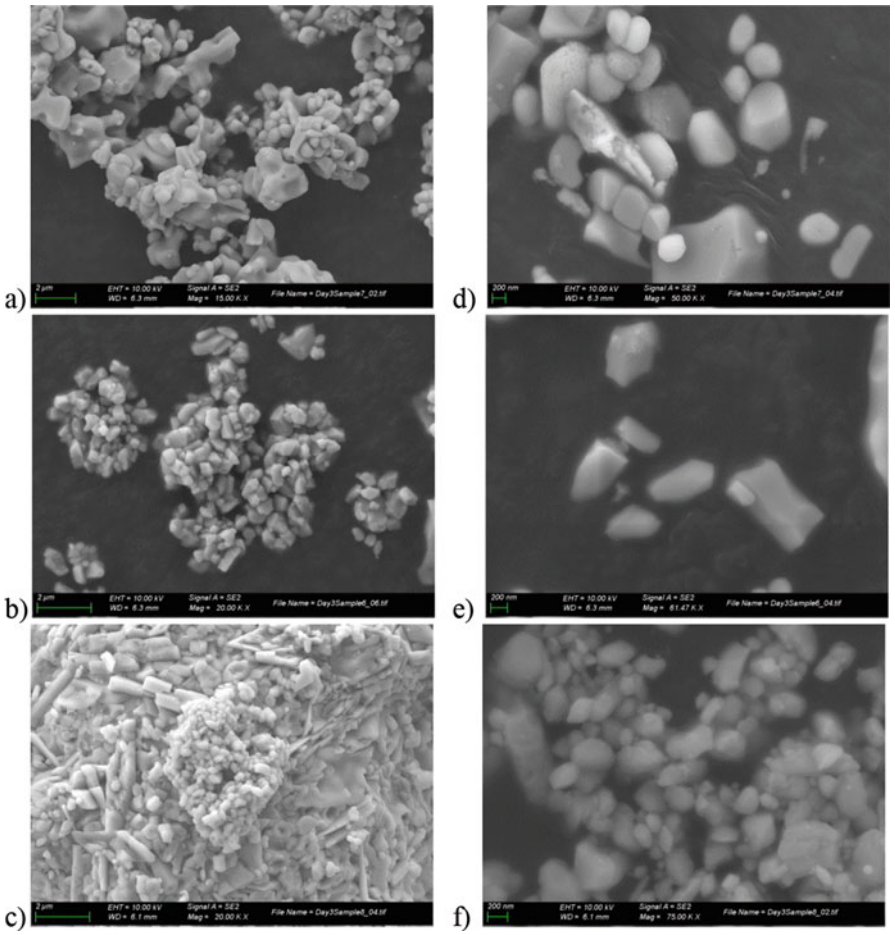

Fig. 2.8 SEM images of $BiPO_4/xPr^{3+}$ polycrystals; $x = 0.5\%$ (**a**, **d**), 1% (**b**, **e**), and 5% (**c**, **f**)

2.3.2 Crystal Structure

Bismuth orthophosphate possesses three structure types at normal conditions, hexagonal and two monoclinic, which are so-called high-temperature monoclinic (HTMP) and low-temperature monoclinic (LTMP, monazite) [66–68]. It was reported recently that two more crystal modifications appear when pressure is applied to $BiPO_4$ crystals [69]. It is known that the hexagonal phase of $BiPO_4$ stabilized by the presence of water molecules in structure and structure formula for this compound is $BiPO_4 \times 0.67H_2O$ [70]. After about 2 months, hexagonal structure loses all water from channels inside of crystal lattice, transforming into LTMP. Hydration of LTMP does not lead to transformation of it to the hexagonal

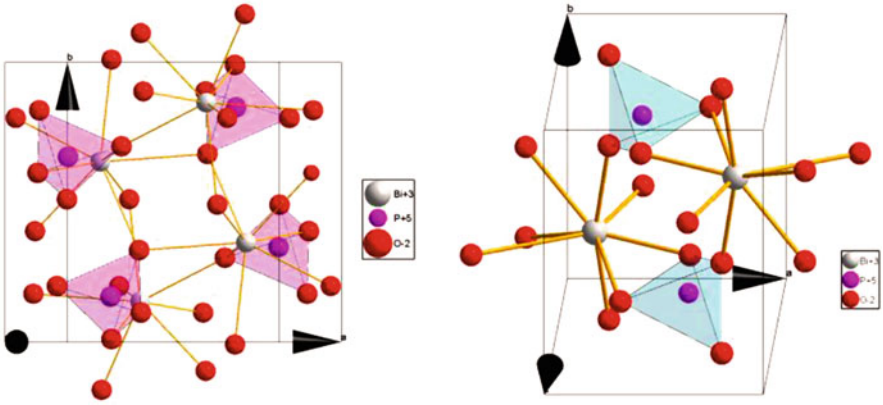

Fig. 2.9 Primitive cell for LTMP (left) and HTMP (right) $BiPO_4$ crystals

phase [67]. Obviously, unstable crystals as abovementioned phases required high pressure are not suitable for WLED application; thus, we do not describe details of hexagonal and high-pressure structures.

Calculations of total energies for LTMP and HTMP have shown very similar values indicating competing stability [70]. The HTMP is the most symmetrical phase of $BiPO_4$, and it is stable at room temperature during 10 months at least [67]. The LTMP is the most stable phase and can be transformed into HTMP after heating to 600 °C. During such heating, PO_4 tetrahedra undergo small rotations.

The primitive cells of both LTMP and HTMP are shown in Fig. 2.9. It can be seen that in both structures, Bi^{3+} cations are surrounded by eight oxygen atoms that belong to $(PO_4)^{3-}$ tetrahedra. Primitive cell contains two and four formula units for LTMP and TMP, respectively. In case of LTMP, there are six nonequivalent positions (one for Bi, one for P, and four for O), and there are five non-equivalent positions for HTMP modification (one for Bi, one for P, and three for O).

More detailed analysis of the structures showed that both of them contain layers of Bi and PO_4. In the case of LTMP, five of the eight oxygen atoms of BiO_8 polyhedra belong to the same layer as Bi, and the other three O atoms belong to PO_4 tetrahedra of adjoining layers. These oxygen atoms connect layers to each other. There are also Bi-(PO_4)-Bi chains along the c axis inside every layer. A similar situation is observed for HTMP, but six of the eight oxygen atoms of BiO_8 polyhedra belong to the same layer as Bi. Thus, adjoining layers are connected by sharing two oxygen atoms from each BiO_8 polyhedra. In both crystal modifications, PO_4 and BiO_8 polyhedra are distorted. In the case of HTMP distances, P-O bonds varied from 1.53 to 1.56 Å (average value is 1.545 Å), and Bi-O bonds have lengths in 2.15–2.19 Å range (average, 2.50 Å). The P-O bond lengths for LTMP are in the 1.47–1.54 range (average, 1.495 Å), and Bi-O bonds are 2.33–2.68 Å (average 2.50 Å). On the first sight, it looks like BiOx polyhedra is more symmetrical for LTMP, but one more oxygen atom is present at 3.02 Å from Bi, and thus bismuth can be interpreted as

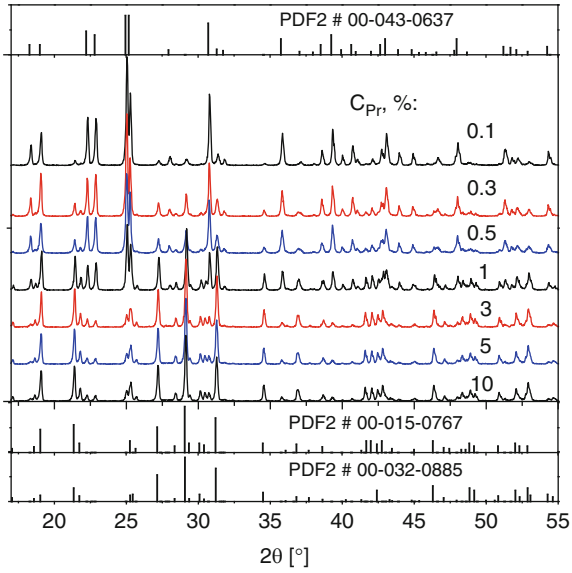

Fig. 2.10 XRD patterns for Pr^{3+}-doped $BiPO_4$. Standards for high-temperature monoclinic $BiPO_4$ (PDF2 card # 00-043-0637), for low-temperature monoclinic $BiPO_4$ (PDF2 card # 00-015-0767), and for $PrPO_4$ (PDF2 card # 00-032-0885) are shown at the top and bottom parts of the figure

the one surrounded by nine oxygen atoms. From the viewpoint of crystal structure, RE ions should have more intensive luminescence in the case of LTMP because of more distorted BiO_x polyhedra. It is worth noting that doping of $BiPO_4$ with RE can lead to structural transformations. In particular, it was reported that Eu^{3+}-doped $BiPO_4$ increases LTMP phase with increase in dopant concentrations [71].

The phase composition of prepared samples was determined by X-ray powder diffraction (XRD) using SHIMADZU XRD-6000 diffractometer with a linear detector and Cu Kα radiation ($\lambda = 1.5418$ Å). The XRD patterns obtained for synthesized $BiPO_4$/xPr nanopowders are shown in Fig. 2.10.

It can be seen that peaks related to HTMP modification prevail (namely, peaks nearly $2\Theta = 25$ and 31°) at low concentrations of Pr^{3+} ions. Increase in concentration led to arising of peaks nearly 26.5 and 28° which indicates the presence of LTMP $BiPO_4$. From XRD patterns, it is clear that all studied samples are mixtures of two $BiPO_4$ modifications. The most essential changes in XRD patterns are observed when the Pr concentration increases from 1% to 3%. We can assume that starting from 3% of Pr^{3+} an LTMP prevails in the mixture. The $PrPO_4$ possess crystal structure of monazite type [72].

2.3.3 Electronic Band Structure and Optical Properties

Calculation of the electronic band structure of solids can provide valuable information for understanding its physical properties. As for $BiPO_4$ compounds, such calculations were performed for bulk HTMP by various methods [22, 73]. To the

best of our knowledge, no result for electronic structure of LTMP was reported so far. Before the discussion of results of calculation, something further must be noted. The SEM images showed that the studied powdered samples consist of crystallites of micro/nano sizes. A very large number of atoms for modeling are needed, even the smallest particle of samples, taking into account the cell parameters a, b, and c about 0.7 nm. Thus, it is more reasonable to use methods for electronic structure calculations for bulk materials. Furthermore, relatively large sizes of crystallites make such step more justified. The drawback of such method is related to unavailability to find changes in electronic structure when moving toward nanoscale particles. The electronic structures of the crystals were calculated with the use of WIEN2k program package [74], in which the full-potential linear-augmented-plane-wave (FP-LAPW) method is implemented within the framework of density-functional theory (DFT). The Perdew and Wang generalized gradient approximation was employed [75] for the exchange-correlation potential. The relativistic effects were treated in the scalar relativistic approximation. The partial densities of electronic states (PDOS) were calculated using well-known relations implemented in the WIEN2k program code [74]. The crystal structure parameters and atomic positions for LTMP and HTMP $BiPO_4$ as well as for $PrPO_4$ were taken from literature [67, 68, 72]. Calculations of PDOSes were carried out for 26 nonequivalent sampling $\boldsymbol{k}$-points in the irreducible parts of the Brillouin zones, and it was assured that further increase in the number of $\boldsymbol{k}$-points does not lead to significant changes in calculated PDOS distributions. Oxygen vacancies are common for oxide materials; therefore, knowledge about changes in electronic structure caused by such defects are helpful for further discussion. Calculation of HTMP $BiPO_4$ with oxygen vacancy was performed for case of one vacancy per unit cell with further geometry optimization.

The partial densities of states (PDOS) for two monoclinic modifications of $BiPO_4$ are shown in Fig. 2.11. It is known that the DFT-based calculations lead to underestimation of energy band gap, and therefore correction of the E_g value has to be applied. Currently, there are a lot of data on E_g for all three modifications of $BiPO_4$, most of them based on UV-vis diffuse reflectance spectra (DRS). In particular, it was reported that E_g values range from 3.5 to 4.6 eV, depending on particle size, morphology, and concentration of defects [76]. It was shown in our works that E_g values of some oxide crystals correspond to the energy point situated between the region of the steep rise and the first peak of intrinsic PL excitation spectra [77, 78]. Obtained from simultaneous analysis of DRS and PL excitation spectra, the E_g value for HTMP is 4.7 eV [22]. In the cited work [79], authors reported that E_g values are 3.8 and 4.2 eV for LTMP and HTMP $BiPO_4$ crystals prepared by hydrothermal method. It is well known that absorption of oxide crystals reaching the fundamental absorption edge should increase by few (at least two) orders of magnitude with respect to absorption in the optical transparency region. However, absorbance spectra obtained in diffuse reflectance experiments do not reflect this feature. We suppose that E_g for LTMP must be closer to 4.2 eV as point at low-energy edge of plateau in corresponding DRS spectra (see Fig. 2.4 from ref. [79]). Calculated values of band gaps are 4.41 and 4.18 eV for HTMP and LTMP,

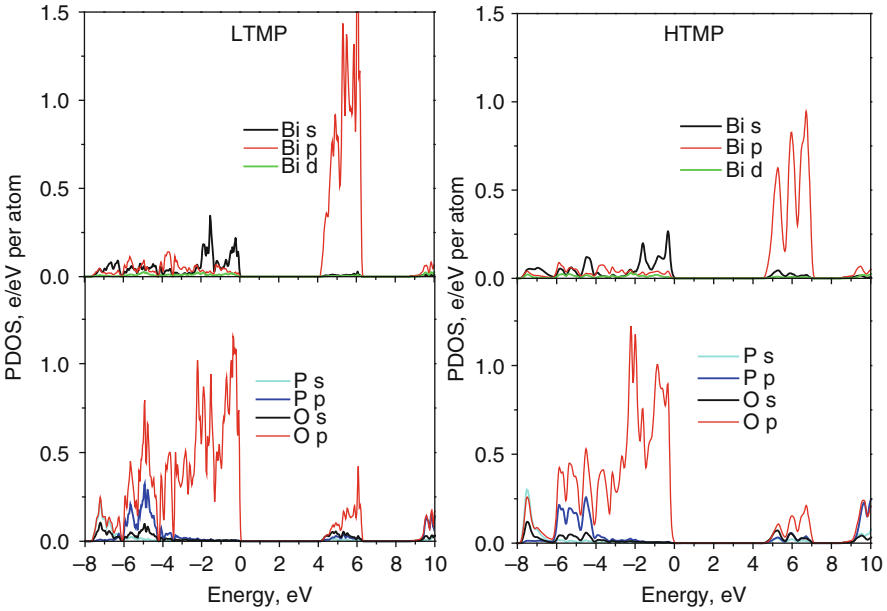

Fig. 2.11 Calculated PDOS for LTMP and HTMP of $BiPO_4$

respectively. A scissor operator $\Delta = 0.29$ eV was applied in order to correct the calculated band gap for HTMP. Fermi energy was chosen as zero energy level.

The distribution of partial densities of electronic states looks similar for both studied phases of $BiPO_4$ in the energy range -8–10 eV. The O *p* states dominate at the top of the valence band (VB), and the bottom of conduction band (CB) is formed mainly by Bi *p* states. The Bi *s* states are present mainly at the top of VB, and their density is roughly five times lower than for O *p* states. The P states are located deep in the VB, resulting in low absorption due to phosphate groups in the energy region near E_g. At the same time, for both phases, band-to-band absorption is due to inner transitions of Bi^{3+} ions and O^{2-} to Bi^{3+} charge transfer process. Thus, Bi^{3+} ions should be greatly involved in all absorption, PL excitation, and PL emission processes. Such conclusions were made in the case of the HTMP bismuth orthophosphate luminescence studies [22]. In particular, violet PL emission was attributed to inner $6s^2 \rightarrow 6s^1p^1$ inner transitions in Bi^{3+} ions, and the blue PL band was assigned to Bi^{3+} ions near defect of crystal lattice. Comparison of PDOS distribution for both monoclinic phases of $BiPO_4$ allowed us to assume that LTMP should be very similar to HTMP case luminescence centers and energy transfer processes. It is well known that oxygen vacancies are common defects in crystal lattice of oxide compounds. Such defects usually modify electronic structure of solids, leading to lowering of band gap energy as well as to creation of electronic states inside the band gap.

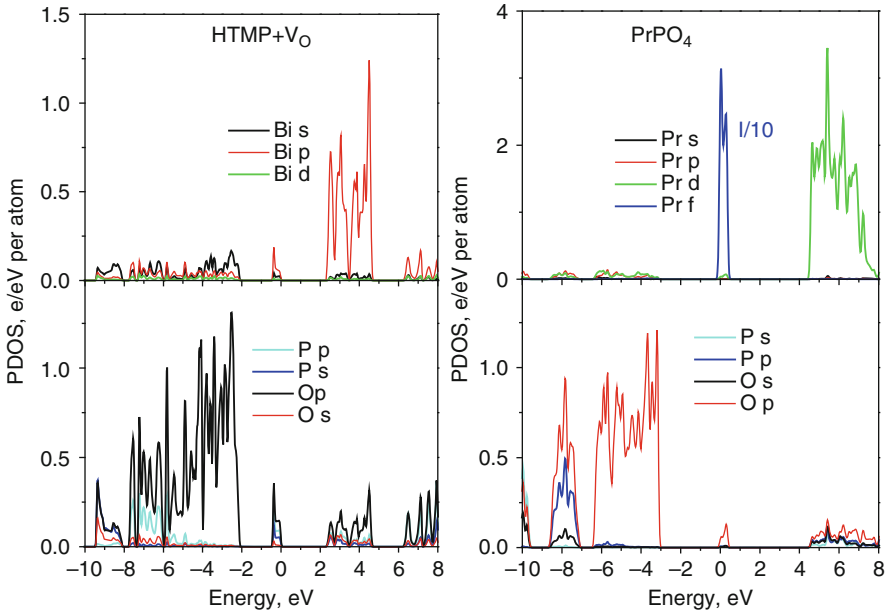

Fig. 2.12 PDOS for HTMP $BiPO_4$ with oxygen vacancy (left) and $PrPO_4$ crystals (right)

The PDOS for HTMP of $BiPO_4$ with oxygen vacancy is shown in Fig. 2.12. It is seen from the figure that the region at energies below −2.1 eV is similar to PDOS distribution in the top of VB in the case of perfect crystal. The region of energies above 2.3 eV corresponds to the bottom of CB for perfect $BiPO_4$. The fully occupied states are observed inside the crystal band gap. These states have Bi *p* and O *p* states character mainly. Thus, energy distance between "VB" and "CB" in case of crystal with oxygen vacancy can spread from a calculated value of 4.4 eV up to 4.7 eV (E_g for perfect HTMP). The abovementioned defect states can lead to formation of absorption/emission band with maxima in the region about 2.3–2.6 eV (539–477 nm wavelength range). This assumption is in a good agreement with results on PL spectroscopy of $BiPO_4$ as the PL emission band in blue spectral region (maxima nearly 2.6 eV) was observed for crystals of 0.1–1 mm in size [22].

The PDOS distributions of $PrPO_4$ crystals are shown in Fig. 2.12. The intensity of Pr *f* states was lowered ten times for better comparison, and scissor operator $\Delta = 1.2$ eV was added to calculated band gap ($E_g{}^{calc} = 3.3$ eV) in order to reach the experimental value for 4f–5d charge transitions of Pr^{3+} ion in $PrPO_4$ crystals [72]. If we have to consider partially occupied Pr *f* states as inter-band ones, we can assert that the top of VB is formed mainly by O *p* states and the bottom of CB formed by Pr *d* states. Similar to the $BiPO_4$ crystals, P states are deeply located in the VB. The overall view of $PrPO_4$ PDOS indicates that all the absorption and emission bands in UV and vis spectral regions should be attributed to inner transitions in Pr^{3+} ions.

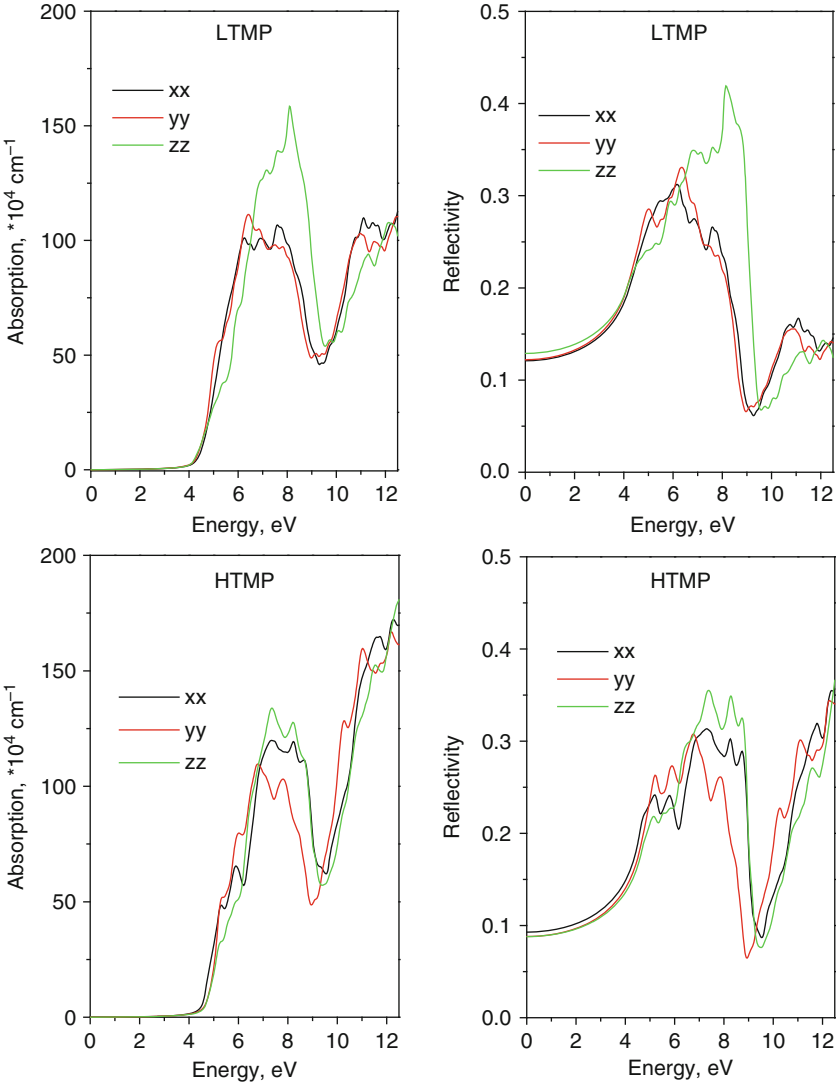

Fig. 2.13 Calculated absorption and reflectivity spectra for two phases of perfect $BiPO_4$

Charge transfer band $O^{2-} \rightarrow Pr^{3+}$ can be observed only at energies about 9.5 eV (130 nm).

Calculated absorption and reflection spectra for LMPT and HTMP $BiPO_4$ crystals are shown in Fig. 2.13. It is seen from the figure that both $BiPO_4$ modifications possess anisotropy. This anisotropy is more expressed in the case of LTMP.

Calculated optical spectra allowed us to assume that HTMP have somewhat better absorption in comparison with LTMP in the low-energy side of the band-to-

band transitions. Higher reflectivity for the region of visible light takes place in the case of LTMP. Thus, excitation of photoluminescence in the visible and UV spectral regions should have slightly better effectiveness in case of more symmetrical phase of $BiPO_4$.

2.3.4 Luminescence Properties

The PL characteristics were measured using DFS-12 double-diffraction grating monochromator equipped with photomultiplier FEU-79. Diode-pumped lasers ($\lambda_{em} = 473$ and 532 nm), N_2 laser ($\lambda_{em} = 337.1$ nm), and Xe lamp were used as excitation light sources. The PL studies were performed at room temperature of the samples.

Some luminescence is still observed for HTMP $BiPO_4$ under excitations in UV and visible regions even at room temperature, but intensity is more than ten times lower than at 8 K. Figure 2.14 shows such spectra for polycrystalline samples of $BiPO_4$ measured for excitations at 337.1, 473, and 532 nm (3.68, 2.62, and 2.33 eV respectively). Details of the synthesis procedure for these samples can be found in [80].

It is seen that under PL excitations inside the crystal band gap, multicomponent PL band is observed with the main maxima nearly 550 nm (green spectral region). The highest intensity of PL was observed for excitation at 473 nm (2.62 eV) that coincides with maxima of PL emission ascribed to "Bi^{3+} near defect" luminescent centers. Some defects related to crystallite surface occur in the case of polycrystalline samples, and concentration of such defects obviously increases when moving toward nanocrystals. It can be seen that visible luminescence better expressed in the

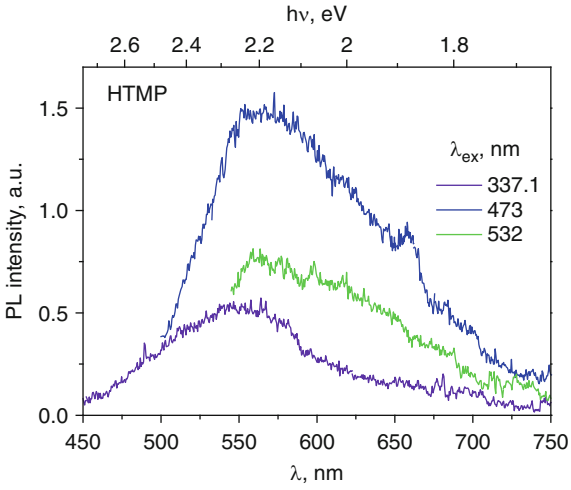

Fig. 2.14 PL spectra of polycrystalline $BiPO_4$ obtained at $T = 300$ K

case of nanopowders than in case of powders of relatively large crystallites. Thus, we can expect that Pr^{3+}-doped $BiPO_4$ nanopowders should have some wideband PL related to host.

Before the discussion of results on PL of Pr^{3+}-doped $BiPO_4$ and $PrPO_4$ it is worth analyzing luminescence properties of $BiPO_4$ samples doped with other RE ions revealing red luminescence. Due to good PL emission characteristics of various materials doped with Eu^{3+} ions, the $Bi_{1-x}Eu_xPO_4$ systems were studied in numerous works (e.g., [34, 39, 63, 64]). Studies of PL at low temperatures showed that $Bi_{0.99}Eu_{0.01}PO_4$ polycrystalline samples reveal only luminescence of Eu^{3+} ions under excitation at 260 and 400 nm. At room temperature also only luminescence related to *f-f* radiation electronic transitions in Eu^{3+} ions was reported. This luminescence is effectively excited through charge transfer band as well as by direct excitation of Eu^{3+} ions. Intensity of luminescence for Eu^{3+}-doped $BiPO_4$ strongly depends on the type of structural phase and increases in the row "hexagonal → HTMP → LTMP" [38, 64]. Quenching of the PL $Bi_{1-x}Eu_xPO_4$ compounds starts for concentrations of Eu^{3+} $x = 0.07$ [81]. Interestingly, that crystal structure completely transformed from HTMP to LTMP also at this concentration of Eu and particle sizes are lower for higher concentration of dopant [81]. It was reported that with Eu^{3+} ion concentrations increasing, the decay times decrease (for $\lambda_{ex} = 393$ nm, $\lambda_{em} = 590$ nm the $\tau = 2.62$ and 1.3 ms for 5% and 15% of Eu, respectively) [82].

$BiPO_4$ nanoparticles doped with Sm^{3+}, another RE ion with intensive red luminescence, were studied in [83] in the case of hexagonal polymorph. Only the PL bands, related to *f-f* transition in Sm^{3+} ions, were observed at room temperature and excitation in visible spectral region. The most intensive luminescence was reported for Sm^{3+} concentration of 3%. No phase transformation was observed during doping process. It was found that co-doping of hexagonal $BiPO_4$ with Eu and Sm led to significant increase in Eu^{3+}-related luminescence band. In case of monazite $BiPO_4$/0.05 Sm^{3+}, only luminescence of Sm^{3+} was also observed with the most intense PL band at 610 nm, which is magnetic dipole allowed, but the electric dipole mechanism plays the dominant role [82].

Interesting luminescence results for the case of monazite $BiPO_4$ co-doped with Eu^{3+}/Tb^{3+} was reported in [84]. Particles of $Bi_{0.97}Eu_{0.03}PO_4$ nearly 50 nm in size revealed red emission while green emission was observed for $Bi_{1-x}Tb_xPO_4$ ($x = 0.03 - 0.18$). Co-doping leads to decreasing Tb^{3+} emission when Eu content increased. The most intensive Tb^{3+} PL emission was observed for $Bi_{1-x}Tb_xPO_4$ at $x = 0.15$. The emission intensities of $Bi_{0.88}Eu_{0.03}Tb_{0.09}PO_4$ increased with prolonging the hydrothermal time. It is consistent with the fact that larger crystal size is in favor of the higher PL emission intensity. The 9% Tb^{3+} and 3% Eu^{3+} co-doped $BiPO_4$ assembly has coordinates of $x = 0.3563$ and $y = 0.3411$, which are close to the standard white light color ($x = 0.333$, $y = 0.333$). It was reported also that the efficient Tb^{3+} to Eu^{3+} energy transfer can be used to tune the emission color from green to yellow to orange by simply changing the concentration of europium in $BiPO_4$: Tb^{3+} and Eu^{3+} [85]. It is worth noting that $BiPO_4$ host luminescence was not observed for RE-doped micro-/nanoparticles when PL excitation was done

in the range of either $h\nu > E_g$ or $h\nu < E_g$. Such situation can be explained by energy transfer from host to RE ions [82].

As was mentioned above, there are no literature data on luminescence properties of $BiPO_4/Pr^{3+}$ nanopowders except our recent paper [40]. In the present work, we expanded the luminescence study on other concentrations of praseodymium as well as the PL properties of $PrPO_4$ samples synthesized in the same away as $BiPO_4/Pr^{3+}$ nanopowders were studied. Figure 2.15 shows the PL emission spectra of Pr^{3+}-doped $BiPO_4$ and $PrPO_4$ samples under direct excitation from ground state $^3H_4$ to $^3P_1$ level of Pr^{3+} ions ($\lambda_{ex} = 473$ nm). The most intensive emission bands were related to radiation transition from $^3P_0$ to $^3H_4$ (483 nm), $^3H_6$ (~ 610 nm), $^3F_2$ (640 nm), and $^3F_4$ (728 nm) and from $^1D_2$ to $^3H_4$ (~ 595 nm) levels of Pr^{3+} ions. The bands related to transitions $^1D_2 \rightarrow {}^3H_4$ overlapping with those for $^3P_0 \rightarrow {}^3H_6$ transitions and therefore forming structured wide band in 570–635 nm spectral range (roughly bands in 570–600 nm range) were attributed mainly to $^1D_2 \rightarrow {}^3H_4$ transitions. It can be noted the PL spectrum of $PrPO_4$ in our study is very similar to that reported in the literature [41].

The PL spectra are strongly dependent on Pr^{3+} content, and intensity of almost every band is different for each spectrum as shown in Fig. 2.15. The most prominent

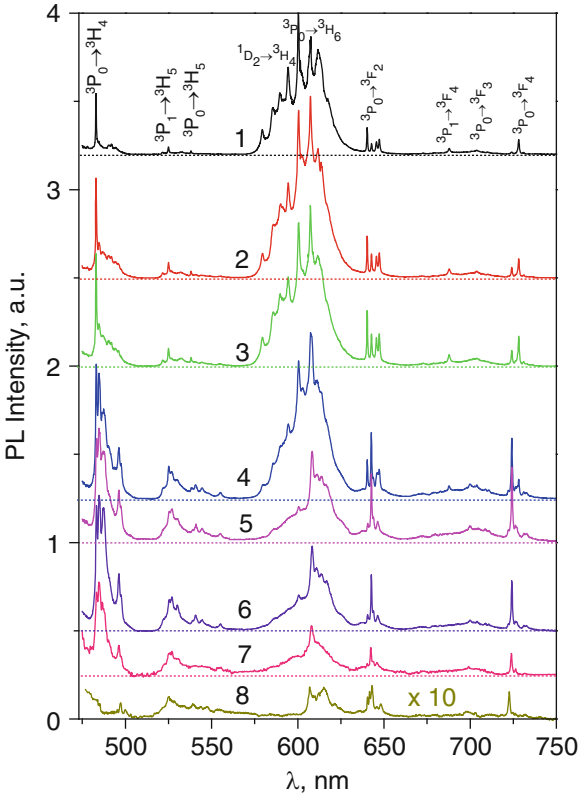

Fig. 2.15 PL emission spectra of $BiPO_4/xPr^{3+}$ ($x = 0.001$ (1), 0.003 (2), 0.005 (3), 0.01 (4), 0.03 (5), 0.05 (6), 0.1 (7)) and $PrPO_4$ polycrystals (8); $\lambda_{ex} = 473$ nm, $T = 300$ K

changes appear when concentration of Pr^{3+} reaches 1%. In particular, the bands of $^3P_0 \rightarrow {}^3H_4$ transitions which were observed as a shoulder at the lowest concentration became more intensive. The bands of $^3P_{0,1} \rightarrow {}^3H_5$ and $^3P_0 \rightarrow {}^3F_4$ transitions also increase in intensity when Pr^{3+} concentration increase to 1%. There also redistribution in bands intensity of the same transitions (clearly seen for $^3P_0 \rightarrow {}^3F_2$ transition) when moving from the lowest concentration to 1% of Pr^{3+} and higher. The changes in PL spectra can be explained by superposition of at least three processes in studied compounds: $BiPO_4$ phase transformation, multiphonon relaxation, and cross-relaxation processes.

In the studied case of excitation to $^3P_1$ level at the first stage of luminescence process, a non-radiation relaxation leads to population of $^3P_0$ level. Further depopulation of the $^3P_0$ level can lead to either radiation emission or population of $^1D_2$ level. There are two possible ways for the population of $^1D_2$ level from $^3P_0$ which are usually discussed – multi-phonon relaxation and phonon-assisted (energy of phonon is about 200 cm^{-1}) cross-relaxation $[^3P_0, {}^3H_4] \rightarrow [^3H_6, {}^1D_2]$ processes [18]. Due to relatively low-energy gap between $^3P_0$ and $^1D_2$ levels (~3800 cm^{-1}) and a presence of asymmetric stretching of P-O bond with phonons energy up to 1160 cm^{-1} [19], the multi-phonon relaxation which releases four phonons is probable. At the same time, at low concentrations of Pr^{3+} ions in studied compounds, distance between two RE ions is too large for effective cross-relaxation (see Table 2.2). According to some studies [20, 21], critical distances for an efficient energy transfer between lanthanide ions are nearly 10 Å, so cross-relaxation processes could play a significant role for concentrations above 1%. Interestingly, the quenching of PL bands related to $^1D_2$-$^3H_4$ transitions clearly observed concentrations of 3% and higher. Taking into account large energy gap (about 6800 cm^{-1}) between $^1D_2$ level and next lower level $^1G_4$, the multiphonon relaxation between these levels is not so probable. So, depopulation of $^1D_2$ level should occur mostly due to the cross-relaxations $[^1D_2, {}^3H_4] \rightarrow [^1G_4, {}^3F_{3,4}]$. Decrease in intensity of $^3P_0 \rightarrow {}^3H_6$ transitions for concentrations above 1% is related to cross-relaxation $[^3P_0, {}^3H_4] \rightarrow [^3H_6, {}^1D_2]$.

The PL excitation spectra for Pr-doped $BiPO_4$ are presented in Fig. 2.16, and in 300–550 nm spectral region, it consists only of the bands related to transitions from ground $^3H_4$ level to $^3P_{0,1,2}$ multiplet of Pr^{3+} ion. The PL excitation spectra of $PrPO_4$ in the studied region do not reveal any band of *f-f* transition in Pr^{3+} ions but only two weak wide bands of presumably defect-related nature. In contrast to the PL emission spectra, the excitation spectra are little dependent on Pr^{3+} concentration. Only one substantial change can be marked – in comparison with $BiPO_4$/0.1%Pr

Table 2.2 The average distances between Pr^{3+} ions in $BiPO_4$/Pr nanopowders

C_{Pr}, %	0.1	0.3	0.5	1	3	5	10	100
d, Å[a]	26.78	18.57	15.66	12.07	8.37	7.06	5.60	4.06[b]

[a]Average distances calculated by the formula reported in [86]
[b]The shortest distances between Pr in $PrPO_4$ [87]

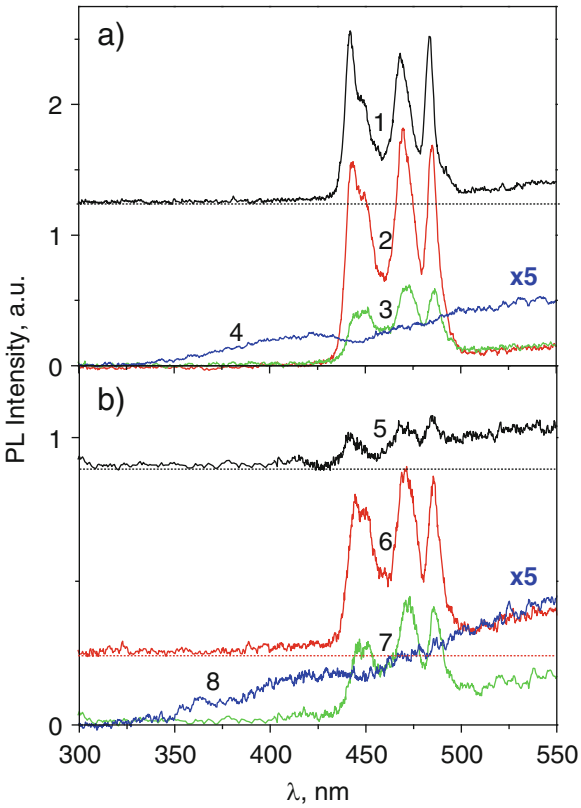

Fig. 2.16 PL excitation spectra of $BiPO_4/xPr^{3+}$ ($x = 0.001$ (1, 5), 0.01 (2, 6), 0.1 (3, 7)) and $PrPO_4$ (4, 8) polycrystals; $\lambda_{em} = 611.5$ (**a**) and 642.8 nm (**b**); $T = 300$ K

Table 2.3 Calculated chromaticity coordinates for $BiPO_4$/Pr nanopowders

C_{Pr}, %	0.1	0.3	0.5	1	3	5	10	100
x	0.603	0.588	0.574	0.530	0.450	0.434	0.405	0.448
y	0.369	0.369	0.372	0.373	0.374	0.380	0.383	0.449

where $^3H_4 \rightarrow {}^3P_1$ transition has somewhat lower intensity than $^3H_4 \rightarrow {}^3P_0$ and $^3H_4 \rightarrow {}^3P_2$ ones; for higher concentrations, the former is dominant in the spectra.

The studied Pr-doped $BiPO_4$ possess intensive orange-red luminescence and have perspectives to be used in WLED. From this viewpoint, it is interesting to evaluate color coordinates for PL emission of these compounds. The calculated coordinates in the case of $\lambda_{ex} = 473$ nm are collected in Table 2.3.

If we compare with standard for red color ($x = 0.67$, $y = 0.33$), obtained values are quite close for low praseodymium concentrations. Increasing the Pr^{3+} content led to more expressed $^3P_0 \rightarrow {}^3H_4$ transition in blue spectral region, resulting in the move of chromaticity coordinates toward those for orange spectral region. So, we can state that $BiPO_4/Pr^{3+}$ samples of low Pr^{3+} content (C_{Pr} less than 0.5%) are perspective red phosphors.

2.4 Conclusions

The prepared Pr-doped nanopowders are mixture of two high-temperature and low-temperature (monazite) monoclinic polymorphs of $BiPO_4$ lattice. Dopant concentration increase leads to increase in the monazite content in the samples. The prepared $PrPO_4$ samples have monazite structure too.

Calculated partial densities of states indicate that for both monoclinic polymorphs of $BiPO_4$ crystals, the top of the valence band is formed mainly by O *p* states with the presence of Bi *s* states, and the Bi *p* states dominate at the low-energy part of the conduction band. In the case of oxygen vacancy in high-temperature polymorph, $BiPO_4$ fully occupied defect band is formed in the band gap region.

Calculated partial densities of states for $PrPO_4$ crystal show that the top of the valence band formed by O *p* states and bottom of the conduction band consist mostly of Pr *d* states. Partially occupied Pr *f* states are located near the middle of the crystal band gap.

At room temperature, un-doped $BiPO_4$ samples reveal weak intrinsic photoluminescence in visible region under excitations at $\lambda_{ex} = 337.1$, 473, and 532 nm. The praseodymium-containing samples reveal only emission related to inner *f*-*f* electronic transition of Pr^{3+} ions under excitation at $\lambda_{ex} = 473$ nm. The PL excitation spectra for $BiPO_4$/Pr nanopowders consist only of bands which correspond to absorption of Pr^{3+} ions in the wavelength region of 300–550 nm.

The most intensive luminescence was observed for Pr^{3+} concentration equal to 1.0%. The concentration quenching of luminescence is attributed to the presence of cross-relaxation $[^3P_0, {}^3H_4] \rightarrow [^3H_6, {}^1D_2]$ processes.

Calculated chromaticity coordinates indicate the possibility for $BiPO_4$/Pr nanopowders. The Pr^{3+} concentration increase leads to the coordinates shifting toward the orange spectral region.

References

1. Pan C, Zhu Y (2011) Size-controlled synthesis of $BiPO_4$ nanocrystals for enhanced photocatalytic performance. J Mater Chem 21(12):4235–4241. https://doi.org/10.1039/C0JM03655B
2. Huang H, Chen G, Zhang Y (2014) Two Bi-based phosphate photocatalysts: crystal structure, optical property and photocatalytic activity. Inorg Chem Commun 44:46–49. https://doi.org/10.1016/j.inoche.2014.02.047
3. Li X, Elshahawy AM, Guan C, Wang J (2017) Metal phosphides and phosphates-based electrodes for electrochemical supercapacitors. Small 13(39):1701530. https://doi.org/10.1002/smll.201701530
4. Nedilko S, Hizhnyi Y, Chukova O et al (2009) Luminescent monitoring of metal dititanium triphosphates as promising materials for radioactive waste confinement. J Nuclear Mater 385(2):479–484. https://doi.org/10.1016/j.jnucmat.2008.12.034
5. Ginebra MP, Traykova T, Planell JA (2006) Calcium phosphate cements as bone drug delivery systems: a review. J Control Release 113(2):102–110. https://doi.org/10.1016/j.jconrel.2006.04.007

6. Ludwig J, Nilges T (2018) Recent progress and developments in lithium cobalt phosphate chemistry-syntheses, polymorphism and properties. J Power Sources 382:101–115. https://doi.org/10.1016/j.jpowsour.2018.02.038
7. Kaneyoshi M (2006) Luminescence of some zirconium-containing compounds under vacuum ultraviolet excitation. J Lumin 121(1):102–108. https://doi.org/10.1016/j.jlumin.2005.09.017
8. Miao CR, Torardi CC (2000) A new high-efficiency UV-emitting X-ray phosphor, $BaHf_{1-x}Zr_x(PO_4)_2$. J Solid State Chem 155(1):229–232. https://doi.org/10.1006/jssc.2000.8938
9. Torardi CC, Miao CR, Li J (2003) Efficient UV-emitting X-ray phosphors: octahedral $Zr(PO_4)_6$ luminescence centers in potassium hafnium–zirconium phosphates $K_2Hf_{1-x}Zr_x(PO_4)_2$ and $KHf_{2(1-x)}Zr_{2x}$ $(PO_4)_3$. J Solid State Chem 170(2):289–293. https://doi.org/10.1016/S0022-4596(02)00087-7
10. Hizhnyi Y, Chornii V, Nedilko S et al (2013) Luminescence spectroscopy and electronic structure of ZrP_2O_7 and $KZr_2(PO_4)_3$ crystals. Radiat Meas 56:397–401. https://doi.org/10.1016/j.radmeas.2013.01.068
11. Nedilko S, Nagornii P, Nedyelko I et al (2009) Nature of intrinsic and impure luminescence of $MAlP_2O_7$ crystals. Opt Mater 31(12):1828–1830. https://doi.org/10.1016/j.optmat.2008.12.023
12. Boyko V, Nedilko SG, Hizhnyi Y et al (2015) Synthesis, luminescence and electronic band structure of $Al(PO_3)_3$ crystals. Solid State Phenom 230:73–78. https://doi.org/10.4028/www.scientific.net/SSP.230.73
13. Nedilko S, Hizhnyi Y, Chornii V et al (2013) Possibility of application of ZrP_2O_7 and $KZr_2(PO_4)_3$ intrinsic luminescence for monitoring of γ-irradiation. Sens Lett 11(10):1937–1944. https://doi.org/10.1166/sl.2013.2756
14. Nedilko S, Chornii V (2013) Electronic band structure and luminescence properties of powdered ZrP_2O_7 crystals. Ukr J Phys Opt 14(4):187–195. https://doi.org/10.3116/16091833/14/4/187/2013
15. Hizhnyi Y, Gomenyuk O, Nedilko S et al (2007) Electronic structure and optical properties of ABP_2O_7 double phosphates. Radiat Meas 42(4-5):719–722. https://doi.org/10.1016/j.radmeas.2007.02.012
16. Hizhnyi YA, Oliynyk A, Gomenyuk O et al (2008) The electronic structure and optical properties of ABP_2O_7 (A= Na, Li) double phosphates. Opt Mater 30(5):687–689. https://doi.org/10.1016/j.optmat.2007.02.009
17. Nakazawa E, Shiga F (1977) Vacuum ultraviolet luminescence-excitation spectra of $RPO_4:Eu^{3+}$ (R= Y, La, Gd and Lu). J Lumin 15(3):255–259. https://doi.org/10.1016/0022-2313(77)90024-2
18. Moncorge R, Boulon G, Denis JP (1979) Fluorescence properties of bismuth-doped $LaPO_4$. J Phys C Solid State Phys 12(6):1165. https://doi.org/10.1088/0022-3719/12/6/028
19. Boulon G, Pedrini C, Guidoni M, Pannel C (1975) Étude de la cinétique des centres luminogènes Bi^{3+} dans les cristaux. J Phys France 36(3):267–278. https://doi.org/10.1051/jphys:01975003603026700
20. Blasse G, Dirksen GJ (1982) The luminescence of broad-band emitters in $LiLaP_4O_{12}$. Phys Stat Sol (b) 110(2):487–494. https://doi.org/10.1002/pssb.2221100214
21. Hizhnyi Y (2016) Luminescence spectroscopy and electronic structure of Zr-and Bi-containing phosphate crystals. Ukr J Phys Opt 17(1):32–38. https://doi.org/10.3116/16091833/17/1/32/2016
22. Hizhnyi YA, Nedilko SG, Chornii VP et al (2014) Electronic structures and origin of intrinsic luminescence in Bi-containing oxide crystals $BiPO_4$, $K_3Bi_5(PO_4)_6$, $K_2Bi(PO_4)(MoO_4)$, $K_2Bi(PO_4)(WO_4)$ and $K_5Bi(MoO_4)_4$. J Alloys Compd 614:420–435. https://doi.org/10.1016/j.jallcom.2014.06.111
23. Zatovsky IV, Strutynska NY, Hizhnyi YA et al (2018) New complex phosphates $Cs_3M^{II}Bi(P_2O_7)_2$ (M^{II}–Ca, Sr and Pb): synthesis, characterization, crystal and electronic structure. Dalton Trans 47(7):2274–2284. https://doi.org/10.1039/c7dt04505k

24. Chornii V, Hizhnyi Y, Nedilko SG et al (2015) Synthesis, crystal structure, luminescence and electronic band structure of $K_2BiZr(PO_4)_3$ phosphate compound. Solid State Phenom 230:55–61. https://doi.org/10.4028/www.scientific.net/SSP.230.55
25. Pimpalshende DM, Dhoble SJ (2015) Stability of luminescence in $LaPO_4$, $LaPO_4$: RE^{3+} (RE= Dy, Eu) nanophosphors. Luminescence 30(2):144–154. https://doi.org/10.1002/bio.2705
26. Zhang L, Fu L, Yang X et al (2014) Controlled synthesis and tunable luminescence of uniform $YPO_4 0.8H_2O$ and $YPO_4 0.8H_2O$: Tb^{3+}/Eu^{3+} nanocrystals by a facile approach. J Mater Chem C 2(43):9149–9158. https://doi.org/10.1039/C4TC01427H
27. Guan M, Sun J, Tao F, Xu Z (2008) A host crystal for the rare-earth ion dopants: synthesis of pure and Ln-doped urchin like $BiPO_4$ structure and its photoluminescence. Cryst Growth Des 8(8):2694–2697. https://doi.org/10.1021/cg070642z
28. Xue F, Li H, Zhu Y et al (2009) Solvothermal synthesis and photoluminescence properties of $BiPO_4$ nano-cocoons and nanorods with different phases. J Solid State Chem 182(6):1396–1400. https://doi.org/10.1016/j.jssc.2009.02.031
29. Wang WN, Widiyastuti W, Ogi T et al (2007) Correlations between crystallite/particle size and photoluminescence properties of submicrometer phosphors. Chem Mater 19(7):1723–1730. https://doi.org/10.1021/cm062887p
30. Kharieky AA, Saraee KRE, Strek W (2017) The size effect on luminescence properties of praseodymium doped LuAG prepared by Pechini method. J Lumin 190:443–450. https://doi.org/10.1016/j.jlumin.2017.05.078
31. Chen X, Liu Y, Tu D (2016) Lanthanide-doped luminescent nanomaterials. From fundamentals to bioapplications. Springer-Verlag, Berlin Heidelberg
32. Riwotzki K, Meyssamy H, Schnablegger H et al (2001) Liquid-phase synthesis of colloids and redispersible powders of strongly luminescing $LaPO_4$:Ce,Tb nanocrystals. Ang Chem Intl Ed 40(3):573–576. https://doi.org/10.1002/1521-3773(20010202)40:3<573::AID-ANIE573>3.0.CO;2-0
33. Shi X, Liu Y, Zhang J et al (2015) Enhanced luminescence properties of $BiPO_4$:Eu^{3+} phosphors prepared by hydrothermal method. Ceram Int 41(5):6683–6686. https://doi.org/10.1016/j.ceramint.2015.01.089
34. Zhao M, Li G, Li L et al (2012) Structures and polymorph-sensitive luminescence properties of $BiPO_4$/Eu grown in hydrothermal conditions. Cryst Growth Des 12(8):3983–3991. https://doi.org/10.1021/cg300451d
35. Liu S, Zhang W, Hu Z et al (2013) Synthesis and luminescent properties of Eu^{3+} and Dy^{3+} doped $BiPO_4$ phosphors for near UV-based white LEDs. J Mater Sci Mater Electron 24(11):4253–4257. https://doi.org/10.1007/s10854-013-1393-x
36. Hizhnyi Y, Chornii V, Nedilko S et al (2016) Luminescence spectroscopy of Ln-doped Bi-containing phosphates and molybdates. Radiat Meas 90:314–318. https://doi.org/10.1016/j.radmeas.2016.01.014
37. Roming M, Feldmann C (2009) Synthesis and characterization of nanoscaled $BiPO_4$ and $BiPO_4$:Tb. J Mater Sci 44(5):1412. https://doi.org/10.1007/s10853-009-3258-5
38. Arunkumar P, Jayajothi C, Jeyakumar D, Lakshminarasimhan N (2012) Structure–property relations in hexagonal and monoclinic $BiPO_4$: Eu^{3+} nanoparticles synthesized by polyol-mediated method. RSC Adv 2(4):1477–1485. https://doi.org/10.1039/C1RA00389E
39. Naidu BS, Vishwanadh B, Sudarsan V, Vatsa RK (2012) $BiPO_4$: a better host for doping lanthanide ions. Dalton Trans 41(11):3194–3203. https://doi.org/10.1039/c2dt11944g
40. Chornii V, Nedilko S, Bychkov K et al (2018) Synthesis and luminescence properties of Pr^{3+}-doped $BiPO_4$ polycrystals. Acta Phys Pol A 133(4):843–846. https://doi.org/10.12693/APhysPolA.133.843
41. Chadeyron-Bertrand G, Vial S, Cellier J et al (2005) Influence of processing parameters on the luminescence of sol–gel derived $PrPO_4$. Mater Res Bull 40(9):1477–1482. https://doi.org/10.1016/j.materresbull.2005.04.023
42. Boutinaud P, Mahiou R, Cavalli E, Bettinelli M (2007) Red luminescence induced by intervalence charge transfer in Pr^{3+}-doped compounds. J Lumin 122:430–433. https://doi.org/10.1016/j.jlumin.2006.01.198

43. Yang R, Xiaoye HU, Tao LIU et al (2011) Pr^{3+}-doped Li_2SrSiO_4 red phosphor for white LEDs. J Rare Earths 29(3):198–201. https://doi.org/10.1016/S1002-0721(10)60430-9
44. Fidelus JD, Yatsunenko S, Godlewski M et al (2009) Relation between structural properties of Pr^{3+}-doped yttria-stabilized zirconia nanopowders and their luminescence efficiency. Scr Mater 61(4):415–418. https://doi.org/10.1016/j.scriptamat.2009.04.034
45. Chen J, Gong X, Lin Y et al (2010) Synthesis and spectral property of Pr^{3+}-doped tungstate deep red phosphors. J Alloys Compd 492(1-2):667–670. https://doi.org/10.1016/j.jallcom.2009.12.009
46. Terebilenko KV, Zatovsky IV, Slobodyanik NS et al (2007) Phase relations in the system K_2MoO_4–KPO_3–MoO_3–Bi_2O_3: a new phosphate $K_3Bi_5(PO_4)_6$. J Solid State Chem 180(12):3351–3359. https://doi.org/10.1016/j.jssc.2007.10.001
47. Becker P (2003) Thermal and optical properties of glasses of the system Bi_2O_3–B_2O_3. Cryst Res Technol 38(1):74–82. https://doi.org/10.1002/crat.200310009
48. Gorodylova NA, Baumer VN, Zatovsky IV et al (2011) Crystallization from high-temperature solutions in the K_2O-P_2O_5-V_2O_5-Bi_2O_3 system. Inorg Mater 47(2):156–162. https://doi.org/10.1016/j.jssc.2007.10.001
49. Terebilenko KV, Zatovsky IV, Baumer VN et al (2008) Phase relations in the $K_2W_2O_7$–K_2WO_4–KPO_3–Bi_2O_3 system and structure of $K_{6.5}Bi_{2.5}W_4P_6O_{34}$. J Solid State Chem 181(9):2393–2400. https://doi.org/10.1016/j.jssc.2008.05.035
50. Umar A, Ahmad R, Kumar R et al (2016) $Bi_2O_2CO_3$ nanoplates: fabrication and characterization of highly sensitive and selective cholesterol biosensor. J Alloys Compd 683:433–438. https://doi.org/10.1016/j.jallcom.2016.05.063
51. Chen Q, Wang Y, Wang H (2018) Synthesis and properties of nanocrystal $BiPO_4$ in diamagnetic PbO-Bi_2O_3-B_2O_3 glass. J Non-Cryst Solids 481:85–93. https://doi.org/10.1016/j.jnoncrysol.2017.10.025
52. Zhong J, Weiren Z, Licai L, Jianqing W (2014) Hydrothermal synthesis and luminescence properties of Eu^{3+} and Sm^{3+} codoped $BiPO_4$. J Rare Earths 32(1):5–11. https://doi.org/10.1016/S1002-0721(14)60026-0
53. Schultze D (1988) Thermal synthesis of non-stoichiometric $Bi_{5.8}PO_{11.2}$. J Therm Anal Calorim 33(3):895–901. https://doi.org/10.1007/BF02138606
54. Schultze D, Uecker R (1985) Thermoanalytical and single crystal growth investigations in the system Bi_2O_5-P_2O_5 and Bi_2O_3-Nd_2O_3-P_2O_5. Thermochim Acta 93:509–512. https://doi.org/10.1016/0040-6031(85)85128-5
55. Wang Y, Guan X, Li L, Li G (2012) pH-driven hydrothermal synthesis and formation mechanism of all $BiPO_4$ polymorphs. CrystEngComm 14(23):7907–7914. https://doi.org/10.1039/C2CE25337B
56. Zhang Y, Sillanpää M, Obregón S, Colón G (2015) A novel two-steps solvothermal synthesis of nanosized $BiPO_4$ with enhanced photocatalytic activity. J Mol Catal A Chem 402:92–99. https://doi.org/10.1016/j.molcata.2015.03.011
57. Liu Y, Sun M, Liu Y et al (2015) Effects of aging time on phase, morphology, and luminescence by two-photon processes of $BiPO_4$:Er^{3+},Yb^{3+} in the solvothermal synthesis. Opt Mater 45:32–36. https://doi.org/10.1016/j.optmat.2015.03.004
58. Xie J, Cao Y, Jia W et al (2018) Solvent-free strategy of photocarriers accumulated site and separated path for porous hollow spindle-shaped $BiPO_4$. ChemCatChem 10(17):3777–3785. https://doi.org/10.1002/cctc.201800750
59. Zhu Y, Ling Q, Liu Y et al (2016) Photocatalytic performance of $BiPO_4$ nanorods adjusted via defects. Appl Catal B Environ 187:204–211. https://doi.org/10.1016/j.apcatb.2016.01.012
60. Yang M, Shrestha NK, Hahn R, Schmuki P (2010) Electrochemical formation of bismuth phosphate nanorods by anodization of bismuth. Electrochem Solid-State Lett 13(4):C5–C8. https://doi.org/10.1149/1.3290775
61. Wang Q, Li Y, Zeng Z, Pang S (2012) Relationship between crystal structure and luminescent properties of novel red emissive $BiVO_4$:Eu^{3+} and its photocatalytic performance. J Nanopart Res 14(8):1076. https://doi.org/10.1007/s11051-012-1076-1

62. Zhao M, Li L, Zheng J et al (2012) Is $BiPO_4$ a better luminescent host? Case study on doping and annealing effects. Inorg Chem 52(2):807–815. https://doi.org/10.1021/ic3019315
63. Fu C, Li G, Zhao M et al (2012) Solvent-driven room-temperature synthesis of nanoparticles $BiPO_4:Eu^{3+}$. Inorg Chem 51(10):5869–5880. https://doi.org/10.1021/ic300465r
64. Zhao M, Li G, Zheng J et al (2011) Preparation and polymorph-sensitive luminescence properties of $BiPO_4$:Eu, part I: room-temperature reaction followed by a heat treatment. CrystEngComm 13(20):6251–6257. https://doi.org/10.1039/C1CE05629H
65. Sun X, Sun X, He J et al (2014) Synthesis and luminescence of $BiPO_4:xEu^{3+}$ powders by solid state reaction method. Ceram Int 40(5):7647–7650. https://doi.org/10.1016/j.ceramint.2013.12.095
66. Mooney-Slater RC (1962) Polymorphic forms of bismuth phosphate. Z Kristallogr 117(1-6):371–385. https://doi.org/10.1524/zkri.1962.117.16.371
67. Romero B, Bruque S, Aranda MA, Iglesias JE (1994) Syntheses, crystal structures, and characterization of bismuth phosphates. Inorg Chem 33(9):1869–1874. https://doi.org/10.1021/ic00087a023
68. Masse R, Durif A (1985) Etude structurale de la forme haute température du monophosphate de bismuth $BiPO_4$. C R Acad Sci 300(17):849–851
69. Errandonea D, Gomis O, Santamaría-Perez D et al (2015) Exploring the high-pressure behavior of the three known polymorphs of $BiPO_4$: discovery of a new polymorph. J Appl Phys 117(10):105902. https://doi.org/10.1063/1.4914407
70. Achary SN, Errandonea D, Muñoz A et al (2013) Experimental and theoretical investigations on the polymorphism and metastability of $BiPO_4$. Dalton Trans 42(42):14999–15015. https://doi.org/10.1039/c3dt51823j
71. Zheng Y, Li L, Zhao M et al (2014) Enhancement of thermal stability in bismuth phosphate by Ln^{3+} doping for tailored luminescence properties. CrystEngComm 16(23):5040–5049. https://doi.org/10.1039/C3CE41960F
72. Horchani-Naifer K, Férid M (2009) Crystal structure, energy band and optical characterizations of praseodymium monophosphate $PrPO_4$. Inorg Chim Acta 362(6):1793–1796. https://doi.org/10.1016/j.ica.2008.08.021
73. Long B, Huang J, Wang X (2012) Photocatalytic degradation of benzene in gas phase by nanostructured $BiPO_4$ catalysts. Prog Nat Sci-Mater 22(6):644–653. https://doi.org/10.1016/j.pnsc.2012.11.007
74. Blaha P, Schwarz K, Madsen G et al (2001) WIEN2k, an augmented plane wave local orbitals program for calculating crystal properties. Techn. Universitadt Wien, Karlheinz Schwarz, Austria. ISBN 3-9501031-1-2
75. Perdew JP, Wang Y (1992) Accurate and simple analytic representation of the electron-gas correlation energy. Phys Rev B 45(23):13244. https://doi.org/10.1103/PhysRevB.45.13244
76. Pan C, Zhu Y (2015) A review of $BiPO_4$, a highly efficient oxyacid-type photocatalyst, used for environmental applications. Cat Sci Technol 5(6):3071–3083. https://doi.org/10.1039/C5CY00202H
77. Hizhnyi Y, Nedilko SG, Chornii V et al (2013) Electronic structure and luminescence spectroscopy of $M'Bi(MoO_4)_2$ (M' = Li, Na, K), $LiY(MoO_4)_2$ and $NaFe(MoO_4)_2$ molybdates. Solid State Phenom 200:114–122. https://doi.org/10.4028/www.scientific.net/SSP.200.114
78. Spassky DA, Vasil'ev AN, Kamenskikh IA et al (2011) Electronic structure and luminescence mechanisms in $ZnMoO_4$ crystals. J Phys Condens Matter 23(36):365501. https://doi.org/10.1088/0953-8984/23/36/365501
79. Pan C, Li D, Ma X et al (2011) Effects of distortion of PO_4 tetrahedron on the photocatalytic performances of $BiPO_4$. Cat Sci Technol 1(8):1399–1405. https://doi.org/10.1039/C1CY00261A
80. Nedilko S, Chornii V, Hizhnyi Y et al (2013) Luminescence spectroscopy and electronic structure of Eu^{3+}-doped Bi-containing oxide compounds. Funct Mater 20(1):29–36. https://doi.org/10.15407/fm20.01.029

81. Liang YL, Zhang W, Hu ZF et al (2014) Effect of Eu^{3+} on microstructure and luminescence properties of $BiPO_4$ for near-UV LED. Appl Mech Mater 543(547):3745–3749. https://doi.org/10.4028/www.scientific.net/AMM.543-547.3745
82. Cybinska J, Lorbeer C, Mudring AV (2016) Ionic liquid assisted microwave synthesis route towards color-tunable luminescence of lanthanide-doped $BiPO_4$. J Lumin 170:641–647. https://doi.org/10.1016/j.jlumin.2015.06.051
83. Yan SQ, Long CG (2016) Effects of Sm^{3+} concentration on the microstructure and luminescence properties of $BiPO_4$ phosphor prepared by hydrothermal method. J Mater Sci Mater Electron 27(11):12079–12084. https://doi.org/10.1007/s10854-016-5357-9
84. Wang Y, Huang H, Quan C, Tian N, Zhang Y (2016) Hydrothermal fabrication of multifunctional Eu^{3+} and Tb^{3+} co-doped $BiPO_4$: photocatalytic activity and tunable luminescence properties. J Cryst Growth 433:1–6. https://doi.org/10.1016/j.jcrysgro.2015.09.031
85. Zhong J, Zhao W, Song E, Deng Y (2014) Luminescence properties and dynamical processes of energy transfer in $BiPO_4$:Tb^{3+}, Eu^{3+} phosphor. J Lumin 154:204–210. https://doi.org/10.1016/j.jlumin.2014.04.031
86. De Sousa DF, Batalioto F, Bell MJV et al (2001) Spectroscopy of Nd^{3+} and Yb^{3+} codoped fluoroindogallate glasses. J Appl Phys 90(7):3308–3313. https://doi.org/10.1063/1.1397289
87. Ni Y, Hughes JM, Mariano AN (1995) Crystal chemistry of the monazite and xenotime structures. Am Mineral 80(1-2):21–26. https://doi.org/10.2138/am-1995-1-203

Chapter 3
Anomalous Change of Refractive Index for Au Sols Under Laser Illumination

Yuliia Harahuts, Valeriy Pavlov, Elena Mokrinskaya, Irina Davidenko, Nikolay Davidenko, Nataliya Kutsevol, Ihor Pampukha, and Victor Martynyuk

3.1 The Holographic Interferometry Technique

At present, effective holographic recording media (HRM) have been created and used for the photothermoplastic (PTP) method of information recording [1–18]. In these HRM, films of polymer composites (FPC) with photo-semiconductor and thermoplastic properties are used as a photosensitive material. Special electronic devices are used to control their work. The principle of holographic recording using PTP technique is presented in Fig. 3.1.

The holographic recording media (HRM) consists of three layers (Fig. 3.1): the lower layer 1 is a glass or lavsan substrate, the middle layer 2 is a transparent electrically conductive film ((tin oxide (SnO_2)/indium oxide (In_2O_3)-tin-doped indium oxide (ITO) films are usually used), and the top layer 3 is a film of polymer composites (FPC). The functioning of the HRM during the registration of holograms consists of three stages. Before recording the holograms, the FPC surface is charged in a corona discharge (Fig. 3.1a), for example, by positive ions. During the hologram registration (Fig. 3.1b), electrons pass within the FPC volume toward the surface neutralizing the positive ions on this surface. The spatial distribution of the light intensity is transformed into the spatial distribution of the density of the surface electric charge. In this case, a spatial distribution of the normal (F_n) and tangential (F_t) electrostatic forces appears. A current pulse is passed through the transparent electrically conductive ITO film for development of the latent electrostatic image of the hologram (Fig. 3.1c). As a result, the ITO layer is heated and heats the FPC until reaching the softening temperature. In real devices, the heating velocity

Y. Harahuts (✉) · V. Pavlov · E. Mokrinskaya · I. Davidenko · N. Davidenko · N. Kutsevol
I. Pampukha · V. Martynyuk
Taras Shevchenko National University of Kyiv, Kyiv, Ukraine
e-mail: ndav@univ.kiev.ua

© Springer Nature Switzerland AG 2019

O. Fesenko, L. Yatsenko (eds.), *Nanophotonics, Nanooptics, Nanobiotechnology, and Their Applications*, Springer Proceedings in Physics 222,
https://doi.org/10.1007/978-3-030-17755-3_3

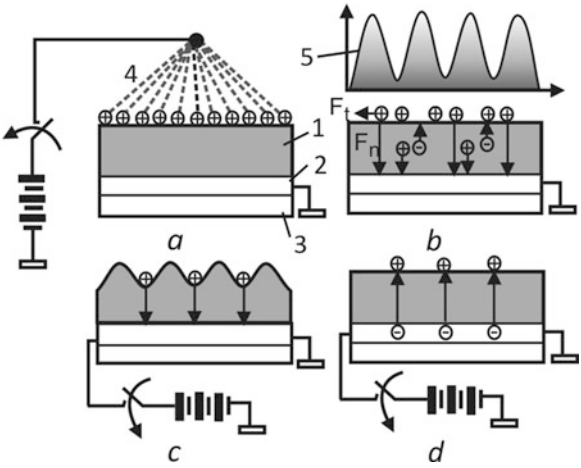

Fig. 3.1 The scheme of the PTP holographic recording technique: (**a**) charging the FPC surface in the corona discharge, (**b**) illumination of the FPC surface with spatially modulated light, (**c**) development of the hologram, (**d**) erasing of the hologram. (1) Transparent solid substrate, (2) transparent conductive layer, (3) FPC, (4) corona electrode, (5) light intensity I modulated along the X coordinate

reaches 10^6 °C/s. In this case, the electrostatic forces F_n and F_t deform the free FPC surface, and the latent electrostatic image is transformed into a geometric relief of the film surface (Fig. 3.1c). After the film cooling down, the geometric relief persists for a long time. In real HRM, recorded holograms can persist for decades at temperatures below the softening point and higher the temperatures of mechanical cracking. For the hologram erasing, it is sufficient to pass through the ITO film a current pulse longer than the duration of the current pulse of the hologram development (Fig. 3.1d). In this case, the FPC is heated until temperatures above the softening point, and the geometric relief disappears. After cooling the HRM until room temperature, it can be used for repeated holographic recording. The number of write-erase cycles can be several hundreds or even thousands.

The high information properties of the HRM can be evidenced by a small "noisy" of the reconstructed images of holograms (Figs. 3.2 and 3.3). This allows them to be used not only in visual holography (Figs. 3.3 and 3.4) but also in holographic interferometry methods.

To test the possibility of using the created HRM in holographic interferometry, experiments were carried out using a small-sized holographic setup (SHS) [5, 9, 19]. This setup allows investigating diffusely reflecting objects, liquids, and gases. The sketch of the SHS is shown in Fig. 3.5, and its photograph is shown in Fig. 3.6.

The practical application of HRMs based on FPC is demonstrated by the following examples of their use in SHS.

3.1.1 Example 1

A transparent cuvette filled with water was used as a model object in the SHS. A resistor is placed at the bottom part of the cuvette to heat the water while passing an

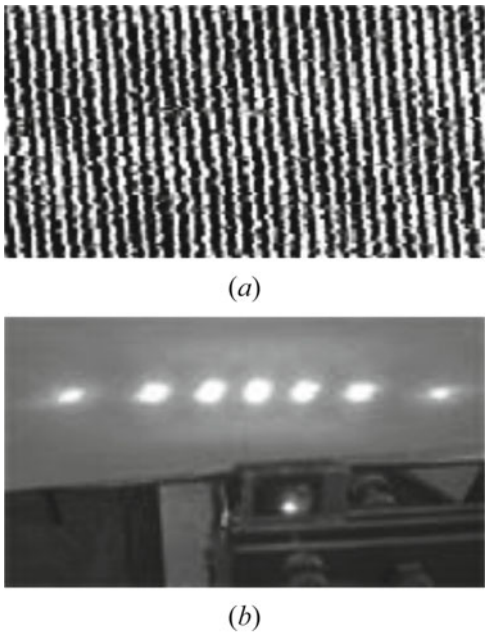

Fig. 3.2 The photograph of the surface area of the FPC after recording the hologram of a plane wave front (**a**) and the photograph of the screen with the projected holographic image of the plane wave front (**b**)

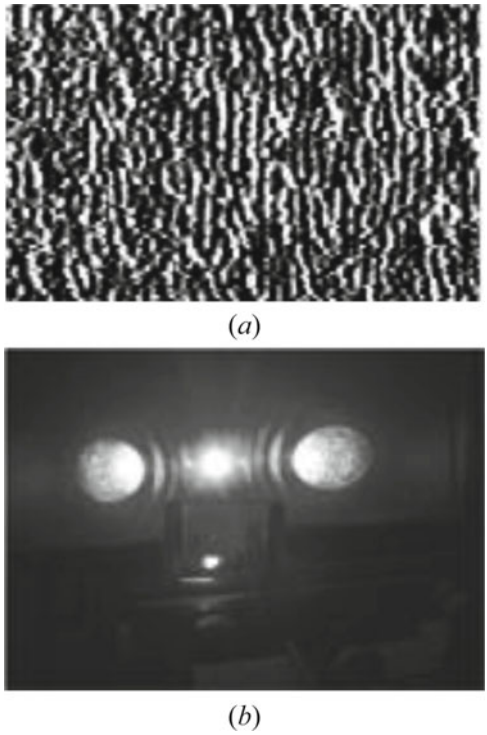

Fig. 3.3 The photograph of the surface area of the FPC after recording the hologram of a coin in the HRM (**a**) and the photograph of the screen with the projected holographic image of a coin (**b**)

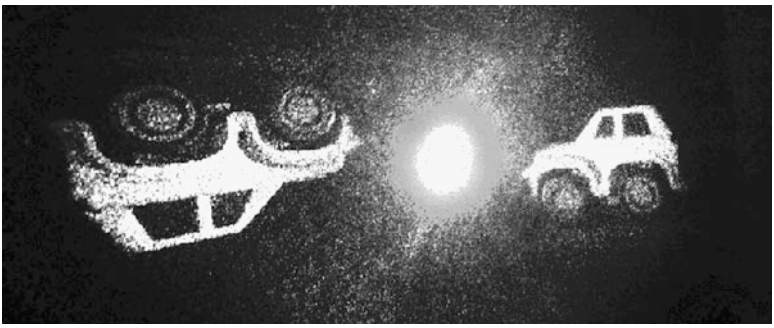

Fig. 3.4 The photograph of the screen with the projected holographic image of a car model

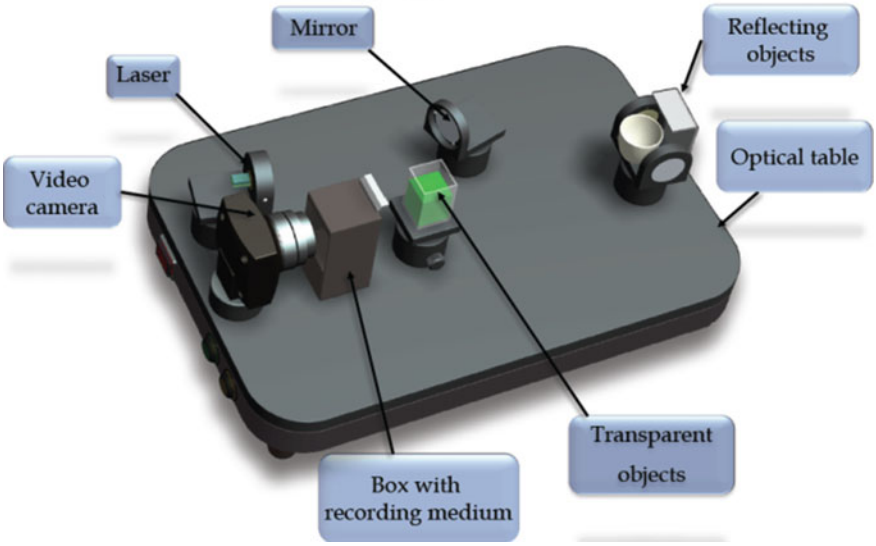

Fig. 3.5 The sketch of a small-sized holographic setup

electric current. The hologram of the cuvette is registered, and the state of the cuvette with water is monitored by the camcorder. Further, a constant electric voltage is applied to the resistor inside the cuvette. The heating of the water in the cuvette does not exceed several degrees. In the image of the cuvette fixed by the camcorder, light and dark interference fringes appear corresponding to the convection flows of water in the cuvette. Figure 3.7 shows the image of the cuvette with water before application of the electrical voltage (*a*) and with the applied electrical voltage (*b*). After switching off the electrical voltage, the interference fringes disappear because the same temperature is there in the cuvette.

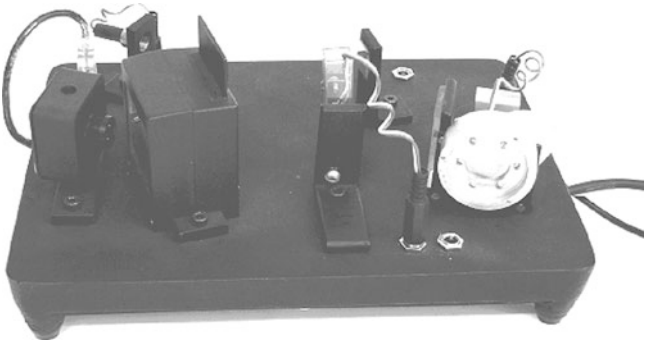

Fig. 3.6 The photograph of the small-sized holographic setup

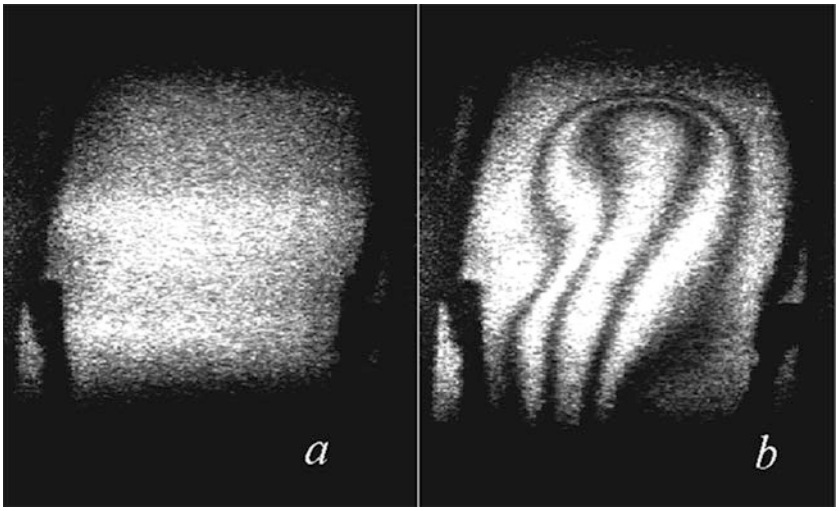

Fig. 3.7 The image of the cuvette with water before application of the electrical voltage to the resistor in the bottom part of the cuvette (**a**) and when the voltage is applied (**b**)

3.1.2 Example 2

A stearin candle placed before the HRM was used as a model object in SHS. A hologram of space above the candle is registered, and a camcorder monitors its condition. Then the candle is ignited, and light and dark interference fringes are observed around the flame arising due to the formation of air heat flows in the flame region. Photographs of the space above the candle without a flame and after burning the candle are shown in Fig. 3.8.

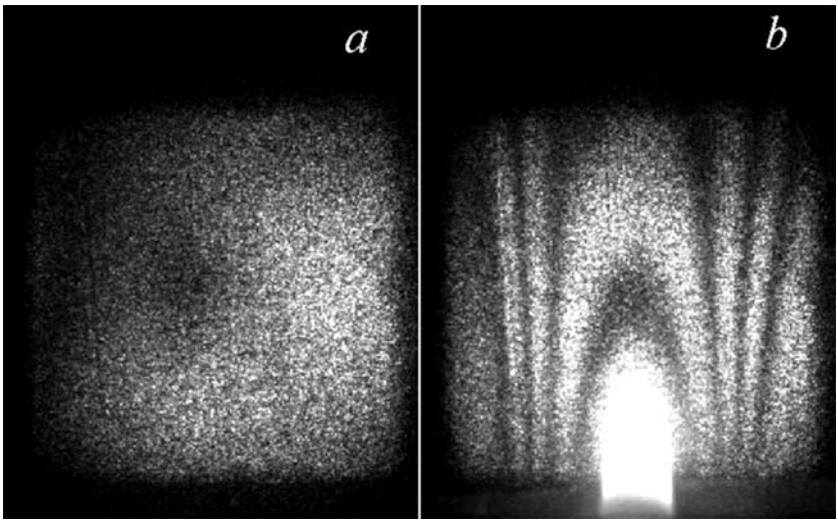

Fig. 3.8 Photographs of the space above the candle before it is ignited (**a**) and a burning candle (**b**)

3.1.3 Example 3

A ceramic bowl was used as the model object in the SHS. The hologram of the bowl was registered, and its surface was monitored using the camcorder. A few drops of hot water were lowered to the bottom of the bowl. In this case, light and dark interference fringes appear in the image of the bowl surface characterizing the change of the linear dimensions of the cup due to the propagation of heat in its walls. The photographs of the bowl before hot water drops enter it and after such a procedure are shown in Fig. 3.9. Over time, the interference fringes disappear indicating that the bowl surface is cooled until room temperature.

3.1.4 Example 4

A piezoelectric loudspeaker was used as a model object in the SHS. The hologram of the loudspeaker diffuser was registered, and the diffuser surface was monitored using the camcorder. A constant electrical voltage was applied to the loudspeaker contacts. In the image of the diffuser surface, concentric light and dark interference fringes appear indicating the bending of the diffuser. The spatial frequency of interference fringes (their number) increases with increasing electrical voltage applied to the contacts. This is directly related to the magnitude of the diffuser deformation. After switching off the electrical voltage, the interference fringes disappear because

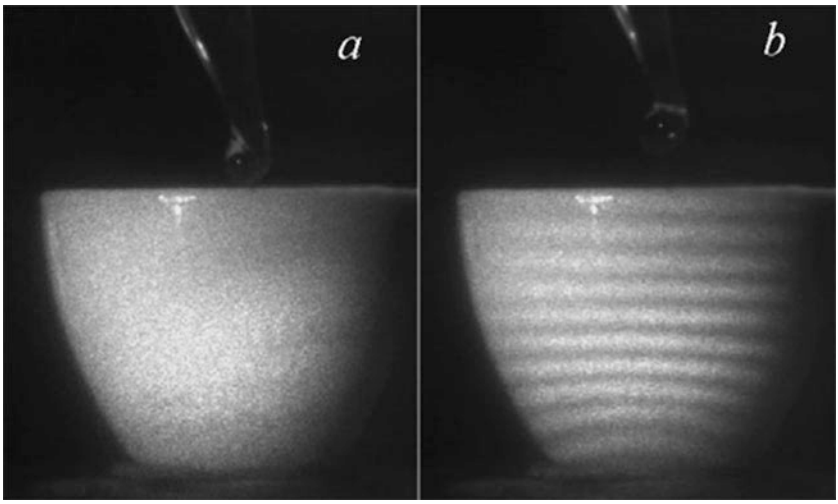

Fig. 3.9 The photographs of the bowl before hot water drops enter it (**a**) and immediately after such a procedure (**b**)

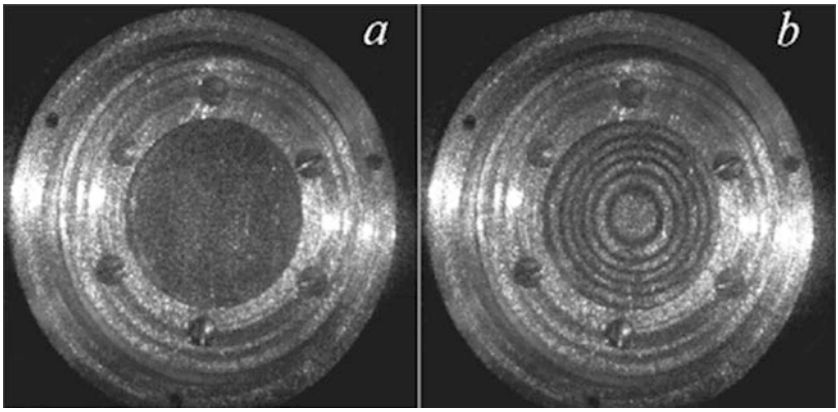

Fig. 3.10 Images of the piezoelectric loudspeaker before the direct electric voltage is applied (**a**) and with the applied electric voltage (**b**)

the diffuser restores its initial shape. The images of the loudspeaker before and after application of the electrical voltage are shown in Fig. 3.10.

3.1.5 Example 5

The L-shaped metal plate (beam) is used as a model object in the SHS. It is fixed in a vertical position relative to the optical table. The hologram of a flat surface of

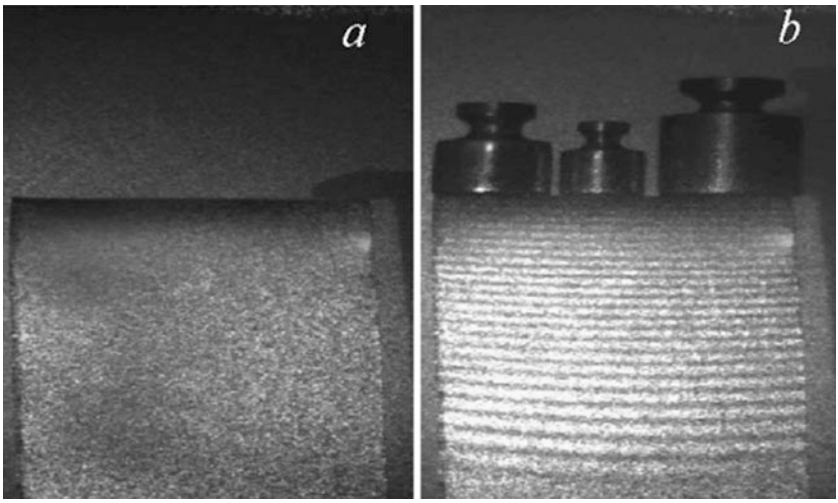

Fig. 3.11 Images of the L-shaped metal plate before its loading (**a**) and after its loading by the weights (**b**)

a plate was registered, and this surface was observed using a camcorder. On the top part of the L-shaped plate, weights from 1 to 5 g were placed. As a result, light and dark interference fringes appear in the image of the plate surface indicating the bending of the L-shaped plate under loading. The spatial frequency of interference fringes (their number) increases with increasing weight. After removing the weights from the top of the plate, the interference fringes immediately disappear because the plate returns to its original state. The images of the L-shaped plate before and after the weights are placed are shown in Fig. 3.11.

3.1.6 Example 6

Small-sized holographic setup (SHS) with recording media based on FPC can also be used for studies of nanoobjects, in particular, in technologies for producing biologically active substances. As an example, the possibility of using various optical methods for detection of the presence and estimation of the concentration of particles based on SiO_2 in aqueous solutions was considered. The following methods were used: (1) comparison of scattering of a focused laser beam passing through a cuvette with H_2O without particles and after their introduction into the liquid (Fig. 3.12), (2) observation of the electrophoresis process in a cuvette with H_2O without particles and after their introduction (Fig. 3.13), and (3) a holographic method for observing the changes of interference fringes in a cuvette with H_2O without particles and after their introduction (Fig. 3.14). It is possible to detect the presence of particles using all three methods. An increase of their

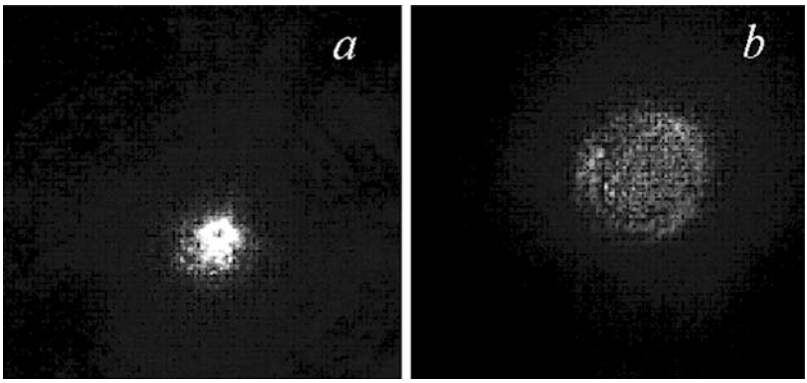

Fig. 3.12 Scattering of the focused laser beam passing through the cuvette with H_2O (**a**) and after the addition of SiO_2-based nanoparticles (**b**)

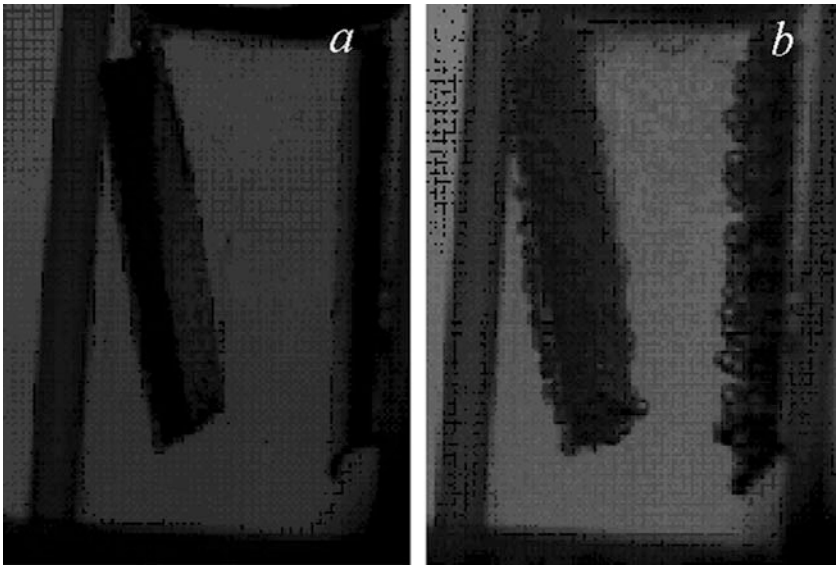

Fig. 3.13 Images of the cuvette with H_2O upon the electrical voltage applied to the gold electrodes near the opposite walls of the cuvette (**a**) and after the addition of SiO_2-based nanoparticles (**b**)

concentration is accompanied by an increase of the change in the optical image. Appropriate mathematical apparatus for image processing allows using considered optical methods for performing express analysis of solutions of biologically active substances.

To extend the possibilities of the method of holographic interferometry, it was proposed to use holographic recording media (HRM) in the method of determination of the refractive index (n) of liquid and gaseous media [20]. This method supposes

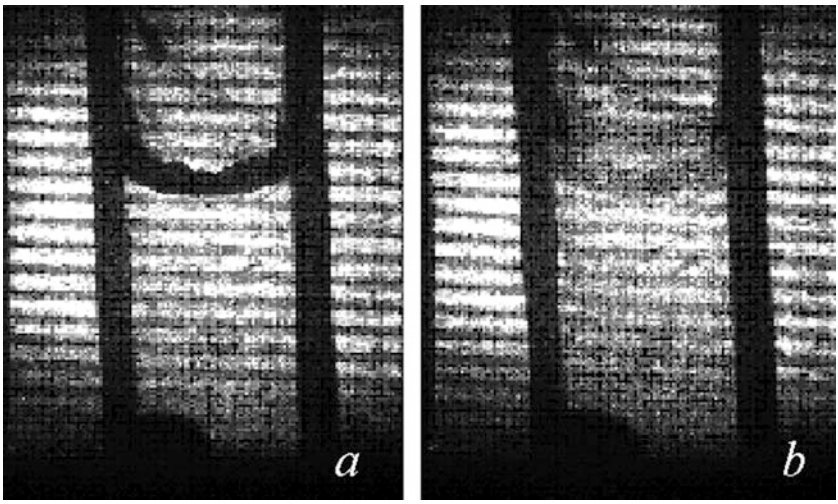

Fig. 3.14 Images of the interference pattern of the cuvette with H_2O without SiO_2-based nanoparticles (**a**) and after their addition (**b**)

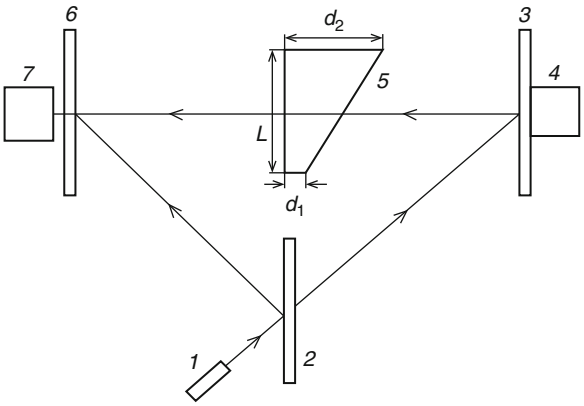

Fig. 3.15 Optical scheme of the small-sized holographic set-up: (1) laser, (2) light splitter, (3) mirror, (4) piezo element, (5) trapezoidal cuvette with high L and cross section of planes d_1 and d_2, (6) HRM, (7) camcorder

the transmission of coherent light through a trapezium-shaped cuvette. In this cuvette, the reference and test media are alternately placed, the hologram is recorded and reconstructed, and n is determined by measuring the spatial frequency of the interference fringes using the phase-shifting interferometry method [21, 22]. SHS (Fig. 3.6) was used to determine n. Its optical scheme is shown in Fig. 3.15.

After recording the hologram of the cell with a reference medium (e.g., a solvent) with a refractive index n_1, this medium is replaced by the investigated medium with

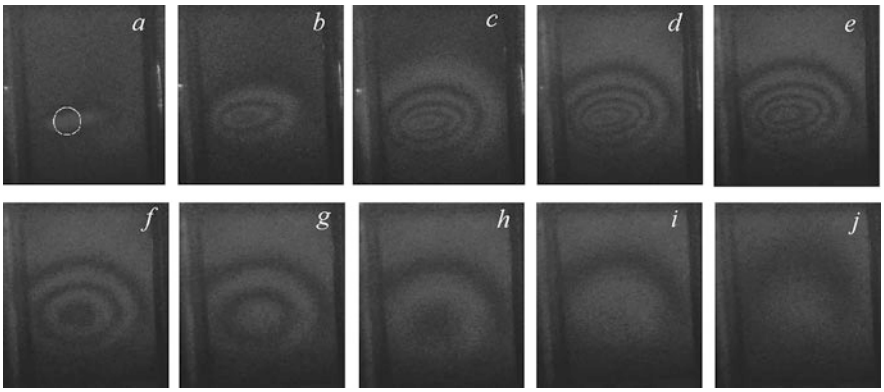

Fig. 3.16 Holography interference snapshot from video clip images for Methylene Blue experiment arranged in seconds of illumination: (**a**) 2 s, (**b**) 10 s, (**c**) 30 s, (**d**) 59 s, (**e**) 60 s (laser is switched off), (**f**) 65 s (5 seconds later after laser is switched off), (**g**) 70 s, (**h**) 80 s, (**i**) 90 s, (**j**) 120 s

refractive index n_2. Then, the interference pattern is observed using the camcorder, the result is processed by the computer for further calculation of the refractive index difference $\Delta n = n_2 - n_1$:

$$\Delta n = \lambda N / \cos\ (\alpha/2)\,(d_2 - d_1)\,, \tag{3.1}$$

where λ is the laser wavelength, α is the observation angle, and N is the number of interference fringes in the interferogram of the cuvette at the altitude L between the segments d_1 and d_2. If it is necessary to measure new media relative to the reference one, the new hologram of the cell with the reference medium is not recorded, but the previously obtained and digitized image is used.

Another promising direction in the use of holographic interferometry methods is the investigation of photochemical reactions [23]. The holography interference images for Methylene Blue experiment are shown in Fig. 3.16. These images demonstrate a significant reaction forming five interference rings which approximately matches a modification of the refraction index by fivefolds. Preliminarily we could conclude that contributions of photochemical reactions are considerably higher than a pure heating effect. Once the green laser irradiation was switched off, in the experimental samples, the refraction index returned back to its original values within 60 s.

The long pass filter was set in front of the camera to let a minor leak of the irradiation green light to expose onto the side walls of the cuvette for monitoring the irradiation condition consistency (*a–d*). In Fig. 3.16, the laser was switched off in the frames *e–j*. The white circle in the center of the interference pattern of the first frame (*a*) is the irradiation spot location (not scaled, the diameter of the spot was 1.5 mm).

This method of studying the kinetics of photothermal and photochemical reactions is very informative and illustrative. Figure 3.17 shows a graph of the

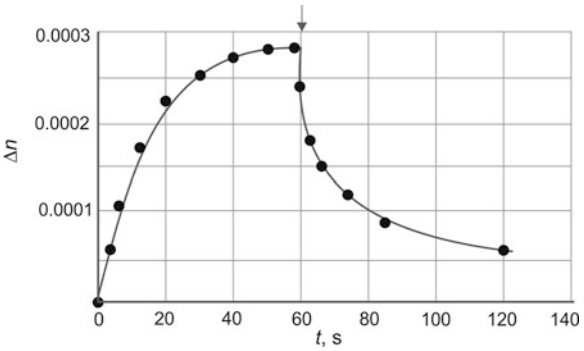

Fig. 3.17 The dependency $\Delta n(t)$ for the aqueous solution of Rhodamine C after switching on the laser with $\lambda_{irr} = 667.5$ nm at time $t = 0$ and after turning off the laser at time $t = 60$ s (the time of switching off the light is marked by a vertical arrow)

dependency $\Delta n(t)$ obtained using the interferogram image processing. It can be seen that these results are of high accuracy.

With the help of the SHI, unusual physical properties of biologically active objects were observed using the samples: (1) H_2O + dextran-graft-polyacrylamide (D-g-PAA), (2) H_2O + Au/D-g-PAA. Let us analyze these results in more detail.

3.2 Polymer Matrix

As a polymer matrix, we used a branched copolymer obtained by grafting polyacrylamide (PAA) chains onto dextran ($M_w = 7 \times 10^4$, g mol^{-1}) backbone [24] using a ceric-ion-reducing agent initiation method. This redox process initiates free radical sites exclusively on the polysaccharide backbone, thus preventing from the formation of homopolymer (PAA).

The detail of synthesis, identifications, and analysis of internal polymer structure was described in [24, 25]. The theoretical number of grafting sites per polysaccharide backbone for the sample we used as polymer nanocarrier in the present work was equal to 5, and the related dextran-graft-polyacrylamide copolymer was referred as D-*g*-PAA. The choice of this copolymer among the series of the branched samples was synthesized based on our previous research. Namely, this sample was the most efficient polymer matrices for Ag and Au sol in situ synthesis as well as for the nanoscale catalyst preparation [26–28].

3.3 Gold Nanoparticle Synthesis

The AuNPs were synthesized by the chemical reduction of Au precursor (tetrachloroauric acid). All synthesized polymers play a role of matrices capable to act as nucleating, capping, and stabilizing agents simultaneously.

A 0.012 mL tetrachloroauric acid aqueous solution ($C = 0.1$ M) was added to 0.5 mL of aqueous polymer solution ($C = 1 \times 10^{-3}$ g/cm^3) and stirred for 20 min. Then, 0.047 mL of 0.1 M aqueous solution of sodium borohydride was added. The final solution was stirred for 30 min. It turned ruby-red in color; thus the formation of Au NPs was indicated. The reduction process was performed at $T = 25$ °C.

Nanosystems were characterized by transmission electron microscopy and UV-vis spectroscopy and quasi-elastic light scattering. The size of AuNPs was 5–10 nm [28].

3.4 Experiment

Standard cuvettes filled with aqueous solutions **1** and **2** were used as the samples for investigations. The changes of the refractive index of the solutions Δn depending on the time of illumination t_{irr} with a laser (radiation wavelength was 650 nm, power was 10 mW, beam diameter was $\sim$ 2 mm) and on the time t_{rel} after turning off this laser were measured. The measurement process in sample **2** is represented by selective photographs in Fig. 3.18.

Figure 3.18 shows the appearance of a region with interference rings after turning off the laser (bright illumination). The localization of interference rings only in the region of light absorption is unusual. Therefore, there is no heat propagation after the absorption of laser radiation to other areas of the cuvette. For samples **1** and using a laser with $\lambda_{irr} = 650$ nm, such experiments were not successful due to the absence of light absorption in D-g-PAA. Holographic interferometry technique was used to measure Δn. During the whole experiment, the images of the cuvette with the solution were videotaped through the HRM. The measurement procedure was the following. First, a hologram of the cuvette with a height L with a polymer solution in water was recorded. Then a laser with $\lambda_{irr} = 650$ nm was switched on, and its beam was directed parallel to the optical table of the setup from the side opposite to

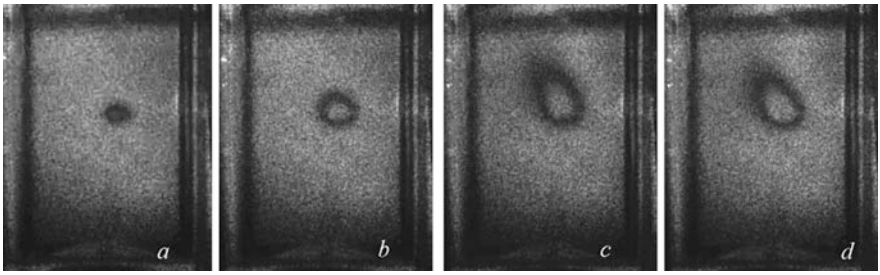

Fig. 3.18 Photographs of cuvettes with the solution during illumination with laser light $\lambda_{irr} = 650$ nm with power 10 mW: $t_{irr} = 2$ s (**a**), $t_{irr} = 4$ s (**b**), $t_{irr} = 11$ s (**c**), $t_{irr} = 15$ s (**d**)

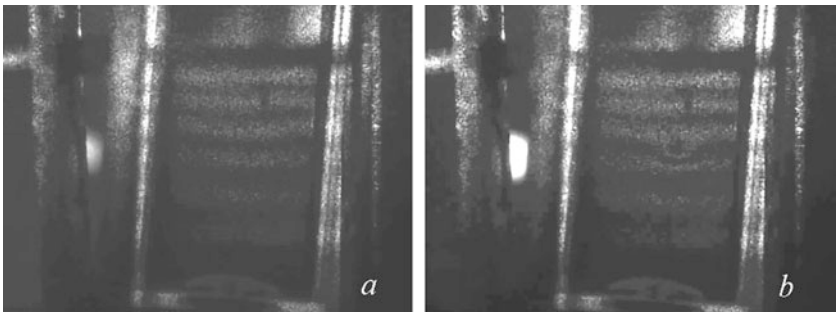

Fig. 3.19 Photographs of the interferogram of the cuvette, where the drift of interference fringes is created as a result of tilting the mirror behind the cuvette before (**a**) and after (**b**) switching on the laser with $\lambda_{irr} = 650$ nm

the cell. If a change of n occurs in the cuvette under the light action, then light and dark interference stripes are observed in the image of the cuvette (Fig. 3.18). The larger change of n provides the greater number of interference stripes. To obtain the exact value of Δn, we used the original and specially developed technique. For these purposes, immediately after registering the hologram of the cuvette and before switching on the laser with λ_{irr}, the difference of the light path of the object beam through the height of the cuvette was artificially created. To do this, the mirror creating an object beam at recording the hologram of the cuvette was simply tilted. As a result of such a procedure, parallel interference stripes appear in the cuvette image (Fig. 3.19a). The number N of interference stripes depends on the inclination angle of the mirror. Then a laser with $\lambda_{irr} = 650$ nm was switched on. If a change of n occurs in the cuvette under the light influence, then a deformation of artificially created interference stripes is observed in the image of the cuvette (Fig. 3.19b). This deformation of the interference stripes increases for greater changes of n.

The results of measurements in sample **2** are presented in Fig. 3.20.

The change of the refractive index Δn within the area of action of laser irradiation increases with increasing t_{irr}, but the characteristic relaxation time of this change $\Delta n/\Delta n_{max}$ after turning off the laser is the same for all studied samples. Moreover, the characteristic time $t_{1/2}$ estimated as the time of changing the maximum value n_{max} by two times is ~ 2 s and does not depend on the irradiation time t_{irr}, i.e., does not depend on the absorbed energy.

A similar effect is observed when a microwave source is used instead of laser irradiation. Figure 3.21 demonstrates some of these experiments in which a generator with a 40 GHz microwave frequency was used. The output of the waveguide was directly on the glass wall of the cuvette. In the photographs, this is the right wall of the cuvette with a thickness of 1 mm.

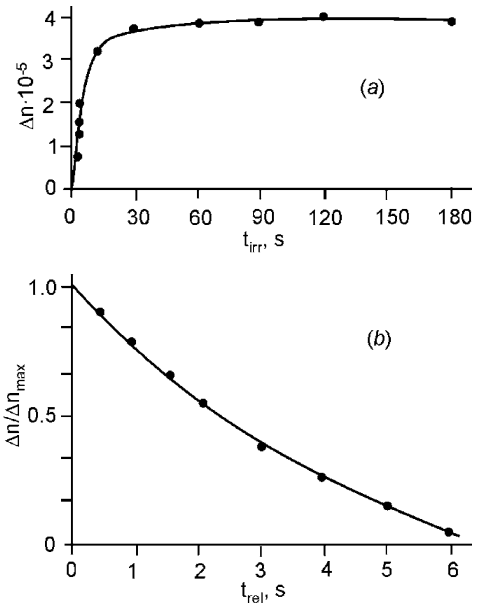

Fig. 3.20 Dependencies of changes of the refractive index Δn on the time t_{irr} (**a**) of illumination of solution **2** with a laser with $\lambda_{irr} = 650$ nm and on the time t_{rel} after switching off this laser (**b**)

It can be seen that if the cuvette is filled only with water or with an aqueous solution of the polymer D-g-PAA, then there is a change of the refractive index in almost the whole volume with the solution as a result of energy absorption from the radiation source during the time t_{irr}. In the case of an aqueous solution of Au/D-g-PAA, in the interference pattern, interference bands are localized only near the cuvette wall (in the photographs, this is the right wall) to which microwave radiation is directed. In this case, an experiment similar to as shown above in Fig. 3.7 is demonstrative. In this experiment, a cuvette filled with distilled water is used in which a resistor is placed. After the start of the passage of electric current, the resistor heats up and heat is transferred from it to the aquatic environment and heats it. Heating results in a change of the refractive index of the aqueous medium in the cuvette. This change is greater for the longer time t_i of the current passage through the resistor. Figure 3.22 shows photographs of interferograms of a cuvette filled with an aqueous solution of the polymer D-g-PAA in which a resistor of small geometric dimensions is placed. The dimension of the resistor is ~ 2 mm and is close to the cross section of the laser beam in the experiments in Fig. 3.18.

It is seen from Fig. 3.22 that the heat diffusion from a heated resistor when the electric current passes through it in an aqueous solution of the polymer D-g-PAA occurs in a significant volume of the cuvette, just as shown in Fig. 3.7. It is not limited to local volume as in the case with aqueous solutions of polymers with Au nanoparticles (Figs. 3.18 and 3.21).

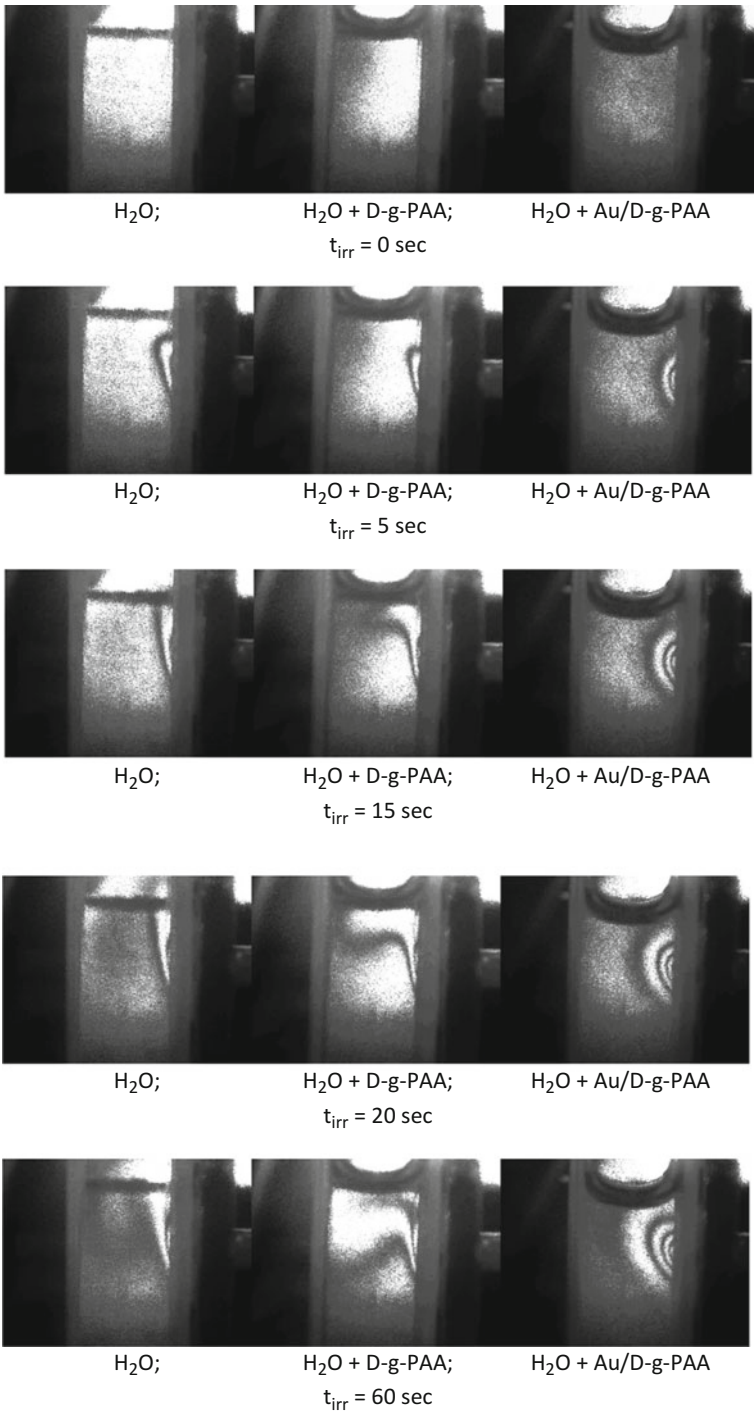

Fig. 3.21 Photographs of interferograms of a cuvette with samples H_2O, H_2O + D-g-PAA, and H_2O + Au/D-g-PAA obtained during their illumination for different t_{irr}

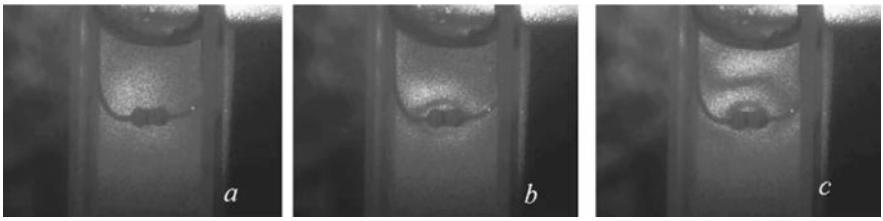

Fig. 3.22 Photographs of interferograms of a cuvette filled only with water or an aqueous solution of the polymer D-g-PAA: $t_i = 0$ (**a**), $t_i = 15$ s (**b**), $t_i = 35$ s (**c**)

3.5 Conclusions

To explain the experimental results, a phenomenological model is proposed which takes into account the features of the molecular structure of starlike dextran-graft-polyacrylamide copolymer with incorporated Au nanoparticles. Since under illumination with light with $\lambda_{irr} = 650$ nm the variation of n is observed mainly in the small volume of the cell near the laser beam transmission region, the following model consideration can be proposed:

- Absorption of laser light $\lambda_{irr} = 650$ nm occurs in Au nanoparticles. Since the fluorescence in the investigated samples is not observed and there are no reasons for photochemical transformations, it can be considered that the dissipation of all absorbed light energy happens by excitation of oscillations. Namely, all absorbed light energy is transformed into thermal energy.
- Since Au nanoparticles have a high thermal conductivity and they are placed close to fragments of polymeric molecules, it can be supposed that thermal vibrations from Au nanoparticles are transferred to the nearest similar fragments and from them to other Au nanoparticles within one large polymeric molecule. Such a stepped mechanism of transferring heat energy within one large polymer molecule must also take into account the energy dissipation to excite vibrations of H_2O molecules located inside the free space of the polymer molecule.
- After thermal excitation of an individual polymer molecule with Au nanoparticles, excitation of vibrations of neighbor H_2O molecules and further excitation of neighboring polymer molecules occur. Therefore, as a result of this cascade process, the aqueous medium in the cell is not immediately heated but only after the local heating of the polymer molecules with Au nanoparticles where the light was absorbed.
- In our experiments, the change of n is observed mainly from the change of n of the aqueous medium. Therefore, this change is seen only near the volume in the cell where the laser light with $\lambda_{irr} = 650$ nm is absorbed.

Acknowledgments With the support of the Military and Research Directorate of the General Staff of the Armed Forces of Ukraine.

References

1. Getmanchuk YP, Davidenko NA, Kunitskaya LR, Mokrinskaya EV (2013) Information media based on electron donor oligomers. Polym Sci Ser B 55(1-2):88–94
2. Davidenko NA, Dekhtyarenko SV, Getmanchuk YP et al (2009) Photosemiconducting properties of holographic media based on ferrocenyl-containing cooligomers of glycidyl carbazole with these oligomers sensitized organic dye. Semiconductors 43(11):1473–1478
3. Getmanchuk YP, Davidenko NA, Davidenko II et al (2015) Effect of the structure and content of carbazolyl-containing co-oligomers on the diffraction efficiency of holographic recording media. Theor Exp Chem 51(1):60–63
4. Getmanchuk YP, Davidenko NA, Davidenko II et al (2015) Effect of oligomer structure on the diffraction efficiency of holographic recording media. Theor Exp Chem 51(2):104–108
5. Davidenko N, Davidenko I, Ishchenko A et al (2012) Reversible holographic recording media based on polymeric composites and their use in energy-saving technologies. Appl Opt 51:48
6. Getmanchuk YP, Davidenko NA, Kunitskaya LR et al (2013) Peculiarities of holographic media based on electron donor oligomers of linear and radial structures. High Energy Chem 47(4):182–186
7. Davidenko NA, Ishchenko AA, Kostenko LI et al (2005) Holographic recording media based on systems with intramolecular and intermolecular charge transfer. High Energy Chem 39(4):254–262
8. Nastas AM (2003) Diffraction efficiency and light-scattering power of photothermoplastic holographis gratings. Opt Spectrosc 95(6):952–955. https://doi.org/10.1134/1.1635482
9. Davidenko NA, Getmanchuk YP, Mokrinskaya EV et al (2014) Information media based on electron donor oligomers with different structures. Appl Opt 53:B242
10. Davidenko NA, Derzhipol'skii AG, Melenevskii DA et al (2005) Forming a latent associative image in photothermoplastic media in comparison with an image in a photorefractive crystal. J Opt Technol 72(10):754–758
11. Panasyuk LM, Nastas AM (2003) Image recording on photothermoplastic media with different thicknesses of the thermoplastic layer. Opt Spectrosc 94(6):959–961. https://doi.org/10.1134/1.1586751
12. Chirita A (2010) Real-time scaling of micro-objects by multiplexed holographic recording on photo-thermoplastic structure. J Mod Opt 57:854
13. Davidenko NA, Ishchenko AA, Pavlov VA et al (2007) Holographic recording in thermoplastic medium with organic dyes of different polarity. Ferroelectrics 353:100–105
14. Chirita A, Galstean T, Caraman M et al (2013) Photo-thermo-plastic media based on chalcogenide glassy semiconductors for real-time holography. J Optoelectron Adv Mater 7(3-4):293
15. Davidenko NA, Dehtarenko SV, Getmanchuk YP et al (2011) Sensitization of photosemiconducting properties of holographic recording media based on glycidylcarbazole cooligomers by organic dyes. Mol Cryst Liq Cryst 535:148–155
16. Davidenko NA, Davidenko II, Studzinsky SL et al (2016) Some features of information properties of holographic recording media based on a photoconducting carbazolyl-containing oligomer doped with an organic electron acceptor. Appl Opt 55(12):B31–B35
17. Davidenko NA, Spitsyna NG, Lobach AS et al (2008) Sensitization of photosensitivity of photothermoplastic holographic recording media by metal (Zinc, Disprosium) mono- and diphthalocyanines in the presence of praseodymium sesqioxide. High Energy Chem 42(1):45–50
18. Barachevsky VA (2018) The current status of the development of light-sensitive media for holography (a review). Opt Spectrosc 124(3):373–407. https://doi.org/10.1134/S0030400X18030062
19. http://photonics.kiev.ua

20. Davidenko NA, Davidenko II, Pavlov VA et al (2018) Photothermoplastic recording media and its application in the holographic method of determination of the refractive index of liquid objects. Appl Opt 57(8):1832–1837. https://doi.org/10.1364/AO.57.001832
21. Reid GT (1986) Automatic fringe pattern analysis. A review. Opt Lasers Eng 7(7):53–68
22. Yamaguchi I, Kato J, Ohta S, Mizuno J (2001) Image formation in phase-shifting digital microscopy. Appl Opt 40(34):6177–6186
23. Davidenko N, Mahdi H, Zheng X et al (2018) Holographic interferometry imaging monitoring of photodynamic (PDT) reactions in gelatin biophantom. Proc SPIE 10612:106120H. https://doi.org/10.1117/12.2305576
24. Kutsevol NV, Chumachenko VA, Rawiso M et al (2015) Star-like polymers dextran-polyacrylamide: the prospects of application for nanotechnology. J Struct Chem 56(5):1016–1023
25. Kutsevol N, Bezugla T, Bezuglyi M, Rawiso M (2012) Branched dextran-graft-polyacrylamide copolymers as perspective materials for nanotechnology. Macromol Symp 317-318(1):82–90
26. Bulavin L, Kutsevol N, Chumachenko V et al (2016) SAXS combined with UV-vis spectroscopy and QUELS: accurate characterization of silver sols synthesized in polymer matrices. Nanoscale Res Lett 11:35
27. Kutsevol N, Chumachenko V, Rawiso M, Shyichuk A (2016) Green synthesis of silver nanoparticles using glucose as reducing agent and dextran-graft-polyacrylamide as template. Micro Nano Lett 11(5):256–259
28. Chumachenko VA, Shton IO, Shishko ED et al (2016) Branched copolymers dextran-graft-polyacrylamide as nanocarriers for delivery of gold nanoparticles and photosensitizers to tumor cells. In: Fesenko O, Yatsenko L (eds) Nanophysics, nanophotonics, surface studies, and applications, vol 183. Springer Proceedings in Physics, pp 379–390. https://doi.org/10.1007/978-3-319-30737-4_32

Chapter 4
Development of the Waveguide Photonic Crystal Structures Formed by Distribution of Nanoparticles in Polymer Matrix

V. Hryn, O. Sakhno, A. Bendziak, V. Fito, P. Yezhov, and T. Smirnova

4.1 Introduction

Waveguide photonic crystal (PC) structures possess the anomalous resonant phenomena termed guided-mode resonance, which manifests itself as a series of strong peaks in reflection (transmission) spectrum of the structure. The central wavelengths of these peaks can be changed by varying PC structure parameters and environment permittivity. Such PC structures can be used for chemical and biological sensing of analytes deposited on PC surface by monitoring the resonance wavelength shift.

Nowadays, the main considered candidates for polymer-based sensors are 1D and 2D relief structures (e.g., [1–4]) fabricated by the techniques adopted from the microelectronics. Their fabrication procedures (UV or electron beam lithography, nanoimprinting, hot or UV embossing, reactive ion etching, etc.) are complicated and rather expensive. In addition, it is difficult to achieve the homogeneity of the grating over the entire surface with the mentioned methods. Grating grooves may vary in depth and shape that causes spectral widening of resonance peaks and decrease of reflection coefficient and, consequently, reduces the sensitivity of the sensor. As an alternative, we propose to develop the resonant waveguide PC structures with volume periodic modulation of permittivity and flat surface, which

V. Hryn · P. Yezhov · T. Smirnova (✉)
Coherent and Quantum Optics Department, Institute of Physics, National Academy of Sciences of Ukraine, Kyiv, Ukraine
e-mail: smirnova@iop.kiev.ua

O. Sakhno
Fraunhofer Institute for Applied Polymer Research, Potsdam-Golm, Germany

A. Bendziak · V. Fito
Lviv Polytechnic National University, Lviv, Ukraine

© Springer Nature Switzerland AG 2019

O. Fesenko, L. Yatsenko (eds.), *Nanophotonics, Nanooptics, Nanobiotechnology, and Their Applications*, Springer Proceedings in Physics 222,
https://doi.org/10.1007/978-3-030-17755-3_4

can be fabricated using photosensitive polymer-based nanocomposites containing inorganic nanoparticles (NPs) of different nature. This approach possesses a number of advantages. Volume structures can be fabricated by a one-step holographic lithography method that enables the production of large-sized PC structures with excellent homogeneity and easily varied symmetry and period. The permittivity (refractive index) modulation of these materials is achieved due to redistribution of the nanocomposite components during holographic patterning [5]. The structures comprising the NPs of different nature possess specific physical and optical properties, i.e., plasmon resonances and optical nonlinearity, which can enhance the sensitivity of sensors. The structures with a flat surface do not mechanically alter the deposited biological objects thus keeping their fluorescent properties intact. All these open perspectives to increase the sensitivity of sensors based on volume PC structures.

The goals of our work are (i) the theoretical analysis of resonant properties of volume PC structures and their dependence on the structure and material parameters and (ii) the development of waveguide PC structures formed in nanocomposites as a result of the NPs distribution within polymer matrix.

4.2 Theoretical Analysis of Resonant Properties of PC Structures

4.2.1 Some Features of Theory of the Plane Waves Diffraction in Sinusoidal Volume Gratings

Figure 4.1 explains the light diffraction by a volume phase grating with the thickness value d. To get a coupled wave resonance, that is the basis of the sensor's operation, the waves diffracted to the $\pm$1st order of the grating should propagate like in a waveguide.

From the diffraction theory in the gratings, in accordance with RCWA [6], the following relations must be fulfilled:

$$k_{0x} + |K| = k_{1x} - \text{first-order diffraction condition}, \tag{4.1}$$

$$k_{0x} - |K| = k_{-1x} - \text{negative first-order diffraction condition}. \tag{4.2}$$

These relations can be expressed through the incidence angle ϕ, diffraction angles in the $\pm$ first orders θ_1 and θ_{-1}, respectively, and wavelength λ:

$$2\pi n_0 \sin\phi/\lambda + 2\pi/\Lambda = 2\pi n_1 \sin\theta_1/\lambda, \tag{4.3}$$

$$2\pi n_0 \sin\phi/\lambda - 2\pi/\Lambda = 2\pi n_1 \sin\theta_{-1}/\lambda. \tag{4.4}$$

In order for the multilayer structure shown in Fig. 4.1 to become a non-symmetric waveguide, in which excitation of localized waveguide modes is possible, the

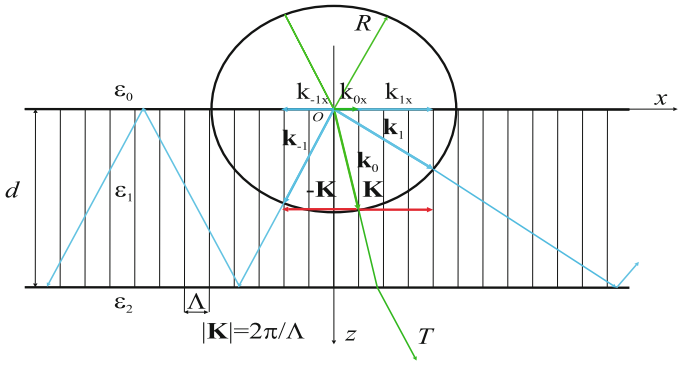

Fig. 4.1 Vector diagram of the beam propagation in the grating-waveguide: Λ, grating period; d, grating thickness; $\mathbf{K}$, reciprocal grating vector; $|\mathbf{K}| = 2\pi/\Lambda$; ε_0, dielectric permittivity of the environment; ε_1, dielectric permittivity of the grating medium; ε_2, dielectric permittivity of the substrate; $\mathbf{k}_0$, wave vector of the zero-order diffracted wave; $\mathbf{k}_1$, wave vector of the first-order diffracted wave; $\mathbf{k}_{-1}$, wave vector of the negative first-order diffracted wave; k_{0x}, k_{1x}, k_{-1x}, projections of wave vectors $\mathbf{k}_0$, $\mathbf{k}_1$, $\mathbf{k}_{-1}$ on $0x$ axis, respectively; R, reflection coefficient of the grating; T, transmittance coefficient

following conditions must be satisfied $\varepsilon_1 > \varepsilon_2 > \varepsilon_0$ or the corresponding relation for the refractive index $n_1 > n_2 > n_0$. This means that the waves diffracted in the $\pm$ first orders do not leave the grating because of the total internal reflection on the interfaces environment/medium and medium/substrate. Only re-diffracted waves propagate under the same diffraction angles as zero-order diffracted waves. In order for the resonance of waveguide modes to occur, the projection of the wave vector $\mathbf{k}_{\pm 1}$ on the axis $0x$ should be equal to the propagation constant of the waveguide mode.

$$2\pi n_0 \sin\phi/\lambda \pm 2\pi/\Lambda = 2\pi n_1 \sin\theta_{\pm 1}/\lambda = \pm\beta. \tag{4.5}$$

Equation (4.5) is greatly simplified if angle $\phi = 0$.

$$2\pi/\Lambda = \beta. \tag{4.6}$$

This relation is fundamental to our next research and computer calculations.

4.2.2 *Propagation Constants of Localized Waveguide Modes and Its Relations with Wavelength*

To find the propagation constants of the planar waveguide as well as multilayer and gradient ones, numerical methods based on a wave equation solution in frequency domain were developed [7, 8]. In all these methods, propagation constants and

corresponding field distributions can be calculated in one computing cycle. If waveguide parameters are known, for a given wavelength λ_0, we will have several propagation constants: $\beta_0 > \beta_1 > \beta_2 > \ldots > \beta_{N-1}$. The number of the waveguide modes, N, increases with an increase in the waveguide thickness d. All calculated propagation constants (for a given wavelength) satisfy the following condition:

$$2\pi n_2/\lambda < \beta_j < 2\pi n_1/\lambda, \tag{4.7}$$

where j changes from 0 to N–1.

On the other hand, each propagation constant for a given waveguide β_j can be matched to a certain number of the wavelengths λ_r, and in each set of wavelengths corresponding to the propagation constant β_j, λ_0 is always present [9]. The wavelengths λ_r for the given β satisfy this condition:

$$2\pi n_2/\beta < \lambda_r < 2\pi n_1/\beta. \tag{4.8}$$

If we take into account that for a certain value of β we form a grating with a period Λ, which is already the same for all wavelengths, then on the basis of expressions (4.6) and (4.8) we obtain a new important relation:

$$n_2\Lambda < \lambda_r < n_1\Lambda. \tag{4.9}$$

Formula (4.8) defines a range of wavelengths in which the resonance wavelengths exist at a given grating period.

4.2.3 *Waveguide Resonance Conditions at Small Incidence Angle of the Plane Wave*

The situation is a little more complicated, if the light beam falls on a grating at the angle $\phi \ll 1$. Obviously, the wavelength of the waveguide resonance will be changed as well as the propagation constants. On the basis of the expression (4.5), we can write:

$$\frac{2\pi n_0 \sin\phi}{\lambda_0 + \delta\lambda} + \frac{2\pi}{\Lambda} \cong \beta_{0i} + \frac{d\beta}{d\lambda}\delta\lambda. \tag{4.10}$$

After simple mathematical transformations, taking into account the expression (4.6) and condition $0 < \phi \leq 1$, we will find that the change in the wavelength of the waveguide resonance is equal to:

$$\delta\lambda \cong \frac{2\pi n_0}{\lambda_0}\sin\phi / \frac{d\beta}{d\lambda}. \tag{4.11}$$

The approximate value of the resonant wavelength can be found using the following expression:

$$\lambda_{res} \cong \lambda_0 + \delta\lambda. \tag{4.12}$$

Values $d\beta/d\lambda$ may be found using the numerical method [7]. We use the approximate value λ_{res} in RCWA to find the exact value of the waveguide resonance wavelength, at which the reflection coefficient is equal to 1.0.

4.2.4 *Results of the Numerical Modeling of the Waveguide Resonance*

Figure 4.1 shows a volume phase grating. The refractive index of the grating medium changes along x-axis by the following equation:

$$n_1(x) = n_{10} + \tilde{n}\cos\left(\frac{2\pi}{\Lambda}x\right) \tag{4.13}$$

Respectively, the dielectric constant of the grating medium will be equal to:

$$\varepsilon_1(x) = n_{10}^2 + 0.5\tilde{n}^2 + 2\tilde{n}n_{10}\cos\left(\frac{2\pi}{\Lambda}x\right) + 0.5\tilde{n}^2\cos\left(\frac{4\pi}{\Lambda}x\right), \tag{4.14}$$

where n_{10} is average refractive index of the grating medium and $\tilde{n}$ is refractive index amplitude modulation. We used the following parameters in our analysis: $\tilde{n} = 0.01$, $\varepsilon_0 = n_0^2 = 1$, $n_{10} = 1.561$, $\varepsilon_{20} = 2.436771$, $n_3 = 1.5147$, $\varepsilon_3 = n_3^2 = 2.29431609$.

Using the grating with parameters shown above and the thickness d =1 μm, we calculated the propagation constants for the light wavelength is 0.6328 μm. The calculations were performed using the method described in [8, 9]. We found that such waveguide has one propagation constant $\beta_0 = 15.32944476\,\mu m^{-1}$. Obviously, the wavelength of 0.6328 μm will be the initial approximation to calculate an exact wavelength of the waveguide resonance in the grating. For this purpose, we have used rigorous coupled-wave analysis, RCWA. We have found that the waveguide resonance occurs at wavelength 0.63278308 μm; the difference between an approximate and an exact value is 0.000017 μm.

Figure 4.2a shows the spectral dependence of reflection coefficient R on the wavelength of the incident wave. Figure 4.2b shows the distribution of the electric field strength along one grating period. Spectral width of the reflection coefficient is equal to $\Delta\lambda = 1.2 \times 10^{-6}\,\mu m$ that is very narrow. If we increase a waveguide thickness to 2 μm, then two waveguide modes will propagate in it with $\beta_0 = 15.44219327\,\mu m^{-1}$, $\beta_1 = 15.27327231\,\mu m^{-1}$. Respectively, two wavelengths correspond to each propagation constant; however there will be one common wavelength 0.6328 μm. The resonant wavelengths that correspond to the propagation

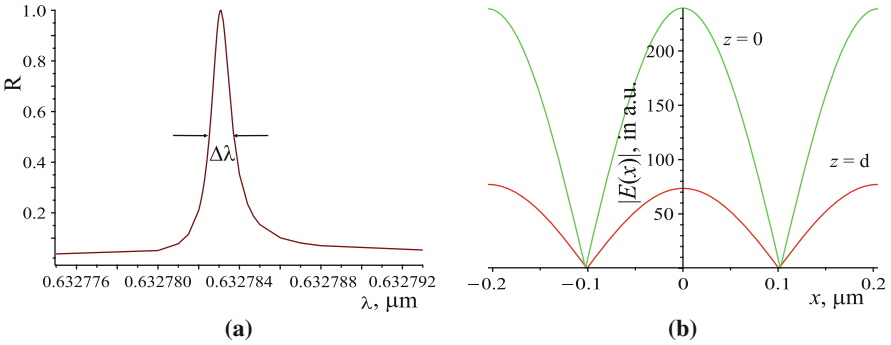

Fig. 4.2 (**a**) Spectral dependence of grating reflection. (**b**) Field distribution along grating period on the boundary with homogeneous media

constant $\beta_0 = 15.44219327\,\mu m^{-1}$ are equal to 0.63278485 and 0.62602545 μm. Respective Δλ will be equal to 0.2×10^{-6} and 0.94×10^{-6} μm. We can assert that, if several propagation constants correspond to a certain "initial" wavelength, then we will have the corresponding number of wavelength for any propagation constant from this set, and among these wavelengths there will be a common "initial" wavelength. The inverse problem, that is, finding the wavelengths that correspond to the propagation constant, is described in [8]. These calculations show that increasing the thickness of the grating increases the number of resonant wavelengths; the spectral width of the resonance response decreases. Also, the width of the resonance curve decreases with a decrease in the modulation coefficient $\tilde{n}$ of the refractive index of the grating.

4.3 Technology for the Fabrication of the Waveguide Layers with the Thickness of ≤2 μm Using Photosensitive Polymer Nanocomposites

The required thickness of the layer for holographic recording of the PC structures was selected according to the theoretical predictions obtained in Part 2. It has been shown that increasing in the layer thickness leads to an increase in the number of resonance peaks and to a decrease in the distance between them. The spectral distance of about 2–3 nm was predicted for the layer thickness of 5 μm. The broadening of the peaks up to several nanometers, which can be caused by various factors (like a limited size of the grating or divergence of testing light wave, incident on the structure), will lead to their overlapping and, correspondingly, to the decrease in the sensitivity of the sensor. Thus, the PC structures with a thickness of 1–2 μm are the most suitable for effective operation of the sensors.

Usually for the fabrication of thin-film waveguide layers, the solutions of polymers in proper solvents are typically used. In the current case, thin layers of homogeneous thickness must be fabricated applying a low-viscous photocurable monomer blend (without any solvent) in order to provide following holographic patterning of the samples. The fabrication of the layers of controllable and reproducible thickness and good thickness uniformity by applying proposed composites is a great challenge. Therefore, different preparation methods have been tested. We have proposed and investigated basically three methods for the fabrication of thin ($d \leq 2\,\mu$m) layers based on organic-inorganic nanocomposites:

1. spin-coating of the nanocomposite layers deposited on glass substrate;
2. filling a cell consisting of two glass substrates with a capillary gap between them;
3. formation of a layer between two substrates with the help of a hydraulic press with a controlled load.

Note that the oxygen presented in air inhibits the polymerization process. This creates additional difficulties by the fabrication of thin photosensitive layers based on photopolymer composites. The study of all methods was performed using a model holographic composite PPC-488, previously developed in IP NASU [10], the organic-inorganic nanocomposite (NC), and the organic matrix of the NC (UV photocurable monomer mixture). The organic-inorganic nanocomposites were developed some years ago in the cooperation between Institute of Physics NASU and Fraunhofer Institute for Applied Polymer Research [5, 11]. The photosensitive NCs consist of a blend of two acrylate monomers of different functionality (of about 70–80 wt.%), inorganic nanoparticles (NPs) of proper parameters (30–20 wt.%) and a small amount of a UV or vis photoinitiator (PI). We used the commercial NPs CANdot Serie X (CAN GmbH, Hamburg).

4.3.1 Spin-Coating of Photosensitive Composites

Two methods for obtaining waveguide periodic structures were considered: fabrication of a thin photosensitive layer with open surface on a glass substrate with the following polymerization (holographic recording) in the inert gas atmosphere and using a second substrate protecting a photocurable layer for holographic patterning in air atmosphere. As the materials for the film preparation, the NC matrix (a mixture of two acrylate monomers with UV photoinitiator (PI)) and the same NC matrix but with 50% solvent (pentane) were used in the first case. After spin-coating procedure the monomer layer with open surface was polymerized using UV exposure in the argon atmosphere (Fig. 4.3a). Polymerization conditions: lamp intensity 40 mW/cm^2, emission spectral range 315÷420 nm, exposure time 250 s. The thicknesses of the final films were measured using Profiler Dektak Veeco 150. The glass substrates applied possess a standard surface quality; the substrates with only chemical cleaning as well as with chemical cleaning and following O_2 1 min plasma treatment, (PlTr) were tested. Application of PlTr to the glass substrates

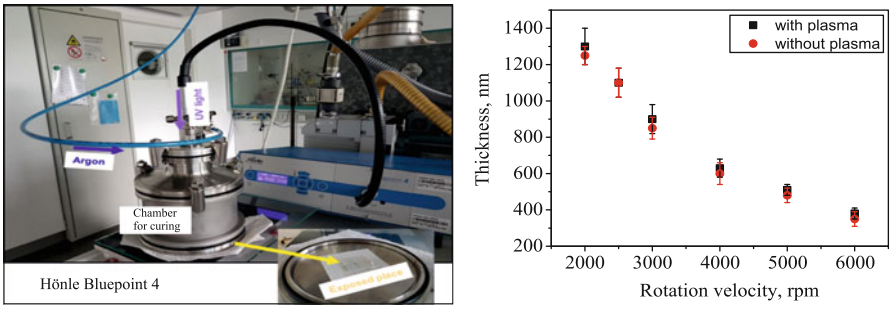

(a) **(b)**

Fig. 4.3 (**a**) Polymerization in the argon atmosphere. (**b**) Dependence of the film thickness on the rotation velocity (rpm) for the substrates with and without of plasma treatment

provides almost complete covering of the substrate with the material and strong adhesion of the polymer/substrate interface. In the case of the substrates without PlTr, a not complete covering of the substrate with the material is usually observed. The adhesion of the film to the substrate is slightly weaker compared to the substrates with PlTr. According to the profiler measurements, the thicknesses of the films deposited of the substrates with and without PlTr differ only slightly: the samples with PlTr are a little thicker than the samples without a PlTr (Fig. 4.3b). For example, the samples made using spin-coating by 2000 rpm speed and a material volume 10 μL provided the thickness d of 1.35 ± 0.1 μm and 1.4 ± 0.15 μ on the distance of about 15 mm, with and without a PlTr, respectively. In order to obtain the thickness of the film of a ∼1 μm, the velocity of spin-coating should be in the range of 2500–3000 rpm (Fig. 4.3b). The reproducibility of the thickness and the surface roughness at these velocities were similar for the substrates with and without PlTr. The thickness deviations of about 50–150 nm were usually observed for different samples at a distance of 15 mm over the sample. The disadvantage of the PlTr procedure is that the samples with a photosensitive film must be cured almost immediately after the treatment. Applying a solution of the NC matrix in a solvent provides bad thickness reproducibility at the selected rpm range (2000–5000 rpm).

For holographic recording in the air atmosphere, a low-viscous spin-coated composite layer on a glass substrate was covered with a second glass substrate with an anti-adhesive coating and then exposed to an uniform UV radiation or to the interference pattern with $\lambda_{rec} = 472$ nm. After a complete curing of the film, a pre-treated substrate was removed. In these experiments we used a photopolymer composition PPC-488 [5], as a model medium. Since the viscosity and the holographic characteristics of the PPC-488 are close to the nanocomposites characteristics, it can be also used for the production of the PC structures.

The thickness of the layer was measured using a micro-interferometer with CCD of a microscope. The results of the measurements are shown in Fig. 4.4. Since only a

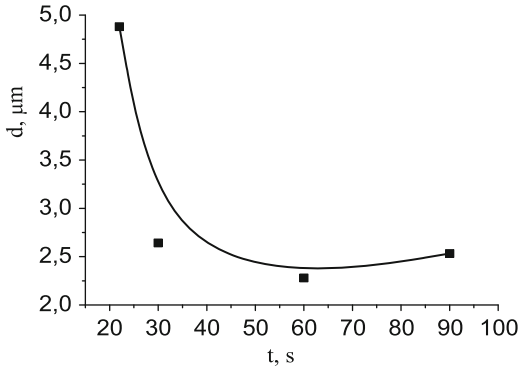

Fig. 4.4 Dependence of film thickness on a rotation time. Rotation velocity: 3000 rpm

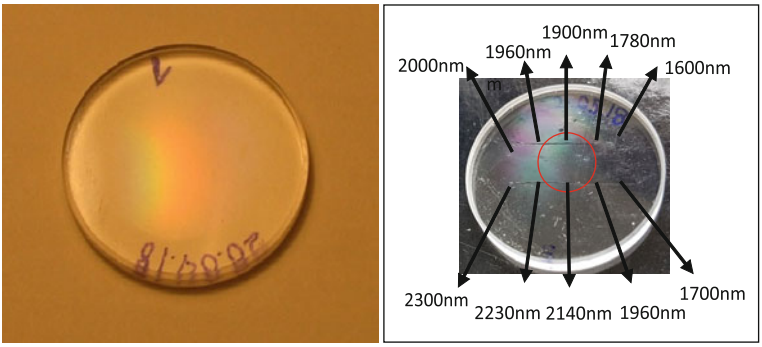

Fig. 4.5 (**a**) Holographic volume grating on a glass substrate. (**b**) Measurements of the thickness of the film at different points: thickness is varied from 1.9 to 2.2 μm at a distance of about 10 mm

rotation velocity of 3000 rpm was available, the minimal layer thicknesses obtained were (2.10÷2.30 μm) ±0.01 μm at a spin-coating time t = 60 s. The final thickness of the films depends on the spin-coating rotation time. Using the layers with a thickness of 2.1 μm, the volume gratings were fabricated by holographic method in order to demonstrate that this layer thickness provides the formation of an effective PC structures (Fig. 4.5a).

It was found that the measurement results made with a micro-interferometer and a profiler are very similar and evident a formation of a small wedge of the film (Fig. 4.5b). The measurements of the sample surfaces showed that the quality of the surface in the case of this modified spin-coating method is better compared to that of the samples made by a spin-coating and curing with an open surface.

4.3.2 *Filling a Cell Consisting of Two Substrates with a Capillary Gap Between Them*

The second tested preparation method was the formation of thin monomer layers in glass cells filled with a nanocomposite. A glass cell was formed with a pair of binder clips without using any spacers, and the material fills into a gap due to the capillary forces (Fig. 4.6a). The substrates of a standard quality were used. In order to ensure a free film surface after polymerization, one of the substrates used for the formation of a cell was previously treated with a special hydrophobic substance. The filled glass cells were exposure to UV lamp or interference pattern. A conventional two-beam interference scheme based on an optically pumped solid-state laser with $\lambda_{em} = 335$ nm was used for the holographic recording of volume gratings with period of 1.1 μm. After the polymerization (recording) completing a treated substrate was easily removed, and the sample thickness was measured with a profiler. This fabrication method provides enough low reproducibly of the film thickness; the samples with the average thickness from 2 up to 6 μm, using substrates of standard quality and a material volume of 2–3 μL, were fabricated. Applying the substrates with polished surface provides better thickness reproducibility. Generally, the formation of a wedge layer was observed of all tested samples. The thickness variations of about 0.5–1.5 μm on a sample distance of 15 mm were found using different samples.

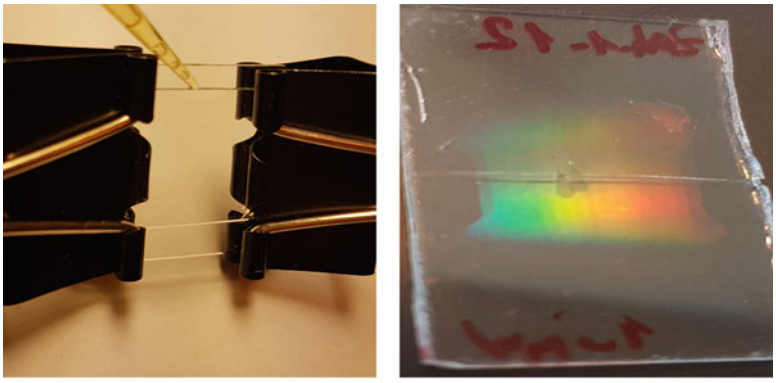

(a) (b)

Fig. 4.6 (**a**) Filling glass cell with a nanocomposite due to the capillary forces. (**b**) Transmission volume grating, thickness $d = 4\,\mu m$

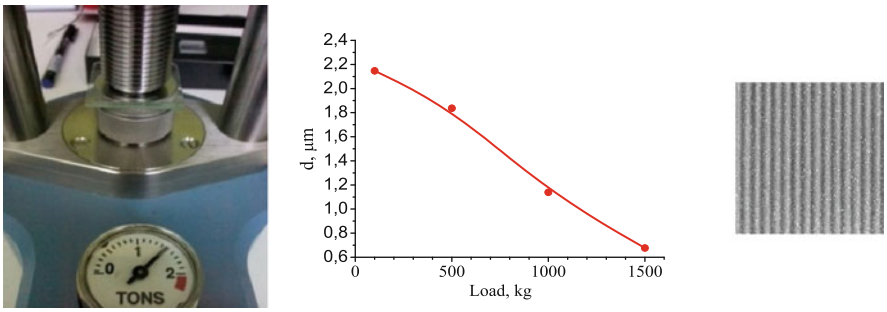

Fig. 4.7 (**a**) Recording layer under the press; (**b**) thickness of polymer film via a load; (**c**) microscopic image of grating with thickness 1.15 ± 0.01 μm (load is 1000 kg); structure period is 3.3 μm

4.3.3 The Pressing Method

In this section, we consider the fabrication of thin photosensitive layers by crushing a layer of nanocomposite between substrates. This technology includes the following steps: (i) deposition of a PPC dosed drop (3.5 μL) on a substrate and it's covering with a second substrate, pre-treated by an anti-adhesive substance; (ii) formation of recording layer by a hydraulic press with a controlled load (Fig. 4.7a); (iii) exposure of the sample to homogeneous UV radiation or interference pattern; and (iv) removing of a pre-treated substrate. We used chemically purified substrates with a size 25 × 25 mm. The layers were pressed at room temperature. The dependence of the layer thickness on a load is shown in Fig. 4.7b. With an increasing load, the thickness varies from 2 to 0.7 μm in the range of a 100–1500 kg load. The uniform loading provides a high homogeneity in thickness (no wedge) for the grating with a diameter of 20 mm. A test holographic recording using the nanocomposite described above confirmed the possibility of the grating formation in a layer with a thickness of approximately 1 μm (Fig. 4.7c). The amplitude of the refractive index modulation, n_1, in fabricated structures reaches 0.01 that is a characteristic value for the used nanocomposite.

4.3.4 The Surface Topologies of the Polymer Films

The surface topology of the polymer films was controlled with help of AF-microscope. The examples of typical surface topologies of the layers fabricated with free surface and between two substrates presented above are shown in Fig. 4.8.

It was found that the final polymer films obtained using polymerization between two substrates are generally characterized by higher surface quality than the

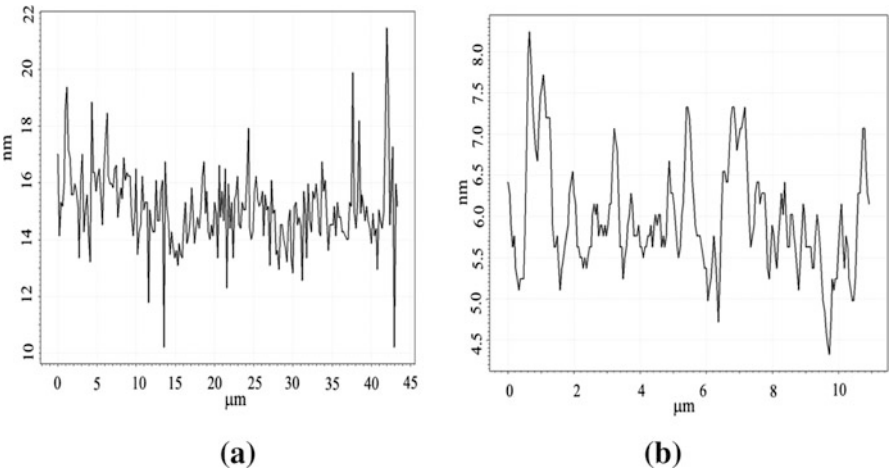

Fig. 4.8 Surface topologies (profile) of the polymer film polymerized with open surface (Y scale 10–22 nm) on plasma treatment substrate (**a**) and between two glass substrates (Y scale 4.5–8 nm) (**b**)

samples, made by polymerization of a layers with free surface in argon atmosphere. The surface roughness is equal to approximately ±1–2 nm for the closed layers and of about ±3–6 nm for the layers with open surface.

4.4 Conclusions

The developed theory of planar waveguides makes it possible to calculate the resonance wavelength, at which the reflection coefficient is close to unity, with sufficient accuracy. Using the obtained approximate value of resonance wavelength, it is possible to calculate the spectral characteristic of the reflection coefficient of a grating using RCWA and determine the resonance wavelength and spectral width of the resonance peak with higher accuracy.

The width of the resonance curve is rather narrow and is equal to $1.2 \times 10^{-6}\,\mu\text{m}$ for the $1\,\mu\text{m}$ thick grating. The width of the resonance peak decreases with the increase of grating thickness. Spectral width of the resonance peak can be increased by increasing the amplitude of refractive index modulation in the grating. Three methods for the fabrication of light-sensitive waveguide layers for holographic recording of volume photonic crystal (PC) structures were investigated: spin-coating, filling a glass cell with composite using capillary forces, and pressing.

It is established that the spin-coating and pressing methods allow obtaining the photocurable layers with a thickness of 0.5–2 μm with a sufficiently good reproducibility and with high quality of the surface. The pressing of the composition between two substrates is the simplest method for the fabrication of thin photocurable layers with high thickness uniformity.

It was shown that the polymer layers obtained by polymerization between glass substrates are characterized by higher surface quality than the layers with an open surface polymerized in an argon atmosphere. The surface roughness was found of about $\pm 1-2$ nm and to $\pm 3-6$ nm, respectively.

Holographic recording of the first PC structures in both holographic composites has shown the formation of volume structures with an enough high refractive index contrast in the layers of the indicated thickness range.

Acknowledgements This work was supported by the grant in the framework of the a Multi-years Project from the SPS Programme – SPS G5351 "Science for Peace and Security" "Nanocomposite Based Photonic Crystal Sensors of Biological and Chemical Agents" (Project 12/18–52).

References

1. Chaudhery V, George S, Lu M, Pokhriyal A, Cunningham BT (2013) Nanostructured surfaces and detection instrumentation for photonic crystal enhanced fluorescence. Sensors 13:5561–5584
2. Zhuo Y, Cunningham BT (2015) Label-free biosensor imaging on photonic crystal surfaces. Sensors 15:21613–21635
3. Nair RV, Vijaya R (2010) Photonic crystal sensors: an overview. Prog Quantum Electron 34:89–134
4. Yaremchuk I, Tamulevičius T, Fitio V, Gražulevičiūte I, Bobitski Y, Tamulevičius S (2013) Guide-mode resonance characteristics of periodic structure on base of diamond-like carbon film. Opt Commun 301–302:1–6
5. Sakhno OV, Goldenberg LM, Stumpe J, Smirnova TN (2009) Effective volume holographic structures based on organic–inorganic photopolymer nanocomposites. J Opt A Pure Appl Opt 11:024013
6. Moharam MG, Gaylord TK (1983) Rigorous coupled-wave analysis of grating diffraction – E-mode polarization and losses. J Opt Soc Am A 73(4):451–455
7. Fitio VM, Romakh VV, Bobitski YV (2014) Numerical method for analysis of waveguide modes in planar gradient waveguides. Mater Sci Medž 20(3):256–261
8. Fitio VM, Romakh VV, Bartkiv LV, Bobitski YV (2016) The accuracy of computation of mode propagation constants for planar gradient waveguides in the frequency domain. Mater Sci Eng Technol (Materialwissenschaft und Werkstofftechnik) 47(2–3):237–245
9. Fitio VM, Romakh VV, Bobitski YV (2016) Search of mode wavelengths in planar waveguides by using Fourier transform of wave equation. Semicond Phys Quantum Electron Optoelectron 19(1):28–33
10. Smirnova T, Sakhno O (2000) PPC: self-developing photopolymers for holographic recording. Proc SPIE 4149:106–112. https://doi.org/10.1117/12.402466
11. Sakhno OV, Smirnova TN, Goldenberg LM, Stumpe J (2008) Holographic patterning of luminescent photopolymer nanocomposites. Mater Sci Eng C 28:28–35

Chapter 5
Optical Phenomena in Nanoscale Tin Dioxide Films Obtained by Means of Polymers

L. Filevska, A. Chebanenko, M. Klochkov, V. Grinevich, and V. Smyntyna

5.1 Introduction

Tin dioxide (SiO_2) is one of the principal nanoscale materials for sensors and electrodes which demonstrate a number of new properties that may expand its practical applications. One such novel property of SiO_2 at nanoscale is the photoluminescence (PL) registered at room temperature.

Requirements for modern electronic display devices stimulate the search for new luminescent materials. Nanoscale forms of tin dioxide that are not classical phosphors help in solving new electronics' problems. One of these compounds is tin dioxide. In recent years, studies of the luminescence of various nanoscale forms of pure and doped SnO_2, as well as composite compounds and heterojunctions using it, have been activated. This interest is due to the promising use of such materials as phosphors [1], in light emitting diode (LED) applications [2], in solid-state optical amplifiers and tunable lasers [3], etc. Thermoluminescence of tin dioxide doped by europium [4] is used as a detection phenomenon for dosimetry purposes.

Low-temperature luminescence of crystalline tin dioxide was described in 1979 [5]. The intrinsic luminescence band of SnO_2 is located in the ultraviolet region of the spectrum (approximately 350–355 nm), [6, 7]. In the visible range, at low temperatures, wide photoluminescence (PL) bands in the range of 2 and 2.5 eV [8, 9] are observed in bulk samples of tin dioxide, which are associated with electron transitions in the interstitial tin/oxygen vacancy. With increasing temperature, the intensity of such PL decreases, and the PL becomes almost invisible at room temperature. The PL spectra of nanoscale samples of tin dioxide differ from the spectra of the bulk material, which was shown by a number of researchers [10].

L. Filevska (✉) · A. Chebanenko · M. Klochkov · V. Grinevich · V. Smyntyna
Odessa I.I. Mechnikov National University, Odessa, Ukraine

© Springer Nature Switzerland AG 2019

O. Fesenko, L. Yatsenko (eds.), *Nanophotonics, Nanooptics, Nanobiotechnology, and Their Applications*, Springer Proceedings in Physics 222,
https://doi.org/10.1007/978-3-030-17755-3_5

The number of observations of photoluminescence in a nanoscale SnO_2 at elevated temperatures increases [11–15].

Optical properties of SnO_2 films [16] are characterized by relatively high transmittance coefficients (80–90%). Optically colorless glass of mark K8, used as substrates, has a transparency of more than 90%. The maximum light absorption is no more than 20%, and the minimum is about 10%. A slight decrease in the thickness of the tin dioxide layer leads to a significant increase in the optical transmittance. At thicknesses of 0.07–0.09 μm, the average optical transmittance of tin dioxide films is 81–83%.

The study of the optical transmission spectra of SnO_2 films allows determining the coefficient of light absorption in the films. The form of the spectral dependence of the absorption coefficient makes it possible to determine the set of parameters. They are types of optical transitions, direct or indirect transitions, leading to the appearance of excess carriers in the conduction band, estimating the forbidden band as well as the degree of composition deviation from film stoichiometry.

The authors have obtained nanostructured films of tin dioxide by sol-gel method using polyvinyl acetate as a structuring additive. In this paper, the results of studies of optical absorption, reflection, and room temperature photoluminescence of the films, depending on the polymer content in the initial solution used for films' production, are presented.

5.2 The Sample Preparation Technology and Experimental Techniques

To obtain SnO_2 films by the sol-gel method, bis(acetylacetonato)dichlorotin (IV) was used as a precursor [17] and polyvinyl acetate (PVA) was used as a structuring substance [18]. The initial materials' solution in acetone was mixed in the required proportions. The resulting gel was put on glass substrates, and then high-temperature annealing was performed in air. As a result of annealing, which provides the removal of decomposition products of the PVA polymer, as well as additional oxidation, the thin layers of tin dioxide were formed. Surface profiles obtained using atomic force microscopy (AFM) showed that the surfaces of SnO_2 films have a porous columnar structure with an average transverse crystallite size of about 20 nm This indicates that the tin dioxide films obtained by the modified sol-gel method are nanostructured with a high degree of surface development.

The optical density spectra of samples of tin dioxide were measured on an SF-46 spectrophotometer. The measurement step was 10 nm in the spectral range from 350 to 1000 nm. The photoluminescence spectra were excited by the glow of a SVD-120 mercury lamp with a UFS-6 optical filter with $\lambda = 360$ nm.

5.3 Results and Discussion

Figure 5.1 shows the optical density spectra of SnO_2 films with different contents of PVA. The band gap, estimated from the slope of the absorption edge, had different values for films obtained from solutions with different polymer contents. For a film from a solution with a PVA concentration of 1%, the size of the forbidden zone was $E_1 = 3.07$ eV and for a film from a solution with a concentration of PVA of 0.1% was $E_2 = 2.98$ eV. Since large values of the forbidden band are specific for smaller crystallites (which is typical for tin dioxide and other semiconductor materials [10, 19]), it can be assumed that the size of SnO_2 nanocrystals is smaller in the first case than in the second. The reason for this is that PVA in the initial solution plays the role of a matrix that divides the space into separate cells, where the synthesis of SnO_2 nanocrystals occurs. Obviously, it is the greater the concentration of PVA, the smaller the volume of the individual cell, which limits the size of SnO_2 nanocrystals. The straightening of the indicated dependence in the coordinates $D^{1/2} - h\nu$ indicates that the indirect allowed optical transitions take place in the studied films. The obtained numerical values of the energy of the forbidden band E_1 and E_2 are lower than those of single-crystal tin dioxide. This is due to the high degree of porosity of the layers under study and the presence of an amorphous phase in them [20]. The last statement is also supported by the presence of a plateau on the curve of the optical density spectrum from the long-wave side of the absorption edge. Processes at grain boundaries with a high density of barriers and boundary

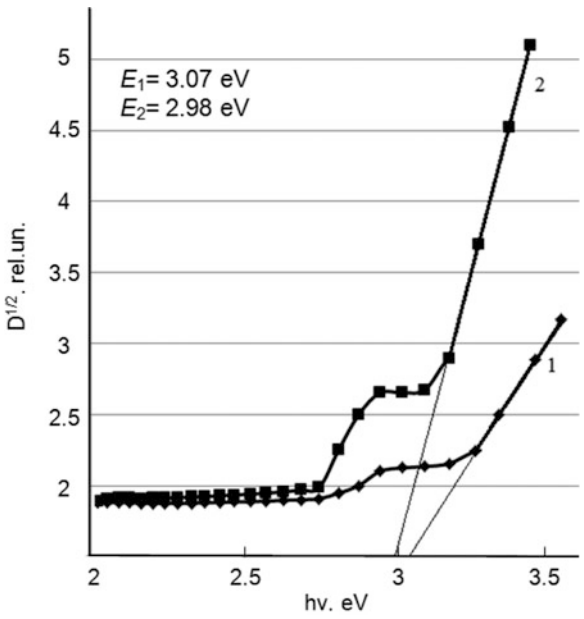

Fig. 5.1 Absorption spectra of SnO_2 films with different contents of PVA: (1) –1%, (2) –0.1%

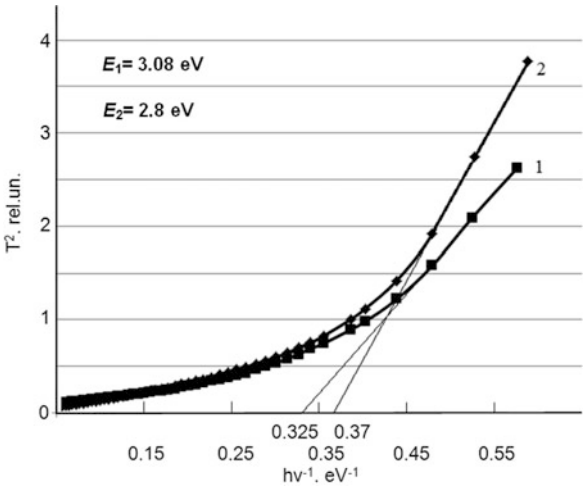

Fig. 5.2 Transmission spectra of SnO_2 films obtained from solutions with a PVA content: (1) –1%, (2) –0,1%

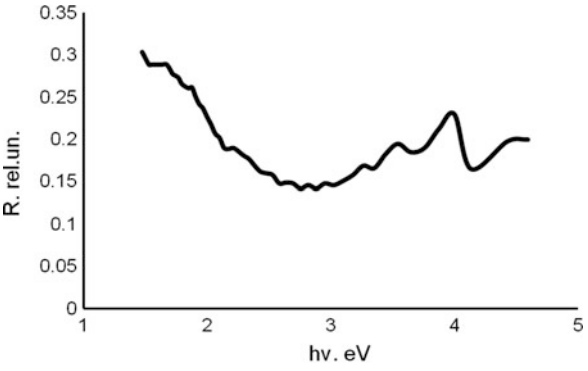

Fig. 5.3 Characteristic reflection spectrum of films SnO_2

defects that affect optical absorption can also contribute to the narrowing of the band gap.

Figure 5.2 shows the optical transmission spectra of SnO_2 with different amounts of PVA in the initial solution. The numerical values of the band gap, estimated from the transmission spectra, were 3.08 eV (for films from a solution containing 1% PVA content) and 2.8 eV (0.1% PVA). As it can be seen, these values of the band gap agree well with those determined from the absorption spectra.

Figure 5.3 shows the specific reflection spectrum of tin dioxide films under study. In the energy range $h\nu > 3$ eV, it has an oscillating character. This may be due to the interference, which appears when the film thickness is comparable to the wavelength, as it was in the case, for example, of thin films of zinc sulfide [21].

The curve of the reflection spectrum shows a minimum at $E = 2.8$ eV, which corresponds to the frequency $\omega_{\min} = 4.25 \cdot 10^{15}$ s^{-1}. The minimum of reflection in films with a relatively high carrier concentration corresponds to the absorption

of light by electron plasma with a plasmon frequency ω_p determined according to [22]

$$\omega_p = \sqrt{\frac{n_0 e^2}{m^* \varepsilon_s \varepsilon_\infty}} \tag{5.1}$$

In the above formula: m^* is the effective electron mass; e is the electron charge; and ε_s and ε_∞ are the static and dynamic dielectric constant of the semiconductor (tin dioxide in our case). The reflection minimum frequency, $\omega_{\min}$, is proportional to ω_p and is determined [23] as

$$\omega_{\min} \approx \omega_p \sqrt{\frac{\varepsilon_\infty}{\varepsilon_\infty - 1}} \tag{5.2}$$

Using (5.1) and (5.2), one can estimate the concentration of free electrons n_0 in the studied SnO_2. The following values were used for calculations [22]: $m^* = 0.59\ m_0$; $\varepsilon_s = 13{,}0$; and $\varepsilon_\infty = 24{,}0$. The obtained value of carrier concentration appeared to be equal to $n_0 = 9.4 \cdot 10^{12}\ \text{cm}^{-3}$.

Figure 5.4 shows the photoluminescence (PL) spectra of two SnO_2 samples containing different concentrations of PVA. It can be seen that the spectral position of the maxima of the PL bands does not depend on the concentration of PVA, but the

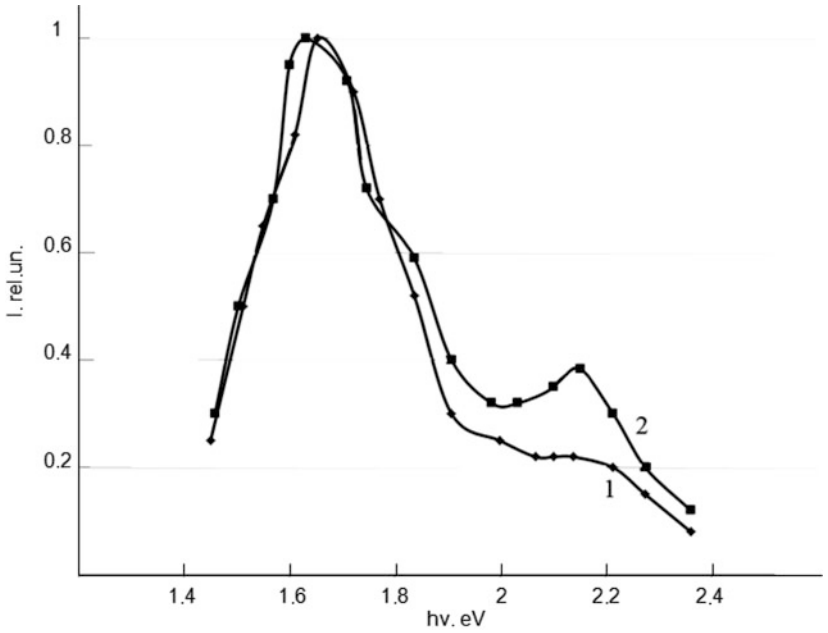

Fig. 5.4 Photoluminescence spectra of SnO_2 films with different contents of PVA in the initial solution: (1) –0.1%, (2) –1%

intensity of the band at $\lambda_{max} = 580$ nm increases with PVA concentration growth. It is known [8] that in tin dioxide, oxygen vacancies (except for donor levels associated with V_0^+ and V_0^{++}) can be mutually located with tin atoms at angles of 100° and 130°, forming centers that participate in radiative recombination. The corresponding energy levels are located at an energy distance of 1.4 eV (V_0 (100°)) and 0.9 eV (V_0 (130°) from the top of the valence band. Taking into account the energy position of the maxima of the PL bands in the SnO_2 films (1.63–1.68 eV and 2.14 eV) under study, as well as the width of the forbidden band (about 3.1 eV), the observed PL bands can be attributed to radiative transitions of electrons from conduction bands of SnO_2 to V_0 (100°) and V_0 (130°) levels, respectively.

5.4 Conclusions

The band gap of the films estimated from the reflection spectra was 2.98 eV (for 0.1% PVA) and 3.07 eV (for 1% PVA). Therefore, the size of the nanocrystals of the film obtained from the solution with a higher polymer concentration is less due to the limitation of the crystallite size by the structuring polymer molecules at the film production.

The reflection spectrum of the investigated tin dioxide film has an oscillating character in the energy region $h\nu > 3$ eV. This may be due to interference, which manifests itself at a film thickness comparable with the wavelength, as it was in the case, for example, in thin films of zinc sulfide [6]. A minimum is observed on the reflection curve spectrum at a frequency $\omega_{min} = 4.25 \cdot 10^{15}$ s^{-1}. The calculated concentration of free electrons was $9.4 \cdot 10^{12}$ cm^{-3}.

The spectral position of the maxima of the PL bands does not depend on the PVA concentration; however, the intensity of the $\lambda_{max} = 580$ nm band increases with increasing PVA concentration. Taking into account the energy position of the maxima of the PL bands in the investigated SnO_2 films (1.63–1.68 eV and 2.14 eV), and also the band gap (about 3.1 eV), the observed PL bands may be associated with the radiative transitions of electrons from the conduction band of SnO_2 to the levels of V_0 (100°) and V_0 (130°), respectively.

The results obtained are valuable as good perspective for the possible application of nanosized tin dioxide as sensors for optical signal registration.

References

1. Arai T, Adachi S (2014) Simple wet chemical synthesis and photoluminescence characterization of SnO_2:Eu^{3+} reddish-orange phosphor. J. Lumin 153(9):46–53
2. Yang Y, Li S, Liu F, Zhang N, Fang G (2017) Bidirectional electroluminescence from p-SnO_2/i-MgZnO/n-ZnO heterojunction light-emitting diodes. J. Lumin 186(6):223–228
3. Bouzidi C, Elhouichet H, Moadhen A (2011) Yb^{3+} effect on the spectroscopic properties of Er–Yb codoped SnO_2 thin films. J Lumin 131(12):2630–2635

4. Bajpai N, Khan SA, Kher RS, Bramhe N, Tiwari A (2014) Thermoluminescence investigation of sol–gel derived and γ-irradiated SnO_2:Eu^{3+} nanoparticles. J. Lumin 145(1):940–943
5. Agekyan VT (1979) Slozhny spektr exitonno-primesnykh komplexov v defektnykh kristallakh dvuokisi olova. Pis'ma v ZHETF 29(8):475–479. (The Complicated spectrum of exiton impurity complexes in the defect crystals of tin dioxide. Letters to the Journal of experimental and theoretical physics (ZHETPh) Soviet.Acad.Sc, 29(8), 475-479(1979))
6. Alhuthali A, El-Nahass MM, Atta AA, Abd El-Raheem MM, Hassanien AM (2015) Study of topological morphology and optical properties of SnO_2 thin films deposited by RF sputtering technique. J. Lumin 158(2):165–171
7. Zhu Z, Ma J, Luan C, Kong L, Yu Q (2011) Structure and photoluminescence properties of epitaxial SnO_2 films grown on α-Al_2O_3 (012) by MOCVD. J Lumin 131(1):88–91
8. Ryabtsev SV (2011) Electrofizicheskie i opticheskie svoystva razlichnykh nanoform oksida olova, Avtoreferat diss . . . . Doctor fiz.-mat, nauk, Voronezh, 2011. (Electrophysical and optical properties of different nanoforms of tin dioxide, Doctor of Sc. Thesises, Voronezh, 2011)
9. Agekyan VT, Serov AY, Filosofov NG (2014) Light emission from tin-dioxide crystals. Semiconductors 48(4):442–445
10. Meier C, Luttjohann S, Kravets VG, Nienhaus H, Lorke A, Ifeacho P, Wiggers H, Schulz C, Kennedy MK, Kruis FE (2006) Vibrational and defect states in SnO_x nanoparticles. J Appl Phys 99:113108
11. Gu F, Wang SF, Song CF, Lü MK, Qi YX, Zhou GJ, Xu D, Yuan DR (2003) Synthesis and luminescence properties of SnO_2 nanoparticles. Chem Phys Lett 372(3–4):451–454
12. Jeong J, Choi SP, Hong KJ, Song HJ, Park JS (2006) Structural and optical properties of SnO_2 thin films deposited by using CVD techniques. J Korean Phys Soc 48(5):960–963
13. Bonu V, Das A, Amirthapandian S, Dhara S, Tyagi AK (2015) Photoluminescence of oxygen vacancies and hydroxyl group surface functionalized SnO_2 nanoparticles. Phys Chem Chem Phys 17:9794–9801
14. Grinevich VS, Smyntyna VA, Filevska LM (2005) Photoluminescence of tin dioxide thin films obtained with the use of polymers. Photoelectronics 14:42–44
15. Kar A, Kundu S, Patra A (2011) Surface defect-related luminescence properties of SnO_2 Nanorods and nanoparticles. J Phys Chem C 115(1):118–124
16. Pankratov EM (1969) Tekhnologiya poluprovodnikovykh sloev dvuokisi olova, Pankratov EM, R'yumin VP, Schelkina NP, M.: Energiya, 1969 (Technology of the semiconductor layers of Tin dioxide, Pankratov EM, R'yumin VP, Schelkina NP, Moscow, Energy, 1969)
17. Ulug B, Türkdemir HM, Ulug A, Büyükgüngör O, Yücel MB, Smyntyna VA, Grinevich VS, Filevskaya LN (2010) Structure, spectroscopic and thermal characterization of bis(acetylacetonato)dichlorotin(IV) synthesized in aqueous solution. Ukr Chem J 76(7):12–17
18. Filevskaya LN, Smyntyna VA, Grinevich VS (2006) Morphology of nanostructured SnO_2 films prepared with polymers employment. Photo-Dermatology 15:11–14
19. Bisi O, Ossicini S, Pavesi L (2000) Porous silicon: a quantum sponge structure for silicon based optoelectronics. Surf Sci Rep 38:1–126
20. Grinevich VS, Serdega BK, Filevskaya LN, Smyntyna VA (2015) Nanostrukturirovannyj tonkoplenochnyj dioksid olova: metody poluchenija i opticheskie svoistva Neravnovesnye protsessy v sensornykh nanostrukturakh. Pod redaktsiey Smyntyny V.A., Odessa, ONU, 2015, 41-119. (Nanostructured thin-film tin dioxide: production methods and optical properties in the book: Non-equilibrium processes in sensory nanostructures, Smyntyna VA (ed) Odessa, Odessa Mechnikov National University, pp 41–119)
21. Krylov PN, Gil'mutdinov FZ, Romanov EA, Fedotova IV (2011) The influence of thermal annealing on the optical properties of nanocrystalline zinc sulfide films. Semiconductors 45(11):1512–1516
22. Ukhanov YI (1977) Opticheskie svoystva poluprovodnikov. Nauka, Moscow. (Optical properties of semiconductors. Moscow, Nauka, 1977)
23. Gamartz AT, Kanagaeva YM, Moshnikov VA (2005) Determination of the charge carrier concentration in lead selenide polycrystalline layers using reflectance spectra. Semiconductors 39(6):636–637

Chapter 6
Optical Properties of Polytetrafluoroethylene–Carbon Nanotube Composite in the Light Spectrum Range 320–1000 nm

I. Ye. Galstyan, M. M. Nishenko, M. M. Yakimchuk, and G. P. Prikhodko

The influence of carbon nanotube (CNT) concentration (in wt.%) on optical properties of polytetrafluoroethylene (PTFE) was investigated by the spectrophotometric analysis. The effect of transparency increasing at 4–25 times was detected in the spectrum range $\lambda = 320$–1000 nm during the addition of CNT to PTFE. It was shown that the increasing CNT concentration and the thickness of the sample lead to decreasing of the composite's transparency in the ultraviolet (UV) band and also to increasing of transparency in infrared (IR) band.

6.1 Introduction

The search for and study of new materials become relevant and are the requirements of the present time due to the need of improvement of the component basis for micro- and nanoelectronics. It is also actual in view of modernization of materials' properties by using nanostabilizers— fullerenes and nanotubes.

It is known that the changing of the properties of different materials by modification by nanobjects with sizes smaller than 100 nm (or multiple to 100 nm) leads to the appearance of features that are not characteristic of either systems themselves or nanosensitizer [1]. New composite systems have unique structural, spectral, photoconductor, and photorefractive properties and also exhibit changes in their surface properties. In the case of using of carbon nanotubes, the surface characteristics of materials change especially [2].

I. Y. Galstyan (✉) · M. M. Nishenko · M. M. Yakimchuk
G. V. Kurdyumov Institute for Metal Physics of the N.A.S. of Ukraine, Kiev, Ukraine

G. P. Prikhodko
Chuiko Institute of Surface Chemistry of the N.A.S. of Ukraine, Kiev, Ukraine

© Springer Nature Switzerland AG 2019

O. Fesenko, L. Yatsenko (eds.), *Nanophotonics, Nanooptics, Nanobiotechnology, and Their Applications*, Springer Proceedings in Physics 222,
https://doi.org/10.1007/978-3-030-17755-3_6

6.2 Materials and Methods

The samples of powder of polytetrafluoroethylene (PTFE)–carbon nanotube (CNT) composite with different concentrations of CNT (from 0 to 5 wt.%) were studied.

Nanocomposites of PTFE–CNT were prepared on the basis of SFN-1-type PTFE emulsion ($d = 1.51$ g/cm^3, mass fraction of dry basis is 55.25%) and multilayer CNTs that were purified and dispersed by cavitation. The samples of composites were obtained by mixing of PTFE (4PN20) powders with multilayer CNTs in the presence of surfactant; then the coagulation of PTFE and CNT emulsion with further hot pressing was performed.

The optical properties were investigated by the spectrophotometer ULAB 101.

6.3 Results and Discussion

The optical properties were studied for the samples of PTFE and composites of PTFE and CNT (0.05, 0.1, 0.5, 2, 5 wt.%).

Dependences of the light transmission factor in the range 320–1000 nm for PTFE films in the wide range of thickness 25–500 μm are presented in Fig. 6.1. For the

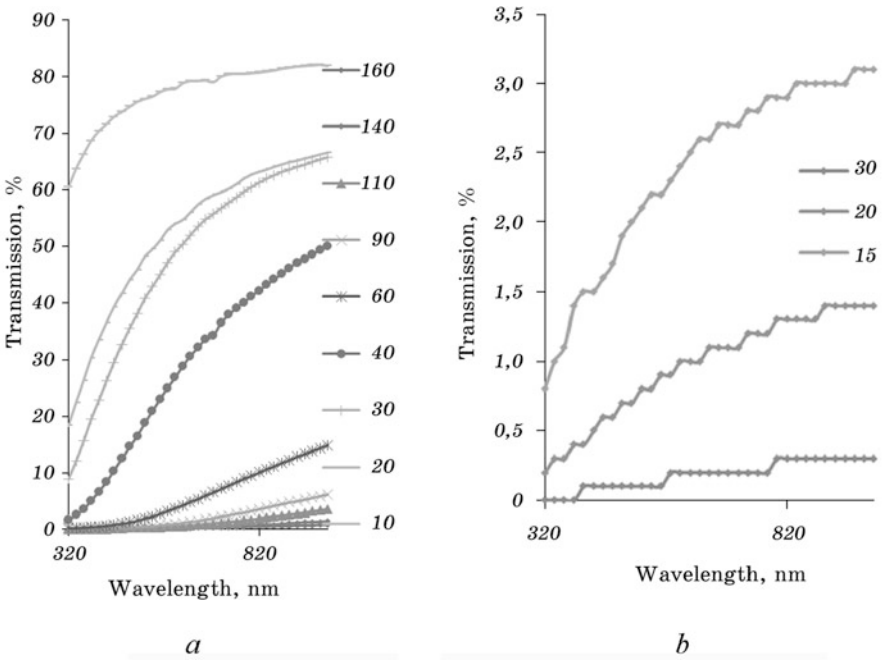

Fig. 6.1 Dependences of the light transmission factor for PTFE–CNT composites with different thickness (**a** 0.05 wt.% CNT; **b** 5.0 wt.% CNT)

thinnest (15 and 20 μm) samples, the highest transmission (80%) was observed at $\lambda = 1000$ nm. As the wavelength is reduced, the light transmission coefficient monotonically decreases to values of 38–45% at $\lambda = 320$ nm. For the samples with maximum of thickness (500 μm), the light transmittance drops to 1–2%. It should be noted that for samples with small thickness (<25 μm) the $K_{tr.} = f(\lambda)$ curves are convex but – for larger (>35 μm) thickness – the curves, on the contrary, have a concave shape. The thickness of the sample at which the inversion occurs is approximately 30 μm. Thus, at low concentrations of CNT in PTFE, the light transmission increases in the infrared (IR) band for a wide range of thicknesses, contrary to the Beer–Lambert–Bouguer law. In the ultraviolet (UV) band also, there is some brightening, but with a lesser effect.

Introduction of carbon nanotubes to PTFE polymer at concentrations of 0.05, 0.1, 0.5, 2, and 5 wt.% in general leads to the decreasing of the light transmission coefficient. The lowest value was observed, as expected, for the PTFE–CNT composite with the highest concentration of CNT (5 wt.%). For the samples with minimum thickness (15 μm), the transmission coefficient is reduced from 3% for $\lambda = 1000$ nm to 1% for $\lambda = 320$ nm. The transmittance decreases with the increase of the sample's thickness. The thickness of the sample at which the inversion of the $K_{tr.} = f(\lambda)$ curve occurs increases to 50 μm for the minimal concentration of the CNT (0.05 wt.%). For the higher CNT concentration (0.1 wt.%), this critical thickness increases up to 70 μm.

Dependences of light transmission coefficients on the thickness of the samples for the two extreme wavelengths $\lambda = 1000$ nm and 320 nm (Fig. 6.2) were constructed based on the data obtained. It is shown that in a wide range of thicknesses of samples for concentrations 0.05–0.5 wt.%, PTFE–CNT composite significantly better transmits the light in comparison to pure PTFE at thicknesses of 25–100 μm. This is especially noticeable in the IR band ($\lambda = 1000$ nm); and in the UV band, this effect is observed in a narrower thickness range (30–60 μm).

Data analysis showed that for the samples with 30 μm thickness:

- The low CNT concentrations (0.05–0.1 wt.%) lead to increase in transmission coefficient in all spectral range (320–1000 nm) from 5–25% to 10–65%.
- The high CNT concentrations (2 and 5 wt.%) lead to reduction of the transmission coefficient at many times, as could be expected.

Qualitatively a similar situation holds for samples with a thickness of 60 μm, but brightening decreases due to doubling of the thickness of the sample.

The dependences of ratio of the PTFE–CNT composite light transmission to pure PTFE light transmission from wavelength are shown in Fig. 6.3. The samples were with different CNT concentration and thicknesses – 30 μm (Fig. 6.3a) and 60 μm (Fig. 6.3b). It can be seen that the thickness of the samples has a strong effect on not only the light transmission coefficient but also on the shape of the curves of the dependences of relative transmission from the wavelength. For the samples with 30 μm thickness, the maximum of transmission was observed for the composite with 0.05 wt.% CNT concentration; and for 60 μm samples, the maximum of transmission was observed for the composite with 0.1 wt.% CNT

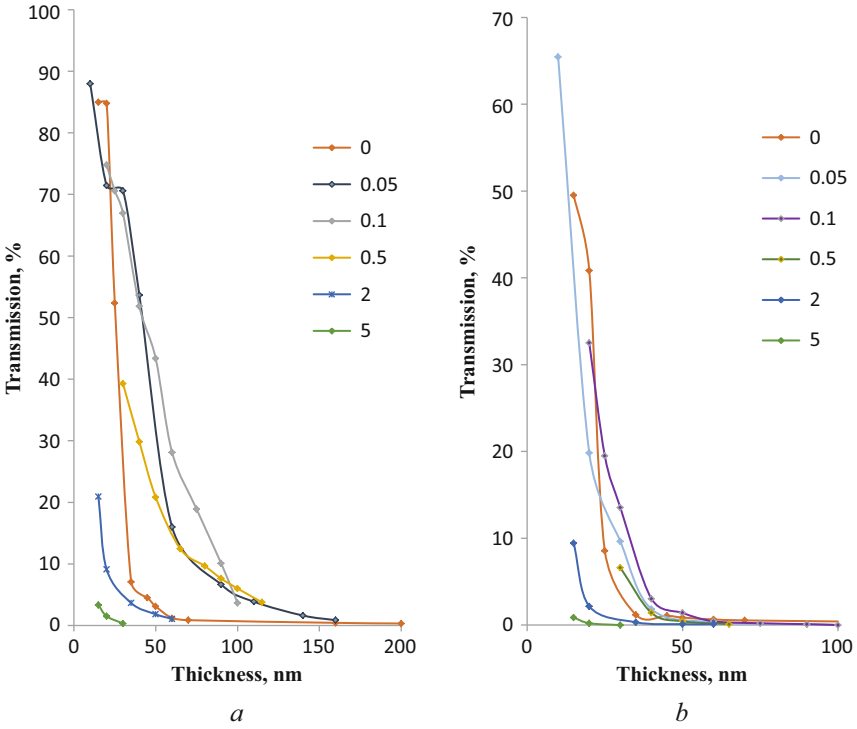

Fig. 6.2 Dependences of light transmission coefficients on the thickness for PTFE–CNT composites with different CNT concentration (**a** $\lambda = 1000$ nm; **b** $\lambda = 320$ nm)

concentration. In the first case, the maximum value of transmission ratio is more than 3.0 at $\lambda \approx 500$ nm, while the second maximum value of transmission ratio reaches almost 25.0 at $\lambda = 1000$ nm.

These effects are more clearly indicated on the dependence of the composite light transmission coefficient from the concentration of CNT for different thicknesses of samples for two values of the wavelength. In the similar way, an experiment was performed for wavelengths $\lambda = 1000$ nm and $\lambda = 320$ nm. For IR band ($\lambda = 1000$ nm), it was found that after adding a small amount of CNT (0.05 and 0.1 wt.%) to the polymer, the light transmission coefficient sharply increases for samples with 30–90 μm thicknesses. It can be concluded that for the sample with thickness 30–40 μm the best light transmitting through a composite appears for CNT concentrations 0.1 and 0.05 wt.%. For example, at 30 μm sample thickness of 30 μ, the light transmission coefficient increases from 30% (PTFE) to 70% after adding of 0.05 wt.% CNT; at 40 μm thickness – the coefficient increases from 5.4% (PTFE) to 53% after adding of 0.05 wt.% CNT; and at 50 μm thickness, the coefficient increases from 3% (PTFE) to 43% after addition of 0.1 wt.% CNT.

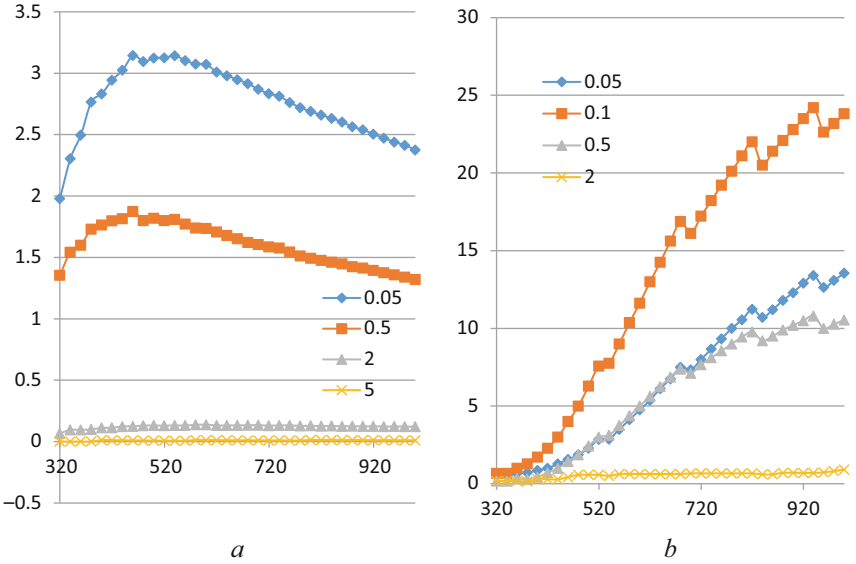

Fig. 6.3 The dependences of ratio of the PTFE–CNT composite light transmission to pure PTFE light transmission from wavelength with different sample thickness (**a** 30 μm; **b** 60 μm)

The light transmission coefficient decreases while further increasing CNT concentration in the composite. The subsequent increasing of the CNT concentration up to 2 and 5 wt.% leads to the coefficient becoming smaller than in PTFE – in full accordance with the Beer–Lambert–Bouguer law. For the smallest thicknesses (15–20 μm), the effect of increasing the transmission coefficient almost disappears, and the dependences of the coefficient for composite from the concentration of CNT acquire another character.

The brightening appears to a far lesser degree in the UV band. The maximum effect was observed for a sample with a thickness of 30 μm. After adding to the polymer of only 0.1 wt.% CNT leads to changes of the transmission coefficient from 4.8% to 3.5%.

The dependence of the logarithm of light transmission on the thickness of the sample is shown in Fig. 6.4. According to the Lambert–Bouguer law, the angle of inclination of a line to the abscissa axis is equal to the light absorption coefficient.

It was found that samples of PTFE +0.1 wt.% CNT significantly better transmit the light than pure PTFE with the thickness more than 20 μm. This is especially true in the IR band. The sample of PTFE +0.1 wt.% CNT with 70 μm thickness transmits the light ($\lambda = 1000$ nm) more than 25 times in comparison to pure PTFE with the same thickness. In the UV band ($\lambda = 320$ nm), the increase in almost two times of the transmission of light was observed at thickness of 20–30 μm. However in the UV band, the 60-μm-thick sample of PFTE with CNT passed less light than pure PFTE.

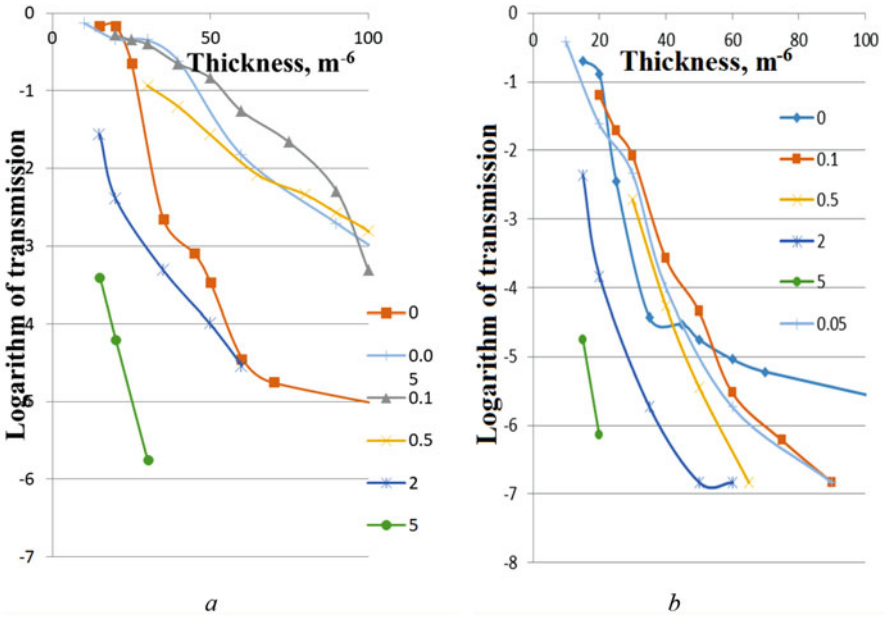

Fig. 6.4 The dependence of the logarithm of light transmission from the thickness of the samples of PTFE–CNT composites with different CNT concentration (**a** $\lambda = 1000$ nm; **b** $\lambda = 320$ nm)

Also at work were studied the darkened and mirrored sunglasses and, for comparison, the transmission spectrum of glass.

It appeared that the common dark glasses perfectly transmit the UV (315–400 nm), with the maximum transmission in the range 360–380 nm. That means that such glasses pass the light which causes the lenticular opacity and damage of the eye's retina. In the IR band, sunglasses are also quite transparent – 70%.

The specific damage caused by such glasses should be noted. The fact is that the pupil of the eye, reacting to a decrease in the amount of light in the visible range, dilates, allowing the entry of intense beam of ultraviolet rays into the eye.

Quite good results have been noted in the 60-μm-thick samples of PTFE–CNT with CNT concentration 0.1 and 0.5 wt.% being particularly good. Based on these samples, we can create protective optical filters.

6.4 Conclusions

1. Transparency increasing by 4–25 times was detected in the spectrum range $\lambda = 320$–1000 nm during the addition of carbon nanotubes to polytetrafluoroethylene.

2. It was shown that the increasing carbon nanotube concentration and the thickness of the sample leads to decreasing of the composite's transparency in the UV band and also to increasing of transparency in infrared IR band.

References

1. Serova VN (2010) Optical and other materials based on transparent polymers. Kazan. Gos.Tekh.Univ., Kazan. [in Russian]
2. Akatenkov RV, Aldoshin SM, Aleksashin VN et al (2011) Effect of small additions of thin multilayer carbon nanotubes on the structure and properties of glassy polymers. Dokl Akad Nauk 437(5):632–635. [in Russian]

Chapter 7
Based on Pneumatic Photonic Structures, High-Accuracy Measurement Procedure for the Universal Gas Constant

E. Ya. Glushko

7.1 Introduction

After the adopted revision of the International System of Units (SI) which took place in 2018, the problem of tight interrelation of subjects like equation of state produced by a physical model, chosen reference points on the P-T plane of a matter, and accuracy of measured volume/mass, pressure, and temperature has important meaning for fundamental constants in the physicochemical area. The uncertainties of purely thermodynamical constants N_A, R, and k_B, it should be noted, are several orders bigger than that for mixed constants like the molar Planck constant is [1–9]. Below we consider how the improved accuracy of measurement of light reflection using a sensitive device could lead to improving accuracy for the molar gas constant. It might, moreover, be thought that a progress in raising the accuracy of only one of the fundamental constants should impact on the whole family of constants due to their interrelation. Besides the fundamental constant describing the phenomenon measured by a device, we should also include into the self-consistent consideration other constants and parameters peculiar to the experimental setup and participating reference equations. The reference equations and participating constants are of utmost importance for the problem by no means phenomenological they are or derived from the first principles. Further we will operate by three kinds of reference equations playing a considerable role for physical phenomena that pressure detector work is based on and also in the organization of conditions for calibration and measurement. The first one concerns the extra low pressure and most little scale division. As far as the most fine measurement of pressure in optical reflection experiment is supposed to be of the order of $P \sim 10^{-5}\ Pa$, it corresponds to light

E. Y. Glushko (✉)
Institute of Semiconductor Physics, Kyiv, Ukraine

© Springer Nature Switzerland AG 2019

O. Fesenko, L. Yatsenko (eds.), *Nanophotonics, Nanooptics, Nanobiotechnology, and Their Applications*, Springer Proceedings in Physics 222,
https://doi.org/10.1007/978-3-030-17755-3_7

beam pressure at intensities beginning with *1 kW/m*^{2}. Therefore the first reference equation should describe light influence onto the detector's sensitive part. Taking into account that transmitted photons do not leave impulse inside the structure, we have for pressure P_l:

$$P_l = \frac{I_0 \cos(\theta_l)}{c} (\kappa + 2R_l) \tag{7.1}$$

where I_0 is light beam intensity, θ_l is incidence angle, κ is absorbance inside the structure, R_l is reflection coefficient, and c is light velocity. The next one, gas state equation, follows from the physical nature of measuring device based on a pneumatic photonic medium. Here, we chose the van der Waals representation of equation of state taking into account that this approach is well studied and its parameters are determined with appropriate accuracy [10].

$$\left(P + \frac{a\nu^2}{V^2}\right)\left(\frac{V}{\nu} - b\right) = RT \tag{7.2}$$

where V is system volume, a and b are van der Waals parameters, ν is number of moles, and T is temperature.

Here, we propose a procedure of high-accuracy measurement of pressure based on an extra high-accuracy volume determination counting in significant digits and precise processing the reflected/transmitted optical beam. The improvement procedure for accuracy of the molar gas constant R from the existing eight digits to ten is based on the described above 10^{-10} relative uncertainty of volume and pressure measurement. The problem of inconsistency between the existing relatively low accuracy of parameters like a, b, and others and the needed output accuracy in ten significant digits for R is solved by the use of sequential connection of different measurement scales – echeloning. The principle of scale echeloning for precise measurements considered in [11, 12] is based on a uniting of several sequentially improving accuracy scales in a prolonged measurement. It is important that in the process of echeloning the every next stage of measurement is accomplished in the absolute uncertainty area of the previous one.

In Fig. 7.1a, the relative uncertainty of fundamental constants and relevant reference data are presented. Nowadays, the accuracy of definition of atomic and electromagnetic constants is several orders bigger than that for physicochemical constants like the Boltzmann constant or the considered below molar gas constant R (brackets 1 and 2). The uncertainty of electric constant, molar mass constant, and light velocity is adopted equal to zero, i.e., in this case, the uncertainty must be transferred to related physical values. For instance, if the Avogadro number will be soon adopted as an exact number then the molar mass constant will lose its exact magnitude and the uncertainty will arise. We suppose that accuracy of all working physical parameters elastic, van der Waals, and others which participate the reference equations is characterized by not less than five significant digits. Therefore

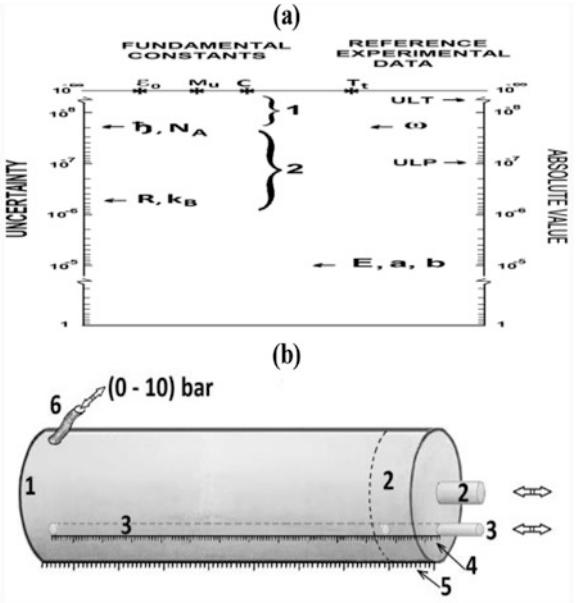

Fig. 7.1 (**a**) Relative uncertainty of constants and relevant reference data. Bracket 1, atomic and electromagnetic area; 2, physicochemical (thermodynamic) area; ω, photon energy; a and b, van der Waals parameters; E, Young modulus; ULP and ULT, reached magnitudes of ultralow pressure (Pa) and ultralow temperature (K); ε_0, M_u, and c, adopted uncertainty of electric constant, molar mass constant, and light velocity, respectively. (**b**) Ten-digit accuracy volume detecting system. 1, measurement tube calibrated in area from *4.9999 cm*^{3} to *999,999,999.999 cm*^{3} (linear sizes *2 m•0.5 m*^{2}); 2, plunger of the main tube; 3, plunger of the volume fine control system calibrated in area from *0.00005 cm*^{3} to *4.9999 cm*^{3} (linear sizes *1 m•5 mm*^{2}); 4, scale of volume precise control; 5, scale of main volume control; 6, connection to pump and *10 bar* pressure reservoir

an opportunity arises to obtain the awaited ten significant digit accuracy uniting two scales during the echeloning procedure. In our case, the minimal pressure scale division is of the order of $P \sim 10^{-5}$ *Pa*, whereas the position of ULP is several orders lower (Fig. 7.1a) that has an important significance to determine the minimal pressure scale division using sensitive opto-pneumatic materials.

In Fig. 7.1b, shown is a sketch of ten significant digit accuracy volume detecting system which includes two scales. The first one is five significant digit accuracy scale calibrated from *4.9999 cm*^{3} to *999,999,999.999 cm*^{3} which is linked to the 2-meter-long measuring tube of *0.5 m*^{2} section. A moving rod inside the tube performs a fine control of the volume in limits of minimal scale division of the main tube scale (*0.00005–4.9999) cm*^{3}.

In Fig. 7.2, a general scheme of pressure indication in an echeloning procedure is shown. The inert gas enters the measuring tube 3 from reservoir 1 through the controlled pressure pump 2. The two-scale pressure detector 4 reflects the meter readings of two opto-pneumatic devices: A calibrated in the bar region with the minimal scale division *0.1 mbar* and device B calibrated in the area from *0.99 nbar*

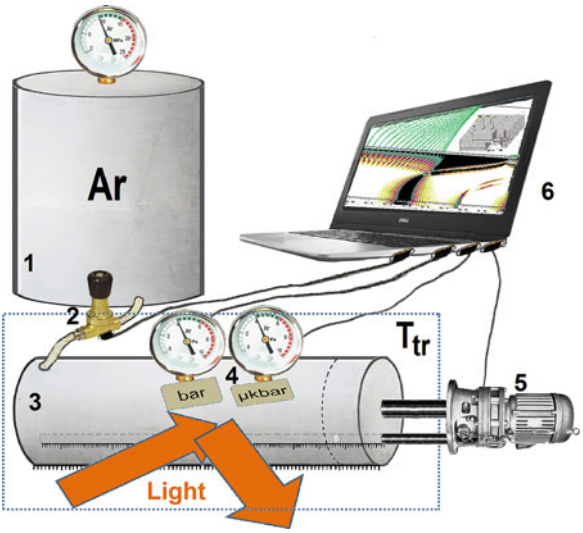

Fig. 7.2 Schematically precise pressure indication in the echeloning approach. 1, Inert gas reservoir; 2, controlled pressure pump; 3, two-scale volume measurement cylinder: upper scale calibrated from *0.00005* cm^3 to *4.9999* cm^3 and lower scale calibrated from *4.9999* cm^3 to *999,999,999.999* cm^3; 4, two-scale manometer: detector A calibrated in area from *0.099 mbar* to *9.9999 bar* and device B calibrated in area from *0.99 nanobar* to *99.999 μkbar*; 5, plunger position controlling system; 6, main control station. Dotted line, area of stable temperature, triple point of water

to *99.999 μkbar*. A light beam falls on the opto-pneumatic device situated inside the tube 3, and its reflection depends on the pressure in the tube. The gas volume changes due to the plunger position controlling system 5 and the process is governed by the main control station 6. We suppose that all the system is keeping with high accuracy at constant temperature, for instance, triple point of water.

In this study, we focus on the use of opto-mechanical properties of pneumatic photonic media as a means to measure gas pressure and gas volume with ten significant figures accuracy what yields needed accuracy for the molar gas constant R in the framework of a self-consistent procedure raising at the same time the accuracy of constants participating the reference equations.

7.2 Opto-pneumatic Medium as a Multiscale Pressure Indicator

Though the outstanding optical features of photonic crystals have been first mentioned in Rayleigh study [13], a tide of the modern applications in a wide area was began from works of Eli Yablonovitch and Sajeev John [14, 15]. Various properties

of photonic structures useful to create perfect dielectric mirrors, high-performance optical filters, key elements of logic gates, controlled mirrors or flexible waveguides, and many other applications were discussed since then (see [16–19]).

The pneumatic kind of a photonic crystal can exhibit significant optical sensitivity to variations of the external pressure and temperature. It was shown in [11, 12] that a gas-filled 1D elastic photonic crystal may be used as an optical indicator with several measuring scales which may be organized on the same substrate due to the well-expressed identity of the bandgap structure behavior. Below, we study a possibility to apply the extra high sensitivity of pneumatic photonic crystal to improve the accuracy of physicochemical fundamental constants using precise measurements of volume and pressure inside a special gas-filled tube. The system under consideration is shown in Fig. 7.3. It is several one-substrate made on 1D strip photonic crystals consisting of prolonged thin layers of a transparent elastic material of width d_1 divided by air voids (d_2) which can nonuniformly vary the lattice period under the action of the external pressure. The light beam reflects at the incident angle θ_l from the resonator center in longitudinal normal plane. The strip length is L and strip halfwidths are l_A and l_B for PhCr's A and B, correspondingly. We assume that for the photonic crystals under consideration all the strip widths $2l$ are much lesser than the strip length L and at the same time the laser beam cross-section size is considered as much lesser than the strip widths. Therefore, we can neglect the non-planarity of surfaces in the area of light beam incidence. Also, the strip design allows the beam inclined incidence in the longitudinal normal plane. In Fig. 7.3, a general schematic of a two-scale pressure indicator based on a layered

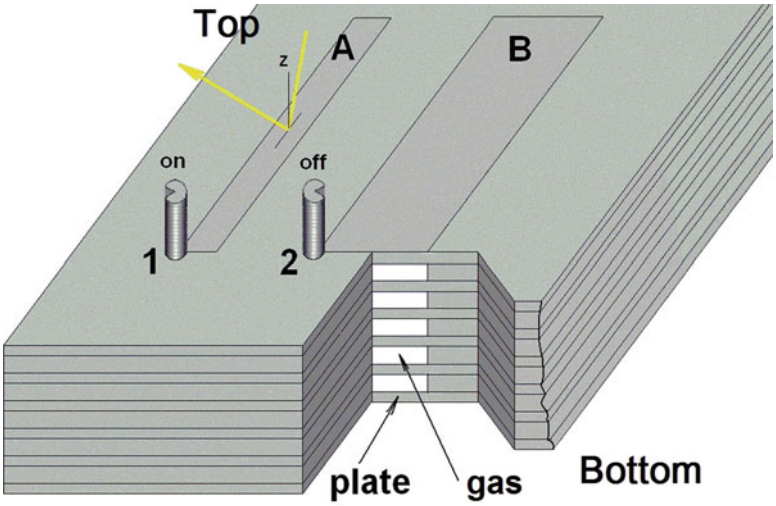

Fig. 7.3 A layered OPM as a multiscale pressure indicator schematically. OZ is perpendicular to plates. A stack of membranes contains two-strip pneumatic photonic crystals A and B. 1 and 2 are switches of access to external gaseous medium atmosphere. Geometry of light beam incidence is shown for strip A

OPM is shown. The stack of plates contains two-strip pneumatic photonic crystals A and B which embrace two scales of pressure indication covering several orders of magnitude. The access to the atmosphere is controlled with the help of switches 1 and 2. Geometry of light beam incidence is shown for strip A. The plate deflection ξ, being directed along the vertical z-axis, is a function of the plate coordinates (x, y). In general case the equation for ξ was studied in [20]

$$D\Delta^2\xi = \delta P, \tag{7.3}$$

where the stiffness parameter of the plate $D = Ed_1{}^3/(12(1 - \sigma^2))$, σ is Poisson's ratio, and δP is the pressure difference. For our mathematically 1D case, the Laplace operator is written as d^2/dx^2, and, following [12], one can find the solution of (1) satisfying the edge boundary conditions for a fixed, long, and separate elastic strip membrane.

A stack of N optically transparent thin plates divided by closed air voids is a system, whose optical properties depend on the external pressure and temperature. Initially, the pressures inside the system coincide with the external pressure, and for the abovementioned geometry of incidence, we have a 1D photonic crystal with period $d_0 = d_1 + d_2$ and the corresponding reflection coefficient $R_l(P_0)$, where P_0 is the external pressure The increase of the external pressure causes the compression and a decrease in the thickness of air layers d_2, which changes, in turn, the total reflection pattern. Under the external pressure action, every membrane bends due to the difference of pressure from both sides. Combining pressures and volumes in the neighboring gaseous voids divided by elastic membranes, we arrive at a chain of equations

$$P_i = \frac{Q_1\tilde{P}_{00}}{Q_1 - P_{i-1} + 2P_i - P_{i+1}} - \frac{a\nu_0^2 Q_2}{(Q_1 - P_{i-1} + 2P_i - P_{i+1})^2}, \quad i = 1, 2, 3 \ldots N \tag{7.1}$$

where pressure P_i is expressed, with the help of (7.2), through the corresponding volumes V_i found by integration along the deformed membrane surface. The parameter $Q_1 = 45Dd_2(1 - b\nu_0/V_0)/l^4$ plays a role of an effective elastic pressure of a membrane; $Q_2 = 45Dd_2/l^4$; P_{00} is the device calibrating pressure; ν_0 is mole number in a separate void of the detector; $V_0 = 2Lld_2$, initial volume of a void; $\tilde{P}_{00} = P_{00} + a(\nu_0/V_0)^2$. It is worth noting that boundary conditions of the system (7.4) may be chosen as $P_{N+1} = P_0$ in case of two-sided access of external pressure to the PhCr and $P_{N+1} = P_{00}$ for the one-sided access. In a limit when the number of plates is large enough, system (7.4) describes a continuous pneumatic medium [11, 15] with distributed gas pressure inside and corresponding deformation of membranes. In Fig. 7.3, a scheme of the two-sided measurement of pressure is represented where the PhCr body has a free access to the measured medium both from top and bottom sides. The strip A device plays a role of the first-level scale which embraces interval $(0.1, 10^4)$ *mbar*, whereas the scale B serves to measure more fine-tuned deviations of pressure. Another scheme of measurement – one-

sided – supposes free access of the PhCr to external medium only from the top or bottom side. The gas-filled 1D elastic pneumatic photonic crystal can be used as an optical indicator of pressure uniting several scales of pressure magnitudes. In general, device includes a layered pneumo-elastic platform, optical fibers and switching valves, all enclosed into a chamber having free access to surrounding medium.

7.3 Bandgap Structure and Map of Reflection

We consider the p-polarized electromagnetic field in the compressed 1D PhCr pneumatic structure consisting of N alternated glass plates divided by air voids. Taking into account the expression for field $\overrightarrow{E_s}$ in s-layer with refraction vector $\overrightarrow{n_s}$

$$n_s \overrightarrow{E_s} = (n_{sz}, -n_{sx})\, A_s e^{ik_{sz}z} - (n_{sz}, n_{sx})\, B_s e^{-ik_{sz}z}, \tag{7.5}$$

where z indicates projection of refraction vector and wave vector $\overrightarrow{k_s}$ into axes OZ (Fig. 7.3) in the geometry of p-polarization. The light transition through the system is determined by Maxwell boundary conditions forming a chain of $2N + 1$ matrix equations for field amplitudes A and B (from top to bottom):

$$\begin{aligned} &\left\{ \widehat{L}_t \begin{pmatrix} A_t \\ B_t \end{pmatrix} = \widehat{L}_1 \begin{pmatrix} A_1 \\ B_1 \end{pmatrix}; \quad \widehat{M}_1 \begin{pmatrix} A_1 \\ B_1 \end{pmatrix} = \widehat{L}_2 \begin{pmatrix} A_2 \\ B_2 \end{pmatrix}; \right. \\ &\left. \widehat{M}_2 \begin{pmatrix} A_2 \\ B_2 \end{pmatrix} = \widehat{L}_3 \begin{pmatrix} A_3 \\ B_3 \end{pmatrix} \quad \cdots \quad \widehat{M}_{2N+1} \begin{pmatrix} A_{2N+1} \\ B_{2N+1} \end{pmatrix} = \widehat{L}_b \begin{pmatrix} A_b \\ B_b \end{pmatrix}, \right. \end{aligned} \tag{7.6}$$

where indexes t and b mark the top and bottom media and A_b is the amplitude of the wave running away into the bottom medium at θ_b incidence angle, whereas $B_b = 0$. For electromagnetic field trapped inside the total internal region (TIR) of the OPM, we must demand $A_t = 0$ (Internal problem). In the case of external incidence of light beam at θ_t incidence angle, the amplitude A_t should be taken equal to 1. The transfer matrices of upper side and lower boundary of the s-layer are as follows:

$$\widehat{L}_s = \begin{pmatrix} \cos\theta_s, & -\cos\theta_s \\ \varepsilon_s \ \sin\theta_s \ , & \varepsilon_s \sin\theta_s \end{pmatrix}, \quad \widehat{M}_s = \begin{pmatrix} \cos\theta_s e^{ik_{sz}d_s}, & -\cos\theta_s e^{-ik_{sz}d_s} \\ \varepsilon_s \sin\theta_s e^{ik_{sz}d_s}, & \varepsilon_s \sin\theta_s \ e^{-ik_{sz}d_s} \end{pmatrix} \tag{7.7}$$

Here the case of TM polarization is considered. In the case of TE-polarized field, the boundary conditions are written for the magnetic field.

The eigenstates of the internal problem are described by the dispersion equation derived in [11]. Every band of eigenstates includes a number of modes equal to the period number; the width of gaps dividing the bands depends on the optical contrastivity of the structure. We have calculated the spectrum of TM waves both

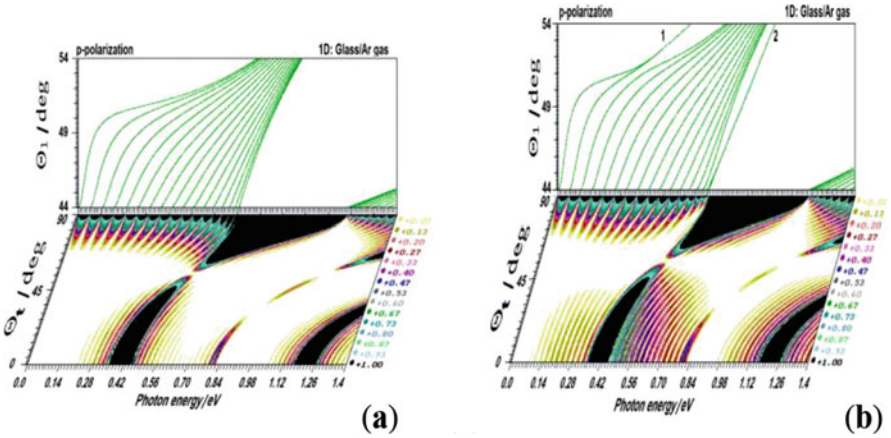

Fig. 7.4 Spectrum of TM-polarized wave in glass/air *16* period 1D PhCr at different pressures. *Vertical panels a, b*: the bandgap structure inside the TIR region at the propagation angles θ_1 in glass from *44°* to *54°*. $d_1 = 0.5\ \mu m$, $d_2 = 0.8\ \mu m$, and photon energy is up to *1.4 eV*. *Horizontal panels a, b*: color diagram for reflection *R* of the external incident beam at external (air medium) incident angles θ_t from *0°* to *90°*. Right column: color scale for reflection coefficient R_l. (**a**) Non-perturbed structure: $P_{N+1} = P_0 = P_{00} = 100\ \mu bar$; (**b**) stressed structure: $P_{N+1} = P_0 = 100\ \mu bar$; $P_{00} = 110\ \mu bar$; 1 and 2, surface states detached from the band; string width $2l = 600\ \mu m$

inside the TIR region and for external incidence of light taking into account the chain correlations (7.6) and loss of periodicity due to the external pressure-caused membrane deformations inside the photonic crystal. In Fig. 7.4 (vertical panels), the bandgap structure of glass/gas *16* period 1D PhCr is shown inside the propagation angle interval $\theta_1 \in (44°, 54°)$ of the TIR region at photon energies between *0* and *1.4 eV*. The width of glass plates was taken $d_1 = 0.5\ \mu m$ and air voids $d_2 = 0.8\ \mu m$ at initial external pressure of calibration $P = P_{00} = 1\ bar$, glass dielectric function $\varepsilon_1 = 2.1$. The bandgap structure exhibits *16* trapped modes in every band. According to Fig. 7.4, the first one is placed in the interval $\omega\varepsilon\ (0, 0.71)\ eV$ at $\theta_1 = 44°$, whereas in upper part, the band at $\theta_1 = 54°$ is narrowed and now occupies the interval of energies *(0.78, 0.99) eV*. The second band begins with *1.15 eV* at $\theta_1 = 44°$. It is clear from Fig. 7.4 that on the boundary of the total internal reflection area and area of external incidence in the vicinity of $\theta_t \sim 90°$ a typical whispering reflection arises which replicates the beginning of the bandgap structure inside the total internal reflection region on vertical panel.

The external incidence of light beam is described in terms of reflection and transmission. In particular, the reflection coefficient R_l is determined by square module of the amplitude B_t at given $A_t = 1$ (Eq. 7.6). In Fig. 7.4, the horizontal panels show the calculated reflection color diagrams in energy interval *(0–1.4) eV* and angular interval of external incidence $\theta_t \varepsilon$ *(0°–90°)*. An all-energy transparency band near *54.4°* illustrates the well-known Brewster effect. The reflection map depends on the system geometry, number of periods and optical properties of

membranes. In general the whole map contains the alternating transmission stop bands corresponding to strong reflection $R_l \sim 1$ and transmission windows.

Our investigation of TM-polarized waves in the OPM shows that the behavior of the bandgap structure inside the TIR region as well as the reflection map of external incidence exhibits high sensitivity to external pressure. The TE-polarized waves show a little different interaction with the pneumatic photonic crystal. It was found that in general the bandgap structure and map of reflection for s-polarized waves are characterized by wider gaps in the TIR region and wider windows of reflection at external incidence than for p-polarized waves. For angles in the vicinity of normal incidence, the difference between polarizations vanishes.

The local (surface) states are absent in a non-deformed photonic crystal if one of two materials (air) coincides with the external medium. Any changes of external pressure deform membranes which may cause the appearance of local states if pressure exceeds the threshold of state detachment from the band. For the PhCr geometry considered in Fig. 7.4, the local states begin to shift out of the band top and bottom approximately at $5\ \mu bar$ difference between external and internal pressures. At the TIR angle $\theta_1 = 54°$ (Fig. 7.4b, vertical panel), energy shift reaches $0.15\ eV$ for the lower pair of closed states and $0.042\ eV$ for upper pair of local modes. This effect provides a good opportunity in usage of detached states for the need of sensoring. In a scheme with fixed frequency of light beam, the detachment is accompanied by the deviation of the transmittance angle from $52.5°$ to $54°$.

We have also analyzed the case of one-sided access of the detector to external medium and have found that sensitivity of the device is lower than for the two-sided geometry under consideration.

7.4 Sensible Reference Points on the Reflectivity Map

The extra high sensitivity of periodic optical structures to a distortion of periodicity is explained by fine character of interference phenomenon causing enough significant changes in separate zones of reflection spectra. In the TIR region, highly sensible to external pressure are local states detached from the first band top for intrinsic incident angles of wave beginning with $\theta_1 = 48.5°$ and from the bottom for θ_1 beginning with $52.5°$ (Fig. 7.4b). In our study, we focus onto some sensible zones of reflection map in geometry of external incidence presented in Fig. 7.4 by horizontal panels. An analysis of the reflection map in the interval of photon energies from 0 to $1.4\ eV$ shows several sensible patterns in the θ_l–ω plane. The most visible one locates in the second window of transmission from $0.42\ eV$ to $0.56\ eV$ at incidence angles close to normal. Another two patterns locate in the vicinity of the second reflection window: from the bottom side $(1.05, 1.19)\ eV$ and from the top side $(1.19, 1.4)\ eV$.

Due to the constructional features, several OPM devices united on a substrate (see Fig. 7.3) have coinciding spectra measured at pressure of calibration. Besides, the bandgap structure and reflection map of a 1D photonic crystal both possess

a well-expressed scale invariance described in [11] that arises due to the plane wave arguments $k_{sz}d_s$ in the Eq. 7.7 at any transformation keeping these arguments constant: $\omega \to t{\cdot}\omega$, $d_s \to d_s/t$, where ω is the light frequency. This feature may serve as an important instrument to fabricate the laser frequency matched opto-pneumatic platforms with needed properties. Further we implement this property to choose the most convenient pressure calibration interval for the given laser wavelength *1064 nm*. A variation of external pressure causes the nonuniform deformation of membranes that in turn spoils the periodicity of the PhCr. Therefore the calibration scale for a fixed interval of pressure differs for different parts of the pressure scale.

7.5 Pressure Calibration Curve in the Nanobar Interval

To reach the final ten significant digit accuracy of measured pressure, an opportunity should be to detect its minimal values expressed in the nanobar interval. If the membrane thickness to be of the order of microns, then the most sensitive strip width $2l_B$ will have the order of several hundred microns (strip detector B in Fig. 7.3).

Principally the pressure interval near the left side of the junior scale of pressure should be measured especially because the nanobar interval is not investigated in detail. Here, we will use a nature pressure reference value which is maximally close to zero – the pressure of ultrahigh vacuum ULP (Fig. 7.1a). It indicates a limit of relative uncertainty in 10^{-13} relatively the right side of scale value *10 bar*. Therefore the first stage of calibration should be a correct determination of minimal division of the scale *1 nbar*. This minimal pressure corresponds to the gas volume concentration approximately $10^{10}\ cm^{-3}$ that is a statistically essential value. The ultralow pressure technically can be realized by weak admission of gas into the measuring tube beginning with picobar pressures which are far enough from the nanobars to be indicated by the device. In Fig. 7.5a, reflection coefficient dependence on photon energy is shown for the pattern of sensibility located at the beginning of second transmission window discussed above for geometry $d_1 = 0.5\ \mu m$, $d_2 = 0.8\ \mu m$. A recalculation of reflection map Fig. 7.4a made to tune the sensible pattern especially for the wavelength 1064 nm gave needed sizes $d_1 = 0.203\ \mu m$ and $d_2 = 0.325\ \mu m$. The nanobar calibration curves linking light reflection and pressure in the area of left part of the junior scale *(0–1)* μbar are presented in Fig. 7.5b for both p- and s-polarizations and the chosen photon energy. One can evaluate photodetector sensitivity needed to satisfy the nanobar accuracy. If the incident beam intensity is about $10^5\ W/m^2$ then the device sensitivity to be on a level of $1\ W/m^2$. Repeating *100* times determination of the calibration curve for other parts of the junior scale *(1–2)* μbar, *(2–3)* μbar, and so on, we fill all the junior scale *(0–100)* μbar. An inevitable partial presence of another polarization of incident light can be accounted by corresponding correction in the process of pressure measurement.

7.6 Pressure Calibration Curve in the Microbar Interval

In our consideration, the microbar area is defined from *100 μbar* to *10 bar*. The major scale like it was described for the junior scale is covered by a thousand *10 mbar* length intervals each of them having its own calibration scale. In Fig. 7.6a,

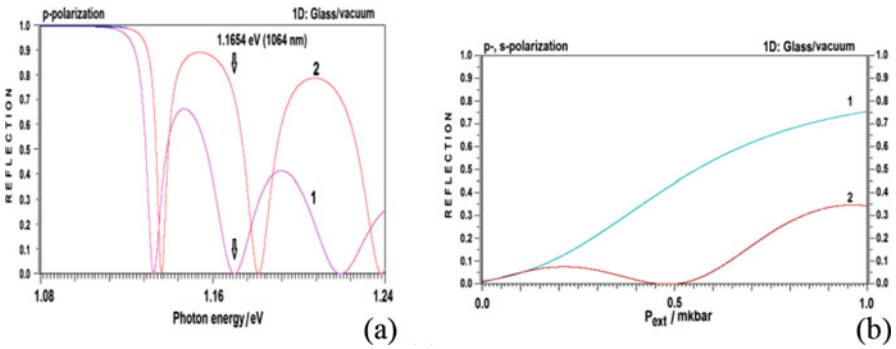

Fig. 7.5 Reflectance spectrum of detector B, half width $l = 400\ \mu m$, nanobar interval. Quasi-normal incidence ($\theta_l = 1°$), $P_{00} = 0$. (**a**) Reflection vs photon energy. Two-sided measurement. *16* period glass/vacuum 1D PhCr: $d_1 = 0.203\ \mu m$, $d_2 = 0.325\ \mu m$. Reflection window ($R \approx 1$) is distinguished by color; arrow shows the chosen operating energy $\omega = 1.1654\ eV$; 1, external pressure $P_0 = 0$; 2, external pressure $P_0 = 1\ \mu bar$. (**b**) Calibration curve reflection R_l vs pressure at fixed photon energy $\omega = 1.1654\ eV$ (Fig. 7.5a, arrows); 1, TM-polarized wave; 2, TE polarization

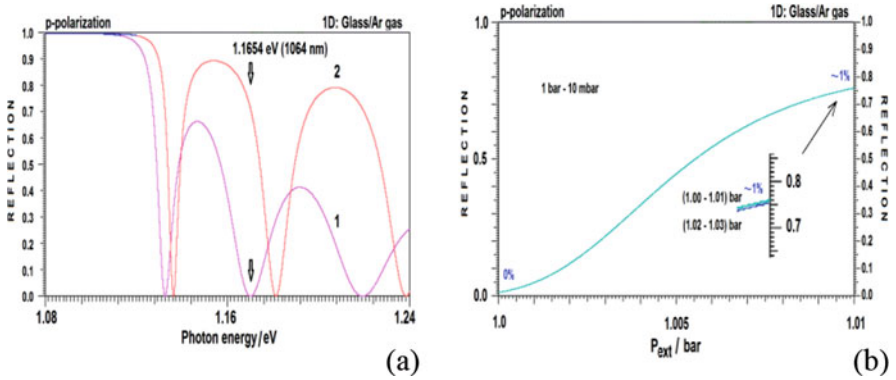

Fig. 7.6 Reflectance spectrum of detector A, halfwidth $l = 40\ \mu m$, and mbar interval of pressures, $P_{00} = 1\ bar$. TM polarization. Quasi-normal incidence ($\theta_l = 1°$). (**a**) Reflection vs photon energy in vicinity of wavelength *1064 nm*. Two-sided measurement. *16* period glass/gas 1D PhCr. $d_1 = 0.203\ \mu m$ and $d_2 = 0.325\ \mu m$; 1, $P_0 = P_{00}$; 2, $P_0 = P_{00} + 10\ mbar$. Energy gap ($R \approx 1$) is distinguished by color; arrows show the chosen operating photon energy *1.1654 eV*. (**b**) A calibration curve reflection R_l vs pressure. Quasi-normal incidence at operating photon energy. Insertion: right side (arrow), 1% difference between *(1.00–1.01) bar* and *(1.02–1.03) bar* curves

reflection coefficient dependence on photon energy is shown for the recalculated pattern of sensibility in the beginning of the second transmission window of the detector A with membrane and void widths $d_1 = 0.203$ μm and $d_2 = 0.325$ μm and strip width $l = 80$ μm. The shown calibration curve is taken from a middle part of the total major scale (0–10) bar and occupies interval (1.00–1.01) bar. The calibration curve "reflection coefficient-pressure" for this interval is presented in Fig. 7.6b for the p-polarized wave having the photon energy *1.1654 eV*. The reflection coefficient varies monotonously along the interval from 0 to approximately 0.76. The calibration curves slightly differs one from another for different intervals. For the chosen parts of major scale *(1.0–1.01) bar* and *(1.01–1.02) bar*, this difference reaches 1% in the right-hand side of the interval.

7.7 Factors Accompanying the Procedure

A situation with the improving of accuracy for fundamental constants is to some extent similar to the famous effect of deceleration of Pioneers [21] which needed to take into account a bundle of various undistinguished but nevertheless influential factors beginning with mechanical and heat up to radiometric ones. Besides, in our case, some additional obstacles arise caused by correlation between accuracies of constants, participating parameters, chosen type of the gas state equation, other factors, and finally measurement procedure. Actually, the experimental procedure of improving the accuracy above the average number of significant digits of parameters is interrelated and recursive. It means that increasing a fundamental constant accuracy is performed by a circle of repeating measurements instantly decreasing relative uncertainty of the measured constant and parameters (like a and b in Eq. 7.2) to the limit uncertainty dictated by accuracy of volume and pressure detection.

Among the small but influential factors besides the discussed above light pressure on the PhCr membrane, one should give the proper weight to pressure deviation caused by convection flows in the vicinity of the detector membranes. So even if the gas microflow velocity $u = 1$ cm/s, then the pressure deviation is measured by the expression $\delta P \sim \rho u^2/2$ and, at normal conditions, can reach 10^{-4} *Pa* which is comparative with minimal divisions of pressure scale.

Immediate heat influence of beam to material of plates and gas substance inside is defined by coefficient κ in Eq. 7.1. Its magnitude can be evaluated for optical glasses as less than 10^{-5} and therefore the coefficient κ may be neglected as a factor of optical pressure in Eq. 7.1. Nevertheless, it should be considered as a reason of possible heating both plate material and gas inside the sensor. The result depends on the design of heat sink system.

One more reason of gas density inhomogeneity arises due to gravity. A stable pressure and concentration gradient in gas volume establishes along the gravity field direction: $\delta P \sim \rho g h$. At the height difference of the order of tube diameter 0.5 m the difference may reach several Pa what is close to the minimal division of pressure

major scale. Therefore the process of measurement should be carried out in stable position of the detector and stable measuring tube orientation.

Sound pollution also can influence the detector meter readings. Even at 1 Db sound level an additional pressure *20 μPa (10^{-12} W/m^2)* on the membrane arises, that corresponds in our case to several divisions of the junior scale of pressure.

Being a characteristic of matter reply to electromagnetic field, the dielectric function of gas inside the detector depends on the density that, in turn, is determined by pressure. In the area of precise measurements in the vicinity of chosen reference points (*P, V*), a linear dependence is valid both for the dielectric function and refraction index.

The combination of small volume of the gaseous medium inside the *20*-period OPM detector ($\sim 10^{-5}$ cm^3, Fig. 7.3) and small measured pressure less than *10 a* lays at the statistical limit of pressure phenomenon when the number of gas atoms is close to 10^{10} and the limit is evidently crossed at $P \sim 10^{-4}$ *Pa* with only 10^5 gas particles inside the whole volume of the detector. Evaluating the mean free path of argon atoms l_{Ar} in the gaseous voids $l_{Ar} \sim (2\pi\sigma C)^{-1/2}$ where σ is the atomic diameter and C is the concentration, one can find that l_{Ar} varies from approximately *0.1 μk* at bar pressures to millimeters at low pressures that much exceed the distance between neighboring membranes of the detector, and it looks like a gas vacuum state along one of the freedoms degree. Another factor arises if geometric size of the sensor intrinsic gaseous volumes becomes small at nanometer distances between membranes. This may influence the gas master equation modifying its parameters. Therefore the parameters a and b in Eq. 7.2 written for the sensor gaseous voids in general may be different from that in a big volume. For instance, the parameter of additional compressing may change its sign due to dominated van der Waals attraction to membranes in such narrow systems. In any case, this subject needs a detailed investigation.

A serious problem of pressure measurement with high accuracy is the use of less accuracy devices at intermediate stage of a complicated procedure. Even for a potentially high-accuracy device with a total relative uncertainty 10^{-10}, the process of scale calibration may include some comparison procedures with less accuracy scales. For instance, the initial six-digit accuracy of a high-precision manometer does not instill confidence as to the microbars and especially as to lower pressure in the considered area of *(0–10) bar*.

There exist some natural restrictions as to the number of significant digits for membranes' sizes in micrometer range. In the best case, there could be only four significant digits for the device parameters d_1, d_2, l_A, and l_B. One can speak the same about the ratio of the laser beam cross section and the strip width *2Ll*. Taking into account that at each measurement both pressure and volume vary in a narrow interval of values, this problem can be solved with the help of a phenomenological description of the sensor behavior for the given laser frequency.

Here p-polarized light is considered. The s-polarized incident light generates another location of reflection windows, and therefore the polarization purity of the incident beam requires a serious attention.

7.8 Final Calibration of the Conventional Two-Scale Manometer

We have obtained all 200 calibration curves with the set of parameters determined with accuracy not less than five significant digits, i.e., $a^{(5)}$, $b^{(5)}$, $\nu^{(5)}$, $E^{(5)}$, and $R_l^{(5)}$. This approximately corresponds to the relative uncertainty for them 10^{-5}, whereas the volume-measuring scale gives the relative uncertainty near 10^{-10}. Therefore the calibration of the major *(0–10) bar* scale needs some additional after process adjusting which will be described below as part of this section. In the process of continual measuring of reflection, gas intake is performed from the reservoir to the measuring tube (Fig. 7.3b) up to the moment when it reaches the known value P_{right} that corresponds to the pressure $P_{\min} = 10^{-5}$ and $P_{\max} = 10$ Pa, and the minimal division of major scale may be marked. With further gas intake, the conventional major scale of pressure is filled by divisions in correspondence with obtained calibration curves up to the limit value *10 bar* (Fig. 7.7, Input). In our case, this procedure is considered as carried out on default. The gas temperature is taken equal to triple point of water $T_{\text{tr}} = 273.16$ *K*.

As it was described above, the junior scale is calibrated by B detector B (Fig. 7.3) in a process of fine increasing the pressure in the every interval of 0.1 Pa beginning with zero pressure. For our goal this interval can be chosen in the vicinity of several reference pressures. In Fig. 7.7, a scheme of accuracy improving for all measurement system at reference pressures and volumes (P_1, V_1), (P_2, V_2), (P_3, V_3) and (P_4, V_4) is shown. A significant calibration problem is a discrepancy between

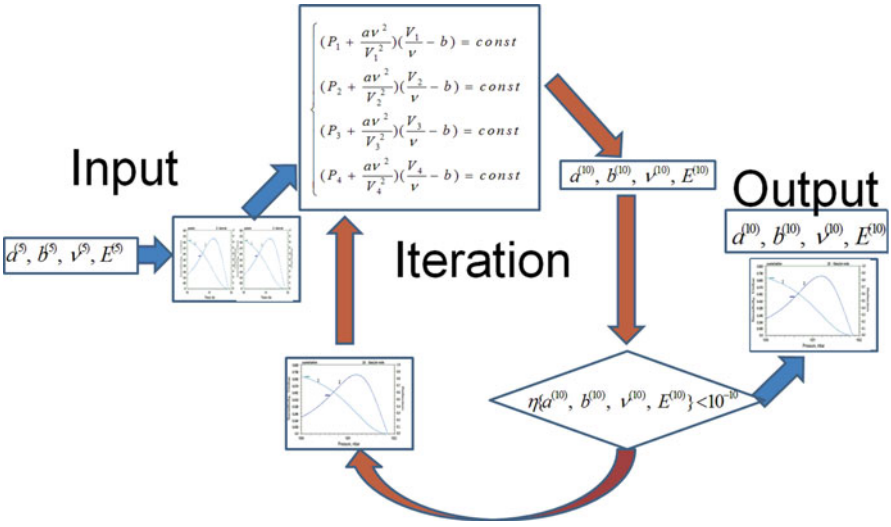

Fig. 7.7 A scheme of self-consistent procedure improving the accuracy of participating parameters

the needed accuracy of junior scale and low accuracy of parameters at the initial stage. Therefore the scale calibration curves are correcting in a self-consistent procedure step by step with correcting in 6th–tenth significant digits of parameters. The entry into the procedure is performed with a set of five-digit parameters $a^{(5)}$, $b^{(5)}$, $\nu^{(5)}$, and $E^{(5)}$ (Fig. 7.7, left part). The first calibration curve (Fig. 7.5b) is used on the input stage with several ten-digit reference points taken from the first interval of pressures *(0, 1) μbar*. Solving the system of four equations (upper part of Fig. 7.7), we find the parameters a, b, and ν in their preliminary ten-digit view that in turn adds five significant digits more to the Young modulus $\boldsymbol{E}$ and also leads to a modification of junior level first calibration curve. The latter calls a pressure shift in 6th–10th significant digits that demands a next correction in parameters a, b, ν, E, and so on (Fig. 7.7, circular arrows). The iteration procedure stops when deviation in the set of parameters became less than 10^{-10} (Fig. 7.7, right side). At the outlet of the procedure, we have corrected parameters $a^{(10)}$, $b^{(10)}$, $\nu^{(10)}$, and $E^{(10)}$, corrected first calibration curve Fig. 7.5b, and corrected first thousand divisions of the total scale. Then the procedure input-iteration-output is repeated for the next one from hundred calibration intervals of the junior scale. All the junior scales represent the minimal division of major level scale *(0, 100) μbar* determined now with ten significant digit accuracy. After the corresponding correction of the first calibration curve of major scale, we begin the next hundred step calibration process for the next division of major level scale *(100, 200) μbar* with the use of previously obtained five-digit calibration curve as the input data. The last interval *(9.99, 10.00) bar* finishes the ten-digit accuracy calibration process.

The iteration procedure serves to determine a group of interrelated physical values with a higher accuracy, i.e., the pressure phenomenon (I) is measured through the phenomenon of pressure caused by the membrane deformation inside a gas-filled opto-photonic medium (II) and the phenomenon of reflection modification (III) with the corresponding optical signal transformation and processing (IV). We consider that the stages III and IV already have the needed accuracy of their opto-electronic scales, but taking into account that the initial calibration of the detector was based on inaccurate digits beginning with the sixth and up to the tenth (Young modulus, for instance), then the measurement procedure should be built on the ten-digit reference points (P_3, V_3) with consecutive improving of parameters to the needed ten-digit accuracy.

It worth noting that the discussed iteration method is irrelative to the physical type of pressure gauges used: thermodynamical, electrical, magnetic, etc. Iterations are applicable if the procedure converges to (a) a unique constant value in the limits of needed significant digits and (b) this value is the correct one. An important argument in favor of the efficiency of iteration procedure in our case is extremely a narrow area of pressure and volume dispersion at final stage of calibration: values P_i and V_i in the central part of Fig. 7.7 differ from one another only beginning with sixth significant digit. Therefore the describing Eqs. (7.2) and (7.3) may be considered as an almost flat surface in a five-dimensional space of parameters a, b, ν, E, and R having unique solution which can be found in the process of iterations.

7.9 Implementation

Let the definite values a and b exist for the gas state Eq. (7.2) describing the gas evolution inside a chosen 10 Pa division of major pressure scale (device A), and let the exact pressure in the measuring tube be established at level $P_{AB} = 3.987640321\ bar$. The initial mode of all setup is device A in state "On" and device B in state "Off" with open access to gas in the tube and zero meter readings on the both of them. As the result of measurement, the meter readings of the first echelon device A (Fig. 7.3) will reach a magnitude *3.9876 bar* and stop in an uncertain position between *3.9876* and *3.9877 bar*. In order to link up the next echelon device B it should be switched to state "On" at initial meter readings *0.000000000 bar*. The following procedure serves to find the difference between exact but undefined position of conventional device A arrow and exactly defined position of the next bigger mark *3.987700000 bar*. It needs at the fixed number of moles a smooth rising of pressure inside the tube compensating the difference. This operation can be realized by shifting plunger 3 into the tube (Fig. 7.1b) which causes the corresponding exquisite volume to decrease and leads to increase of pressure measured by device A. For a not dense gas under consideration, the correlation $dP/P \sim dV/V$ is valid for all variants of gas state equation with needed five-digit accuracy; therefore the volume decreasing in an interval from *0.00005* cm^3 to *4.9999* cm^3 corresponds to a pressure region in *10 Pa*. Aborting the procedure when the first echelon device A meter readings reach the value $P_A = 3.9877$, we do obtain the meter readings on the second echelon device $P_B = 0.000059679\ bar$ which should be subtracted from P_A: $P_{AB}{=}P_A - P_B = 3.987640321\ bar$. Restoring the position of plunger 3, one can repeat several times the pressure measurement at the junior level scale to reach a statistically large enough number of measurements.

The four equations of state figuring in Fig. 7.7 also yield magnitude of a constant in the right-hand side at every step of the iteration procedure. At the final stage of the procedure, this constant gets ten significant digit accuracy, and the expected molar gas constant can be found from correlation

$$R^{(10)} = \frac{\text{const}^{(10)}}{T_{\text{tr}}} \tag{7.8}$$

in a view containing ten significant digits. A statistically large number of measurements should be performed under the given conditions of experiment. Besides, the variation of the experiment conditions in repeating procedures at the junior level scale to reach a statistically large enough number of measurements.

7.10 Summary

In ancient Egypt, mathematicians had determined the number of π measuring the ratio of a circle length to its diameter with three significant digit accuracy and about one percent relative uncertainty. Since then trillions of significant digits of π

were obtained mathematically, the physical measurement techniques cannot boast a sufficient progress in mining the digits of fundamental constants.

We have discussed above a possibility of the gas-filled elastic photonic structures to serve as a sensitive optical pressure indicator uniting several pressure scales of different accuracy. The echeloning procedure for two united scales of pressure/volume was considered in a variant when the minimal division of a major scale covers the total scale of junior scale. It gives an opportunity to unite significant digits of both scales. The overlapping of scales is also possible, the resulting number of significant digits in this case must be found with account of overlapping.

The considered pressure gauge includes several layered elastic photonic structures united in a platform, optical fibers, and switching valves, all enclosed into a chamber and situated inside the ^{40}Ar-filled volume detecting system at fixed temperature. At the chosen parameters, both scales of the device may cover the pressure interval *(0, 10) bar* with accuracy *1 nbar* which allows to operate the physical values and parameters with ten significant digits. Meanwhile the described procedure is indifferent to the physical nature of phenomenon used in the design of pressure detectors related to the calibration scales.

We have used the two-parameter phenomenological van der Waals equation of state with constants a and b improved in a self-consistent procedure for every P-V area under study. One can expect the same result for other kinds of equation of state.

There exists the interrelation between different fundamental constants due to the physical phenomena uniting them. Therefore an opportunity arises to improve the accuracy of the Boltzmann constant to nine significant digits from the existing seven and reduce the relative uncertainty to approximately $3 \cdot 10^{-8}$ considering k_B as a ratio R/N_A. Besides, several ways exist connecting the proposed procedure with gravitation through the indication of hydrostatic pressure. A 10-m free fluid column puts pressure upon the device strip A in the bar interval, and corrective deviations can be detected by strip B up to nanobars. The sufficient length of the fluid column allows 7–8 significant digits of height measurement with corresponding improvement of the relative uncertainty for the Newtonian constant of gravitation.

This work was supported by the Ukrainian Foundation of Fundamental Research, project Φ76/70-2017.

References

1. Newell DB, Cabiati F, Fischer J, Fujii K, Karshenboim SG, Margolis HS, de Mirandes E, Mohr PJ, Nez F, Pachucki K, Quinn TJ, Taylor BN, Wang M, Wood BM, Zhang Z (2018) The CODATA 2017 values of h, e, k, and N_A for the revision of the SI. Metrologia 55:L13–L16
2. Mohr PJ, Taylor BN, Newell DB (2012) CODATA recommended values of the fundamental physical constants. J Phys Chem Ref Data 41:043109
3. Karshenboim SG (2017) Adjusted recommended values of the fundamental physical constants. EurPhysJST 172:385–397
4. Bartl G et al (2017) A new ^{28}Si single crystal: counting the atoms for the new kilogram definition. Metrologia 54:693–727

5. Vocke RD Jr, Rabb SA, Turk GC (2014) Absolute silicon molar mass measurements, the Avogadro constant and the redefinition of the kilogram. Metrologia 51:361–375
6. Azuma Y, Barat P, Bartl G et al (2015) Improved measurement results for the Avogadro constant using a ^{28}Si-enriched crystal. Metrologia 52:360–375
7. Flowers JL, Petley BW (2001) Progress in our knowledge of the fundamental constants of physics. Rep Prog Phys 64:1191–1246
8. Sortais Y et al (2000) ^{87}Rb verses 133Cs in cold atom fountains: a comparison. IEEE Trans Ultrason Ferroelectr Freq Control 47:1093–1097
9. Taylor BN, Phillips WD (eds) (1984). Precision measurement and fundamental constants II. National Bureau of Standards (U.S.), Special Publication 617
10. Aliezer S, Ghatak A, Hora H (2002) Fundamentals of equations of state, vol 384. World Scientific Publishing Co Pte LTD, River Edge
11. Glushko EY (2010) Pneumatic photonic crystals. Opt Express 18:3071–3079
12. Glushko EYa. The conception of scales echeloning for precise optical indication of pressure and temperature. 11th international conference on Laser and Fiber-Optical Networks Modeling (LFNM), 1–3, 2011
13. Rayleigh JWS (1887) On the maintenance of vibrations by forces of double frequency and on the propagation of waves through a medium endowed with a periodic structure. Philos Mag 24:145–159
14. Yablonovitch E (1987) Inhibited spontaneous emission in solid-state physics and electronics. Phys Rev Lett 58:2059–2062
15. John S (1987) Strong localization of photons in certain disordered dielectric superlattices. Phys Rev Lett 58:2486–2489
16. Werber A, Zappe H (2006) Tunable, membrane-based, pneumatic micro-mirrors. J Opt A Pure Appl Opt 8:313–317
17. Pervak V, Ahmad I, Trubetskov MK, Tikhonravov AV, Krausz F (2009) Double-angle multilayer mirrors with smooth dispersion characteristics. Opt Express 17:7943–7951
18. Tokranova N, Xu B, Castracane J (2004) Fabrication of flexible one-dimensional porous silicon photonic band-gap structures. MRS Proc 797. https://doi.org/10.1557/PROC-797-W1.3
19. Grzybowski B, Qin D, Haag R, Whitesides GM (2000) Elastomeric optical elements with deformable surface topographies: applications to force measurements, tunable light transmission and light focusing. Sensors Actuators 86:81–85
20. Landau LD, Lifshitz EM (1970) Theory of elasticity. Pergamon Press, New York, p 165
21. Turyshev SG, Toth VT (2010) The pioneer anomaly. Living Rev Relativ 13:4–171

Chapter 8
Nanoscale Photocatalytic Layers with Titania on Stainless Steel Foil

V. Honcharov, V. Zazhigalov, O. Sanzhak, F. Azimov, D. Brazhnyk, M. Parlinska-Wojtan, and E. Drzymala

8.1 Introduction

The widespread use of catalytic technologies in industry requires a thorough study of all properties of catalysts. The main requirements for modern catalysts are mechanical strength, thermal stability, activity and selectivity. Catalytic systems deposited on metals and alloys satisfy these requirements [1–6]. An important problem is the structure, quantity and composition of these systems on the support surface. Therefore, great attention is paid to the issue of catalyst synthesis technology. At present, nanoscale structures [7–9] have found wide application in various branches of science and technology. In particular, they have proven themselves in catalysis [10]. Hence, technologies of nanostructured catalysts synthesis are promising trend of modern materials science [11].

In fact, the most important problem of ecology is the removal of harmful wastes of chemical and pharmaceutical industries. Photocatalysis is a very effective technology in this direction. In particular, titanium oxide catalysts attract attention for organic compounds and dyes degradation [12, 13]. However, such catalysts have a number of disadvantages, among which are low activity in the visible optical range [14, 15], the use of dispersed titania what accompanied by an increase of treated

V. Honcharov (✉)
State Establishment "Lugansk State Medical University", Rubizhne, Ukraine

V. Zazhigalov · O. Sanzhak · F. Azimov · D. Brazhnyk
Institute for Sorption and Problems of Endoecology, National Academy of Sciences of Ukraine, Kyiv, Ukraine
e-mail: zazhigal@ispe.kiev.ua

M. Parlinska-Wojtan · E. Drzymala
Institute of Nuclear Physics, PAS, Krakow, Poland

© Springer Nature Switzerland AG 2019

O. Fesenko, L. Yatsenko (eds.), *Nanophotonics, Nanooptics, Nanobiotechnology, and Their Applications*, Springer Proceedings in Physics 222,
https://doi.org/10.1007/978-3-030-17755-3_8

solution turbidity and as result a decrease of light radiation effective and problems with separation catalyst from deactivated solution.

Prospect of development of photocatalytic processeas of environment protection is connected with the synthesis of new compositions more effective at visible light irradiation and the creation of supported catalysts which content the active phase on the surface of formed flat supports as ceramics, glasses, metallic foils etc [16, 17]. It is necessary to note that metallic foil supports have advantages over other materials what in first order it is connected with simple possibility of the prepared catalyst dimensions change according to catalytic reactor. The main problem of the preparation of supported titania containing catalysts is obtaining of layer with high adhesion to support which determines the high stability of the catalyst.

A number of papers cite data on the use of ion-plasma methods in catalytic technologies [11, 18–20]. One of the leading places among the ion-plasma technology takes ionic implantation [21–25]. It has significant advantages [21, 23, 26, 27] compared to other methods. Namely, it leads to the formation of nanoscale structures with a very small consumption of the target component. In this case, the synthesized systems have high mechanical strength, heat resistance and low price in comparison with the traditional ones [8, 9, 11, 24]. Unfortunately, there is small amount of literature sources on the use of ionic implantation for catalysts preparation and, in particular, their absence for photocatalysts synthesis. Therefore, the problems of the synthesis and study of the properties of supported titanium oxide photocatalysts obtained by ionic implantation presented in this paper is relevant.

8.2 The Experimental Part

The nanoscale photocatalytic layers with titania on stainless steel foil (SS) were prepared by low temperature ionic implantation method. The samples with thickness 100 mkm was treated by titania ion flow under fluence $5 \cdot 10^{17}$ cm^{-2}. Other conditions were next. Pressure in the vacuum chamber was 10^{-4} Pa, energy of the ions was 20 keV and processing time was 1 hour. After implantation some of samples were calcinated on air under differ temperatures (200, 300, 400, 500, 600 °C). Calcination time of the sample at each temperature was equal to 2 hours.

The implants were studied by means of traditional SEM. Scanning electron microscopy was carried out on a TESCAN VEGA 3 SBH instrument equipped with a tungsten cathode. The samples were deposited a SEM stub sample holder covered with a carbon patch. Uncoated samples were imaged in high vacuum mode at 30 kV accelerating voltage using the SE detector. The specific surface area of the samples was determined by krypton adsorption on NOVA 2200C Quantachrome Instruments. The detail of the samples study by XRD, SAXS and XPS methods were reported in [8, 11, 25]. The procedure of distribution of elements in surface layer by XPS method was described in [25].

The photocatalytic properties of the samples in degradation of benzene in aqueous solutions (50 threshold limit values (TLV)) was determined under visible

and UV irradiation. The study was carried out in a cylindrical reactor (9 cm diameter) with a wall-placed 10 cm height sample (implantation on both sides of the foil) and immersed thermostatically controlled radiation source. The source of radiation (high pressure mercury or sodium lamps were used) was placed in reactor centre, which permits to implement the investigation in both UV and visible range. The reaction products were analyzed on a SelmiChrom-2 gas chromatograph equipped with a FID on a stainless steel column (length 1 m, diameter 3 mm) filled with Porapak Q.

8.3 Results and Discussion

The data obtained by XRD method demonstrate the presence of (111) (200) and (220) planes austenite reflexes (initial stainless steel) in diffractogram of synthesized sample with implanted titanium, only [25]. The SAXS data show the some shift of these reflexes compared initial support after titanium implantation what corresponds to the results obtained for other implants [25, 26] and it is connected with titanium introduction in support matrix. The realized in this work thermal treatment of the sample (200–600 °C) has any influence of XRD and SAXS data.

In the same time the SEM data (cross section) [11, 25] shown the formation of the new layer (thickness of this layer is near to 80 nm) of the stainless steel surface after titanium implantation. The results of XPS study demonstrate the presence of titanium, oxygen and nitrogen in this nanolayer [25] and the formation of amorphous titanium oxynitride and nitride of titanium in this layer on stainless steel surface as result of titanium implantation was supposed. It was shown [25] that treatment of this sample at 600 °C led to formation of titanium oxide in this surface layer. The influence of other temperatures of the sample treatment on its properties was no studied.

In this study firstly it was found (Fig. 8.1) that the implants containing titanium on the base of stainless steel foil have the much higher benzene photodegradation activity at visible light than at UV-irradiation.

In the second it is characteristic that in the visible irradiation spectrum the samples have a maximum activity after their annealing at temperature equal to 200 °C. The initial steel and samples with a treatment temperature of 300–500 °C have a significantly lower activity. The foil after annealing at a temperature equal to 600 °C almost does not show activity in this process.

One of the possible causes of the observed effect is the replacement of nitrogen atoms, trapped from the plasma, initiating a discharge, during ionic implantation with oxygen atoms [28]. Another reason may be morphological changes (changes in the size of oxides and nitrides of titanium, changes in surface roughness, migration of defects, etc.) of samples caused by temperature.

In order to test these hypotheses a study of the surface of the samples after their temperature treatment at different temperatures was conducted. The results of SEM investigations are shown in Fig. 8.2.

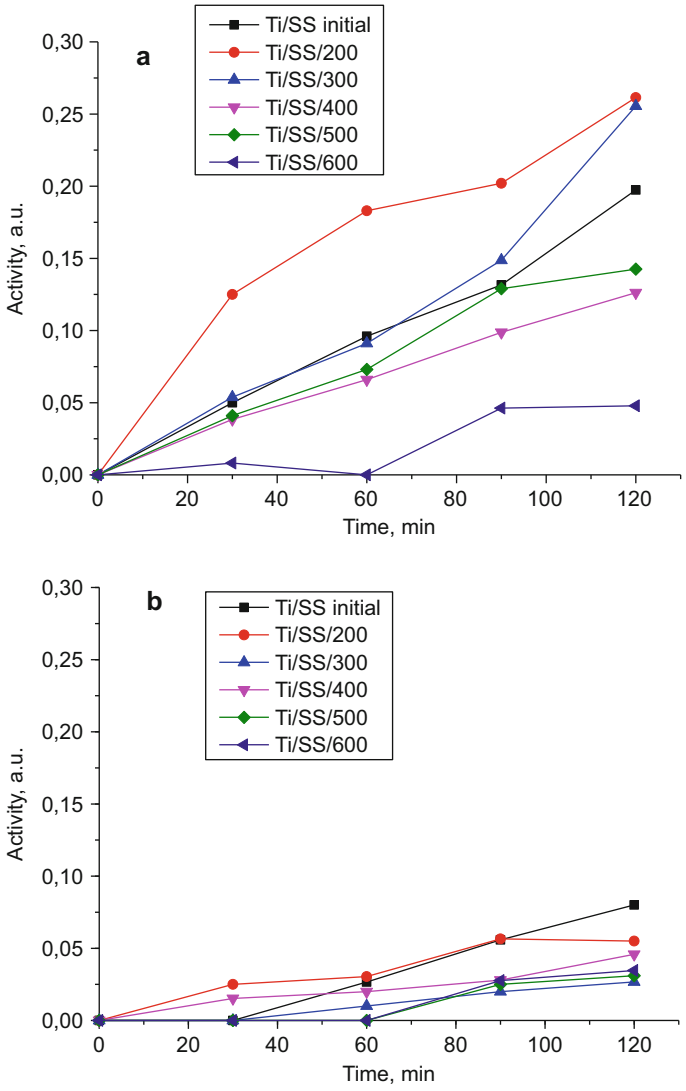

Fig. 8.1 The Ti/SS samples activities under the aqueous benzene solution photodegradation: (**a**) visible light, (**b**) UV irradiation

Initial sample demonstrate that after titanium nanolayer deposition all defects connected with stainless steel foil manufacture rests without changes and its morphology practically no difference from initial support. But the treatment of the sample at 200 °C drastically changes its surface morphology and the appearance of surface snow-like layer can be observed. The increase of the treatment temperature accompanied by destruction of this snow-like layer and the formation of tightly

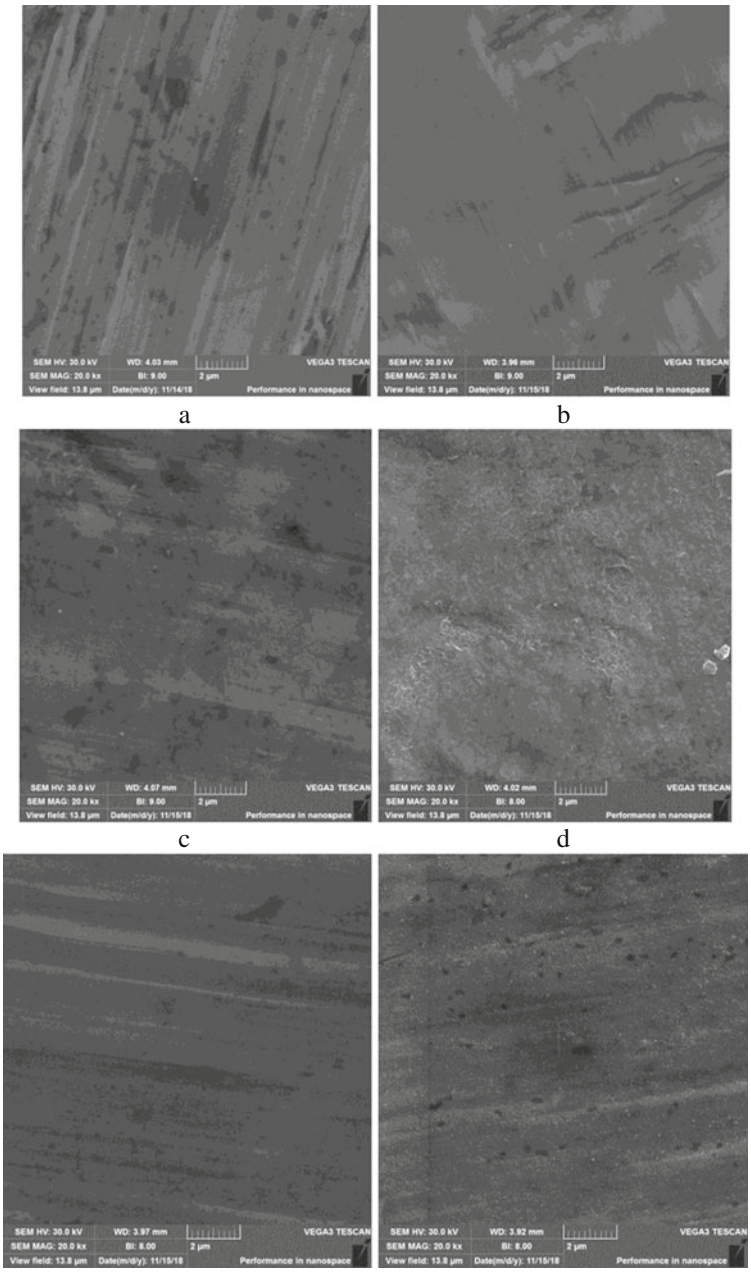

Fig. 8.2 The data of SEM investigation of Ti/SS samples: initial sample (**a**) and after its temperature treatment under 200 °C (**b**), 300 °C (**c**), 400 °C (**d**), 500 °C (**e**), 600 °C (**f**)

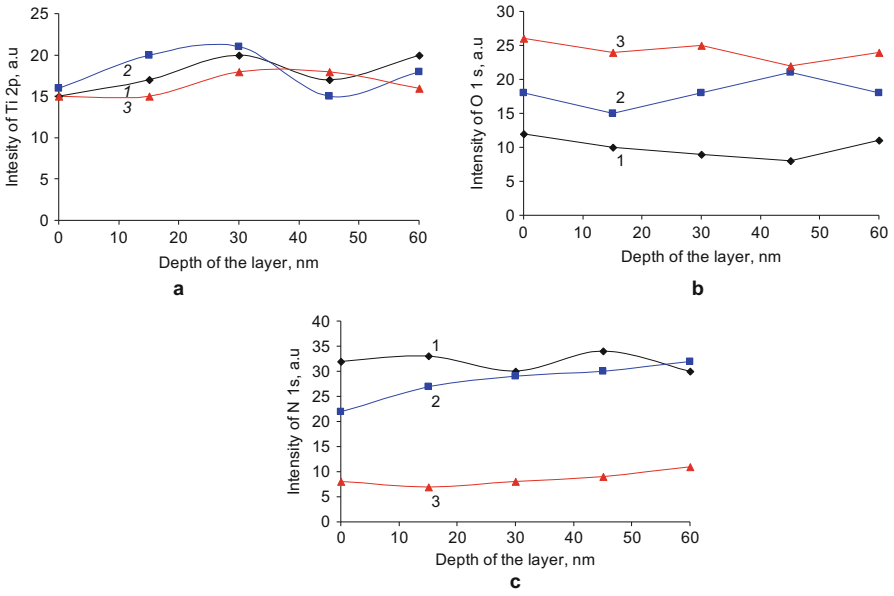

Fig. 8.3 Influence of thermal treatment of the Ti/SS sample on elements content on surface layer of the samples: (**a**) Ti, (**b**) O, (**c**) N. Initial sample – 1, samples after thermal treatment at 200 °C – 2, 500 °C – 3

evenly coated surface was observed clearly after 400 °C and 500 °C treatment. The formation of the defects on surface (dark places) can be observed after treatment at 500 °C but their quantity and distribution increased after 600 °C.

It is necessary to note that the specific surface area of the support (stainless steel) increases after titanium implantation in two order (from $2 \cdot 10^{-4}$ up to $3.6 \cdot 10^{-2}$ m^2/g). But the temperature treatment of implant leads to further increase of this value: 0.4 m^2/g after 200 °C and 0.15 m^2/g after 500 °C.

The study of elements distribution in depth of surface layer of the implanted samples shows (Fig. 8.3) that temperature treatment has less influence on Ti content on surface layer (Fig. 8.3a). In the same time the treatment accompanied by the increase of oxygen content in surface layer (Fig. 8.3b) and vice versa leads to the decrease of nitrogen content (Fig. 8.3c). Taking into account the previously obtained data [25] it is possible to suppose that temperature treatment in air leads to rapid oxidation of titanium nitride on surface of the sample with formation of titanium oxynitride (200 °C). The increase of the treatment temperature accompanies by further oxidation of oxynitride and nitride of titanium which leads to formation of titanium oxide surface layer.

So, it is possible to suppose that high photocatalytic activity of the sample after treatment at 200 °C is connected with higher content of titanium oxynitride on surface.

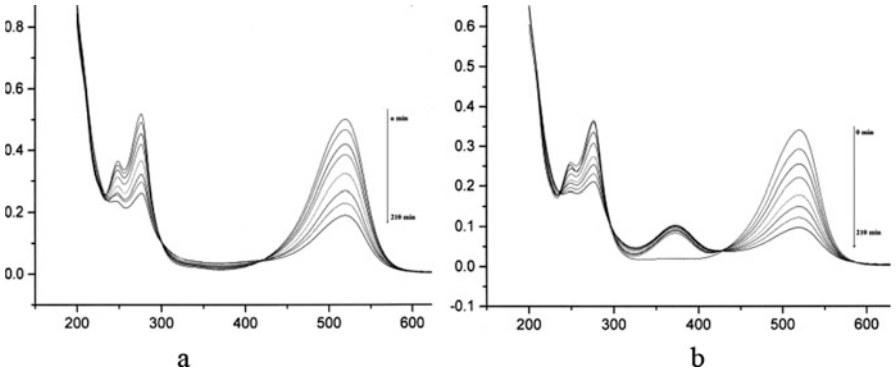

Fig. 8.4 Photocatalytic degradation of the Safranin T on the Ti/SS samples treated at 200 (**a**) and 500 °C (**b**)

In the other hand it was established by us that the dye (Safranin T) degradation (reaction was effected according the Protocol [29]) at visible light irradiation (all samples were inactive in UV irradiation) proceeds with higher activity on the sample Ti/SS thermally treated at 500 °C (Fig. 8.4). As result it is possible to suppose that photocatalytic activity of the catalysts prepared by ionic implantation of titanium on stainless steel determined not only of surface composition but the influence of the nature of waste influenced on the effective of process. In the last case the formation of nanodispersed titania on support surface determines the activity of this reaction.

8.4 Conclusions

It was established that the samples synthesized on stainless steel using ionic implantation have a high catalytic activity in the reaction of aqueous benzene solution photodegradation. At what the implants containing titanium on the base of stainless steel foil have the much higher benzene photodegradation activity at visible light than at UV-irradiation. It is shown that the maximum activity is observed in samples that were additionally calcined at a temperature of 200 °C. It was found that during calcination of implants, they are changed not only by the composition, but also by the microstructure of their surface (the specific surface area of the support increases after titanium implantation in two order), that causes catalytic properties. It was established that high photocatalytic activity of the sample after treatment at 200 °C is connected with higher content of titanium oxynitride on surface. The influence of the nature of waste on the effective of process was shown.

Thus, ionic implantation has significant prospects in ecological catalysis, energetics, chemical and pharmaceutical industries as a technology for the synthesis of photocatalysts.

Acknowledgments The investigations were realized with partial financial support of NAS of Ukraine Fundamental Programme “Fine Chemicals”, Project 20-(14-16).

References

1. Giornelli T, Lofberg A, Bordes-Richard E (2006) Preparation and characterization of VO_x/TiO_2 catalytic coatings on stainless steel plates for structured catalytic reactors. Appl Catal A Gen 305:197–203
2. Vaneman GL (1991) Comparison of metal foil and ceramic monolith automotive catalytic converters. Catal automot pollut control II 71:537–555
3. Muraoka S, Kitamura K, Kishi S et al (2007) Development of efficient metal catalyst support. Mater Sci Forum 561–565(1):547–550
4. Wyrwa DW, Schmid G (2007) Metal nanoparticles on stainless steel surfaces as novel heterogeneous catalysts. J Clust Sci 18(3):476–493
5. Kaltner W, Veprek-Heijman M, Jentys A et al (2009) Effect of chromium migration from metallic supports on the activity of diesel exhaust catalysts. Appl Catal Environ 89:123–127
6. Zamaro JM, Ulla MA, Miro EE (2008) ZSM5 growth on a FeCrAl steel support. Coating characteristics upon the catalytic behavior in the NO_x SCR. Microporous and Mesoporous Mater 115:113–122
7. Bogdanov NY (2008) Nonastructuring of metal materials by intense ion beams. Fizika i Khimiya Obrabotki Materialov 40(44):8–44
8. Zazhigalov VA, Honcharov VV (2014) Formirovaniye nanorazmernogo pokrytiya na stali 12H18N10T pri ionnoy implantatsii. Metallofizika i Noveishie Tekhnologii 6(36):757–766
9. Cherny AA, Maschenko SV, Honcharov VV et al (2015) Nanodimension layers on stainless steel surface synthesized by ionic implantation and their simulation. In: Nanoplasmonics, nano-optics, nanocomposites and surface studies. Springer, Cham, pp 203–213
10. Chena J, Li Y, Li Z et al (2004) Production of COx-free hydrogen and nanocarbon by direct decomposition of undiluted methane on Ni–Cu–alumina catalysts. Appl Catal Gen 269:179–186
11. Honcharov V, Zazhigalov V, Sawlowicz Z, Socha R, Gurgol J (2017) Structural, catalytic, and thermal properties of stainless steel with nanoscale metal surface layer. In: Fesenko O, Yatsenko L (eds) Nanophysics, nanomaterials, interface studies, and applications. NANO 2016. Springer proceedings in physics, vol 195. Springer, Cham
12. Malato S, Fernandez-Ibanez P, Maldonado MI, Blanco J, Gernjak W (2009) Decontamination and disinfection of water by solar photocatalysis: recent overview and trends. Catal Today 147:1–59
13. Thompson TL, Yates JT (2006) Surface science studies of the pho-toactivation of TiO_2 new photochemical processes. Chem Rev 106:4428–4453
14. Hiroshi I, Yuka W, Kazuhito H (2003) Carbon-doped anatase TiO_2 powders as a visible-light sensitive photocatalyst. Chem Lett 32(8):772–773
15. Lin X, Rong F, Fu D, Yuan C (2012) Enhanced photocatalytic activity of fluorine doped TiO_2 by loaded with Ag for degradation of organic pollutants. Powder Technol 219:173–178
16. Rachel A, Subrahmanyan M, Boule P (2002) Comparison of photocatalytic efficiencies of TiO2 in suspended and immobilised form for photocatalytic degradation of nitrobenzenesulfonic acids. Appl Catal B Environ 37:301–308
17. Shan AY, Ghazi TIM, Rashid SA (2010) Immobilisation of titanium dioxide onto supporting materials in heterogeneous photocatalysis. A review. Appl Catal A General 389:1–8
18. Magali BK, Sven GJ (1996) A review of the use of plasma techniques in catalyst preparation and catalytic reactions. Appl Catal Gen 147:1–21
19. Liu CJ, Vissokov G, Jang BWL (2002) Catalyst preparation using plasma technologies. Catalysis Today 72:173–184

20. Durme JV, Dewulf J, Leys C et al (2008) Combining non-thermal plasma with heterogeneous catalysis in waste gas treatment: a review. Appl Catal Environ 78:324–333
21. Kalin BA (2001) Radiatsionno-puchkovyye tekhnologii obrabotki konstruktsionnykh materialov. Fizika i khimiya obrabotki materialov 4:5–16
22. Wang H, Zhang S, Yu D et al (2011) Surface modification of (Tb, Dy)Fe_2 alloy by nitrogen ion implantation. J Rare Earths 29(9):878–882
23. Khirvonen DK (1985) Ionnaya implantatsiya. Metallurgiya, Moskva
24. Kang TJ, Kim JG, Lee HY et al (2014) Modification of optical and mechanical surface properties of sputter-deposited aluminum thin films through ion implantation. Int J Precis Eng Manuf 15(5):889–894
25. Zazhigalov VA, Honcharov VV, Bacherikova IV, Socha R, Gurgul J (2018) Formation of nanodimension layer of catalytically active metals on stainless stail surface by ionic implantation. Theor Experim Chem 34(2):128–137
26. Dudognon J, Vayer M, Pineau A et al (2008) Grazing incidence X-ray diffraction spectra analysis of expanded austenite for implanted stainless steel. Surf Coat Technol 202(20):5048–5054
27. Dudognon J, Vayer M, Pineau A et al (2008) Mo and Ag ion implantation in austenitic, ferritic and duplex stainless steels: a comparative study. Surf Coat Technol 203:180–185
28. Li X, Xiong R, Wei G (2008) S–N Co-doped TiO_2 photocatalysts with visible-light activity prepared by sol–gel method. Catal Lett 125(1–2):104–109
29. Zazhigalov VA, Sidorchuk VV, Khalamieda SV, Kuznetsova LS (2008) Mechanochemical synthesis of $BaTiO_3$ from barium titanyl oxalate. Inorg Chem 44(6):641–645

Chapter 9
New Methacrylic Polymers with Heterocyclic Analogs of Stilbene in Side Chain – Promising Materials for Optoelectronics

O. Krupka, O. Kharchenko, V. Smokal, A. Kysil, and A. Kolendo

9.1 Introduction

Organic and polymeric nonlinear optical (NLO) materials have continuously drawn great interest due to their several advantages superior to conventional inorganics, such as large nonlinear optical coefficient, ultrafast response, wide response wave band, high optical damage threshold, and easy combination and modification. Generally, desired NLO materials should exhibit a high NLO property, good optical transparency, and thermal stability. Designs and syntheses of effective chromophores are very important for acquiring desired NLO materials [1].

π-Conjugated organic compounds based on aromatic systems attract significant attention with respect to the application as semiconductors in organic field transistors (OFETs), organic light-emitting diodes (OLEDs), and photogalvanic batteries, and also as biological active compounds [2].

Stilbene and its derivatives are good materials for molecular electronics due to their properties of organic conductors, photoswitches, organic displays, or biosensors [3]. Stilbene and its derivatives have so many advantages and have been of interest for more than half a century [4]. Nowadays, heterocyclic analogs of stilbene are commonly requested in different areas of science and technology [5].

Styrylquinolines are derivatives of stilbene and these dyes have two active centers – endocyclic nitrogen atom and ethylene group. Thus, styrylquinolines can enter into variety photochemical reactions [6–9].

The styryl dyes [10] with quinoline nucleus were applied to various sensitive materials such as sensitizers or desensitizers formerly. With the development of new technologies, the researchers have found a new application of styrylquinoline dyes

O. Krupka (✉) · O. Kharchenko · V. Smokal · A. Kysil · A. Kolendo
Taras Shevchenko National University of Kyiv, Kyiv, Ukraine

© Springer Nature Switzerland AG 2019

O. Fesenko, L. Yatsenko (eds.), *Nanophotonics, Nanooptics, Nanobiotechnology, and Their Applications*, Springer Proceedings in Physics 222,
https://doi.org/10.1007/978-3-030-17755-3_9

to electroluminescence [11] and photochromism [12, 13] as well as in the field of pharmaceutics [14, 15]. For example, the study of the photochemical properties of 2-styrylquinoline and its several derivatives showed that the substituents in the styryl moiety increased the quantum yield of photoisomerization [16].

Here, stilbene derivatives have been chosen for the synthesis of methacrylic polymers and investigation of their photochemical properties as promising materials.

The side chain methacrylic polymers with different active functional group have been well studied and widely applied in many fields, such as optoelectronics, nonlinear optics, optical storage materials, biochemicals, and medicine. Thus, creating these polymers is one of the actual problems in modern polymer chemistry. Photopolymers are studied for their macromolecular properties and for the properties of the photosensitive group. Among them, polymers having photochromic dyes, such as azo [17], cinnamoyls, chalcones, coumarins, spyrooxazines, diarylethenes, etc., represent an active field of research in polymer science because of their technological applications in the fields of photolithography, nonlinear optical materials, liquid crystalline materials, and holographic elements [18–22].

The copolymer composition and comonomer unit distribution depend on monomer reactivity ratios. The most common mathematical model of copolymerization is based on finding the relationship between the composition of copolymers and the composition of the monomer feed in which the monomer reactivity ratios are the parameters to be determined [23]. The calculation of the monomer reactivity ratios requires the mathematical treatment of experimental data on the composition of copolymers and monomer in feed mixtures. The most fundamental quantities characterizing a copolymer is its composition on a molar basis, which eventually is used for the determination of the relevant monomer reactivity ratios. Spectroscopic methods, preferably ^{1}H NMR spectroscopy, and elemental analysis are probably the most widely used methods for the analysis of copolymers and the determination of reactivity ratios r_1 and r_2.

9.2 Experimental

Methods: ^{1}H NMR spectra were obtained on a “Mercury” 400 MHz Bruker, using $CDCl_3$, DMSO-d_6 as the solvents. Chemical shifts are reported in ppm (δ) to internal standard $Si(CH_3)_4$. Infrared spectra were recorded on Perkin Elmer BX with KBr. UV-VIS spectra were recorded on a Shimadzu UV-1800 spectrometer (Shimadzu, Kyoto, Japan) at room temperature in solution in a quartz liquid cell. KM-6 cathetometer was used for measuring kinetics of polymerization.

The synthesis of 2-styrylquinolines was described earlier [8, 9, 24, 25] according to general technique [26]. Compounds **1a**–**1h** were obtained from 8-hydroxy-2-methylquinoline with appropriate aromatic aldehydes by Knoevenagel condensation during 14 hours; see Scheme 1, *a* and *b*. Methacrylic monomers **2a**–**2h** were synthesized from **1a**–**1h** by using methacryloyl chloride as acylating agent and

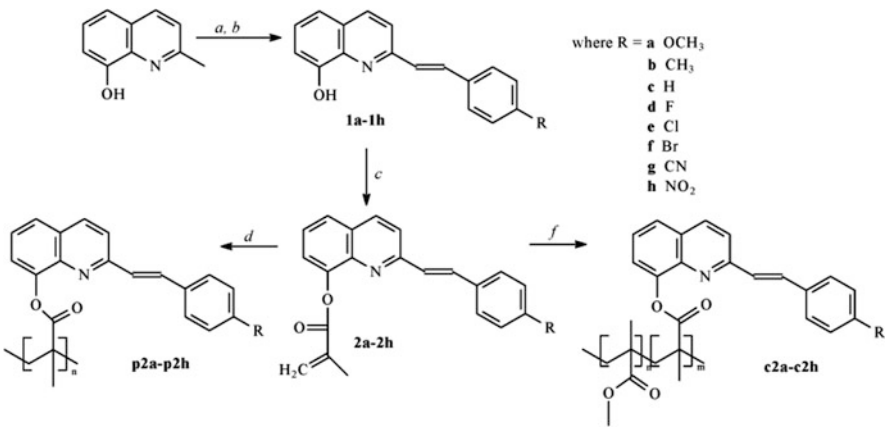

Fig. 9.1 Synthesis 2-styrylquinolines and polymers based on them. Reagents and conditions: a) Ac_2O, 140 °C, R-PhCHO; b) *1 step*, EtOH, HCl (c); *2 step*, EtOH, $(Et)_3N$; c) DMF, $CH_2 = C(CH_3)COCl$, −5–0 °C, $(Et)_3N$; d) DMF, 80 °C, argon; f) DMF, MMA, 80 °C, argon

triethylamine as acceptor of hydrogen chloride. These monomers are stable for keeping at room temperature and are good soluble in organic solvents.

Free radical polymerization. The synthesis of homopolymers and copolymers (mole ratio 1:3) based on methacrylic monomers **2a**–**2h** and methylmethacrylate (MMA) was conducted in 10% DMF solution with AIBN as radical initiator at 80°C (argon atmosphere). The mixture was degassed with repeated freeze and three cycles. The polymerization was stopped by pouring the reaction mixture into methanol. The precipitation was repeated from DMF into methanol to give purified polymers. Polymers were dried under vacuum at 50 °C overnight. Synthetic route and chemical structures of the styrylquinoline containing polymers are shown in Fig. 9.1d, f.

Kinetics of homopolymerization and copolymerization (1:3) of 2-styrylquinolines containing monomers with MMA were investigated by dylatometric method at conditions that were mentioned above. The conversion rates were controlled gravimetrically. The polymerization was carried out during 4 hours. Purification of polymers was done analogically.

9.3 Results and Discussion

Series of methacrylic monomers **2a**–**2h** with different donor–acceptor substituents in benzene ring were synthesized. Homopolymers and copolymers with MMA (1 moiety of 2-styrylquinoline monomer to 3 moieties of MMA) were synthesized by free radical thermoinitiated polymerization of 10% solutions of monomers in DMF at 80 °C and inert atmosphere. Dilatometric method was used for investigation

kinetic's parameters such as conversion, speed of polymerization (V_{gr}), total constant of polymerization's speed (K_{sum}). Kinetic's curves of homopolymerization of monomers **2a**–**2h** are shown in Fig. 9.2.

Kinetic's parameters were calculated from kinetic's curves by computing program, and Table 9.1 presents its results.

The biggest speed of polymerization was obtained for **2c** and 8-methacryloxyquinaldine, a bit lower for **2b** and **2e**, monomers with methyl and chlorine substituents accordingly. The monomer with nitro group as substituent has got the lowest speed of polymerization, because it is well known that nitro group is a trap of free radicals. As was shown, 2-styrylquinoline-containing monomers have bigger speed of polymerization (V_{gr}) than the polymerization of MMA, but lower value V_{gr} than the polymerization of 8-methacryloxyquinaldine. In general, polymerization of **2a**–**2h** were carried out to high conversions – from 63% to 83%.

Reactivity of styrylquinoline-containing methacrylic monomers. The free radical copolymerization of various ratios of **2a, 2c, 2h**, and MMA initiated by AIBN has

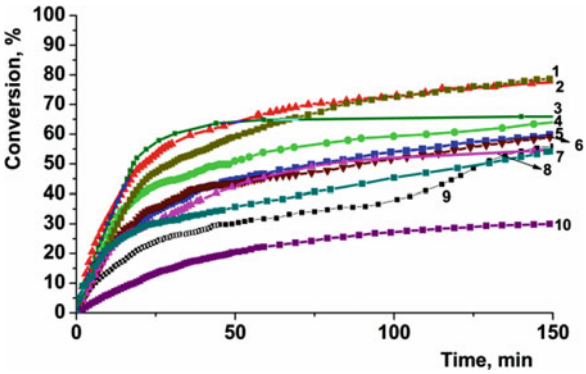

Fig. 9.2 Kinetic's curves of homopolymerization of 10% DMF solutions of 2-styrylquinoline monomers at 80 °C: 1, 8-methacryloxyquinaldine; 2, 2c; 3, 2a; 4, 2f; 5, 2e; 6, 2a; 7, 2g; 8, 2d; 9, 2h; 10, MMA

Table 9.1 Kinetic's parameters of polymerization of methacrylic monomers

Monomer	Substituent	Conversion for 4 h, %	$V_p \times 10^4$, mol/l × s	$K_\Sigma \times 10^3$, l/mol × s
2a	$-OCH_3$	67	0.95	2.55
2b	$-CH_3$	66	1.62	8.33
2c	–H	83	1.78	4.50
2d	–F	64	1.08	5.60
2e	–Cl	68	1.24	3.45
2f	–Br	75	1.04	3.27
2g	–CN	63	1.01	2.75
2h	$-NO_2$	63	0,8	1.36
MMA		33	1.08	0.51
Ph-methacrylate[a]		–	0.52	1.10
8-methacryloxyquinaldine		85	1.81	3.28

[a]Ref. [27]

been carried out at 80 °C during 5–15 minutes for reaching yields of polymers 5–10%. Purification of polymers was carried out according to standard methods. The copolymer compositions to determine monomer reactivity ratios were analyzed by ^{1}H NMR spectra. Thus, the mole fractions of **2a, 2c, 2h**, and MMA in the copolymer were determined from the ratio of the integral intensities of aromatic and –CH=CH– protons in monomer's units, at 6.9–8.35 ppm (11 protons – for **2a** and **2h**, 12 protons – for **2c**), and methyl protons adjacent to oxygen at 3.8 ppm for MMA units [28]. For example, the mole fraction of 2h:MMA in copolymer have been calculated from the following equation:

$$\mathbf{2h} : \mathrm{MMA} = \frac{\text{Integral intensites at } 6.9 - 8.35 \text{ ppm}}{11} : \frac{\text{Integral intensites at } 3.8 \text{ ppm}}{3} \tag{9.1}$$

For the copolymerization, the behaviors of the system were evaluated through plots of the copolymer composition (Fig. 9.3). The composition of copolymer obtained from the copolymerization technique showed azeotropic composition at F_1 0.4–0.5. The monomer reactivity ratios, the content of the reaction mixture, and the copolymer were calculated according to the Fineman–Ross (FR) and calculation methods.

The FR parameters were calculated for free radical copolymerization of **2a, 2c, 2h**, and MMA. It is well known that monomer reactivity ratios can be indicative of the relative reactivity of comonomers. In order to estimate the relative reactivity ration of **2a, 2c, 2h**, and MMA in free radical copolymerization, the FR [23, 29], the next equation have been used:

$$y = r_2 - r_1{}^* x, \tag{9.2}$$

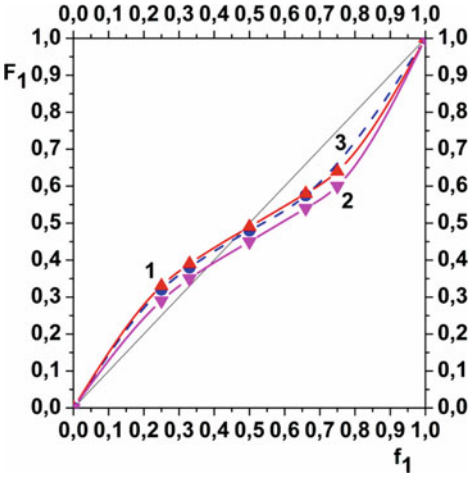

Fig. 9.3 Composition diagrams of the free radical copolymerization of 2a, ▲; 2c, ▼;2h, •, with MMA

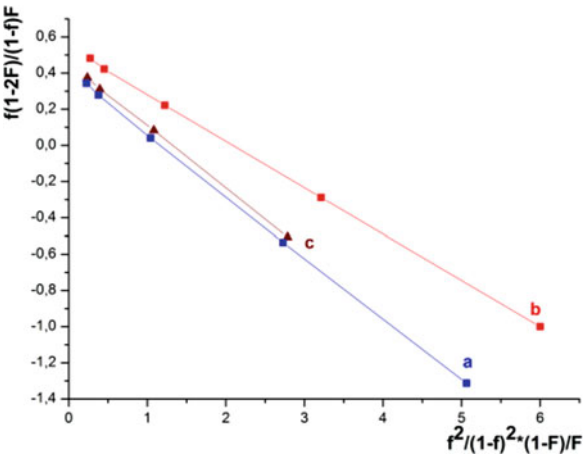

Fig. 9.4 Fineman-Ross plots for the free radical copolymerization of **2a** (**a**), **2c** (**b**), **2h** (**c**) with MMA

where $x = (f^2/(1-f)^2*(1-F)/F$ and $y = f(1-2F)/(1-f)F$, respectively. From the slope and intercept of the straight line, the monomer reactivity ratios of **2a, 2c, 2h**, and MMA were determined and found to be $r_1 = 0.34$, $r_2 = 0.41$ for **2a** monomer; $r_1 = 0.26$, $r_2 = 0.55$ for **2c** monomer; and $r_1 = 0.33$, $r_2 = 0.44$ for **2h** monomer (Fig.9.4). According to the calculating method, the copolymerization parameters were found – for **2a** $r_1 = 0.339 \pm 0.004$, $r_2 = 0.411 \pm 0.011$; for **2c** $r_1 = 0.255 \pm 0.004$, $r_2 = 0.547 \pm 0.014$; and for **2h** $r_1 = 0.327 \pm 0.004$, $r_2 = 0.444 \pm 0.006$. As we can see, the monomer reactivity ratios determined by calculation methods almost completely coincide with the ratios previously determined by the FR method.

The copolymer composition equation has the form $y = r_1*x + r_2$: in the calculations method for the determination of r_1 and r_2.

$$[M_1]/[M_2] * ([m_2]/[m_1] - 1) = -r_1{}^*([M_1]/[M_2])^{2*}[m_2]/[m_1] + r_2$$

where $y = [M_1]/[M_2]*([m_2]/[m_1]–1)$ and $x = ([M_1]/[M_2])^2*[m_2]/[m_1]$.

It is well known that Price and Alfrey developed a simple scheme (Q–e) to predict reactivity ratios of monomers participating in a free radical copolymerization [23]. From the Q–e scheme were calculated the resonance stabilization parameter Q and electronegativity parameter e. The Q–e scheme postulates that the reactivity ratios r_1 and r_2 can be expressed by the equation:

$$r_1 = Q_1/Q_2 \exp[-e_1(e_1 - e_2)] \tag{9.3}$$

$$r_2 = Q_2/Q_1 \exp[-e_2(e_2 - e_1)] \tag{9.4}$$

The Q–e values of MMA have been found in the literature [30] to be following $Q = 0.74$ та $e = 0.4$. The Q–e values of styrylquinoline-containing methacrylic

monomers have been found to be $Q = 3.16$, $e = 1.8$ for **2a**; $Q = 2.37$, $e = 1.8$ for **2c**; and $Q = 2.91$, $e = 1.79$ for **2h**.

The values of parameter r_1 illustrate similar values which were obtained with using two different methods. These values can be explained not enough influence of substitute effect.

The values of reverse constants $1/r_2$ were calculated. It was installed to be 2.44 for **2a**, 1.82 for **2c**, and 2.27 for **2h**. It was found that all three new monomers can join to the radical of MMA actively, moreover, the most active monomer with CH_3-group. The similar and low values of $r_1 * r_2$ (for **2a** – 0.14, for **2c** – 0.14, for **2h** – 0.15) illustrate the common tendency of styrylquinoline-containing monomers to interchange with links of MMA. The values of Q parameters have correlated with the values of $1/r_2$, and the values of the polar factor e have been almost identical for all monomers.

Photochemical properties of styrylquinoline-containing methacrylic polymers have been investigated. Absorption spectra of **p2b–p2f** polymers have long-wavelength absorption band (LWAB) at 340 nm and vibrational structure at 285 nm (Fig. 9.5, spectra 3–7). As was shown in Fig. 9.4, the introduction of methoxy (**p2a**) or nitro (**p2h**) group into the styrylquinoline molecule in the neutral form leads to a bathochromic shift of LWAB by ~23 or 30 nm, respectively, and the disappearance of the LWAB vibrational structure in the case of **p2h** (Fig. 9.5, spectra 1, 2).

Isomerization of p2a–p2h solutions in THF (tetrahydrofuran) has been got after UV irradiation at a wavelength of 366 nm. Absorption spectra of p2b during UV irradiation in THF are represented in Fig. 9.6. Initial spectrum (Fig. 9.5) is thermostable trans-isomer. Decrease of absorption intensity for p2b was observed at 260–380 nm and increase of absorption intensity at 225–245 nm with isosbestic point at 252 nm during irradiation process (1153 s). The photostationary state (D_{pss}) was reached under irradiation. Concentrations of trans- and cis-isomers in the mixture depend on irradiation wavelength [31]. It was found that the biggest changes in the absorption spectra go at 295 nm under irradiation of styrylquinoline containing derivatives. The proportion between the decreases of optical density at a

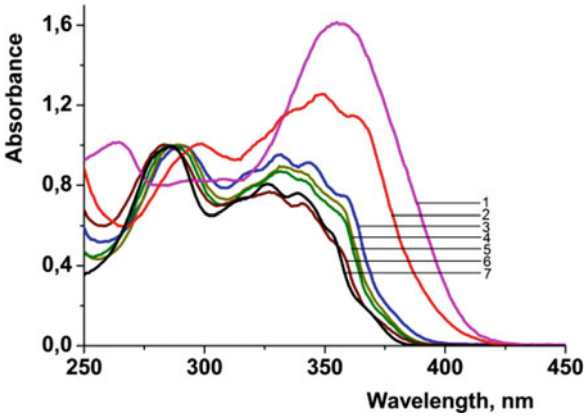

Fig. 9.5 Normalized absorption spectra of solutions of homopolymers **p2a–p2h** in THF: 1, p2h; 2, p2a; 3, p2b; 4, p2f; 5, p2e; 6, p2d; 7, p2c

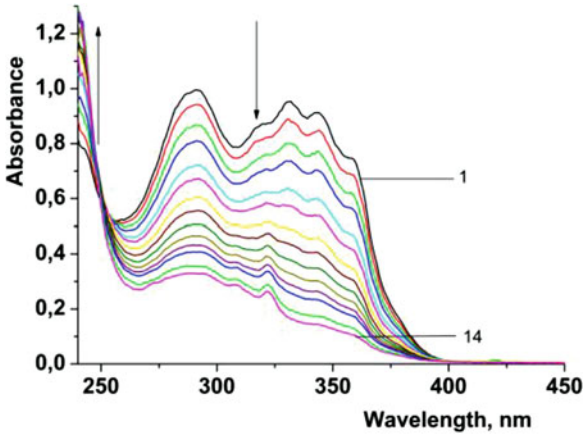

Fig. 9.6 Changes of absorption spectra of polymer p2b in THF under irradiation at the wavelength of 366 nm at room temperature

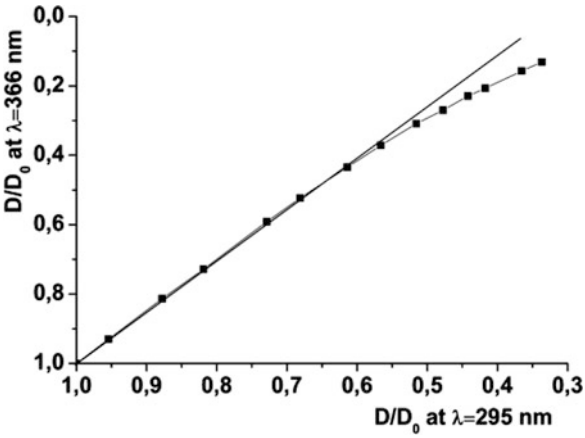

Fig. 9.7 The proportion between the decreases of optical density of p2b at a wavelength of 290 nm and its decreases of 366 nm after irradiation by $\lambda = 366$ nm

wavelength of 295 nm and its decreases of 366 nm after irradiation by $\lambda = 366$ nm was checked (Fig. 9.7). The linearity is kept till significant irradiation times, which allowed to study changes in optical density at the wavelength of 295 nm.

It was obtained that graphic dependence $\ln(D_{pss} - D_0)/D_{pss} - D_t)$ on the irradiation time under irradiation with light $\lambda = 366$ nm is not linear, see Fig. 9.8.

Figure 9.9 presents the semi-logarithmic dependence of changes in optical density $\mathrm{Ln}(D/D_0)$ of polymers on time of irradiation. It was found that speed of trans-cis-photoisomerization reaction increases with increasing electron acceptor properties of substitutes in the aromatic ring. Constants of speed of trans-cis-photoisomerization were obtained by tgα of dependence $(D_{pss}-D_0)/D_{pss}-D_t)$ on

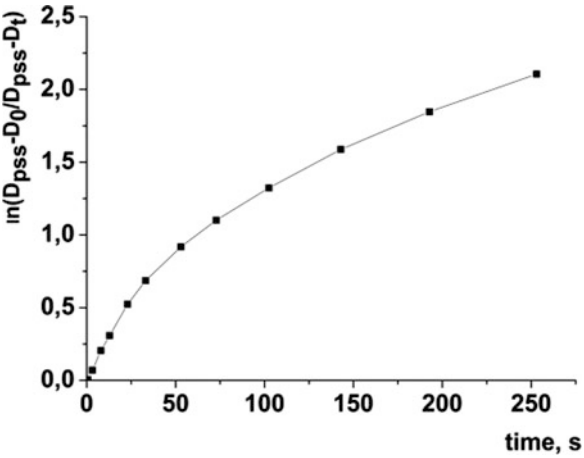

Fig. 9.8 Graphic dependence $\ln(D_{pss} - D_0)/D_{pss} - D_t)$ on the irradiation time under irradiation of p2b in THF with light $\lambda = 366$ nm

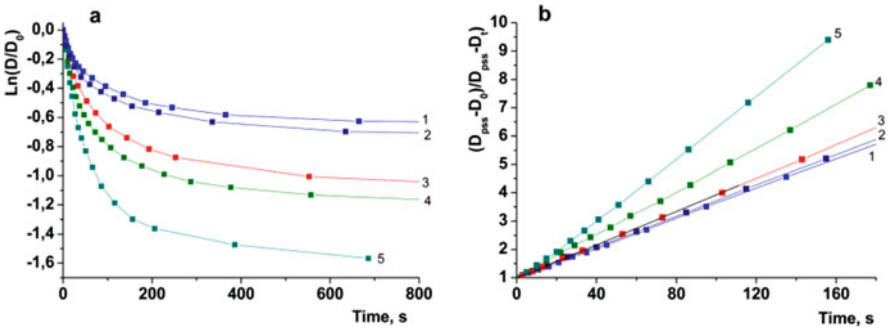

Fig. 9.9 Graphic dependence $\ln(D_t/D_0)$ (**a**) and $\ln(D_{pss} - D_0)/D_{pss} - D_t)$ (**b**) at 295 nm on time of irradiation $\lambda = 366$: 1, **p2a**; 2, **p2d**; 3, **p2b**; 4, **p2e**; 5, **p2f**

Table 9.2 Values of constants of speed of trans-cis-photoisomerization and half-reaction periods

Polymer	K_{t-c}, $\times 10^2$, s^{-1}	$\tau_{0.5}$, s	σ_0-Hammett constant
p2a	2.5	28	−0.28
p2b	2.7	26	−0.14
p2d	2.8	25	0.15
p2e	4.0	17	0.24
p2f	5.8	12	0.26

irradiation time at linear sections (to 200 s of irradiation). The half-reaction periods were calculated by formula: $\tau_{0,5} = \ln 2/k_{t-c}$.

Moreover, constants of speed of isomerization and half-reaction periods are not constants of basic photoprocess (Table. 9.2), but they are characteristics of speed disappearance trans-isomer at such conditions of experiment.

Table 9.2 presents that speed of photoisomerization increases with the growth of the Hammett constant of the substituent.

The cis-trans photo-induced isomerization of styrylquinoline derivatives under UV irradiation with the wavelength 254 nm was investigated. Solutions of the investigated polymers in THF, which were previously irradiated at 366 nm wavelengths and photostationary state was reached, were used for investigation of cis-trans-isomerization. The maximum absorption of cis-forms of polymers is in the region of 270–330 nm. Changes in absorption spectra in all cases are the same and typical for cis-trans isomerization processes. Isobestic point was present during irradiation time.

Figure 9.10 presents changes in the absorption spectra of c2a in THF of trans-cis-isomerization under UV irradiation with the wavelength 366 nm (Fig. 9.10a) and cis-trans-isomerization under UV irradiation with the wavelength 254 nm; see Fig. 9.10b. The semi-logarithmic dependence of changes in the optical density $\mathrm{Ln}(D/D_0)$ (Fig. 9.10a) and $\ln(D_{\mathrm{pss}}-D_0)/D_{\mathrm{pss}}-D_t)$ (Fig. 9.10b) on the time of irradiation are shown in Fig. 9.11 for copolymers with the mole ratio 1:3.

The processes of cis-trans isomerization take place for homopolymers and copolymers. It was installed that the speed of this isomerization process increases linearly with increasing electron donation of substitutes (values of its Hammett substituent constant σ_0) in the aromatic ring. Table 9.3 presents the constant's values of speed of cis-isomerization and half-reaction periods of cis-isomers.

Figure 9.12 presents dependence of half-reaction periods during cis-trans-isomerization process on Hammett constant. It was shown that speed of photoisomerization increases with reduction of σ_0 values of substituent; moreover, good linear dependence can be seen.

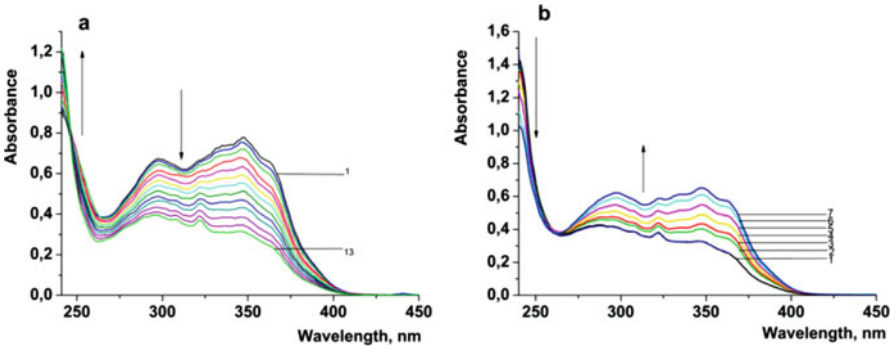

Fig. 9.10 Changes in absorption spectra of **c2a** in THF under irradiation: (**a**) trans-cis- isomerization at wavelength of 366 nm, 1, 0 s; 2–13, 2685 s; (**b**) cis-trans-isomerization at wavelength of 254 nm: 1, 0 s; 2, 10 s; 3, 40 s; 4, 70 s; 5, 130 s; 6, 250 s; 7, 550 s

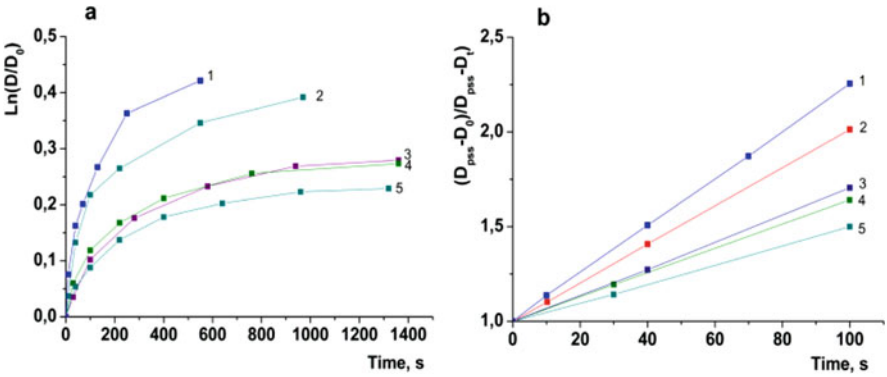

Fig. 9.11 Graphic dependence $\ln(D_t/D_0)$ (**r**) and $\ln(D_{pss}-D_0)/D_{pss}-D_t)$ (**b**) at wavelength 295 nm under irradiation $\lambda = 254$ nm: (**a**) 1, c2a; 2, c2b; 3, c2f; 4, c2e; 5, c2d; (**b**) 1, c2a; 2, c2b; 3, c2d; 4, c2e; 5, c2f

Table 9.3 Values of constants of speed of cis-trans-photoisomerization and half-reaction periods

Polymer	K_{t-c}, $\times 10^2$, s^{-1}	$\tau_{0.5}$, s	σ_0-Hammett constant
p2a/c2a	15/12,5	46/55	−0,28
p2b/c2b	7,9/10	88/69	−0,14
p2d/c2d	8,4/7,0	83/99	0,15
p2e/c2e	5,1/6,4	135/108	0,24
p2f/c2f	5,7/5	122/139	0,26

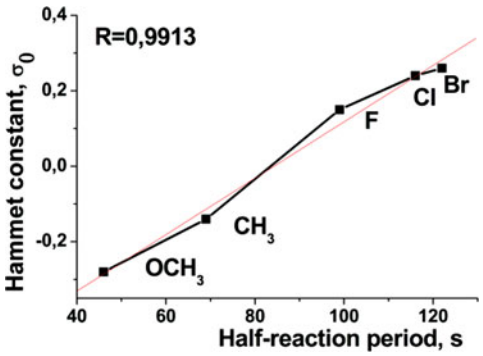

Fig. 9.12 Dependence of half-reaction periods during cis-trans-isomerization process on Hammett constant for styrylquinoline-containing polymers

9.4 Conclusion

Homopolymers and copolymers with MMA based on 2-styrylquinoline monomers were obtained by free radical polymerization. The polymerization ability of styrylquinoline-containing monomers was investigated by using dilatometric

method. The monomer reactivity ratios and copolymerization parameters for MASTQ–MMA system were computed using Fineman–Ross (F-R) and calculation methods. The photochemical properties of styrylquinoline-containing polymers were studied. The trans-cis-trans photo-induced isomerization of new methacrylic polymers with styrylquinoline chromophore in side chain was investigated under UV irradiation. It was found that speed of trans-cis-photoisomerization reaction increases with increasing electron acceptor properties of substitutes in the aromatic ring. It was approved that irradiation solutions of trans- and cis-forms by UV with wavelength 254 nm lead to reverse reaction. It was installed that speed of the last reaction increases linearly with increasing electron donation of substitutes (values of its Hammet substituent constant σ_0) in the aromatic ring.

References

1. Zhang C-Z et al (2010) Significant effect of Bromo substituents on nonlinear optical properties of polymer and chromophores. J Phys Chem B 114:42–48
2. Gulakova EN et al (2011) Synthesis and structure of styryl-substituted azines. Russ J Organ Chem 47(2):245–252
3. Liao L, Li Y et al (2014) STM investigation of the photoisomerization and photodimerization of stilbene derivatives on HOPG surface. J Phys Chem C 118:15963–15969
4. Grad ME, Simu GM et al (2008) Synthesis and colour assessment of some new stilbene azo dyes. Rev Roum Chim 53(2):107–111
5. Budyka M, Oshkin I (2011) Comparative semiempirical and DFT study of styrylnaphthalenes and styrylquinolines and their photocyclization products. Int J Quantum Chem 111:3673–3680
6. Gulakova EN et al (2014) Regiospecific C-N photocyclization of 2-styrylquinolines. J Org Chem 79(12):5533–5537
7. Budyka MF et al (2010) The effect of substituents in the styryl moiety on the photocyclization of 4-styrylquinoline derivatives. High Energy Chemistry 44(5):404–411
8. Oshkin V, Budyka M (2010) Quantum_chemical study of the photoisomerization and photocyclization reactions of styrylquinolines: potential energy surfaces. High Energy Chemistry 44(6):472–481
9. Walko M (2009) Molecular and biomolecular switches, Dissertation, University of Groningen
10. Deligeorgiev T, Vasilev A et al (2010) Styryl dyes – synthesis and applications during the last 15 years. Soc Dyers Col, Color Technol 126:55–80
11. Ayaz N et al (2012) Polymers based on methacrylate bearing coumarin side group: synthesis via free radical polymerization, monomer reactivity ratios, dielectric behavior, and thermal stabilities. ISRN Polym Sci 352759:1–13. https://doi.org/10.5402/2012/352759
12. Budyka M, Potashova N (2012) Design of fully photonic molecular logic gates based on the supramolecular bis-styrylquinoline dyad. Nanotechnol Russ 7:280–287
13. Podeszwa B et al (2007) Investigating the antiproliferative activity of quinoline-5,8-diones and styrylquinolinecarboxylic acids on tumor cell lines. Bioorg Med Chem Lett 17:6138–6141
14. Mao F, Yan J, Li J et al (2014) New multi-target-directed small molecules against Alzheimer's disease: a combination of resveratrol and clioquinol. Org Biomol Chem 12:5936–5944
15. Mekouar K, Mouscadet J-F et al (1998) Styrylquinoline derivatives: a new class of potent HIV-1 integrase inhibitors that block HIV-1 replication in CEM cells. J Med Chem 41:2846–2857
16. Budyka M et al (2008) Photoisomerization of 2-styrylquinoline in neutral and protonated forms. High Energy Chem 42(6):446–453

17. Derkowska-Zielinska B, Skowronski L, Biitseva A et al (2017) Optical characterization of heterocyclic azo dyes containing polymers thin films. Appl Surf Sci 421:361–366. https://doi.org/10.1016/j.apsusc.2016.12.080
18. Krupka O, Smokal V, Derkowska-Zielinska B, et al (2017) Optical and photochemical properties of diarylethylenes. Proceedings of SPIE 10440: 104400C. https://doi.org/10.1117/12.2278118
19. Derkowska-Zielinska B, Krupka O, Smokal V et al (2016) Optical properties of disperse dyes doped poly(methyl methacrylate). Mol Cryst Liq Cryst 639:87–93. https://doi.org/10.1080/15421406.2016.1254585
20. Smokal V, Czaplicki R, Derkowska B ea (2007) Synthesis and study of nonlinear optical properties of oxazolone containing polymers. Synth Met 157(18–20):708–712. https://doi.org/10.1016/j.synthmet.2007.07.006
21. Derkowska-Zielinska B, Skowronski L, Sypniewska M et al (2018) Functionalized polymers with strong push-pull azo chromophores in side chain for optical application. Opt Mater 85:391–398. https://doi.org/10.1016/j.optmat.2018.09.008
22. Derkowska-Zielinska B, Skowronski L, Kozlowski T et al (2015) Influence of peripheral substituents on the optical properties of heterocyclic azo dyes. Opt Mater 49:325–329. https://doi.org/10.1016/j.optmat.2015.10.001
23. Alfrey TC, Price C (1947) Relative reactivities in vinyl copolymerization. J Polym Sci 2(1):101–106
24. Kharchenko O et al (2018) Reactivity and polymerisation ability of styrilquinaline containing metacrylic monomers. Chem Chem Technol 12(1):47–52. https://doi.org/10.23939/chcht12.01.047
25. Kharchenko O et al (2018) Synthesis and photophysical properties of new styrylquinoline-containing polymers. Mol Cryst Liq Cryst 661:38–44. https://doi.org/10.1080/15421406.2018.1460236
26. Barberis V, Mikroyannidis J (2006) Synthesis and optical properties of aluminum and zinc quinolates through styryl substituent in 2-position. Synth Met 156:865–871. https://doi.org/10.1016/j.synthmet.2006.05.007
27. Derkowska-Zielinska B, Figà V, Krupka O et al (2015) Optical properties of polymethacrylate with styrylquinoline side chains. Proc SPIE 9652:965216. https://doi.org/10.1117/12.2194840
28. Fineman M, Ross S (1950) Linear method for determining monomer reactivity ratios in copolymerization. J Polym Sci 5(2):259–265
29. Brandrup J, Immergut EH, Grulke EA (1999) Polymer handbook, 4th edn. John Wiley & Sons, New York
30. Budyka M (2008) Photochemical properties of amino and nitro derivatives of 2- and 4-styrylquinolines and their hydrochlorides. High Energy Chem 42(3):220–226. https://doi.org/10.1134/S0018143908030065
31. Fedus M, Smokal V, Krupka O et al (2011) Synthesis and non-resonant nonlinear optical properties of push-pull side-chain azobenzene polymers. J Nonlinear Opt Phys Mater 20:1–13. https://doi.org/10.1142/S021886351100584X

Chapter 10
The Effect of Ultraviolet Irradiation on the Electro-transport Properties of Carbon Nanotubes

Transport Properties of Ultraviolet Irradiated Carbon Nanotubes

Oleh D. Marinin, Iryna V. Ovsiienko, Tatiana A. Len, Lyudmila Yu. Matzui, Yuriy I. Prylutskyy, Dina D. Naumova, and Uwe Ritter

10.1 Introduction

The development of new promising composite materials based on polymer matrices with nanocarbon including carbon nanotube (CNT) filler is one of the urgent needs of modern material science. When creating polymer composites, the stability of their mechanical, electro-physical, and electro-dynamic characteristics under the influence of electromagnetic radiation of different frequencies is very important. The question of the interaction of electromagnetic radiation with polymers is completely unexplored. It is known that under prolonged action of ultraviolet (UV) radiation, there is "aging" of some polymers, for example, epoxy resin [1, 2]. The epoxy matrix begins to brittle fracture, to be recovered, while all its physical and chemical properties are lost. Short-term powerful UV irradiation strongly heats the surface of composites based on epoxy resin that leads to ablation of the same sites on the surface of the composite [3]. The papers contain data on the polarization of polymers, in particular, the epoxy resin under the action of UV irradiation [4, 5].

O. D. Marinin (✉) · I. V. Ovsiienko · T. A. Len · L. Y. Matzui
Departments of Physics, Taras Shevchenko National University of Kyiv, Kyiv, Ukraine

Y. I. Prylutskyy
Department of Biophysics, Taras Shevchenko National University of Kyiv, Kyiv, Ukraine

D. D. Naumova
Department of Chemistry, Taras Shevchenko National University of Kyiv, Kyiv, Ukraine

U. Ritter
Technical University of Ilmenau, Ilmenau, Germany

© Springer Nature Switzerland AG 2019

O. Fesenko, L. Yatsenko (eds.), *Nanophotonics, Nanooptics, Nanobiotechnology, and Their Applications*, Springer Proceedings in Physics 222,
https://doi.org/10.1007/978-3-030-17755-3_10

A short-time UV irradiation of the polymer composite based on PTFE leads to the solidification of the polymer and the growth of the crystalline phase that causes the improvement of its elastic characteristics [6, 7]. An increase in UV irradiation exposure time results in gradual amorphization and destruction of the crystalline phase.

The UV irradiation of polymer composite leads to certain changes in its structural and phase composition and, consequently, to changes in its electro-physical properties. So, the UV irradiation of the polymer composite results in a reduction of almost 1000 times the value of its resistivity and a displacement of about 30 K toward the increase in the temperature minimum in the temperature dependence of the resistivity [8]. Such a change in the resistivity of the composite is connected, first of all, with the decrease in the contribution of the contact resistance to the total resistivity of the composite. During the UV irradiation of the polymeric composite, there is a local heating of some sections of the composite, while, obviously, a thin polymer layer between the particles of a nanocarbon filler is destroyed.

On the other hand, the UV irradiation promotes the formation on the surface of nanocarbon filler the oxygen-containing functional groups. Some reactions of the nanocarbon surface functionalization occur only under UV irradiation.

As is known, at the covalent functionalization, the destruction of the delocalized π-electron system and the partial σ-bond break in the graphite layer occur, thus forming the free bonds, due to which various functional groups are joined with carbon atoms on the surface CNTs [9–12]. Thus, covalent functionalization causes the formation of a significant number of defects on the surface of CNTs. This process, on the one hand, improves the connection between nanocarbon filler and polymeric matrix and enhances the mechanical properties of nanocomposites. On the other hand, a significant number of defects in the nanocarbon filler results in deterioration of its properties associated with charge transfer. This causes a deterioration in the electrical properties of the polymeric composite as a whole. Therefore, since the UV irradiation causes a partial functionalization of the CNT's surface by oxygen-containing groups, then, obviously, the bonds at the interface between the nanocarbon filler and the polymer matrix are intensified. However, the question of changing of the electro-transport properties of nanocarbon structures themselves under UV irradiation, in particular, of CNTs remains open.

Thus, the effect of UV irradiation on the electro-transport properties of the polymer composites is determined by how such action reduces the influence of the polymer on the total resistance of the composites by reducing the contact resistance between the filler's particles, on the one hand, and worsens the electrical conductivity of the individual particles of the nanocarbon filler due to the destruction of their structure, on the other.

In the literature, there is a fairly large number of works in which the effect of UV irradiation on the electro-transport properties of polymeric composites near the percolation threshold is investigated. However, there are practically no papers on the study of the effect of UV irradiation on the electric transport and the conduction mechanisms in composites with a high concentration of CNTs.

The aim of presented work is a detailed study of the possibility of functionalization of CNTs with different numbers of layers and different degrees of structural perfection under the UV irradiation and the determination of the effect of UV irradiation on their electrical conductivity.

10.2 Experimental

10.2.1 Preparation and Characterization of CNT Specimens

For investigation of influence of UV irradiation on the transport properties, three types of CNTs were chosen. These are multiwalled carbon nanotubes (MWCNTs), functionalized multiwalled carbon nanotubes (FMWCNTs), and metal single-walled carbon nanotubes (SWCNTs).

MWCNT The source MWCNTs were obtained by arc discharge method with use of nickel as catalyst. Figure 10.1 presents the part of the X-ray diffraction pattern for source MWCNT (curve 1).

As it is shown from Figure, the X-ray diffraction pattern contains graphite *00l* and *hkl* lines. This indicates a fairly high degree of ordering of the source MWCNT crystal structure. The positions of 002 and 004 graphite lines correspond to the interlayer distance $d_{002} = 0.340$ nm. The crystallite size L determined by broadening of the 002 graphite line is ~10 nm. On the diffraction pattern also, there are lines that correspond to reflection from the nickel planes.

FMWCNTs The FMWCNTs were obtained from the source MWCNTs by treating them according to the following scheme. At the first stage, the tubes were boiled in an aqueous solution of nitric acid for 3 hours. Next, the tubes were washed in water.

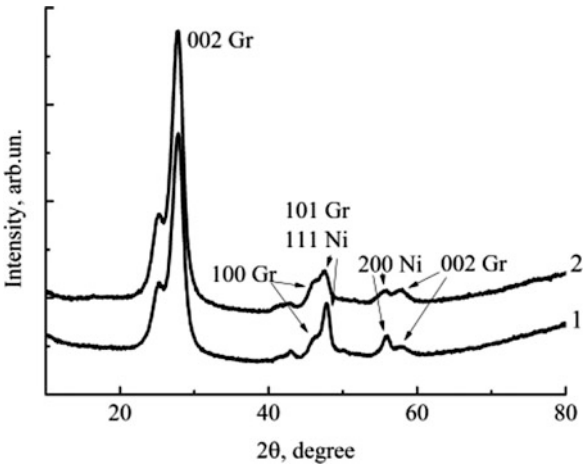

Fig. 10.1 X-ray diffraction patterns (Ni tube) for source (curve 1) and functionalized (curve 2) MWCNTs

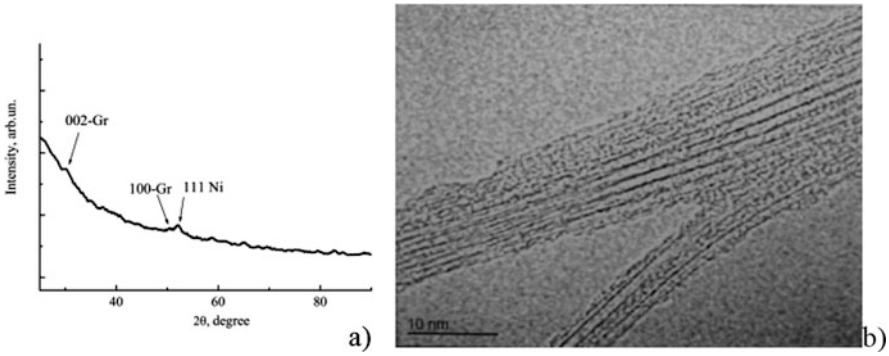

Fig. 10.2 X-ray diffraction pattern (**a**) and HRTEM image (**b**) [13] for SWCNTs

Then, the tubes were again boiled in concentrated nitric acid, washed in distilled water to neutral pH, and then dried.

The part of the X-ray diffraction pattern for functionalized MWCNT is presented on Fig. 10.1 (curve 2).

As it is seen from the Figure, the diffraction pattern only slightly changes compared to the source MWCNT. The relative intensity of graphite lines increases, and therefore the intensity of lines corresponding to nickel plane reflections decreases. The analysis of the X-ray diffraction pattern of FMWCNTs shows that neither the position of graphite lines nor their broadening is unchanged in comparison with MWCNT X-ray diffraction pattern. Thus, functionalization does not result in change in the distance between layers in MWCNTs and reducing the size of crystallites in them. We note that the functionalization of the above scheme at the same time led to a decrease in the content of nickel in the tubes.

SWCNTs SWCNTs were obtained by the method of thermal spraying of graphite electrodes in the plasma of an arc discharge using nickel as a catalyst. For the purification of impurities, the synthesized SWCNTS were treated for 8 hours with aqueous hydrochloric acid, and then washed several times with deionized water.

Figure 10.2 presents the part of the X-ray diffraction pattern (Fig. 10.2a) and fragments of HRTEM image [13] (Fig. 10.2b) for SWCNT.

As it follows from the X-ray diffraction pattern, there is only weak intensive line corresponding to nickel. There are no intense lines that correspond to reflections from graphite planes. So, the obtained CNTs are single walled. Their diameter is 1.4–2 nm (Fig. 10.2b).

10.2.2 Characterization Methods

The specimens of MWCNTs, FMWCNTs, and SWCNTS were exposed to UV irradiation for 20 minutes. UV treatment was performed by DRT-1000 (ultraviolet lamp) equipped with electric-discharge arc lamp of high pressure inflated with

mercury and argon compound that could release ultraviolet radiation of 50 W at 240–320 nm wavelength. The distance between the UV lamp and the sample was fixed at 11 cm.

The quantitative composition of functional groups on the surface of source and UV-irradiated CNTs is determined by the infrared (IR) spectroscopy method. The experiments have been performed by Perkin Elmer Spectrum BX FT-IR infrared spectrometer at the frequency range 4000–400 cm^{-1}. The specimens in a form of pellets of 10 mm in diameter were prepared from the powder mixture of pre-dried CNTs and KBr.

For the electro-transport investigations from CNT powders, the bulk specimens in the form of rectangular parallelepipeds (2 mm × 3.5 mm × 15 mm) were prepared by cold pressing using a polyvinyl acetate adhesive (75% mass of CNTs and 25% mass of polyvinyl acetate) [14]. The density of obtained compacted specimens was ∼1. g/cm^3 The resistivity has been investigated in the temperature interval from 4.2 K up to 300 K with standard four-probe method [15]. The resistivity measurement error did not exceed 0.5%.

10.3 Results and Discussion

10.3.1 Infrared Spectroscopy

Figure 10.3 presents the IR spectra for source MWCNTs (curve) 1 and treated with UV MWCNTs (curve 2).

As it is shown from the Figure, IR spectra form is significantly different for source and UV-treated MWCNTs. A characteristic feature of the source MWCNT

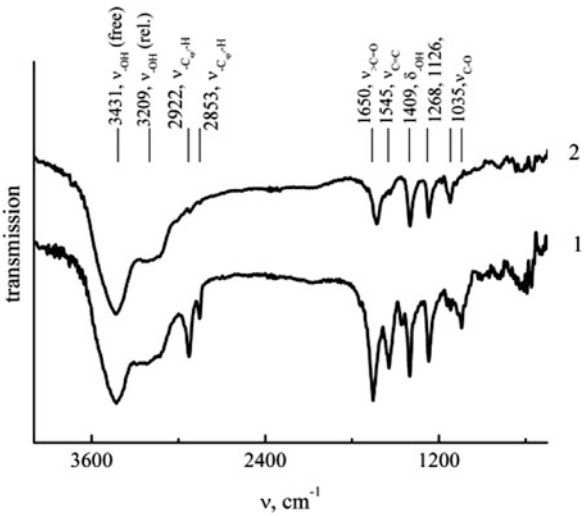

Fig. 10.3 IR spectra for source (1) and treated with UV (2) MWCNTs

spectrum is the presence in them of bands corresponding to the vibrations not only to functional groups, but also to the carbon atoms in the MWCNTs. In the spectra of UV-irradiated MWCNTs, the bands that correspond to the vibrations of carbon atoms in the tubes are practically absent.

Let us analyze in more detail the spectra of the source and UV-irradiated MWCNTs. In the short-wave region of the spectrum for both specimens, there is a broad intense band with a shoulder to the right. This band is associated with valence vibrations of the hydroxyl group. The band contains two lines. The first (3431 cm^{-1}) more intensive band corresponds to adsorbed water (tabular value 3400 cm^{-1}) or valence vibrations of so-called free groups –OH. Such groups are not part of other functional groups, for example, the carboxyl group –COOH. The second less intensive band corresponds to the vibrations of the related groups –OH, that is, those that are part of other functional groups. The following two lines (2922 $cm^{-1}$and 2853 cm^{-1}) are associated, respectively, with valence vibrations of sp^2 and sp^3 hybridized carbon atoms related with hydrogen. Such carbon atoms with attached hydrogen, including the rehybridized sp^3 carbon atoms, are located along the crystallites boundaries. Thus, the presence of these intensive lines can be considered as a criterion of the perfection of the nanocarbon structure. One more line associated with vibrations of the graphite skeleton is the C=C line (1545 cm^{-1}). This line is observed both for layered nanocarbon structures and for CNTs. As can be seen from the figure, the intensity of this line for the source MWCNTs is approximately equal to the intensity of the C_{sp2}-H and C_{sp3}-H lines, as well as the intensities of the bands corresponding to the different functional groups. Another intensive band, which is observed in the spectrum of the source MWCNTs, corresponds to the vibrations of the carbonyl group >C=O (1650 $см^{-1}$). The next band (1409 cm^{-1}) is associated with the deformation vibrations of the hydroxyl group ((δ -OH). -OH. Note that the intensity of this band correlates with the intensity of the valence vibration band (υ -OH). And the last broad, intense band consisting of two lines is associated with the vibrations of the functional group C-O, which is part of, in particular, the lactones group or ethers.

Thus, the relative intensities of the bands corresponding to the vibrations of carbon atoms in the graphite skeleton are approximately equal to the relative intensities of the bands corresponding to the vibrations of the functional groups. For the spectrum of UV irradiated MWCNTs, there are practically no bands corresponding to the vibrations of carbon atoms in the graphite skeleton. (C=C, C_{sp2}-H and C_{sp3}-H bands). This spectrum contains only bands corresponding to the vibrations of the functional groups OH, >C=O and C-O. The relative intensity of the bands associated with the vibrations of the carbon atoms is negligible.

The spectra of functionalized (curve 1) and UV-irradiated functionalized (curve 2) MWCNTs are presented in Fig. 10.4.

As it is seen from the Figure, in contrast to the specimens MWCNTs and UV-MWCNTs, the differences in the IR spectra of specimens FMWCNTs and UV-FMWCNTs are minimal. For both specimens, there are intense bands associated with the vibrations of functional groups: the hydroxyl group (valence and deformation), the carbonyl group (valence and deformation), and the group C-O (valence).

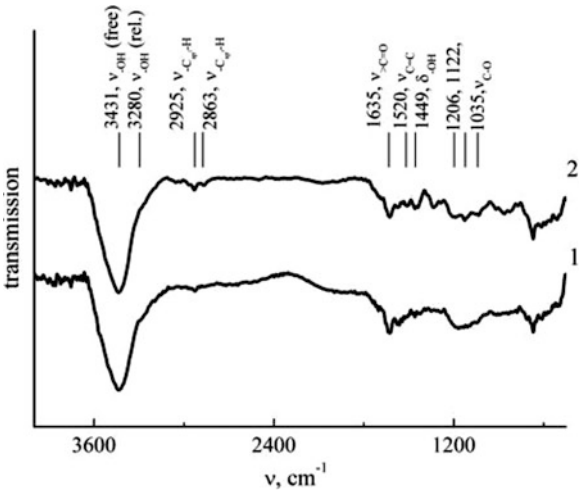

Fig. 10.4 IR spectra for functionalized (1) and fuctionalized and treated with UV (2) MWCNTs

At that the relative intensities of the C_{sp2}-H and C_{sp3}-H bands are significantly smaller than the relative intensities of the bands corresponding to the vibrations of the functional groups, and the UV irradiation weakly affects the correlation of the intensities of these bands. Thus, the relative intensity of the line corresponding to the vibration of C_{sp2}-H after UV irradiation is slightly increased compared with the relative intensity of the –OH line. And a broad intensive line associated with the vibration of the C-O group in the spectrum of the FMWCNTs after UV irradiation is split into several separate less intensive lines. It should be noted that the line corresponding to the C=C vibrations of graphite skeleton is not observed in the spectrum of both the source FMWCNTs and the UV-irradiated one.

Figure 10.5 presents the IR spectra for source (curve 1) and UV-irradiated (curve 2) SWCNTs.

As it follows from the picture, the spectra for SWCNTs are significantly differ from both spectra for MWCNTs and functionalized MWCNTs.

In the spectrum of the initial SWCNTs, there is only one broad intensive band that corresponds to the vibration of the functional group. This is a ν-OH. (3438 cm^{-1}). This band, in contrast to the spectrum of MWCNTs, is symmetrical and has no characteristic shoulder on the right, which indicates the presence of a related hydroxyl group. Thus, the broad intensive symmetric band in the spectrum of the source SWCNTs is only due to the presence of adsorbed water or the free –OH group. In the spectrum of UV-irradiated SWCNTs, this characteristic shoulder on the right appears, which indicates the joining of functional groups containing the –OH group to the SWCNT surface. The first of all, it is a carboxyl group –COOH. The spectrum of source SWCNTs contains only two bands associated with vibrations of carbon atoms in graphite skeleton C_{sp2}-H and C_{sp3}. Moreover, their intensity can be compared with the intensity of the –OH group (curve 1). After UV irradiation, the intensity of these groups becomes much smaller compared to the –OH group. The relative intensities of the C=C bands in the both spectra are negligible.

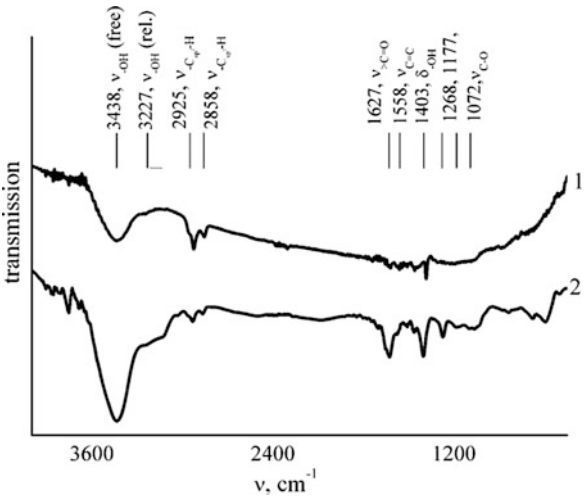

Fig. 10.5 IR spectra for source (1) and treated with UV (2) SWCNTs

After UV irradiation in the IR spectrum of SWCNTs, two new bands corresponding to the vibrations of the functional groups appear. These are an intensive band associated with the vibrations of carbonyl group (1627 cm^{-1}) and a wide band, which contains two lines associated with the vibrations of CO group (1268 cm^{-1}, 1072 cm^{-1}).

For a more detailed analysis of the effect of UV irradiation on the composition of functional groups on the CNT surface on Fig. 10.6, the diagrams of the ratio of relative intensities of the bands corresponding to the various functional group vibrations before and after UV irradiation are presented. Also Table 10.1 shows the ratio of the relative intensities of these bands before and after UV irradiation.

For the unit of intensity for all spectra, the relative intensity of the band corresponding to the vibrations of the carbon atoms in the graphite skeleton is chosen. Indeed, the number of bonds corresponding to vibrations C=C does not change during the UV irradiation process. Although the literature has the data on the disappearance of the line C=C after irradiation of CNTs with powerful UV greater than 20 minutes. Due to a powerful UV irradiation, a part of the substance evaporates from the surface of the CNTs that leads to a decrease in the intensity of the C=C band. However, the conditions of UV irradiation in our studies are such that the number of C=C connections is obviously unchanged. Therefore, it is logical to choose as the unit of intensity the relative intensity of the C=C band.

As can be seen from the following diagrams and Table, in the spectra of the source MWCNTs and SWCNTs, the intensities of the bands corresponding to the vibrations of the functional groups are approximately equal to the intensity of the C=C band. The exception is the –OH free line for SWCNTs. The UV irradiation of the source MWCNTs results in a significant (from 18 times for C-O group up to 50 times for –OH group) increase in the intensity of the bands corresponding to the vibrations of the functional groups. The same trend is observed for SWCNTs

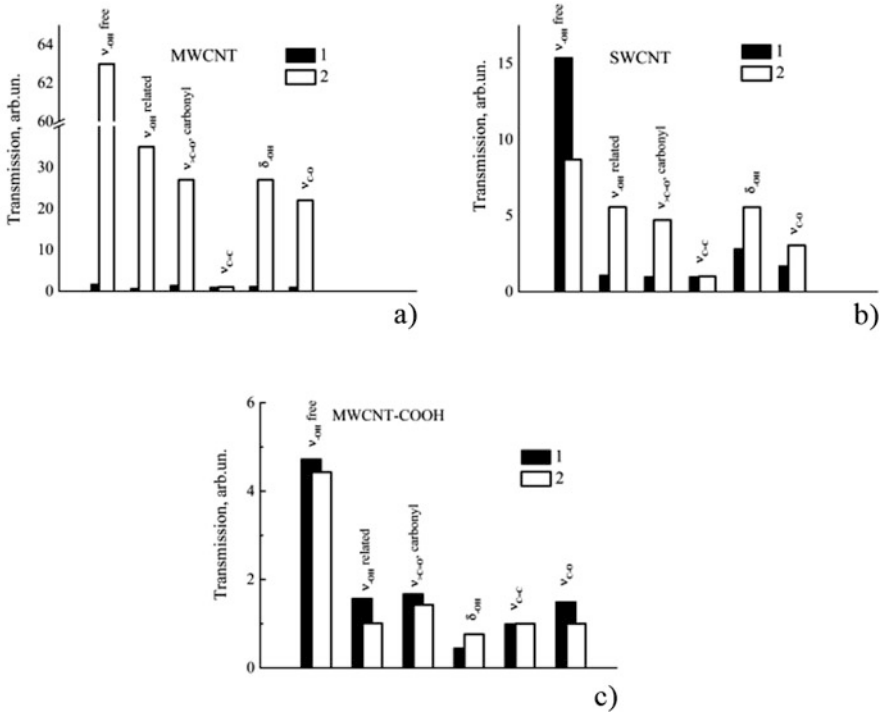

Fig. 10.6 Ratio of relative intensities of the bands corresponding to the various functional group vibrations before and after UV irradiation for MWCNTs (**a**), SWCNTs (**b**), and FMWCNTs (**c**)

Table 10.1 The ratio of relative intensities of functional group bands before and after UV irradiation. Normalization on the intensity of the C=C band

Specimen	MWCNTs			SWCNTs			FMWCNTs		
Intensity ratio	Source	UV	I_{UV}/I_s	Source	UV	I_{UV}/I_s	Source	UV	I_{UV}/I_s
$I_{C=C}/I_{C=C}$	1.0	1.0	1	1.0	1.0	1	1.0	1.0	1
$I_{\text{-OH free}}/I_{C=C}$	1.7	63	37	15.4	8.7	0.56	4.7	4.4	0.93
$I_{\text{-OH rel.}}/I_{C=C}$	0.7	35	50	1.1	5.6	5.1	1.6	1.	0.63
$I_{>C=OH}/I_{C=C}$	1.5	27	18	1.0	4.7	4.7	1.7	1.4	0.82
$I_{C-O}/I_{C=C}$	1.0	22	22	2.8	5.6	2	1.5	1	0.7

except for –OH free group. However, the growth in the intensity of the bands associated with the vibrations of functional groups for SWCNTs is considerably smaller. It ranges from 2 times for C-O group up to 5 times for –OH group. Note that the intensities of the –OH related, >C=O and –OH bands in the spectra as for MWCNTs that as SWCNTs are correlated with each other. This, obviously, points to the fact that on the surface of source CNTs as results of UV irradiation, precisely carboxyl groups are formed. Other processes are observed for source functionalized MWCNTs. For FMWCNTs, the intensities of the bands corresponding to functional

groups are approximately the same except for –OH free band, the intensity of which is essentially larger. And all these intensities are larger than the intensity of the C=C band. After UV irradiation, the intensities of the bands of all functional groups decrease. Pay attention to such detail. If before the UV irradiation the intensities of the –OH related band and >C=O was almost the same, then after the irradiation, the intensity of the hydroxyl group band decreased almost twice, while the intensity of carbonyl group band decreased by only 17%. That is, the UV irradiation results in the destruction of the carboxyl group itself and the dissociation of the hydroxyl group from it, while the carbonyl group remains bound to the surface of CNTs.

Thus, the analysis of the IR spectra of MWCNTs and SWCNTs found that in the source specimens of CNTs, the relative concentration of functional groups was very small. The short-term UV-radiation of CNTs resulted in a significant increase in the relative concentration of functional groups, in particular, hydroxyl and carbonyl groups and the C-O group. This process is more pronounced for MWCNTs whose structure is less perfect and contains a significant number of defects. As is known, the UV irradiation leads to a partial conversion of oxygen contained in the air to ozone. Ozone is a strong oxidant and its interaction with the surface of VNT leads to the formation of a significant amount of oxygen-containing groups on it. The effect of UV irradiation on the surface of functionalized MWCNTs is different. Under the UV irradiation, the part of the functional groups on the surface of MWCNTs is destroyed.

10.3.2 Resistivity of CNTs

Figure 10.7 presents the temperature dependences of resistivity $\rho(T)$ for source and functionalized MWCNTs before and after UV irradiation and the main parameters

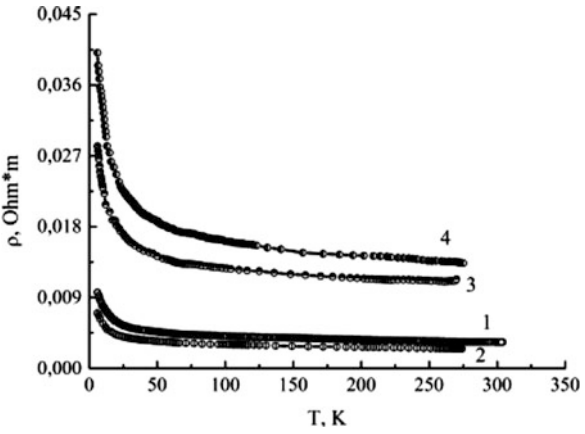

Fig. 10.7 Dependences ρ(T) for source (1) and UV-irradiated (2) MWCNTs and for FMWCNTs (3) and UV-irradiated FMCNTs (4)

Table 10.2 Parameters of resistivity for MWCNTs

Specimen	$\rho_{4.2}$,Ohm·m	$\rho_{4.2}/\rho_{273}$
MWCNTs	$9.64 \cdot 10^{-3}$	2.88
UV-MWCNTs	$7.11 \cdot 10^{-3}$	2.80
FMWCNTs	$2.82 \cdot 10^{-2}$	2.49
UV-FMWCNTs	$4.01 \cdot 10^{-2}$	2.98

of resistivity (resistivity $\rho_{4.2}$ at temperature $T = 4.2$ K and ratio of resistivity at $T = 4.2$ K to resistivity at $T = 273$ K $\rho_{4.2}/\rho_{273}$ are also in Table 10.2).

As can be seen from the Figure, for all specimens of CNT, there is a similar character of the temperature dependence of resistivity. The sharp drop in the resistivity occurs at low temperature, and with a further increase in temperature, a weak temperature dependence of the resistivity is observed. The ratio $\rho_{4.2}/\rho_{273}$ for all specimens of MWCNTs is about (2.5÷3), which is greater than, for example, fine crystalline anisotropic graphite, for which this ratio is 1.6 [16], but is substantially less than for MWCNTs obtained by decomposition of CO (∼30) [17]. However, the values of resistivity at the same temperatures are essentially different for all specimens. The UV irradiation of the source MWCNTs leads to a decrease in resistivity by 30%, while the functionalization of source MWCNTs increases their resistivity in three times. The UV irradiation of functionalized MWCNTs results in a further increase in resistivity. That is, in one case, the UV irradiation leads to a decrease in resistivity in comparison with source CNTs; otherwise, it increases resistivity.

Let us consider the mechanisms of the formation of the resistivity temperature dependence for the investigated MWCNTS. As it is known, the electrical conductivity of MWCNTs with a sufficiently large number of layers is considered within the framework of models used to describe the electrical conductivity of graphite materials. For MWCNTs with a large number of defects, the variable range hopping conductivity mechanism (VRH) for both a two-dimensional and a three-dimensional case is proposed [18, 19]. In [20], the authors describe the temperature dependence of resistivity in terms of the "two-band" conductivity model, which is used to describe the transport properties of fine crystalline graphite materials. In addition, for some MWCNTs the abnormal temperature and magnetic field dependencies of the electrical resistance, that are associated with the manifestation of the quantum effects of charge carriers weak localization and interaction, were observed [21].

A detailed analysis of the temperature dependence of the resistivity has revealed that linear dependence $\ln(\rho) = f(T^{-1/3})$ is observed for all specimens of MWCNTs as before, that after UV irradiation (Fig. 10.8).

As it is shown from the Figure, the linear dependence $\ln(\rho) = f(T^{-1/3})$ is strictly fulfilled for FMWCNTs and UV-FMWCNTs throughout all temperature ranges. For source MWCNTs and UV-MWCNTs, a slight deviation from linear dependence is observed in the high-temperature interval. Such linear dependence of $\ln(\rho)$ from

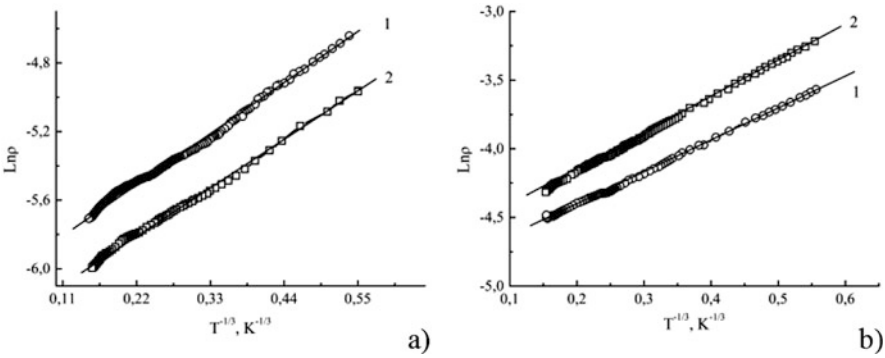

Fig. 10.8 Dependences $\ln(\rho) = f(T^{-1/3})$ for source (1) and UV-irradiated (2) MWCNTs (**a**) and FMWCNTs (**b**)

Table 10.3 Parameters T_0 and ρ_0 for specimens of MWCNTs

Specimen	MWCNTS	UV-MWCNTS	FMWCNTS	UV-FMWCNTS
ρ_0, Ohm·m	$2.288 \cdot 10^{-3}$	$1.711 \cdot 10^{-3}$	$7.227 \cdot 10^{-3}$	$9.005 \cdot 10^{-3}$
T_0, K	17.98	16.70	12.68	19.90

$T^{-1/3}$ indicates that resistivity varies with temperature according to the law:

$$\rho = \rho_0 \exp\left(T_0/T\right)^{\frac{1}{3}}. \tag{10.1}$$

This dependence is characteristic for variable range hopping in a two-dimensional case (VRH 2D). Here:

$$T_0 = 13.8\frac{\alpha^2}{k_b N\left(E_F\right)}, \tag{10.2}$$

where α is the localization length, $N(E_F)$ is the density of states at the Fermi level, and ρ_0 depends on the phonon spectrum, scaling as ${\nu_{\text{ph}}}^{-1}$ [18].

Table 10.3 contains parameters T_0 and ρ_0 for all MWCNT specimens obtained from the experimental dependences $\ln(\rho) = f(T^{-1/3})$.

As it is follows from the Table, for source MWCNTs after UV irradiation, ρ_0 varies significantly (~25%), while the T_0 changes somewhat. The opposite picture is observed for functionalized MWCNTs after UV irradiation. The characteristic resistivity ρ_0 for these MWCNTs increases slightly. At the same time, the temperature T_0 increases by more than 50%.

The temperature dependences of resistivity $\rho(T)$ for specimens of source and UV irradiation SWCNTs are presented in Fig. 10.9. And in Table 10.4, there are main parameters of resistivity (resistivity $\rho_{4.2}$ at temperature $T = 4.2$ K, the temperature of minimum $T_{\min}$ and ratio of resistivity at $T = 4.2$ K to resistivity at $T_{\min}$).

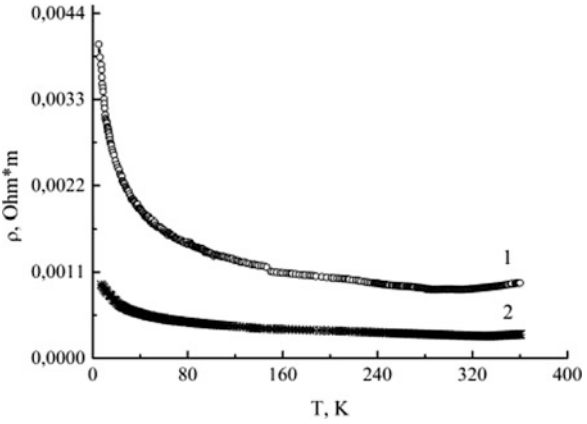

Fig. 10.9 Dependences $\rho(T)$ for source (1) and UV-irradiated (2) SWCNTs

Table 10.4 Parameters of resistivity for SWCNTs

Specimen	SWCNTs	UV-SWCNTs
$\rho_{4.2}$,Ohm·m	$4.02 \cdot 10^{-3}$	$9.42 \cdot 10^{-4}$
$T_{\min}$, K	287	333
$\rho_{4.2}/\rho_{T\min}$	4.56	3.25

As can be seen from the Figure, the dependence $\rho(T)$ for source SWCNTs is more complicated than for MWCNTs. There is a sharp decrease in resistivity up to of 80 K, and then the resistivity is weakly dependent on the temperature. At the temperature $T = 287$ K minimum in the dependence $\rho(T)$ is observed. With further increase in temperature, the resistance increases slightly. The effect of UV irradiation on the resistivity of SWCNTs is more significant compared to the MWCNTs. The UV irradiation results both in significant (∼4 times) reducing the value of the resistivity, and in changing the form of the resistivity temperature dependence.

Let us consider the more detailed mechanisms of conductivity in SWCNTs.

As is known, an ideal defect-free single-walled CNT is a one-dimensional conductor, whose conductivity is described within the terms of the theory of the Luttinger liquid [22]. However, experimentally, such conductivity is observed only for unit single-walled CNT. More often, the conductivity of macrospecimens, which are either binders or ropes or mats from individual SWCNTs, is investigated. Various models are used to describe the temperature dependence of the conductivity in such bulk specimens [23]. For description of the conductivity of studied SWCNT specimens, let us use the model that takes into account the conductivity of individual SWCNT as a one-dimensional conductor (first term) and the conductivity of tubes junctions as a non-interacting Fermi liquid (second term):

$$\rho(T) = aT^{-\alpha} + bT. \tag{10.3}$$

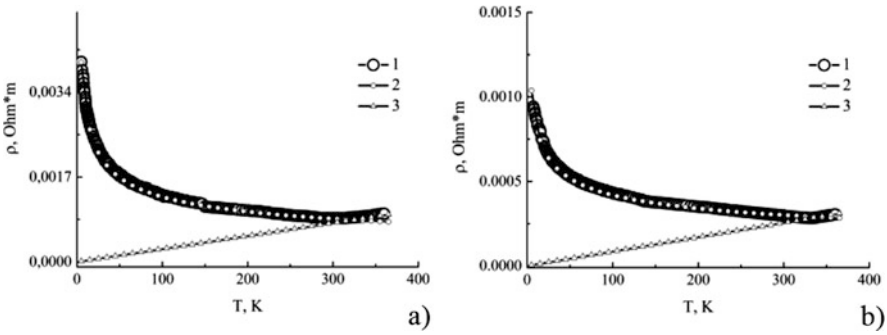

Fig. 10.10 Experimental (1) and calculated conductivity of individual SWCNTs (2) and calculated conductivity of tubes junctions (3) for source (**a**) and UV-irradiated (**b**) SWCNTs

Table 10.5 Calculated resistivity parameters α, g, a, b, and ratio a/b for source and UV-irradiated SWCNTs

Specimen	SWCNTS	UV-SWCNTS
a,	$7.3 \cdot 10^{-3}$	$1.6 \cdot 10^{-3}$
α	0.374	0.303
g	0.209	0.239
b	$2.6 \cdot 10^{-6}$	$8.5 \cdot 10^{-7}$
a/b	2808	1882

In the case of bulk conductor, which is 1D Luttinger liquid, the exponent α is related to the Luttinger parameter g through the equation

$$\alpha = \frac{\left(g + g^{-1} - 2\right)}{8} \tag{10.4}$$

One of the most distinctive peculiarities arising in 1D electron systems is the presence of the long-range Coulomb interaction that leads to the anomalous (power-like) dependence of resistivity at medium temperatures, which is not similar to that for non-interacting Fermi liquid. The Luttinger parameter g that expresses the extent of electron interaction could acquire different values for different systems. Generally, g values range from 0.2 to 0.3 that is much lower in comparison with the value $g = 1$ for the Fermi liquid.

Figure 10.10 presents the calculation in terms of model (3) temperature dependences $\rho(T)$ for source and UV-irradiated SWCNTs, and Table 10.5 presents the calculated resistivity parameters.

As it follows from the Figure, the obtained experimental dependences $\rho(T)$ are well described within the terms of the proposed model. Moreover, in the temperature range from T = 4.2 K to the temperature, at which minimum in dependence $\rho(T)$ is observed ($T_{\min}$), resistivity as for source SWCNTs that for UV-SWCNTs can be described only in the terms of the model of 1D Luttingerliquid. Above the $T_{\min}$ temperature, a significant contribution to the resistivity is given by a linear temperature term.

10.3.3 Discussion

Let us analyze the effect of UV irradiation on the conductivity mechanisms in the specimens of MWCNTs and SWCNTs.

As shown above, the short-term UV-radiation of CNTs resulted in a significant increase in the relative concentration of oxygen containing functional groups on their surface. This process is more pronounced for defected CNTs with less perfect structure. Thus, short-term UV irradiation causes a partial functionalization of CNT surface.

It is generally accepted that the formation of a strong covalent bond between functional groups and carbon atoms on the CNT surface causes a large number of defects in the tube structure and destruction of delocalized π electron system of graphite layers. This obviously leads to degradation of tube properties associated with charge transfer. Thus, on the one hand, functionalization of CNTs is a necessary process that provides uniform distribution of the CNTs in the polymer matrix. On the other hand, functionalization leads to disruption of the transport properties of the CNT. Therefore, the question arises whether such possible functionalization methods allow to modify the surface of the CNTs while not restricting their transport properties.

Let us clear how the transport properties of CNTs change after functionalization by UV irradiation and what are the possible reasons for such changes.

As is known, the resistance of composite materials R_{CM} is defined as [8]

$$R_{\mathrm{CM}} = \frac{\gamma^2 \pi \cdot h}{4 \cdot F} \cdot \left(\frac{F - \phi_c}{\phi - \phi_c} \right)^t \cdot \left(r_{\mathrm{CNT}} + R_k \cdot B\left(\delta\right) \right), \tag{10.5}$$

where ϕ is the volume content of filler, ϕ_c is the critical concentration or the so-called percolation threshold, t is the critical index, F is the packing parameter, r_{Gr} is the resistance of single particle (CNT), h is the tubes length, R_k is the electric resistance of a single contact between graphite particles (CNTs), function $B(\delta)$, where δ is the thickness of the polymeric layer between CNTs, if $\delta \to 0$ that $B(\delta) = 1$, γ is the factor that varies from 1 to 2. The electric resistance of the single contact between the CNTs depends on its own resistivity ρ_{CNT}, the contact area S (or the radius of the contact spot a) between CNTs and the pressure on the contact. Resistance R_k in the first approximation can be written as:

$$R_k = \frac{\rho_{\mathrm{CNT}}}{2a} \quad \text{at} \quad a \gg l \quad \text{(Holm-type contact)} \tag{10.6}$$

and

$$R_k = \frac{\rho_{\mathrm{CNT}}}{2a} \cdot \frac{l}{2a} \quad \text{at} \quad a \ll l \quad \text{(Sharvin-type contact)}, \tag{10.7}$$

where l is the free path of current carriers in the CNT.

The mass part of the filler in investigated bulk specimens of CNTs is 0.75, which corresponds to the volume part of filler ~0.70. This volume concentration of filler φ is much higher than percolation threshold φ_c as for MWCNTs, that for SWCNTs. For CNTs, percolation threshold is a few tenths of a percent in dependence of CNT structure and properties. Thus, investigated bulk specimens of CNTs are in the part of the percolation curve, in which the resistivity value is practically independent on the concentration of the filler. So, the factor in the Eq. (10.5) after UV irradiation obviously is not changed. Let us rewrite an expression (10.5) in the following form:

$$R_{\mathrm{CM}} = A \cdot (r_{\mathrm{CNT}} + R_k) \tag{10.8}$$

It is taken into account that according to our estimates, the thickness of the polymer layer δ is very small. Therefore, we can assume that the function $B(\delta) = 1$. The resistance of the single CNT along the tubes axis can be written in the first approximation as

$$r_{\mathrm{CNT}} = \frac{\rho_{\mathrm{CNT}} h}{\pi b^2}, \tag{10.9}$$

where b is the radius of CNT.

Contact resistance is considered as the Holm contact (10.6), where maximal value of contact spot area can be equal to the entire CNT surface area. Let us rewrite (10.8) with use (10.6) and (10.9).

$$R_{\mathrm{CM}} = A \cdot \left(\frac{\rho_{\mathrm{CNT}} h}{\pi b^2} + \frac{\rho_{\mathrm{CNT}}}{2a} \right) = A \rho_{\mathrm{CNT}} \left(\frac{h}{\pi b^2} + \frac{1}{2a} \right). \tag{10.10}$$

Thus, the change in the resistance of CNTs bulk specimens after UV irradiation can be caused by both the change in the resistance of the tubes itself and the change in the contact resistance between the individual tubes, primarily due to the change in the contact slot size. Moreover, it is obvious that changing the size of the contact spot can only cause a change in the value of the CNT bulk specimen resistance in the all temperature ranges. This is explained by the fact that the specimens contain only a very small amount of polymer binder, and therefore the effects associated with different temperature dependences of the thermal expansion coefficient are not significant. On the other hand, the change in the temperature dependence of the CNT's resistivity ρ_{CNT} leads to the change in the resistance temperature dependence of the entire bulk specimen.

Let us analyze from Tables 10.3 and 10.5 how the bulk resistivity parameters for CNT specimens are changed after UV irradiation. As it is shown from Table 10.3 for MWCNT specimen, parameter ρ_0 somewhat decreases while the parameter T_0 associated with the localization length α and the density of charge carriers at the Fermi level $N(E_F)$ is practically unchanged. This allows to assume that the short-time UV irradiation is only a change in contact resistance between the individual tubes, while it does not affect the structure and, consequently, the

transport properties of MWCNTs themselves. A completely different picture is observed for MWCNTs functionalized with treatment by nitric acid. As can be seen from Table 10.3, parameter ρ_0 increases by more than three times and parameter T_0 also grows essentially. This indicates as an increase at such strong covalent functionalization, the contact resistive between the individual tubes, that is expected, and the change in the conduction mechanisms in the tube itself. This change may be due to an increase in the amount of defects in the CNT's structure caused by the treatment of tubes with a strong oxidant, as well as with the possible change in the electronic structure of the tubes themselves as a result of the accession of functional groups to carbon atoms. For such a change in the electronic structure of the CNTs in the functionalization process a number of articles indicates, in particular, [14, 15]. The UV irradiation of functionalized MWCNTs leads to a further increase in the resistivity of bulk specimens which is caused both by an increase of contact resistance between the tubes, and by the growth of the resistivity of the tubes themselves.

An even more difficult situation is observed for SWCNTs. On the one hand, as shown by the analysis of the IR spectra, the number of functional groups on the surface is significantly smaller in comparison with the functionalized and UV-irradiated MWCNT tubes. This is obviously due to less defective structure of SWCNTs. However, for SWCNTs bulk specimens after UV irradiation, the most significant (almost 4 times) decrease in resistivity is observed. As it follows from Table 10.5 for SWCNTs, parameter a is reduced by 4 times, which reflects the reduction in the contact resistance. And parameter g which is responsible for the interaction degree between carriers increases, which indicates the beginning of the formation of 2D conductive structure.

Such results are somewhat unexpected, as in the literature, most studies [24] point to an increase in the contact resistance between individual SWCNT after functionalization. The contact resistance between the individual tubes increases with the functionalization due to the creation of a small negative charge on the surface of the tubes (electrostatic repulsion). But the removal of surface (organic) contaminants from the CNT surface at UV irradiation promotes the formation of stronger conductive network in the SWCNT bulk specimen.

10.4 Conclusion

Thus, carried out investigations have shown that short-term ultraviolet irradiation leads to partial functionalization of the CNTs with oxygen-containing functional groups. Moreover, the qualitative composition and the relative number of functional groups depend essentially on the degree of defect of the tubes and the state of their surface. The largest number of functional groups is observed for highly defective MWCNTs with a lot of torn chemical bonds. For SWCNTs with a perfect structure, the degree of functionality after UV irradiation is significantly smaller

in comparison with defective MWCNTs. The UV irradiation of functionalized MWCNTs leads to a slight decrease in the degree of their functionalization.

It is revealed that short-time UV irradiation induces a decrease in the resistivity of bulk CNT specimens. However, there is no direct correlation between the degree of fictionalization and the relative decrease in resistivity. This is due to the various effects of UV irradiation on the contact resistance between separate tubes and resistance of the tubes themselves. For essentially defective MWCNTs, the bulk specimen's resistance is reduced by reducing the contact resistance between the tubes, while the UV irradiation practically does not affect the conductivity of the tubes itself. For SWCNTs, the contact resistance decreases under the influence of UV irradiation also. Moreover, this occurs in the presence of a very small amount of polymer. But for SWCNTs, unlike MWCNTs after UV irradiation, the conductivity of the tubes itself changes. In SWCNTs, there is a transition from 1D conductivity, which is described in terms of model of strongly interacting Luttinger liquid in the formation of two-dimensional conducting structure.

References

1. Odegard GM, Bandyopadhyay A (2011) Physical aging of epoxy polymers and their composites. J Polym Sci B Polym Phys 49(24):1695–1716
2. Ning X, Xiang Z, Peng Z, Zhang S, Chen S (2013) Effect of UV ageing on space charge characteristics of epoxy resin and its nanocomposites, 2013 IEEE International Conference on Solid Dielectrics (ICSD), 30 June – 4 July 2013. https://doi.org/10.1109/ICSD.2013.6619663
3. Zhang W, Shentu B, Weng Z (2018) Preparation and properties of heat and ultraviolet- induced bonding and debonding epoxy/epoxy acrylate adhesives. J Appl Polym Sci 135:46435
4. Durmus H, Safak H, Akbas HZ, Ahmetli G (2011) Optical properties of modified epoxy resin with various oxime derivatives in the UV-ViS spectral region. J Appl Polym Sci 120:1490–1495
5. Gaidukovs S, Medvids A, Onufrijevs P, Grase L (2018) UV-light-induced curing of branched epoxy novolac resin for coatings. Express Polym Lett 12(10):918–929
6. Ferry L, Alexander-Katz R, Vigier G, Garapon C (1997) Interaction between UV radiation and filled polytetrafluoroethylene (PTFE). I. Degradation processes. J Polym Sci B 36(12):2057–2067
7. Ferry L, Vassoille R, Vigier G, Bessede JL (2003) Study of polytetrafluoroethylene crystallization. Acta Polym 46(4):300–306
8. Perets Y, Matzui L, Vovchenko L, Ovsiienko I, Yakovenko O, Lazareno O, Zhuravkov O, Brusylovets O (2016) Influence of ultraviolet/ozonolysis treatment of nanocarbon filler on the electrical resistivity of epoxy composites. Nanoscale Res Lett 11:370–1-370-4
9. Bikiaris D, Vassiliou A, Chrissafis K, Paraskevopoulos KM, Jannakoudakis A, Docoslis A (2008) Effect of acid treated multi-walled carbon nanotubes on the mechanical, permeability, thermal properties and thermo-oxidative stability of isotactic polypropylene. Polym Degrad Stab 93:952–967
10. Datsyuk V, Kalyva M, Papagelis K, Parthenios J, Tasis D, Siokou A, Kallitsis I, Galiotis C (2008) Chemical oxidation of multiwalled carbon nanotubes. Carbon 46:833–840
11. Zhang J, Zou H, Qing Q, Yang Y, Li Q, Liu Z, Guo X, Du Z (2003) Effect of chemical oxidation on the structure of single-walled carbon nanotubes. J Phys Chem B 107:3712–3718

12. Tchoul MN, Ford WT, Lolli G, Resasco DE, Arepalli S (2007) Effect of mild nitric acid oxidation on dispersability, size, and structure of single-walled carbon nanotubes. Chem Mater 19:5765–5772
13. Minchenko OH, Tsymbal DO, Prylutska SV, Hnatiuk OS, Prylutskyy YI (2018) Single-walled carbon nanotubes affect the expression of genes associated with immune response in normal human astrocytes. Toxicol In Vitro 52:122–130
14. Ovsiienko IV, Len TA, Matzui LY, Tkachuk VY, Berkutov IB, Mirzoiev IG, Prylutskyy YI, Tsierkezos N, Ritter U (2016) Magnetoresistance of functionalized carbon nanotubes. Matwiss u Werkstofftech 47:254–262
15. Matzui LY, Ovsienko IV, Len TA, Prylutskyy YI, Scharff P (2005) Transport properties of composites with carbon nanotube-based composites. Fuller Nanotub Car N 13(Supplement 1):259
16. Matzui DV, Ovsiyenko IV, Lazarenko OA, Prylutskyy YI, Matzui VI (2011) Abnormal electron transport in graphite intercalation compounds with iron. Mol Cryst Liq Cryst 535:64–73
17. Len TA, Ovsiienko IV, Matzui LY, Berkutov IB, Mirzoiev IG, Gnida D, Kunitskyi YA (2017) Magnetoresistance of modified carbon nanotubes. Journal of Nano- and Electronic Physics 9:01018-1–01018-7
18. Liu B, Sundqvist B, Andersson O, Wagberg T, Nyeanchi EB, Zhu X-M, Zou G (2001) Electric resistance of single-walled carbon nanotubes under hydrostatic pressure. Solid State Commun 118:31–36
19. Chauvet O, Benoit JM, Corraze B (2004) Electrical, magneto-transport and localization of charge carriers in nanocomposites based on carbon nanotubes. Carbon 42:949–952
20. Ovsienko IV, Len TA, Matsuy LY, Prylutskyy YI, Berkutov IB, Andrievskii VV, Komnik YF, Mirzoiev IG, Grechnev GE, Kolesnichenko YA, Hayn R, Scharf P (2015) Magnetoresistance and electrical resistivity of N-doped multi-walled carbon nanotubes at low temperatures. Phys Status Solidi B 252:1402–1409
21. Len TA, Ovsiienko IV, Matzui LY, Tugay A (2014) Electrical resistance and magnetoresistance of modified carbon nanotubes. J Nano- Electron Phys 6:04024-1–04024-5
22. Ovsienko IV, Len TA, Matzui LY, Prylutskyy YI, Ritter U, Scharf P, Normand F, Eklund P (2007) Resistance of nanocarbon material containing nanotubes. Mol Cryst Liq Cryst 468:289–297
23. Shiraishi M, Ata M (2002) Conduction mechanisms in single-walled carbon nanotubes. Synth Met 128:235–239
24. Simmons JM, Nichols BM, Baker SE, Marcus MS, Castellini OM, Lee CS, Hamers RJ, Eriksson MA (2006) The effect of ozone oxidation on single-walled carbon nanotubes. J Phys Chem B 110:7113–7118

Chapter 11
New Method for Rapid Digital Hologram Processing

Yu. M. Kotsiuba, H. A. Petrovska, V. M. Fitio, and Ya. V. Bobitski

11.1 Introduction

Digital holographic interferometry (DHI) is widely used to study microdisplacements [1], the quality of parts in MEMS [2], or microscopy of living objects [3]. Depending on the application, there are many modifications of DHI including Fresnel and Fourier holography [4, 5].

In the digital Fresnel holography, there is an issue, if two- or three-wavelength method with spatial multiplexing is used. In this case, several complex object fields must be retrieved at different wavelengths, and they are located in different places of the reconstructed hologram. In order to get the accurate measurement result, one needs to perform the displacement of the reconstructed objects to the center [6]. To solve this problem, different complex algorithms were proposed, which also require different parameters to be manually calculated [7, 8]. One of them is the method with adjustable magnification, which involves finding the desired part from the hologram reconstructed by the S-FFT algorithm [9].

In the digital Fourier or focused image holography, it is necessary to select the correct filtering window to retrieve the complex amplitude of the object beam. During filtration, it's important to select the entire area of the useful signal while avoiding the unwanted components. Depending on the experiment conditions, the required components can be located anywhere in the hologram spectrum. Usually

Y. M. Kotsiuba · H. A. Petrovska (✉) · V. M. Fitio
Department of Photonics Lviv Polytechnic National University, Lviv, Ukraine
e-mail: halyna.a.Petrovska@lpnu.ua

Y. V. Bobitski
Department of Photonics Lviv Polytechnic National University, Lviv, Ukraine

Faculty of Mathematics and Natural Sciences University of Rzeszow, Rzeszow, Poland

© Springer Nature Switzerland AG 2019

O. Fesenko, L. Yatsenko (eds.), *Nanophotonics, Nanooptics, Nanobiotechnology, and Their Applications*, Springer Proceedings in Physics 222,
https://doi.org/10.1007/978-3-030-17755-3_11

the filter is selected manually. Thus, the digital holograms processing slows down, in particular when living objects are under study. In addition, in the reconstructed object field, there is an undesirable component caused due to the tilted reference wave.

Thus, it is obvious that developing of the algorithm for the automatic detection of the useful signal components from the reconstructed complex data in digital holography is important. This algorithm will facilitate the processing of digital holograms and increase the accuracy of measurements. In the further sections, we describe our method for automatically centering the components of the hologram spectrum and selecting the correct filtering window.

11.2 Mathematical Description of Digital Holographic Interferometry

In digital holography, the phase information is calculated by retrieving the complex amplitude of the object wave using Fresnel or Fourier transforms [10]. It is known that there are two main optical configurations for digital holograms recording: in line and off-axis. The second approach allows simplifying the procedure of obtaining the useful information. In this case, the tilted reference beam $A_r(x,y)$ interferes with the object wave $U(x,y)$. The obtained hologram has the following intensity distribution:

$$I_H(x, y) = \left[|U(x, y)|^2 + {A_r}^2 + A_r(x, y)\, U^*(x, y) + {A_r}^*(x, y)\, U(x, y)\right] \tag{11.1}$$

where $U(x,y)$ and $A_r(x,y)$ are the complex amplitudes of the object and reference beams.

As can be seen from (11.1), the useful spectrum terms of the digital hologram $A_r(x, y)U^*(x, y)$ or $A_r{}^*(x,y)U(x,y)$ contain the reference beam component that leads to the presence of a systematic measurement error. This error is due to the off-axis configuration of the recording scheme. The distance between useful components and the center of coordinates is proportional to the value of the interference angle θ [11]. This angle also determines the maximum carrier spatial frequency of the digital hologram [12]:

$$f_{R\max} = \frac{2}{\lambda} \sin\left(\frac{\theta_{\max}}{2}\right) \tag{11.2}$$

For retrieving the object field, a filtering in the frequency domain is performed. The complex amplitude of the object beam is calculated from:

$$\Gamma(x, y) = F^{-1}\{H(x, y) \cdot F\{I_H(x, y)\}\} \tag{11.3}$$

where $F\{\ldots\}$ denotes Fourier transform and $H(x,y)$ represents the binary filter.

11.3 Description of the Proposed Method

The first step of the proposed method is to ensure a fixed position of the component of the useful signal in the center of the spectrum. This can be done with help of the Fourier transform translation property:

$$F^{-1}\{F(u+a, v+b)\} = f(x, y)\exp[i2\pi(xa+yb)] \tag{11.4}$$

where $F^{-1}\{\ldots\}$ denotes the inverse Fourier transform and *F(u,v)* stands for the Fourier transform of the function *f(x,y)*.

From this, it also follows that by multiplying the recorded hologram by some phase factor Φ, one can shift the spectral components by the value of *(a,b)*. In order to shift the useful component to the proper place, it is necessary to determine the coordinates of its center (assuming the spectrum center coordinate equal to zero).

To solve this task, it was proposed to use the Count objects.vi function from the IMAQ Vision package of the LabView programming environment. This function allows you to recognize objects in images according to selected size and grayscale threshold. The main problem that arises in this case is to choose the correct threshold value for recognizing the proper object in the spectrum image. Nowadays, there are several approaches to solve this problem. In [13, 14], approaches based on histogram analysis were proposed. However, a series of steps is used, and in addition, some parameters must be entered manually. In another paper [15], the algorithm based on threshold binarization is considered with a sequential increase of the threshold until three separate binary objects remain. Then, the necessary component is selected, which is further used for spatial filtering of a digital hologram. A similar algorithm is implemented in our method. However, the proposed function from the IMAQ Vision package has the possibility to set the maximum and minimum size of the recognition objects. This feature allows avoiding recognition of the undesirable zero-order component. The "Count objects.vi" function gives all the information about the selected "+1" and "−1" order: width and the coordinates of the center point in the Cartesian system.

After that, it is necessary to find the proper distance between the center of recognized object and zero coordinate of the frequency domain. It should be noted that in the proposed function, the zero coordinate is located in the upper left part of the image. In the frequency domain, it is located in the center. Taking into account this fact, the calculation of the shift value distance is carried out by the following relation:

$$\begin{aligned} f_c &= \frac{x_c}{M} - \frac{1}{2} = \frac{2x_c - M}{2M} \\ g_c &= \frac{y_c}{N} - \frac{1}{2} = \frac{2y_c - N}{2N} \end{aligned} \tag{11.5}$$

Thus, the appropriate phase is calculated from:

$$\Phi_1(x, y) = \exp\left[-i2\pi\left(xf_c + yg_c\right)\right] \tag{11.6}$$

After the digital hologram is multiplied by the obtained function, a new image of the spectrum is formed, where the required component is located in the center. Then, knowing the width of the selected object, one can calculate the binary filter:

$$H(x, y) = \begin{cases} 1, \text{if} \sqrt{x^2 + y^2} \leq R \\ 0, \text{otherwise} \end{cases} \tag{11.7}$$

where R stands for the half-width of the recognized object.

Applying a binary filter, we select the useful signal part from the spectrum, and after the inverse Fourier transform, the complex amplitude of the object beam is obtained.

However, during the study of objects with digital holographic interferometry, some situation may occur when the recognition of the spectrum components becomes complicated due to the optical scheme configuration. It is known that a digital-focused image hologram is a particular case of a lensless Fourier hologram, where the exit pupil of the optical system is an object. The Fourier hologram is recorded using a spherical wave. To compensate the curvature of the reference wave, the point light source is placed on the same plane with the object [16]. In the optical schemes for digital holographic microscopy, the exit pupil can be located at large distances from the object, even outside the optical scheme that makes impossible to fulfill the curvature compensation condition. This leads to the defocusing of the spectrum components. This issue makes the recognition process not correct and also causes some errors in the retrieved the object wave [17].

Obviously, for the correct recognition and in order to avoid errors, it is necessary to compensate the curvature of the reference wave. This procedure can be carried out by multiplying a digital hologram by the following phase factor:

$$\Phi_2(x, y) = \exp\left[-\frac{i\pi\left(x^2 + y^2\right)}{\lambda r}\right] \tag{11.8}$$

where r denotes the curvature compensation radius.

At this stage, there is a problem of determining the proper value of r. There are several algorithms that introduce certain coefficients to get a focused image by finding their maximum. Thus, in work [18], a special coherence coefficient is introduced, which is calculated from the phase noise density. The determination of this coefficient involves a complex procedure of separation the noise from the phase image. In another work [19], a slightly simpler algorithm based on the correlation coefficient of the reconstructed speckle fields is proposed. The reconstruction of the object field is carried out sequentially for different values of r. At each iteration, this value is increased by Δr. After that, the correlation coefficient is calculated between a pair of reconstructed speckle images at a distance $r \pm \Delta C$, taking ΔC as a correlation interval. Obviously, the first algorithm is more informative when the phase of the object wave is needed. On the other hand, if

the speckle-field information is required, one should use the second method. The proposed algorithms allow applying our method even under nonoptimal conditions for the digital hologram recording.

11.4 Results and Discussion

The validation of the proposed methods was carried out using test holograms obtained with the software described in [20]. In this program, an array of complex values with dimension 1000 × 1000 points was used as the object wave. At each point, the complex amplitude had magnitude equal to one, and the phase varied within the range [−π; π]. The plane reference wave and the size of the diaphragm were chosen so to avoid overlapping of the useful signal with zero order.

The different steps of the hologram processing by the proposed method are shown in Fig. 11.1. Figure 11.1a shows the spectrum of the original digital hologram. The object recognition algorithm was applied to this spectrum. The input parameters for this case were the minimum $M_{\min}$ and the maximum $M_{\max}$ object size and were equal to 300 and 110,000 pixels, respectively. These values were sufficient to determine the necessary components while ignoring the zero order. Selection of the threshold was carried out automatically, using the method described in the previous section. After that, using the relations (11.5) and (11.6), the phase factor $\Phi_1(x,y)$ was calculated. The spectrum of a digital hologram after multiplying by the calculated phase term is shown in Fig. 11.1b. We see that the desired component is in the center of the spectrum. The width of the square that captures the component in the case of using a circular diaphragm is used to calculate the binary filter using relation (11.7). After applying the binary filter (Fig. 11.1c), the inverse Fourier transform is performed and the phase field is calculated. In the case of using a noncircular diaphragm, the task becomes a bit more complicated, since it is impossible to calculate the filter by a simple mathematical function. In

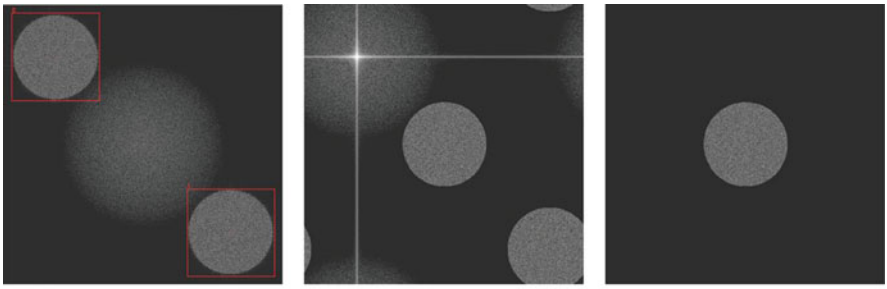

Fig. 11.1 Spectrum of the digital hologram (useful components selected) (**a**), same spectrum with object field component located in the center (**b**), and after applying the window filter (**c**)

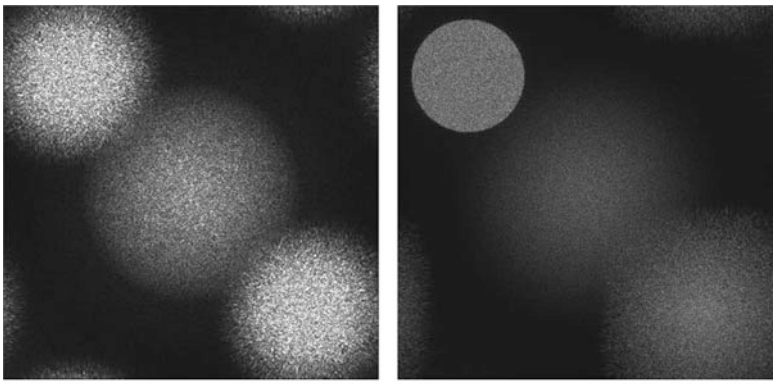

Fig. 11.2 Spectrum of the digital hologram before (**a**) and after (**b**) the compensation of the curvature of the reference beam

this case, one should use the threshold binarization of the image. Also in He et al. [15], it was proposed to use a Gaussian blur to minimize possible inaccuracies during the definition of a binary filter.

As was said previously, the curvature of the reference beam used to record a digital hologram distorts the useful component of the spectrum. An example of the spectrum of the digital hologram recorded using a spherical reference wave with radius $r = 500\ mm$ is shown in Fig. 11.2a. Obviously, the determination of the exact center coordinates of the required component is more complicated. In order to carry out this procedure correctly, the phase term $\Phi_2(x,y)$ was calculated. The result of phase compensation is shown in Fig. 11.2b.

After the compensation of the curvature of the reference wave field, the proposed method of fast digital hologram processing can be applied without any problems.

11.5 Conclusion

A method has been developed for rapid processing of Fourier and Fresnel digital holograms. The proposed algorithm allows automation of the process of retrieving the phase information from digital holograms and eliminates the systematic errors caused by the off-axis recording schemes configuration. The calculation of the correction phase factor will allow using the proposed method even with significant values of the reference beam curvature, which may occur under certain experimental conditions. The method can be applied to the digital two- or three-wavelength holography, as well as in digital holographic microscopy.

References

1. Schnars U, Falldorf C, Watson J, Jüptner W (2015) Digital holography. In: Digital holography and wavefront sensing. Springer, Berlin, Heidelberg, pp 39–68
2. Asundi A (2011) Digital holography for MEMS and microsystem metrology, vol 7. Wiley, New York
3. Micó V, Ferreira C, Zalevsky Z, García J (2010). Basic principles and applications of digital holographic microscopy. Microscopy: Science, Technology, Applications and Education 1411–1418
4. Picart P, Li JC (2013) Digital holography. Wiley, New York
5. Kotsiuba Y, Petrovska H, Fitio V, Bobitski Y (2017, August) Digital interferometry methods for the surface relief study. In: International conference on nanotechnology and nanomaterials. Springer, Cham, pp 207–217
6. Khodadad D, Bergström P, Hällstig E, Sjödahl M (2015) Fast and robust automatic calibration for single-shot dual-wavelength digital holography based on speckle displacements. Appl Opt 54(16):5003–5010
7. Li JC, Peng ZJ, Tankam P, Song QH, Picart P (2011) Digital holographic reconstruction of a local object field using an adjustable magnification. JOSA A 28(6):1291–1296
8. Zhang F, Yamaguchi I, Yaroslavsky LP (2004) Algorithm for reconstruction of digital holograms with adjustable magnification. Opt Lett 29(14):1668–1670
9. Picart P, Tankam P, Mounier D, Peng ZJ, Li JC (2009) Spatial bandwidth extended reconstruction for digital color Fresnel holograms. Opt Express 17(11):9145–9156
10. Schnars U, Jüptner WP (2002) Digital recording and numerical reconstruction of holograms. Meas Sci Technol 13(9):R85
11. Gusev ME, Voronin AA, Gurevich VS, Isaev AM, Alexeenko IV (2012) Modern methods of registration, reconstruction and representation of results in digital holographic interferometry, 7-th international scientific-practical conference «Holography – study and practice», Moscow, 28–30 September 2010, p 83
12. Abramov AY, Savonin SA, Dikov OV, Perepelnitsina OA, Ryabukho VP (2010) Digital focused image holographic interferometry of microscopic transparent objects, collection of works of international conference «FOP-2010». Saint-Petersburg 1:272–274
13. Li J, Wang Z, Gao J, Liu Y, Huang J (2014) Adaptive spatial filtering based on region growing for automatic analysis in digital holographic microscopy. Opt Eng 54(3):031103
14. Weng J, Li H, Zhang Z, Zhong J (2014) Design of adaptive spatial filter at uniform standard for automatic analysis of digital holographic microscopy. Optik-International Journal for Light and Electron Optics 125(11):2633–2637
15. He X, Nguyen CV, Pratap M, Zheng Y, Wang Y, Nisbet DR et al (2016) Automated Fourier space region-recognition filtering for off-axis digital holographic microscopy. Biomed Opt Express 7(8):3111–3123
16. Gusev ME, Voronin AA, Gurevich VS, Isaev AM, Alexeenko IV, Redkorechev VI (2011) Methods of digital holographic interferometry and its application to measure nanodisplacement. Nanosystems Phys Chem Math 2(1):23–39
17. Khodadad D, Bergström P, Hällstig E, Sjödahl M (2014) Single shot dual-wavelength digital holography: calibration based on speckle displacements. International Journal of Optomechatronics 8(4):326–339
18. Picart P, Montresor S, Sakharuk O, Muravsky L (2017) Refocus criterion based on maximization of the coherence factor in digital three-wavelength holographic interferometry. Opt Lett 42(2):275–278
19. Yang Y, Kang BS, Choo YJ (2008) Application of the correlation coefficient method for determination of the focal plane to digital particle holography. Appl Opt 47(6):817–824
20. Kotsiuba Y, Petrovska H, Fitio VM, Bulavinets T, Bobitski YV (2016, August) Optimization of the parameters of digital holographic microscope. In: International conference on nanotechnology and nanomaterials. Springer, Cham, pp 231–247

Chapter 12
Theory of Exciton States in Nanosystems Containing Dielectric Quantum Dots

Sergey I. Pokutnyi

12.1 Introduction

Investigation of quasi-zero nanosystems consisting of semiconductor (dielectric) spherical form quantum dots (QDs) with the radii $a = 1$–10 nm, containing CdS, ZnSe, and aluminum oxide in their volume, which were grown in the transparent dielectric matrix, such as borosilicate glass, vacuum, and immersion oils, has received increased attention due to their unique photoluminescent properties and their ability to efficiently emit light in the visible or near-infrared regions at room temperature [1–4]. Such linear dimensions a of QD are comparable with the de Broglie wavelength of the electron and the hole or/and their Bohr radii. The optical properties of quasi-zero nanosystems are largely determined by the energy spectrum of the spatially separated electron-hole pairs (excitons) [5–13].

In the experimental work [1], it is found that the nonequilibrium electrons generated by the interband excitation of CdS QDs with radii $a = (1.5$–$30)$ nm have a finite probability of overcoming the potential barrier and penetration into the matrix of borosilicate glass, where the QD is immersed (wherein the hole moves in the QD volume).

In [7–13], the theory of the exciton from spatially separated electrons and holes (the hole is within the volume of the semiconductor (dielectric) QD, and the electron is localized over the spherical surface boundary of (QD/matrix)) is developed. The effect of a significant increase in the binding energy of an exciton is revealed in a nanosystem that contains semiconductor (CdS, CdSe, ZnSe) and aluminum oxide (almost by two orders) dielectric QD in comparison with the binding energy of an exciton in such single crystal materials.

S. I. Pokutnyi (✉)
Chuiko Institute of Surface Chemistry of National Academy of Sciences of Ukraine, Kyiv, Ukraine

© Springer Nature Switzerland AG 2019

O. Fesenko, L. Yatsenko (eds.), *Nanophotonics, Nanooptics, Nanobiotechnology, and Their Applications*, Springer Proceedings in Physics 222,
https://doi.org/10.1007/978-3-030-17755-3_12

It was noted [14] that, at such levels of QD content in the samples, one must take into account the interaction between charge carriers localized above the QD surfaces. Therefore, in [15–21], we develop the theory of an exciton quasimolecule (or biexciton) (formed from spatially separated electrons and holes) in a nanosystem that consists of ZnSe and CdS QDs synthesized in a borosilicate glassy matrix.

Using the variational method, we obtain the total energy and the binding energy of the exciton quasimolecule (or biexciton) singlet ground state in such a system as functions of the spacing between the QD surfaces and of the QD radius. We show that the biexciton formation is of the threshold character and possible in a nanosystem, in which the spacing between the QD surfaces exceeds a certain critical spacing. The spectral shift of the low-temperature luminescence peak is established [15–21].

In experimental works [2–4], the nonlinear optical properties and their dependences on the matrix material (vacuum oil) of heterogeneous liquid nanophase composites based on wideband aluminum oxide QD with average radii not exceeding $a = 25$ nm were studied. In [2–4], it is shown that aluminum oxide QDs in such matrix have a wide absorption band in the visible and near-infrared wavelengths.

In [2–4], the nature of the absorption bands in the visible and near-infrared regions remains unclear. Therefore, the study of light absorption mechanisms in such nanoheterostructures is problematic.

This chapter summarizes the theory of excitons from spatially separated electrons and holes (the hole moves in volume QD, and the electron is localized over the spherical surface boundary of [QD/matrix]). In [7–11], the role of centrifugal energy of the electron in the potential energy of the exciton is developed. It has been shown that the centrifugal energy in the potential energy of the exciton leads to the occurrence of the quasistationary states in the band of the surface exciton states, which with the increase of QD radius transfers into stationary state. It is established that the light spectrum of the interband absorption (emission) of nanosystems consisting of the energy bands are formed by the electron between the quasistationary and stationary states, and intraband absorption spectra are formed from the bands caused by electron transitions between stationary states.

12.2 Energy of Ground State Exciton in Nanosystems

Consider the model of quasi-zero nanosystems: semiconductor spherical QD with a radius, which contains semiconductor (dielectric) material in its volume with permittivity ε_2, surrounded by a dielectric matrix with permittivity ε_1. In the QD volume, h hole moves with the effective mass m_h, and e electron with the effective mass $m_e{}^{(1)}$ is situated in the matrix (r_e and r_h – the distance of the electron and the hole from the QD center). Let us assume that in QD, the valence band has a parabolic form. We also assume that on the spherical surface boundary of QD/matrix, infinite high potential barrier exists. Therefore, in the studied model, h hole cannot deviate from the QD volume, and e electron cannot penetrate into the QD volume [7–11].

The energy of polarization interaction of the electron and the hole $U(\boldsymbol{r_e}, \boldsymbol{r_h}, a)$ with a spherical surface boundary of QD/matrix in the case of relative $\varepsilon = (\varepsilon_2/\varepsilon_1) \gg 1$ permittivity can be represented as the algebraic sum of the hole and electron interaction energies with their $V_{hh'}(r_h, a)$, $V_{ee'}(r_e, a)$ and "foreign" $V_{eh'}(r_e, r_h, a)$, $V_{he'}(\boldsymbol{r_e}, \boldsymbol{r_h}, a)$ images, respectively [7–11]:

$$U(r_e, r_h, a, \varepsilon) = V_{hh'}(r_h, a, \varepsilon) + V_{ee'}(r_e, a, \varepsilon) + V_{eh'}(r_e, r_h, a, \varepsilon) + V_{he'}(r_e, r_h, a, \varepsilon), \tag{12.1}$$

where

$$V_{hh'}(r_h, a, \varepsilon) = \frac{e^2\beta}{2\varepsilon_2 a}\left(\frac{a^2}{a^2 - {r_h}^2} + \varepsilon\right), \tag{12.2}$$

$$V_{ee'}(r_e, a, \varepsilon) = -\frac{e^2\beta}{2\varepsilon_1 a} \cdot \frac{a^4}{r_e^2\left(r_e^2 - a^2\right)}, \tag{12.3}$$

$$V_{he'}(\boldsymbol{r_e}, \boldsymbol{r_h}, a, \varepsilon) = \frac{e^2\beta}{2\varepsilon_2 a} \cdot \frac{a^2}{r_e\left|\boldsymbol{r_h} - (a/r_e)^2\boldsymbol{r_e}\right|}, \tag{12.4}$$

$$V_{eh'}(\boldsymbol{r_e}, \boldsymbol{r_h}, a, \varepsilon) = -\frac{e^2\beta}{2\varepsilon_1 a} \cdot \frac{a^2}{r_h\left|\boldsymbol{r_e} - (a/r_h)^2\boldsymbol{r_h}\right|}. \tag{12.5}$$

Here, the parameter of the nanosystem $\beta = (\varepsilon_2 - \varepsilon_1)/(\varepsilon_2 + \varepsilon_1)$.

For simplicity, without losing the generality, we assume that the hole h with the effective mass m_h is located in the center of the QD (wherein $r_h = 0$) and the e electron with an effective mass $m_e{}^{(1)}$ is localized in the matrix of the spherical surface QD ($r_e = r$ – the distance of e electron from the QD center). Such an assumption is justified, as the ratio of the effective masses of electrons and holes in the nanosystem $\left(\left(m_e^{(1)}/m_h\right) \ll 1\right)$. In the observed quasi-zero nanosystems model, in the frame of the above mentioned approximations, as well as in the effective mass approximation and the center of mass of nanosystem [6], the Hamiltonian of exciton (from spatially separated hole, moving in QD volume, and the electron situated in the dielectric matrix) takes the form [12, 13]:

$$H(r, a) = -\frac{\hbar^2}{2\mu_0}\Delta + V_l(r) + V_{eh}(r) + U(r, a) + E_g, \tag{12.6}$$

where the first member is the operator of exciton's kinetic energy (($\mu_0 = m_e{}^{(1)}m_h/(m_e{}^{(1)} + m_h)$ – the reduced mass of the exciton from spatially separated electrons and holes), the second describes the centrifugal energy of the exciton

$$V_l(r) = \frac{\hbar^2 L^2}{2\mu_0 r^2} \tag{12.7}$$

($L^2 = l(l+1)$, $l = 0, 1, 2, -$ orbital quantum number of the electron), and E_g is the width of semiconductor bandgap with ε_2 permittivity. In the Hamiltonian (12.6), the energy of the Coulomb interaction between the electron and the hole is described by the equation [7]:

$$V_{eh}(r) = -\frac{1}{2}\left(\frac{1}{\varepsilon_1} + \frac{1}{\varepsilon_2}\right)\frac{e^2}{r} = -\frac{e^2}{\tilde{\varepsilon} r} \tag{12.8}$$

Polarization interaction energy (12.2), (12.4), (12.5) of the electron and the hole with spherical surface boundary of QD/matrix, when $r_h = 0$, takes the form [12, 13]:

$$V_{hh'}(a) = \frac{e^2\beta}{2\varepsilon_2 a}\left(1 + \frac{\varepsilon_2}{\varepsilon_1}\right) \tag{12.2a}$$

$$V_{he'}(a) = \frac{e^2\beta}{2\varepsilon_2 a} \tag{12.4a}$$

$$V_{eh'}(a) = -\frac{e^2\beta}{2\varepsilon_1 a} \tag{12.5a}$$

Then taking into account (12.3), (12.2a), (12.4a), and (12.5a), the energy of polarization interaction (12.3) may be written in the following form [12, 13]:

$$U\,(r, a) = -\frac{e^2\beta}{2\varepsilon_1 a} \cdot \frac{a^4}{r^2\left(r^2 - a^2\right)} + \frac{e^2\beta}{\varepsilon_2 a} \tag{12.9}$$

Consideration of interaction energy of the hole with its (12.2a) and "foreign" (12.4a) images, as well as the electron with the "foreign" (12.5a) image, leads to the increase of the polarization interaction energy (12.9) by $(e^2\beta/\varepsilon_2 a)$, which decreases with the increase of QD radius.

In the nanosystem, the Hamiltonian $H(r, a)$ (12.6) of the exciton from spatially separated electron and hole, considering the formulas (12.9), (12.7), and (12.8), takes the following form [12, 13]:

$$H\,(r, a) = -\frac{\hbar^2}{2\mu_0}\Delta + U_l\,(r, a) + E_g, \tag{12.10}$$

where the effective potential energy of the exciton

$$U_l\,(r, a) = -\frac{e^2}{\tilde{\varepsilon} r} - \frac{e^2\beta}{2\varepsilon_1 a} \cdot \frac{a^4}{r^2\left(r^2 - a^2\right)} + \frac{e^2\beta}{\varepsilon_2 a} + \frac{\hbar^2 L^2}{2\mu_0 r^2} \tag{12.11}$$

with the increase of the QD radius (so that $a \gg a_{ex}$, where $a_{ex} = (\varepsilon_2\ \hbar^2/\mu\ e^2)$ is exciton Bohr radius, $\mu = m_e^{(2)}\ m_h/(m_e^{(2)} + m_h)$ is the reduced exciton mass,

and $m_e{}^{(2)}$ is the effective mass of electron in the semiconductor with permittivity ε_2), the spherical surface between the boundary of two media goes into the flat boundary surface. In this regard, the exciton from the spatially separated electrons and holes (the hole moves in the semiconductor, and the electron is situated in the matrix) becomes two-dimensional. In the Hamiltonian (12.6) potential energy, describing the motion of the exciton in the nanosystem, containing QD with large radius ($a \gg a_{\text{ex}}$), the main contribution is the energy of the Coulomb interaction $V_{eh}(r)$ (12.8) between the electron and the hole. Interaction energy between the electron and the hole with their (12.2a), (12.5), and "foreign" (12.5a), (12.4a) images gives a much smaller contribution to the potential energy (12.11) of the Hamiltonian (12.6). By the first approximation, this contribution may be neglected. In the potential energy (12.11) of the Hamiltonian (12.6), the energy of the Coulomb interaction (12.8) between the electron and the hole only remains. The Schrodinger equation with this Hamiltonian describes a two-dimensional exciton (2D exciton) from spatially separated electron and hole energy spectrum, which takes the form [22]:

$$E_n = -\frac{Ry_{\text{ex}}^{2D}}{(n+(1/2))^2},\ Ry_{\text{ex}}^{2D} = \frac{(\varepsilon_1+\varepsilon_2)^2}{4\varepsilon_1^2\varepsilon_2^2}\cdot\left(\frac{\mu_0}{m_0}\right)Ry_0, \tag{12.12}$$

where $n = 0,1,2\ \ldots$ is the principal quantum number of exciton and $Ry_0 = 13.606$ eV is the Rydberg constant. Bohr radius of such 2D exciton is described by the following equation:

$$a_{\text{ex}}^{2D} = \frac{2\varepsilon_1\varepsilon_2}{\varepsilon_1+\varepsilon_2}\cdot\frac{\hbar^2}{\mu_0 e^2}, \tag{12.13}$$

and the binding energy of the ground state of 2D exciton, according to (12.12), is given by:

$$E_{\text{ex}}^{2D} = -4Ry_{\text{ex}}^{2D} \tag{12.14}$$

If $l \neq 0$, the contribution of the centrifugal energy into the effective potential energy $U_l(r,a)$ (12.11) creates a positive potential barrier, the maximum value of which is the following:

$$U^{\max}(l,S) \sim L^2 S^{-2} \tag{12.15}$$

for QD with large radius $S \gg 1$ ($S = \left(a/a_{\text{ex}}^{2D}\right)$ – the dimensionless radius of QD). The formation of such a barrier means that along with the stationary states $E_{1,l}(S) < 0$ the exciton (from spatially separated electrons and holes), over the spherical surface of the QD, quasistationary states of the exciton with energy $E_{1,l}(S) > 0$ can occur. With the increase of radius S of QD, starting from the value of S greater than a certain critical radius of $S_c^*(1,l)$, i.e., at

$$S > S_c^*(1,l) \tag{12.16}$$

the first quasistationary states should appear. At bigger radii of QD

$$S > S_c(1,l) > S_c^*(1,l) \tag{12.17}$$

they need to pass into stationary states. When $S \geq \tilde{S}_c(1,l) \gg 1$, stationary states pass into two-dimensional exciton state with energy $E_{1,l}(a) = \left(-E_{\text{ex}}^{2D}\right)$ (12.14), localized on a flat surface between two media [5, 6], i.e., the energy spectrum $E_{1,\,l}(S)$ of the stationary states of the exciton energy is bounded from below $\left(-E_{\text{ex}}^{2D}\right)$ (12.14). The existence of the critical radius $S_c^*(1,l)$ shows that for QD with determined radius S, the energy spectrum $E_{1,\,l}(S)$ of the exciton is bounded above by the maximum value $l^{\max}(1,S)$, forming a band of surface states, localized on the surface spherical boundary of (QD/matrix), part of which has a quasistationary character. Such band of surface states contains a finite number of levels $(1,\ l)$, and this band is completed by $(1, l^{\max}(l,S))$ level. Radius $S_c^*(1,l)$ corresponds to the highest acceptable value of energy $E_{1,l}^{\max}(S)$ of ground state at fixed l. This maximum value of the energy coincides with the $U^{\max}\left(l,\ S = S_c^*(1,l)\right)$ (12.15) [12, 13].

Let us define the energy of the ground $(n = 1)$ state of the exciton Hamiltonian (12.10) for arbitrary values of S and l by means of the variational method. By making a standard replacement of the radial wave function $R_l(r) = (\chi_l(r)/r)$, the variational function $\chi_l(r)$ will be given as [12, 13]:

$$\chi_l(r) = A_l r\,(r-a)\exp\left(-j_l\,(r-a)\,/a\right), \tag{12.18}$$

$$A_l = 2(j_l/S)^{5/2}\left(a_{\text{ex}}^{2D}\right)^{-5/2},$$

where $j_l(a)$ is a variational parameter. Choosing the wave function $\chi_l(r)$ in the form (12.18) provides its passage to the limit when $S \to \infty$, $(j_l/S) \to$ const in the wave function of electrons localized on the plane surface between two media [23, 24]. We write the mean value of the exciton Hamiltonian (12.10) on the wave functions (12.18) in the following form:

$$E_{1,l}\,(a,\ j_l(a)) = \langle R_l(r)\,|H\,(r,a)|\,R_l(r)\rangle \tag{12.19}$$

The results of the variational calculation of energy $E_{1,\,l}(a)$ (12.19) of the ground state of the exciton in nanosystems containing aluminum oxide QD with average a radius not exceeding 20 nm are obtained for the nanosystem containing aluminum oxide QD (with permittivity $\varepsilon_2 = 10$ and the effective mass of hole $(m_h/m_0) = 6.2$; the value of the effective mass of the electron in the matrix $(m_e{}^{(1)}/m_0) = 0.537$ [14]), situated in the matrix (vacuum oil), which was studied in experimental studies [2–4] (see Fig. 12.1). Figure 12.1 shows the dependence of $E_{1,\,l}(a)$ (12.19) for the states

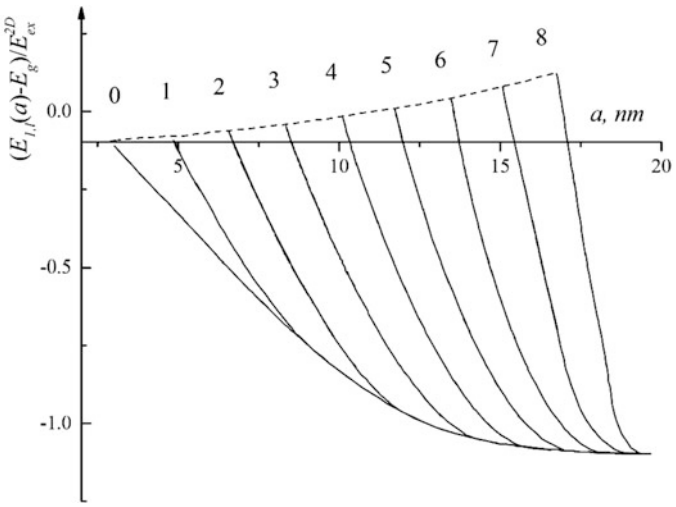

Fig. 12.1 The dependence of the energy spectrum $(E_{1,\,l}(a) - E_{\mathrm{g}})$ of the exciton (from spatially separated electrons and holes) in the states ($n = 1$, $l = 0,1,2,3,4,5,6,7,8$) (where n and l are the principal and orbital quantum numbers of the electron) (solid line) on the a radius of the aluminum oxide QD, situated in the dielectric matrix (vacuum oil). The numbers at the curves indicate the value of l. The dashed lines indicate the boundaries of the spectrum of quasistationary states $E_{1,l}^{\max}(a)$ of the exciton. Here, E_{g} is the bandgap of the aluminum oxide QD and $E_{\mathrm{ex}}^{2D} = 2.5038$ eV is the binding energy of the ground state of the two-dimensional exciton (from spatially separated electrons and holes)

with $l = 0$, 1, 2, 3, 4, 5, 6, 7, 8 with quasistationary states spectrum border $E_{1,l}^{\max}(a)$. The obtained results (see Fig. 12.1) clearly illustrate the abovementioned qualitative features of considered dependences $E_{1,\,l}(a)$ (12.19). The critical radii of QD for $l \leq 8$ have, respectively, values [12, 13]:

$$\begin{gathered} a_{\mathrm{c}}^{*}(1,l)\left(S_{c}^{*}(1,l)\right) = 4.9 \text{ nm } (13.94);\ 6.64 \text{ nm } (18.9); \\ 8.48 \text{ nm } (24.12);\ 10.22 \text{ nm } (29.1);\ 11.82 \text{ nm } (33.6); \\ 13.5 \text{ nm } (38.4);\ 15.2 \text{ nm } (43.2);\ 16.8 \text{ nm } (47.8) \\ a_{\mathrm{c}}(1,l)\,(a_{\mathrm{c}}(1,l)) = 3.1 \text{ nm } (8.82);\ 5.0 \text{ nm } (14.22); \\ 6.83 \text{ nm } (19.43);\ 8.63 \text{ nm } (24.55); \\ 10.4 \text{ nm } (29.6);\ 12.14 \text{ nm } (34.5); \\ 13.84 \text{ nm } (39.4);\ 15.5 \text{ nm } (44.1);\ 17.16 \text{ nm } (48.8). \end{gathered} \tag{12.20}$$

In nanosystems with the increase of radius a of QD, starting from the value not exceeding a certain critical radius of QD $a_{\mathrm{c}}^{*}(1,l)$ at

$$a_{\mathrm{c}}^{*}(1,l) \leq a \leq a_{\mathrm{c}}(1,l) \tag{12.21}$$

quasistationary states of the exciton firstly appear (see Fig. 12.1). For instance, the smallest radius $a_c^*(1, l)$ of QD wherein quasistationary states of the exciton appear (in the state $(1, l = 1)$) according to (12.20) is equaled to $a_c^*(1, 1) \cong 4.9$ nm, whereas the largest radius of QD $a_c^*(1, l)$, at which the quasistationary state exciton occurs (in the state $(1, l = 8)$, is equaled to $a_c^*(1, l = 8) \cong 16.8$ nm) [12, 13].

In the range of values of QD radii

$$a_c(1, l) \leq a \leq \tilde{a_c}(1, l) \tag{12.22}$$

(at $a \geq \tilde{a_c}(1, l) = 19.1$ nm quasistationary states $(1, l)$ of the exciton goes into the two-dimensional exciton state (12.12) localized on a flat surface bounding two media [5, 6]), and the quasistationary state goes into the exciton stationary states (see Fig. 12.1). The smallest radius of QD $a_c(1, l)$ at which the exciton stationary states appear (in the state $(1, l = 0)$, according to (12.20)) is equaled to $a_c(1, 0) \cong 3.1$ nm [5, 6], whereas the largest radius of QD $a_c(1, l)$ (in exciton state $(1, l = 8)$) is equaled to $a_c(1, l = 8) \cong 17.16$ nm. In the nanosystem, the stationary states of the exciton (from spatially separated electrons and holes) are located in the bandgap of aluminum oxide QD (below the bottom of the conduction band E_c of aluminum oxide QD (see Fig. 12.2, area 1)). They are limited below by level $E_{ex}^{2D} \cong 2.504$ eV (12.14), which is equal to the binding energy of the ground state of two-dimensional exciton (from spatially separated electrons and holes). Quasistationary states of the exciton are in the conduction band E_c (above the bottom of the conduction band E_c of aluminum oxide QD) (see Fig. 12.2, area 2). They are limited to the top by the border of the spectrum $E_{1,l}^{\max}(a)$ of quasistationary states. The magnitude of $E_{1,l}^{\max}(a)$ takes a maximum value in the state $(1, l = 8)$, wherein the $E_{1,l=8}^{\max}\left(a = a_c^*(1, l = 8) \cong 0.21\ E_{ex}^{2D} \cong 0.526\ \text{eV}\right)$ (see Fig. 12.1). In the nanosystem, the hole moves in the valence band E_v of QD, and the electron is in the quasistationary and stationary states (in areas 1 and 2 of the conduction band and the band gap of QD; see Fig. 12.2) [12, 13].

Such high quasistationary states could be significant in the processes of scattering of electrons in the QD with sufficient large radius $a \cong a_c^*(1, 8) \cong 16.8$ nm and may lead to a strong suppression of electron mobility in dielectric matrices. The electron trapping on the quasistationary states is possible also without changing the total energy [12, 13].

Thus, for aluminum oxide QD, wherin the radius is in the interval (12.22), the energy spectrum $E_{1,l}(a)$ of the exciton is limited above by the maximum value of the orbital quantum number $l^{\max} = 8$, which forms the band of surface states. Such band of the surface states of the exciton (from spatially separated electron and hole) consists of stationary and quasistationary states and has a finite number of levels $(1, l)$, which is equal to 9 [12, 13].

The obtained results allow us to follow the transition from the exciton states localized on the surface of a spherical QD to the states of the exciton localized on the boundary plane surface. For QD with large radius S (in the limit of $S \to \infty$), not only arbitrary values of l but also (l/S), which within $(S, l \to \infty)$ define the

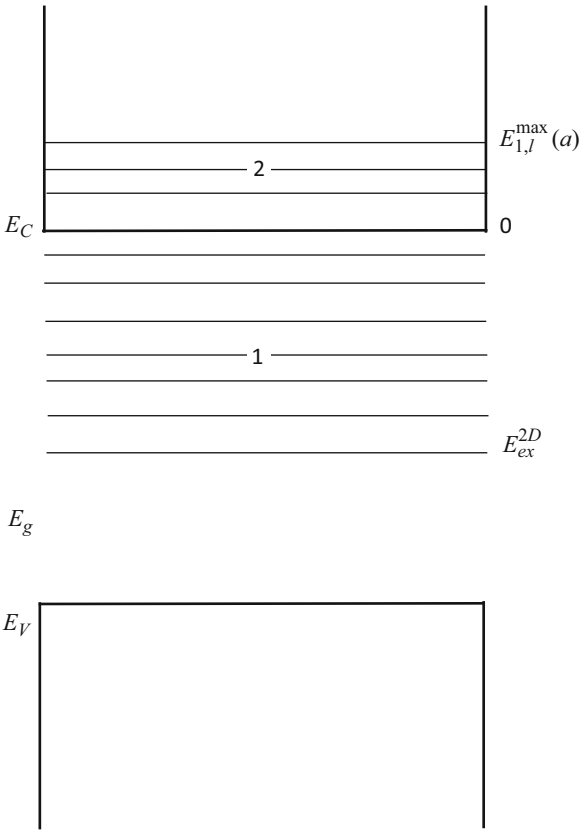

Fig. 12.2 Schematic representation of the energy levels $E_{1,\,l}(a)$ of the exciton (from spatially separated electron and hole) in the state ($n = 1$, $l \leq 8$) in the nanosystem consisting of aluminum oxide QD with a radius situated the dielectric matrix (vacuum oil). The stationary states of the exciton (area 1) are located in the bandgap of aluminum oxide QD (below the bottom of the conduction band E_c of aluminum oxide QD). They are bounded below by level E_{ex}^{2D}, which is the binding energy of the ground state of the exciton (from spatially separated electrons and holes) in the nanosystems. Quasistationary states of the exciton (area 2) are in the E_c conduction band of aluminum oxide QD (above the bottom of the conduction band E_c). They are limited to the top boundary of the spectrum of quasistationary states $E_{1,l}^{\max}(a)$. In such an exciton, a hole moves in the valence band of a QD, and the electron is located on energy levels (in areas 1 and 2)

finite quasimomentum $p = \hbar k_{\|} = (\hbar l/a)$ of free movement of the electron parallel to the boundary surface, become permitted. As a result, the expression $E_{1,\,l}(a)$ (12.19) proceeds into the spectrum of exciton states localized on the boundary plane surface, which in the dimensional units has the following form [12, 13]:

$$E_{1,l}\left(k_{\|}\right) = -E_{\text{ex}}^{2D} + \left(\hbar^2 {k_{\|}}^2\right)/2\mu \tag{12.23}$$

Thus, all surface states become stationary, as in the case of specified passage to the limit potential barrier (12.11) becomes infinitely wide, and its height (12.15) $U^{\max}(l,S) \to (L^2/S^2) = (\hbar^2 k_{\|}{}^2)/2\mu$ (in the dimensional units) defines the kinetic energy of the "free" motion of the electron along the plane of the media boundary.

The more elementary method to detect and study observed exciton states in nanosystems consisting of aluminum oxide with an average radius of a (12.22) placed in the matrix(vacuum oil) [2–4] can be investigated the interband. This is formed by electron transitions in the surface exciton states band between the quasistationary states located in the conductivity band E_c of QD and stationary states, being in the band gap of the QD (see Fig. 12.2) and intraband (which is caused by the electron transitions between the stationary states) of light absorption. Such transitions with a change in the orbital quantum number ($l^{'} = l \pm 1$) per unit are allowed by the selection rules. The photon energy for such transitions

$$\Delta E_l^{l+1}(a) = E_{1,l+1}(a) - E_{1,l}(a) \tag{12.24}$$

where l takes values from 0 to 8.

Consider the qualitative picture of the appearance of transition states in the nanosystem (see Figs. 12.1 and 12.2 and Table 12.1). Starting from the radius of aluminum oxide QD $a \geq a_c^*(1,1) \cong 4.9$ nm in the range of QD radii [12, 13]:

$$a_c^*(1,1) \leq a < \left(a_c^*(1,2) \cong 6.64 \text{ nm}\right) \tag{12.25}$$

interband transition occurs between the states of (1,1) and (1,0) with photon energies in the range of

$$248 \text{ meV} < \Delta E_0^1(a) \leq 551 \text{ meV} \tag{12.26}$$

With the increase of the radius a of QD in the range of radii a

$$a_c^*(1,2) \leq a < \left(a_c^*(1,3) \cong 8.48 \text{ nm}\right) \tag{12.27}$$

there are two interband transitions: the transition between the states (1,1) and (1,0) with photon energies in the range of

$$248 \text{ meV} \leq \Delta E_0^1(a) < 25 \text{ meV}; \tag{12.28}$$

and transition between states (1, 2) and (1,1) in the range of QD radii

$$a_c^*(1,2) \leq a < (a_c(1,2) \cong 6.83 \text{ nm}) \tag{12.29}$$

with the energy of the quantum

$$\Delta E_1^2(a) \cong 826 \text{ meV}, \tag{12.30}$$

Table 12.1 Energy transitions $\Delta E^{l}_{l-1}(a)$ (expressed by meV), in which the orbital quantum number l changes by one (wherein l takes values from 1 to 8) between quasistationary and stationary states of the exciton (from the spatially separated electrons and holes) (see Fig. 12.1), which appears in the nanosystem containing aluminum oxide QD with a radius (expressed by nm), situated in the dielectric matrix (vacuum oil)

a (nm)	$\Delta E^{1}_{0}(a)$ (meV)	$\Delta E^{2}_{1}(a)$ (meV)	$\Delta E^{3}_{2}(a)$ (meV)	$\Delta E^{4}_{3}(a)$ (meV)	$\Delta E^{5}_{4}(a)$ (meV)	$\Delta E^{6}_{5}(a)$ (meV)	$\Delta E^{7}_{6}(a)$ (meV)	$\Delta E^{8}_{7}(a)$ (meV)
5,2	501							
5,3	426							
5,6	401							
5,8	351							
6,0	325							
6,5	250							
6,9	200	826						
7,2	180	801						
7,5	150	751						
8,0	75	676						
8,6	24	570	1150					
9,0	0	451	926					
9,5	0	325	851					
10	0	225	751					
10,3	0	201	701	1172				
11	0	75	576	976				
11,9	0	0	350	750	1192			
12,5	0	0	225	651	1080			
13	0	0	124	502	976			
13,6	0	0	52	388	851	1352		

(continued)

Table 12.1 (continued)

a (nm)	$\Delta E_0^1(a)$ (meV)	$\Delta E_1^2(a)$ (meV)	$\Delta E_2^3(a)$ (meV)	$\Delta E_3^4(a)$ (meV)	$\Delta E_4^5(a)$ (meV)	$\Delta E_5^6(a)$ (meV)	$\Delta E_6^7(a)$ (meV)	$\Delta E_7^8(a)$ (meV)
14	0	0	0	275	626	1302		
15,2	0	0	0	63	376	1001	1480	
16	0	0	0	0	150	501	1281	
16,9	0	0	0	0	0	224	628	2000
17,5	0	0	0	0	0	63	300	1552
18	0	0	0	0	0	0	150	1052
18,5	0	0	0	0	0	0	34	401
18,8	0	0	0	0	0	0	0	72
19,1	0	0	0	0	0	0	0	0

and in the range of QD radii

$$a_c(1,2) \le a < a_c^*(1,3) \tag{12.31}$$

such transition is intraband with energies of the quantum in the range of

$$526\ \text{meV} < \Delta E_1^2(a) \le 826\ \text{meV} \tag{12.32}$$

in the range of QD radii

$$a_c^*(1,3) \le a < \left(a_c^*(1,4) \cong 10.22\ \text{nm}\right) \tag{12.33}$$

interband transition between (1, 3) and (1, 2) is added to two transitions that occur in the range of QD a radii (12.27), which range in radii of QD

$$a_c^*(1,3) \le a < (a_c(1,3) \cong 8.63\ \text{nm}) \tag{12.34}$$

will be interband with photon energy

$$\Delta E_2^3(a) \cong 1.0\ \text{meV}, \tag{12.35}$$

in the range of QD radii

$$a_c(1,3) \le a < a_c^*(1,4) \tag{12.36}$$

such transition is intraband with photon energies

$$0.694\ \text{meV} < \Delta E_2^3(a) \le 1.0\ \text{meV}.$$

In the range of a radii of QD (12.33), intraband transition between the states (1, 2) and (1, 1) will be observed with photon energies in the range of

$$175\ \text{meV} < \Delta E_1^2(a) \le 526\ \text{meV} \tag{12.37}$$

Intraband transitions between the states (1, 1) and (1, 0) disappear when $a \cong 9.1$ nm.

In the range of radii of QD

$$a_c^*(1,4) \le a < \left(a_c^*(1,5) \cong 11.82\ \text{nm}\right) \tag{12.38}$$

three transitions exist: intraband transitions between the states (1, 2) and (1, 1), which, with energy not exceeding (188 meV), disappear when $a \cong 11.6$ nm, and intraband transitions between the states (1, 3) and (1, 2) with photon energies

$$351\ \text{meV} \le \Delta E_2^3(a) \le 701\ \text{meV}. \tag{12.39}$$

Arising new transition between the states (1, 4) and (1, 3) in the range of a radii of QD

$$a_{\mathrm{c}}^{*}(1,4) \leq a < (a_{\mathrm{c}}(1,5) \cong 10.4 \ \mathrm{nm}) \tag{12.40}$$

is interband with a photon energy

$$\Delta E_3^4(a) \cong 1.108 \ \mathrm{eV}, \tag{12.41}$$

and in the range of radii

$$a_{\mathrm{c}}(1,4) \leq a < a_{\mathrm{c}}^{*}(1,5) \tag{12.42}$$

such transition will be intraband with photon energies

$$0.801 \ \mathrm{eV} < \Delta E_3^4(a) \leq 1.108 \ \mathrm{eV}. \tag{12.43}$$

In the range of a

$$a_{\mathrm{c}}^{*}(1,5) \leq a < \left(a_{\mathrm{c}}^{*}(1,6) \cong 13.5 \ \mathrm{nm}\right) \tag{12.44}$$

two transitions that occur in the range of a radii of QD (12.39) is added to the transition between the states (1, 5) and (1, 4), which range is in the range of QD radii

$$a_{\mathrm{c}}^{*}(1,5) \leq a < (a_{\mathrm{c}}(1,5) \cong 12.14 \ \mathrm{nm}) \tag{12.45}$$

will be interband, with photon energy

$$\Delta E_4^5(a) \cong 1.128 \ \mathrm{eV}, \tag{12.46}$$

in the range of radii

$$a_{\mathrm{c}}(1,5) \leq a < a_{\mathrm{c}}^{*}(1,6) \tag{12.47}$$

such transition is intraband with photon energies

$$0.876 \ \mathrm{eV} < \Delta E_4^5(a) \leq 1.128 \ \mathrm{eV}. \tag{12.48}$$

In the same range of QD radii (12.44), intraband transitions between the states (1, 3) and (1, 2) occur with the photon energies

$$20 \ \mathrm{meV} \leq \Delta E_2^3(a) \leq 351 \ \mathrm{meV}, \tag{12.49}$$

and intraband transitions between the states (1, 4) and (1, 3) are observed with photon energies

$$351\ \text{meV} \leq \Delta E_3^4(a) \leq 801\ \text{meV}. \tag{12.50}$$

In the range a of QD

$$a_c^*(1,6) \leq a < \left(a_c^*(1,7) \cong 15.2\ \text{nm}\right) \tag{12.51}$$

there are three transitions: intraband transitions between the states of (1, 4) and (1, 3), and between (1, 5) and (1, 4) with photon energies which are in the following ranges respectively:

$$20\ \text{meV} \leq \Delta E_3^4(a) \leq 351\ \text{meV}, \tag{12.52}$$

$$326\ \text{meV} \leq \Delta E_4^5(a) \leq 876\ \text{meV}, \tag{12.53}$$

transitions between (1, 6) and (1, 5) in the range of QD radii

$$a_c^*(1,6) \leq a < (a_c(1,6) \cong 13.84\ \text{nm}) \tag{12.54}$$

will be intraband with the photon energy

$$\Delta E_5^6(a) \cong 1.302\ \text{eV}, \tag{12.55}$$

and in the range of QD radii

$$a_c(1,6) \leq a < a_c^*(1,7) \tag{12.56}$$

Such transition is intraband with photon energies

$$0.901\ \text{eV} < \Delta E_5^6(a) \leq 1.302\ \text{eV}. \tag{12.57}$$

In the range of QD a radii

$$a_c^*(1,7) \leq a < \left(a_c^*(1,8) \cong 16.8\ \text{nm}\right) \tag{12.58}$$

there are three transitions: two intraband between the states (1, 5) and (1, 4), and also between the states of (1, 6) and (1, 5) with photon energies that lie in the ranges, respectively:

$$0\ \text{meV} \leq \Delta E_4^5(a) \leq 326\ \text{meV}, \tag{12.59}$$

$$876\ \text{meV} \leq \Delta E_5^6(a) \leq 901\ \text{meV}, \tag{12.60}$$

Transition between the states (1, 7) and (1, 6) in the range of QD radii

$$a_{\mathrm{c}}^{*}(1,7) \leq a < (a_{\mathrm{c}}(1,7) \cong 15.5 \ \text{nm}) \tag{12.61}$$

in intraband with the photon energy

$$\Delta E_6^7(a) \cong 1.502 \ \text{eV}, \tag{12.62}$$

in the range of a

$$a_{\mathrm{c}}(1,7) \leq a < a_{\mathrm{c}}^{*}(1,8) \tag{12.63}$$

this transition will be intraband with photon energies with the range of

$$0,876 \ \text{eV} < \Delta E_6^7(a) \leq 1,502 \ \text{eV}. \tag{12.64}$$

In the range of a

$$a_{\mathrm{c}}^{*}(1,8) \leq a < (\tilde{a_{\mathrm{c}}} \cong 19.1 \ \text{nm}) \tag{12.65}$$

there are three transitions: two intraband between the states (1, 6) and (1, 5), and between the states (1,7) $\rightarrow$ (1,6) with photon energies lying in the ranges, respectively:

$$263 \ \text{meV} \leq \Delta E_5^6(a) \leq 876 \ \text{meV}, \tag{12.66}$$

$$776 \ \text{meV} \leq \Delta E_6^7(a) \leq 876 \ \text{meV}, \tag{12.67}$$

transition between the states (1, 8) and (1, 7) in the range of QD

$$a_{\mathrm{c}}^{*}(1,8) \leq a < (a_{\mathrm{c}}(1,8) \cong 17.16 \ \text{nm}) \tag{12.68}$$

will be intraband with photon energies

$$\Delta E_7^8(a) \cong 1.903 \ \text{eV} \tag{12.69}$$

In the range of a

$$a_{\mathrm{c}}(1,8) \leq a \leq \tilde{a_{\mathrm{c}}}, \tag{12.70}$$

there are three intraband transitions: the transition between the states (1, 6) and (1, 5) with photon energies in the interval

$$0 \leq \Delta E_5^6(a) \leq 263 \ \text{meV}, \tag{12.71}$$

transition between the states (1, 7) and (1, 6) with photon energies

$$0 \leq \Delta E_6^7(a) \leq 776 \text{ meV} \tag{12.72}$$

and transition between the states (1, 8) and (1, 7) with photon energies

$$0 \leq \Delta E_7^8(a) \leq 1.903 \text{ eV}. \tag{12.73}$$

Thus, in the nanosystem in which average values of aluminum oxide QD radii vary in the range of:

$$a_c^*(1,1) \leq a \leq \tilde{a}_c, \tag{12.74}$$

interband and intraband transitions create energy bands, lying in the QD bandgap. Energy of photons $\Delta E_l^{l+1}(a)$ (12.23) of such interband and intraband transitions reaches high values comparable to the binding energy $E_{ex}^{2D} \cong 2.504$ eV (12.14) of the ground state of two-dimensional exciton (Fig. 12.1 and Table 12.1). Energies of the interband transitions $\Delta E_l^{l+1}(a)$ (12.23) significantly exceed the energies corresponding to the intraband transitions for a given average radius of QD a (in the interval (12.74)) [12, 13]. Spectra of emission, absorption, and transmittance of light, which are located in the visible and infrared wavelengths, are formed from such energy bands. Such spectra were observed in experimental works [2–4].

It should be noted that in the nanosystems, in which average a radii of aluminum oxide QD vary in the interval (12.74) at T temperature satisfying

$$\Delta E_l^{l+1}(a) \gg k_B T \tag{12.75}$$

(where k_B – Boltzmann constant), the observation of nanosystems is possible in the processes of absorption and emission on the transitions with frequencies $\left(\Delta E_l^{l+1}(a)/\hbar\right)$, depending on the values of the average radius of the QD (in the interval (12.74)), lying in the range from the infrared to the visible spectrum. Such processes do not occur on QD with small radii $a < a_c^*(1,1) \cong 4.9$ nm. New transition states $(1, l)$, starting from $(1, 0)$ at $a \geq a_c^*(1,1)$ to (1,8) state at $a \geq a_c^*(1,8)$ (see Table 12.1), will contribute to the absorption (and also emission) at large values of QD radii $a \geq a_c^*(1, l \leq 8)$. Therefore, for instance, it is possible to spectroscopically control the nucleation of QD in the dielectric matrix, fixing the formation stage of the QD, starting from the radii $a \geq a_c^*(1,1)$, that is, the emergence of a new phase in the nanosystem. The dependence of the energy spectrum of $E_{1,l}(a)$ (12.19) of the exciton on the a radius of QD and its threshold feature provide an opportunity to select laser spectroscopy methods in nanosystems for determining the degree of dispersion of nanosystems (Fig. 12.1) [12, 13].

It should be noted that in the energy of the ground state of the exciton (12.19) (of spatially separated electrons and holes) in nanosystems containing aluminum oxide QD with a radii (12.22), the main contribution is the average value of the energy

of the Coulomb interaction $\overline{V}_{eh}(a) = \langle R_l(r_e, r_h, r, a) | V_{eh}(r) | R_l(r_e, r_h, r, a) \rangle$ between the electron and the hole. In this regard, the average value of the energy interaction between the electron and the hole with "foreign" images providea a much smaller contribution to the energy of the ground state of the exciton (12.19) (the ratio of which to the contribution of the average value of the Coulomb interaction energy does not exceed 8%). The latter circumstance is due to the fact that the values of the average energies of the interaction of holes and electrons with their images, as well as the values of average interaction energies of the hole and electron with "foreign" images, contributes to the exition (12.19) with different signs, which largely compensate each other [12, 13].

Thus, the energy of the ground state of the exciton (12.19) (of spatially separated electrons and holes) is due to the renormalization of the Coulomb interaction energy (12.8) between the electron with a hole, as well as the polarization interaction energy (12.5) of the electron and the hole with spherical surface of boundary QD/matrix associated with the spatial restriction of the area of the volume quantization volume of QD.

One can see from Fig. 12.1, which shows the dependence of the total energy $E_{1,l}(a)$ (12.19) of the ground state of exciton (of spatially separated electrons and holes) in a nanosystem containing aluminum oxide QD with the average radius a from the interval (12.22), it follows that with the increase of QD radius $E_{1,l}(a)$ (12.19) total energy of the ground state of the exciton increases. Herewith, the energy (12.19) of the ground state of the exciton significantly exceeds (3–49 times) the value of the binding energy of the exciton $\tilde{E}_{\mathrm{ex}}^{2D} \approx (-51.16$ meV) in an aluminum oxide single crystal. Starting from the radius $a \geq \tilde{a}_{\mathrm{c}}(1, l) = 19.1$ nm, the value of the total energy (12.19) of the ground state of the exciton asymptotically tends to the values of $E_{\mathrm{ex}}^{2D} = (-2.5038$ eV) (12.14) (characterizing the binding energy of the ground state of the two-dimensional exciton (from spatially separated electrons and holes)) (Fig. 12.1) [12, 13].

12.3 Comparison of the Theory with Experiment

In experimental works [2–4], nanostructures containing aluminum oxide QD with small concentrations ($x = 0.03\%$) are placed in the matrix (vacuum oil). At such low concentrations of QD, the interaction between the QDs can be neglected. Optical properties of such nanosystems are mainly determined by the energy spectrum of electrons and holes localized near the surface of the spherical single QDs, situated in the dielectric matrices. In [2–4], it was observed that the nonlinear optical properties and their dependences on the matrix material of heterogeneous liquid nanophase composites based on wideband aluminum oxide QD with average radii are not greater than $a = 25$ nm. In [2–4], it is shown that in the matrix (vacuum oil) aluminum oxide QD has a wide absorption band (from 1.4 to 3.7 eV) in the visible and near-infrared regions.

To interpret the results of the experiments [2–4], we may assume that QDs have a spherical form. In [2–4], the average a radii of QD vary from 1 to 25 nm. This follows from the results of the variational calculation of the ground state energy $E_{1,l}(a)$ (12.19) of the exciton in a nanosystem containing aluminum oxide QD. Varying radii a in the range of (12.22) (Figs. 12.1 and 12.2 and Table 12.1), the band of surface exciton states appears (consisting of the stationary states band with $E_{1,l} = E_{\text{ex}}^{2D} = 2.5038$ eV width, located in the band gap of QD, and from a band from quasistationary states $E^{\max} = 0.526$ eV, located in the conduction band of QD). In [2–4], the formation of donor-type additional band width with (0.3.0.4) eV inside the bandgap aluminum oxide QD at the depth (2.3 eV and 1.96 eV) from the bottom of the conduction band of the QD is revealed. Let us assume that such a band can be described by the band of surface exciton states. Then, in the nanosystem levels, $E_{\text{d}} = -2.3$ eV and $(-1.96$ eV) correspond to the QDs with average radii: (14.0 nm, 14.9 nm, 16.1 nm, 17.0 nm, 18.1 nm) and (5 nm, 5.2 nm, 12.5 nm, 13 nm, 15.2 nm, 16.3 nm, 17.4 nm), respectively (Fig. 12.1), and besides the values of the radii lie in the range of average radii of QD studied in experimental conditions [2–4].

In the frequency region corresponding to the quasistationary and stationary states $(1, l)$ from the band of surface exciton states, the light wavelength is much larger than the dimensions of these states (about a_{ex}^{2D} (12.13)) (see Table 12.1). Therefore, the behavior of such states $(1, l)$ in the electromagnetic field can be well described by the dipole approximation [16, 17]. In the case of the optical absorption of a nanosystem containing aluminum oxide QD with average radii but not exceeding 20 nm, an electron is transferred from the stationary levels $(1, l)$ to the higher levels of the excited stationary states $(1, (l + 1))$ (the condition (12.75) is satisfied). As a result, the electron transitions to such highly excited exciton levels (particularly, transitions from the levels ($E_d = -2.3$ eV and $(-1.96$ eV)) [2–4]) excite the dipole moments of the transitions, the values of which are proportional to the a radii of QD and exceed by an order than the typical values for aluminum oxide single crystal [25, 26]. Such a mechanism of the excitation of the dipole moments of transitions causes QD polarization in the field of the light wave, which creates an additional polarization of the nanosystem, and leads to the nonlinear increment to the refractive index of the nanosystem [2–4]. The increment in the range of frequencies below the resonance is positive. In the case of sufficient large length of interaction of light waves with the nanosystem, the increase in the refractive index due to self-focusing of the beam can cause a waveguide channel. As a result, with an increase of the radiation intensity [2–4], "enlightenment" of nanosystem occurs.

The optical absorption of the nanosystem causes interband transitions between the levels of the surface exciton states – between stationary states, lying in the bandgap of QD, and quasistationary states, located in the QD conduction band (Figs. 12.1 and 12.2 and Table 12.1). Such transitions lead to an increase in the concentration of nonequilibrium electrons in the QD conduction band. In the case of scattering of electrons in the QD with large radii $a > a_{\text{c}}^{*}(1, l = 8) = 16.8$ nm, the trapping of electrons on the quasistationary states can occur without change in their total energy. As a result, the concentration of nonequilibrium electrons in the conduction band of QD can also increase. In [2–4], electron transition from

quantum energy 4.1 eV with an additional band to the QD conduction band at the level of 0.4 eV was observed. This level is in the area of quasistationary states. As it is shown in [2–4], the increase of the electron concentration in the QD conduction band induces nonlinear increment to the refractive index of the nanosystems, which is negative. As a result, in [2–4], the saturation of radiation intensity was experimentally observed by increasing the intensity of the light wave due to the finite number of electronic levels in surface exciton states in the QD (Fig. 12.1).

12.4 Conclusion

The picture of the occurrence of the surface exciton states was described in the nanosystem. It was found that with the increase of a radius of QD, starting from the magnitude a greater than a certain critical radius of QD $a_{\mathrm{c}}^{*}(1,l)$, quasistationary states initially appear, which with the increase of QD radius $a \geq a_{\mathrm{c}}(1,l) > a_{\mathrm{c}}^{*}(1,l)$ relapses into the stationary state. Quasistationary and stationary states form a band of surface states of the exciton. In the nanosystem, the stationary states of the exciton are located in the bandgap of aluminum oxide QD (below the bottom of the conduction band of QD, see Fig. 12.2, area 1). They are bounded below by the level E_{ex}^{2D}, which is equal to the binding energy of the ground state of the two-dimensional exciton (from spatially separated electrons and holes). Quasistationary states of the exciton are in the conduction band of aluminum oxide QD (Fig. 12.2, area 2). They are bounded to the top by boundary of the $E_{1,l}^{\max}(a)$, wherein $E_{1,l}^{\max}(a)$ takes the significant value comparable to the $E_{\mathrm{ex}}^{2D} \cong 2.504$ eV. The mechanisms of the formation of intra- and interband absorption spectra (emission light) are presented in the nanosystem containing aluminum oxide QD, situated in the matrix (vacuum oil) [2–4]. It was found that in the nanosystem, the spectra of interband absorption (emission) of light composed of the energy bands, which were formed by the electron transitions between the quasistationary and stationary states, and intraband absorption spectra composed of the zones, which were caused by the electron transitions between stationary states.

It was shown that the electron transitions from fixed levels $(1, l)$ to the higher levels of the excited stationary $(1, (l+1))$ states, belonging to the surface exciton states, which lie near the bottom of the conduction band in the bandgap of the QD (Figs. 12.1 and 12.2 and Table 12.1), can excite the dipole moments of the transitions, the values of which are proportional to the a radii of QD and are higher by an order than the typical values for aluminum oxide single crystal [16, 17]. Such a mechanism of excitation of the dipole moments of transitions causes QD polarization in the field of the light wave and leads to the nonlinear increment to the refractive index of the nanosystem. Such increment in the range of frequencies below the resonance is positive. As a result, with increasing the radiation intensity, the “enlightenment” of the nanosystem was observed [2–4].

It was shown that the electron interband transitions between the levels of the surface exciton states of QD, between stationary states and quasistationary states (Figs. 12.1 and 12.2 and Table 12.1), lead to the increase of nonequilibrium concentration of the electrons in the conduction band of QD. The trapping of the electrons on the quasistationary states (without changing the total energy) of the QD with large radii $a > a_c^*(1, l = 8) = 16.8$ nm also increases the concentration of nonequilibrium electrons in the conduction band of QD. Such an increase in the concentration of the electrons in the conduction band of QD is the nonlinear increment to the refractive index nanosystems [2–4], which is negative. The finite number of electronic levels in surface exciton states of QD (Fig. 12.1) leads to the increase of the light wave intensity to the saturation of the intensity of radiation observed experimentally in [2–4]. It was found that the electron transitions in the surface exciton states caused significant absorption of the radiation in the visible and near-infrared wavelengths and produced blurring of the experimentally observed absorption edges [2–4].

References

1. Grabovskis V, Dzenis Y, Ekimov A (1989) Photoionization of semiconductor microcrystals in glass. Sov Phys Solid State 31(1):272–275
2. Kulchin YN, Shcherbakov AV, Dzyuba VP (2008) Nonlinear-optical properties of heterogeneous liquid nanophase composites based on high-energy-gap nanoparticles. Quantum Electronics 38(2):154–158
3. Dzyuba VP et al (2010) Nonlinear refractive index of dielectric nanocomposites in weak optical fields. Tech Phys Lett 36(11):973–977
4. Dzyuba VP, Kulchin YN, Milichko VA (2013) Quantum size states of a particle inside the nanopheres. Adv Mater Res A 677:42–48
5. Efros AL, Efros AL (1982) Interband absorption of light in a semiconductor sphere. Sov Phys Semicond 16(7):772–775
6. Pokutnyi SI (2007) Exciton states in semiconductor quantum dots in the framework of the modified effective mass method. Semiconductors 41(11):1323–1328
7. Pokutnyi SI (2013) On an exciton with a spatially separated electron and hole in quasi-zero-dimensional semiconductor nanosystems. Semiconductors 47(6):791–798
8. Pokutnyi SI (2013) Binding energy of the exciton with a spatially separated electron and hole in quasi-zero-dimensional semiconductor nanosystems. Tech Phys Lett 39(3):233–235
9. Pokutnyi SI, Kulchin YN, Dzyuba VP (2015) Binding energy of excitons formed from spatially separated electrons and holes in insulating quantum dots. Semiconductors 49(10):1311–1315
10. Pokutnyi SI (2015) Exciton states formed by spatially separated electron and hole in semiconductor quantum dots. Tech Phys 60:1615–1618
11. Pokutnyi SI (2016) Excitons based on spatially separated electrons and holes in Ge/Si heterostructures with germanium quantum dots. Low Temp Phys 42(12):1151–1154
12. Pokutnyi SI (2018) Optical spectroscopy of excitons with spatially separated electrons and holes in nanosystems containing dielectric quantum dots. J Nanophotonics 12(2):026013–1 - 026013-16
13. Pokutnyi SI (2018) Exciton spectroscopy with spatially separated electron and hole in Ge/Si heterostructure with germanium quantum dots. Low Temp Phys 44(8):819–823
14. Yakimov AI, Dvurechensky AV et al (2001) Effects of electron-electron interaction in the optical properties of dense arrays of quantum dots Ge/Si. JETP 119:574–589

15. Pokutnyi SI, Kulchin YN (2016) Special section guest editorial: optics, spectroscopy, and nanophotonics of quantum dots. J Nanophotonics 10(3):033501–1–033501-8
16. Pokutnyi SI (2013) Biexcitons formed from spatially separated electrons and holes in quasi-zero-dimensional semiconductor nanosystems. Semiconductors 47(12):1626–1635
17. Pokutnyi SI (2016) Biexciton in nanosystem of quantum dots of cadmium Sulfide in a dielectric matrix. Tech Phys 61(11):1737–1739
18. Pokutnyi SI, Kulchin YN, Dzyuba VP, Amosov AV (2016) Biexciton in nanoheterostructures of dielectric quantum dots. J Nanophotonics 10(3):036008-1–036008-8
19. Pokutnyi SI (2017) Excitonic quasimolecules in nanosystems of quantum dots. Opt Eng 56(9):091603-1–091603-7
20. Pokutnyi SI (2017) Biexciton in nanoheterostructures of germanium quantum dots. Opt Eng 56(6):067104-1–067104-5
21. Pokutnyi SI (2016) Quantum – chemical analysis of system consisting of two CdS quantum dots. Theor Exp Chem 52(1):27–32
22. Lozovik YE, Nishanov VN (1976) Exciton Wannier-Mott near the interface. Sov Phys Solid State 18(11):1905–1911
23. Efremov NA, Pokutnyi SI (1990) Spectrum of local states of charge carriers in the ultradisperse media. Sov Phys Solid State 32(10):1697–1706
24. Efremov NA, Pokutnyi SI (1991) The broadening of the quasi-stationary states of carriers in ultradisperse media. Sov Phys Solid State 33(10):1607–1612
25. Pokutnyi SI (1995) Size quantization of the exciton in quasi-zero-dimensional structures: theory. Phys Lett A 203:388–394
26. Pokutnyi SI (1997) Absorption and scattering of light in quasi-zero-dimensional structures: II. Absorption and scattering of light by single-particle local states of the charge carriers. Sov Phys Solid State 39(4):528–531

Sergey I. Pokutnyi is a professor of theoretical physics (doctor of sciences in physics and mathematics) at the Chuiko Institute of Surface Chemistry, National Academy of Sciences of Ukraine, Kyiv. His current research interests are theoretical optics and spectroscopy nanosystems (electron, exciton, and biexciton states in nanosystems and nanophotonics nanosystems), theory of condensed matter (theory of excitons and biexcitons in nanosystems, theory of local electron states in nanosystems, theory of transfer energy electron excitation states in nanosystems), and magneto-electro-optics nanosystems. He has published more than 254 papers in ISI journals and ten books. He is an associate editor of *Journal of Nanophotonics* and *Nanooptics and Nanophotonics* and an editorial board member of *Nanomaterials and Nanotechnology* (SAGE publishing).

Part II
Nanobiotechnology

Chapter 13
Magnetic Resonance Nanotherapy for Malignant Tumors

V. Orel, A. Shevchenko, T. Golovko, O. Ganich, O. Rihalsky, I. Orel, A. Burlaka, S. Lukin, V. Kotovsky, V. Dunaevsky, and S. Nazarchuk

13.1 Introduction

The advances in magnetic nanoparticle technology have brought new prospects for nanotherapy which is defined as a combination of therapeutic and diagnostic agents within a single platform. Most importantly, magnetic nanoparticles are capable of external control over electromagnetic field generation and the forces of attraction fields applied in delivering the nanoparticles to a tumor and its microenvironment [1].

Nanotherapy is best known from the thermal therapy approach, where a dispersion of iron oxide (magnetite) nanoparticles is injected into the tumor which is subsequently heated by an alternating magnetic field. Reported side effects were not severe, and signs of iron release from the intratumoral deposits were not observed

V. Orel (✉)
National Cancer Institute, Kyiv, Ukraine

National Technical University of Ukraine "Igor Sikorsky Kyiv Polytechnic Institute", Kyiv, Ukraine
e-mail: v-orel@voliacable.com

A. Shevchenko
G. V. Kurdyumov Institute for Metal Physics, National Academy of Science of Ukraine, Kyiv, Ukraine

T. Golovko · O. Ganich · O. Rihalsky · I. Orel
National Cancer Institute, Kyiv, Ukraine

A. Burlaka
R.E. Kavetsky Institute of Experimental Pathology, Oncology and Radiobiology, Academy of Science of Ukraine, Kyiv, Ukraine

© Springer Nature Switzerland AG 2019

O. Fesenko, L. Yatsenko (eds.), *Nanophotonics, Nanooptics, Nanobiotechnology, and Their Applications*, Springer Proceedings in Physics 222,
https://doi.org/10.1007/978-3-030-17755-3_13

[2]. Over recent years, the hybrid method has been proposed for a combined use of ultrahigh-field magnetic resonance imaging (MRI) together with controlled and localized radio-frequency heating in the tumor. However, this clinical success in nanotherapy requires a sufficient coverage of the tumor area by the nanoparticles which can be difficult in clinics. Hyperthermia can also be seen as a limiting factor for treatment efficiency since the induction of heat-shock proteins may lead to chemotherapy resistance [3].

Metallic nanoparticles are known to induce oxidative stress through reactive oxygen species (ROS) generation during redox reaction by interruption of the electronic flux, perturbation of the permeability transition, and diminution of protective cellular components such as glutathione [4]. The magnetic nanoparticles have demonstrated their use in molecular level cell signaling controlling the ultimate fates of the tumor cells [5].

MRI is based on the effects of magnetic field and radio waves upon hydrogen atoms in the host. The distribution of hydrogen varies between body tissues, and this dependence is applied for tumor diagnostics. Magnetic properties of a hydrogen atom depend on the spin of its nucleus; such properties are to be used when the body of a patient placed under conditions of a strong electromagnet. The patient's body can acquire a magnetization due to slightly predominant alignment of hydrogen nuclei along the external magnetic field rather than against it. Under the influence of radio waves, the hydrogen nuclei change their distribution and generate radio signal [6].

The magnetic spin effects can play an important role in chemical reactions producing or destroying radicals because redox reactions involve the production or destruction of magnetic moments of electrons in magnetic fields [7]. Magnetic resonance imaging can induce double-strand breaks in DNA through induction of reactive oxygen species by the electromagnetic field [8].

This paper aims to study the possible use of the magnetic resonance effect for magnetic nanotherapy of Lewis lung carcinoma.

S. Lukin
R.E. Kavetsky Institute of Experimental Pathology, Oncology and Radiobiology, National Academy of Science of Ukraine, Kyiv, Ukraine

V.Ye. Lashkaryov Institute of Semiconductor Physics, National Academy of Science of Ukraine, Kyiv, Ukraine

V. Kotovsky · S. Nazarchuk
National Technical University of Ukraine "Igor Sikorsky Kyiv Polytechnic Institute", Kyiv, Ukraine

V. Dunaevsky
V.Ye. Lashkaryov Institute of Semiconductor Physics, National Academy of Science of Ukraine, Kyiv, Ukraine

13.2 Materials and Methods

13.2.1 Magneto-Mechano-Chemical Synthesis

The magnetic nanocomplex (MNC) is comprised of iron oxide (II, III) nanoparticles Fe_3O_4 (Sigma-Aldrich) with diameters of 30–50 nm and antitumor drug DOXO (Pfizer, Italy). The synthesis of MNC was performed in a magneto-mechano-chemical reactor (NCI) based on the magnetic resonance phenomena. Magnetic properties of MNC are as follows: saturation magnetic moment 8.17 emu/g; area under hysteresis curve 610.12 erg/g; coercive field 19.14 Oe; and *g*-factor 2.50 [9].

13.2.2 Magnetic Resonance System

The Intera 1.5T (Philips Medical Systems, Netherlands) magnetic resonance system with a synergy body coil was used in this study. Magnetic field intensity was 1.5T, magnetic field gradients strength 33 mT/m, slew rate (Pulsar) 80 T/m/s, and slew rate (Nova) 160 T/m/s. The characteristics of radio-frequency system are nominal frequency 63.87 MHz, maximal frequency offset 270 kHz, and amplifier peak power 18/25 kW. The nuclear magnetic resonance properties that determine the image appearance are proton density, spin-lattice relaxation time (T1), spin-spin relaxation time (T2), and flow. The T1-weighted images were produced by using TE (echo time) 20 ms and TR (repetition time) 100 ms.

Treatment and visualization were carried out simultaneously while animals were in a prone position, anesthetized by the isoflurane inhalation (1–2%) and immobilized in horizontal volume coil for 15 min.

13.2.3 Fluorescence and Thermography

The Nikon ECLIPSE 80i microscope was utilized for fluorescence microscopy of MNC and its components after magnetization by MRI.

The fiber-optic thermometers TM-4 (Radmir) and thermal imager FLIR (Flir Systems Inc.) were used to control temperatures inside and on the surface of tumors.

13.2.4 Electron Spin Resonance Spectroscopy

Electron spin resonance (ESR) spectra, *g*-factors, and concentration of paramagnetic centers in the samples were studied with the spectrometer RE1307. Measurements were carried out at liquid nitrogen temperatures (77 K) in a cylinder resonator with the mode H_{011} and frequency 9.15 GHz, the power of microwave radiation 40 mW, and modulation frequency of magnetic field 100 kHz. The samples were placed in a

quartz Dewar with an inner diameter of 4.5 mm. *g*-Factor was calculated according to the formula of the resonance condition when 500 mg of tissue was placed in a special mold and frozen by liquid nitrogen. Qualitative and quantitative changes in the functioning of mitochondrial electron transport chain (ETC) were evaluated by the shape and location of ESR signal (Landé *g*-factor of spectroscopic splitting) and amplitude of ESR signal in the control and experimental samples of the tissue.

13.2.5 Laboratory Animals, Tumor Transplantation, and Treatment of Lewis Lung Carcinoma

Animal studies were approved by the Regional Committee for Animals and Medical Research Ethics of National Cancer Institute, Ukraine (Protocol N44 of 28 Nov 2012). All animal procedures were carried out with the humane care according to the Law of Ukraine N 3447–IV on the protection of animals from cruelty and European Directive 2010/63/EU on the animal protection for scientific purposes.

The study was carried out on male C57Bl/6 mice ($n = 40$, 18–20 g, vivarium of National Cancer Institute). Lewis lung carcinoma was transplanted to animals by injection of a 30% cell suspension (0.4 ml) in medium 199 into the hip as described in the paper [10]. The animals were divided into four groups, 10 per group: control (intact mice) (1), conventional DOXO (2), magnetic complex comprised of the ferromagnetic nanoparticles and paramagnetic DOXO without magnetic resonance tomography (MRT) treatment (3), magnetic complex comprised of the ferromagnetic nanoparticles and paramagnetic DOXO with MRT (4). DOXO (3 mg/kg) or MNC (3 mg/kg DOXO and 3 mg/kg Fe_3O_4, 0.2 ml in sodium chloride solution) was intraperitoneally injected on the 3rd day after tumor transplantation. Subsequent total ER (electromagnetic irradiation) of the animals was performed over 15 min on the Intera 1.5T. Tumor size was measured by the caliper.

13.2.6 Tumor Growth Rate and Statistics

The nonlinear kinetics of the tumor growth was evaluated by the growth factor φ according to the autocatalytic equation. The effect of anticancer magnetic nanotherapy was evaluated with the braking ratio κ [7]. The image heterogeneity was calculated according to [11]. Statistical comparisons of data were performed with Statistica 13.0 (© StatSoft, Inc., 2015) software by using the student's *t*-test when the data complied with the conditions of normality.

13.3 Results and Discussion

13.3.1 Magnetic Nanocomplex Imaging

Figure 13.1 shows the photographs, fluorescence microscopy images, and MRI of MNC and its components after magnetization by MRI. The volume and concentration of solution samples were equal to a single intraperitoneal injection. MRI of MNC had slightly greater heterogeneity due to the presence of iron oxide nanoparticles.

13.3.2 Nonlinear Kinetics of Tumor Volume

The growth kinetics of animal tumors and metastasis dissemination are shown in Fig. 13.2. The conventional DOXO treatment (group 2) resulted in minimal tumor

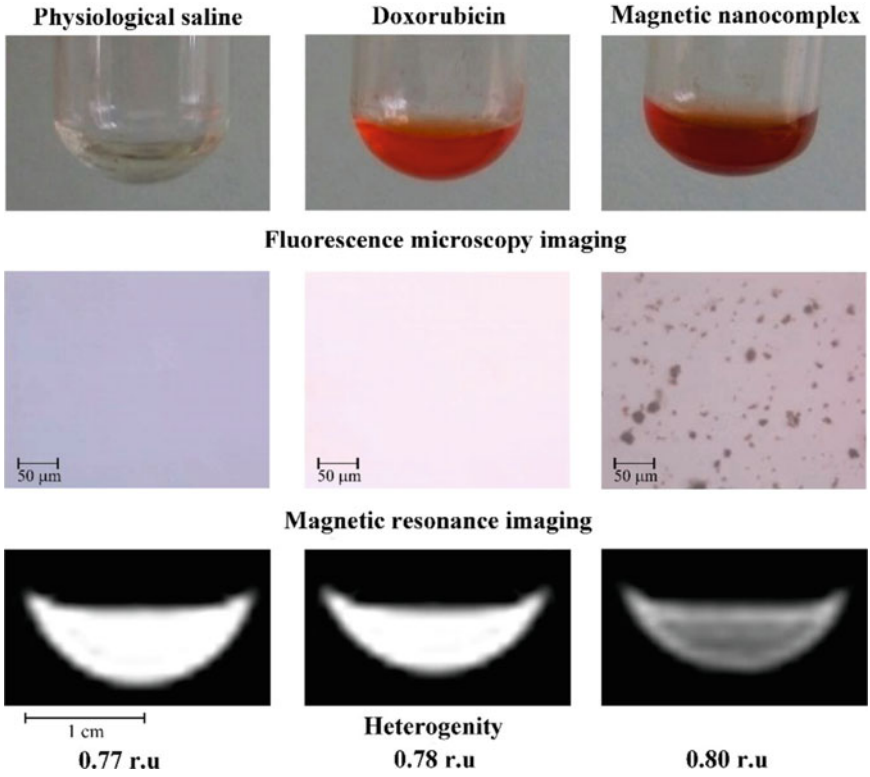

Fig. 13.1 Photograph, fluorescence microscopy (×400), and MRI of MNC and its components

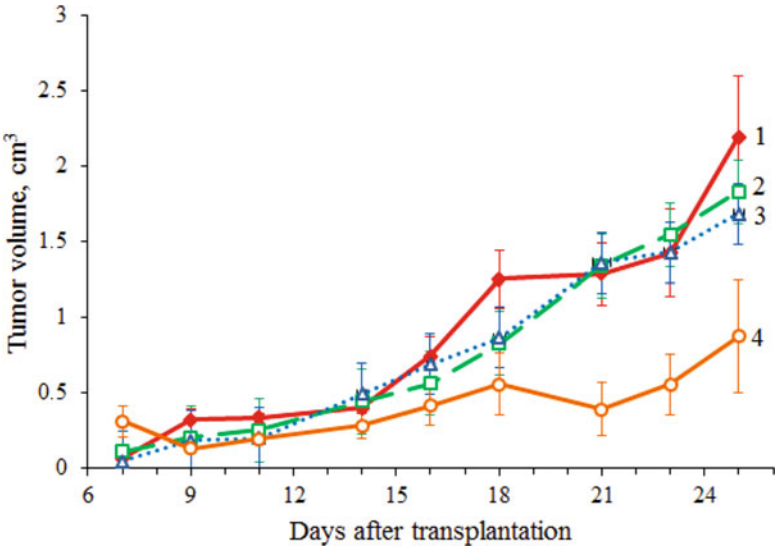

Fig. 13.2 Effect of MNC and ER by MRT on the growth kinetics of Lewis lung carcinoma. (1) Control (without treatment); (2) conventional DOXO; (3) MNC; (4) MNC + ER by MRT

response. The combination therapy of MNC and electromagnetic radiation (ER) by MRT (group 4) had maximal antitumor effect. The treatment by MNC alone (group 3) resulted in equal antitumor effect as compared with group 2. The average number of lung metastatic foci per mouse in groups 3 and 4 compared to group 1 (control) and group 2 (conventional DOXO) tended to decrease up to 25 days after tumor transplantation.

13.3.3 Tumor Imaging

A tomogram was made in three orthogonal projections. A whole-body photograph and MRI scan of a mouse from the control group with Lewis lung carcinoma 1 day after tumor transplantation is shown in Fig. 13.3. MNC was not administered, so Lewis lung carcinoma can be clearly found.

The change in surface temperature was measured to define the mechanism of antitumor effect (Fig. 13.4) before and after a 15 min session of ER by MRT. The temperature change did not exceed 1.6 °Celsius. The temperature inside the tumor reached 37 °C. These findings match earlier studies supporting that heating of metallic implants during 1.5T MRI session demonstrated changes in the body temperature of less than 1 °C [12]. Therefore, ER could have only generated moderate hyperthermia within the tumor and its microenvironment. Considerably, moderate hyperthermia is not associated with induction of heat-shock proteins and

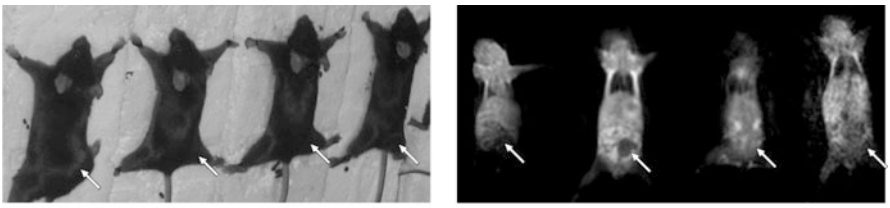

Fig. 13.3 Whole-body images of mice with Lewis lung carcinoma in near hind leg: (**a**) photograph; (**b**) magnetic resonance imaging. Mice belong to the control group. The image was taken 1 day after tumor transplantation and no antitumor treatment was given. Arrow indicates tumor

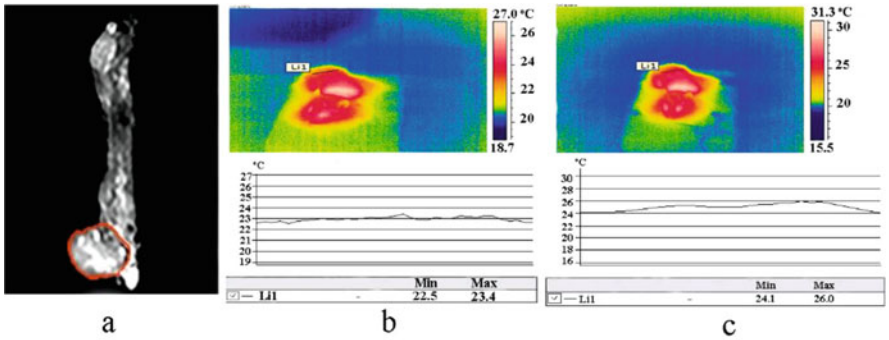

Fig. 13.4 Magnetic resonance (**a**) and surface thermal imaging of Lewis lung carcinoma ($V = 0.88$ cm^3) under MNC before (**b**) and after (**c**) ER by MRT on 25th day after tumor transplantation. The tumor is marked in red

following chemotherapy resistance. This was the reason to investigate changes in redox reactions within the tumor and its microenvironment by ESR.

13.3.4 Electron Spin Resonance Spectroscopy Tumor

ESR spectra of Lewis lung carcinoma are presented in Fig. 13.5. A triplet signal characterizing the ETC state was recorded near $g = 2.007$ in the ESR spectra in the control and investigated samples. It is well known that ETC is the cellular mechanism used for extracting energy from redox reactions, such as the oxidation of sugars (respiration) [13]. This is the evidence of the loss in functional activity of NADH-ubiquinone oxidoreductase in respiratory chain of mitochondria as a result of the formation of nitric oxide-iron(II) sulfur protein (NO-FeS-protein) N complex and indicates high level of glycolysis among animals in the first control group. *g*-Factor in a range of 2.2–2.4 has shown an accumulation of free iron complexes. Iron is a metal in proteins responsible for the storage and transport

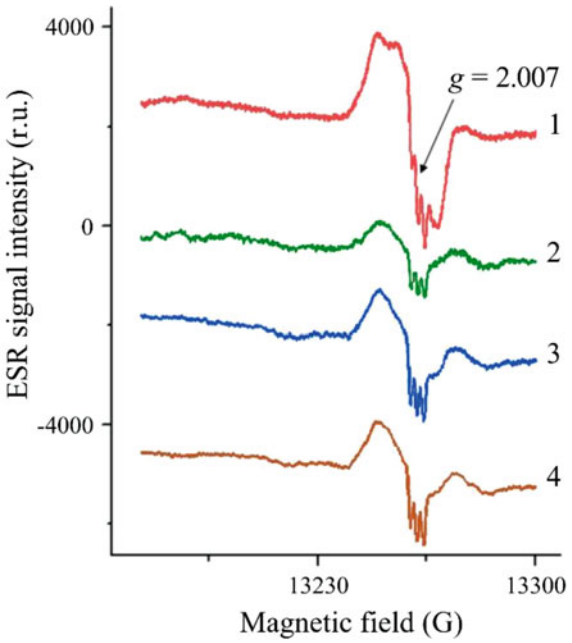

Fig. 13.5 Electron spin resonance spectrum of Lewis lung carcinoma on 25th day after tumor transplantation: (1) control (no treatment); (2) conventional DOXO; (3) MNC; (4) MNC + ER by MRT. $T = 77$ K

of molecules, ions, and electrons. Multicellular organisms exploit the properties of metals, most commonly iron, for oxygen transport [14]. The level of free iron in the tumor tissue obtained from control animals reached 0.5 ± 0.13 arb. units. Free iron was not detected in the tumors obtained from treated groups of animals. ESR-signal with *g*-factor of 2.25–2.42 indicating the presence of P-450 cytochrome was not detected among all investigated groups. This suggests the violation in electron transfer regulation of mitochondrial ETC of tumor cells during anticancer therapy.

The central question in the current paper asks: why did the ferromagnetic iron oxide nanoparticles with DOXO under ER of the MR system have greater antitumor effect than the MNC without ER and conventional DOXO? The answer to the above-raised question relies on the obtained experimental data and a hypothetical model of the MNC action based on our previous results during magnetic nanotherapy (Fig. 13.6).

The proposed hypothetical model is based on the well-known fact that organic radicals on the surface of iron oxide nanoparticles can persist for a long time. Changes in the pair recombination rates in the extent of singlet↔triplet interconversion can modulate radical concentrations under magnetic resonance effect [15] with an impact on tumor growth kinetics [16]. Free radicals are highly reactive and can destroy DNA as it is considered in the model. The organic and metal-organic magnetic nanoparticles with organic radicals are also used as active components for spintronic effects. Spintronics is a field focusing on the phenomena of spin-dependent electron transport and related magnetic moment, in addition to its electronic charge. The spins of free radicals, in our case paramagnetic doxorubicin,

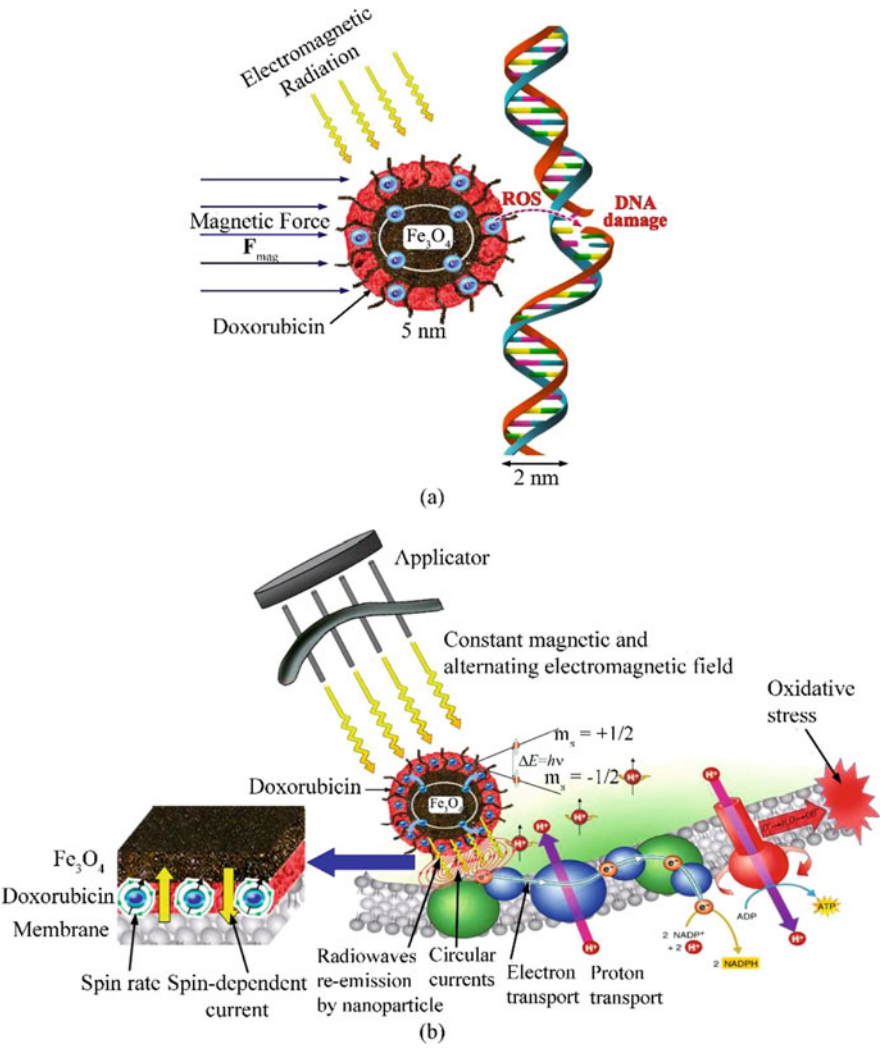

Fig. 13.6 The hypothetical model of MNC action for magnetic nanotherapy: DNA damage (**a**); the deregulation of electron and proton spin-dependent transport in mitochondrial membrane (**b**)

are operated by both magnetic and electric fields [17]. The redox character of organic radical-based biopolymers and ER is exploited to develop the models of spin-dependent transport in mitochondrial membrane of tumor cells. Multiple metabolic and redox sensitive pathways regulate the production of mitochondrial ROS. Cancer cells reprogram glycolytic fluxes and mitochondrial metabolism to uncouple electron transport chain (ETC) complexes from ATP synthesis, but couple the Krebs cycle with ETC complexes resulting in ROS formation necessary for cell survival and proliferation signaling to promote cancer progression. The spintronic

effects in applied heterostructures such as ferromagnetic nanoparticles and paramagnetic doxorubicin violate electron and proton transport in mitochondria leading to an increased oxidative stress and apoptotic signaling in tumor cells compared to conventional DOXO. This can allow to locally activate drugs without an increase in the concentration of the agent. Furthermore, setting various parameters of the external magnetic field can switch spin-controlled states of free radical pairs and reduce toxic side effects of ROS in normal tissue [18, 19].

13.4 Conclusions and Future Perspectives

The technology of magnetic resonance nanotherapy allows to improve antitumor effect of the chemotherapeutic drug and monitors the treatment effectiveness. This opens prospects for clinical use of nanotechnology in personalized cancer treatment and individually optimized treatment protocols for cancer patients with disseminated tumor cells.

References

1. Gobbo OL, Sjaastad K, Radomski MW et al (2015) Magnetic nanoparticles in cancer theranostics. Theranostics 5:1249–1263. https://doi.org/10.7150/thno.11544
2. Maier-Hauff K, Ulrich F, Nestler D et al (2011) Efficacy and safety of intratumoral thermotherapy using magnetic iron-oxide nanoparticles combined with external beam radiotherapy on patients with recurrent glioblastoma multiforme. J Neuro-Oncol 103:317–324. https://doi.org/10.1007/s11060-010-0389-0
3. Winter L, Oezerdem C, Hoffmann W et al (2015) Thermal magnetic resonance: physics considerations and electromagnetic field simulations up to 23.5 Tesla (1 GHz). Radiat Oncol 10:201. https://doi.org/10.1186/s13014-015-0510-9
4. Limbach LK, Wick P, Manser P et al (2007) Exposure of engineered nanoparticles to human lung epithelial cells: influence of chemical composition and catalytic activity on oxidative stress. Environ Sci Technol 41:4158–4163. https://doi.org/10.1021/es062629t
5. Thomas R, Park IK, Jeong YY (2013) Magnetic iron oxide nanoparticles for multimodal imaging and therapy of cancer. Int J Mol Sci 14:15910–15930. https://doi.org/10.3390/ijms140815910
6. Gworth WH, Todd CJ, Bell MI et al (2000) The diagnostic and therapeutic impact of MRI: an observational multicenter study. Clin Radiol 55:825–831
7. Emanuel N (1982) Kinetics of experimental tumor processes. Pergamon Press, Oxford
8. Jaffer H, Murphy KJ (2017) Magnetic resonance imaging-induced DNA damage. Can Assoc Radiol J 68:2–3. https://doi.org/10.1016/j.carj.2016.12.004
9. Orel VE, Shevchenko AD, Rykhalskiy AY et al (2015) Investigation of nonlinear magnetic properties magneto-mechano-chemical synthesized nanocomplex from magnetite and antitumor antibiotic doxorubicin. In: Fesenko O, Yatsenko L (eds) Springer proceedings in physics: nanocomposites, nanophotonics, nanobiotechnology and applications, vol 156. Springer Proceeding in Physics, Cham, pp 103–110. https://doi.org/10.13140/2.1.4251.2643
10. Matsuzaki T, Yokokura T (1987) Inhibition of tumor metastasis of Lewis lung carcinoma in C57BL/6 mice by intrapleural administration of Lactobacillus casei. Cancer Immunol Immunother 25:100–104. https://doi.org/10.1007/BF00199948

11. Li H, Calder CA, Cressie N (2007) Beyond Moran's I: testing for spatial dependence based on the spatial autoregressive model. Geogr Anal 39:357–375. https://doi.org/10.1111/j.1538-4632.2007.00708.x
12. Shellock FG (2000) Radiofrequency energy-induced heating during MR procedures: a review. J Magn Reson Imaging 12:30–36. https://doi.org/10.1002/1522-2586(200007)12:1<30::AID-JMRI4>3.0.CO;2-S
13. Nicholls DG, Ferguson SJ (2002) Bioenergetics 3. Academic Press, London
14. Nelson DL, Cox MM (2008) Lehninger principles of biochemistry, 5th edn. W.H. Freeman and Company, New York
15. Woodward JR, Jackson RJ, Timmel CR et al (1997) Resonant radiofrequency magnetic field effects on a chemical reaction. Chem Phys Lett 272:376–382. https://doi.org/10.1016/S0009-2614(97)00542-3
16. Orel V, Tselepi M, Mitrelias T et al (2018) Nanomagnetic modulation of tumor redox state. Nanomedicine 14:1249–1256. https://doi.org/10.1016/j.nano.2018.03.002
17. Barnes FS, Greenebaum B (2015) The effects of weak magnetic fields on radical pairs. Bioelectromagnetics 36:45–54. https://doi.org/10.1002/bem.21883
18. Chen Y, Zhang H, Zhou HJ et al (2016) Mitochondrial redox signaling and tumor progression. Cancers (Basel) 8:40. https://doi.org/10.3390/cancers8040040
19. Sensenig R, Sapir Y, MacDonald C et al (2012) Magnetic nanoparticle-based approaches to locally target therapy and enhance tissue regeneration in vivo. Nanomed (Lond) 7:1425–1442. https://doi.org/10.2217/nnm.12.109

Chapter 14
Nanoporous Biochar for Removal of Toxic Organic Compounds from Water

Yuliya S. Dzyazko, Olexii V. Palchik, Vladimir M. Ogenko, Leon Y. Shtemberg, Valerii I. Bogomaz, Sergii A. Protsenko, Vladimir G. Khomenko, Irina S. Makeeva, Oxana V. Chernysh, and Olexander G. Dzyazko

14.1 Methods for Biochar Production

Biochar means carbonized organic substances that are produced for addition to soil in order to enhance its beneficial features [1, 2], for instance, reducing mobility of toxic ions [1], improvement of microbiological composition, or decrease of nitrogen leaching [2]. As noted in [3], according to the International Biochar Initiative (IBI) "biochar is a solid material obtained from the carbonization of biomass." Besides additions to soil, biochar is used as fuel [4–6]. The widest application field of biochar is related to adsorption processes: this material is used as a sequestrant of carbon dioxide to reduce a greenhouse effect during biomass putrefaction [6]. Moreover, it is employed for adsorption removal of inorganic contaminants from water, such as oxygen-containing compounds of arsenic [7], phosphorus [7, 8], chromium [7], ions of ammonium [9], copper, zinc [10], and nitrate [11]. This material is also used for adsorption of both polar and nonpolar organic molecules, for instance, dyes [12–14], ethers, benzene [15], naphthalene,

Y. S. Dzyazko (✉) · O. V. Palchik · V. M. Ogenko
VI Vernadskii Institute of General and Inorganic Chemistry of the National Academy of Science of Ukraine, Kyiv, Ukraine

L. Y. Shtemberg · S. A. Protsenko
Crop Care Institute, Cherkasy, Ukraine

V. I. Bogomaz
"Ukravit" Agro LTD, Kyiv, Ukraine

V. G. Khomenko · I. S. Makeeva · O. V. Chernysh
Kyiv National University of Technologies and Design, Kyiv, Ukraine

O. G. Dzyazko
Taras Shevchenko Natiional University of Kyiv, Kyiv, Ukraine

© Springer Nature Switzerland AG 2019

O. Fesenko, L. Yatsenko (eds.), *Nanophotonics, Nanooptics, Nanobiotechnology, and Their Applications*, Springer Proceedings in Physics 222,
https://doi.org/10.1007/978-3-030-17755-3_14

nitrobenzene, dinitrobenzene [16], benzoquinone, tetracycline, and even polyvinyl alcohol [17].

Organic and inorganic substances that can be adsorbed by biochar are summarized in [3]. Biochar is also applied to preparation of composites, which are widely used as adsorbents [18]. This material is successfully combined, for instance, with metal oxides: [19–22], graphenes [23, 24], or phosphates [25]. The mentioned constituents are purposefully inserted to biochar [19–24] or remain in it during carbonization of wastes, such as bones [25]. In the last case, phosphate groups form complexes with ions being adsorbed, this is known phenomenon for phosphate materials [26].

The feedstock of biological origin (mainly wastes of agriculture and food industry) is applied to biochar manufacture: straw [7, 10, 15, 23], ground grains [8], hardwood [10], wood chips [11] or bark [19], municipal sludge [11–13], spent mushroom substrate [14], needles of coniferous trees [16], sugarcane bagasse [11, 17], and meat and bonemeal [25].

Biochar is often prepared from sugarcane bagasse [11, 17, 27–31]. Commercially available carbohydrates (saccharides) are also used [32–34]. As stressed [34], cyclic fragments of the precursors are attractive for carbonization, since polyaromatic compounds are formed. They give graphite clusters. It is also noted that carbonization of glucose in the presence of fumed silica gives carbon nanoparticles attached to the surface of the oxide support [35].

The methods of carbonization are considered in [3]: main of them are pyrolysis and gasification. Pyrolysis is the thermal decomposition of materials in the absence of oxygen or when significantly less oxygen is present than required for complete combustion. This process involves a number of thermal decomposition stages, which cannot be defined exactly. Conventional pyrolysis provides slow heating up to 500 °C in the absence of air. Vapor residence times vary from 5 to 30 min. Fast pyrolysis requires dry feedstock, fast temperature increase by heating small biomass particles (1–2 mm) to 400–500 °C and vapor residence times of 1 s (maximum 5 s). In the case of gasification, biomass is reacted with steam or air. Gasification converts biomass by careful control of the oxygen amount.

Other important method is hydrothermal carbonization [3, 31, 32, 36], which requires not only elevated temperature but also high pressure. Hydrochars are less stable (dominated by alkyl moieties) than biochars (dominated by aromatics) [3]. These materials are not included in the "European Biochar Certificate" (EBC) standardization due to their nonreproducible functional properties.

At last, torrefaction (heating at 200–300 °C in air-free medium) is applied to biomass carbonization. Chemical carbonization (charring in aggressive media) is also known [28]. Despite much lower specific surface area comparing with activated carbon, the material obtained from sugar bagasse shows sufficient adsorption capacity toward chromium-containing ions (up to 0.73 mmol g^{-1}) [28]. Similar approach can be applied to saccharides.

The aim of the investigation is synthesis of biochar with chemical method and testing of obtained materials for adsorption organic and inorganic species.

14.2 Synthesis and Characterization of Biochar

Such dry product of dairy industry as lactose (disaccharide, Fig. 14.1a), which was produced by the "Agrocapital of Ukraine" LTD Company (Ukraine), was applied to investigations. Dextrin (polysaccharide, Fig. 14.1b), that was manufactured from corn starch by the "Vimal" PPCE, was also used.

Sulfocarbonization method was applied to the saccharides, since it allows us to avoid their melting during heating under high temperatures in a liquid-free media and conglomerate formation. First of all the materials were milled. Then they were mixed with two volumes of concentrated sulfuric acid drop by drop under intensive stirring similarly to [28]. As opposed to [28], temperature was kept at an ambient level by cooling of the mixture-containing vessel with ice. This was necessary to slow down gas evolution, which results in a heave of the mixture. Its color gradually changed from white through yellow to dark brown. Then the mixture was activated with ultrasound at 25000 Hz using an UZG-2-4 m generator (Ultra Resonance LTD, Russia). After this, the vessel was heated in an oil bath at 120 °C during 12 h. The rate of heating was regulated (1 °C min^{-1}). Periodically the mixture was activated with ultrasound. Then the carbonaceous material was removed from the vessel and washed with deionized water up to neutral pH of the effluent. The samples were marked as 1 (produced from lactose) and 2 (from dextrin). Particularly for better identifying of the stripes of infrared (IR) spectra, the sample obtained from dextrin was pyrolized at 700 °C in the flow of argon (sample 3). No reagents were used for impregnation of carbon before this thermal treatment. Sorption properties of this material were also investigated.

The photos of particles of micron size were obtained by means of a Crystal-45 optical microscope (Konus, USA). The particles were additionally highlighted with a laser. Transmission electron microscopy (TEM) images were obtained with a JEOL JEM 1230 transmission electron microscope (Jeol, Japan). Preliminarily the samples were milled.

Porous structure was studied using a method of capillary condensation (nitrogen adsorption–desorption) by means of a Quantachrome gas analyzer (Quantachrome Instruments, USA). Before the measurements, the samples were dried at 150 °C to remove condensed water from pores. The Barrett-Joyner-Halenda (BJH) method was used for mathematical treatment of desorption isotherms. As found, this method gives the best agreement between calculated and experimental isotherms.

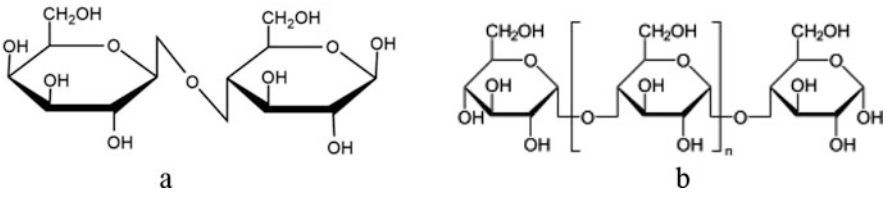

Fig. 14.1 Lactose (**a**) and dextrin (**b**)

Micropores, which give the largest contribution to specific surface area, were determined according to the Dubinin-Radushkevich method (DR).

IR spectra of the samples, which were preliminarily pressed with KBr, were recorded using a Spectrum BX Fourier-transform (FT)-IR spectrometer supplied with a Fourier converter (Perkin Elmer, USA).

14.3 Testing of Biochar for Practical Application

Adsorption of some pesticides was also studied. Such substances as tebuconazole (TBC), epoxiconazole (EPC), carboxin (CBX), acetamiprid (AMP), and thiamethoxam (TMT) were studied (Fig. 14.2).

Combining solution containing CBX, AMP, and TMT (100 mg dm^{-3} of each component) was used for testing of sample 1. Two-component solution containing TBC (70 mg dm^{-3}) and EPC (120 mg dm^{-3}) was used for testing of sample 1. These combinations of pesticides (produced by the "Ukravit" Agro LTD, Ukraine) are typical for commercial products. The solution (10 cm^{-3}) was added to different sample weights (0.2–1 g). In other words, the adsorbent dosage was 20–100 g dm^{-3}. The time of contact was 48 h. Then the solid and the liquid were separated, the equilibrium solution was analyzed using an Agilent 1290 liquid chromatograph supplied with an Agilent 6400 triple quadrupole detector (Agilent, USA). The value of adsorption degree (S) was calculated according to the formula:

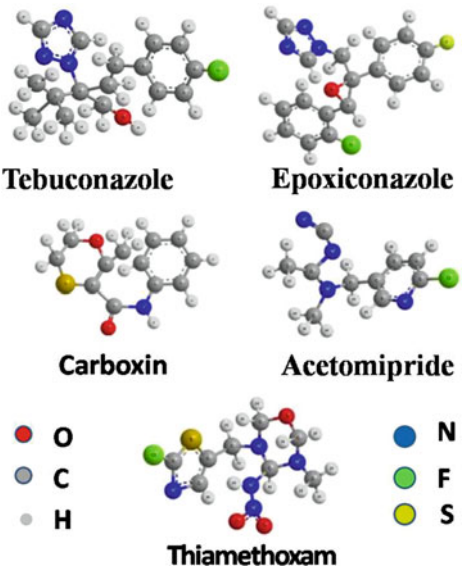

Fig. 14.2 Pesticides, which were used for biochar testing

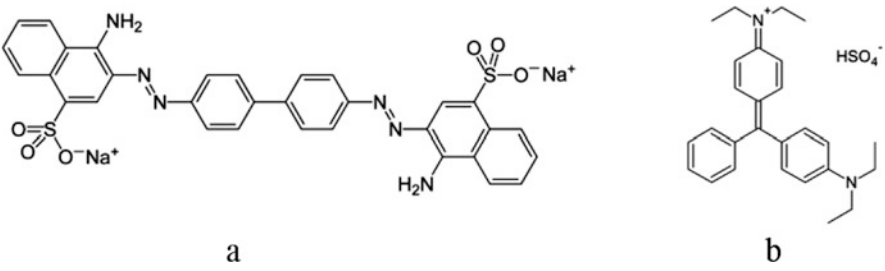

Fig. 14.3 Congo Red (**a**) and Brilliant Green (**b**)

$$S = \frac{C_0 - C}{C_0}, \tag{14.1}$$

where C_0 and C are the initial and residual concentration. Adsorption capacity (A) was estimated via:

$$A = \frac{(C_0 - C)\,V}{m}, \tag{14.2}$$

where V is the solution volume and m is the mass of a sample.

Similar experiments were performed using dyes such as anionic dye Congo Red (CR; Fig. 14.3). Cationic dye (Brilliant Green, BG) was also used. In this case, one-component solutions contained 5 mg dm^{-3} of a dye.

The sorbent mass was varied from 0.05 to 1 g. The solutions after adsorption of brilliant green were analyzed using a Shimadzu UV-mini1240 spectrophotometer (Shimadzu, Japan) at a wavelength of 625 nm. Congo Red was determined with the same method at 505 nm.

Electrochemical investigations were carried out as follows. The mixture containing a sample (90 mass %), an inert binder (polytetrafluoroethylene), and an electroconductive addition (C65 soot produced by Timcal) was pressed in a form of thin tablets (about 100 μm). The electrodes of equal mass and sizes were impregnated with a 30% H_2SO_4 solution similarly to [37, 38] and placed to a cell of "sandwich" type. The electrodes were divided with a Celgard porous separator (Celgard). The electrochemical studies were carried out using a computerized MST**AT** 32 potentiostat (Arbin Corporation, USA); Galvanostatic measurements were performed within the voltage interval of −0.6 to 0.6 V. Specific capacitance (C_{cp}) was calculated via:

$$C_{cp} = \frac{2 \cdot I \cdot \Delta t_d}{m \cdot \Delta U}, \tag{14.3}$$

where I is the current of charging and discharging, Δt_d is the discharging time, and ΔU is the voltage.

14.4 Visualization of Particles: Porous Structure at a Nanoscale

Chemical carbonization of dextrin results in formation of brilliant irregular particles, a size of which is from several tens of microns to 150 μm (Fig. 14.4a). The largest particles of 150 miscons dominate. Similar results were obtained for sample 1. Pyrolysis decreases the particle size: it reaches only ≈100 μm. Smaller particles prevail (Fig. 14.4b).

The type of initial saccharide as well as the thermal treatment of carbon material affects porous structure of an end product. Figure 14.5 illustrates typical isotherm of nitrogen adsorption–desorption. The isotherm is characterized by a slow growth followed by a rapid build-up. No plateau is observed. This isotherm is related to the

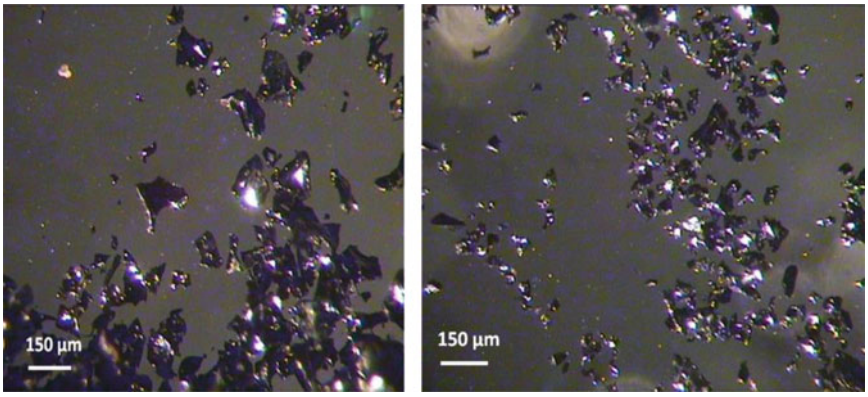

Fig. 14.4 Optical images of samples 2 and 3

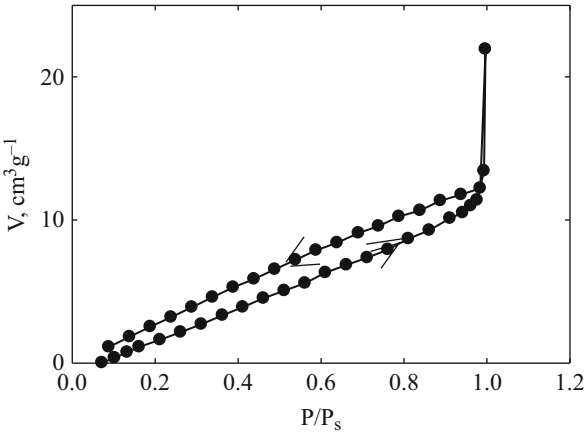

Fig. 14.5 Isotherm of nitrogen adsorption–desorption for sample 1

third type: they are characteristics for the pair of adsorbent–adsorbate, when the heat of adsorption is close to zero [39]. In general, the interaction between adsorbate and adsorbent is weaker than that between the adsorbate molecules. The hysteresis loop is related to B-type according to de Boer classification (the loop is along the whole adsorption isotherm). This type means slit pores.

Pore size distributions are plotted in Fig. 14.6. As seen, the sample obtained from dextrin is characterized by slightly more developed porous structure. Nanosized pores, a radius (r) of which is ≈2 nm, predominate. Larger pores ($r > 10$ nm) were recorded. Regarding the pyrolyzed material, larger volume of micropores, which is determined as an intersection of the integral curve with the ordinate axis, is observed. It is the same for mesopores. Here additional dominant pores appear ($r = 6$ nm). Nanosized pores in sample 3 are seen in TEM image (Fig. 14.7).

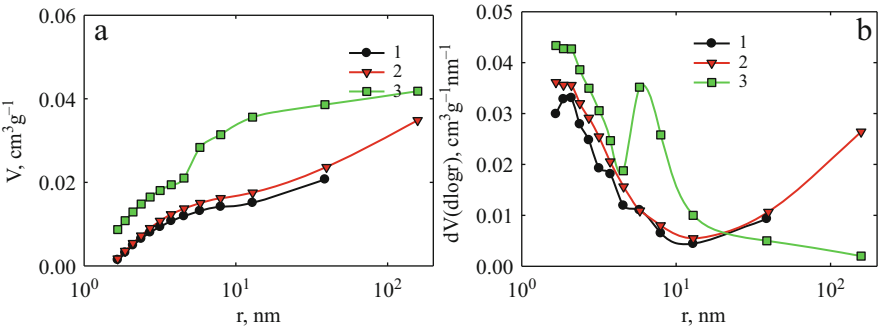

Fig. 14.6 Integral (**a**) and differential (**b**) pore size distributions. Numeration of the curves corresponds to sample numbers

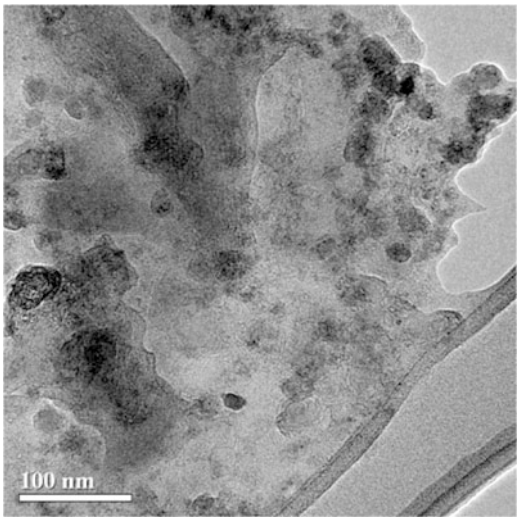

Fig. 14.7 TEM image of sample 3

The values of specific surface area are 50 (sample 1), 70 (sample 2), and 130 $m^2\ g^{-1}$. For known activated carbons, these values are about 1000 $m^2\ g^{-1}$ and even higher [39–42]. Thus, pyrolysis without any activator (water vapor, alkali, zinc salts, etc.) causes only insufficient opening of closed pores, which are formed during activation. Nevertheless, the surface area increases two times comparing with sample 2.

14.5 IR Spectroscopy

Figure 14.8 illustrates the IR spectra for the biochar samples. Regarding the samples obtained from lactose, a number of stripes that are attributed to characteristic vibrations are seen in the IR spectra. The intensive band at 3407 cm^{-1} is attributed to stretching vibrations of OH groups (both phenolic and carboxylic and adsorbed water) [43]. The stripes at 3028 and 2972, 2876 and 2815 cm^{-1} are due to stretching vibrations of aliphatic and aromatics CH groups. Some of these bands as well as the stripe at 2533 cm^{-1} can be the a result of stretching vibrations of COOH groups. They are evidently bonded with water, since the stripe at 2533 cm^{-1} is very wide.

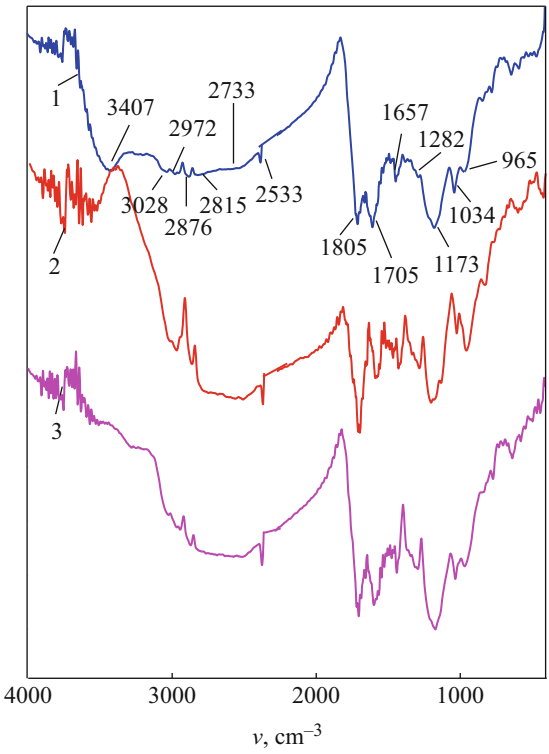

Fig. 14.8 IR spectra of carbon materials. Numeration of the curves corresponds to sample number

The presence of CH groups is confirmed by weak bands at 1440 and 839 cm^{-1} (deformation vibrations of these groups). The band of 2733 cm^{-1} shows stretching CH vibrations for aldehydes (Fermi stripe). The bands attributed to SO_2 are at 1346 and 1034 cm^{-1}. These stripes are independent on pressure in the case of SO_2 adsorption, which is realized even at 150 °C [44]. They can be also related to -SO_3H groups attached to the carbon matrix. At last, sulfuric acid can be encapsulated inside closed pores, which are formed during chemical carbonization. As noted above, this encapsulated amount is insufficient to provide high surface area that is typical for activated carbon.

Aldehyde and ketone groups as well as C=O of carboxyl group are shown as intensive stripes at 1805 and 1705 cm^{-1}. The bands at 1440–1657 cm^{-1} are related to C–C stretching vibrations of benzene rings. The appearance of vibrations of carbonyl groups within this interval is also possible. C–O–C stretching vibrations of epoxy groups give the stripe at 1282 cm^{-1}. The bands of 1173 and 1034 cm^{-1} are related to C–O–C stretching vibrations and to SO_3H groups. In general, C–O–C vibrations can be related not only to ethers, but also to epoxy groups. The vibrations of C–C skeleton can also appear within this interval. The stripe at 965 cm^{-1} is due to C–O–C stretching vibrations. The bands, which are placed at $\nu < 965$ cm^{-1}, are related to deformation vibrations.

Similar results were obtained for the samples obtained from dextrin. However, the bands that correspond due to stretching vibrations of aliphatic and aromatic CH groups and stretching C–C vibrations (particularly attributed to C–C vibrations in benzene rings) are more expressed indicating their higher content relatively to oxygen-containing groups than that for the sample obtained from lactose. Thus, the carbonization of polysaccharide gives the material with higher amount of C–C and CH groups. The intensity of the peak attributed to OH groups decreases, it is shifted to the region of higher frequencies. It means decrease of content of water and carboxyl groups. The band, which is typical for aldehydes (2733 cm^{-1}), is observed, but it is not very clear. The band at 1173 cm^{-1} shows a shoulder, which disappears after pyrolysis (transfer from sample 2 to sample 3). It means the shoulder is related, namely, to SO_2, which is removed under high temperatures. It is also similar for -SO_3H groups. Simultaneously the band for epoxy groups is clearer comparing with sample 1.

The peak at 965 cm^{-1} becomes invisible after pyrolysis indicating at least partial removal of carboxyl groups. This assumption is confirmed by the equality of the intensity of the bands for C=O groups and ambiguity of the stripe for OH groups in the region of high frequencies. After pyrolysis, the intensities of the stripes for C=O groups (1805 and 1705 cm^{-1}) become practically equal.

Thus, carbonization of disaccharide caused by sulfuric acid gives both aromatic and aliphatic fragments. The last ones are evidently attached to benzene or alkane rings. This is in agreement with data [45] that have been obtained for carbonization of sugar cane bagasse at 200–800 °C in inert atmosphere. The aliphatic fragments contain aldehyde groups. The C=O fragments are also attributed to carboxyl groups (they are confirmed by characteristic band or OH groups). The carbonyl fragments

can be also related to ketones. C–O–C stretching vibrations indicate epoxy groups, which are confirmed exactly by the IR spectrum. They can be also attributed to ether fragments.

In the case of polysaccharide, chemical carbonization provides formation of larger amount of aromatic and aliphatic fragments. At the same time, smaller amount of carboxylic, sulfuric, or phenolic groups was found comparing with sample 1. Moreover, they partially disappear during pyrolysis. Carbonyl groups are present both before and after the treatment under high temperature. These factors evidently determine adsorption properties of carbon materials.

14.6 Adsorption of Dyes and Pesticides

Figure 14.9a illustrates the effect of dosage on pesticide adsorption. Despite more developed surfaces, pyrolysis deteriorates sorption ability of biochar toward both TBC and EPC. The S value increases from 0.73 to 0.98 (EPC) or from 0.93 to 0.99 for sample 3 with increasing of its dosage. Regarding unpyrolyzed samples, the adsorption degree provides $S \approx 1$ indicating almost complete removal of toxic species. Taking the size of adsorbate molecule into consideration (it is about 1 nm), the nanopores, a radius of which is ≈2 nm (samples 1 and 2), plays a key role for the pesticide adsorption. Decline of adsorption after thermal treatment is probably caused by additional hydrophilization of the surface mainly due to C=O and C–O–C groups. This is possible due to thermally induced opening of closed pores, which are formed during chemical carbonization. As proved by means of IR spectroscopy, these pores can contain encapsulated H_2SO_4, which provides their partial opening.

It was found for sample 1 that the value of adsorption degree toward CBX, AMP, and TMT reaches 0.99 and higher. The residual concentration of pesticides and their maximal allowable concentration (MAC) are plotted in Fig. 14.9b for the maximal

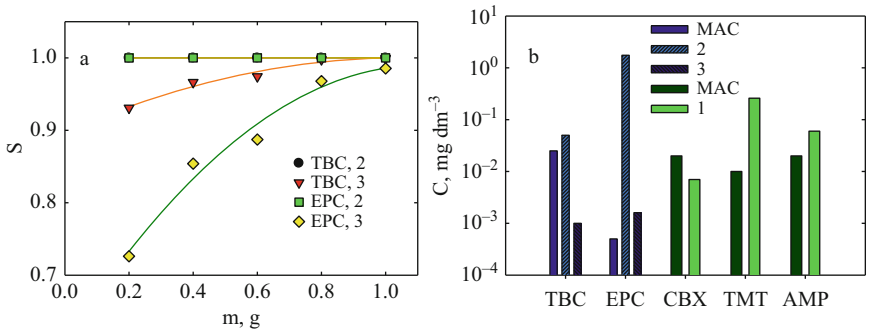

Fig. 14.9 Adsorption degree toward some pesticides (**a**), residual concentration of pesticides under maximal adsorbent dosage (100 g of an adsorbent per 1 dm^3 of a solution) and their maximal allowable concentration (**b**). Legends: the numbers of adsorbents are after comma

dosage of the adsorbents. In the case of sample 1, it is possible to decrease the content of EMK in two-component solution down to the MAC and even lower. The same result was obtained for CBX adsorption on sample 1.

Since the pesticides are removed practically completely, adsorption capacity predictably increases with dosage (Fig. 14.10). The curves of capacity vs. adsorbent mass are fitted with an inversed polynomial function:

$$A = a_1 + \frac{a_2}{m}, \tag{14.4}$$

where a_1 and a_2 are the empirical coefficient. Extrapolation of the curves, for instance, to $m = 0.01$ g (the dosage is 1 g dm^{-3}) gives the values that are given in Table 14.1. Further decreasing in dosage is unrealistic, since $A \to \infty$, when $m \to 0$. As follows from the table, the values of adsorption capacity are several tens mg per 1 g of biochar or even 120 mg g^{-1}. Note that the pyrolyzed sample is more efficient under low dosage comparing with unpyrolyzed biochar.

Regarding dye adsorption, the cationic dye (BG) is adsorbed preferably comparing with the anionic one (CR), since biochar contains mainly cation exchange groups (Table 14.2). Electrostatic attraction is an important reason of dye adsorption [45], this allows us to use cation exchange resins and their composite for BG removal [46]. Pyrolysis deteriorates dye adsorption evidently due to additional hydrophilization of the biochar surface. C–O–C and C=O groups make impossible hydrophobic

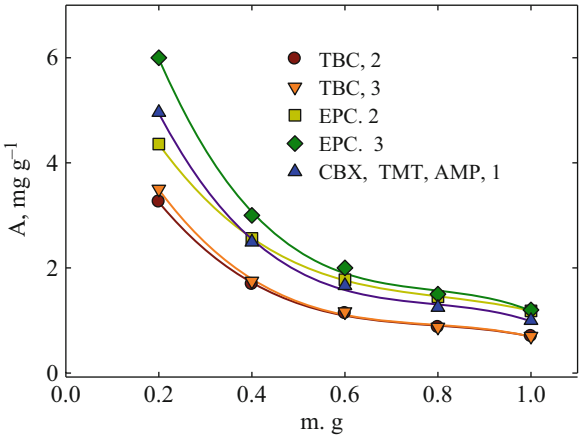

Fig. 14.10 Adsorption capacity of biochars as a function of the sample mass. Legends: the numbers of adsorbents are after comma

Table 14.1 Adsorption of pesticides effect of adsorbent dosage

Substance	Dosage, g dm^{-3}	A, mg g^{-1} for samples		
		1	2	3
TBC	1	–	63	70
EPC	1	–	79	100
CBX, AMP, and TMT	1	120		

Table 14.2 Adsorption of dyes: effect of adsorbent dosage

Substance	Dosage, g dm^{-3}	*S* for samples		
		1	2	3
CR	5	0.88	0.86	0,55
	10	0.96	0,97	0.75
	25	0.99	0,99	0,89
	100	0.99	0,99	0,99
BG	5	0.92	0.90	0.65
	10	0.99	0.99	0.78
	25	0.99	0.99	0.95
	100	0.99	0.99	0,99

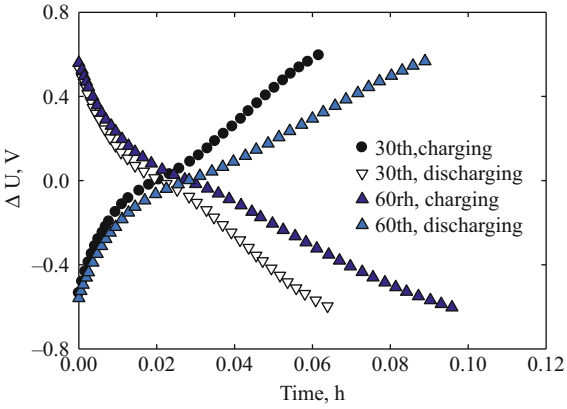

Fig. 14.11 Typical charging–discharging curves of electrochemical condenser at the constant discharging current of 200 μA. The cycle number is pointed in the legend. Sample 2 was used for the electrode preparation

interaction on the one hand. On the other hand, they cannot provide electrostatic attraction. Nevertheless, sample 3 removes the dyes practically completely under high adsorbent dosage.

14.7 Capacitance of Condensers Prepared From Nanoporous Biochars

Typical charging–discharging curves for the electrochemical condenser based on nanoporous biochar are plotted in Fig. 14.11. They are linear, each line is characterized by a slope to the abscissa axis. The slope reflects the capacitance of a condenser. However, the galvanostatic curves show different slopes. It means the sufficient contribution of redox reactions to the capacitance (this contribution is called "pseudocapacitance"). Comparing the discharging curves under conditions of constant discharging current, it is possible to suggest that the specific capacitance is different within the whole diapason of cycling (Table 14.3). The highest capacitance value has been found for sample 2. This indicates sufficient concentration of hydrophilic groups located at its surface. This is in agreement with the data of IR

Table 14.3 Specific capacitance of carbon materials in different cycling diapasons

	C_{cp}, F g^{-1}					
	30th cycle			60th cycle		
Sample	0–0.2 V	0.2–0.6 V	0.0–0.6 V	0–0.2 V	0.2–0.6 V	0.0–0.6 V
1	2.28	1.06	1.42	2.19	0.80	1.31
2	1.27	7.07	5.07	1.27	7.07	5.07
3	2.76	2.18	2.53	3.89	3.56	3.68

spectroscopy. Sample 3 shows lower capacitance despite more developed surface, since its dominant oxygen-containing groups cannot be a source of charge. At last, sample 1 demonstrates the lowest capacitance due to the lowest surface area and probably lower content of functional groups, which can be dissociated.

Normally the capacitance of activated carbon is an order of magnitude higher [38]. However, in our case a part of pores are closed, they are excluded from charge accumulation. It is possible to estimate the specific capacitance per unit of surface area (C_s, $C_s = C_{cp}/S$, where S is the specific surface area) similarly to [40]. From the data obtained for 60th cycle at 0–0.6 V, it is possible to estimate the C_s value as 0.026 (sample 1), 0.072 (sample 2), and 0.028 (sample 3). These values have practically the same order of magnitude as the data obtained in [40]. However, hydrophobic surface and pseudocapacitance were excluded in [40]. Thus, the comparison of our literature data can be made only as a first approximation.

14.8 Conclusions

Biochars obtained from both disaccharide and polysaccharide are characterized by nanoporous structure. Nanopores, a radius of which is 2 nm, determine functional properties of the materials: they make sufficient contribution to specific surface area and provide adsorption of rather large organic molecules, such as pesticides. Another important factor is functional oxygen-containing groups: they are responsible for hydrophilization of surface and support dye adsorption. As confirmed by IR spectroscopy and electrochemical measurements, the adsorbent produced from polysaccharide is characterized by higher content of these groups comparing with that obtained from disaccharide. Despite lower surface area comparing with commercial activated carbon, the adsorbents, which were synthesized by chemical method without pyrolysis, are characterized by significant capacity toward dyes and pesticides. The synthesis method requires no expensive special devises for thermal treatment. Moreover, it excludes the energy consumptions that are caused by furnaces. The technique can be used in any laboratory, which is supplied by elementary equipment. In a future, the nanoporous samples could be used for modification of some materials. Earlier inorganic ion exchangers have been proposed for modification of ion exchange resins [46, 47], polymer ion exchange membranes

[48], or microfiltration membranes [49–51] as well as ceramic separators [52]. It is expected that the additions of nanoporous biochar to inorganic modifiers will change porous structure of sorbents and membranes at the nanoscale and improve their functional properties.

Acknowledgments The work was performed within the framework of the project entitled "Developments of materials and processes for removal of valuable and toxic components from the solutions of biogenic and technogenic origin" supported by the NAS of Ukraine.

References

1. Carami N, Clemente R, Moreno-Jimenez E et al (2011) Efficiency of green waste compost and biochar soil amendments for reducing lead and copper mobility and uptake to ryegrass. J Hazard Mater 191(1–3):41–48
2. Xu N, Tan G, Wang H et al (2016) Effect of biochar additions to soil on nitrogen leaching, microbial biomass and bacterial community structure. Eur J Soil Biol 74:1–8
3. Mohan D, Sarswat A, Ok YS et al (2014) Organic and inorganic contaminants removal from water with biochar, a renewable, low cost and sustainable adsorbent – a critical review. Bioresour Technol 160:191–202
4. Liu Z, Quek A, Hoekman SK et al (2013) Production of solid biochar fuel from waste biomass by hydrothermal carbonization. Fuel 103:943–949
5. Qian K, Kumar A, Zhang H (2015) Recent advances in utilization of biochar. Renew Sust Energ Rev 42:1055–1064
6. Nunes LJR, Oliveira Matias JC, Silva Catalao JP (2017) Torrefaction of biomass for energy applications. Academic Press, London/San-Diego/Cambridge/Oxford
7. Zhu N, Yan T, Qiao J et al (2016) Adsorption of arsenic, phosphorus and chromium by bismuth impregnated biochar: adsorption mechanism and depleted adsorbent utilization. Chemosphere 164:32–40
8. Fang C, Zhang T, Li P (2014) Application of magnesium modified corn biochar for phosphorus removal and recovery from swine wastewater. Int J Environ Res Public Health 11(9):9217–9237
9. Taghizadeh-Toosi A, Clough TJ, Sherlock RR et al (2012) Biochar adsorbed ammonia is bioavailable. Plant Soil 350(1–2):57–69
10. Chen X, Chen G, Chen L (2011) Adsorption of copper and zinc by biochars produced from pyrolysis of hardwood and corn straw in aqueous solution. Bioresour Technol 102(19):8877–8884
11. Kameyama K, Miyamoto T, Iwata Y et al (2016) Influences of feedstock and pyrolysis temperature on the nitrate adsorption of biochar. Soil Sci Plant Nutr 62(2):180–184
12. Fan S, Wang Y, Wang Z et al (2017) Removal of methylene blue from aqueous solution by sewage sludge-derived biochar: adsorption kinetics, equilibrium, thermodynamics and mechanism. J Environ Chem Eng 5(1):601–611
13. Leng L, Yuan X, Huang H et al (2015) Bio-char derived from sewage sludge by liquefaction: characterization and application for dye adsorption. Appl Surf Sci 346:223–231
14. Sewu D, Boakye P, Jung H et al (2017) Synergistic dye adsorption by biochar from co-pyrolysis of spent mushroom substrate and Saccharina japonica. Bioresour Technol 244(1):1142–1149
15. Xiao L, Bi E, Du B et al (2014) Surface characterization of maize-straw-derived biochars and their sorption performance for MTBE and benzen. Environ Earth Sci 71(12):5195–5205
16. Chen B, Zhou D, Zhu L et al (2008) Transitional adsorption and partition of nonpolar and polar aromatic contaminants by biochars of pine needles with different pyrolytic temperatures. Environ Sci Technol 42(14):5137–5143

17. Li G, Zhu W, Zhu L et al (2016) Effect of pyrolytic temperature on the adsorptive removal of p-benzoquinone, tetracycline, and polyvinyl alcohol by the biochars from sugarcane bagasse. Korean J Chem Eng 33(7):2215–2221
18. XF T, YG L, YL G et al (2016) Biochar-based nano-composites for the decontamination of wastewater: a review. Bioresour Technol 212:318–333
19. Reddy DHK, Lee S-M (2014) Magnetic biochar composite: facile synthesis, characterization, and application for heavy metal removal. Colloids Surf A: Physicochem Eng Asp 454:96–103
20. Zhang M, Gao B, Varnoosfaderani S et al (2013) Preparation and characterization of a novel magnetic biochar for arsenic removal. Bioresour Technol 130:457–462
21. Yu Z, Zhou L, Huang Y et al (2015) Effects of a manganese oxide-modified biochar composite on adsorption of arsenic in red soil. J Environ Manag 163:155–162
22. Li R, Wang JJ, Zhou B et al (2016) Enhancing phosphate adsorption by Mg/Al layered double hydroxide functionalized biochar with different Mg/Al ratios. Sci Total Environ 559:121–129
23. Tang J, Lv H, Gong Y (2015) Preparation and characterization of a novel graphene/biochar composite for aqueous phenanthrene and mercury removal. Bioresour Technol 196:355–363
24. Zhang M, Gao B, Yao Y (2012) Synthesis, characterization, and environmental implications of graphene-coated biochar. Sci Total Environ 435–436:567–572
25. Betts AR, Chen N, Hamilton JG et al (2013) Rates and mechanisms of Zn^{2+} adsorption on a meat and bonemeal biochar. Environ Sci Technol 47(24):14350–14357
26. Dzyazko YS, Trachevskii VV, Rozhdestvenskaya LM et al (2013) Interaction of sorbed Ni(II) ions with amorphous zirconium hydrogen phosphate. Russ J Phys Chem A 87(5):840–845
27. Ueno M, Kawamiysu Y, Komita Y et al (2007) Carbonization and classification of bagasse for effective utilization of sugarcane biomass. Proc Int Soc Sugar Cane Technol 26:1194–1201
28. Altundogan NS, Bahar N, Mujde B (2007) The use of sulfuric acid-carbonization products of sugar beet pulp in Cr(VI) removal. J Hazard Mater 144:255–264
29. Ozer A, Tanyildizi MS, Tumen F (1998) Study of cadmium adsorption form aqueous solution in activated carbon from sugar beet pulp. Environ Technol 19:1119–1125
30. Ozer A, Tumen F (2005) Cu(II) adsorption from aqueous solutions on sugar beet pulp. Eur J Miner Process Environ Prot 5(1):26–34
31. Cao X, Ro KS, Libra JA et al (2013) Effects of biomass types and carbonization conditions on the chemical characteristics of hydrochars. J Agric Food Chem 61:9401–9411
32. Hu B, Wang K, Wu L et al (2010) Engineering carbon materials from the hydrothermal carbonization process of biomass. Adv Mater 22:1–16
33. Buasri A, Pholprasert C, Suwunnakee N et al (2013) Effects of carbonization temperature and nanoporous silica templating on the synthesis of porous carbon from commercial sugar. Adv Mater Res 650:113–118
34. Myronyuk IF, Mandzyuk VI, Sachko VM et al (2016) Structural features of carbons produced using glucose, lactose, and saccharose. Nanoscale Res Lett 11:508. https://doi.org/10.1186/s11671-016-1723-z
35. Nosach LV, Voronin EF, Pakhlov EM et al (2016) Nano-particulate structures with glucose-derived char and compacted fumed silica in gaseous and aqueous media. Springer Proc Phys 195:729–742
36. Fiori L, Basso D, Castello D et al (2014) Hydrothermal carbonization of biomass: design of a batch reactor and preliminary experimental results. Chem Eng Trans 37:55–60
37. Kotz R, Carlen M (2000) Principles and applications of electrochemical capacitors. Electrochim Acta 45(15–16):2483–2498
38. Vol'fkovich YM, Serdyuk TM (2002) Electrochemical capacitors. Electrokhimiya 38(9):1043–1068
39. Gregg SJ, Sing KSW (1991) Adsorption, surface area and porosity. Academic Press, London
40. Volfkovich YM, Bograchev DA, Mikhalin AA et al (2018) Electrodes based on carbon nanomaterials: structure, properties, and application to capacitive deionization in static cells. Springer Proc Phys 210:127–146
41. Volfkovich YM, Mazin VM, Urisson NA (1998) Operation of double-layer capacitors based on carbon materials. Russ J Electrochem 34(8):740–746

42. Volfkovich YM, Bograchev DA, Mikhalin AA et al (2017) Capacitive deionization of aqueous solutions: modeling and experiments. Desalin Water Treat 69:130–141
43. Nakanishi K (1960) Infrared absorption spectroscopy. Nankodo, Tokyo
44. Sracy WO, Vastola FJ, Walker PL (1968) Interaction of sulfur dioxide with active carbon. Carbon 6:917–923
45. Namasivayam C, Kavitha D (2002) Removal of Congo red from water by adsorption onto activated carbon prepared from coir pith, an agricultural solid waste. Dyes Pigments 54:47–58
46. Ponomarova L, Dzyazko Y, Volfkovich Y, Sosenkin V, Scherbakov S (2018) Effect of incorporated inorganic nanoparticles on porous structure and functional properties of strongly and weakly acidic ion exchangers. Springer Proc Phys 214:63–77
47. Dzyazko YS, Ponomareva LN, Volfkovich YM et al (2012) Effect of the porous structure of polymer on the kinetics of Ni^{2+} exchange on hybrid inorganic-organic ionites. Russ J Phys Chem A 86(6):913–919
48. Dzyazko YS, Rozhdestvenska LM, Vasilyuk SL et al (2017) Composite membranes containing nanoparticles of inorganic ion exchangers for electrodialytic desalination of glycerol. Nanoscale Res Lett 12:438. https://doi.org/10.1186/s11671-017-2208-4
49. Myronchuk VG, Dzyazko YS, Zmievskii YG et al (2016) Organic-inorganic membranes for filtration of corn distillery. Acta Periodica Technologica 47:153–165
50. Dzyazko YS, Rozhdestvenskaya LM, Zmievskii YG et al (2015) Organic-inorganic materials containing nanoparticles of zirconium hydrophosphate for baromembrane separation. Nanoscale Res Lett 10:64. https://doi.org/10.1186/s11671-015-0758-x
51. Zmievskii Y, Rozhdestvenska L, Dzyazko Y et al (2017) Organic-inorganic materials for baromembrane separation. Springer Proc Phys 195:675–686
52. Dzyazko YS, Volfkovich YM, Sosenkin VE et al (2014) Composite inorganic membranes containing nanoparticles of hydrated zirconium dioxide for electrodialytic separation. Nanoscale Res Lett 9(1):271. https://doi.org/10.1186/1556-276X-9-271

Chapter 15
The Regularities of Sorption of Substances of Different Nature by pH-Sensitive Acrylic Hydrogels for Plant Nanofertilizer Formation

K. V. Kalinichenko, G. N. Nikovskaya, V. O. Oliinyk, Yu. M. Samchenko, and Z. R. Ulberg

15.1 Introduction

For the nanocomposites preparation, individual polymers have been used most often as the polymer matrix [1–6]. Meanwhile, an essential interest for this purpose could represent multicomponent polymer matrices [7, 8]. At present, the most interesting example of multicomponent polymer matrices, especially for environmental biotechnologies, are hydrogels — insoluble three-dimensional hydrophilic polymers, swollen in agues medium [7, 9]. Conventional hydrogels absorb water from aqueous medium without any change in the equilibrium swelling with the change in pH, temperature, electric fields, or other external stimuli of the environment, while the stimulus responsive "smart or intelligent" hydrogels sharply change their equilibrium swelling in response to the environment changes [7, 9–13]. As applied to soil ecosystems, the most valid hydrogels are the pH-sensitive ones [14–17].

The pH-sensitive acrylic hydrogels in swollen state offer physical, chemical, and mechanical stability [9, 17]. Besides, they are biocompatible and biosafe [9]. Depending on their design and construction, acrylic hydrogels are able to absorb, retain, and gradually excrete water solutions with ions, molecules, nanoparticles,

K. V. Kalinichenko (✉) · G. N. Nikovskaya · Z. R. Ulberg
Colloidal Technologies of the Natural Systems Department, F.D. Ovcharenko Institute of Biocolloidal Chemistry, National Academy of Sciences of Ukraine, Kiev, Ukraine

V. O. Oliinyk
Department of Physical and Chemical Geomechanics, F. D. Ovcharenko Institute of Biocolloidal Chemistry, National Academy of Sciences of Ukraine, Kiev, Ukraine

Y. M. Samchenko
Department of Functional Hydrogel, F.D. Ovcharenko Institute of Biocolloidal Chemistry, National Academy of Sciences of Ukraine, Kiev, Ukraine

© Springer Nature Switzerland AG 2019

O. Fesenko, L. Yatsenko (eds.), *Nanophotonics, Nanooptics, Nanobiotechnology, and Their Applications*, Springer Proceedings in Physics 222,
https://doi.org/10.1007/978-3-030-17755-3_15

and other active substances in living systems [9]. Therefore, they have found an application in decisions of the following tasks: enzymes immobilization in biotechnology, address drugs delivery to sick organs and their prolonged release in medicine, aerial desiccation in closed volumes in environment protection technologies, for water reservation, fertilizers and artificial soil formation in agriculture [4, 6, 7, 9, 10, 14, 16, 18]. One of the main criterions of soil fertility is the presence of water stable aggregates, including heavy metal compounds (micro- and macroelements — essential plant nutrients). Using the pH-sensitive acrylic hydrogels as matrices in nanofertilizer synthesis, we, in essence, follow nature, developing a biomimetic approach in nanofertilizers formation.

The aim of our work was the investigation for valid nanofertilizers preparation features of pH sensitive acrylic hydrogels in water solutions with substances of different nature at pH-value alterations, conditions for processes of hydrogels "swelling–collapse", and "matter sorption–desorption".

15.2 Experimental

In our study, hydrogels of acrylic row, prepared at concentration of swelling agent N,N'-methylene-acrylamide 0.654%, were used as polymeric matrices for nanocomposites formation. These are: homopolyacrylamide gel (PAAG), copolymers of acrylamide and acrylic acid (AA-AA), and acrylamide and acrylonitrile (AA-AN), as discrete particles of 1–2 mm size. They have negative and positive active groups, which are able to interact with the substances from external solution. For example, the quantity of negatively charged COOH-groups in the hydrogels AA-AA, AA-AN, PAAG, responsible for binding positively charged substances, corresponds to the proportion: 20: 3: 2, respectively.

As model heavy metal compounds, essential for plant growth, we used nanosized negatively charged humic complexes of ferrous and copper (Fe-humate, Cu-humate) and Fe (III), Cu (II), and Mn (II) cations as simple salts ($CuSO_4 \cdot 5H_2O$, $Fe_2(SO_4)_3 \cdot 9H_2O$, $MnCl_2 \cdot 4H_2O$). All of them are able to form polynuclear nanosized hydroxy complexes as a consequence of hydrolysis; besides, manganese as a negatively charged anion of $KMnO_4$ salt, phosphorus as K_2HPO_4 and dyes as molecules with positively and negatively charged chromophore macroions — anionic (azorubine, brilliant blue, acid fuchsin) and cationic (methyl violet, methylene blue, basic fuchsin). The dyes molecules have size ~3 nm. Adsorption of the substances was studied at stirring and dynamics of desorption at passive contact conditions — without stirring. The efficiency of these processes was estimated by changing the compound concentrations in the outer solution.

The concentration of heavy metals was determined by the method of atomic-absorption spectrophotometry and phosphorus and organic dyes by calorimetrically. The swelling of the synthetic hydrogels was studied by the volumetric method.

15.3 Results and Discussion

The swelling dynamic of the dry acrylic hydrogels, which was in sync with heavy metal (copper) sorption, is represented in Fig. 15.1. The data demonstrated that maximal value of swelling (Fig. 15.1a) can be achieved within the first hour of the contact, as well as the metal sorption (Fig. 15.1b). Thus, in the sorption experiment the time of swelling was limited to 1 hour.

The efficiency of sorption and desorption of metal compounds in the form of cations, anions, humic complexes, and phosphate ions by acrylic hydrogels was studied (Fig. 15.2). It was established that among acrylic gels, the highest degree of the sorption was observed for the copolymer of acrylamide-acrylic acid (AA-AA), which also had the highest swelling ability (Fig. 15.1a). It should be noted that in all cases, the rate of Fe (III) sorption was higher in comparison with copper (II). At the same time, the humic complexes of the studied metals were sorbed much less and more easily desorbed by distilled water; manganese in the form of cation was sorbed much better than its permanganate anion.

The hydrogel interactions with organic molecules were estimated (Fig. 15.3). In this experiment, different organic dyes with acidic and basic nature were chosen for better visualization. It was established that cationic organic compounds were better sorbed by the studied hydrogels, whereas the highest sorption activity was detected in the case of the AA-AA hydrogel, which was characterized with the maximum number of active carboxylic groups. The desorption in distilled water of the studied sorbates was rather small. These results indicated the essential role of the binding chemical mechanism of organic substrates of various natures by polymeric gels of acrylic series.

These results (Figs. 15.2 and 15.3) point out that compounds with different nature can be effectively sorbed by acrylic hydrogels, quite firmly held in the hydrogel matrix, and only partially desorbed into the environment.

The sorption efficacy and the holding strength of the metal and organic compounds in cationic form were higher in comparison with anionic ones. According to

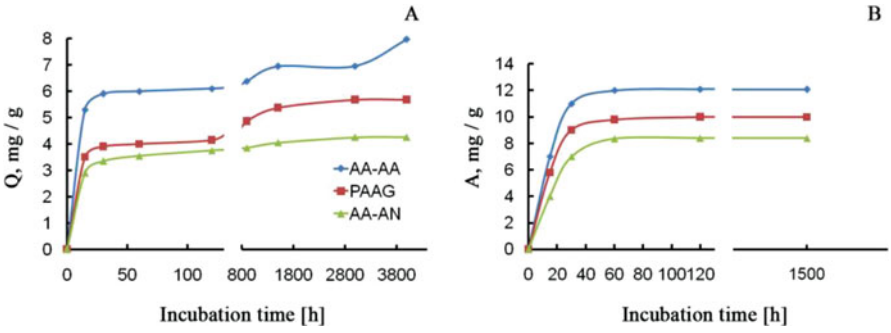

Fig. 15.1 The dynamic of swelling (**a**) and sorption of copper (**b**) by polymeric gels

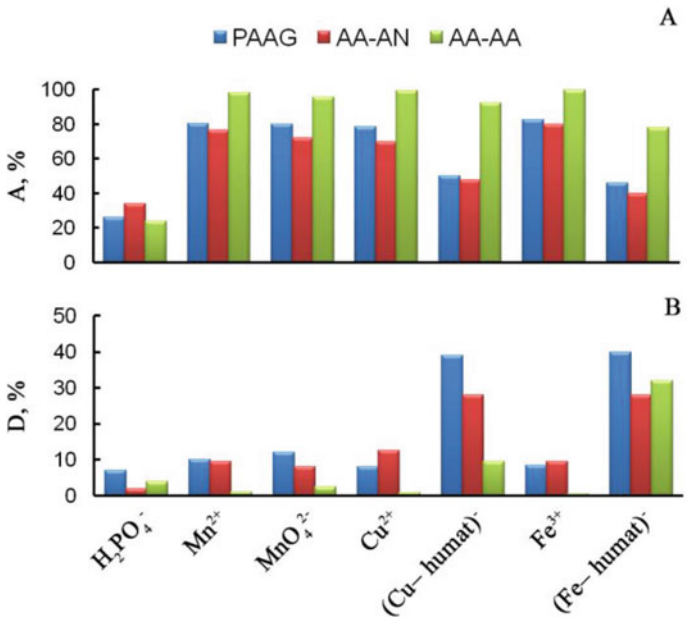

Fig. 15.2 The efficiency of sorption (**a**) compounds of different nature by acrylic hydrogels and their desorption (**b**) by distilled water

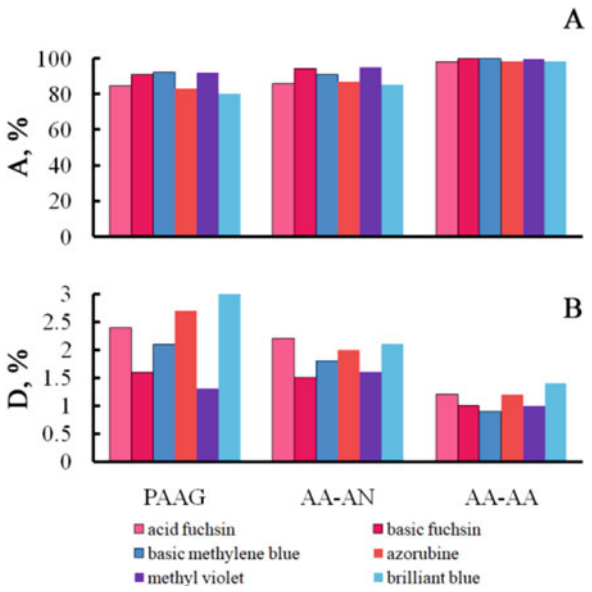

Fig. 15.3 The efficiency of dyes sorption (**a**) and their desorption (**b**) by distilled water. Initial dyes concentration – 100 mg/L

the affinity to the substrates with various natures, the hydrogels could be placed in the following sequence:

$$\text{AA-AA} > \text{PAAG} > \text{AA-AN}.$$

The affinity of substances to the polymeric gels was:

$$\text{Organic dyes} > Fe^{3+} > Cu^{2+} > Mn^{2+} > MnO_4^- > (\text{Cu-Humate})^- > (\text{Fe-Humate})^- > H_2PO_4^-.$$

Dyes molecules, when concentrated inside the gel matrix, interact with each other and form nanoparticles with the size ~ 10 nm. Similarly, at joint presence of metal salts and complexes in gel matrix they associate with nanoparticles, which are able to gradually desorb into surrounding medium. In general, the degree of the substances' desorption had the opposite order:

$$(\text{Fe-Humate})^- > (\text{Cu-Humate})^- > H_2PO_4^- > MnO_4^- > Mn^{2+} > Cu^{2+} > Fe^{3+} > \text{organic dyes}.$$

The efficacy of heavy metals sorption and desorption depending on the procedure of substrate introduction into gel matrix was studied with copper ($CuCl_2$) as an example (Table 15.1). The procedure included incorporation of the metal into a swollen hydrogel; otherwise, the hydrogel swelling occurred in copper chloride solution with a concentration two times smaller than in the first case (in order to level the initial concentrations of metal ion). There were not distinct differences of copper sorption efficiency under the variants with dry and swollen hydrogels. However, the desorption data showed that holding strength of metal ion in the variant with simultaneous sorption and swelling processes was much higher than in the case of the already swollen hydrogel.

This means that the gel swollen in distilled water holds water very strongly, and at the used concentration the electrolyte of $CuCl_2$ is not able to squeeze it out but is capable of being evenly spaced in the hydrated sphere of the swollen hydrogel. The swelling of the cumulated polymers is a process of three-dimensional grid hydration:

$$\text{AA-AA} + H_2O \leftrightarrow (\text{AA-AA})_{sw}.$$

Table 15.1 The influence of sequence of adding electrolyte ($CuCl_2$) into a system of copolymers hydrogels of acrylamide-acrylic acid (AA-AA) and polyacrylamide (PAAG). Initial concentration Cu (II) – 120 mg/L

	Parameters of copper (II) interaction with hydrogel	
Hydrogel	A, %	B, %
AA-AA swollen	97.00	40.00
AA-AA dry	98.00	1.50
PAAG swollen	80.00	65.00
PAAG dry	86.00	32.00

Hydrogel syneresis — the inverse to the swelling process of displacement of water-bound polymer — can be caused by various factors, for example, the action of electrolytes in the external environment:

$$(\text{AA-AA})_{sw} + CuCl_2 \leftrightarrow (CuCl_2)\,(\text{AA-AA})_{sw}. + H_2O.$$

The sorption of metals by hydrogel from mixed solutions was studied (Fig. 15.4). It was established that the efficacy of the heavy metals sorption from the mixed solution (Fig. 15.4, 2 variant) was slightly lower than from the individual ones (Fig. 15.4, 1 variant). In the case with natural water (Fig. 15.4, 3 variant), which can be considered as a natural solution of metals, the sorption efficiency of the studied metals was similar to those from the individual solutions.

Since the state of the acrylic polymers strongly depends on the pH value of the internal solution, the pH dependence of the swelling and sorption degree was evaluated (Fig. 15.5). For all gels, the swelling rate was in strong correlation with the change of solution acidity, increasing along with increasing pH value and vice versa (Fig. 15.5a). The most pH-sensitive was hydrogel AA-AA, which characterized with the maximum amount of free carboxyl groups. In the pH range of 5.0–6.0, these hydrogels undergo a phase transition between swollen and collapsed states. In acidic

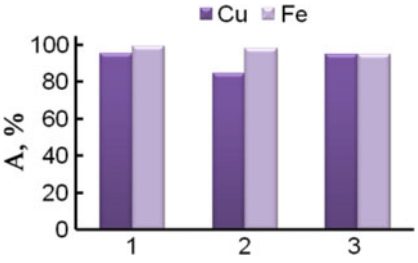

Fig. 15.4 Sorption efficiency of copper and ferric (A, %) by copolymer gel AA-AA from the following solutions: (1) Individual; (2) Mixed pH = 6.0; (3) Natural water pH = 6.6. Initial concentration (mg/mL): in solutions Cu-630, Fe-58.0; in natural water Cu - 2.0, Fe - 1.0

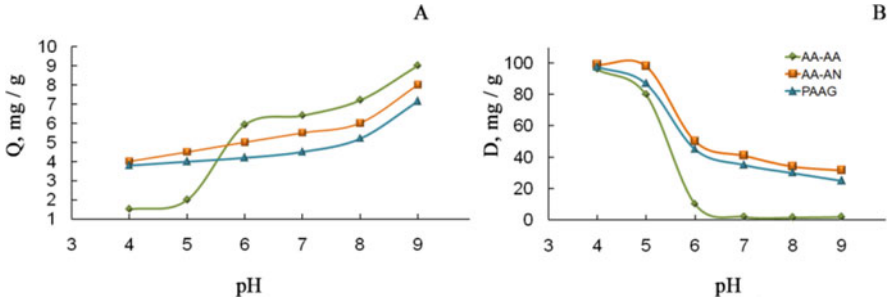

Fig. 15.5 Dependence of the coefficient of hydrogel swelling (**a**) and the desorption degree of copper (**b**) at changing pH of the external solution. The initial concentration of copper was 2 mmol

medium, the suppression of acidic groups' ionization of the hydrogels surface took place. The contraction (collapse) of the hydrogels occurred owing to the formation of a hydrogen bonds system and, consequently, there was the release of the sorbed substances to the external solution. The swelling of hydrogels PAAG and AA-AN was much less dependent on the pH; however, it also decreased when the solution acidity increased.

The desorption of copper cation from PAAG and AA-AN hydrogels occurred even in distilled water, whereas the AA-AA gel quite firmly held the metal ion at these conditions (Fig. 15.5b). Decreasing the pH from 5.0 to 4.0 provided almost complete desorption of copper ions from all hydrogels.

Comparison of the swelling–compression curves of the hydrogels and their sorption–desorption of cationic substances under the changes of external solution pH value indicated the synchronicity of these processes. The swelling of acrylamide hydrogels and sorption of sorbates took place at neutral and weakly alkaline pH zones and compression of the hydrogel matrix with desorption (release) of sorbed substances under decreasing of external solution pH. The tested hydrogels had similar desorption degree of the bioelements in acidic media.

The AA-AA gel had the maximal efficiency of bioelements sorption and the firmest hold on them. Therefore, one may expect that this gel with sorbed bioelements will be the most suitable to use for nanofertilizer preparation.

For understanding the possibility of hydrogels regeneration and their reuse for re-sorption of nutrients for plant development, their swelling and sorbing abilities were studied in the following cycles: (1) dry gel swelling in the solution of copper sulfate; (2) separation from the liquid phase; (3) metal ion desorption in a similar initial volume of water with pH 4.0–4.2; (4) drying in the air. The preservation of ability for swelling and sorption metals for all tested hydrogel matrices was established (Table 15.2). The data pointed to the possibility of hydrogel sorbents for complete regeneration and, if necessary, their reuse.

Thus, the acrylic hydrogels are able to sorb substances of different nature from the external solution at neutral and weakly alkaline environments and partially desorb them under decreasing pH. The most effective hydrogel is the copolymer of acrylamide and acrylic acid (AA-AA). The ability to sorb water and sorbate from the external solution is maintained after several "swelling–collapse" cycles.

Table 15.2 Swelling of hydrogels (Q, g/g) and copper sorption (A, g/g) in cycles swelling–sorption–drying–desorption

	I cycle		II cycle		III cycle	
Hydrogels	Q, g/g	A, g/g	Q, g/g	A, g/g	Q, g/g	A, g/g
PAAG	5.00	9.80	5.20	10.00	4.80	9.50
AA-AA	6.20	12.00	6.00	13.50	6.60	11.80
AA-AN	4.00	8.40	4.20	8.90	3.80	9.00

15.4 Conclusions

Biocompatible and environmentally safe acrylic hydrogels can effectively sorb at swelling substances of different nature — heavy metal compounds in the form of cations, anions, and organocomplexes, as well as organic molecules. By sorption efficiency and holding strength of sorbed substances, the hydrogels of acrylic series correspond to the following sequences: AA-AA > PAAG > AA-AN.

Hydrogels' swelling occurs synchronously with sorption of sorbate under alkalizing external solution; collapse and sorbate desorption — under acidification. The alternation of "swelling–collapse" cycles was not reflected on the efficiency of water and metal sorption by the hydrogels.

References

1. Kokabia M, Sirousazarb M, Hassan ZM (2007) PVA–clay nanocomposite hydrogels for wound dressing. Eur Polym J 43(3):773–781
2. Haraguchi K, Takehisa K (2002) Nanocomposite hydrogels: a unique organic–inorganic network structure with extraordinary mechanical, optical, and swelling/de-swelling properties. Adv Mater 14(16):1120–1124
3. Schexnailder P, Schmidt G (2009) Nanocomposite polymer hydrogels. Colloid Polym Sci 287(1):1–11
4. Gaharwar AK, Peppas NA, Khademhosseini A (2013) Nanocomposite hydrogels for biomedical applications. Biotechnol Bioeng 111(3):441–453
5. Haraguchi K (2007) Nanocomposite hydrogels. Curr Opinion Solid State Mater Sci 11(3–4):47–54
6. Satarkar NS, Hilt JZ (2008) Hydrogel nanocomposites as remote-controlled biomaterials. Acta Biomater 4(1):11–16
7. Jilie K, Li M (2007) Smart hydrogels. In: Galaev I, Mattiasson B (eds) Smart polymers: applications in biotechnology and biomedicine. CRC Press, Boca Raton, pp 247–268
8. Winey KI, Vaia RA (2007) Polymer nanocomposites. MRS Bull 32(04):314–322
9. Samchenko Y, Ulberg Z, Korotych O (2011) Multipurpose smart hydrogel systems. Adv Colloid Interf Sci 168(1–2):247–262
10. Luchini A, Geho DH, Bishop B, Tran D, Xia C, Dufour RL, Liotta LA (2008) Smart hydrogel particles: biomarker harvesting: one-step affinity purification, size exclusion, and protection against degradation. Nano Lett 8(1):350–361
11. Roy S, Banerjee A (2011) Amino acid based smart hydrogel: formation, characterization and fluorescence properties of silver nanoclusters within the hydrogel matrix. Soft Matter 7(11):5300–5308
12. Zhou X, Hon YC, Sun S, Mak AFT (2002) Numerical simulation of the steady-state deformation of a smart hydrogel under an external electric field. Smart Mater Struct 11(3):459–467
13. Li H (2009) Smart hydrogel modeling. Springer Verlag, Heidelberg
14. Rudzinski WE, Chipuk T, Dave AM, Kumbar SG, Aminabhavi TM (2002) pH-sensitive acrylic-based copolymeric hydrogels for the controlled release of a pesticide and a micronutrient. J Appl Polym Sci 87(3):394–403
15. Gemeinhart RA, Chen J, Park H, Park K (2000) pH-sensitivity of fast responsive superporous hydrogels. J Biomater Sci Polym Ed 11(12):1371–1380

16. Demitri C, Scalera F, Madaghiele M, Sannino A, Maffezzoli A (2013) Potential of cellulose-based superabsorbent hydrogels as water reservoir in agriculture. Int J Polym Sci 3:1–6
17. Wang W, Wang A (2010) Nanocomposite of carboxymethyl cellulose and attapulgite as a novel pH-sensitive superabsorbent: synthesis, characterization and properties. Carbohydr Polym 82(1):83–91
18. Zwieniecki MA (2001) Hydrogel control of xylem hydraulic resistance in plants. Science 291(5506):1059–1062

Chapter 16
Effect of Porosity on Ion Transport Through Polymers and Polymer-Based Composites Containing Inorganic Nanoparticles (Review)

Yuliya Dzyazko, Yurii Volfkovich, Olga Perlova, Ludmila Ponomaryova, Nataliia Perlova, and Evgen Kolomiets

16.1 Introduction

The development of nanotechnologies gives a new impulse to chemistry of polymer ion exchange resins and membranes, which are related to nanomaterials. When they are in contact with water or other polar solvent, the system of nanopores is formed. First, this feature has been found for homogeneous perfluorinated membranes (PFMs) of Nafion type [1, 2]. Then, it was proved for other polymer ion exchange materials (heterogeneous membranes and resins) [3, 4]. The nanopores are hydrophilic; they provide ion transport and ion exchange ability of swollen polymers. Their porous structure involves also hydrophobic pores; their size is from several tens of nanometers to several tens of microns. Both hydrophilic and hydrophobic pores are available for any inorganic modifier: the filler affects functional properties of the composite. The most intensive work in the field of practical application of organic-inorganic ion exchange materials has been started since the 2000s [5]. The necessity of investigations was caused by requirements of technologies for alternative energy and separation.

Y. Dzyazko · E. Kolomiets
VI Vernadskii Institute of General and Inorganic Chemistry of the National Academy of Science of Ukraine, Kyiv, Ukraine

Y. Volfkovich
AN Frumkin Institute of Physical Chemistry and Electrochemistry of the RAS, Moscow, Russia

O. Perlova · N. Perlova (✉)
Odessa II Mechnikov National University, Odesa, Ukraine

L. Ponomaryova
Sumy National University, Sumy, Ukraine

© Springer Nature Switzerland AG 2019

O. Fesenko, L. Yatsenko (eds.), *Nanophotonics, Nanooptics, Nanobiotechnology, and Their Applications*, Springer Proceedings in Physics 222,
https://doi.org/10.1007/978-3-030-17755-3_16

Correctly chosen ion exchange support, inorganic modifier, and modification technique allow one to accelerate ion transport through the polymer materials, expand the range of operation temperature, increase ion exchange capacity, and enhance selectivity of the composites [6]. Since porous structure of polymer ion-exchanger and membranes is very complex, inorganic particles can be in one or other pores. Thus, their effect on the porous structure and functional properties of polymer support can be different. This problem is outside the focus of attention except probably [7].

16.2 Dry and Swollen Ion Exchange Polymers: Swelling Pressure

Dry ion exchange materials contain heterogeneities that are formed during synthesis [1, 2, 8, 9]. Dipole-dipole interaction between fixed ions and counter-ions results in multiplet (cluster) formation. Different estimations give 2–8 pairs in the multiplets [8, 9].

The nanosized heterogeneities in dry polymers were recognized by small-angle X-ray scattering (SAXS) [2, 10], and the method of small-angle neutron scattering was also applied [11]. The spectra show two peaks at scattering vector of 0.01–0.1 A^{-1} indicating a size of the formations of several nanometers and several tens of nanometers. The smallest heterogeneities are related to clusters, and the larger ones are associated with crystallinity (the larger the crystallinity, the more distinct is the SACS maximum) [10]. The last formations and also claw-like structure defects can be observed using scanning electron microscopy (SEM) [12] as seen in Fig. 16.1a. In the case of macroporous resins, structure defects of micron size are formed purposefully in ion exchange polymer during synthesis.

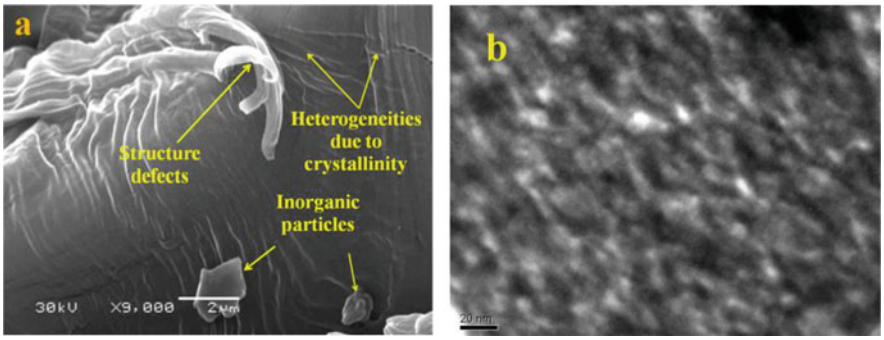

Fig. 16.1 SEM (**a**) and TEM (**b**) images of CMI-7000 cation exchange membrane (**a**, adapted from [13]) and Dowex HCR-S gel-like cation-exchange resin (**b**, original photo)

There are pores, the size of which is several tens of microns, in heterogeneous membranes [5, 13, 14]. They are attributed to voids between ion-exchanger and binder. The macropores of dry polymers are recognized with mercury porosimetry [15]. The smallest heterogeneities are visualized with transmission electron microscopy (TEM) (Fig. 16.1b) after shading with transition metal ions [12].

Thus, the structure of dry ion exchange polymers contains practically no micro- and mesopores, however, macropores are characteristic for them.

Thermodynamic approaches to swelling of ion exchange materials were summarized by Helfferich in 1950s [16]. A solution of water in polymer has been suggested. In other words, water and polymer are not different phases; no nanopores are related to swollen ion-exchanger.

According to modern approaches, swelling of ion exchange polymers is multistage. Primarily, functional groups (for instance, $–SO_3H$) are hydrated forming the pairs of fixed ions ($–SO_3^-$) and H_3O^+ counter-ions [17]. Next water molecules join H_3O^+ forming clusters of counter-ions with several H_2O molecules. Continuous aqueous phase is formed by this manner. Water and polymer are different phases, as proved by Hsu and Gierke based on SAXS data for Nafion PFM [2]. The model of nanopores (alternating nanosized clusters, which are formed from the smallest heterogeneities of dry polymers, and smaller channels) has been proposed (Fig. 16.2). The clusters and channels are organized similarly to inverted micelles (ion exchange groups are inside them) and arranged on a lattice. In other words, hydrophilic fragments of hydrocarbonic chains form the so-called gel regions, which are penetrated by clusters and channels. The nanopores are responsible for ion transport – they are called "transport pores."

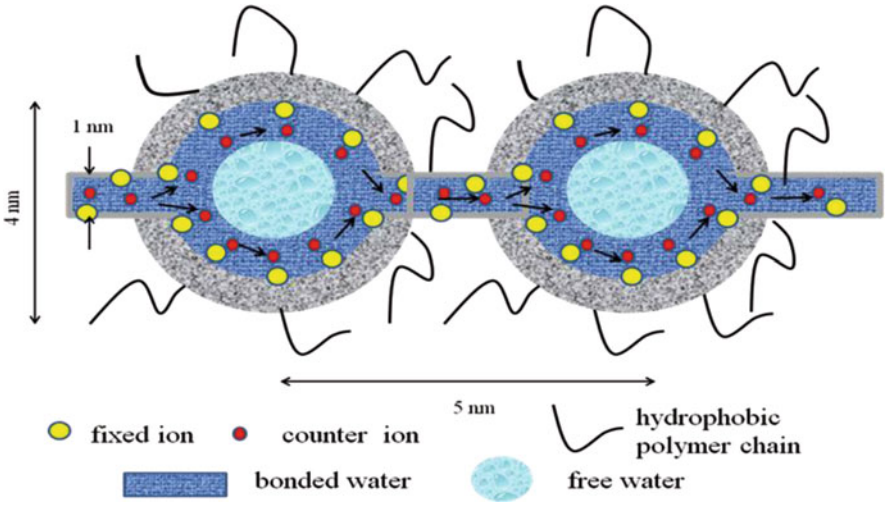

Fig. 16.2 Cluster-channel model for ion exchange polymer. Arrows show ion transport through Debye's layer along pore walls

Despite some criticism and alternative approaches [18], the Hsu-Gierke model has endured for many years as a conceptual basis for rationalizing the properties of Nafion-type, membranes, especially ion and water transport. The approach was developed further. Parallelism of cluster-channel paths [19] as well as aggregation and agglomeration of clusters [10] were suggested. The Hsu-Gierke model was also applied not only to homogeneous PFMs, but also to ion exchange resins and heterogeneous membranes [3, 4, 20].

Transport pores contain bonded water, namely, water clusters around fixed and counter-ions. A thickness of its layer is 1.5 nm [20]. Ion movement along pore walls is slower comparing with aqueous solutions. The cluster centers are filled with free water, in which the transport rate is close to that for aqueous solutions.

According to [21], the ion transport occurs through clusters and channels, where the distribution of counter- and co-ions is irregular. Regarding a cation-exchanger, this is caused by negative charge of pore walls due to fixed ions on them. The negative charge is compensated by adjacently located positively charged counter-ions. The thickness of this Debye's layer is about 1 nm. Anions and nonpolar molecules are excluded from it. When the ion-exchanger is in contact with a concentrated solution, there is almost electrically neutral liquid in the pore center (cations and anions are in equal amounts). The conductivity of the ion exchanger materials is predominantly determined by transport of counter-ions through the Debye's layer along pore walls (see Fig. 16.2), but co-ions and nonpolar molecules moved through free solution in the centers of pores.

As opposed to Ref. [21], the Debye's layers in clusters are overlapped, when an outer solution is low-concentrated. Ions move not only along pore walls but also through free water in the centers. In this case, the ratio of clusters and channels plays a key role due to different mobility of counter-ions in free and bonded water [12, 14, 22, 23]. However, the approach [21] is important for electrodialysis, when at least one side of a membrane is in contact with rather concentrated solution.

Porous structure of swollen ion exchangers involves also voids between gel regions, which are formed by bundles of hydrophobic fragments of polymer chains. Other elements of porosity are macropores, which are also attributed to dry polymers. Both gel regions and macropores are filled with a neutral solution. Ions of this solution make insignificant contribution to transport [12, 20, 22, 23]. This causes selectivity of ion exchange membranes toward either cations or anions [20]. As shown theoretically, the transport number of charged species is equal to the contribution of clusters and channels to total porosity [24]. Pores, a radius (r) of which is less than 10 nm, determine charge selectivity of membranes. The approach has been confirmed experimentally [7].

In fact, fixed and counter-ions in hydrophilic pores are osmotic centers. The osmotic theory of swelling suggests concentrated electrolyte inside transport pores, when the ion-exchanger is in contact even with pure water [16]. The "solution" is able to be diluted. In this case, the Debay's layers are overlapped in the clusters; thus the transport pores are filled with a "solution."

In the framework of macroscopic models, the tendency of the "solution" to be diluted is considered as the difference between the osmotic pressures of the

liquids inside and outside the granules of resin or the membrane sheets (so-called swelling pressure, π according to Gluekauf and Gregor models). The π value has been suggested for the ion-exchange materials, which change their volume freely. This magnitude has not to be related to the swelling pressure of gel in a volume bounded with rigid walls, as valid for polymers [25]. When water content in the ion-exchanger increases, osmotic pressure decreases [16]:

$$\pi v_{H_2O} = -RT \ln a_{H_2O}, \tag{16.1}$$

where a_{H_2O} is the activity of water in the ion-exchanger (related to free water, $a_{H_2O} = 1$ outside granules, $a_{H_2O} < 1$ inside them [26]), R is the gas constant, T is the temperature, and v_{H_2O} is the partial molar volume of water.

Elastic pressure, which is attributed to the polymer net, grows with increase of water content. This magnitude is estimated quantitatively according to Flory-Rehner theory [27]. When the values of osmotic and elasticity pressure become equal, the swelling stops.

The π value for any ion-exchanger can be calculated, when this magnitude is known for other sample of similar composition, and the water content in two samples is equal. The swelling pressure grows linearly with increase of cross-linkage [16]. Regarding strongly acidic gel-like cation-exchangers produced by Dow Chemical Company, this magnitude is ≈50 bar for the resin containing 4% of divinylbenzene, 150 bar (8%), 350 bar (16%), and 650 bar (24%). The Nafion PFM shows higher swelling pressure than the resin containing 8% of DVB [28].

16.3 Purposeful Formation of Inorganic Particles in Ion Exchangers

Depending on interaction of inorganic constituent with polymer, the organic-inorganic materials are divided into two classes [29, 30]. In class I, the components are bonded together through strong covalent or coordinative bonds: the inorganic fragments can be built-in a polymer backbone or grafted to it. Alternately, the inorganic matrix can be functionalized with organics. Regarding class II, inorganic and polymer constituents are different phases. The interactions between them are hydrogen bonding, van der Waals, π–π or weak electrostatic attraction. The materials of class II are related to composites. They can be obtained by solution-casting using finely dispersed inorganic ion-exchanger and sol-gel technique that often provides simultaneous formation of both polymer and inorganic constituents. Inorganic particles can be also embedded to the preliminarily synthesized polymer. In the last case, it is possible to use any commercial ion exchange material. Any inorganic constituent can be inserted into the polymer, if the synthesis method provides no its destruction. Since complex porous structure is attributed to ion exchange polymers, the particles can be deposited in one or other types of pores.

The features of precipitation of zirconium hydrophosphate (ZHP) and hydrated zirconium dioxide (HZD) are analyzed in Refs. [31, 32]. As an example, let us consider ZHP deposition: the synthesis method involves impregnation of polymer with a $ZrOCl_2$ solution followed by treatment with phosphoric acid. For simplicity, denote ZHP as $CatAn_z$ (where z is the charge number) and assume that there are only $H_2PO_4^-$ ions in the precipitator solution (*HAn*).

During precipitation, dissolution of small particles and their reprecipitation on larger particles is advantageous from a thermodynamic point of view. Gibbs energy of the system reduces due to decrease of the particle surface. The Ostwald-Freundlich Eq. [33] reflects the effect of the radius of particles (r_p) on their solubility:

$$\ln \frac{\overline{C}_{CatAn_z}}{C_{CatAn_z,\infty}} = -\frac{\beta V_m \sigma \cos\varphi}{RT r_p} \tag{16.2}$$

Here $\overline{C}_{CatAn_z}$ and $C_{CatAn_z,\infty}$ are the concentration of dissolved compound in the ion-exchanger and its saturated solution, respectively; β is the shape factor of particles, V_m is the molar volume of $CatAn_z$, σ is the surface tension of solvent, and φ is the wetting angle ($\approx$1 for hydrophilic compound).

The equations that take into consideration the conditions of precipitation have been proposed [31, 32]. They include the concentration of metal salt (C_{Cat}) and precipitator (C_{pr}), the volumes of ion-exchanger (V_i) and precipitator (V_{pr}), the solubility product of $CatAn_z$ (K_{sp}), and the exchange capacity of polymer [31]:

$$r_p = -\frac{\beta V_m \sigma \cos\varphi}{RT\left[\ln K_{sp} - \ln C_{CatAn_z,\infty} - z\ln\left(C_{pr} - \frac{(A+zC_{Cat})V_i}{V_{pr}}\right)\right]} \tag{16.3}$$

As follows, smaller particles are formed in the ion-exchanger with higher exchange capacity. For instance, the composite based on rigid resin contains smaller ZHP particles than flexible polymer (Fig. 16.3). However, Eq. (16.3) shows only the way that allows us to control the particle size; the formula gives no possibility for exact calculations. This is mainly due to ambiguity of the K_{sp} value for multivalent metal ions. For example, a large variety of species were found in the solution over HZD precipitate: $Zr(OH)_3^+$, $Zr(OH)_2^+$, $Zr(OH)_3^+$, $Zr(OH)_4$(aq) as well as the polymeric species $[Zr_4(OH)_8]^{8+}$ and $Zr_2(OH)_2^{6+}$ [34]. Different dissolution reactions, which is characterized by own K_{sp}, have to be considered.

However, we can estimate the particle radius for HZD from Eq. (16.2). The ratio under logarithm (the content of Zr in the solution for undersaturation and oversaturation conditions) is not higher than 0.1 [35]. We can assume $V_m = 21.6\ cm^3\ mol^{-1}$ for amorphous HZD similarly to crystalline ZrO_2. Since $\beta = 2.8$ for globules, the minimal particle diameter is 1.6 nm for the temperature of 293 K.

When sol of insoluble neutral zirconium hydroxocomplexes is used for impregnation of ion-exchanger (oversaturation condition), the ratio at the left side of Eq. (16.2) is close to 1, and the logarithm is close to 0. Since $z = 0$, Eq. (16.3)

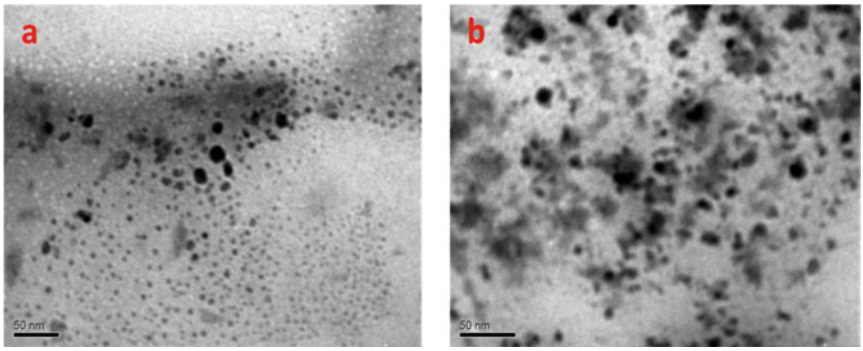

Fig. 16.3 TEM images of ZHP nanoparticles in rigid (Dowex HCR-S) and flexible (Dow WX-2) resins. (Adapted from Ref. [31])

is simplified down to Eq. (16.1). As a result, large particles of micron size are deposited inside ion-exchangers [23]. No single nanoparticles were found, though sol contained very small single particles (≈6 nm) [36]. Comparing with ZrO_2, α-ZHP is characterized by larger molar volume (91 cm^3 mol^{-1}) as calculated in Ref. [37]. The sufficient difference in molar volume is probably attributed for amorphous ZHP and HZD. Larger ZHP particles are formed in the substrate of microfiltration membrane [37, 38]. Smaller HZD particles are precipitated also in active layer improving rejection ability of the membrane.

The formation of the amorphous modification of ZHP and titanium hydrophosphate (THP) in polymers is suggested [39, 40]. Under certain synthesis conditions, crystalline modifications can be formed [41–43]. ZHP crystallizes in hydrophobic pores of Nafion PFM, amorphous modification is formed in clusters and channels [43]. Both hydro- and dihydrophosphate groups (attributed to α- and γ-ZHP modifications, respectively) were found with NMR spectroscopy: the spectra show two signals [23, 44] similarly to individual amorphous ZHP [45]. More complex spectra were obtained for PFM containing single nanoparticles [44]. The signals at −15 and −20 ppm are suggested to be related to crystalline ZHP; other signals correspond to amorphous phase.

As shown further, the state of embedded particles (non-aggregated nanoparticles, aggregates or agglomerates) affects porosity of the polymer on the one hand and ion transport through the composite on the other hand.

16.4 Investigations of Porous Structure of Polymer-Based Composites

Since main pores of polymers ion-exchangers are formed only in a solvent, special techniques are necessary. Regarding membranes, Archimedes' (picnometer) method [46] is enough to determine total porosity including closed pores.

Fractions of transport (α) and non-transport pores can be determined from the measurements of electrical conductivity ($\overline{\kappa}$) using heterogeneous model [20], which involves the conductivity of gel regions (κ_g) and equilibrium solution (κ):

$$\overline{\kappa} = \kappa_g^{\alpha} \kappa^{1-\alpha}. \tag{16.4}$$

Mercury is used as non-polarized electrodes; resistance at the membrane-solution interface is excluded by this manner. The conductivity of gel regions is calculated for Isoconductivity point, where $\overline{\kappa} = \kappa$. Linearity of $\log \overline{\kappa}$-$\log \kappa$ curve means that the $\overline{\kappa}$ and κ values are close to each other, and the model is valid. The conductivity of gel regions and the α-parameter are determined from the logarithmic dependence.

Exclusion of the effect of the membrane-solution interface is especially important to estimate transport and non-transport pores. The model cannot be applied without complying with this condition [13, 14]. In this case, the curve is modeled using semilogarithmic dependence.

Detailed analysis of pore size distributions (up to $r = 100$ nm) is possible by means of the method involving water adsorption-desorption using a vacuum Mac-Ben apparatus supplied with quartz scales [47]. Isotherms are obtained by this manner [16]. Further they are recalculated into integral and differential pore size distributions using the algorithm [47].

Other techniques are isopiestic method [48] and thermoporosimetry based on differential scanning calorimetry (DSC) [49]. The last method, which gives information about pores, a radius of which is up to 3 μm, is described also in Ref. [15].

The method of standard contact porosimetry (MSCP), which has been recommended by the IUPAC [50], gives pore size distributions in a very wide interval ($r = 1$ nm–100 μm). The MSCP provides gravimetric measurements of the content of working liquid (water for polymers) in the sample. The measurements are performed also for the porous standards samples that are attached to the tested sample. The data corresponding to conditions of capillary equilibrium are taken into consideration. The amount of liquid in the system of standards and tested sample is varied by impregnation and drying. When thermodynamic equilibrium is reached, the liquid in the contacting porous materials has the same chemical potential. The pore size distributions for the tested sample can be recalculated from the known distribution for the standards. Theoretical approaches, which dealt the MSCP, and also some practical details are given in Refs. [15, 51–53]. Regarding the composite, all the abovementioned methods allow us to determine only porosity of polymer, since it destroys under the conditions of thermal pretreatment, which are necessary for dehydration of inorganic constituent.

16.5 Evolution of Porosity of Polymer-Based Composites

In order to investigate evolution of porous structure and functional properties of composites, stepwise modification of ion exchange resins with ZHP was performed [22, 23, 41, 54–56]. The water content in one or other types of pores of the polymer was determined by the MSCP. Figure 16.4a shows typical pore size distributions for individual ZHP and for the composites containing non-aggregated nanoparticles [56]. The curve for the inorganic ion exchanger demonstrates diffuse maximum at $\log r \approx 0.3$ (nm). Regarding the composite, the area of the peaks for clusters and voids between gel regions decreases with the growth of ZHP content. No change of the peak centers is observed. Unchangeable position of these peaks is characteristic also for cation exchange membranes modified with silica [57] or ZHP [7]. This is a contradiction with a hypothesis by Yaroslavtsev and co-authors [58]. The surface of non-aggregated nanoparticles is covered with water, and additional water provides increase of size of clusters and channels. However, this hypothesis was not confirmed experimentally in Ref. [58] and subsequent works of these authors. Nevertheless Nagarale et al. [59] have found the increase of channel radius from 4 to 6 Å for polyvinyl alcohol (PVA) membrane, when the content of silica grows from 50% to 70%. The indirect method involving electroosmotic measurements followed by calculations via the formula:

$$r = \left(\frac{8\eta F\beta}{f_{\mathrm{cw}}}\right)^{0.5} \tag{16.5}$$

where β implies that each coulomb of electricity exerts a drag effect, which is enough to carry β cm^3 of water through 1 cm^2 of the membrane, η is the viscosity coefficient for permeate, and f_{cw} is the coefficient of friction between counter-ion and water in a solution, $f_{\mathrm{cw}} = RT/D$, where D is the diffusion coefficient of counter-ions in a solution. Thus, the hypothesis [58] is confirmed only for channels.

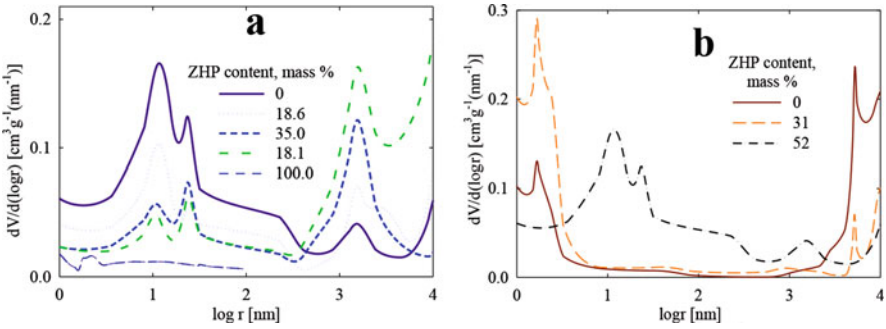

Fig. 16.4 Evolution of porous structure of Dowex HCR-S resin affected by ZHP. The composite contained non-aggregated nanoparticles. (**a**, Adapted from Ref. [56]), only aggregates and agglomerates (**b**, Adapted from Ref. [23])

As opposed to Refs. [22, 23], the increase of water content in transport pores and voids between gel regions has been found for the cation exchange membrane containing ZHP [7]. However, no information about the state of the embedded particles is given. Unreal low porosity ($1.85 \times 10^{-4} - 2.16 \times 10^{-3}$) has been reported for the membrane based on poly-***o***-toluidine containing Th(IV) phosphate [60].

When the composite contains only aggregates and agglomerates, the peaks due to mesopores are shifted toward lower log*r* values (Fig. 16.4b) [23]. The maximum of voids between gel fields is a shoulder of the cluster peak. The structure defects become larger comparing with the pristine resin, their volume increases after the first modification cycle. Further insertion of ZHP results in reduction of volume of macropores due to their filling with ZHP. The shift of the peaks attributed to mesopores is caused by swelling pressure in macropores due to additional osmotic centers (fixed and co-ions of the modifier). The constant position of cluster peaks for the composites containing also nanoparticles (see Fig. 16.4a) is due to additional swelling pressure in transport pores. This prevents their squeezing from the side of macropores.

As opposed to Refs. [22, 23], no influence of the modifier nanoparticles, which are located in transport pores, on structure defects has been found (the macropores were free from ZHP) [14]. The same effect is suggested in Ref. [7]; however, no information about the modifier state is given.

Comparing with MSCP, the method of water vapor adsorption gives lower pore volume and smaller clusters [61]. No shift of the cluster peaks is observed for the composite containing only large particles, since condensation of the vapor occurs only in micro- and mesopores providing lower swelling pressure (see Eq. (16.1)). The π value was estimated as 150 bar (pristine resin), 140 bar (resin filled with aggregates and agglomerates), and 190 bar (resin containing also single nanoparticles). Formally, non-aggregated nanoparticles can be considered as an additional cross-linking agent. The aggregates and agglomerates in hydrophobic pores "loosen" the resin structure. Similar results were obtained also with MSCP for rigid resin modified with large particles [55] and for flexible resin containing also non-aggregated nanoparticles [54].

16.6 Effect of Polymer Porosity on Ion Transport Through Composites

In order to establish the effect of incorporated inorganic particles on ion transport, some structure parameters of the polymer constituent have to be determined. One of them is the distance between functional groups (L) [24], which is determined taking into consideration the polymer fraction (m) in a composite, the exchange capacity of polymer (A_p) and its specific surface area (S):

Table 16.1 Parameters of porous structure for polymer and organic-inorganic ion exchange materials

Sample	Modifier, m	Particles[a]	L. nm	n[b]	α	γ	References
Ion exchange resin							
Dowex HCR-S	0	–	0.78	2.5	1.71	1.01	[22, 56, 61]
	ZHP, 0.39	NP, AR, AL	0.53	4.5	1.06	1.53	
	ZHP, 0.43	AR, AL	–	2.3	0.92	–	[23, 60]
Dowex WX-2	0	–	–	30.0	–	–	[54]
	ZHP, 0.21	NP, AR, AL	–	6.0	–	–	
Dowex MAC-3	0	–	0.37	4.3	0.4	0.6	[62]
	ZHP, 0.08	NP, AR, AL	0.38	3.9	0.4	0.9	
Membranes							
MK-40	0	–	–	5.8	1.9	1.6	[14]
	ZHP, 0.04	NP, AR		5.7	1.8	1.5	
MA-40	0	–		2.7	1.3	1.0	
	ZHD, 0.03	NP, AR		2.6	1.1	0.9	

[a]*NP* non-aggregated nanoparticles, *AR* aggregates, *AL* agglomerates
[b]The data were obtained with a method of water vapor adsorption (CC). Other results were obtained using MSCP

$$L = \left(\frac{qS}{A_p F (1 - m)} \right)^{0.5}, \tag{16.6}$$

where q is the electron charge. The L parameter was applied to polymer membranes (L = 0.4–0.7 nm) [3, 7, 15, 20], membranes modified with HZD [14], and ion exchange resins and their composites [56, 62]. This and other parameters are summarized in Table 16.1. Figure 16.5a reflects the influence of this parameter on electric conductivity. The modified polymers demonstrate smaller L value than the pristine samples (see also Table 16.1). Modification with ZHP leads to increase [14] or even reduction of membrane conductivity [63], earlier no sufficient effect of the modifier has been found [64]. In the case of ion exchange resin, the influence of ZHP is unambiguous (Fig. 16.5b, see also Fig. 16.5a) [12, 22, 23].

Other parameter is a number of water molecules per functional groups (hydration number, n); it characterizes hydration of fixed and counter-ions [7, 15, 20, 57, 65]. For different membranes, n = 3–8 [65], 11 [57], 14–18 [7]. This value is calculated from the plateau of water adsorption isotherm [54, 55, 61]:

$$n = \frac{A_{H_2O}}{A_p V_{H_2O} (1 - m)}, \tag{16.7}$$

where A_{H_2O} is the content of water. Modification of the membranes with silica causes significant increase of the n magnitude [57].

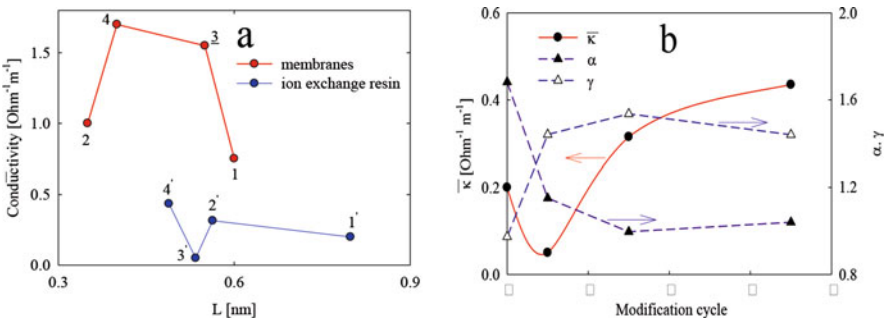

Fig. 16.5 Electrical conductivity of ion-exchange materials as a function of the distance between the functional groups of PFM (1–4, based on data [7]) and Dowex HCR-S resin ($1' - 4'$, based on data [22, 56]) (**a**), conductivity, α- and γ-parameters vs modification cycle of Dowex HCR-S resin [22] (**b**). The modifier is ZHP; pouring (1, 2) and extruding (3, 4) membranes and pristine (1, $1'$, 3) and composite (2, 4, $2' - 4'$) materials were researched, $m = 0.19(2')$, $0.36(3')$, $0.38\ (4')$

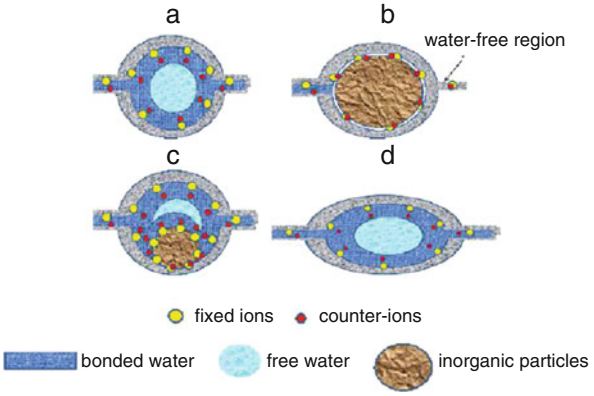

Fig. 16.6 Effect of embedded particles on transport pores: (**a**) pristine polymer, (**b**) complete blockage of the part of clusters and channels (they are free from water), (**c**) partial screening, and (**d**) squeezing affected by swelling pressure from the side of structure defects containing a modifier

Formally, reduction of the L parameter with increase of the modifier content indicates smaller distance between functional groups. However, higher hydration numbers show rebuilding of hydrate shells of fixed and counter-ions due to elongation of transport pores (unwinding of the macromolecule coil). This contradiction is evidently due to blockage of a part of clusters and channels with nanoparticles. As a result, some transport pores are unavailable for water (Fig. 16.6) and excluded from ion exchange. It means that the A_p magnitude is overstated. When the particle is smaller than the transport pores, it partially screens the pore walls. In this case, the counter-ions near the particle surface are involved to ion transport providing the increase of conductivity.

Blockage of the transport pores is confirmed in Ref. [61]. Pore size distributions for clusters have been recalculated as $(1 - m)(dV/d(\log r))$. The recalculated values are higher than the experimental magnitudes for the composites. It means, the modifier decreases water content in transport pores. Structure defects are stretched (see Fig. 16.4a) due to the modifier contribution to swelling pressure.

Comparing with the L parameter, which takes into consideration the value of ${A_p}^{-0.5}$, the calculation error for hydration number is smaller. It means, the n parameter is more suitable to estimate transformation of porous structure of the polymer constituent. The increase of the n value (see Table 16.1) indicates growth of the distance between functional groups.

Based on obtained results, a shift of the peaks of differential pore size distributions can be explained (see Fig. 16.4b). The pristine polymers contain no charge carriers in voids between gel regions and structure defects. Swelling pressure is provided by fixed and counter-ions only in clusters and channels. As opposed to pristine materials, there are charge carriers in voids between gel regions and structure defects. Electric double layer inside transport pores works as a semipermeable barrier. Thus, additional swelling pressure appears also in the largest pores of polymer. This results in squeezing of transport pores and voids between gel regions, their size becomes smaller (see Fig. 16.6). When non-aggregated nanoparticles are placed in clusters and channels, they provide additional swelling pressure preventing squeezing.

Other parameters, which are obtained from porometric measurements, are as follows: (i) the ratio of volumes of transport and hydrophobic pores (α) [14, 22, 23, 55] and (ii) the ratio of volumes of channels and clusters (γ) [14, 22, 55]. Earlier micropores were excluded from the α parameter; asymmetry of the peaks of differential pore size distributions was also considered [12]. The curves were deconvoluted into Lorentz components in order to estimate transformation of porous structure more exactly.

The change of the α and γ parameters due to embedded particles has been found (see Fig. 16.5b and Table 16.1). This change reflects the ion transport through the composites. Indeed, a growth of the α parameter and reduction of the γ value are characteristic for the composites after the first modification cycle. Simultaneously, electrical conductivity decreases. Further modification causes no sufficient change of these parameters, however, the conductivity grows.

The transformation of the polymer pore structure after the first modification cycles depresses ion transport [12, 22, 23]. This is caused by higher fraction of channels, which contain only bonded water, and by lower fraction of transport pores for the composites comparing with the pristine resin. Improvement of conductivity after the third modification cycle occurs, since the counter-ions of the modifier in clusters and channels are involved into ion transport.

16.7 Evolution of Electrical Conductivity: Functions of Particles

Theoretically, the dependence of the electrical conductivity of composites on the modifier content should obey the percolation theories. Known approaches involve volume fraction and electrical conductivity of modifier and polymer, the shape factor of embedded particles, wettability between the particles and matrix [66]. The theories explain the rapid growth of conductivity after certain critical value of modifier content (so-called percolation threshold). The dependence of conductivity on the modifier fraction can be divided to three regions (Fig. 16.7a). At low modifier content, the conductive particles are separated from each other and the conductivity of the composite is close to that of polymer. The rapid increase of conductivity is related to the formation of the continuous conductive network of modifier. Further increase of its content causes no influence on conductivity.

Let us compare the theory and some experimental results (Fig. 16.7b). Only the composites based on PVDF [67] and poly(2, 6-dimethyl-1, 4-phenyleneoxide) (POO) [71], which contain ZHP derivative [67] and silica [71], are the closest to the percolation model. Regarding the composite containing inert silica, highly conductive PPY is considered as the modifier of inorganic matrix [68]. Here, the falling curves are the inversion of the theoretical dependence (see Fig. 16.7a). The PFM membrane shows the decrease of conductivity with increasing of the ZHP content [63]. The curves for PPY-THP [69] and PFM-CeO_2 [70] membranes pass through a maximum. Regarding rigid ion exchange resin, these dependencies show minimum (see Fig. 16.5b). These composites disobey the percolation model due to their heterogeneous structure. Heterogeneity is reinforced with the growth of the modifier content. The conductivity buildup is due to the increase of the

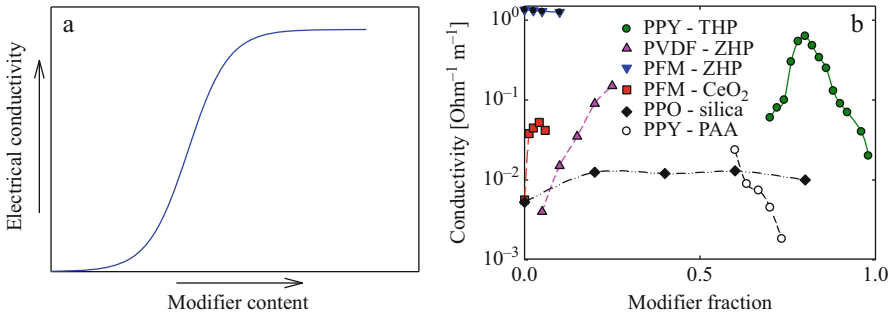

Fig. 16.7 Theoretical (**a**) and experimental (**b**) dependencies of conductivity on the modifier content. The measurements were performed under ambient temperature except the PVDF-ZHP composite (80° C) [67]. Relative humidity was ambient (PPY-PAA [68], PPY-THP [69]), 90% (PVDF-ZHP [67]), and 100% (PFM-ZHP [63]); the materials were immersed with water (PFM-CeO_2 [70], PPO-silica [71]) (Here PVDF is polyvinylidene fluoride, POO is poly(2, 6-dimethyl-1, 4-phenyleneoxide), PPY is polypyrrole, and PAA is polyantimonic acid)

amount of non-aggregated silica nanoparticles; the plateau is caused by aggregates [71]. Similarly, embedded ZHP nanoparticles are responsible for the improvement of conductivity [22]. Aggregates and agglomerates depress conductivity after the first modification cycle [22, 23]. Further modification increases conductivity due to elongation of transport pores [23]. These formations make no contributions to transport of counter-ions [22, 23]. However, large particles affect ion transport indirectly changing the porous structure of polymer.

At last, let us consider the functions of embedded particles. Non-aggregated nanoparticles in transport pores improve conductivity, they are also responsible for water retention under elevated temperatures and low humidity (this is important in the case of the membranes applied to fuel cells). According to Yaroslavtsev and Yampolskii, the nanoparticles provide charge selectivity of ion exchange membranes [72]. This is due to screening of the cluster centers (a neutral solution, which contains both counter- and co-ions, is located there [21]). However, small channels protect the cluster-channel system from co-ions. Berezina et al. suggest that voids between gel regions provide transport of co-ions deteriorating charge selectivity of the membranes [20]. High charge selectivity is reached, when the ratio of volumes of transport and non-transport pores is ≈ 0.9 [42]. Aggregates in voids between gel regions depress ion transport. These formations prevent adsorption of organics on hydrophobic fragments of polymer chains. Thus, the aggregates perform protective function as suggested in refs. [13, 14].

Agglomerates increase electroosmotic transport due to appearance of fixed ions in structure defects. They squeeze transport pores providing formation of sorption centers, which are selective toward large ions, such as UO_2^{2+} [55]. The resin containing agglomerates can be used for preferable removal of toxic ions from water containing also Ca^{2+} and Mg^{2+} [23]. Thus, the largest particles are useful rather for ion exchange resins.

16.8 Conclusions

Particles of inorganic ion-exchanger embedded into ion exchange polymer affect its porous structure due to additional swelling pressure. Depending on size and location of the particles, they are able to block, stretch, and squeeze transport pores of the polymer matrix. Thus, the modifier directly or indirectly influences ion transport through the composites. The particle size can be controlled during synthesis. Each type of inorganic particles performs their own function. Non-aggregated nanoparticles in clusters and channels enhance ion transport. They provide also water retention under elevated temperature and low humidity; this expands the temperature diapason of fuel cell operation. Aggregates of nanoparticles in voids between gel regions prevent transport of co-ions and accumulation of organic substances. This improves charge selectivity of ion exchange membranes and enhances their stability against fouling. Agglomerates in structure defects squeeze transport pores; a part of them is excluded from ion transport. Thereby,

formation of the particles of micron size is undesirable for the materials, which are applied to electrochemical processes. However, all types of particles in ion exchange resin enhance their selectivity toward toxic ions.

References

1. Eisenberg A, Yeager HL (eds) (1982) Perfluorinated ionomer membranes. ACS Symp Ser, vol 180. American Chemical Society, Washington
2. Hsu WY, Gierke TD (1983) Ion transport and clustering in nafion perfluorinated membranes. J Membr Sci 13:307–326
3. Kononenko NA, Berezina NP, Vol'fkovich YM et al (1985) Investigation of ion-exchange materials structure by standard porosimetry method. J Appl Chem USSR 58:2029–2033
4. Berezina NP, Kononenko NA, Vol'fkovich YM (1994) Hydrophilic properties of heterogeneous ion-exchange membranes. Russ J Electrochem 30:329–335
5. Guizard C, Bac A, Barboiu M et al (2001) Hybrid organic-inorganic membranes with specific transport properties: Applications in separation and sensors technologies. Separ Purif Technol 25:167–180
6. Kraytsberg A, Eiu-Eli Y (2014) Review of advanced materials for proton exchange membrane fuel cells. Energy Fuels 28:7303–7330
7. Kononenko NA, Fomenko MA, Volfkovich YM (2015) Structure of perfluorinated membranes investigated by method of standard contact porosimetry. Adv Colloid Interf Sci 222:425–435
8. Eisenberg A (1970) Clustering of ions in organic polymers. A theoretical approach. Macromolecules 3:147–154
9. Dreifus B (1986) Clustering and hydration in ionomers. In: Eisenberg A, Bailey FE (eds) Coulombic interaction in macromolecular systems. ACS Symp Ser, vol 302. American Chemical Society, Washington, DC, pp 103–119
10. James PJ, Elliott JA, McMaster TJ et al (2000) Hydration of Nafion studied by AFM and X-ray scattering. J Mater Sci 35:5111–5119
11. Young SK, Trevino SF, Beck Tan NC (2002) Small-angle neutron scattering investigation of structural changes in Nafion membranes induced by swelling with various solvents. J Polym Sci B Polym Phys 40:387–400
12. Dzyazko YS, Ponomareva LN, Volfkovich YM et al (2013) Conducting properties of a gel ionite modified with zirconium hydrophosphate nanoparticles. Russ J Electrochem 49:209–215
13. Dzyazko YS, Rozhdestvenska LM, Vasilyuk SL et al (2017) Composite membranes containing nanoparticles of inorganic ion exchangers for electrodialytic desalination of glycerol. Nanoscale Res Lett 12:438
14. Dzyazko Y, Rozhdestveskaya L, Zmievskii Y et al (2015) Heterogeneous membranes modified with nanoparticles of inorganic ion-exchangers for whey demineralization. Mater Today: Proc 6:3864–3873
15. Kononenko N, Nikonenko V, Grande D et al (2017) Porous structure of ion exchange membranes investigated by various technique. Adv Colloid Interf Sci 246:196–216
16. Helfferich F (1995) Ion exchange. Dover, New York
17. Laporta M, Pegoraro M, Zanderighi L (1999) Perfluorosulfonated membrane (Nafion): FT-IR study of the state of water with increasing humidity. Phys Chem Chem Phys 1:4619–4628
18. Mauritz KA, Moore RB (2004) State of understanding of Nafion. Chem Rev 104:4535–4585
19. Schmidt-Rohr K, Chen Q (2008) Parallel cylindrical water nanochannels in Nafion fuel-cell membranes. Nat Mater 7:75–83
20. Berezina NP, Kononenko NA, Dyomina OA et al (2008) Characterization of ion-exchange membrane materials: properties vs structure. Adv Colloid Interf Sci 139:3–28

21. Nikonenko VV, Yaroslavtsev AB, Pourcelly G (2012) Ion transfer through charged membranes: structure, properties, and theory. In: Ciferri A, Perico A (eds) Ionic interactions in natural and synthetic macromolecules. Wiley, Hoboken, pp 267–335
22. Dzyazko YS, Ponomaryova LN, Volfkovich YM et al (2013) Polymer ion-exchangers modified with zirconium Hydrophosphate for removal of Cd^{2+} ions from diluted solutions. Sep Sci Technol 48:2140–2149
23. Dzyazko YS, Ponomaryova LN, Volfkovich YM et al (2014) Ion-exchange resin modified with aggregated nanoparticles of zirconium hydrophosphate. Morphology and functional properties. Microporous Mesoporous Mater 198:55–62
24. Volfkovich YM (1984) Influence of the electric double layer on the internal interfaces in an ion-exchanger on its electrochemical and sorption properties. Soviet Electrochem 20(5):621–628
25. Mark JE (2007) Physical properties of polymers handbook, 2nd edn. Springer, New York
26. Kimoto K (1983) Water absorption and Donnan equilibria of per-fluoroionomer membranes for the chlor-alkali process. Electrochem Sci Technol 130:334–341
27. Flory PJ, Rehner JJ (1943) Statistical mechanics of cross-linked polymer networks II. Swelling. J Chem Phys 11:521–526
28. Pushpa KK, Nandan D, Iyer RM (1988) Thermodynamics of water sorption by perfluorosulphonate (Nafion-117) and polystyrene–divinylbenzene sulphonate (Dowex 50W) ion-exchange resins at 298 ± 1 K. J Chem Soc Faraday Trans 1(84):2047–2056
29. Tripathi BP, Shahi VK (2011) Organic–inorganic nanocomposite polymer electrolyte membranes for fuel cell applications. Prog Polym Sci 36:945–979
30. Sanchez C, Julián B, Belleville P et al (2005) Applications of hybrid organic-inorganic nanocomposites. J Mater Chem 15:3559–3592
31. Perlova N, Dzyazko Y, Perlova O et al (2014) Formation of zirconium hydrophosphate nanoparticles and their effect on sorption of uranyl cations. Nanoscale Res Lett 12:209. https://doi.org/10.1186/s11671-017-1987-y
32. Perlova O, Dzyazko Y, Halutska I et al (2018) Anion exchange resin modified with nanoparticles of hydrated zirconium dioxide for sorption of soluble U(VI) compounds. Springer Proc Phys 210:3–15
33. Myerson AS (ed) (2002) Handbook of industrial crystallization. Butterworth-Heinemann, Woburn
34. Ekberg C, Källvenius G, Albinsson Y et al (2004) Studies on the hydrolytic behavior of zirconium(IV). J Solut Chem 33(1):47–79
35. Kobayashi T, Sasaki T, Takagi I et al (2007) Solubility of zirconium(IV) hydrous oxides. J Nucl Sci Technol 44(1):90–94
36. Dzyazko YS, Volfkovich YM, Sosenkin VE et al (2014) Composite inorganic membranes containing nanoparticles of hydrated zirconium dioxide for electrodialytic separation. Nanoscale Res Lett 9:271. https://doi.org/10.1186/1556-276X-9-271
37. Myronchuk VG, Dzyazko YS, Zmievskii YG et al (2016) Organic-inorganic membranes for filtration of corn distillery. Acta Periodica Technologica 47:153–165
38. Zmievskii Y, Rozhdestvenska L, Dzyazko Y et al (2017) Organic-inorganic materials for baromembrane separation. Springer Proc Phys 195:675–686
39. Zhang Q, Jiang P, Pan B et al (2009) Impregnating zirconium phosphate onto porous polymers for lead removal from waters: effect of nanosized particles and polymer chemistry. Ind Eng Chem Res 48:4495–4499
40. Jia K, Pan B, Lv L et al (2009) Impregnating titanium phosphate nanoparticles onto a porous cation exchanger for enhanced lead removal from waters. J Colloid Interface Sci 331:453–457
41. Pan B, Pan B, Chen X et al (2006) Preparation and preliminary assessment of polymer-supported zirconium phosphate for selective lead removal from contaminated water. Water Res 40(15):2938–2946
42. Yang C, Srinivasan S, Aricò AS et al (2001) Composite Nafion/zirconium phosphate membranes for direct methanol fuel cell operation at high temperature. Electrochem Solid-State Lett 4:A31–A34

43. Chabé J, Bardet M, Gébel G (2012) NMR and X-ray diffraction study of the phases of zirconium phosphate incorporated in a composite membrane Nafion®-ZrP. Solid State Ionics 229:20–25
44. Nicotera I, Khalfan A, Goenaga G et al (2008) NMR investigation of water and methanol mobility in nanocomposite fuel cell membranes. Ionics 14:243–253
45. Dzyazko YS, Trachevskii VV, Rozhdestvenskaya LM et al (2013) Interaction of sorbed Ni(II) ions with amorphous zirconium hydrogen phosphate. Russ J Phys Chem A 87(5):840–845
46. Nussinovitch A (2010) Polymer macro- and micro-gel beads: fundamentals and applications. Springer, New York/Dordrecht/Heidelberg/London
47. Gregg SJ, Sing KSW (1991) Adsorption, surface area and porosity. Academic Press, London
48. Harland CE (1994) Ion exchange-theory and practice, 2nd edn. RSC Publisher, Letchworth
49. Brun M, Quinson JF, Blanc R et al (1981) Caractérisation texturale de résines en milieu réactionnel. Macromol Chem Phys 182:873–882
50. Rouquerol J, Baron G, Denoyel R et al (2011) Liquid intrusion and alternative methods for the characterization of macroporous materials (IUPAC technical report). Pure Appl Chem 84:107–136
51. Volfkovich YM, Bagotsky VS (2014) Experimental methods for investigations of porous materials and powders. In: YuM V, Filippov AN, Bagotsky VS (eds) Structural properties of different materials and powders used in different fields of science and technology. Springer, London/Heidelberg/New York/Dordrecht, pp 1–8
52. Volfkovich YM, Sosenkin VE (2012) Porous structure and wetting of fuel cell components as the factors determining their electrochemical characteristics. Russ Chem Rev 81:936–959
53. Volfkovich YM, Sakars AV, Volinsky AA (2005) Application of the standard porosimetry method for nanomaterials. Int J Nanotechnol 2:292–302
54. Dzyazko YS, Volfkovich YM, Ponomaryova LN et al (2016) Composite ion-exchangers based on flexible resin containing zirconium hydrophosphate for electromembrane separation. J Nanosci Technol 2:43–49
55. Dzyazko YS, Perlova OV, Perlova NA et al (2017) Composite cation-exchange resins containing zirconium hydrophosphate for purification of water from U(VI) cations. Desalin Water Treat 69:142–152
56. Dzyazko YS, Ponomareva LN, Volfkovich YM et al (2012) Effect of the porous structure of polymer on the kinetics of Ni^{2+} exchange on hybrid inorganic-organic ionites. Russ J Phys Chem 86:913–919
57. Zabolotskii VI, Protasov KV, Sharafan MV (2010) Sodium chloride concentration by electrodialysis with hybrid organic-inorganic ion-exchange membranes: an investigation of the process. Russ J Electrochem 46:979–986
58. Novikova SA, Safronova EY, Lysova AA et al (2010) Influence of incorporated nanoparticles on the ionic conductivity of MF-4SC membrane. Mendeleev Commun 20:156–157
59. Nagarale RK, Gohil GS, Shahi VK et al (2004) Organic-inorganic hybrid membrane: thermally stable cation-exchange membrane prepared by the sol-gel method. Macromolecules 37:10023–10030
60. Khan AA, Khan A, Inamuddin (2007) Preparation and characterization of a new organic–inorganic nano-composite poly-o-toluidine Th(IV) phosphate: its analytical applications as cation-exchanger and in making ion-selective electrode. Talanta 72(2):699–710
61. Dzyazko Y, Ponomarova L, Volfkovich Y et al (2016) Influence of zirconium hydrophosphate nanoparticles on porous structure and sorption capacity of the composites based on ion exchange resin. Ch Ch Technol 19:329–335
62. Ponomarova L, Dzyazko Y, Volfkovich Y et al (2018) Effect of incorporated inorganic nanoparticles on porous structure and functional properties of strongly and weakly acidic ion exchangers. Springer Proc Phys 214:63–77
63. Sahu AK, Bhat SD, Pitchumani S et al (2009) Novel organic–inorganic composite polymer-electrolyte membranes for DMFCs. J Membr Sci 345:305–314

64. Alberti G, Casciola M, Capitani D et al (2007) Novel Nafion–zirconium phosphate nanocomposite membranes with enhanced stability of proton conductivity at medium temperature and high relative humidity. Electrochim Acta 52:8125–8132
65. Bryk MT, Zabolotsky VI, Atamanenko D et al (1989) Structural inhomogeneity of ion-exchange membranes in swelling state and methods of its investigations. Khim Tekhnol Vody 11:491–498
66. Taherian R (2016) Experimental and analytical model for the electrical conductivity of polymer-based nanocomposites. Compos Sci Technol 123:17–31
67. Casciola M, Alberti G, Ciarletta A et al (2005) Nanocomposite membranes made of zirconium phosphate sulfophenylenphosphonate dispersed in polyvinylidene fluoride: preparation and proton conductivity. Solid State Ionics 176:2985–2989
68. Khan AA, Alam MM, Inamuddin et al (2004) Electrical conductivity and ion-exchange kinetic studies of a crystalline type 'organic–inorganic' cation-exchange material: polypyrrole/polyantimonic acid composite system, (Sb_2O_5) $(–C_4H_2NH–)\cdot nH_2O$. J Electroanal Chem 572:67–67
69. Khan AA, Paquiza L (2011) Electrical behavior of conducting polymer based 'polymeric–inorganic' nanocomposite: polyaniline and polypyrrole zirconium titanium phosphate. Synth Met 161:899–905
70. Kuznetsova EV, Safronova EY, Ivanov VK et al (2013) Transport properties of hybrid materials based on MF-4SC perfluorinated ion exchange membranes and nanosized ceria. Nanotechnol Russ 8:461–465
71. Tong X, Zhang B, Fan Y et al (2017) Mechanism exploration of ion transport in nanocomposite cation exchange membranes. ACS Publ. Appl Mater Interfaces 9:13491–13499
72. Yaroslavtsev AB, Yampolskii YP (2014) Hybrid membranes containing inorganic nanoparticles. Mendeleev Commun 24:319–326

Chapter 17
Features of the Influence of UFS/Raffinose Nanocomposites on In Vitro Cultivation of Gametes of Swine

O. V. Shcherbak, A. B. Zyuzyun, A. O. Sverhunov, and A. O. Sverhunova

Modern nanotechnologies are intensively used in various fields of science and technique, including biotechnology, agriculture, and medicine. A new trend in the realm of the synthesis of nanoparticles is the biological synthesis using polymer matrices, which are nontoxic and can be easily synthesized in any form that is necessary for a certain way of use. Similar matrices include biopolymers such as starch, chitosan, cyclodextrin, and ultrafine silica (UFS), which are acting as a stabilizer and recovering agent. The use of biopolymers in the production of nanoparticles has several advantages over conventional synthetic reagents. The high molecular weight chains of such biopolymers are characterized by a large number of hydroxyl groups, and therefore such structures can form complexes with target molecules. This ensures control of the size, shape, and dispersion of nanoparticles, which makes them less toxic to mammalian cells [5, 7]. UFS possesses a unique complex of physicochemical, medical, and biological properties: high sorption capacity for proteins, toxins, lack of allergenic and harmful effects on cells, and activation of reparative processes [2, 6, 10].

Nedava V. Yu. with colleagues showed that addition of UFS to cryomedium during cryopreservation prolongs survival of sperm after its deconservation [14]. Adsorption modification of the surface of UFS by some carbohydrates provided obtaining on its basis nanomaterials that showed more stimulatory activity on the sperm, rather than the original UFS [1]. During creating new nanomaterials, it is

O. V. Shcherbak · A. B. Zyuzyun
Institute of Animal Breeding and Genetics nd.a. M.V. Zubets, National Academy of Agrarian Science of Ukraine, Kiev, Ukraine

A. O. Sverhunov (✉)
Kharkiv State Zooveterinarian Academy, Kharkiv, Ukraine

A. O. Sverhunova
Kharkiv National Medical University, Kharkiv, Ukraine

© Springer Nature Switzerland AG 2019

O. Fesenko, L. Yatsenko (eds.), *Nanophotonics, Nanooptics, Nanobiotechnology, and Their Applications*, Springer Proceedings in Physics 222,
https://doi.org/10.1007/978-3-030-17755-3_17

necessary to take into account the multifunctionality of biomolecules. It is known that some carbohydrates are energy-intensive mediums, natural cryoprotectants, and structures, which recognize the cell surface in biopolymers and receptors [9].

The mechanism of action of some carbohydrates that penetrate into the cell and form hydrogen bonds with water molecules is currently widely covered, but the effect of carbohydrates that do not penetrate into the cell is not yet fully understood [1]. Such a carbohydrate is oligosaccharide raffinose.

Receiving biologically complete embryos of farm animals in vitro, if compared to in vivo, does not always have high and stable results. Therefore, the attention of biotechnologists is paid to optimizing mediums for the cultivation of reproductive cells. Nanomaterials based on UFS and raffinose deserve attention due to their ability to improve the mediums for gametes of pigs. Domestic scientists have proved that the addition of UFS in low concentrations to the suspension of various cells (yeast, microorganisms, red blood cells, sperm) contributes to stimulating their viability. Immobilization of a number of biomolecules on the surface of NFS allows the creation of biologically active nanomaterials that can enhance this effect [4].

17.1 The Purpose of Research

To study the biological activity of UFS/raffinose nanoparticles on spermatozoa and oocyte-cumulus complexes of pigs in in vitro cultivation conditions.

17.2 Materials and Methods of Research

The research was carried out at the Laboratory of Biotechnology for the reproduction of the Institute of Animal Breeding and Genetics nd.a. M.V. Zubets NAAS. Raffinose, which is composed of residues of D-galactose, D-glucose, and D-fructose trisaccharide, was immobilized to the surface of UFS (the O. Chuik Institute of Surface Chemistry, NAS of Ukraine) (Fig. 17.1).

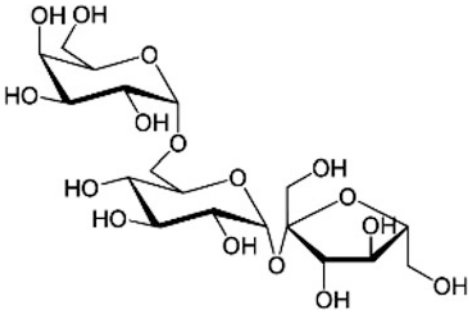

Fig. 17.1 Raffinose (C18H32O16)

In order to experimentally evaluate the biological activity were used cryopreserved ejaculated spermatozoids of the three boars of the Mirgorod breed (Dnipro 641, Komysh 853, Kohaniy 289) that were stored at the Bank of Genetic Resources of Animals at the Institute of Animal Breeding and Genetics nd.a. M.V. Zubets NAAS. To the defrosted spermatozoa of each boar was added a UFS/raffinose in 0.1, 0.01, and 0.001% concentrations (experimental groups). The effect of nanomaterial on sperm of each boar was separately evaluated by changing their activity in percentages with the subsequent establishment of average value in the control group (without addition of UFS/raffinose to defrosted sperm) and in the experimental groups.

Obtaining oocytes, their morphological evaluation and selection and placement for maturation in vitro were carried out in sterile conditions of the box. The temperature in the box was maintained at +20 – +25 °C. Oocyte-cumulus complexes (OCCs) were obtained from ovaries of slaughtered clinically healthy pigs in the age from 6 to 8.5 months. OCCs were removed by dissecting the walls of the antral follicles. Selected oocytes ($n = 245$) were matured in vitro for 46 hours in the TSM 199 medium (Sigma, M-5017) with adding 20% of the cow's estrus serum and 3–5 × 106 granulosa cells/ml. For in vitro cultivation were taken the oocytes with dense and loose cumulus [2, 13]. Gametes were cultivated at temperature of +38.8 °C and 4% CO_2 in the air. Removed OCCs of pigs were divided into two groups: experimental, in which the cultivation was carried out in a medium with addition of UFS/raffinose nanomaterial in 0.001% concentration, and control, in which cultivation of OCCs was performed without adding nanomaterial. The criterion for morphological evaluation of maturation of oocytes was the presence of the first polar body [3, 8]. The level of maturation of oocytes in vitro and fertilization and analysis of condition of embryo nuclei chromatin were studied by analysis of cytogenetic preparations prepared according to the modified method of A. Tarkovsky [11, 12]. The preparations were stained with 2% solution of Gimza's dye and analyzed using a Jenaval light microscope, Carl Zeiss eyeglass × 10, lens × 100. Statistical processing of the obtained data was carried out using the Student's criterion.

17.3 Results and Discussion

It was found, that after defrosting of spermatozoa they showed an average activity of 16.7 ± 3.3%. In the control group, within 30 minutes, this indicator decreased only by 1.7% (15.0 ± 2.9%). After the presence of spermatozoa in an environment containing UFS/raffinose in 0.1, 0.01, and 0.001% concentrations for 30 minutes, the gametes activity decreased by 10.0, 8.4, and 6.7%, compared with the initial activity (Fig. 17.2).

It should be noted that after 1.5 hours from the beginning of the research, sperm activity was 9.2% in control group and in the experimental groups, there was a similar activity at that time, namely, 7.5% with 0.001% UFS/raffinose

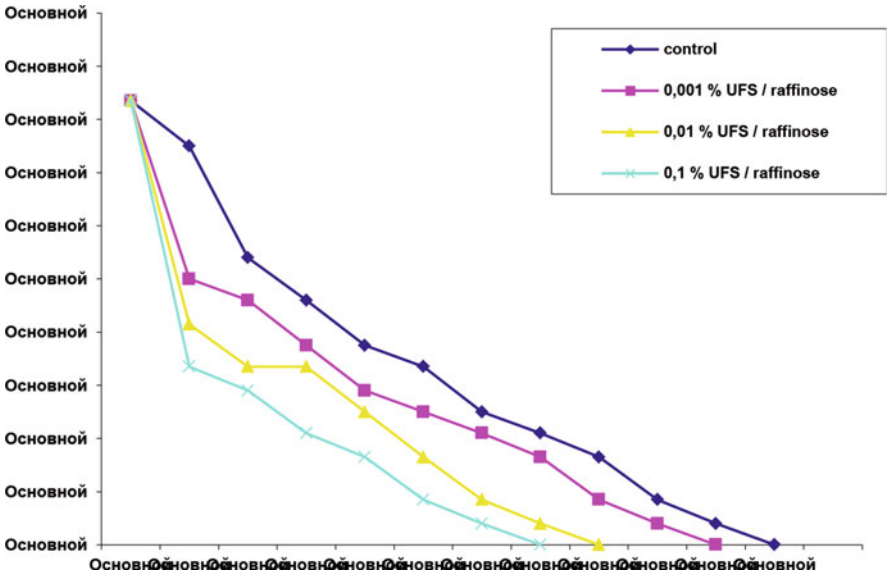

Fig. 17.2 Effect of UFS/raffinose on the viability of defrosted ejaculated spermatozoa of boars

concentration and 6.7% and 4.2 with 0.01 and 0.1% UFS/raffinose concentration. The total survival time of spermatozoa in the control group was 5 hours and in the experimental group with 0.1% concentration, it did not exceed 3 hours; for spermatozoa, which were in 0.01 and 0.001% concentrations of UFS/raffinose, this indicator was 3.5 and 4,5 hours, respectively. In our opinion, this process was manifested due to the properties of sugars to replace water molecules in biological systems that contain proteins. Also, such a process can also be accompanied by the formation of complexes in solutions and the change in the viscosity of such biological systems.

Consequently, we have shown that the smallest effect on the preserved sperm has 0.001% concentration of UFS/raffinose; therefore, the next stage of our studies was to evaluate the effectiveness of meiotic maturation of porcine oocytes in vitro by adding exactly this concentration of nanomaterial based on UFS and oligosaccharide.

According to the morphological evaluation and cytogenetic analysis, the largest part of the oocytes in both groups, after in vitro cultivation for 46 hours, reached the stage of nuclear maturation – metaphase II, indicating a sufficiently high total maturation (over 75%). Between the studied groups was established a probable difference in the number of oocytes which achieved metaphase II in vitro ($p < 0.01$ Student's criterion). Thus, in the control group, there were 15.5% less oocytes that reached metaphase II (115 oocytes out of 166 placed for cultivation) than in experimental groups (67 oocytes out of 79 placed for cultivation). It was also noted that in the control group, there were 11.0% more oocytes that did not restore meiotic maturation and remained at the stage of diplotene (31 oocytes out of 166 placed on cultivation) (Table 17.1).

Table 17.1 The effect of UFS/raffinose on maturation of oocytes of pigs in in vitro conditions

Group	Total amount of oocytes, *n*	Stages of OCC's development in vitro			Number of oocytes with degenerated chromatin, *n* (% ± m)
		Diplotene, *n* (% ± m)	Telophase, *n* (% ± m)	Metaphase II, *n* (% ± m)	
Control group	166	31[a] (18,7 ± 3,0)	5[c] (3,0 ± 1,3)	115[d] (69,3 ± 3,5)	15[f] (9,0 ± 2,2)
Studied group (0,001% UFS/raffinose)	79	6[b] (7,6 ± 2,9)	2[c] (2,5 ± 1,7)	67[e] (84,8 ± 4,0)	4 [f] (5,0 ± 2,4)

Note: a:b, d:e – the difference is statistically significant compared to the maximum value with P < 0.01, the Student's criterion

It should be noted that the total part of gametes with degenerated chromosomal material did not exceed 9.0% and did not have a significant difference between the compared groups. It points to the provision of activating properties of mediums for the complete maturation of the oocytes. Thus, the addition of 0.001% UFS/raffinose contributed to increasing of the level of oocytes, which developed to metaphase II in vitro, to almost 85.0% (67 oocytes out of 79 placed on cultivation), due to providing activating conditions in the maturation medium for oocytes (Figs. 17.3 and 17.4). This indicates the stimulating effect of UFS/raffinose in 0.001% concentration for porcine oocytes under in vitro cultivation conditions.

Consequently, as a result of the evaluation, the dose-dependent effect of UFS/raffinose on cultivated gametes is shown. In our opinion, this effect was observed as a result of the interaction of UFS/raffinose with proteins of the gametes membrane, that is, in smaller concentrations this nanomaterial only causes the structural rearrangement of the membrane, and when the concentration increases, it extracts proteins from the membrane, violating the integrity of the bilipid layer.

Fig. 17.3 Porcine ovary after in vitro maturation in the stage metaphase II of meiosis

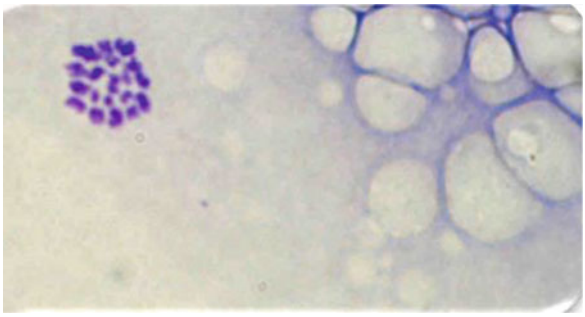

Fig. 17.4 Cytogenetic preparation of porcine oocyte at the stage of metaphase II of meiosis after maturing in vitro ($n = 19$)

17.4 Conclusions

Was applied an assessment of the biological activity of nanomaterials, based on UFS with surface modified by raffinose, under cultivation conditions with swine gametes in vitro. It has been established that 0.001% UFS/raffinose concentration with depreserved sperm of boars ensures a decrease by 5% in its activity (boars 10.0% vs. 15.0% in control). It was found that the addition of nanoparticles of UFS/raffinose in 0.001% concentration to the medium for cultivating of porcine OCCs contributes to a possible increase of their maturing level, compared to control group.

Prospects for further researches consist in the complex assessment of the peculiarities of using the nanomaterials, taking into account the dose-dependent effect of them for specific cell types. The use of the obtained results will provide the basis for developing recommendations for optimization of gametes cultivation technology and the formation of in vitro embryos of farm animals.

References

1. Belous AM, Kriobiologija, Grishhenko VI (1994) Monografija. Pod redakciej Kalugina Ju. V. i Nikitina I. I. – K.: «Naukova dumka». 432 s
2. Zyuzyun AB, Shherbak OV, Osỳpchuk OS, Kovtun SI, Dzicyuk VV (2015) Zastosuvannya nanomaterialu v embriogenetỳchnij sỳstemi in vitro otrỳmannya embrioniv svỳnej – *Faktorỳ eksperỳmentaìnoyi evolyuciyi organizmiv: Zb. nauk. pr. Nacionaìna akademiya nauk Ukrayinỳ* – K.: "Logos". 17:164–168
3. Kovtun SI, Galagan NP, Shherbak OV, Trocžkỳj PA (2015) Metodỳchni rekomendaciyi z kriokonservaciyi spermatozoyidiv ta oocỳtiv siìškogospodarṡkỳx tvarỳn i formuvannya embrioniv in vitro – Chubỳnṡke. – 17 s
4. Novichkova DA, Kuz'mina TI, Shherbak OV, Galagan NP, Epishko OA (2017) Vlijanie nanochastic vysokodispersnogo kremnezema na morfologiju i intracitoplazmaticheskuju lokalizaciju lipidnyh kapel' v oocitah svinej – *Rozvedennja i genetika tvarin*. – 53:284–292
5. Galagan NP, Patej LM, Nastasiyenko NS (2006) Nanokompozỳtỳ na osnovi vỳsokodỳspersnogo kremnezemu i biomolekul ta yix termichni peretvorennya – *Nanosỳstemỳ, nanomaterialỳ, nanotexnologiyi : Zb. nauk. pr.* – 4(3):599–612
6. Shherbak OV, Galagan NP, Trocžkỳj PA, Kovtun SI (2017) Zastosuvannya nanochastỳnok dioksỳdu kremniyu v texnologiyi formuvannya embrioniv svỳnej in vitro – *Nanosỳstemỳ, nanomaterialỳ, nanotexnologiyi Nanosistemi, Nanomateriali, Nanotehnologii* – 15:381–388 (Instỳtut metalofizỳkỳ im. G. V. Kurdyumova NAN Ukrayinỳ).
7. Shherbak OV, Zyuzyun AB, Osỳpchuk OS, Kovtun SI, Galagan NP, Trocžkỳj PA (2017) Vỳvchennya biologichnoyi aktỳvnosti nanomaterialu v umovax kuìtỳvuvannya spermatozoyidiv ta oocỳtiv svỳnej in vitro – *Faktorỳ eksperỳmentaìnoyi evolyuciyi organizmiv: Zb. nauk. pr. // Nacionaìna akademiya nauk Ukrayinỳ* – K.: "Logos". – 20:256–259
8. Beebe LF, Mcllfatrick SM, Vassiliev IM, Nottle MB (2013) Development of an improved porcine embryo culture medium for cloning, transgenesis and embryonic stem cell isolation. Cloning Transgen 2:107
9. Bermejo-Alvarez P, Roberts RM, Rosenfeld CS (2012) Effect of glucose concentration during in vitro culture of mouse embryos on development to blastocyst, success of embryo transfer, and litter sex ratio. Mol Reprod Dev 79(5):329–336

10. Castillo-Martín M, Yeste M, Morató R, Mogas T, Bonet S (2013) Cryotolerance of in vitro produced porcine blastocysts is improved when using glucose instead of pyruvate and lactate during the first 2 days of embryo culture. Reprod Fertil Dev 25(5):737–745
11. Pradeep PJ, Srijaya C, Zain RBM, Papini A, Chatterji AK (2011) Caryologia. A simple technique for chromosome preparation from embryonic tissues of teleosts for ploidy verification. Caryologia 64(2):233–239
12. Romar R, Coy P, Rath D (2012) Maturation conditions and boar affect timing of cortical reaction in porcine oocytes. Theriogenology 78:1126–1139
13. Romar R, Funahashi H, Coy P (2016) In vitro fertilization in pigs: new molecules and protocols to consider in the forthcoming years. Theriogenology 85:125–134
14. Nedava VE (1990) Ispolzovanie aerosilov v praktike iskusstvennogo osemeneniya – Using aerosil in practice artificial insemination. Zootechniya 8:63–65

Chapter 18
The Infrared and Raman Spectra of Acetaminophen–Cholesterol Complex: DFT Study

A. Dawid and Z. Gburski

18.1 Introduction

Atherosclerosis and related cardiovascular diseases remain a major health problem in societies nowadays. Cholesterol clusters have long been identified within atherosclerotic plaque and show significant causative correlation with the development of atherosclerosis and cardiovascular diseases [1–6]. The appearance of cholesterol condensates in nascent plaques and increased concentrations of cholesterols in susceptible and unstable atherosclerotic plaque has been detected by imaging and staining techniques [7–9]. Cholesterol within atherosclerotic plaque is mostly esterified, but as plaques develop, the amount of free cholesterol increases [10, 11] and leads to the formation of cholesterol clusters or crystals [12–14]. The major deliverers of cholesterol to a region of being formed atherosclerotic plaque are the low density lipoproteins (LDL), circulating in the blood vessels. It is known that oxidative modification of LDL contributes to the pathology of atherosclerosis [1, 15]. The properly chosen antioxidants may protect LDL against oxidative modification. Acetaminophen, also known as paracetamol, is used as an analgesic and antipyretic in small doses, it has also significant antioxidant properties [16–29]. In view of the mentioned reasons, it is desirable to study the properties of cholesterol–acetaminophen complexes. Particularly, in this work, we focused on the calculation of the infrared and Raman spectra, i.e., important "fingerprints" of the

A. Dawid (✉)
Department of Transport and Computer Science, WSB University, Dąbrowa Górnicza, Poland
e-mail: adawid@wsb.edu.pl

Z. Gburski
Katowice Institute of Information Technologies, Katowice, Poland

Institute of Physics, University of Silesia in Katowice, Chorzów, Poland

© Springer Nature Switzerland AG 2019

O. Fesenko, L. Yatsenko (eds.), *Nanophotonics, Nanooptics, Nanobiotechnology, and Their Applications*, Springer Proceedings in Physics 222,
https://doi.org/10.1007/978-3-030-17755-3_18

system composed of acetaminophen and cholesterol molecule, using the density functional theory (DFT).

18.2 Calculation Details

The calculations were performed at the B3LYP/6-31G(d,p) and the B3LYP/6-311G(d,p) level of DFT theory. The molecules were modeled using Avogadro software [30]. A few different configurations of cholesterol–acetaminophen were optimized by classical dynamics (MD) methods and then used as starting configurations for further DFT optimization. The configurations studied in this work are shown in Fig. 18.1. The binding energy, hydrogen bond formation, and shapes of HOMO and LUMO molecular orbitals are presented. In the case of interaction of these two molecules, we have added the dispersion correction GD3BJ for density functional theory potential, available within calculation package. The infrared (IR) and Raman spectra calculations were performed within harmonic oscillation approximation. All calculations were carried out using Gaussian09 package [31].

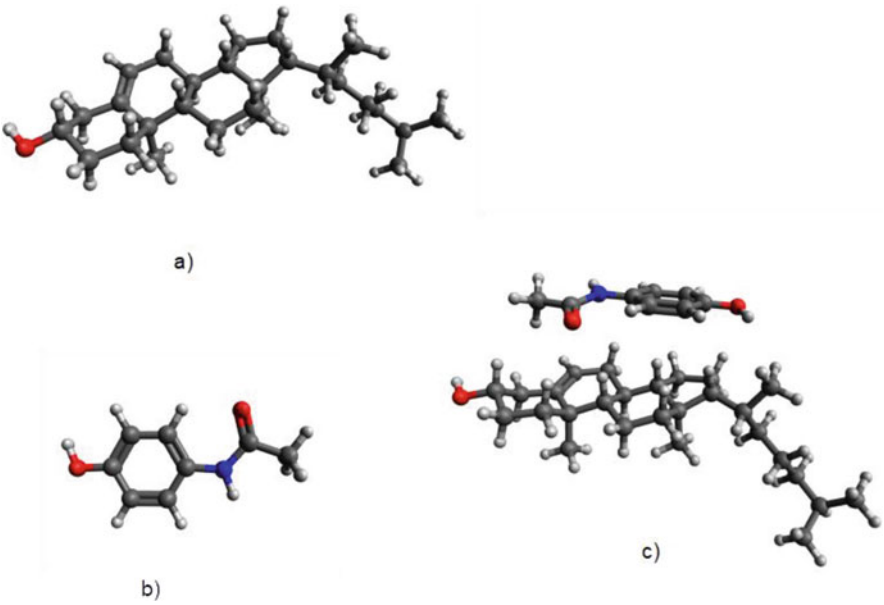

Fig. 18.1 Graphical representation of (**a**) cholesterol $C_{27}H_{46}O$, (**b**) acetaminophen $C_8H_9NO_2$, and (**c**) acetaminophen–cholesterol complex

18.3 Results

The first question that we want to answer in this report is about binding energy of isolated and interacting molecules, i.e., acetaminophen and cholesterol. This quantity is very important for stability of chemical complexes. The values of binding energies are shown in Table 18.1. As we see, the vicinity of acetaminophen near cholesterol does not destabilize the molecules. The $\Delta E_{\mathrm{HOMO-LUMO}}$ energy gap is lower for interacting molecules than for isolated ones, but still the binding energy is quite high to prevent chemical reaction between molecules. Electron density and HOMO/LUMO orbitals of molecules are shown in Fig. 18.2. The HOMO and LUMO orbitals of acetaminophen do not change so much when it comes to the interaction with cholesterol molecule. The influence of acetaminophen on cholesterol can be more visible in the infrared (IR) and Raman spectra. The calculated IR spectrum of acetaminophen reveals three characteristic bands (Fig. 18.3). The low

Table 18.1 HOMO–LUMO energy gap

Molecule name	Method	Dispersion	$\Delta E_{\mathrm{HOMO-LUMO}}$[eV]
Cholesterol	B3LYP/6-31G(d,p)	–	6.948
Acetaminophen	B3LYP/6-31G(d,p)	–	5.395
Cholesterol+acetaminophen	B3LYP/6-311G(d,p)	GD3BJ	5.275

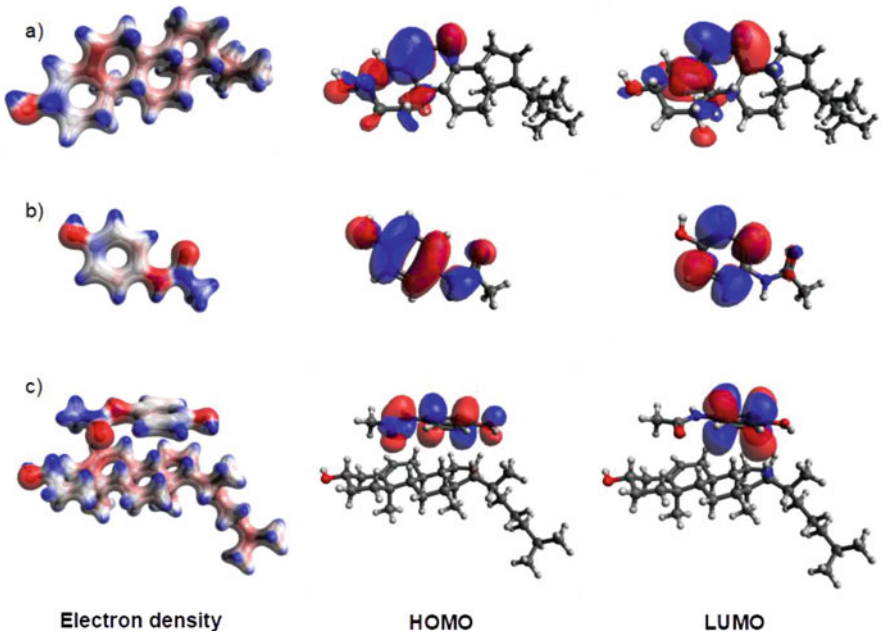

Fig. 18.2 Electron density and HOMO and LUMO orbitals for (**a**) isolated cholesterol, (**b**) isolated acetaminophen, and (**c**) acetaminophen–cholesterol complex

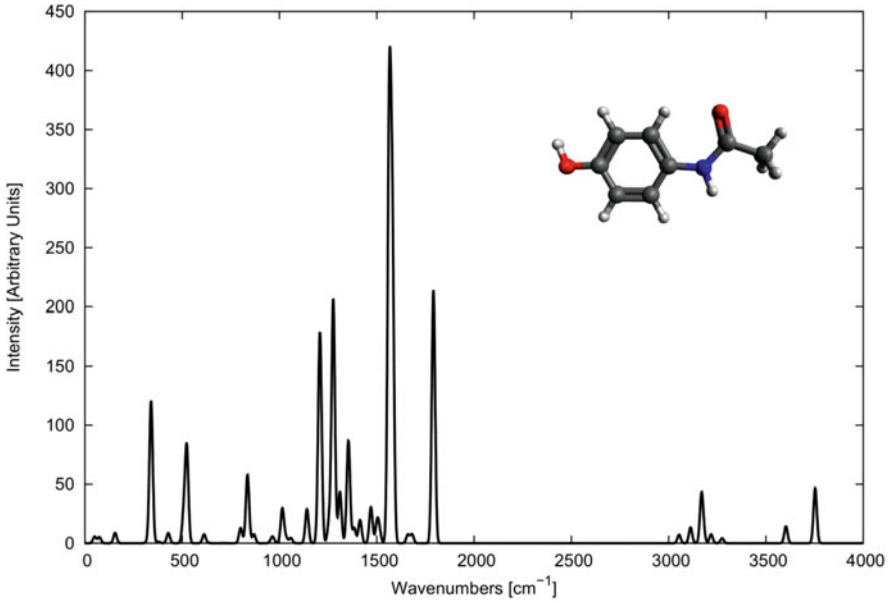

Fig. 18.3 The calculated infrared spectrum of acetaminophen

frequency band (100–600 cm^{-1}) is responsible for C-C-C bending inside benzene ring. The higher frequency band (800–1800 cm^{-1}) reflects C-C stretching vibrations and C-C-H bending vibrations. The stretching vibrations of C-H atoms are visible in the band between 3000 and 3800 cm^{-1}. The existence of these bands reflects hydrophilic character of acetaminophen [32, 33]. The peaks in 3232 cm^{-1} represent hydrogen stretching vibrations in the ring and 3750 cm^{-1} in the tail. The highest amplitude of vibration in acetaminophen molecule is observed in the case of N-benzene ring stretching vibration. Another picture of IR spectra is observed in the case of cholesterol molecule (Fig. 18.4). The highest amplitude of vibration is visible in H-H stretching vibrations (double peak at 3048 and 3120 cm^{-1}). The lower band (300–1700 cm^{-1}) represents stretching and bending in alkane chain. The IR spectrum of interacting acetaminophen and cholesterol molecules shows broadening of C-H stretching vibration peak visible at 3074 cm^{-1} (Fig. 18.5). The difference between them is also visible in low frequency peak (326 cm^{-1}). This peak is responsible for benzene ring-O-H bending vibration. In Raman spectrum of acetaminophen, the C-H vibrations at 3075 cm^{-1} are more pronounced then in IR spectrum (Fig. 18.6). The amplitude of these vibrations in Raman spectrum is comparable with C-O-H bending vibration. One can also notice strong peaks at 3626 cm^{-1} which come from stretching vibration of N-H and 3830 cm^{-1} which in turn is responsible for O-H stretching vibration. The Raman spectrum for cholesterol is shown in Fig. 18.7. In high-frequency band, we can observe two peaks. The one at 3078 cm^{-1} is responsible for stretching vibrations between carbons and

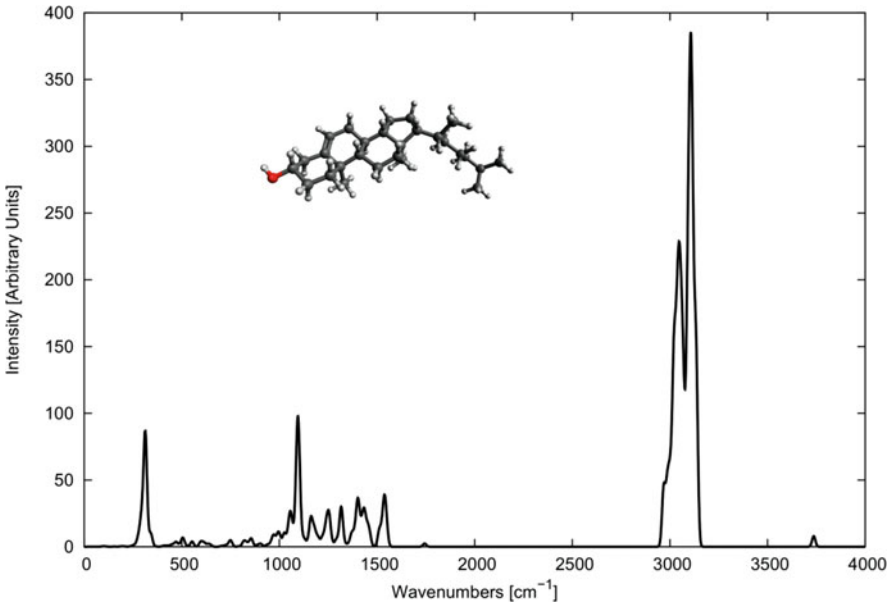

Fig. 18.4 The calculated infrared spectrum of cholesterol

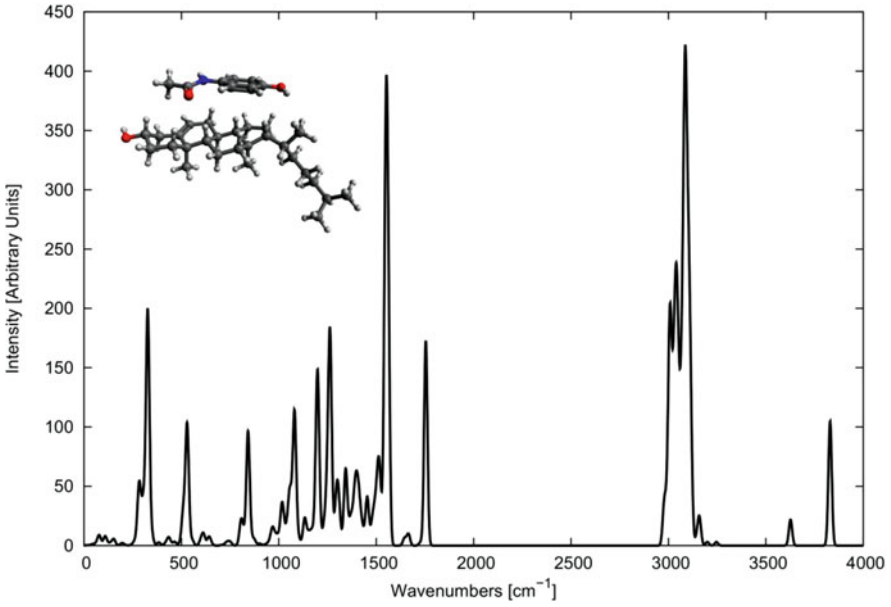

Fig. 18.5 The infrared spectrum of acetaminophen–cholesterol complex

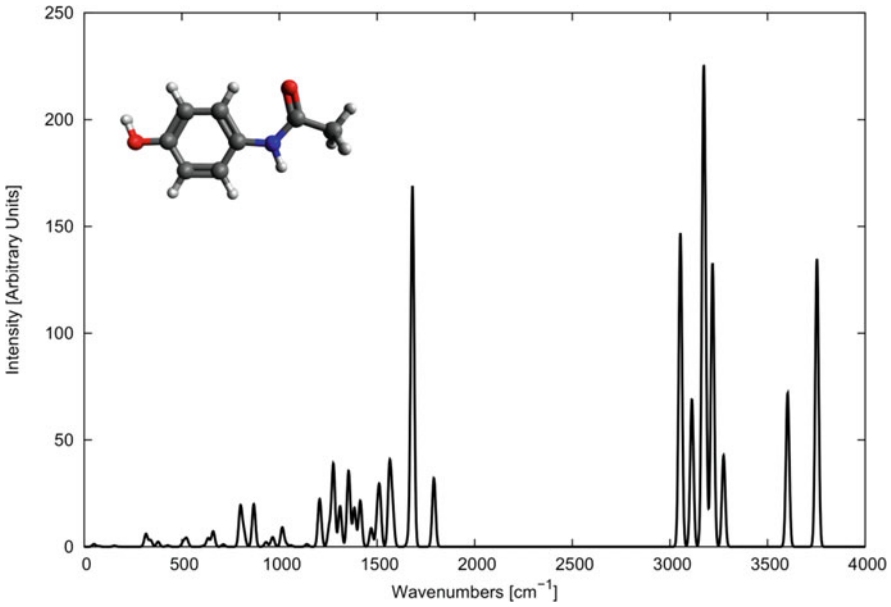

Fig. 18.6 The calculated Raman spectrum of acetaminophen

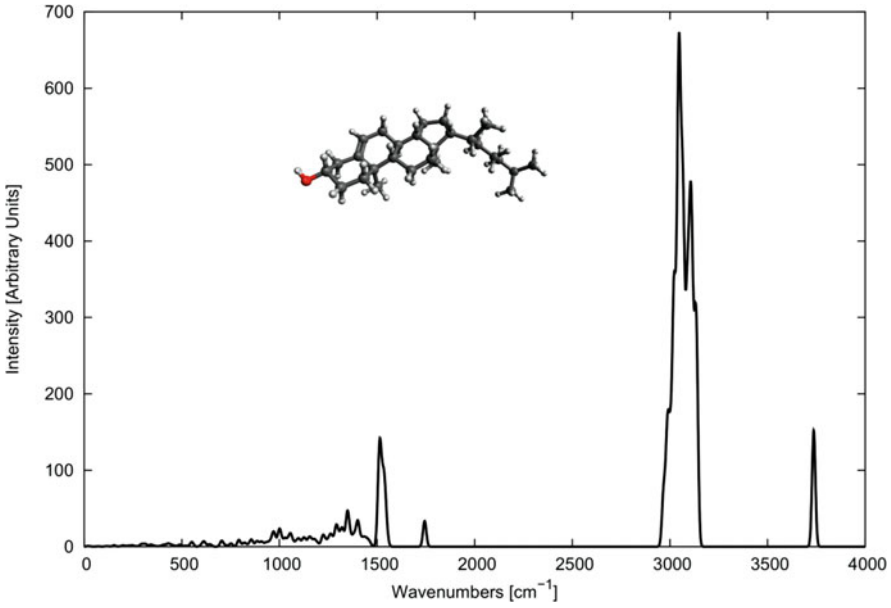

Fig. 18.7 The calculated Raman spectrum of cholesterol

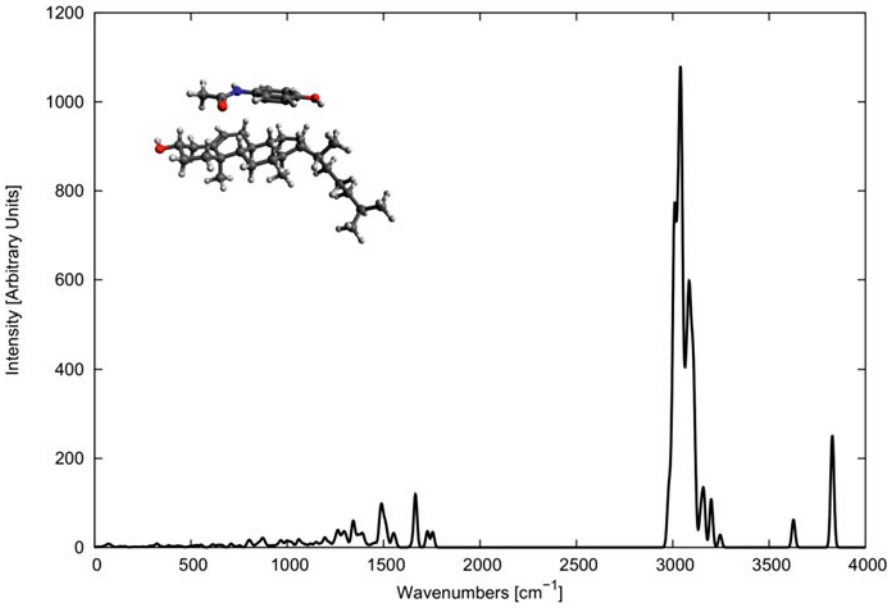

Fig. 18.8 The calculated Raman spectrum of acetaminophen–cholesterol complex

hydrogens. The second one at 3626 cm^{-1} comes from O-H vibrations. It is worthy to notice, that N-H (acetaminophen) and O-H (cholesterol) vibrations occurred at the same wavelength. When two of these molecules are very close to each other, the similar vibrations amplify each other. This effect can be seen in Fig. 18.8, where at 3075 cm^{-1} the amplitude is even higher than the sum of amplitudes for isolated molecules.

In conclusion, we have found that both molecules form a stable complex. The interaction between them is not able to destroy this stability. The high-frequency IR and Raman spectra for interacting molecules show that stretching vibrations C-H, O-H, and N-H tend to amplify each other.

Acknowledgments We would like to thank the PL Grid supercomputers network for sharing computational resources (grant name molecai2018).

References

1. Weber C, Noels H (2011) Atherosclerosis: current pathogenesis and therapeutic options. Nat Med 17:1410–1422. https://doi.org/10.1038/nm.2538
2. Moriya J (2019) Critical roles of inflammation in atherosclerosis. J Cardiol 73:22–27. https://doi.org/10.1016/j.jjcc.2018.05.010
3. Wang T, Butany J (2017) Pathogenesis of atherosclerosis. Diagn Histopathol 23:473–478. https://doi.org/10.1016/j.mpdhp.2017.11.009

4. Gburski Z, Górny K, Raczyński P (2010) The impact of a carbon nanotube on the cholesterol domain localized on a protein surface. Solid State Commun 150:415–418. https://doi.org/10.1016/j.ssc.2009.12.005
5. van Soest G, Marcu L, Bouma BE, Regar E (2017) Intravascular imaging for characterization of coronary atherosclerosis. Curr Opin Biomed Eng 3:1–12. https://doi.org/10.1016/j.cobme.2017.07.001
6. Kachel A, Gburski Z (1997) Chain formation in a model dipolar liquid: computer simulation study. J Phys-Condens Matter 9:10095–10100. https://doi.org/10.1088/0953-8984/9/46/007
7. Suhalim JL, Chung C-Y, Lilledahl MB, Lim RS, Levi M, Tromberg BJ, Potma EO (2012) Characterization of cholesterol crystals in atherosclerotic plaques using stimulated Raman scattering and second-harmonic generation microscopy. Biophys J 102:1988–1995. https://doi.org/10.1016/j.bpj.2012.03.016
8. Lim RS, Suhalim JL, Miyazaki-Anzai S, Miyazaki M, Levi M, Potma EO, Tromberg BJ (2011) Identification of cholesterol crystals in plaques of atherosclerotic mice using hyperspectral CARS imaging. J Lipid Res 52:2177–2186. https://doi.org/10.1194/jlr.M018077
9. Dawid A, Gburski Z (2003) Rayleigh light scattering in fullerene covered by a spherical argon film – a molecular dynamics study. J Phys Condens Matter 15:2399–2405. https://doi.org/10.1088/0953-8984/15/14/315
10. Small DM, Lyman G (1988) Duff memorial lecture. Progression and regression of atherosclerotic lesions. Insights from lipid physical biochemistry. Arterioscler 8:103–129
11. Gburski Z, Zerda T (1980) Vibrational dephasing and intermolecular interactions in liquids. Acta Phys Pol Ser A 57:447–454
12. Frink RJ (2010) Parallel cholesterol crystals: a sign of impending plaque rupture? J Invasive Cardiol 22:406–411
13. Nidorf SM, Eikelboom JW, Thompson PL (2014) Targeting cholesterol crystal-induced inflammation for the secondary prevention of cardiovascular disease. J Cardiovasc Pharmacol Ther 19:45–52. https://doi.org/10.1177/1074248413499972
14. Piatek A, Dawid A, Gburski Z (2011) The properties of small fullerenol cluster (C-60(OH)(24))(7): computer simulation. Spectrochim Acta Part -Mol Biomol Spectrosc 79:819–823. https://doi.org/10.1016/j.saa.2010.08.059
15. Piatek A, Dawid A, Gburski Z (2006) The existence of a plastic phase and a solid–liquid dynamical bistability region in small fullerene cluster (C60)7: molecular dynamics simulation. J Phys Condens Matter 18:8471. https://doi.org/10.1088/0953-8984/18/37/006
16. Dawid A, Górny K, Gburski Z (2011) The structural studies of fullerenol C60(OH)24 and nitric oxide mixture in water solvent – MD simulation. Nitric Oxide 25:373–380. https://doi.org/10.1016/j.niox.2011.08.004
17. Ozsoy MB, Pabuçcuoğlu A (2007) The effect of acetaminophen on oxidative modification of low-density lipoproteins in hypercholesterolemic rabbits. J Clin Biochem Nutr 41:27–31. https://doi.org/10.3164/jcbn.2007004
18. Dawid A, Dendzik Z, Gburski Z (2004) Molecular dynamics study of ultrathin argon layer covering fullerene molecule. J Mol Struct 704:173–176. https://doi.org/10.1016/j.molstruc.2004.01.065
19. Rosenberg L, Rao RS, Palmer JR (2003) A case-control study of acetaminophen use in relation to the risk of first myocardial infarction in men. Pharmacoepidemiol Drug Saf 12:459–465. https://doi.org/10.1002/pds.867
20. Hansson GK (2005) Inflammation, atherosclerosis, and coronary artery disease. N Engl J Med 352:1685–1695. https://doi.org/10.1056/NEJMra043430
21. Gburski Z (1985) Convergence of memory functions for the vibrational dephasing process in liquids. Chem Phys Lett 115:236–240. https://doi.org/10.1016/0009-2614(85)80687-4
22. Rosenson RS, Brewer HB, Davidson WS, Fayad ZA, Fuster V, Goldstein J, Hellerstein M, Jiang X-C, Phillips MC, Rader DJ, Remaley AT, Rothblat GH, Tall AR, Yvan-Charvet L (2012) Cholesterol efflux and atheroprotection: advancing the concept of reverse cholesterol transport. Circulation 125:1905–1919. https://doi.org/10.1161/CIRCULATIONAHA.111.066589

23. Gburski Z, Gray CG, Sullivan DE (1983) Information theory of line-shape in collision-induced absorption. Chem Phys Lett 100:383–386. https://doi.org/10.1016/0009-2614(83)80292-9
24. Dawid A, Gburski Z (1999) Interaction-induced light scattering in xenon clusters: molecular dynamics study. J Mol Struct 482–483:271–276. https://doi.org/10.1016/S0022-2860(98)00668-1
25. Grebe A, Latz E (2013) Cholesterol crystals and inflammation. Curr Rheumatol Rep 15:313. https://doi.org/10.1007/s11926-012-0313-z
26. Abela GS, Aziz K, Vedre A, Pathak DR, Talbott JD, Dejong J (2009) Effect of cholesterol crystals on plaques and intima in arteries of patients with acute coronary and cerebrovascular syndromes. Am J Cardiol 103:959–968. https://doi.org/10.1016/j.amjcard.2008.12.019
27. Kosmider M, Dendzik Z, Palucha S, Gburski Z (2004) Computer simulation of argon cluster inside a single-walled carbon nanotube. J Mol Struct 704:197–201. https://doi.org/10.1016/j.molstruc.2004.02.050
28. Abela GS, Vedre A, Janoudi A, Huang R, Durga S, Tamhane U (2011) Effect of statins on cholesterol crystallization and atherosclerotic plaque stabilization. Am J Cardiol 107:1710–1717. https://doi.org/10.1016/j.amjcard.2011.02.336
29. Dawid A, Gburski Z (1997) Interaction-induced light scattering in Lennard-Jones argon clusters: Computer simulations. Phys Rev A 56:3294–3296. https://doi.org/10.1103/PhysRevA.56.3294
30. Hanwell MD, Curtis DE, Lonie DC, Vandermeersch T, Zurek E, Hutchison GR (2012) Avogadro: an advanced semantic chemical editor, visualization, and analysis platform. J Cheminformatics 4:17. https://doi.org/10.1186/1758-2946-4-17
31. Gaussian 09, Revision D.01, Frisch MJ, Trucks GW, Schlegel HB, Scuseria GE, Robb MA, Cheeseman JR, Scalmani G, Barone V, Mennucci B, Petersson GA, et al, Gaussian, Inc., Wallingford, CT, 2009.
32. Dawid A, Górny K, Gburski Z (2015) The influence of distribution of hydroxyl groups on vibrational spectra of fullerenol C60(OH)24 isomers: DFT study. Spectrochim Acta A Mol Biomol Spectrosc 136., Part C:1993–1997. https://doi.org/10.1016/j.saa.2014.08.023
33. Dawid A, Górny K, Gburski Z (2017) Water solvent effect on infrared and raman spectra of C60(OH)24 fullerenol isomers: DFT study. J Phys Chem C 121:2303–2315. https://doi.org/10.1021/acs.jpcc.6b06484

Chapter 19
Change in Functional State of Bone Marrow-Derived Mesenchymal Stem Cells After Incubation with Silver Nanoparticles

N. A. Volkova, M. S. Yukhta, E. V. Pavlovich, and A. N. Goltsev

19.1 Introduction

Today among all known nanomaterials, industrial silver nanoparticles (AgNPs) have the highest degree of application [1, 2], largely due to their wide bactericidal properties [3]. AgNPs are contained in the numerous modern products including food nutritional supplements, cosmetics, packaging materials, textiles, electronics, home appliances, water disinfectants, room spray, and medical instruments [4]. The widespread use of AgNPs in everyday life has raised the issue of the safety and consequences of their application. Now the carcinogenic potential of AgNPs belongs to group D (not classified as carcinogenic to the organism). Thus, the enlarged use of nanosilver determines the importance of in-depth study of possible genotoxic and carcinogenic hazards of individual compounds, concentrations, and forms.

The transport of AgNPs inside the cell begins with cell membrane receptor recognition, internalization, and translocation and ends with degradation, accumulation, or clearance by cells. For most cells, uptake of AgNPs via endocytosis is a time, dose, energy-dependent process, and the major target organelles are endosomes and lysosomes. The works [5, 6] demonstrate that silver ions are more toxic to mesenchymal stem cells (MSCs) than AgNPs (in terms of absolute silver concentration). This effect is approximately three times higher for silver ions than for AgNPs. However, in other researches the biological effects on eukaryotic cells and microorganisms induced by both nanoparticles and ions of silver are the same according to the concentration range [7]. Previously, the mechanisms underlying the release of silver ions from nanoparticles were investigated [8, 9]. The liberation

N. A. Volkova (✉) · M. S. Yukhta · E. V. Pavlovich · A. N. Goltsev
Institute for Problems of Cryobiology and Cryomedicine of the National Academy of Sciences of Ukraine, Kharkov, Ukraine

© Springer Nature Switzerland AG 2019

O. Fesenko, L. Yatsenko (eds.), *Nanophotonics, Nanooptics, Nanobiotechnology, and Their Applications*, Springer Proceedings in Physics 222,
https://doi.org/10.1007/978-3-030-17755-3_19

of silver ions involves oxidative-reduction processes whose rate increases with a temperature in the range of 0–37 °C and decreases with pH growing [10, 11]. In addition, the presence of ligands (such as SO_4^{2-}, S^{2-}) in the microenvironment reduces significantly the adverse effects of silver ions and AgNPs, indicating that these ligands are able to bind silver or toxic metabolites actively. At present, AgNPs are used more than particles of micrometer size, since particles with dimensions in the range of several nanometers have higher ratio of area to mass. Such increase in the reactive surface area leads to a more efficient release of silver ions (Ag^+) in parallel with the low overall concentrations of silver and to the increase of the effect in relation to the applied mass of silver [12].

In present work the mesenchymal stem cells (MSCs) were chosen as a model for studying the possible cytotoxic effects of AgNPs, since these cells are progenitoric for most body tissues in the early stages of development and are involved in the processes of regeneration in an adult organism. Because of the high differentiated capacity, MSCs are the optimal cell models for analyzing the possible effects of AgNPs on morphofunctional characteristics of cells. MSCs can be cultivated for weeks without passing cells, which is important for long-term studies [13]. In addition, MSCs promote regeneration and restoration of mesenchymal tissues, such as bone, cartilage, muscle, ligament, tendon, adipose tissue, and stroma [14]. As reported in [5, 15, 16], silver has a size-dependent cytotoxicity and only AgNPs less than 10–15 nm are considered toxic.

Recent studies have shown that accumulation of AgNPs in the liver could induce cytotoxicity via oxidative cell damage. The AgNPs' risk assessment includes the verification of their biological properties, possible mechanisms, and efficient approaches to decrease their negative impact. Nanotoxicity focuses majorly on the testing of biological actions and is critical to understanding mechanisms and to predicting potentially side effects of AgNPs for sustainable development in the future [17].

In our previous studies [18] on the biological effects of gold nanoparticles (AuNPs), we have shown that some concentrations of 15 nm AuNPs (6–9 μg/ml) affected the immunophenotype, synthesis of type I collagen, ability to direct differentiation, and spectroscopic characteristics of rat bone marrow MSCs.

In this way nanoscale materials have a dose-dependent effect on biological objects. The finding of the presence/absence of AgNPs' cytotoxic action is an important direction of nanobiotechnological research. Here we present the results of investigation of what effect will have the incubation time and concentrations of 40 nm AgNPs on functional state of the bone marrow MSCs.

19.2 Materials and Methods

MSCs were isolated from resected femur of rats ($n = 7$, weighing 220–225 g) by washing out with Hank's solution (PAA, Austria), followed by flushing through a needle with gradually decreased diameter. The next step was a centrifugation

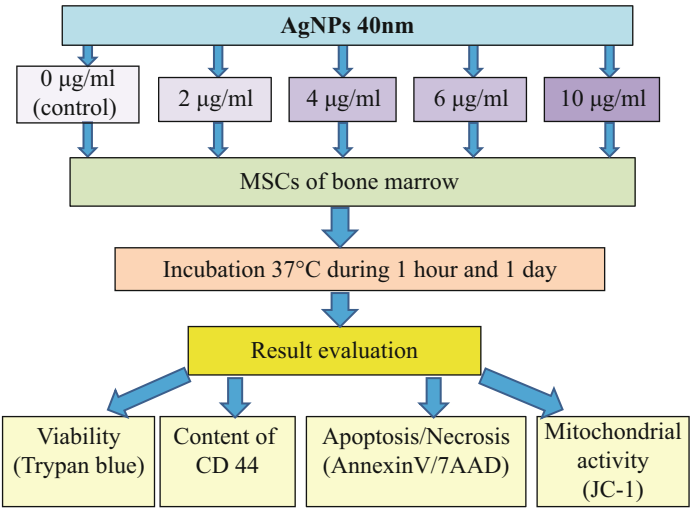

Fig. 19.1 Experimental scheme

at 840 × *g* for 5 min. The cells were resuspended in culture medium and plated on culture flasks (PAA) with 10^3 cells/cm^2 density. Cultural medium contained Iscove's Modified Dulbecco's Medium (PAA), 10% fetal bovine serum (FBS) (HyClone, USA), gentamicin (150 mg/ml) (Farmak, Ukraine), and amphotericin B (10 mg/ml) (PAA). Cultural medium was changed every 3 days. We used standard culture conditions (37 °C, 5% CO_2, 95% humidity) in a CO_2 incubator (Sanyo, Japan). At 80% confluence MSCs were detached with 0.25% trypsin solution (Hyclone) and EDTA (PanEco, Russia) in ratio 1:2 and replanted in other flasks. The third passage of MSCs was used in experiments.

The scheme of experiment is shown in Fig. 19.1. The AgNPs (Sigma-Aldrich, USA) were obtained by citrate synthesis with an initial metal concentration of 20 μg/ml.

The average size of AgNPs was 40 nm. Incubation of MSCs with AgNPs lasted for 1 hour and 1 day at 37 °C. The range of investigated AgNPs' concentrations was 2, 4, 6, and 10 μg/ml. Cells incubated under the same conditions without AgNPs were taken as a control. The percentage of viable cells in the samples was assessed with the trypan blue exclusion test [19].

CD44 expression by MSCs was analyzed using mouse anti-rat CD44-FITC monoclonal antibodies (BD Biosciences, USA) according to the manufacturer's instruction.

The apoptotic/necrotic processes in MSCs were studied using Annexin-V-FITC (Annexin V) (Becton Dickinson, USA) and 7-Amino-Actinomycin (7AAD) (BD) dyes. The functional state of mitochondria was investigated using JC-1 (BD) dye according to the manufacturer's instructions. FACS Calibur (BD) was used for this test. Data were analyzed using WinMDI v.2.8.

Statistical analysis of obtained data was performed using Excel (Microsoft, USA) and Statistica 8 (StatSoft, USA) software. To determine the significance of the differences in continuous variables between the groups, Student's *t*-test or Mann–Whitney *U*-test was used depending on the distribution of parameters. One-way ANOVA or Kruskal-Wallis ANOVA test was applied in the cases of multiple (more than two) comparisons.

19.3 Results and Discussion

The first stage of the study was to determine the effect of AgNPs' addition on the membrane integrity of the MSCs depending on the concentration and incubation time. It has been established that the best viability of cells in the Trypan blue exclusion test was found after 1-hour incubation with AgNPs in concentrations of 2–6 μg/ml (Fig. 19.2). At the same time, the use of 10 μg/ml AgNPs led to a significant decrease of this parameter by 1.24 times in comparison with the control on this term of observation.

After increasing of the incubation time up to 1 day the index of viability in all investigated samples decreased compared to the previous term of observation. AgNPs at the concentration of 2 μg/ml did not affect the viability of MSCs if compare to the corresponding control. However AgNPs' addition at the concentrations of 4, 6, and 10 μg/ml led to a decrease in this indicator by 1.7, 1.9, and

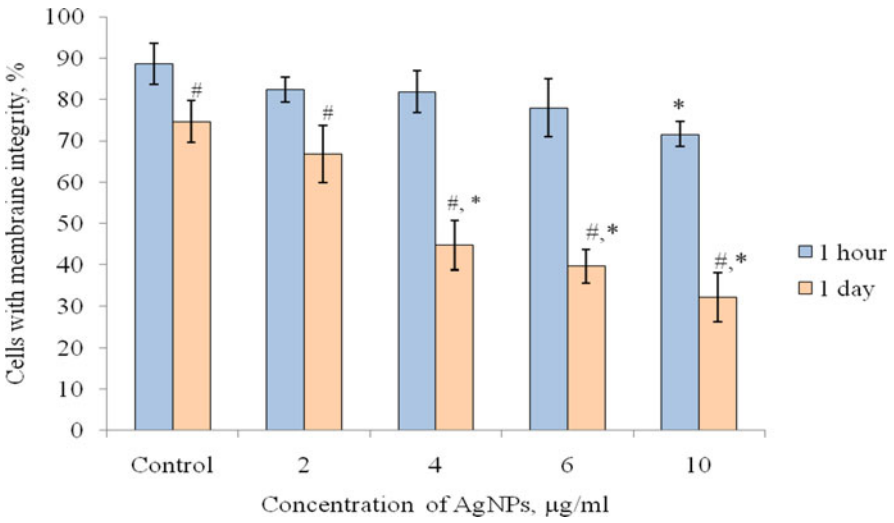

Fig. 19.2 Viability of MSCs after incubation with AgNPs. (Notes: * – difference is significant versus control ($p < 0.05$). # – difference is significant versus previous term of observation ($p < 0.05$))

2.3 times, respectively, versus control. The increase of dead cell number after 1-day incubation which was also detected in the control group may be a result of functional impairment in the MSCs, the degree of which increased with the addition of AgNPs.

Our results showed that cell viability is inversely related to concentration of AgNPs and incubation time. These findings are consistent with the work [20] that shows a decrease of cell viability after exposure to large AuNPs, i.e., 200 nm and 500 nm, but not to smaller AuNPs. In parallel, AgNPs have not been reported to alter cellular functions after 2 weeks of exposure [21], while the viability of MSCs decreased.

The next stage of the study was to determine the content of CD 44^+ MSCs after incubation with AgNPs. The CD44, also known as Pgp1, is a receptor for hyaluronic acid. Other known ligands are collagens, matrix metalloproteinases, and osteopontin. This marker is implied in adhesion function, cell–cell interaction, homing, hematopoiesis, and tumor metastasis [22]. The obtained data (Fig. 19.3) showed that cells in all experimental groups revealed high expression of CD44 (≥90%). AgNPs' addition at the studied concentrations did not lead to any significant changes in the level of CD 44 expression after 1-hour incubation.

The increasing of incubation time did not impair on the level of CD 44 expression by MSCs in the cases of 2, 4, and 6 μg/ml AgNPs' addition. Herewith, the use of AgNPs in the concentration of 10 μg/ml caused a decrease of this indicator by 1.2 times in comparison with the corresponding control.

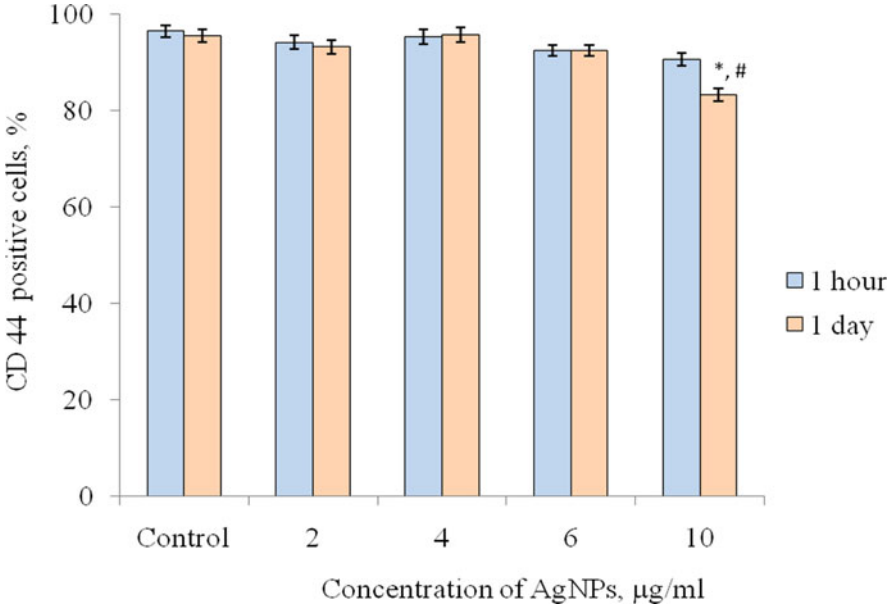

Fig. 19.3 Content of CD 44^+ MSCs after incubation with AgNPs. (Notes: * – difference is significant versus control ($p < 0.05$). # – difference is significant versus previous term of observation ($p < 0.05$))

The effect of 10 μg/ml AgNPs on the level of CD 44 expression is probably due to the oppression of the functional state of cells interacted with nanoparticles. These changes in the phenotype of the bone marrow MSCs give the prerequisites for the detection and prevention of disturbances in the processes of adhesion and proliferation.

The next stage of the work was to monitor the appearance of apoptotic and necrotic processes in bone marrow MSCs in conditions of interaction with AgNPs. It is known [23], nanoparticles of metals can cause apoptosis in cells of different origin. Thus, low doses of titanium dioxide and iron oxide lead to cell death due to the generation of oxidative stress and subsequent apoptosis by the mechanism of caspase-3 activation [24].

The results obtained by flow cytometry (Table 19.1) suggested that AgNPs at the concentrations of 2 and 4 μg/ml did not cause the development of necrosis/apoptosis processes in MSCs after 1-hour incubation. AgNPs' addition in the concentration of 6 and 10 μg/ml led to the decrease in percentage of Annexin $V^-/7AAD^-$ cells (by 27.65 ± 1.45% and 29.17 ± 1.27%, respectively) and to the increase in the number of apoptotic cells (by 17.18 ± 1.38% and 16.6 ± 1.12%, respectively) compared to the control samples of MSCs.

Incubation with AgNPs in concentration of 2 μg/ml during 1 day did not cause the development of necrosis/apoptosis processes in MSCs (Table 19.2). The number of Annexin $V^-/7AAD^-$ cells was significantly lowered by AgNPs addition in concentrations of 4, 6, and 10 μg/ml (by 19.01 ± 1.73%, 38.35 ± 1.25%, and

Table 19.1 Cytofluorometric analysis of MSCs after 1-hour incubation with AgNPs, staining with Annexin V and 7AAD

Sample/region	Annexin $V^+/7AAD^-$	Annexin $V^-/7AAD^-$	Annexin $V^+/7AAD^+$ + Annexin $V^-/7AAD^+$
Control	2.52 ± 0.61	87.79 ± 1.62	9.69 ± 1.32
AgNPs 2 μg/ml	3.76 ± 0.93	86.91 ± 2.35	9.33 ± 1.12
AgNPs 4 μg/ml	3.98 ± 1.18	85.16 ± 1.24	10.86 ± 1.15
AgNPs 6 μg/ml	19.70 ± 1.12[a]	60.14 ± 1.11[a]	20.16 ± 1.21[a]
AgNPs 10 μg/ml	19.12 ± 0.29[a]	58.62 ± 1.15[a]	22.26 ± 2.31[a]

Note: [a] Difference is significant versus control ($p < 0.05$)

Table 19.2 Cytofluorometric analysis of MSCs after 1-day incubation with AgNPs, staining with Annexin V and 7AAD

Sample/region	Annexin $V^+/7AAD^-$	Annexin $V^-/7AAD^-$	Annexin $V^+/7AAD^+$ + Annexin $V^-/7AAD^+$
Control	2.77 ± 0.13	87.88 ± 1.62	9.35 ± 0.25
AgNPs 2 μg/ml	3.45 ± 1.57	85.90 ± 1.18	9.65 ± 1.46
AgNPs 4 μg/ml	7.76 ± 1.29[a]	68.87 ± 1.37[a]	23.37 ± 1.28[a]
AgNPs 6 μg/ml	18.69 ± 1.7[a]	49.53 ± 1.27[a]	31.78 ± 1.35[a]
AgNPs 10 μg/ml	23.56 ± 1.36[a]	45.68 ± 2.27[a]	30.76 ± 2.64[a]

Note: [a] Difference is significant versus control ($p < 0.05$)

42.21 ± 1.56%, respectively) compared with corresponding control. The number of Annexin $V^+/7AAD^-$ cells that present an early stage of apoptosis was increased in the presence of AgNPs in concentrations of 4–10 μg/ml. The percentage of Annexin $V^+/7AAD^+$ and Annexin $V^-/7AAD^+$ cells (late stages of apoptosis, necrosis) after 1-day incubation with 4, 6, and 10 μg/ml AgNPs was significantly different from that in control samples.

Cell alterations during apoptosis are similar for most of cell types. In apoptotic cells, there are changes of lipid composition of plasma membrane: phosphatidyl serine transfers from cytoplasmic part of bilayer to outer side, causing caspase cascade activation, chromatin condensation, and disorder of electron transport chain in mitochondria and eventually arresting ATP synthesis. Programmed cell death can be triggered by receptor-mediated physiological stimuli resulted from genetic disorders, exposure to chemical or physical factors as well as by other changes in cells. We observed this effect after AgNPs' addition in the concentrations of 4–10 μg/ml. In our earlier studies a decrease in the percentage of viable cells and an increase of the number of apoptotic cells were also shown after 7-day culture of the fibroblasts, cryopreserved in the presence of AuNPs in concentration of 6 μg/ml [25].

The last stage of the work was the quantitative evaluation of the mitochondrial activity of bone marrow-derived MSCs after incubation with AgNPs for 1 hour and 1 day. As known, mitochondria play a major role in cellular partitioning of death-regulating signals; the loss of mitochondrial membrane potential is an early event in several types of apoptosis. The high transmembrane potential of healthy cells loaded with JC-1 allows for the formation and sequestration of JC aggregates in the mitochondrion, that detected by a peak in red/orange fluorescence (585 nm) [26]. The results obtained by flow cytometry (Fig. 19.4) suggested that AgNPs addition in the concentrations of 2 and 4 μg/ml did not affect mitochondrial activity in MSCs after 1-hour incubation. The use of AgNPs in the concentrations of 6 and 10 μg/ml led to its decrease by 1.21 and 1.28 times compared to the control samples of MSCs on this observation period.

An increase of the incubation period up to 1 day resulted in a significant decrease in the mitochondrial activity of bone marrow MSCs in all studied groups compared to the previous observation period (1 hour). The obtained data showed that in the control group after 1 day of incubation, 58.1 ± 4.2% of cells was fluoresced in the orange region of the spectrum and 41.9 ± 3.7% was fluoresced in the green one. The use of AgNPs at all concentrations for this incubation period resulted in a significant decrease in the number of cells with fluorescence in the orange region compared with the control. It should be noted that a significant difference of the investigated parameter between the samples with AgNPs' addition in the concentrations of 2, 4, 6, and 10 μg/ml was not observed.

Mitochondria-specific outcomes of AgNPs' exposure have been identified in multiple cell types, including (but not limited) loss of membrane potential, inhibition of enzymes involved in oxidative phosphorylation, and changes in calcium sequestration [27, 28]. Mitochondria appear to be the sensitive targets for nanosilver. Bressan et al. [27] have studied the interaction of nanosilver with human dermal

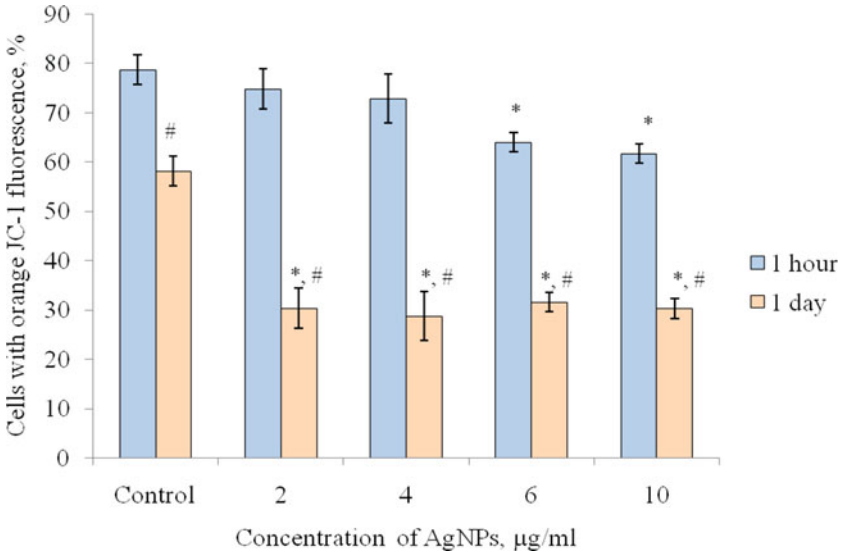

Fig. 19.4 Mitochondrial activity of MSCs after incubation with AgNPs. (Notes: * – difference is significant versus control ($p < 0.05$); # – difference is significant versus previous term of observation ($p < 0.05$))

fibroblasts. They have found that nanosilver particles accumulate outside the mitochondria, cause direct mitochondrial damage, and disturb the function of the respiratory chain, resulting in ROS generation and oxidative stress. AshaRani et al. [28] have suggested that the disruption of the mitochondrial respiratory chain by nanosilver increases ROS production and interruption of ATP synthesis, thus leading to DNA damages. However, the biological significance of mitochondrial toxicity due to AgNPs' exposure is currently incompletely understood.

19.4 Conclusion

In the present study we analyzed the effects of 40 nm AgNPs' concentration and incubation time on morphological and functional state of bone marrow MSCs. It was shown that the use of AgNPs under 1-hour incubation in the concentrations of 2 and 4 μg/ml did not lead to significant changes in viability, level of CD 44 expression, state of apoptotic and necrotic processes, and mitochondrial activity of the cells. The AgNPs' application in the concentrations of 6 and 10 μg/ml resulted in a decrease of mitochondrial activity, percentage of Annexin $V^-/7AAD^-$ cells, and an increase of the number of apoptotic cells compared with the control samples of MSCs. An increase of the incubation period up to 1 day led to a toxic effect of AgNPs (4–10 μg/ml) on MSCs that manifested in an activation of apoptosis

and necrosis processes, decreasing of viability, content of $CD44^+$ cells (AgNPs 10 μg/ml), and mitochondrial activity.

In summary, the internalization of nanosilver into stem cells had a significant influence on various aspects of cellular functions. Therefore, more studies are needed to investigate the effects of nanosilver on stem cell behavior in order to predict the possible health risks. The obtained results are related to the field of applied nanotechnology, which extends to clinical medicine, especially in the development of addressed drug delivery to the target cells or organs.

Acknowledgments This work has been supported by project No 70/18-H NAS of Ukraine "Biosafety and efficiency of interaction of inert metal nanoparticles with mesenchymal stem cells of bone marrow."

References

1. Henig RM (2007) Our silver-coated future. Onearth 29(3):22–29
2. Lara HH, Garza-Trevico EN, Ixtepan-Turrent L, Singh DK (2011) Silver nanoparticles are broad-spectrum bactericidal and virucidal compounds. J Nanobiotechnol 9(3):30–39
3. You C, Han C, Wang X et al (2012) The progress of silver nanoparticles in the antibacterial mechanism, clinical application and cytotoxicity. Mol Biol Rep 39(9):9193–9201
4. Faunce T, Watal A (2010) Nanosilver and global public health: international regulatory issues. Nanomedicine 5(4):617–632
5. Lima R, Feitosa LO, Ballottin D (2013) Cytotoxicity and genotoxicity of biogenic silver nanoparticles. J Phys Conf Ser 429(2):8–11
6. Carlson C, Hussain SM, Schrand AM et al (2008) Unique cellular interaction of silver nanoparticles: size-dependent generation of reactive oxygen species. J Phys Chem B 112(6):13608–13619
7. Park MV, Neigh AM, Vermeulen JP et al (2011) The effect of particle size on the cytotoxicity, inflammation, developmental toxicity and genotoxicity of silver nanoparticles. Biomaterials 32(1):9810–9817
8. Greulich C, Kittler S, Epple M et al (2009) Studies on the biocompatibility and the interaction of silver nanoparticles with human mesenchymal stem cells (hMSCs). Langenbeck's Arch Surg 394(3):495–502
9. Greulich C, Braun D, Peetsch A et al (2012) The toxic effect of silver ions and silver nanoparticles towards bacteria and human cells occurs in the same concentration range. RSC Adv 2(17):6981–6987
10. Kittler S, Greulich C, Gebauer JS et al (2009) Synthesis of PVP-coated silver nanoparticles and their biological activity towards human mesenchymal stem cells. Mater Chem 40(4):258–264
11. Kittler S, Greulich C, Diendorf J et al (2010) Toxicity of silver nanoparticles increases during storage because of slow dissolution under release of silver ions. Chem Mater 22(16):4548–4554
12. Loza K, Diendorf J, Greulich C et al (2014) The dissolution and biological effects of silver nanoparticles in biological media. J Mater Chem 2(12):1634–1643
13. Pittenger MF, Mackay AM, Beck SC et al (1999) Multilineage potential of adult human mesenchymal stem cells. Science 284(5411):143–147
14. Baksh D, Song L, Tuan RS (2004) Adult mesenchymal stem cells: characterization, differentiation, and application in cell and gene therapy. J Cell Mol Med 8(3):301–316
15. Greulich C, Diendorf J, Simon T et al (2011) Uptake and intracellular distribution of silver nanoparticles in human mesenchymal stem cells. Acta Biomater 7(1):347–354

16. De Lima R, Seabra AB, Durn N (2012) Silver nanoparticles: a brief review of cytotoxicity and genotoxicity of chemically and biogenically synthesized nanoparticles. J Appl Toxicol 32(4):867–879
17. Zhang T, Wang L, Chen Q, Chen C (2014) Cytotoxic potential of silver nanoparticles. Yonsei Med J 55(2):283–291
18. Volkova N, Pavlovich O, Fesenko O et al (2017) Studies of the influence of gold nanoparticles on characteristics of mesenchymal stem cells. J Nanomater 2017:6934757
19. Norkus M, Kilmartin L, Fay D et al (2013) The effect of temperature elevation on cryopreserved mesenchymal stem cells. CryoLetters 34(4):349–359
20. Soenen SJ, Manshian B, Montenegro JM et al (2012) Cytotoxic effects of gold nanoparticles: a multiparametric study. ACS Nano 6:5767–5783
21. Hackenberg S, Scherzed A, Kessler M et al (2011) Silver nanoparticles: evaluation of DNA damage, toxicity and functional impairment in human mesenchymal stem cells. Toxicol Lett 201:27–33
22. Dominici M, Le Blanc K, Mueller I et al (2006) Minimal criteria for defining multipotent mesenchymal stromal cells. The International Society for Cellular Therapy position statement. Cytotherapy 8(4):315–317
23. Kim K, Lee M, Park H (2006) Cell-permeable and biocompatible polymeric nanoparticles for apoptosis imaging. J Am Chem Soc 22(11):3490–3491
24. Rim K-T, Song S-W, Kim H-Y (2013) Oxidative DNA damage from nanoparticle exposure and its application to workers' health: a literature review. Saf Health Work 4(4):177–186
25. Pavlovich EV, Volkova NA (2015) Influence of gold nanoparticles on human fibroblast before and after cryopreservation. In: Fesenko O, Yatsenko L (eds) Nanoplasmonics, nano-optics, nanocomposites, and surface studies, Springer proceedings in physics 156. Springer, Cham
26. Cossarizza A, Baccaranicontri M, Kalashnikova G et al (1993) A new method for the cytofluorometric analysis of mitochondrial membrane potential using the J-aggregate forming lipophilic cation 5, 5′, 6, 6′-tetrachloro-1, 1′, 3, 3′-tetraethylbenzimidazolcarbocyanine iodide (JC-1). Biochem Biophys Res Commun 197(1):40–45
27. Bressan E, Ferroni L, Gardin C et al (2013) Silver nanoparticles and mitochondrial interaction. Int J Dent 2013:312747
28. AshaRani PV, Low Kah Mun G, Hande MP et al (2009) Cytotoxicity and genotoxicity of silver nanoparticles in human cells. ACS Nano 3:279–290

Part III
Applications

Chapter 20
Challenges in Studying the Incorporation of Nanomaterials to Building Materials on Microbiological Models

Adrian Augustyniak, Pawel Sikora, Krzysztof Cendrowski, Paweł Nawrotek, Ewa Mijowska, and Dietmar Stephan

20.1 Microbiologically Induced Deterioration (MID)

Microbial overgrowth is one of the main factors leading to the deterioration of building materials that can be caused by a variety of microorganisms. Such deterioration was reported in numerous structures including sewer systems, elevations, bridges, roads, and marine constructions [1, 2]. Biofilms formed on surfaces can generate an acidic attack that changes the chemical environment of cementitious materials and cause their damage. The deterioration can be caused by the production of organic and inorganic acids. These substances act together with several environmental

A. Augustyniak (✉)
Department of Immunology, Microbiology and Physiological Chemistry, Faculty of Biotechnology and Animal Husbandry, West Pomeranian University of Technology, Szczecin, Poland

Building Materials and Construction Chemistry, Technische Universität Berlin, Berlin, Germany

P. Sikora
Building Materials and Construction Chemistry, Technische Universität Berlin, Berlin, Germany

Faculty of Civil Engineering and Architecture, West Pomeranian University of Technology, Szczecin, Poland

K. Cendrowski · E. Mijowska
Nanomaterials Physicochemistry Department, Faculty of Chemical Technology and Engineering, West Pomeranian University of Technology, Szczecin, Poland

P. Nawrotek
Department of Immunology, Microbiology and Physiological Chemistry, Faculty of Biotechnology and Animal Husbandry, West Pomeranian University of Technology, Szczecin, Poland

D. Stephan
Building Materials and Construction Chemistry, Technische Universität Berlin, Berlin, Germany

© Springer Nature Switzerland AG 2019

O. Fesenko, L. Yatsenko (eds.), *Nanophotonics, Nanooptics, Nanobiotechnology, and Their Applications*, Springer Proceedings in Physics 222,
https://doi.org/10.1007/978-3-030-17755-3_20

factors, such as elevated humidity, temperature optimal for microbial growth, high carbon dioxide concentrations, high concentrations of chloride ions and other salts, and the presence of sulfates.

Microorganisms thrive on building materials mostly in the form of biofilms. First, the surface is preconditioned with lipids, sugars, and other organic substances that create an attachment point for cells. Once microorganisms reach the surface (brought with air, soil, water, or wastewater), they start multiplying and creating a biofilm matrix that can be composed of extracellular substances including polysaccharides, amyloids, cellulose, extracellular DNA, lipids, alginate, and many more. The main component is water which makes over 97% of biofilm [3]. Environmental biofilms can be complex and include many genera of bacteria and fungi. These microorganisms use synergistic interactions as they represent producers (autotrophs) and destruents (chemoorganotrophs). Changes in the cementitious materials can be associated with multiple biogenic reactions, including the generation of organic acids, carbon dioxide, nitric acid, hydrogen sulfide, and sulfuric acid [4, 5]. Furthermore, biofilms are emerging on the surface accordingly to the rules of ecological succession. Primarily attached cells produce organic acids (acetic, lactic, butyric, and others) that reduce pH of the environment. The highest contribution to MID is made by sulfur-oxidizing and sulfur-reducing bacteria from genera *Thiobacillus*, *Acidithiobacillus*, *Thiomonas*, and so on. Their metabolic activity can locally decrease the pH of concrete to as low as 1.0. These microorganisms start growing as soon as pH drops below 9, leading to a surface erosion and the formation of cracks. The biogenic release of acid degrades the cementitious material in the process of gypsum generation ($CaSO_4$) (in various hydration states) and possibly ettringite ($3CaO \cdot Al_2O_3 \cdot CaSO_4 \cdot 12H_2O$ or $3CaO \cdot Al_2O_3 \cdot 3CaSO_4 \cdot 31H_2O$). The production of ettringite increases internal pressures leading to the formation of cracks.

Economic losses arising from MID are counted in billions of US dollars annually [4]. Therefore, methods to mitigate this problem are being sought, and nanomaterials were proposed as a solution. This chapter is to underline the chances, risks, and evaluation problems associated with the use of microbiological models in testing nanomaterials incorporated with cementitious composites.

20.2 Mitigating Deterioration with Nanomaterials

Building materials are being constantly improved to withstand harsh conditions, including freezing and thawing, abrasion wear, elevated temperature, and MID. For that reason, nanomaterials were proposed as an admixture to cementitious composites. These substances can play multiple roles in building materials, e.g., silica nanoparticles can be used to increase the mechanical strength, while antimicrobial properties of metal or metal oxide nanoparticles can be used in self-cleaning composites which are designed to be more resistant to a microbial overgrowth than conventional concrete.

The International Organization for Standardization (ISO) created standards (ISO/TS 80004-2:2015; ISO/TR11360:2010) [6, 7], defining nanoobjects as the separate parts of material existing in nanoscale, in one, two, or three dimensions, where at least one dimension is 100 nm or less. Three-dimensional nanoobjects are called nanoparticles, whereas two-dimensional nanostructures are indicated as nanofibers (e.g., nanotubes, nanorods, or nanowires). Monodimensional structures are known as nanoplates. Nanomaterials are also defined for having nanosized external parts or surface (e.g., characterized by pores in nanoscale). Furthermore, nanomaterials express different properties from the same materials synthetized in microscale [6, 7].

The 197-NCM RILEM Technical Committee report entitled "Nanotechnology in Construction Materials" (published in 2004) [8] is the first document describing the potential application of nanotechnology in the development of building materials technology. Thanks to their properties associated with their nanometric size, nanomaterials enable the modification of cementitious composites in direction that is unreachable with conventional admixtures and additives. Introducing nanomaterials even in small concentration can lead to a significant reduction in the amount of cement used in the composite, without degrading (and in some cases with improving) its properties [9].

Titanium dioxide (TiO_2), silica nanoparticles (SiO_2), and carbon nanotubes can be highlighted among nanomaterials used in the industrial scale [10]. Other nanomaterials such as aluminum oxide (Al_2O_3), iron oxide (Fe_2O_3 and Fe_3O_4), calcium carbonate ($CaCO_3$), and carbon materials (graphene oxide or carbon black) are mostly used in a laboratory or technical scale [9, 11]. Furthermore, a great interest was put in the recent years into the incorporating cementitious composites with molecular hybrids, e.g., core-shell-type materials. These structures can simultaneously provide multiple functions within the composite, namely, increase the stability and dispersion rate in water suspension [12, 13]. They also decrease a demand for the addition of nanomaterial which allows to avoid problems associated with the consistency change in cementitious composite. Such nanocomposites, including silica/titania [13], carbon nanotube/silica [14], or silica/magnetite [15], were thoroughly described in the literature.

Depending on the type of nanomaterial used, its influence on cementitious composite can be variable. The introduction of nanoparticles to cementitious composite influences the properties of material through their nanofilling activity that enables an increase in the dimensional packaging of cement particles. The consequence arising from this phenomenon is the compaction of microstructure and the improvement of interfacial transition zone (ITZ) between the cement paste and aggregate. Moreover, nanostructures exhibit nucleation effect, playing the role of crystallization of seeds for calcium hydroxide (CH) [16]. Additionally, certain nanomaterials (such as SiO_2 or Al_2O_3) exhibit a noticeable pozzolanic activity; thus, they react with available CH, forming a secondary type of calcium silicate hydrate (C-S-H) gel in the cement paste [14]. Titanium dioxide is currently used as an cement admixture [17] that provides the self-cleaning and bactericidal properties, whereas copper oxide (CuO) or zinc oxide (ZnO) provides only bactericidal properties.

20.3 Release of Nanomaterials

Nanotechnology is dynamically developing, thanks to the successful outcome of the research. On the other hand, the influence of nanomaterials on the natural environment still has not been fully described [18]. Unfortunately, the introduction of nanoparticles to the environment and their emission to air, water, and soil create hazards to living organisms [19]. The production scale and vast application potential of nanomaterials has made their presence in the environment unavoidable. Nanostructures can intentionally or accidentally enter the natural environment through many routes and then interact with living organisms. These exchange routes are shown in Fig. 20.1.

In the case of nanomaterial-containing cementitious composites, there are several time-points when nanomaterials are likely to be released. The "life cycle" of cementitious composite (e.g., concrete) consist of four main stages that include the production (I), implementation and use (II), the demolition of building containing the material (III), and the storage and utilization of construction and demolition waste (IV) [21]. Such "life cycle" of a cementitious composite in building and the potential release points of nanomaterials are depicted in Fig. 20.2.

Research data confirm that the interaction between nanomaterials and living organisms can be harmful to the latter. Nanoparticles were found to be toxic against protozoans, bacteria, fungi, plants, and animals (including mammals). The interac-

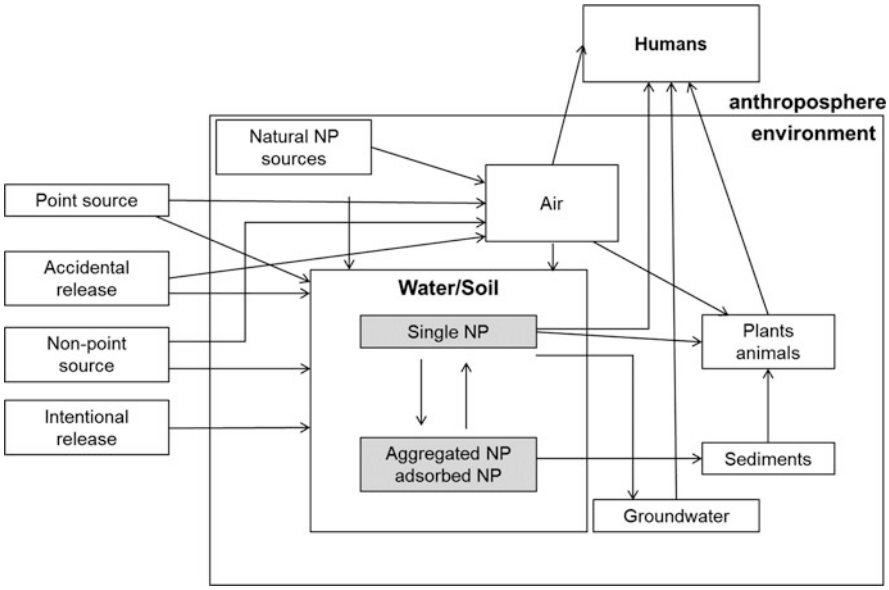

Fig. 20.1 Nanoparticle pathways from the anthroposphere into the environment, reactions in the environment, and exposure of humans. (Redrawn from [20] with the permission by Elsevier)

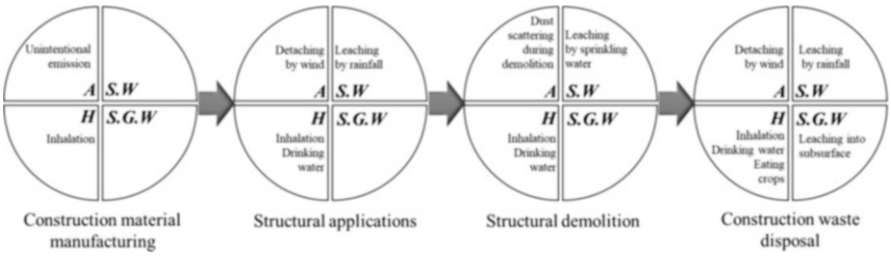

Fig. 20.2 Primary pathways into the environment and corresponding exposure routes to humans expected during the life cycle of manufactured nanomaterials (MNMs) used in construction (A for air, S.W. for surface water, S.G.W. for soil and groundwater, H for human). (Redrawn from [21] with the permission by Springer)

tion effects between nanomaterials and living organisms can be manifold, starting from genetic changes, through affecting cell structures, up to the degradation of tissues and organs. Exposition to the high amounts of nanomaterials may lead to an organism dysfunction or decease [22, 23].

The influence of nanomaterials can have variable effects on bacteria. Recent studies have shown that the exposition of *E. coli* or *Salmonella* Typhimurium to ZnO and TiO_2 can lead to the deformation of cytoplasmic membranes through the osmotic stress [24]. Because of their size, nanomaterials can be released from composites and further transferred in multiple ways (Figs. 20.1 and 20.2), which makes difficult the proper estimation of their effect on the natural environment and humans [18, 20]. Environmental studies on soil microbiota have shown that nanoparticles can influence the qualitative and quantitative composition of these microbial consortia. The addition of metal oxides (TiO_2, CuO, and ZnO) can lead to changes in the structure of soil microbiomes [25, 26]. Similar changes can be caused by carbon nanomaterials (including nanotubes) [27]. This has a high relevance on the environmental level, because a quantitative disruption in the microbiome can influence the natural phenomena that have microbiological origin, including possible interruptions in the cycles of elements (nitrogen, phosphorous, sulfur, and carbon) [28].

20.4 Estimating Toxicity of Nanomaterials

The toxicity of nanomaterials was confirmed in the laboratory environment, although, as it was shown in the previous chapter, estimating the actual environmental risks remains problematic. It is reflected in the recent scientific literature [29, 30], as well as in the recent report of American Concrete Institute, ACI 241R-17 [31], where the potential toxicity of nanomaterials is acclaimed, but there is no particular information or guidance on specific deleterious effect that they cause in living organisms.

The mechanism of toxicity has not been thoroughly described so far. Currently, two hypotheses are predominant in the literature. First is based on the toxicity of metal ions that are being released from metallic nanoparticles. Second hypothesis explains the toxicity of nanomaterials strictly as the activity of formed reactive oxygen species (ROS). In fact, these radicals can debilitate all components of the cells [22, 23, 32]. For example, photocatalytic nanoparticles such as TiO_2 can be activated with UV irradiation to produce ROS. In this process, the energy carried by irradiation is transferred to the surface of nanoparticles that releases an electron (e^-). The electron is transferred to the molecular oxygen which results in the generation of superoxide (O_2^{*-}). Missing electron is restored by its capture from the hydroxyl group that becomes the hydroxyl radical (OH^*) [33].

The evaluation of the potential toxicity of nanoparticles is complex, and many factors can have an impact on their final activity. Their size, shape, chemical composition, tendency to agglomerate, solubility, surface area, and charge can be highlighted among other [18, 34]. Such combination makes the toxicity evaluation of given nanomaterial greatly difficult. Boverhof and David [35] suggest that the toxicity of nanomaterials should define them in at least 12 ways, including their size, shape, surface charge, whether particles are aggregated or agglomerated, solubility rate, and type of solvent. It was observed that 70–90% of existing studies does not comply with this standard [10]. For that reason, the results obtained by different authors often cannot be compared, and the differences in the characteristics of used particles can explain the discrepancies found in many studies between allegedly the same nanomaterials [36]. The toxicity evaluation of carbon nanotubes can be shown as a good example. These nanomaterials gathered great interest, because their activity can pose a threat similar to that of asbestos fibers. Studies seem to confirm this hypothesis, although according to Jones et al. [37] there are over 50,000 possible variants of carbon nanotubes that can greatly differ in terms of their toxicity. As indicated by Świdwińska-Gajewska and Czerczak [38], because of the differential composition and size (mono- or multiwalled), shape (rigid fibers or tangled thread), as well as their properties, the enormous possibilities of their modification, and their possibility to be contaminated with metal catalyst (that can influence the toxicity), the determination of one normative for this group appears unreachable. For that reason, it was suggested to independently evaluate the toxicity of all kinds of nanotubes [38].

The size distribution of nanomaterials is another problem that should be taken into consideration. Once applied, nanoparticles start changing their size, which usually leads to their agglomeration. Therefore, nanomaterials should be separately studied after synthesis, during their release to the environment and after a transformation in the environment, because their properties can be variable in all these stages (Fig. 20.3) [18, 21]. Caballero-Gutzman and Nowack [36] described a tool called material flow analysis (MFA) that was designed to predict the flows of engineered nanomaterials (ENM) to the environment. The authors suggested that MFA modeling should rely mostly on quantitative and empirical data. Furthermore, the dynamic description of ENM release should be used to reproduce the scenarios

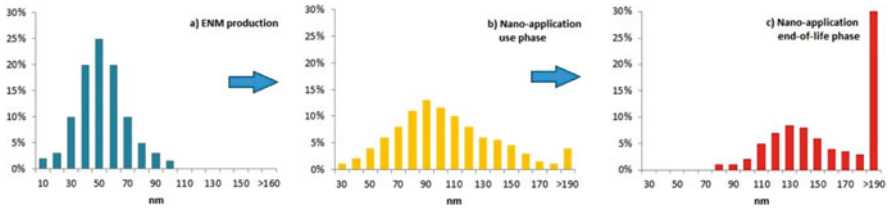

Fig. 20.3 Variation in the size distribution of engineered nanomaterials throughout their life cycle (**a**). During production, the size distribution of the ENM powder will be largely within the nano-range (**b**). During its incorporation into a nano-product, the ENM size can change due to agglomeration or functionalization reactions (**c**). Once released from the application, most of the nanomaterial will be found agglomerated, aggregated, or attached to particles that are no longer in the nano-range. (Reprinted from [36] with the permission by Elsevier)

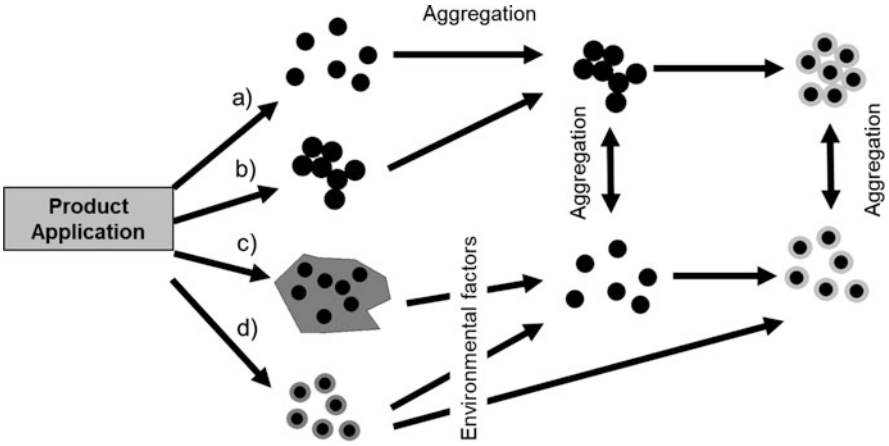

Fig. 20.4 Release of NP from products and (intended or unintended) applications: (**a**) release of free NP, (**b**) release of aggregates of NP, (**c**) release of NP embedded in a matrix, and (**d**) release of functionalized NP. Environmental factors (e.g., light, microorganisms) result in the formation of free NP that can undergo aggregation reactions. Moreover, surface modifications (e.g., coating with natural compounds) can affect the aggregation behavior of the NP. (Redrawn from [20] with the permission by Elsevier)

that are environmentally relevant and include changes in nanomaterials at each stage of their "life cycle."

In the case of cementitious materials, this problem can be even higher. Moreover, this aspect undermines the utility of laboratory results, because of the differentiated distribution of particle sizes on various stages of cementitious composite manufacturing. Before being introduced, nanoparticles often have a desirable dispersion, although during their introduction they become agglomerated which leads to changes in the granulation. Later on nanomaterials, agglomerates, and nanoparticles embedded in the cement matrix are being released (Fig. 20.4a–d). During the production process, the size distribution would be mostly in nanometric scale

(Fig. 20.4a), and after the implementation of nano-product, the size of nanoparticles can be changed by the agglomeration or functionalization processes (Fig. 20.4b). After the release from the composite, the majority of nanomaterial is likely to become agglomerated, aggregated, or attached to particles that exceed nanoscale (Fig. 20.3c). The toxicity of nanomaterials is highly correlated with their size, where it is assumed that the smaller the nanoparticle is, the higher is its toxicity [29, 39]. Thus, there is a high probability that such changes also alter the toxicity of studied nanomaterial. Therefore, all of the showed stages should be evaluated while estimating the toxicological properties of nanosized cement admixtures.

Proper dispersion is one of the main factors required for a nanomaterial to express toxicity. There is much data underlining the toxicity of dispersed nanomaterials. Nevertheless, reaching the proper state of dispersion after implementing them to cementitious composites is very complicated. The preparation of cement mortars requires specific and limited water amount in which the nanomaterial can be dispersed prior to the addition to cement, whereas the mixing process is simplified in order to be energy-efficient. Furthermore, the addition of surfactants that would improve dispersion could have negative influence of the hydration kinetics in cement. Because of these restrictions, the only solution is based on the addition of plasticizers or superplasticizers. Studies conducted by Sikora et al. [40] showed that the dispersion conducted with a method that is commonly used in introducing nanomaterials to cementitious composite (mechanical stirring combined with sonication) is inefficient and the toxicity of used nanomaterials even before their introduction to the cementitious composite can be minimized.

Several groups of organisms are being used in the toxicological analyses. Plant (e.g., *Lepidium sativum* L., *Lemna* sp. L.) and animal models (*Daphnia magna*, *Danio rerio*) are among the most often used [41–44]. In the case of bacteria, the toxicity is usually studied by measuring the bioluminescence of *Aliivibrio fischeri* or testing toxicants on selected bacteria from genus *Salmonella* in the Ames test [45, 46]. All listed model organisms are useful in studies regarding chemicals and all factors that can be homogenously distributed in the tested environment. In the case of nanomaterials it is more complicated, because of their properties and dispersion. As they are solid compounds, they descend to the bottom of test dish which can impede their contact with the tested organism. Microorganisms can be a solution to this problem, because they are homogenously distributed in the liquid, especially model reference strains such as *E. coli*, *P. aeruginosa*, or *C. albicans* [40]. The another advantage of microorganisms is their short generation time and a simplicity in providing them the optimal growth conditions, especially in the case of prototrophic bacteria [47]. Nevertheless, the currently used toxicological methods are based on studying the bactericidal or bacteriostatic effects on model microorganisms. These investigations do not usually include the metabolic activity of tested bacteria or fungi, what can be crucial in the future estimations regarding the nanomaterial toxicity in the environment. For that reason it would be advisable to take microbial metabolism into account.

Microorganisms are the first group of living organisms that deals with any contamination in the natural environment. Therefore, bacteria are proposed and

used in the ecotoxicological studies of nanomaterials [46, 48]. They allow efficient analysis of the toxicity of studied nanomaterial. Among all scientific possibilities, also those indicated above, microorganisms appear to be perfect candidates to be used in toxicological studies describing the activity of nanomaterials and their impacts in the environment. Studying these interactions on microorganisms has many advantages. Firstly, microorganisms are present in every environment within the biosphere, and they are the first living organisms that interact with contaminants entering the environment. Secondly, they can actively interact with toxicants directly in the environment, because of the fact that considerable part of microbial metabolism is kept outside of the cell or in the biofilm matrix. Bacteria and fungi can locally change their environment, e.g., releasing lytic enzymes that degrade complex substances in order to increase their bioavailability [3, 49]. Therefore, the toxicant can be changed even before it is internalized in the cell. This also confirms that apart from abiotic factors, also living organisms can modify the studied nanostructure. Furthermore, it has been shown on the model of *Tetrahymena* sp., that nanomaterials can be biomagnified (i.e., transferred up the trophic chain) [40, 48]. Finally, there is a scientific discussion on the potential consequences of applying nanomaterials and the necessity to provide proper legislative measures [50–52]. Furthermore, the methodology that should be used in the description of nanomaterials in the natural environment is also discussed [53–55].

20.5 Issues with Reference Microorganisms

There are several model organisms that are usually applied in the toxicological studies of nanomaterials. The most commonly used species are *E. coli* (a Gram-negative bacterium), often followed by *Staphylococcus aureus* (a Gram-positive bacterium), and *Candida albicans* (a yeast). The main problem is that even though strains belong to the same species, they can express different sets of metabolic activity and defense mechanisms. It is clearly visible in the case of antibiotic-resistant strains that can greatly differ from each other. This problem was previously described by Sikora et al. where the growth kinetics of four strains of *E. coli*, including two wild and two genetically modified minimal genome strains, was studied [40, 56]. The comparison of the results showed that these bacteria differently responded to metal oxide nanoparticles. *E. coli* is a preferred model because of its fast growth and relatively low nutritional demands. Nevertheless, this microorganisms is a common inhabitant in the gastrointestinal tract, whereas environmental strains should be taken into consideration for the environmental applications [57]. Especially, microorganisms that can have a high importance in the environment, such as bacteria from genera *Pseudomonas* and *Streptomyces*, are advisable. These microorganisms were described below only as two selected examples that could be included in the toxicological studies of materials used in outdoor applications [58, 59].

Streptomyces spp. are soil-dwelling microorganisms that are present in aquatic and terrestrial environments. These spore-producing filamentous bacteria are present in soils of every continent as well as in fresh and marine water [60, 61]. Years of studies and discoveries showed that these actinomycetes are responsible for production of many antibiotics that entered the common medical use, including streptomycin, cephalosporin, tetracycline, neomycin, daptomycin, and many more [62]. They can also produce numerous pigments, such as medermycin, undecylprodigiosin, or actinorhodin, which may have antibiotic activity [63, 64]. Actinomycetes are autochthonic to plants, and many strains can promote their growth in several ways. Their lytic activity leads to the mineralization of organic matter; therefore, they contribute to soil development. Furthermore, streptomycetes provide plants with phosphorous and amino acids [65]. Some strains are also producers of plant growth hormones, e.g., auxin (IAA) [66]. Streptomycetes can also be involved in a mutualistic relation with plants. Their positive effect on the development of mycorrhizae was confirmed, where streptomycetes were endophytes producing secondary metabolites against plant pathogens, including bacteria, fungi, and insects [67–69]. Nevertheless, these bacteria can also contribute to the deterioration of building materials, because these are also associated with the sulfur oxidation. Furthermore, their presence in the material is almost certain when sand was used to prepare the cementitious composite [1]. All of these features make them good candidates to be included in toxicological studies, at least in the initial stage before assessing whole microbiomes.

Pseudomonas spp. are Gram-negative bacilli belonging to type *Gammaproteobacteria*, order *Pseudomonadales* and family *Pseudomonadaceae*. The shape of their cells is usually straight or slightly curved, and their average size is in the range of 0.5–1.0 × 1.5–5 μm. They are motile, having one or several flagella, and their metabolism is strictly aerobic [58]. On the one hand, these bacteria are opportunistic pathogens that can cause diseases leading to great losses in medicine and agriculture, but on the other hand they are highly adapted to the environment they inhabit, what can be used, e.g., in bioremediation purposes [70, 71]. Depending on the species and its adaptation to the environment, they can have various functions in the environment. While *P. syringae* shows pathogenicity to plants, *P. protegens* can secrete substances that inhibit development of pathogenic microorganisms [72]. Other species associated with rhizomicrobiota and expressing growth-promoting factors is *P. fluorescens* [73]. Similar to actinomycetes, some pseudomonads also can produce phytohormones (IAA). Furthermore, they actively solubilize phosphates, produce siderophores, and increase the accessibility of ammonium nitrogen in the environment. These bacteria can also actively attach to plant tissues [74]. They are also known for the high ability to form biofilms. They contribute to the development of biofilm matrix by producing alginate. Pseudomonads can also actively interact with nanomaterials leading to their secondary dispersion [75].

Microorganisms almost never occur in monocultures, and microbial populations are also variable in terms of their growth dynamics. They differ in generation time, nutritional demands on carbon sources, or final electron acceptors. Furthermore, these populations often are a part of biofilm which contains all abovementioned

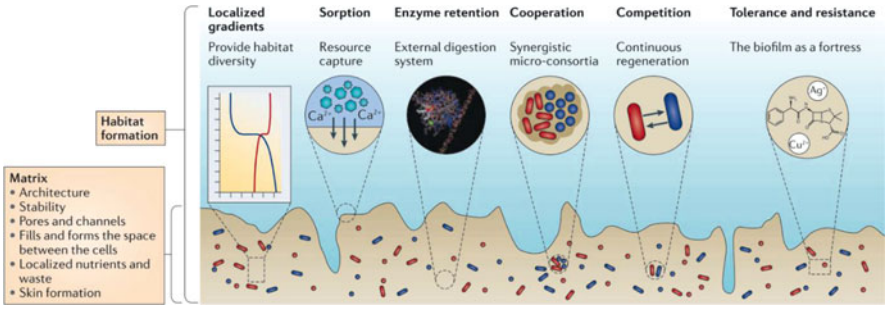

Fig. 20.5 Emergent properties of biofilms and habitat formation. Bacterial cells in biofilms can be considered to be habitat formers, owing to their generation of a matrix that forms the physical foundation of the biofilm. The matrix is composed of extracellular polymeric substances (EPS) that provide architecture and stability to the biofilm. Nutrients and other molecules can be trapped by sorption both to EPS molecules and to the pores and channels of the matrix, whereas skin formation by hydrophobic EPS molecules enhances the ability of the biofilm to survive desiccation. Biofilms derive several emergent properties—that is, properties that are not predictable from the study of free-living bacterial cells—from the EPS matrix. These properties include localized gradients that provide habitat diversity, resource capture by sorption, enzyme retention that provides digestive capabilities, social interactions, and the ability, through tolerance and/or resistance, to survive exposure to antibiotics. (Reprinted from [3] with the permission of Springer Nature)

groups that grow in synergistic or antagonistic relations. The deposition of cells in biofilms depends on the aerobic conditions. Aerobic cells are gathering closer to the air interphase, while anaerobic microorganisms can be found in the interface between the cementitious composite and biofilm matrix. As it seems, this growth is dependent on numerous factors that cannot be artificially recreated in the laboratory, even in a climatic chamber [3]. The basic properties of biofilm and the functions of its matrix are shown in Fig. 20.5.

The evaluation of non-photocatalytic cement-based surfaces has not been standardized to date. On the other hand, microbiological tests presented in the literature are often based on undiversified models [13, 76–78]. The specific morphological and metabolic features of used bacteria seem to be neglected by the authors, and the information is usually limited only to the genus group designation, or GenBank number. Genotyping is based on gene 16S rRNA that usually enables the identification down to the genus level [76, 79]. Nevertheless, this sequence may be not enough to accurately determine the taxonomic position (species) of given bacterium [80, 81]. Moreover, it should be highlighted that there can be a high diversity even between two strains belonging to the same species. For example, different *E. coli* isolates can express variability, e.g., in biofilm formation capacity and the ability to adhere to surface. They can also have dissimilar antibiotic resistance pattern. The genome of some strains can also contain bacteriophages. In that case stress response in the bacterium can induce the phage to multiply which (in some cases) leads to the production of toxins, such as Stx toxin [57, 82, 83]. Moreover, references describing studies on microbiological models should also

include the full name of the bacterium along with an indication to the history of its isolation and the collection where it is kept. This information is necessary because there can be many derivatives of one strain that undergo genetic modifications by genetic engineering or multiple passaging that can change their characteristics; thus, their response to the toxicant can be variable [84]. The NCBI taxonomy browser shows over 3000 records while searching for *E. coli* [85]. The variable response of four *E. coli* possessing different genetic profiles was shown in the tests assessing the toxicity of metal oxide nanoparticles on the bacterial population growth kinetics [40]. Therefore, future endeavors toward developing methods and selecting strains should include their full characteristics that are well known and described.

Nanomaterials act differently than antibiotics, because their diffusion can be minimalized by the agglomeration and aggregation processes. Aggregated nanomaterial has decreased surface area; therefore, it becomes less available to the microorganisms. This process can diminish the known toxicity of well-dispersed nanostructures, which was shown on the example of metal oxide nanoparticles [40]. In this study, pure nanoparticles were used, so that solution did not contain free ions that could lead to the higher toxicity. Prior to use, nanoparticles were mixed and sonicated, precisely the way as it would be done in the industry before mixing with cement. The observed toxicity was diminished due to the agglomeration that was clearly visible in Transmission Electron Microscopy (TEM) images. Another reason for such outcome was the purity of nanomaterial, because purified nanomaterial can have lower tendency to release free ions. This problem was described by Beer et al. [86], who indicated that the presence of ions can give false-positive results where the toxicity of ions is measured instead of nanoparticles.

Considerable changes in the measured toxicity can be attributed to the agglomeration of nanoparticles [87]. Particularly during the introduction of nanomaterials to the cement-based composites, the limited amount of water and lack of surfactants can increase the agglomeration. Furthermore, in the industrial preparation of cementitious composites, the maximum possible dispersion would be achieved by a combination of sonication and mixing [87–90]. When the nanomaterials are studied in the laboratory conditions, agglomerated particles may possibly descend to the bottom and become less accessible to microorganisms. This should be taken into consideration during the biofilm formation assay. The difference was shown between the locations of biofilms formed by *E. coli* and *P. aeruginosa* [40]. *E. coli* tends to produce it at the bottom of test plate, whereas *P. aeruginosa* can increase the biomass in the air/liquid interface, what should be considered while designing the toxicity test [91–94].

Several adaptation mechanisms in microorganisms are known to help them survive in the environment that contains metallic nanoparticles. This defense response includes the secretion of antioxidative substances (pigments) and exopolymers that separate cells from the external environment, creating a space in which they are less exposed to negative environmental conditions [64, 95]. Therefore, gathering cells in a biofilm provides better protection than obtained in the planktonic (unattached) form [3]. Metals and metal nanoparticles that reach cells can be harmful to cellular structures. In order to deal with this threat, microorganisms evolved to regulate

the uptake and efflux of metals through transmembranous proteins. Furthermore, they can chemically modify the toxicant and create a bypass in the metabolic routes that are affected by the metal. Other mechanisms are based on catching the contaminant in the periplasmic space, as well as immobilizing it inside or outside the cells through the production of siderophores [96, 97]. Nanomaterials can enter the cells which was confirmed in the study investigating the interaction between a streptomycete and UV-activated titania/silica nanospheres. In this study an internalization of TiO_2 was confirmed in the cells of streptomycete. Conducted elemental mapping showed the presence of TiO_2 inside the cell. Nanomaterial was concentrated in the areas associated with the deposition of polyphosphate which presumably can be related with the accumulation of nanoparticles in the biomass of this bacterium [95].

In many cases, the studied toxicity of nanomaterials does not fully explain the phenomena that may occur when the activity of nanostructures does not end with the cell death. The question arising from this problem is what the consequences are of such interaction for the cell and its environment. Does the cell go to anabiosis or maybe it becomes more active and starts producing secondary metabolites? Because of the characteristics of nanomaterials, such contact with a high probability will induce a cellular stress response. Such stress can be induced by ROS which are being generated in nanomaterial-containing environments [21, 96]. Findings presented by Ge et al. [98] showed changes in the microbiota after the release of nanomaterials, although the authors did not inform whether the observed phenomena were caused solely by a direct interaction between bacteria and nanomaterials. Current data indicates that there is also another possibility to be taken into account, in which nanomaterials may stimulate bacteria changing their activity in the environment. The creation of reactive oxygen species has been extensively studied, although the defense mechanisms used by bacteria against ROS are still largely unknown. Microorganisms can use enzymes such as superoxide dismutase, catalase, peroxidases, or glutathione reductase to avoid oxidative stress [97, 99]. Pigments also has similar function [64]. Nevertheless, still there is missing data showing how the reaction to stress affects the cellular metabolism, although there are first findings showing that the excess of ROS can be used by cells for adenosine triphosphate (ATP) overproduction and using them, e.g., in the conversion of keto acids to carboxylic acids [97]. For that reason, the metabolic features of model organisms should be also included in the toxicological studies, especially if nanomaterial have potential to induce the secretion of active compounds. Such overproduction of secondary metabolites can potentially cause an indirect reaction of the toxicant with the environment, which triggers changes caused by stimulated microorganisms. There is evidence that nanomaterials can stimulate bacteria. For example, titanium dioxide caused overexpression of flavins in *Shewanella oneidensis* and pigment production in *Streptomyces* sp. [95, 100]. It was confirmed that the release of TiO_2 and ZnO nanoparticles (which were also proposed for cementitious composites) can cause changes in soil microbiota. In this study most of tested taxa were diminished, except of *Streptomycetaceae* family and genus *Streptomyces*. Interestingly, these bacteria are known producers of active secondary metabolites, including antibiotics

and enzymes that interact with other organisms [61]. Therefore, there is a question whether these microorganisms were resistant to the toxicity of nanoparticles, gained a niche where the population could develop, or possibly were stimulated to produce antimicrobial compounds.

20.6 Future Prospects

There is still much to be done to improve the current state of the art. Nevertheless, the incorporation of nanomaterials and other substances in building materials should be monitored to verify their potential and the actual toxicity in these particular applications. For that reason, it is important to continue research on the interaction between microorganisms, materials, and nanomaterials. Furthermore, future experiments should focus not only on the toxicity but also on the metabolic potential of tested microorganisms. Therefore, the outline of experiments should include the influence of environmental factors together with microbiological potential of given environment. It should also take into consideration the application of studied nanocomposites and materials, so that the outcome would give a sufficient measure of the consequences arising from the given use. Finally, extensive measurements should be performed directly in the environment where the nanocomposite is used, in order to avoid oversimplified laboratory conditions. Therefore, it is advisable (where applicable) to study MID on whole microbial communities, especially for outdoor materials and those used in wastewater treatment systems. Nevertheless, the monitoring of whole communities involves the application of expensive laboratory protocols that can be too cost-demanding to be commonly used. For that reason, the research should be also directed into developing simple and fast, genetic or metabolic tests that could be used to indirectly monitor the condition of examined material through the assessment of microorganisms that inhabit it.

Acknowledgments This work was supported by the National Science Centre within the project No. 2016/21/N/ST8/00095 (PRELUDIUM 11).

References

1. Vupputuri S, Fathepure BZ, Wilber GG et al (2015) Isolation of a sulfur-oxidizing *Streptomyces* sp. from deteriorating bridge structures and its role in concrete deterioration. Int Biodeter Biodegr 97:128–134. https://doi.org/10.1016/j.ibiod.2014.11.002
2. Sikora P, Augustyniak A (2017) Utilization of nanomaterials for reduction of microbiologically induced deterioration (MID) of cement-based composites. In: Çınar Ö (ed) III international conference on sustainable development. Book of proceedings, Sarajevo, Bosnia and Herzegovina, pp 33–36
3. Flemming HC, Wingender J, Szewzyk U et al (2016) Biofilms: an emergent form of bacterial life. Nat Rev Microbiol 14:563–575. https://doi.org/10.1038/nrmicro.2016.94

4. Cwalina B (2008) Biodeterioration of concrete. Archit Civ Eng Environ 4:133–140. https://doi.org/10.1201/9781315119557
5. Wei S, Jiang Z, Liu H et al (2013) Microbiologically induced deterioration of concrete-A review. Braz J Microbiol 44:1001–1007
6. ISO ISO/TS 80004-2:2015 Nanotechnologies – vocabulary – part 2: nano-objects
7. ISO ISO/TR 11360:2010 Nanotechnologies – methodology for the classification and categorization of nanomaterials
8. Zhu W, Bartos PJM, Porro A (2004) Application of nanotechnology in construction summary of a state-of-the-art report. Mater Struct Constr 37:649–658. https://doi.org/10.1617/14234
9. Silvestre J, Silvestre N, de Brito J (2016) Review on concrete nanotechnology. Eur J Environ Civ Eng 20:455–485. https://doi.org/10.1080/19648189.2015.1042070
10. Gibb A, Jones W, Goodier C et al (2017) Nanotechnology in construction and demolition – what we know, what we don't. Report for the Institution of Occupational Safety and Health
11. Rashad AM (2013) A synopsis about the effect of nano-Al_2O_3, nano-Fe_2O_3, nano-Fe_3O_4 and nano-clay on some properties of cementitious materials – a short guide for Civil Engineer. Mater Des 52:143–157. https://doi.org/10.1016/J.MATDES.2013.05.035
12. Stynoski P, Mondal P, Wotring E, Marsh C (2013) Characterization of silica-functionalized carbon nanotubes dispersed in water. J Nanopart Res 15:1396. https://doi.org/10.1007/s11051-012-1396-1
13. Sikora P, Cendrowski K, Markowska-Szczupak A et al (2017) The effects of silica/titania nanocomposite on the mechanical and bactericidal properties of cement mortars. Construct Build Mater 150:738–746. https://doi.org/10.1016/j.conbuildmat.2017.06.054
14. Sikora P, Abd Elrahman M, Chung S-Y et al (2019) Mechanical and microstructural properties of cement pastes containing carbon nanotubes and carbon nanotube-silica core-shell structures, exposed to elevated temperature. Cem Concr Compos 95:193–204. https://doi.org/10.1016/j.cemconcomp.2018.11.006
15. Bolhassani M, Sayyahmanesh M (2015) A study on mechanical properties of cement paste using magnetite-silica nano-composites. Adv Cem Res 27:571–580. https://doi.org/10.1680/adcr.14.00106
16. Sanchez F, Sobolev K (2010) Nanotechnology in concrete – a review. Construct Build Mater 24:2060–2071. https://doi.org/10.1016/J.CONBUILDMAT.2010.03.014
17. Hunger M, Hüsken G, Brouwers HJH (2009) Photocatalytic degradation of air pollutants – from modeling to large scale application. Cem Concr Res 40:313–320. https://doi.org/10.1016/j.cemconres.2009.09.013
18. Giese B, Klaessig F, Park B et al (2018) Risks, release and concentrations of engineered nanomaterial in the environment. Sci Rep 8:1565. https://doi.org/10.1038/s41598-018-19275-4
19. Hincapié I, Caballero-Guzmán A, Nowack B (2015) Nanomaterials in landfills module 3: nanomaterials in construction waste. EMPA, Swiss Federal Laboratories for Materials Science and Technology, St. Gallen
20. Nowack B, Bucheli TD (2007) Occurrence, behavior and effects of nanoparticles in the environment. Environ Pollut 150:5–22. https://doi.org/10.1016/j.envpol.2007.06.006
21. Maya B-S, Barcaro G, Bettotti P et al (2013) Springer handbook of nanomaterials. Springer, Berlin
22. Sharifi S, Behzadi S, Laurent S et al (2012) Toxicity of nanomaterials. Chem Soc Rev 41:2323–2343. https://doi.org/10.1039/c1cs15188f
23. Maurer-Jones MA, Gunsolus IL, Murphy CJ, Haynes CL (2013) Toxicity of engineered nanoparticles in the environment. Anal Chem 85:3036–3049. https://doi.org/10.1021/ac303636s
24. Kumar A, Pandey AK, Singh SS et al (2011) Cellular uptake and mutagenic potential of metal oxide nanoparticles in bacterial cells. Chemosphere 83:1124–1132. https://doi.org/10.1016/j.chemosphere.2011.01.025
25. Ge Y, Schimel JP, Holden P (2011) Evidence for negative effects of TiO_2 and ZnO nanoparticles on soil bacterial communities. Environ Sci Technol 45:1659–1664. https://doi.org/10.1021/es103040t

26. Rousk J, Ackermann K, Curling SF, Jones DL (2012) Comparative toxicity of nanoparticulate CuO and ZnO to soil bacterial communities. PLoS One 7:1–8. https://doi.org/10.1371/journal.pone.0034197
27. Hao Y, Ma C, Zhang Z et al (2018) Carbon nanomaterials alter plant physiology and soil bacterial community composition in a rice-soil-bacterial ecosystem. Environ Pollut 232:123–136. https://doi.org/10.1016/j.envpol.2017.09.024
28. Rodrigues DF, Jaisi DP, Elimelech M (2013) Toxicity of functionalized single-walled carbon nanotubes on soil microbial communities: implications for nutrient cycling in soil. Environ Sci Technol 47:625–633. https://doi.org/10.1021/es304002q
29. Pacheco-Torgal F, Jalali S (2011) Nanotechnology: advantages and drawbacks in the field of construction and building materials. Construct Build Mater 25:582–590. https://doi.org/10.1016/j.conbuildmat.2010.07.009
30. Kobetičová K, Černý R (2017) Ecotoxicology of building materials: a critical review of recent studies. J Clean Prod 165:500–508. https://doi.org/10.1016/J.JCLEPRO.2017.07.161
31. ACI (2017) ACI 241R-17 Report on application of nanotechnology and nanomaterials in concrete
32. Fu PP, Xia Q, Hwang HM et al (2014) Mechanisms of nanotoxicity: generation of reactive oxygen species. J Food Drug Anal 22:64–75. https://doi.org/10.1016/j.jfda.2014.01.005
33. Burello E, Worth AP (2011) A theoretical framework for predicting the oxidative stress potential of oxide nanoparticles. Nanotoxicology 5:228–235. https://doi.org/10.3109/17435390.2010.502980
34. Ding Y, Kuhlbusch TAJ, Van Tongeren M et al (2017) Airborne engineered nanomaterials in the workplace—a review of release and worker exposure during nanomaterial production and handling processes. J Hazard Mater 322:17–28. https://doi.org/10.1016/j.jhazmat.2016.04.075
35. Boverhof DR, David RM (2010) Nanomaterial characterization: considerations and needs for hazard assessment and safety evaluation. Anal Bioanal Chem 396:953–961. https://doi.org/10.1007/s00216-009-3103-3
36. Caballero-Guzman A, Nowack B (2016) A critical review of engineered nanomaterial release data: are current data useful for material flow modeling? Environ Pollut 213:502–517. https://doi.org/10.1016/j.envpol.2016.02.028
37. Jones W, Gibb A, Goodier C et al (2016) Nanomaterials in construction–what is being used, and where? Proc Inst Civ Eng Mater:1–14. https://doi.org/10.1680/jcoma.16.00011
38. Świdwińska-Gajewska AM, Czerczak S (2017) Nanorurki węglowe-charakterystyka substancji, działanie biologiczne i dopuszczalne poziomy narażenia zawodowego. Med Pr 68:259–276. https://doi.org/10.13075/mp.5893.00504. [in Polish]
39. Nawrotek P, Augustyniak A (2015) Nanotechnologia w mikrobiologii - wybrane aspekty. Postep Mikrobiol 54:275–282. [in Polish]
40. Sikora P, Augustyniak A, Cendrowski K et al (2018) Antimicrobial activity of Al_2O_3, CuO, Fe_3O_4, and ZnO nanoparticles in scope of their further application in cement-based building materials. Nanomaterials 8:212. https://doi.org/10.3390/nano8040212
41. Michael I, Hapeshi E, Michael C et al (2012) Solar photo-Fenton process on the abatement of antibiotics at a pilot scale: degradation kinetics, ecotoxicity and phytotoxicity assessment and removal of antibiotic resistant enterococci. Water Res 46:5621–5634. https://doi.org/10.1016/j.watres.2012.07.049
42. Oukarroum A, Barhoumi L, Samadani M, Dewez D (2015) Toxic effects of nickel oxide bulk and nanoparticles on the aquatic plant *Lemna gibba* L. Biomed Res Int 2015:1–7. https://doi.org/10.1155/2015/501326
43. Zhu X, Chang Y, Chen Y (2010) Toxicity and bioaccumulation of TiO_2 nanoparticle aggregates in *Daphnia magna*. Chemosphere 78:209–215. https://doi.org/10.1016/J.CHEMOSPHERE.2009.11.013
44. Zhu X, Wang J, Zhang X et al (2009) The impact of ZnO nanoparticle aggregates on the embryonic development of zebrafish (*Danio rerio*). Nanotechnology 20:1–9. https://doi.org/10.1088/0957-4484/20/19/195103

45. Baniamerian H, Safavi M, Alvarado-Morales M et al (2018) Photocatalytic inactivation of *Vibrio fischeri* using Fe_2O_3-TiO_2-based nanoparticles. Environ Res 166:497–506. https://doi.org/10.1016/j.envres.2018.06.011
46. Li Y, Chen DH, Yan J et al (2012) Genotoxicity of silver nanoparticles evaluated using the Ames test and in vitro micronucleus assay. Mutat Res Genet Toxicol Environ Mutagen 745:4–10. https://doi.org/10.1016/j.mrgentox.2011.11.010
47. Pande S, Kost C (2017) Bacterial unculturability and the formation of intercellular metabolic networks. Trends Microbiol 25:349–361. https://doi.org/10.1016/j.tim.2017.02.015
48. Holden P, Schimel JP, Godwin H (2014) Five reasons to use bacteria when assessing manufactured nanomaterial environmental hazards and fates. Curr Opin Biotechnol 27:73–78. https://doi.org/10.1016/j.copbio.2013.11.008
49. Mukhtar S, Zaheer A, Aiysha D et al (2017) Actinomycetes: a source of industrially important enzymes. J Proteomics Bioinform 10:316–319. https://doi.org/10.4172/jpb.1000456
50. Hodge GA, Maynard AD, Bowman DM (2014) Nanotechnology: rhetoric, risk and regulation. Sci Public Policy 41:1–14. https://doi.org/10.1093/scipol/sct029
51. Hannah W, Thompson PB (2008) Nanotechnology, risk and the environment: a review. J Environ Monit 10:291–300. https://doi.org/10.1039/b718127m
52. Amenta V, Aschberger K, Arena M et al (2015) Regulatory aspects of nanotechnology in the agri/feed/food sector in EU and non-EU countries. Regul Toxicol Pharmacol 73:463–476. https://doi.org/10.1016/j.yrtph.2015.06.016
53. Handy RD, Cornelis G, Fernandes T et al (2012) Ecotoxicity test methods for engineered nanomaterials: practical experiences and recommendations from the bench. Environ Toxicol Chem 31:15–31. https://doi.org/10.1002/etc.706
54. Klaine SJ, Alvarez PJJ, Batley GE et al (2008) Nanomaterials in the environment: behavior, fate, bioavailability, and effects. Environ Toxicol Chem 27:1825–1851. https://doi.org/10.1897/08-090.1
55. Holden P, Klaessig F, Turco RF et al (2014) Evaluation of exposure concentrations used in assessing manufactured nanomaterial environmental hazards: are they relevant? Environ Sci Technol 48:10541–10551. https://doi.org/10.1021/es502440s
56. Karcagi I, Draskovits G, Umenhoffer K et al (2016) Indispensability of horizontally transferred genes and its impact on bacterial genome streamlining. Mol Biol Evol 33:1257–1269. https://doi.org/10.1093/molbev/msw009
57. Struk M, Grygorcewicz B, Nawrotek P et al (2017) Enhancing effect of 50 Hz rotating magnetic field on induction of Shiga toxin-converting lambdoid prophages. Microb Pathog 109:4–7. https://doi.org/10.1016/j.micpath.2017.05.018
58. Palleroni NJ (2015). *Pseudomonas*. In: Whitman WB, Rainey F, Kämpfer P, Trujillo M, Chun J, DeVos P, Hedlund B, Dedysh S (eds) Bergey's manual of systematics of archaea and bacteria. https://doi.org/10.1002/9781118960608.gbm01210
59. Kämpfer P (2015). *Streptomyces*. In: Whitman WB, Rainey F, Kämpfer P, Trujillo M, Chun J, DeVos P, Hedlund B, Dedysh S (eds) Bergey's manual of systematics of archaea and bacteria. https://doi.org/10.1002/9781118960608.gbm00191
60. Solecka J, Ziemska J, Rajnisz A et al (2013) Promieniowce - Występowanie i wytwarzanie związków biologicznie czynnych. Postep Mikrobiol 52:83–91. [in Polish]
61. Hopwood DA (2007) Streptomyces in nature and medicine: the antibiotic makers. Oxford University Press, New York
62. de Lima Procópio RE, da Silva IR, Martins MK et al (2012) Antibiotics produced by *Streptomyces*. Braz J Infect Dis 16:466–471. https://doi.org/10.1016/j.bjid.2012.08.014
63. Murakami T, Burian J, Yanai K et al (2011) A system for the targeted amplification of bacterial gene clusters multiplies antibiotic yield in *Streptomyces coelicolor*. Proc Natl Acad Sci 108:16020–16025. https://doi.org/10.1073/pnas.1108124108
64. Stankovic N, Radulovic V, Petkovic M et al (2012) *Streptomyces* sp. JS520 produces exceptionally high quantities of undecylprodigiosin with antibacterial, antioxidative, and UV-protective properties. Appl Microbiol Biotechnol 96:1217–1231. https://doi.org/10.1007/s00253-012-4237-3

65. Kieser T, Bibb MJ, Buttner MJ et al (2000) Practical *Streptomyces* genetics. John Innes Centre Ltd, Norwich
66. Pradesh U, Bhanjan M, Pradesh U (2015) Isolation and characterization of streptomycetes with plant growth promoting potential from mangrove ecosystem. Pol J Microbiol 64:339–349
67. Chater KF (2016) Recent advances in understanding *Streptomyces*. F1000Research 5:1–16. https://doi.org/10.12688/f1000research.9534.1
68. Nonoh JO, Lw W et al (2010) Isolation and characterization of *Streptomyces* species with antifungal activity from selected national parks in Kenya. Afr J Microbiol Res 4:856–864
69. de Jesus Sousa JA, Olivares FL (2016) Plant growth promotion by streptomycetes: ecophysiology, mechanisms and applications. Chem Biol Technol Agric 3:1–12. https://doi.org/10.1186/s40538-016-0073-5
70. Park H, Hong M, Hwang S et al (2014) Characterisation of *Pseudomonas aeruginosa* related to bovine mastitis. Acta Vet Hung 62:1–12. https://doi.org/10.1556/AVet.2013.054
71. Tanti B, Buragohain AK (2013) Biodegradation of petroleum tar by *Pseudomonas* spp. from oil field of Assam, India. Biorem J 17:107–112. https://doi.org/10.1080/10889868.2013.786017
72. Royer M, Larbat R, Le Bot J et al (2016) Tomato response traits to pathogenic *Pseudomonas* species: does nitrogen limitation matter? Plant Sci 244:57–67. https://doi.org/10.1016/j.plantsci.2015.12.008
73. Ganeshan G, Kumar AM (2007) *Pseudomonas fluorescens*, a potential bacterial antagonist to control plant diseases. J Plant Interact 1:123–134. https://doi.org/10.1080/17429140600907043
74. Goswami D, Vaghela H, Parmar S et al (2013) Plant growth promoting potentials of *Pseudomonas* spp. strain OG isolated from marine water. J Plant Interact 8:281–290. https://doi.org/10.1080/17429145.2013.768360
75. Horst AM, Neal AC, Mielke RE et al (2010) Dispersion of TiO_2 nanoparticle agglomerates by *Pseudomonas aeruginosa*. Appl Environ Microbiol 76:7292–7298. https://doi.org/10.1128/AEM.00324-10
76. Guo M-Z, Ling T-C, Poon C-S (2013) Nano-TiO_2-based architectural mortar for NO removal and bacteria inactivation: influence of coating and weathering conditions. Cem Concr Compos 36:101–108
77. Sikora P, Augustyniak A, Cendrowski K et al (2016) Characterization of mechanical and bactericidal properties of cement mortars containing waste glass aggregate and nanomaterials. Materials (Basel) 9:1–16. https://doi.org/10.3390/ma9080701
78. Guo M-Z, Ling T-C, Poon C-S (2012) TiO_2-based self-compacting glass mortar: comparison of photocatalytic nitrogen oxide removal and bacteria inactivation. Build Environ 53:1–6
79. Bhuvaneshwari M, Bairoliya S, Parashar A et al (2016) Differential toxicity of Al_2O_3 particles on Gram-positive and Gram-negative sediment bacterial isolates from freshwater. Environ Sci Pollut Res 23:12095–12106. https://doi.org/10.1007/s11356-016-6407-9
80. Adeolu M, Alnajar S, Naushad SGR (2016) Genome based phylogeny and taxonomy of the "Enterobacteriales": proposal for *Enterobacterales* ord. nov. divided into the families *Enterobacteriaceae*, *Erwiniaceae* fam. nov., *Pectobacteriaceae* fam. nov., *Yersiniaceae* fam. nov., *Hafniaceae* fam. nov., *Morganellaceae* fam. nov., and *Budviciaceae* fam. nov. Int J Syst Evol Microbiol 66:5575–5599. https://doi.org/10.1099/ijsem.0.001485
81. Nawrotek P, Grygorcewicz B, Augustyniak A (2017) Changes in the taxonomy of γ-*Proteobacteria*, modification of the order *Enterobacteriales* and novel families within *Enterobacterales* ord. nov. Postep Mikrobiol 56:465–469. [in Polish]
82. Rzewuska M, Czopowicz M, Kizerwetter-Świda M et al (2015) Multidrug resistance in *Escherichia coli* strains isolated from infections in dogs and cats in Poland (2007–2013). Sci World J 2015:1–8. https://doi.org/10.1155/2015/408205
83. Van Elsas JD, Semenov AV, Costa R, Trevors JT (2010) Survival of *Escherichia coli* in the environment: fundamental and public health aspects. ISME J 5:173–183. https://doi.org/10.1038/ismej.2010.80

84. Bachmann BJ (1996) Derivations and genotypes of some mutant derivatives of *Escherichia coli* K-12, 2nd edn. ASM Press, Washington, DC
85. NCBI Taxonomy Browser, search item "*Escherichia coli*." https://www.ncbi.nlm.nih.gov/Taxonomy/Browser/wwwtax.cgi?mode=Undef&id=562&lvl=3&lin=f&keep=1&srchmode=1&unlock. Accessed 30 Nov 2019
86. Beer C, Foldbjerg R, Hayashi Y et al (2012) Toxicity of silver nanoparticles—nanoparticle or silver ion? Toxicol Lett 208:286–292. https://doi.org/10.1016/j.toxlet.2011.11.002
87. Parveen S, Rana S, Fangueiro R (2013) A review on nanomaterial dispersion, microstructure, and mechanical properties of carbon nanotube and nanofiber reinforced cementitious composites. J Nanomater 2013:1–19. https://doi.org/10.1155/2013/710175
88. Mendoza O, Sierra G, Tobón JI (2014) Effect of the reagglomeration process of multi-walled carbon nanotubes dispersions on the early activity of nanosilica in cement composites. Construct Build Mater 54:550–557. https://doi.org/10.1016/J.CONBUILDMAT.2013.12.084
89. Stephens C, Brown L, Sanchez F (2016) Quantification of the re-agglomeration of carbon nanofiber aqueous dispersion in cement pastes and effect on the early age flexural response. Carbon N Y 107:482–500. https://doi.org/10.1016/J.CARBON.2016.05.076
90. Mateos R, Vera S, Valiente M et al (2017) Comparison of anionic, cationic and nonionic surfactants as dispersing agents for graphene based on the fluorescence of riboflavin. Nanomaterials 7:1–17. https://doi.org/10.3390/nano7110403
91. O'Toole GA (2011) Microtiter dish biofilm formation assay. JoVE 47:1–2. https://doi.org/10.3791/2437
92. Rasamiravaka T, Labtani Q, Duez P, El Jaziri M (2015) The formation of biofilms by *Pseudomonas aeruginosa*: a review of the natural and synthetic compounds interfering with control mechanisms. Biomed Res Int 2015:759348. https://doi.org/10.1155/2015/759348
93. Latimer J, Forbes S, McBain AJ (2012) Attenuated virulence and biofilm formation in *Staphylococcus aureus* following sublethal exposure to triclosan. Antimicrob Agents Chemother 56:3092–3100. https://doi.org/10.1128/AAC.05904-11
94. Wood TK (2009) Insights on *Escherichia coli* biofilm formation and inhibition from whole-transcriptome profiling. Environ Microbiol 11:1–15. https://doi.org/10.1111/j.1462-2920.2008.01768.x
95. Augustyniak A, Cendrowski K, Nawrotek P et al (2016) Investigating the interaction between *Streptomyces* sp. and titania/silica nanospheres. Water Air Soil Pollut 227(230):1–13. https://doi.org/10.1007/s11270-016-2922-z
96. Lemire J, Harrison JJ, Turner RJ (2013) Antimicrobial activity of metals: mechanisms, molecular targets and applications. Nat Rev Microbiol 11:371–384. https://doi.org/10.1038/nrmicro3028
97. Lemire J, Alhasawi A, Appanna VP et al (2017) Metabolic defence against oxidative stress: the road less travelled so far. J Appl Microbiol 123:798–809. https://doi.org/10.1111/jam.13509
98. Ge Y, Schimel JP, Holdena P (2012) Identification of soil bacteria susceptible to TiO_2 and ZnO nanoparticles. Appl Environ Microbiol 78:6749–6758. https://doi.org/10.1128/AEM.00941-12
99. Fodil D, Jaouadi B, Badis A et al (2012) A thermostable humic acid peroxidase from *Streptomyces* sp. strain AH4: purification and biochemical characterization. Bioresour Technol 111:383–390. https://doi.org/10.1016/j.biortech.2012.01.153
100. Maurer-Jones M, Gunsolus IL, Meyer BM et al (2013) Impact of TiO_2 nanoparticles on growth, biofilm formation, and flavin secretion in *Shewanella oneidensis*. Anal Chem 85:5810–5818. https://doi.org/10.1021/ac400486u

Chapter 21
Computational Studies of Adsorption of Toxic Molecules and Anions on the Surface of Doped and Functionalized Carbon Nanotubes

V. Borysiuk, S. G. Nedilko, Yu. Hizhnyi, and A. Shyichuk

21.1 Introduction

Removal of toxic molecules and ions of heavy metals from environment is an urgent technological requirement of human civilization. One of the most promising methods of such kind of removal is adsorption of toxic molecules by artificial adsorbents [1, 2]. The search for new adsorbent materials which can allow economically efficient schemes of such removal is a topical research task [1, 3].

Materials based on carbon nanostructured materials, in particular carbon nanotubes (CNTs), are considered as very promising candidates for such application [1, 2, 4, 5]. Among other adsorbent materials, the CNTs are characterized by a number of advantages, most notably large surface area and generally high adsorption capability of carbon surface for many toxic compounds [1, 3].

Carbon nanotubes (CNTs) are intensively studied at present time as promising materials for gas sensors [6–10]. Specific properties of CNT-based materials allow elaboration of efficient gas sensors with sensitivity in the ppb region [6, 11, 12] and with several additional advantages, such as low dimensions, fast response, good reversibility at ambient temperature, and low power consumption.

Computational studies of adsorptions of various molecules on the surfaces of carbon nanostructures, in particular CNTs and graphene, have become a powerful tool for quantitative description of adsorption characteristics of real carbon nanomaterials [13]. Computational approaches in the studies of adsorption of toxic molecules and anions on the CNT surface have been recognized as having high

V. Borysiuk (✉) · S. G. Nedilko · Y. Hizhnyi
Taras Shevchenko National University of Kyiv, Kyiv, Ukraine

A. Shyichuk
Department of Rare Earth, Faculty of Chemistry, Adam Mickiewicz University, Poznań, Poland

© Springer Nature Switzerland AG 2019

O. Fesenko, L. Yatsenko (eds.), *Nanophotonics, Nanooptics, Nanobiotechnology, and Their Applications*, Springer Proceedings in Physics 222,
https://doi.org/10.1007/978-3-030-17755-3_21

predictive power. Since computational modeling can predict several important physical and chemical properties of the sensor materials, the computations themselves can evaluate the prospects for removal of toxic molecules from the environment, as well as for elaboration of novel gas sensors [14–17]. Adsorption of several types of molecules of industrially important toxic gases on the B- or N-CNTs was treated so far in the density functional theory (DFT)-based electronic structure calculations. In particular, such studies were reported for carbon monoxide (CO) [18–20], nitrogen dioxide (NO_2) [18, 19], chlorine (Cl_2) [20], formaldehyde (HCOH) [17], methanol (CH_3OH), and ammonia (NH_3) [19, 21].

Hydrogen halide gases HX (X = F, Cl, Br) are widely used in the industry as reagents (see [22]) and also are produced as byproducts in many industrial applications (see [23–26]). At the same time, these gases are very toxic and harmful for biological organisms even at low concentrations [22, 27]. Majority of electrochemical gas sensors of hydrogen halides available on the market are relatively expensive and their detection limit usually does not exceed the ppm level [28]. Elaboration of novel, more efficient, and sensitive sensors of hydrogen halide gases is an important present-day task.

Compounds of hexavalent ions of heavy metals M(VI), in particular Cr(VI), are widely spread industrial pollutants, and at the same time, they are very harmful to living bodies [29–31]. Therefore, there is a strong technological need to remove such compounds from industrial waste as well as from the environment [32, 33]. The properties of CNTs as adsorption materials for Cr(VI) compounds have been studied over the last decade [4, 32, 34–38] and it was found that these materials are very promising for the efficient removal of Cr(VI) compounds from the environment [2, 32, 35–37].

However, despite of a large volume of accumulated experimental data, there is a considerable lack of understanding of Cr(VI)-on-CNTs adsorption mechanisms at the single-molecule level. In particular, the peculiarities of chemical bonding between the most common types of Cr(VI) anions and the CNT surface still remain unclear.

Adsorption models developed in the mentioned above research papers usually employ analogies with adsorption of molecules on a carbon surface without explicit consideration of specific CNT structures. However, it is well-known that carbon surface of CNTs (particularly low-diameter ones) may be significantly curved, and this feature determines their distinctive adsorption properties [39].

Chromium is the 21st most abundant element in the earth's crust [40], and its valance state can range from -2 to $+6$, but it is generally found as trivalent Cr(III) and hexavalent chromium Cr(VI) in natural environments.

Trivalent chromium occurs naturally in many vegetables, fruits, meat, grains and is often added to vitamins as a dietary supplement, whereas Cr(VI) most often produced by industrial processes and mining of chromium ore, is an indicator of the environmental contamination. The main industries that contribute to water pollution by Cr(VI) are leather production, mining, electroplating, textile dyeing, metal finishing, wood manufacturing, nuclear power plants, electrical and electronic

equipment manufacturing, catalysis [41–46]. For this reason, hexavalent chromium is among very common environmental pollutants.

Most of the Cr(III) compounds are sparingly soluble in water, whereas the majority of Cr(VI) compounds are highly soluble. In addition, Cr(III) is several times less toxic than Cr(VI) [47]. The tolerance limit for Cr(VI) for discharge into inland surface waters is 0.1 mg/L and 0.05 mg/L in potable water.

The effect of hexavalent chromium on humans can occur not only due to use of contaminated water but also by inhalation of contaminated air and the contact of evaporation with the skin. Hexavalent chromium, Cr(VI), are dangerous to humans at all ways of interaction, even with short-term impact. The above determine the relevance for investigation of the adsorption mechanisms of chromium-containing anions, first of all those containing Cr(VI), and shows the need to study these mechanisms both in gas and water environments. Chromium(VI) generally exists in monomeric ($HCrO_4^-$ and CrO_4^{2-}) or biomeric state ($Cr_2O_7^{2-}$) [48]. The dependency of concentration of these species on the pH and concentration of Cr(VI) solution are presented in Figs. 21.1 and 21.2, respectively.

It is evident (Fig. 21.2) that CrO_4^{2-} predominates above pH 6.5 and $HCrO_4^-$ dominates in the pH range of 1–6.5.

The above description shows the need to study the mechanisms of adsorption on the surface of carbon materials of such molecular chromium groups as CrO_4^{2-}, $HCrO_4^-$, and $Cr_2O_7^{2-}$.

Besides Cr(VI)-containing ions, the DFT-based calculations provide an opportunity to study the adsorption mechanisms of molecules with other hexavalent ions Mo(VI) and W(VI). These ions are isovalent to Cr(VI), which, however, does not determine the identity of the adsorption characteristics of corresponding molecules and anions on the surfaces of various carbon nanostructured materials.

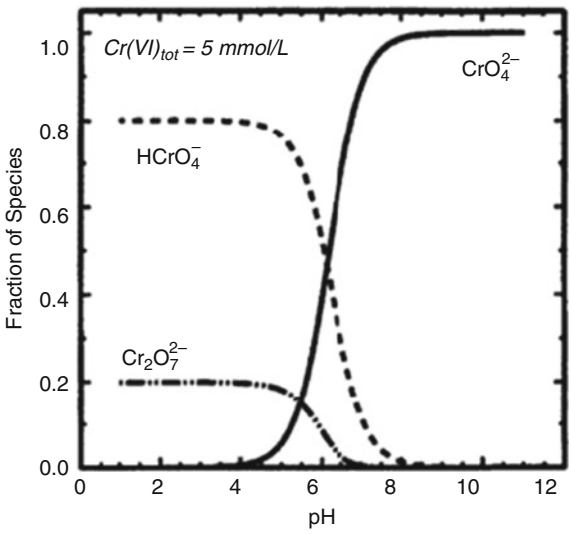

Fig. 21.1 Distribution of Cr(VI) species as a function of pH [48]

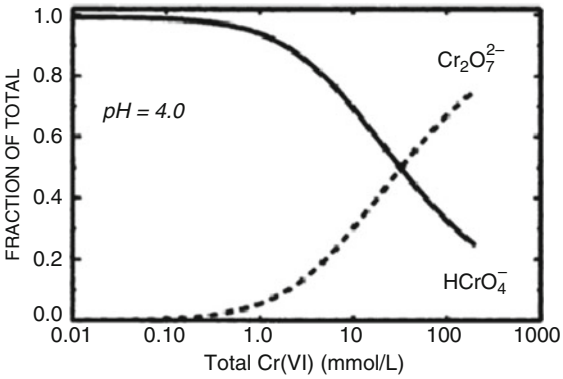

Fig. 21.2 Fraction of $HCrO_4^-$ and $Cr_2O_7^{2-}$ at pH 4 as a function of total Cr(VI) concentration [48]

21.2 Fundamentals of the Structural and Electronic Properties of Carbon Nanotubes

It is well-known that the first observation of the structure of multi-walled carbon nanotubes was in 1991 [49]; however, there are a number of works in which the evidence is provided for an earlier discovery of the CNTs. In 1976, it was clearly shown the existence of hollow carbon fibers of nanometer diameters [50]. In 1987, the US patent [51] was issued for the production of discrete cylindrical carbon fibers with a constant diameter in the range of 3.5–70 nm and a length that is 102 times greater than the diameter. In 1991, the multiwalled carbon nanotubes contained in arc discharge were registered and investigated [49]. Methods for the synthesis of the single-walled carbon nanotubes were also described [52, 53].

Carbon nanotubes have a hollow cylindrical structure with a diameter of 1 to several 10s of nanometers and a length of up to hundreds of micrometers, consisting of one or more hexa-honalnyh graphite planes (graphene sheets) rolled into a tube and ending generally hemispherical surface, which can be seen as half fullerene molecule [53]. For example, CNT(10,10) ends with a half-fullerene C_{240}. The CNT can also have open ends after oxidation [54]. Depending on the number of graphene layers, the nanotubes can be single-walled (SWCNT) or multiwalled (MWCNT). The ideal SWCNT can be represented as a graphene sheet (hexagonal layer of carbon atoms) rolled up into the cylinder without the presence of any seams.

Since the microscopic structure of SWCNT is closely related to graphene, the tubes are usually denoted in terms of graphene lattice vectors, it can be obtained geometrically by curling strips of graphene. The geometry of the SWCNT is completely determined by a pair of indices (n,m) indicating the relative position $C_h = na_1 + ma_2$ pair of atoms of graphene strips, which, upon the tube formation of, are superimposed on each other (a_1 and a_2 are the basis vectors of the hexagonal layer).

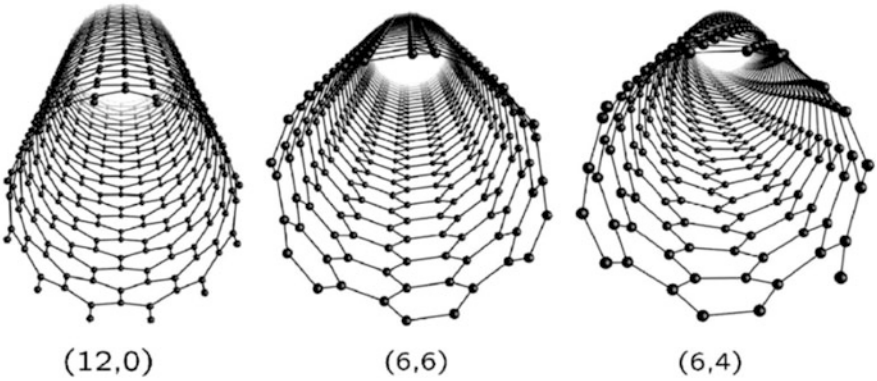

Fig. 21.3 Atomic structures of (12,0) zigzag, (6,6) armchair, and (6,4) chiral nanotubes [55]

This chiral vector C_h defines the circumference of the tube. The diameter d_t of the nanotube can thus be calculated from:

$$d_t = |C_h| / \pi \tag{21.1}$$

The chiral vector C_h uniquely defines a particular (n,m) of the tube, as well as its chiral angle θ, which is the angle between C_h and a_1.

Nanotubes of the (n,n) type ($\theta = 30°$) are called armchair tubes, because they exhibit an armchair pattern along the circumference. Such tubes display carbon-carbon bonds perpendicular to the nanotube axis. Both zigzag and armchair nanotubes are achiral tubes, in contrast with general (n,$m \neq n \neq 0$) chiral ones (Fig. 21.3).

The geometry of the graphene lattice and the chiral vector determine not only the diameter of the CNT but also the unit cell and its number of carbon atoms. The smallest graphene lattice vector T perpendicular to C_h defines the translational period t along the tube axis. The lattice vector T can also be expressed in terms of the basis vectors a_1 and a_2 as $T = t_1 a_1 + t_2 a_2$. Using $C_h, \cdot T = 0$, the expressions for t_1 and t_2 are represented by:

$$t_1 = (2m + n) / N_R, \quad t_2 = -(2n + m) / N_R \tag{21.2}$$

where N_R is the greatest common divisor of $(2m + n)$ and $(2n + m)$. The number of carbon atoms per unit cell N_C can also be expressed as a function of n and m:

$$N_C = 4\left(n^2 + nm + m^2\right) / N_R \tag{21.3}$$

As in the case of bulk crystalline solids, in CNTs, the appearance of "native" defects, which are formed in the places of the transformation of a part of hexagonal cycles into five- and seven-circular cycles with the formation of rings of nanotubes,

may occur. Defects can also be external: introduced accidentally due to the manufacturing process or which are specially incorporated to modify the properties of the nanotubes. The appearance of defects in CNT leads to the bend of the tube, the change of the chirality vector and its diameter, the change in the relation with adjacent tubes in the beam, and, consequently, the change in the properties of the CNTs.

Carbon nanotubes are known for their special electronic properties due to the nature of the bonds of the electron orbitals of carbon atoms in the structure of the tubes. The orbitals (s, p_x, p_y) combine to form in-plane σ (bonding or occupied) and σ_* (antibonding or unoccupied) orbitals. The lateral interaction with neighboring p_z orbitals (labeled the ppπ interaction) creates delocalized π (bonding) and π_* (antibonding) orbitals. In analogy, the σ bonds in the nanotube form a hexagonal network which strongly connects the carbon atoms in the cylinder wall of the CNT. The π bonds are perpendicular to the surface of the nanotube and are responsible for the weak interaction between SWNTs in a bundle, similar to the weak interaction between carbon layers of pure graphite [56].

The energy levels associated with the inplane σ bonds are known to be far away from the Fermi energy in graphite and thus do not play a key role in its electronic properties. In contrast, the bonding and antibonding π-bands cross the Fermi level at the high-symmetry points in the Brillouin zone of graphene [57].

The electronic structures of undoped single-walled CNT(3,3) and CNT(5,5) were calculated relatively long ago, and these low-diameter CNTs may be considered now as objects which are well-studied by various calculation methods [58–60].

The electronic structures of the low-diameter (i.e., with low values of m and n) B- or N-doped CNT(n,m) are also well-studied. In particular, such calculations were reported for the B(N)-doped metallic-type CNT(5,5) [61–63] and also for semiconductor-type B(N)-CNT(5,7) [64] and N-CNT(6,0) [65] and for many other B(N)-doped CNTs with higher values of (n,m). The electronic structures of B(N)-doped graphene sheets were studied recently within a molecular cluster approach by the DFT-based methods (see [66, 67]).

As it was found, doping of CNTs with the B or N impurities enhances their ability to absorb gaseous molecules [14, 15, 68]. This finding has roused an intense interest on the boron- and nitrogen-doped CNTs (B-CNTs and N-CNTs) as promising materials for gas sensors [14, 68, 69].

It is known that CNT(n,m) for which $n - m = 3l$ with l an integer (including armchair-type CNTs for which $m = n$) is characterized by the metallic-type electronic band-structure, whereas all other CNTs with $n - m = 3l \pm - 1$ are semiconductors [55]. Principle of operation of a CNT-based gas sensor is based on measurements of resistance of the working material. So, as the working material is a mixture of CNTs with dispersed (m,n), just the metallic-type CNTs should form conductivity properties of the mixture rather than semiconductor ones. Therefore, studies of armchair-type CNTs obviously should have higher priority.

It should be noted that the majority of modern synthesis procedures of CNTs allow to produce only mixes of CNTs with high dispersion of index (m,n) (see [70] and references therein). Technologies of synthesis of CNTs monodisperse by (m,n)

index (or procedures of selection of already synthesized CNTs by their structure) appeared only in the recent years and still are very complicated and expensive (see [71] and references therein). Sensing materials of existing CNT-based gas sensors are in fact "mixes" of CNTs with high dispersion of (*m*,*n*) index as these materials were produced by "conventional" synthesis methods without preliminary selection by the CNT structure (see [8, 18, 72]). Therefore, it is obvious that studies of a set of CNTs with various (*m*,*n*) indexes are desirable for prediction of properties of real working materials of the CNT-based gas sensors. However, studies of such a set require extensive computing resources and make analysis of results very complicated. So, researchers generally limit themselves to consideration of gaseous adsorption of the CNTs with some single case of (*m*,*n*) index [14, 17]) or graphene [18] reasonably regarding such limitation as being sufficient for adequate prediction of the physical properties of real gas sensing materials.

21.3 Modelling of Adsorption Properties of the CNT Surface by the DFT-Based Electronic Structure Calculations: A Brief Description of Computational Approach

21.3.1 Construction of CNT Clusters

The lengths of CNTs in mixtures may vary from several micrometers to hundreds of micrometers, and their diameters vary from nanometers to tens of nanometers [34]. Commercially available mixtures of carbon nanotubes consist mainly of MWCNTs with average diameters of 5 nm. The present-day computational capabilities are insufficient to perform a first-principle calculation for the full-length carbon nanotubes as well as for the entire variety of the nanotube structures.

The CNT(3,3) and CNT(5,5) are the narrowest possible nanotubes, with diameters of ~0.4 and ~0.7 nm, respectively. However, such nanotubes are convenient objects of calculations, since their clusters will have sufficient length for modeling of molecular adsorption even with relatively small number of atoms. A single-layered graphene sheet is commonly used to model the surface of large-diameter CNTs (with correspondingly, low surface curvature). Consideration of both low-diameter CNTs and graphene is a widely spread approach in prediction of the adsorption properties of real CNT mixtures by computational studies [73–75].

The CNTs and graphene were modeled in our calculations as molecular clusters. For calculations of adsorption of hydrogen halide molecules HX, the clusters of CNT(3,3) comprised 78 carbon atoms (or in other words, 13 C_6 "rings" along the nanotube axis) were taken. To compensate the effects of dangling C–C bonds, 12 outermost C atoms of the clusters were replaced by the H atoms providing $C_{66}H_{12}$ formula of the cluster. Such replacement is a widely used approach in computational modeling of CNTs within molecular cluster approach [69, 76, 77]. To model the

B or N impurities, one carbon atom from the central 6 "ring" of the cluster was substituted by the boron or nitrogen atom.

It should also be noted that the lengths of real CNTs usually exceed their diameters by several orders of magnitude. So, a "section" of the CNT modeled in a cluster must be long enough to provide a negligible influence of side surfaces on the central region of the section where the B(N) impurities and adsorbed HX molecules are adsorbed. To examine this property, we performed supplementary geometry-optimized calculations of undoped CNT(3,3), CNT(5,5), and graphene clusters. According to the supplementary calculations, addition of two extra carbon "rings" to both sides of CNT(3,3) and CNT(5,5) clusters only slightly (within 0.8% of magnitude) changes the C-C distances in the central regions of clusters. Analogous weak changes in the core region were observed when two extra carbon "strips" were added to the opposite sides of graphene cluster. The following characteristic size parameters of undoped CNT(3,3) cluster were obtained in geometry-optimized calculations: distance along the nanotube axis between outermost C_6 "rings" was 12.3 Å, distance between edging H_6 "rings" (clusterlength) was 14.1 Å, and averaged distance between "contralateral" C nuclei of the central C_6 "ring" (cluster diameter) was 4.2 Å. Analogously, the length and diameter of the undoped CNT(5,5) cluster were obtained as 14.2 and 7.0 Å, respectively. Characteristic dimension of undoped graphene cluster (the longest internuclear distances between the H nuclei located on the opposite sides) was obtained as ~11.74 × 13.6 Å, respectively.

Since molecular anions of M(VI) metals have sizes larger than the hydrogen halide molecules HX, molecular clusters of larger sizes were needed to calculate molecular anions adsorption simulations than for hydrogen halide. Therefore, for the calculation of adsorption of M(VI) molecular anions the clusters of CNT(3,3) comprising 23 C_6 "rings" of armchair CNT(3,3) was used. The dangling C–C bonds in the cluster were capped with H atoms, resulting in $C_{126}H_{12}$ formula (see Fig. 21.4a).

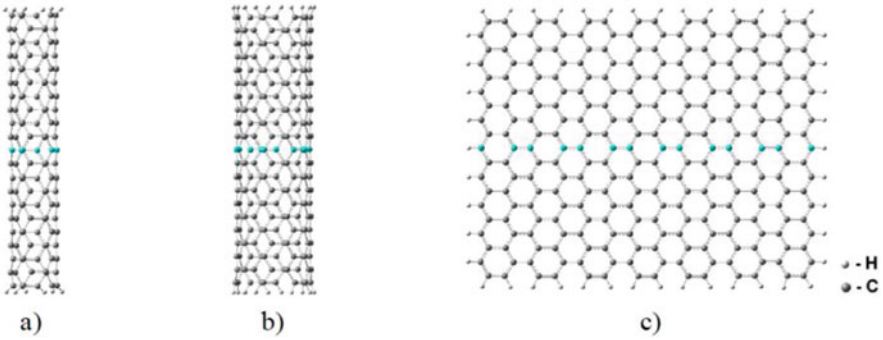

Fig. 21.4 Undoped clusters with optimized geometry: CNT(3,3) (**a**), CNT(5,5) (**b**), and graphene sheet (**c**)

Clusters with the formulas $C_{210}H_{20}$ and $C_{266}H_{46}$, respectively, were constructed to model a CNT(5,5) and graphene (see Fig. 21.4b, c, respectively). Approximate lengths of both CNT clusters were 26.5 Å. The dimensions of GR cluster were 24.1 × 30.8 Å.

Clusters of all undoped carbon nanostructures used in calculations were electrically neutral, while additional charges equal to $-1e$ and $+1e$ were assigned to clusters describing the B- and N-doped clusters, respectively. By using such additional charges, we have modeled a very common situation when an "additional" electron introduced into a real CNT by the N_C impurity is compensated by an additional charge $+1e$ of defect created somewhere far from the N_C site (such compensating defects were not modeled explicitly in our calculations). Correspondingly, additional compensating defects can supply one "missing" electron in the B_C case. Taking into account the $-2e$ charge of "free" $M(VI)O_4^{2-}$ anion, additional $-2e$ charges were assigned to the clusters of undoped adsorbent and chromate anion. So, additional charges of $-3e$ or $-1e$ were assigned to the B- or N-doped clusters, respectively. All systems were treated as closed-shell, that is, with no unpaired electrons.

Characteristic size parameters of undoped CNT(3,3) cluster used in calculations of adsorption of M(VI) anions were the following: distance along the nanotube axis between the outermost C_6 rings was ~24.7 Å, distance between outermost H6 rings (cluster length) was ~26.5 Å, mean distance between "contralateral" C nuclei of the central C_6 ring (cluster diameter) was ~4.21 Å. Analogously, the length and diameter of undoped CNT(5,5) cluster were ~26.5 and ~6.84 Å, respectively. Characteristic dimension of undoped GR cluster (the maximal internuclear distances between the H nuclei located on the opposite sides of the sheet) was ~24.1 × 30.8 Å. It should be noted that the lengths of real CNTs usually exceed their diameters by several orders of magnitude. So, a "section" of the CNT modeled in a cluster must be long enough to guarantee a negligible influence of side surfaces on the central region of the section where the B(N) impurities and adsorbed $M(VI)O_4^{2-}$ anion are situated. To examine this property, we have performed supplementary geometry optimization calculations of undoped CNT(3,3), CNT(5,5), and GR clusters. As the calculations showed, removal of the two outermost carbon rings from both edges of CNT(3,3) and CNT(5,5) clusters (or the two outermost carbon "strips" from GR cluster) changes the C-C distances in the central regions of clusters within 0.3%. Such slight changes ensure a negligible influence of the cluster edges on the calculated adsorption geometries. Consequently, the selected sizes of clusters were considered optimal, as larger clusters require more CPU time.

To complement these edge cases of the CNT surface curvatures by an intermediate one, we have additionally considered a fragment of the hexa-layered multiwalled carbon nanotube which can be denoted using formal rules as MWCNT(17,17)@(21,21)@(25,25)@(29,29)@(33,33)@(37,37) and will be mentioned in the following text as MWCNT. The outer diameter of such MWCNT is ~5.1 nm, which corresponds to an average tube diameter in commercially available mixtures of CNTs [34].

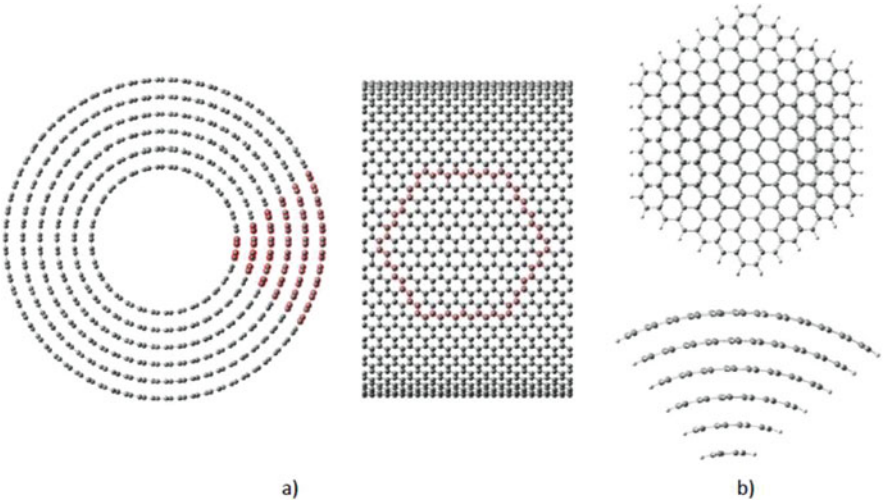

Fig. 21.5 (**a**) Scheme of selection of MWCNT cluster from six-walled carbon nanotube (edge atoms of the cluster are marked by red shadows); (**b**) structure of selected MWCNT cluster given in two projections

As it was found for the low-diameter CNTs [74], the nanotube fragments of at least 30 Å length can guarantee a sufficiently weak influence of the edges on the central part. However, construction of MWCNT cluster of such length would require 6800 carbon atoms. Such a number is too large for efficient DFT-based calculations of adsorption geometries, inasmuch as up to a 100s of combinations of adsorbents and adsorbates that have to be considered in our studies. For this reason, we have constructed a conical section of MWCNT which comprises a hexagonal part of the nanotube outer surface (for construction of the cluster, see Fig. 21.5). This part has transverse dimension of 29.0 Å, and the distance between inner and outer walls of MWCNT is 15.2 Å. All dangling C–C bonds of MWCNT cluster were capped by placement of H atoms providing a $C_{546}H_{126}$ formula.

During geometry optimization calculations, the H atoms of MWCNT cluster were fixed (frozen). As our geometry optimizations showed, the structure of MWCNT cluster was not stable without such freezing, that is, the carbon sheets constituting the conical part of the multiwalled tube moved apart. Normally, coaxial structure of MWCNTs prevents such decomposition. The freezing of the edge hydrogen atoms was applied in studies of molecular adsorption on the outer layer of MWCNT of 2 nm diameter [78]. Such freezing obviously provides some limitations to geometric optimization of the whole cluster. However, it leaves the atomic positions in the cluster core to be optimized thus providing (as it was also shown in [78]) an adequate treatment of molecular adsorption properties.

As a result, it was found that geometry optimization of undoped MWCNT cluster resulted in a little bulging of the outer carbon layers of the cluster (several deeper layers were also bulged but to a lower extent). However, despite the bulging, the

cluster preserved the curvature of the outer surface (after optimization, corresponding curvature radius decreased only by 10%). This feature shows that freezing of outer atoms provides a reasonable approximation in modeling of adsorption on medium-diameter MWCNT. An analogous approach to model the medium-diameter MWCNT has been successfully applied in [73].

21.3.2 Calculation Method, Basis Sets, and Other Computational Parameters

The geometry-optimized calculations were performed with use of Gaussian 09 [79] software package within density functional theory (DFT) level with B3LYP nonlocal correlation functional [80, 81]. The calculations used a basis set of 6-31G, which is typical for computational studies of adsorption of molecules (hydrogen halide) on the surface of CNT in recent years [69]. However, other base sets were used to calculate the molecular anions, since the heavy metals contained in the molecular anions are beyond the range that can be calculated using the base set of 6-31G. The basic set of cc-pVDZ was used for Cr and O atoms [82]. The atoms Mo and W are represented by the basis set of cc-pVDZ-PP with pseudo-potentials [83, 84]. Such combination of basis sets is generally utilized in computational studies of adsorption of molecules with d-metals on the CNT surfaces [85, 86]. All other settings were Gaussian 09 defaults, that is, no additional keywords were specified. Effects of water solvent on the studied adsorption properties were considered within the polarizable continuum model (PCM) [87].

As starting geometry, the HX (X = F, Cl, Br) molecules were put at 1.5 Å distance from the CNT surface in the vicinity of the B(N) atom, and the HAX bond was initially oriented parallel to the CNT axis. In the geometry optimization studies, several starting positions of $M(VI)O_4^{2-}$ (M(VI) = Cr, Mo, W) anions with respect to the carbon surface were considered for each adsorption case. In all cases, the anions were initially put in such a way that the shortest C/B/N-O distance lied between 1.5 and 2.2 Å. Using such initial geometry, we ensure binding of the anion particularly to the dopant atoms, not at just some other site of the doped CNT or graphene sheet.

Excited electronic states of CrO_4^{2-} anions in "free" and in adsorbed configurations were studied by the time-dependent DFT method (TD-DFT) method. In these calculations, the two-level ONIOM-2 approach in treatment of interatomic interactions was used [88]. The "adsorbent $+CrO_4^{2-}$ anion" system with optimized geometry was divided into two regions, the quantum mechanical (QM) and the molecular mechanical (MM). The QM region comprised the atoms of CrO_4^{2-} anion, while the MM region comprised all atoms of the adsorbent molecule (C and H) (see Fig. 21.6). The electronic embedding was used in order to take into account electrostatic interaction between the QM and MM regions, i.e., the atoms of the QM region were treated by TD-DFT calculations, while the atoms of the

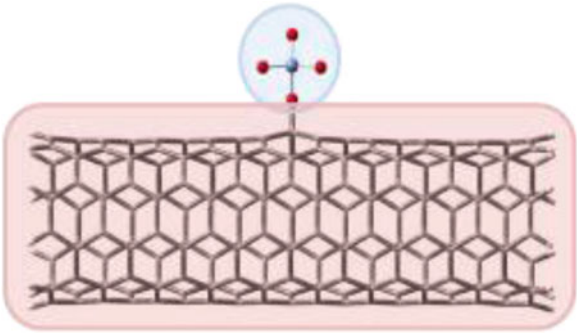

Fig. 21.6 Geometry-optimized structures of CNT(3,3) with adsorbed on the surface of CrO_4^{2-} anion are considered in the approximation of quantum mechanics (the region is painted blue), and CNT(3,3) is considered in the approximation of molecular mechanics (the region is painted with pink color)

MM region were treated as partial charges contributing to the quantum-mechanical Hamiltonian. Successful applications of the ONIOM approach to calculations of the excited states of molecules are reviewed in [89]. The TD-DFT is a well-established method for treatment of the excited states of tetrahedral oxyanions of d^0 metals (see [90] and references therein). The TD-DFT calculations of the singlet excited states of CrO_4^{2-} anions (QM region) were carried out in a single-point (no geometry optimization) calculation with the previously optimized geometry. The B3LYP exchange-correlation functional was used and only single excitations were taken into account. The same basis sets as for the geometry optimization calculations were used. Energies and oscillator strengths of electronic transitions from the ground to 50 lowest energy excited states were obtained.

21.4 Electronic Structure and Sensing Properties of Carbon Nanotubes with Adsorbed Hydrogen Halide Molecules HX (X = F, Cl, Br)

The results of geometry-optimized calculations of the electronic structure of carbon nanotubes (CNTs) and graphene (GR) with adsorbed HX (X = F, Cl, Br) are presented in this section. The influence of boron and nitrogen impurities on the formation and character of chemical bonds between carbon materials the molecules of halogen halides is analyzed.

The binding energies, E_b, were obtained as the difference of the calculated total energies using expression: $E_b = E_{CNT\text{-}B(N)\text{-}HX} - E_{CNT\text{-}B(N)} - E_{HX}$.

The calculated E_b value should be negative in a stable adsorption configuration. The charge states of HX (X = F, Cl, Br) adsorbates are obtained as an algebraic sum of calculated Mulliken charges of H and X atoms. Negative value of charge of the adsorbate molecule means transfer of negative electronic charge from the CNT to the molecule.

The calculated binding energies, charges on the HX adsorbate molecules (X = F, Cl, Br) and the optimized geometry of the internuclear distances of CNT(3,3), CNT(5,5) and graphene are presented in Table 21.1.

As Table 21.1 shows, our calculations provide relatively low values of binding energies between adsorbed HX (X = F, Cl, Br) molecules and undoped clusters: they range from −0.07 to −0.19 eV. Internuclear distances in adsorbed molecules $R_{H–X}$ are only slightly changed with respect to corresponding distances in free molecules (the difference does not exceed 1.5%). For all considered cases of adsorption on undoped clusters, the "axis" of HX molecule is settled practically perpendicular to the carbon surface. The shortest $R_{C–H}$ distance exceeds 2 Å for all studied HX cases.

For all adsorption configurations, calculations indicate lower binding energies and higher $(R_{C–H})^{min}$ distances for undoped graphene clusters in comparison with CNT(3,3) and CNT(5,5) (see Table 21.1). Values of E_b obtained for undoped CNT(3,3) and CNT(5,5) fall into the region of binding energies typical for hydrogen bonds (0.1–0.6 eV [91]) but are close to its lower limit. The E_b value in GR-HCl and GR-HBr cases are even slightly below this lower limit and fall into the region of the van der Waals bonds (0.01–0.1 eV, see [92]). Relatively low values of E_b and slight changes of internuclear distances in adsorbed molecules indicate the absence of covalent bonding between HX (X = F, Cl, Br) adsorbates and undoped carbon nanotubes.

Calculations also give low values for charges or HX molecules adsorbed on undoped clusters: they are in the −0.02 to −0.07 *e* range (see Table 21.1).

The calculated binding energies, charges on the HX adsorbate molecules (X = F, Cl, Br), and the optimized geometry of the internuclear distances of B-doped CNT(3,3), CNT(5,5), and graphene are shown in Table 21.2. In general, calculations show a completely different situation with respect to the adsorption of HX molecules on the surface of boron-doped carbon nanotubes in comparison with undoped nanostructures.

Calculations reveal far different situation for adsorption of HX molecules on the B-doped CNTs. In this case, the binding energies with adsorbate molecules range from −0.36 to −2.53 eV (see Table 21.2), and they are generally higher by an order of magnitude than corresponding energies of adsorption on undoped clusters. The E_b values for CNT(3,3) and CNT(5,5) definitely fall into the region of hydrogen bonds (0.1–0.6 eV, Ref. 202) or are slightly above this region [−0.87 eV, for CNT(3,3)-B-HCl], while the −2.13 eV value observed in CNT(3,3)-B-HBr case is typical for covalent bonds [93].

For CNT(5,5), all adsorption cases reveal lower binding energies relatively to CNT(3,3) (compare corresponding rows in Table 21.2). The B-doped graphene clusters reveal binding energies typical for covalent bonds (ranging from −2.53 for GR-B-HF to −2.38 for GR-B-HCl, see Table 21.2).

As Table 21.2 shows, in each case of HX adsorption on the B-doped CNT(3,3) and CNT(5,5), the H atom of the adsorbate is located closer to one of the atoms of the nanotube, than to the impurity atom B, that is, $(R_{C–H})^{min} < (R_{B–H})^{min}$. In the CNT(3,3)-B-HBr case, the $(R_{C–H})^{min}$ distance is even almost twice shorter than the $(R_{B–H})^{min}$ distance. So, it is arguable that C and H atoms create chemical bonds in

Table 21.1 Calculated binding energies, charges of adsorbate molecules HX (X = F, Cl, Br) and internuclear distances for undoped configurations

Type of adsorbate	Configuration	Binding energy E_b (eV)	Charge state of HX adsorbate (e)	$R_{H–X}/(R_{H–X})^{free}$	$(R_{C–H})^{min}$
HF	CNT(3,3)-HF	−0.19664	−0.038	0.9567/0.94927	2.07545
	CNT(5,5)-HF	−0.15972	−0.033	0.95255/0.94927	2.07033
	GR-HF	−0.1231	−0.024	0.95178/0.94927	2.24942
HCl	CNT(3,3)-HCl	−0.1356	−0.071	1.3404/1.32057	2.18253
	CNT(5,5)-HCl	−0.1422	−0.046	1.33027/1.32057	2.36785
	GR-HCl	−0.0707	−0.033	1.32667/1.32057	2.48136
HBr	CNT(3,3)-HBr	−0.1536	−0.068	1.4578/1.44006	2.20396
	CNT(5,5)-HBr	−0.16345	−0.044	1.44780/1.44006	2.36396
	GR-HBr	−0.0868	−0.031	1.44429/1.44006	2.46213

$R_{H–X}$(Å) – internuclear distance in adsorbed HX molecule
$(R_{H–X})^{free}$(Å) – internuclear distance in free HX molecule
$(R_{C–H})^{min}$(Å) – shortest distance from a carbon atom of the adsorbent to the H atom of HX

Table 21.2 Calculated binding energies, charges of adsorbate molecules HX (X = F, Cl, Br), and internuclear distances for the B-doped configurations

Type of adsorbate	Configuration	Binding energy E_b (eV)	Charge state of HX adsorbate (e)	$R_{H-X}/(R_{H-X})^{free}$	$(R_{C-H})^{min}$
HF	CNT(3,3)-B-HF	−0.5950	−0.03	0.9729/0.94927	1.90231
	CNT(5,5)-B-HF	−0.4963	−0.018	0.96624/0.94927	2.00599
	GR-B-HF	−2.5311	−0.003	0.9598/0.94927	2.24942
HCl	CNT(3,3)-B-HCl	−0.8800	−0.503	2.027/1.32057	1.15766
	CNT(5,5)-B-HCl	−0.3764	−0.137	1.37235/1.32057	1.96542
	GR-B-HCl	−2.3824	−0.12	1.35292/1.32057	2.56420
HBr	CNT(3,3)-B-HBr	−2.1342	−0.112	2.7779/1.44006	1.0962
	CNT(5,5)-B-HBr	−0.3622	−0.14	1.4933/1.44006	1.98348
	GR-B-HBr	−2.3907	−0.125	1.47253/1.44006	2.78799

R_{H-X}(Å) – internuclear distance in adsorbed HX molecule
$(R_{H-X})^{free}$(Å) – internuclear distance in free HX molecule
$(R_{C-H})^{min}$(Å) – shortest distance from a carbon atom of the adsorbent to the H atom of HX

all studied cases of adsorption on the B-doped CNT(3,3) and CNT(5,5) clusters. For the B-doped graphene, on contrary $(R_{C–H})^{min} > (R_{B–H})^{min}$ and the H atoms of the adsorbates create chemical bonds with the B dopants.

The most significant elongations of the H–X distances are obtained for CNT(3,3)-B-HBr and CNT(3,3)-B-HCl cases (∼53% and ∼93%, respectively). In contrast, adsorption of HX molecules on the B-doped graphene clusters, despite high binding energies, does not lead to significant changes of internuclear distances in the adsorbates (the relative change does not exceed 12.5%).

The calculated binding energies, charges on the HX molecules (X = F, Cl, Br), and the optimized geometry of the internuclear distances of N-doped CNT(3,3), CNT(5,5), and graphene are presented in Table 21.2.

In general, calculations show a situation similar to the case of adsorption of HX molecules on the surface of undoped clusters.

For all studied adsorptions cases, calculations give relatively low values of the binding energies (do not exceed −0.41 eV; see Table 21.3), small adsorbate charges (do not exceed |0.05| e), slight changes if internuclear distances in adsorbates (do not exceed 2.5%), and relatively high internuclear distances between the adsorbates and nanotubes (above 2 Å). Although for some cases (CNT(3,3)-N-HF, CNT(5,5)-N-HF, GR-N-HF, and CNT(5,5)-N-HBr) the values of E_b can be formally attributed to the energy range of weak hydrogen bonds (see above), the rest of the adsorption cases reveal binding energies typical for van der Waals' interaction (0.01–0.1 eV range of binding energies [92]), that is, physisorption.

Results of the study of the system "HX molecule (X = F, Cl, Br), adsorbed on the surface of undoped, B-, and N-doped CNT(3,3), CNT(5,5), and graphene" allow the following conclusions. The calculated binding energies and charges on adsorbates reveal the mechanism of physisorption of HX molecules on undoped graphene and undoped CNTs and on N-doped materials. Therefore, undoped, B-, and N-doped carbon nanotubes are less attractive to elaboration of sensors of hydrogen halide gases.

Materials based on the B-doped CNTs are perspective for sensing of HCl and HBr hydrogen halides as the molecules are chemisorbed on the nanotube surfaces.

21.5 Electronic Structure of Carbon Nanotubes with Adsorbed Molecular Anions of Hexavalent Metals and Perspectives for Removal of Toxic M(VI) Metals by Carbon Nanomaterials

This section presents calculation results and corresponding analysis for the electronic structure of single- and multiwalled carbon nanotubes and graphene with adsorbed anions of M(VI) metals. The influence of impurities (boron and nitrogen) and oxygen- and ammonia-containing functional groups on the formation of the interatomic bonds between carbon materials and the anions is analyzed in view of

Table 21.3 Calculated binding energies, charges of adsorbate molecules HX (X = F, Cl, Br), and internuclear distances for N-doped configurations

Type of adsorbate	Configuration	Binding energy E_b (eV)	Charge state of HX adsorbate (e)	$R_{H-X}/(R_{H-X})^{free}$	$(R_{C-H})^{min}$
HF	CNT(3,3)-N-HF	−0.1703	0.007	0.9555/0.94927	2.53622
	CNT(5,5)-N-HF	−0.4126	0.02	0.95049/0.94927	3.73704
	GR-N-HF	−0.2116	0.021	0.95008/0.94927	3.92233
HCl	CNT(3,3)-N-HCl	−0.0603	−0.064	1.3519/1.32057	2.66707
	CNT(5,5)-N-HCl	Geometry optimization unconverged			
	GR-N-HCl	−0.06534	−0.001	1.32000/1.32057	5.16923
HBr	CNT(3,3)-N-HBr	−0.0942	0.013	1.4392/1.44006	3.88017
	CNT(5,5)-N-HBr	−0.1868	−0.009	1.43967/1.44006	3.08926
	GR-N-HBr	−0.0716	0.005	1.43913/1.44006	4.17118

R_{H-X}(Å) – internuclear distance in adsorbed HX molecule
$(R_{H-X})^{free}$(Å) – internuclear distance in free HX molecule
$(R_{C-H})^{min}$(Å) – shortest distance from a carbon atom of the adsorbent to the H atom of HX

potential application of carbon nanomaterials for removal of M(VI) metals from air and water media.

The binding energies E_b of anions to adsorbents, both in vacuo and in aqua, were obtained as the difference of the calculated total energies using expression:

$$E_b = E_{ads-anion} - E_{ads} - E_{anion}, \tag{21.4}$$

where $E_{ads\text{-}anion}$ are total energies of the optimized adsorption system "adsorbent with anion," E_{ads} are total energies of the optimized adsorbent, and E_{anion} are total energies of optimized anions calculated within the same approximations.

Clusters of all undoped carbon nanostructures in calculations were electrically neutral, while additional charges equal to $-1e$ and $+1e$ were assigned to clusters describing the B- and N-doped clusters, respectively. Taking into account the $-2e$ charge of "free" $M^{VI}O_4^{2-}$ (M^{VI} = Cr, Mo, W) anion, additional $-2e$ charges were assigned to the clusters of undoped adsorbent and chromate anion. Consequently, additional charges of $-3e$ or $-1e$ were assigned to the B- or N-doped clusters, respectively.

Differences in charge density on the $M^{VI}O_4^{2-}$ (M^{VI} = Cr, Mo, W), $Cr_2O_7^{2-}$, and $HCrO_4^-$ anions (in respect to the isolated anion) in adsorbed state were defined as $\Delta q = -2e - q$ ($\Delta q = -e - q$ for $HCrO_4^-$), where q is an algebraic sum of charge states of all atoms of anion (calculated in adsorbed configuration using Mulliken population analysis). If the calculated value of Δq is negative, the electronic charge is transferred from the anion to the adsorbent.

21.5.1 Adsorption of $M(VI)O_4^{2-}$ (M(VI) = Cr, Mo, W) Anions on Undoped and B(N)-Doped CNTs

Single adsorption configurations were found in each case (see Fig. 21.7), except for the adsorption on undoped graphene.

In all cases, the binding energies are negative and fall within -0.5 to -7.2 eV range (Table 21.4). Such E_b values are typical for the chemisorption mechanism of adsorption [93].

All three anions, CrO_4^{2-}, MoO_4^{2-}, and WO_4^{2-}, have very similar dependencies of both E_b, and Δq on type of doping and type of the adsorbent structure. This feature is quite expected since Cr, Mo, and W metals are isoelectronic and the valence properties of $M(VI)O_4^{2-}$ anions are determined by interplaying $3d$ ($4d$ or $5d$) orbitals of the M(VI) cation and $2p$ orbitals of the oxygen ligands. At that, the cationic d orbitals are localized at the central core of the anion, so creation of the chemical bonds to outer atoms is determined mainly by the oxygen $2p$ orbitals which have very common energy and spatial structure for all three $M(VI)O_4^{2-}$ anions [90].

Two stable configurations (GR-1 and GR-2) were found for the case of the adsorption of $M^{VI}O_4^{2-}$ (M^{VI} = Cr, Mo, W) molecules on graphene sheet (Fig. 21.8).

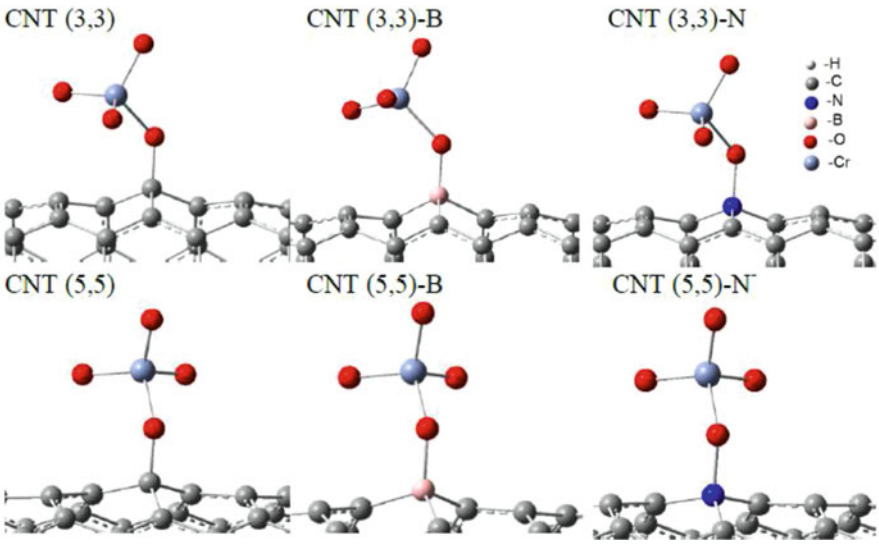

Fig. 21.7 Geometry-optimized structures of CrO_4^{2-} anions adsorbed on CNT(3,3) and CNT(5,5) in vacuo (only central parts of the clusters are shown)

So, our results indicate that one would expect quite similar absorption characteristics for the three anions and also for other types of adsorbents; for this reason we have limited the set of anions to only CrO_4^{2-} in studies of adsorption on the functionalized carbon nanostructures.

The optimized geometries of CrO_4^{2-} adsorbed on pristine and doped graphene (Fig. 21.8) illustrate typical peculiarities of adsorption configurations.

As Fig. 21.8 shows, in configuration 1 (such kind of atomic configuration is the most common among all adsorption cases), the chemical bond between the O atom of the anion and C atom of the adsorbent is created (the internuclear distance R_{C-O}^{min} is 1.47 Å which is a typical value for C–O covalent bonding [94]).

In configuration 2 (see Fig. 21.8), three O atoms are located at approximately equal distance from the carbon surface, that is, one of the faces of the CrO_4^{2-} tetrahedron is parallel to the graphene surface. In this configuration, each of the three O atoms is located about 2.80 Å above the center of C_6 "honeycomb" of graphene surface, and all three O atoms have approximately the same local surrounding. Within this accuracy, the structure is characterized by the C_3 symmetry axis perpendicular to the graphene plane and containing one C atom of the adsorbent, the Cr atom, and the "upper" O atom of the CrO_4^{2-} anion.

In the GR-B-CrO_4^{2-} case, one O atom of the anion creates a covalent bond to the boron dopant of the adsorbent (Fig. 21.8), and such kind of bonding is common for all cases of adsorption on the B-doped adsorbents. The situation is different for the N-doped adsorbents: one O atom of the anion can create bond either with N atom or with C atom which is the nearest neighbor to N (see Fig. 21.7 and 21.8).

Table 21.4 Binding energies E_b (eV), charge differences Δq (e) of $M(VI)O_4^{2-}$ (M(VI) = Cr, Mo, W) anions adsorbed on undoped and B(N)-doped carbon nanostructures, and the shortest internuclear distances R^{min} between anions and adsorbents (Å) calculated in vacuo

Configuration	E_b	Δq	R^{min}(bond type)
CNT(3,3)-CrO_4^{2-}	−3.79083	−0.8291	1.4161 (C–O)
CNT(5,5)-CrO_4^{2-}	−3.7329	−0.8974	1.43652 (C–O)
MWCNT-CrO_4^{2-}	−2.63828	−0.9464	1.45463 (C–O)
GR-CrO_4^{2-}-1	−2.89096	−0.9723	1.4678 (C–O)
GR-CrO_4^{2-}-2	−2.87873	−0.8554	3.14651 (C–O)
CNT(3,3)-B-CrO_4^{2-}	−0.76203	−0.5907	1.44814 (B–O)
CNT(5,5)-B-CrO_4^{2-}	−1.36138	−0.6446	1.47594 (B–O)
MWCNT-B-CrO_4^{2-}	−0.85638	−0.7705	1.50932 (B–O)
GR-B-CrO_4^{2-}	−1.50437	−0.8147	1.51794 (B–O)
CNT(3,3)-N-CrO_4^{2-}	−6.25441	−1.1137	1.48069 (N–O)
CNT(5,5)-N-CrO_4^{2-}	−5.62802	−1.119	1.51974 (N–O)
MWCNT-N-CrO_4^{2-}	−6.54564	−0.9901	1.39640 (C–O)
GR-N-CrO_4^{2-}	−6.79154	−0.9940	1.40748 (C–O)
CNT(3,3)-MoO_4^{2-}	−3.35158	−0.7910	1.42157 (C–O)
CNT(5,5)-MoO_4^{2-}	−3.23772	−0.8594	1.44191 (C–O)
GR-MoO_4^{2-}-1	−2.37352	−0.9282	1.47396 (C–O)
GR-MoO_4^{2-}-2	−2.34263	−0.7462	3.10782 (C–O)
CNT(3,3)-B-MoO_4^{2-}	−0.5478	−0.5701	1.45440 (B–O)
CNT(5,5)-B-MoO_4^{2-}	−1.05357	−0.6156	1.47825 (B–O)
GR-B-MoO_4^{2-}	−0.78632	−0.9420	1.55429 (C–O)
CNT(3,3)-N-MoO_4^{2-}	−5.61597	−1.0815	1.48592 (N–O)
CNT(5,5)-N-MoO_4^{2-}	−7.21026	−0.9307	1.40001 (C–O)
GR-N-MoO_4^{2-}	−6.49465	−0.9589	1.42121 (C–O)
CNT(3,3)-WO_4^{2-}	−3.23703	−0.7827	1.42612 (C–O)
CNT(5,5)-WO_4^{2-}	−3.12088	−0.8412	1.44547 (C–O)
GR-WO_4^{2-}-1	−2.27914	−0.9033	1.48033 (C–O)
GR-WO_4^{2-}-2	−2.36037	−0.7513	3.10519 (C–O)
CNT(3,3)-B-WO_4^{2-}	−0.53325	−0.5699	1.45440 (B–O)
CNT(5,5)-B-WO_4^{2-}	−1.01168	−0.6051	1.47534 (B–O)
GR-B-WO_4^{2-}	−1.10752	−0.7515	1.52304 (B–O)
CNT(3,3)-N-WO_4^{2-}	−5.42915	−1.0719	1.50997 (N–O)
CNT(5,5)-N-WO_4^{2-}	−7.07997	−0.9122	1.4075 (C–O)
GR-N-WO_4^{2-}	−6.21075	−0.9324	1.42828 (C–O)

Creation of covalent O-C bonds is observed for adsorption of CrO_4^{2-} and MoO_4^{2-} on CNT(3,3)-N and CNT(5,5)-N and for WO_4^{2-} on CNT(3,3)-N. The O-N covalent bonds are created in all other adsorption cases on the N-doped adsorbents. As Table 21.4 shows, creation of O-N bonds provides the highest absolute values of binding energies.

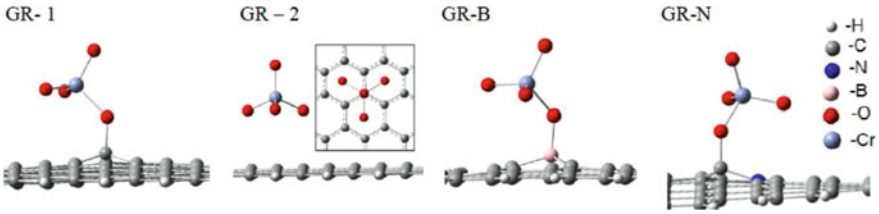

Fig. 21.8 Geometry-optimized structures of CrO_4^{2-} anions adsorbed on graphene in vacuo (only central parts of the clusters are shown)

The calculated oscillator strengths of CrO_4^{2-} anions are given in Fig. 21.9. As can be seen from the figure, calculations predict appearance of additional red bands of optical absorption of CrO_4^{2-} anions after on N-doped CNT. Such an appearance can be related to the fact that adsorption of CrO_4^{2-} on the N-doped CNT is accompanied by significant distortions of the anion nuclei. When considering distances and angles for adsorption on carbon nanostructures (see Table 21.5), one can see that the most significant distortions of the CrO_4^{2-} geometry are observed for adsorption on nitrogen-doped structures in comparison with undoped and B-doped configurations.

Since our results reveal the chemisorptions mechanisms, they indicate that the CNT-based materials can efficiently adsorb CrO_4^{2-}, MoO_4^{2-}, and WO_4^{2-} anions in gaseous media, i.e., from air atmosphere. However, the situation is quite different for adsorption in water.

The binding energies (E_b) and the charge difference (Δq) for the adsorbed configurations of $M(VI)O_4^{2-}$ on the surface of undoped, boron-nitrogen-doped, carbon nanostructures calculated *in aqua* are shown in Fig. 21.10.

As Fig. 21.10 shows, much lower absolute values of binding energies are observed for all studied combinations relatively to corresponding cases in vacuo. The E_b values of all adsorption cases on MWCNT cluster and graphene are positive indicating that adsorption of $M(VI)O_4^{2-}$ anions by such adsorbents is energetically unfavorable. Positive are also the energies of adsorption cases on all undoped adsorbents. Only the B- and N-doped CNT(3,3) and CNT(5,5) reveal negative E_b values and these values are below -2 eV for adsorption of CrO_4^{2-} and MoO_4^{2-} on CNT(3,3). All three anions reveal no stable adsorption configurations *in aqua* on undoped graphene, i.e., geometry optimization was not convergent.

From these results, we can conclude that undoped CNTs could be less-efficient materials for adsorption of $M(VI)O_4^{2-}$ anions in water. The efficiency can be improved if the materials would contain a valuable amount of low-diameter CNTs, or they would be doped by aliovalent impurities like B or N. Both ways of improvement are expensive and hardly realizable for massive production of CNT mixtures [96, 97]. So, another mechanism should be proposed to explain a substantial uptake of Cr(VI) anions by CNT-based materials from water solutions observed in experiments [36, 38, 98, 99]. These mechanisms are examined in the following subsection.

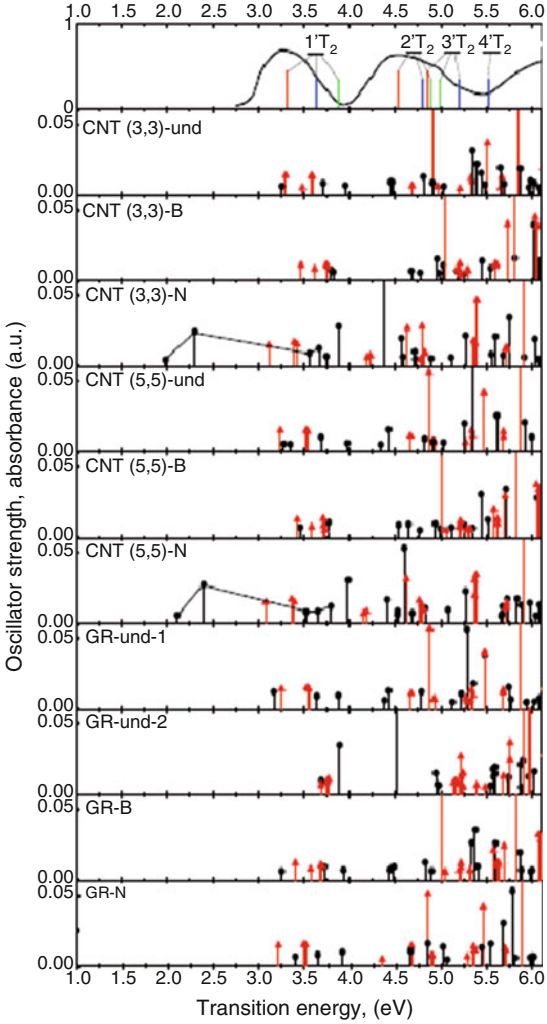

Fig. 21.9 Top plot: calculated energies of electronic transitions from the ground ($^1A_1$) to the low-energy excited states of free CrO_4^{2-} anions (blue bars); energies of the same transitions calculated with another basis sets [90] (green bars) and determined experimentally (red triangles); experimental absorption spectrum of chromate anion in aqueous solution (black solid line) [95]. Other plots: oscillator strengths of electronic transitions of CrO_4^{2-} anions adsorbed on the surface of carbon nanostructures calculated with (black circles) and without (red triangles) account of influence from the adsorbents

Table 21.5 Characteristic parameters of distortions of adsorbed CrO_4^{2-} anions

Configuration	Relative standard deviation of distances (%)	Relative standard deviation of angles (%)
CNT(3,3)-CrO_4^{2-}	6.3	2.1
CNT(5,5)-CrO_4^{2}	6.8	2.3
GR-CrO_4^{2-}	1.7	2.1
CNT(3,3)-B-CrO_4^{2-}	4.8	1.3
CNT(5,5)-B-CrO_4^{2}	5.1	1.5
GR-B-CrO_4^{2-}	5.3	1.6
CNT(3,3)-N-CrO_4^{2-}	7.7	3.1
CNT(5,5)-N-CrO_4^{2}	7.9	3.2
GR- N-CrO_4^{2-}	7.0	2.4

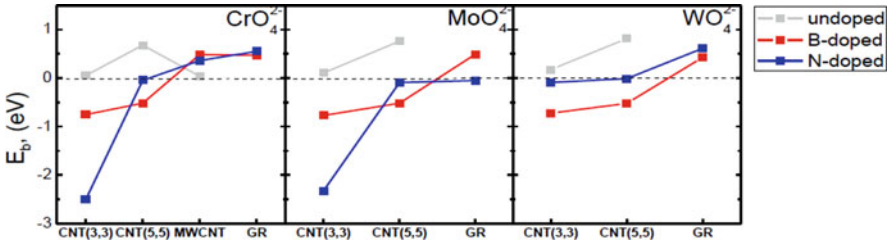

Fig. 21.10 Dependencies of binding energies E_b on adsorbent type and type of doping calculated in aqua

21.5.2 Adsorption of CrO_4^{2-} Anions on Functionalized CNTs

It is believed that one of the most efficient ways for enhancement of the adsorption capability of CNTs with respect to Cr(VI) compounds is functionalization of the CNT-based materials by the oxygen-containing surface functional groups (OSG) [2, 4, 34, 35]. In such functionalization, mixes of CNTs are treated by acids, for instance, by HNO_3 [34, 35] and then filtered, washed out, and dried up. As a result, various OSGs are created on the CNTs surfaces (a schematic explanation of the process can be found in [35]).

According to existing concepts [34, 36, 47], such kind of functionalization can enhance uptake of Cr(VI) compounds by the materials due to the following factors: (a) chemical reactions of Cr(VI) compounds with OSG can change the valence state of chromium ions Cr(VI) → Cr(III), whereas trivalent chromium ions are by several orders less toxic than hexavalent ones; (b) compounds of Cr(VI) can be chemically bound directly to atoms of OSG, that is, the groups can create additional adsorption cites for chromium compounds if compared with nonfunctionalized CNT surface; and (c) positively charged OSG^+ can be the centers of Coulomb attraction for negatively charged chromate anions like CrO_4^{2-} that enhances adsorption capability of functionalized CNT material (this concept is analyzed in [36]).

However, there were several experimental indications that Coulomb attraction to positively charged groups is a less important factor for enhancement of Cr(VI) uptake by the OSG-functionalized CNTs, and this enhancement occurs mainly due to creation of additional OSG-related adsorption sites [34]. In this subsection, we examine computationally, could the OSGs form such sites.

Particular objects of the calculations and motivation for their choice are the following. As it was shown in [35], the FTIR spectra of OSG functionalized CNT materials reveal spectral peaks corresponding to several oxygen-containing groups, in particular –OH (hydroxyl group), –COOH (carboxyl group), and $–COO^{-}$ (deprotonated carboxyl group). So, in our calculations we consider such groups and some of their combinations.

Here, we consider only one type of carbon nanotube, namely, CNT(5,5), since the main focus of the study is bonding of the anions to the OSGs, and the curvature of carbon surface is obviously expected to have a low importance.

The following functional groups are considered (see also Fig. 21.11):

1. CNT(5,5)-COOH. A neutral carboxyl group –COOH has one unpaired electron, whereas neutral cluster of CNT(5,5) has even number of electrons. An even number of electrons is a necessary condition for stability of the chemical bonds; so to model functionalization of the CNT by –COOH group, we assigned the $+1$e charge to CNT(5,5)-COOH adsorbent (accordingly, the -1e charge was assigned to CNT(5,5)-COOH-CrO_4^{2-} complex). So in fact we model a removal of an extra electron from the region of adsorption (from the OSG). Physically, this electron can be localized on some other defect in the CNT which is left beyond the study.
2. CNT(5,5)-B-COOH. Creation of B_C requires an extra electron, so it compensates the COOH group providing chemical stability for the complex. In this case, the adsorbent was taken electrostatically neutral, and correspondingly -2e charge was assigned to CNT(5,5)-B-COOH-CrO_4^{2-} system.
3. CNT(5,5)-COOH-OH. Carboxyl and hydroxyl groups are bound to two nearest C atoms of the nanotube. Unpaired electrons of both groups are mutually compensated, and such complex is considered as one of the most probable kings of coexistence of -COOH and -OH groups on the CNT surface (see [35] and references therein).

   As it was found experimentally [35, 36], adsorption capability of OSG-functionalized CNT materials with respect to Cr(VI) compounds in water solution substantially depends on the pH level. It is well-known that at high pH levels, OSG can be deprotonated (this process can be schematically denoted as $–COOH \rightarrow COO^{-} + H^{+}$ or $–OH \rightarrow –O^{-} + H^{+}$). To study the influence of deprotonation on adsorption of CrO_4^{2-}, we consider the following two complexes with deprotonated carboxyl groups:
4. CNT(5,5)-COO^{-}-OH. Analogous to case (3) but with carboxyl group missing H^{+} proton. The negative charge of carboxyl group is modeled by adding one extra electron, that is, assigning $-1e$ charge to the system.

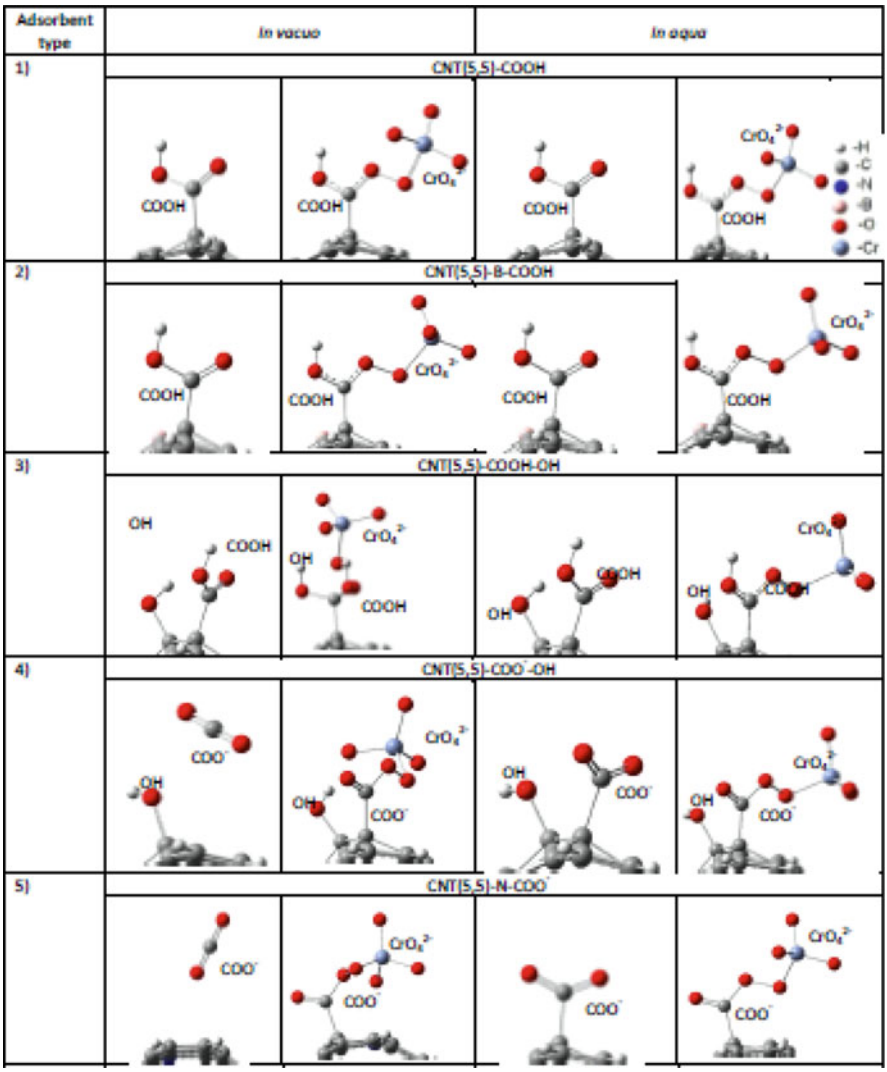

Fig. 21.11 Geometry-optimized structures of OSG-functionalized CNT(5,5) with (columns 2 and 4) and without (columns 1 and 3) adsorbed CrO_4^{2-} anions

5. CNT(5,5)-N-COO^-. The negative charge of carboxyl group is supplied by aliovalent impurity N_C.

Functionalization of the CNTs by ammonia is a commonly applied method of influence on the adsorption properties of the CNT-based materials [76]. To study adsorption of CrO_4^{2-} on ammonia-functionalized CNTs, we consider the following cases:

Table 21.6 Binding energies E_b (eV), charge differences Δq (e) of CrO_4^{2-} anions adsorbed on functionalized CNT(5,5), and the shortest internuclear distances R^{min} between the anion and adsorbents (Å) calculated in vacuo

Type of adsorbent	E_b	Δq	R^{min}(bond type)
1. CNT(5,5)-COOH	−5.09424	−1.27908	1.44011 (O–O)
2. CNT(5,5)-B-COOH	−2.03214	−1.23958	1.44219 (O–O)
3. CNT(5,5)-COOH-OH	−4.15042	−1.04078	1.43590 (O–O)
4. CNT(5,5)-COO^--OH	–	−1.08516	1.44225 (O–O)
5. CNT(5,5)-N-COO^-	–	−1.14172	1.44671 (O–O)
6. CNT(5,5)-OH-NH_3^+	–	−0.6631	0.97521 (H–O) 1.60492 (H–O)
7. CNT(5,5)-1-NH_3^+	−10.53795	−0.57807	0.98510 (H–O) 1.99308 (H–O)
8. CNT(5,5)-2-NH_3^+	−10.30772	−0.5677	0.98504 (H–O) 2.0149 (H–O)

6. CNT(5,5)-OH-NH3$^+$. The ammonia –NH_3^+ and hydroxyl –OH groups are bound to the neighboring C atoms of the nanotube providing even number of electrons.
7. CNT(5,5)-1-NH_3^+ (1 = $C_8H_{16}O_2N$ = -C_2H_4-N-CH_2-CH_2-O-CH_2-CH_2-O-CH_2-CH_2-). Such kind of functionalization with ammonia can substantially enhance hydrophilicity of the CNT-based materials [100], even when functionalization procedures are rather complex [76, 101].
8. CNT(5,5)-2-NH3+ (2 = C_4H_8N = -C_2H_4-N-CH_2-CH_2-). Another group with NH_3^+ at the end, however, with different (approximately, a half-shorter) atomic chain between ammonia and the nanotube. Such shorter chain represents an intermediate case of distance between the NH_3^+ and the CNT surface if compared with corresponding distances in groups (6) and (7).

Calculation results on adsorption of CrO_4^{2-} anions on functionalized CNTs both in vacuo and *in aqua* are given in Table 21.6. As the calculations show, adsorbents (4), (5), and (6) are not stable in vacuo without CrO_4^{2-} anions (geometry optimizations unconverged), so the corresponding binding energies cannot be calculated.

As Table 21.6 shows for adsorbents (1)–(5), in all these cases, the R^{min} distances are typical for the covalent bonding between two oxygen atoms, that is, the anions are bound to the OSG by O-O covalent bonds both in vacuo and in aqua. At that, the R^{min} distances for in-vacuum and in-water adsorption on adsorbents (1)–(5) are very close (they differ by only few thousandths of Å); however, the binding energies E_b are significantly different. For vacuum, the E_b energies are negative, whereas for water they are positive, indicating that adsorption on adsorbents (1)–(5) in vacuo is energetically unfavorable.

Adsorption configurations of CrO_4^{2-} on adsorbents (7) and (8) in vacuo are characterized by the binding energies (near −10 eV) which are substantially higher

Table 21.7 Binding energies E_b (eV), charge differences Δq (e) of CrO_4^{2-} anions adsorbed on functionalized CNT(5,5), and the shortest internuclear distances R^{min} between the anion and adsorbents (Å) calculated *in aqua*

Type of adsorbent	E_b	Δq	R^{min}(bond type)
1. CNT(5,5)-COOH	3.67783523	−1.17828	1.44335 (O–O)
2. CNT(5,5)-B-COOH	3.76432267	−1.13843	1.44124 (O–O)
3. CNT(5,5)-COOH-OH	3.9323826	−1.15227	1.43907 (O–O)
4. CNT(5,5)-COO^--OH	2.28683293	−0.99205	1.44092 (O–O)
5. CNT(5,5)-N-COO^-	1.61844338	−1.02606	1.44856 (O–O)
6. CNT(5,5)-OH-NH_3^+	−0.92044761	−0.17524	1.70045 (H–O)
7. CNT(5,5)-1-NH_3^+	−1.00481	−0.19679	1.66845 (H–O)
8. CNT(5,5)-2-NH_3^+	−0.97787	−0.18121	1.70959 (H–O)

than E_b values of other adsorption configurations on functionalized CNTs found in vacuo (cases (1)–(3); see Table 21.6).

A distinctive feature of these configurations is that two O-H bonds between the anion and NH_3^+ group are created. One of them has R^{min} distance (0.985 Å) typical to covalent O–H bonding. However, the H atom of this bond lies closer to the anion than to the N atom of NH_3^+ group (corresponding H-N distance is 2.004 Å, whereas other H-N distances in the group are in the range 1.2–1.3 Å). So, attached to CNT surface OSGs of (1), (2), and (3) types as well as ammonia-containing groups (7) and (8) can be the centers of efficient adsorption of CrO_4^{2-} anions in vacuo.

The negative E_b values (about −1 eV) are also obtained for *in aqua* adsorption of CrO_4^{2-} on ammonia-functionalized CNTs (cases (6)–(8)). In each of these three cases, two O-H bonds between the oxygen atoms of the anion and the hydrogen atoms of NH_3^+ groups are created (correspondingly, two values are given in the R^{min} column of Table 21.7 for cases (6)–(8)). Such R^{min} values are typical for the hydrogen-type bonds [94].

So, taking into account generally weak adsorption of CrO_4^{2-} on undoped and B(N)-doped carbon nanostructures, it can be concluded that functionalization by ammonia-containing functional groups can enhance the adsorption capability of the CNT-based materials with respect to CrO_4^{2-} anions in water surrounding.

21.5.3 *Adsorption of $HCrO_4^-$ and $Cr_2O_7^{2-}$ Anions on Pristine, B(N)-Doped, and Functionalized Carbon Nanostructures*

Results obtained in Sect. 5.1 definitely indicate that almost all adsorption cases of $M(VI)O_4^{2-}$ anions on MWCNT reveal E_b, Δq, and R_{C-O}^{min} values which are intermediate between CNT(5,5) and graphene cases, both in vacuo and *in aqua*. This result implies that considering only two absorbents representing the "edge" cases of the nanotube surface curvature [CNT(5,5) and graphene] may provide

Table 21.8 Binding energies E_b (eV), charge differences Δq (e) of $HCrO_4^-$ and $Cr_2O_7^{2-}$ anions adsorbed on undoped and B(N)-doped carbon nanostructures, and the shortest internuclear distances R^{min} between the anions and adsorbents (Å) calculated in vacuo

Type of anion	Type of adsorbent	E_b	Δq	R^{min}(bond type)
$HCrO_4^-$	CNT(5,5)	−0.36325	−0.07179	3.06261 (C–O)
	CNT(5,5)-B	Unconverged		
	CNT(5,5)-N	−2.22284	−0.14129	2.99330 (C–O)
	GR	−0.34054	−0.07392	3.22327 (C–O)
	GR-B	Unconverged		
	GR-N	−2.04522	−0.0942	2.99330 (C–O)
$Cr_2O_7^{2-}$	CNT(5,5)	−1.37037	−0.32272	2.71228 (C–O)
	CNT(5,5)-B	0.092683	−0.46276	1.51208 (B–O)
	CNT(5,5)-N	−5.78497	−0.82444	1.43616 (C–O)
	GR	−0.87035	−0.78919	1.54294 (C–O)
	GR-B	0.175954	−0.59377	1.55506 (B–O)
	GR-N	−4.67928	−0.26619	2.77642 (C–O)

Table 21.9 Binding energies E_b (eV), charge differences Δq (e) of $HCrO_4^-$ and $Cr_2O_7^{2-}$ anions adsorbed on undoped and B(N)-doped carbon nanostructures, and the shortest internuclear distances R^{min} between the anions and adsorbents (Å) calculated *in aqua*

Type of anion	Type of adsorbent	E_b	Δq	R^{min}(bond type)
$HCrO_4^-$	CNT(5,5)	−0.0351	0.024866	3.94411 (C–O)
	CNT(5,5)-B	−0.09661	0.015293	3.95882 (C–O)
	CNT(5,5)-N	−0.10812	0.007237	3.22034 (C–O)
	GR	0.005776	0.00764	3.97388 (C–O)
	GR-B	0.027164	0.009331	3.97438 (C–O)
	GR-N	−0.01816	0.006586	3.95648 (C–O)
$Cr_2O_7^{2-}$	CNT(5,5)	−0.03814	0.036403	3.85276 (C–O)
	CNT(5,5)-B	−0.09642	0.038606	3.79722 (C–O)
	CNT(5,5)-N	−0.13169	0.013523	3.33032 (C–O)
	GR	0.01776	0.022416	3.96976 (C–O)
	GR-B	0.048613	0.03503	3.97388 (C–O)
	GR-N	−0.06209	0.003633	3.29386 (C–O)

quite sufficient information about adsorption properties with respect to oxoanions of hexavalent chromium. For this reason, we limit our studies of $HCrO_4^-$ and $Cr_2O_7^{2-}$ adsorption on undoped and B(N)-doped carbon nanostructures to only two types of adsorbents, namely, CNT(5,5) and graphene sheets.

As it follows from calculations (see Tables 21.8 and 21.9), adsorption of $Cr_2O_7^{2-}$ and $HCrO_4^-$ anions on undoped and B(N)-doped carbon nanostructures *in aqua* is characterized by either positive or nominally negative but very low in absolute values binding energies (not greater than |0.13| eV). Such E_b values, together with relatively long R^{min} (in 3.2–4 Å range; see Table 21.8), unambiguously reveal the absence of chemical bonding between the adsorbents and the anions. At that,

the cases with negative E_b values presented in Table 21.9 can be regarded as physisorption. Such results, together with results for adsorption of CrO_4^{2-} anion (see above) can lead to a conclusion that neither undoped nor B(N)-doped CNTs cannot by efficient adsorbents of the considered anions of hexavalent chromium in water surrounding.

However, adsorption configurations with chemical bonds and substantially negative binding energies exist in vacuo (see Table 21.8). As the table shows, the aliovalent doping of adsorbents in the case of $HCrO_4^-$ and $Cr_2O_7^{2-}$ adsorption has in general the same effect on the E_b values as it was in CrO_4^{2-} case (see above). Doping with N substantially lowers the E_b values (by ~2 and ~4 eV for $HCrO_4^-$ and $Cr_2O_7^{2-}$ adsorption, respectively) relatively to corresponding adsorption cases on undoped adsorbents. Doping with B, in contrast, leads to positive binding energies (in $Cr_2O_7^{2-}$ case) or to the absence of adsorbed configurations ($HCrO_4^-$ case).

Rather long R^{min} (near 3 eV; see Table 21.8) are obtained for all adsorption configurations of $HCrO_4^-$ in vacuo. At that, simultaneously, two [CNT(5,5)-N-$HCrO_4^-$ case] or even three (all other converged cases) oxygen atoms of $HCrO_4^-$ anion are located at approximately equal distance from the adsorbent.

Long R^{min} together with substantially negative E_b values are obtained in vacuo also for $Cr_2O_7^{2-}$ adsorption on CNT(5,5) and GR-N adsorbents. So, taking into account these results (and also results for CrO_4^{2-} presented above), we can conclude that carbon nanostructures will be efficient materials for removal of all three considered anions of Cr(VI) in gaseous state, whereby doping with N will enhance the adsorption capability of the materials.

Results for adsorption of $Cr_2O_7^{2-}$ and $HCrO_4^-$ anions on functionalized CNT(5,5) *in aqua* are presented in Table 21.10 (the adsorbents have the same notation as in Sect. 5.3) As Table 21.10 shows for both anions, all adsorbents

Table 21.10 Binding energies E_b (eV), charge differences Δq (e) of $HCrO_4^-$ and $Cr_2O_7^{2-}$ anions adsorbed on functionalized CNT(5,5), and the shortest internuclear distances R^{min} between the anion and adsorbents (Å) calculated *in aqua*

Type of adsorbate	Type of adsorbent	E_b	Δq	R^{min}(bond type)
$HCrO_4^-$	1. CNT(5,5)-COOH	−0.46465	−0.03652	1.62764 (H–O)
	2. CNT(5,5)-B-COOH	−0.38381	−0.01867	1.66788 (H–O)
	3. CNT(5,5)-COOH-OH	−0.11714	0.068841	2.64463 (C–H)
	4. CNT(5,5)-COO-OH	−0.77144	0.197648	1.6253 (H–O)
	5. CNT(5,5)-N-COO^-	2.714456	−0.13429	1.46669 (O–O)
	6. CNT(5,5)-OH-NH_3^+	−0.52561	−0.06348	1.84429 (H–O)
$Cr_2O_7^{2-}$	1. CNT(5,5)-COOH	−0.52714	−0.01422	1.63343 (H–O)
	2. CNT(5,5)-B-COOH	−0.44699	−0.0132	1.64909 (H–O)
	3. CNT(5,5)-COOH-OH	−0.35767	0.050108	1.80878 (H–O)
	4. CNT(5,5)-COO-OH	−0.1915	0.114867	3.78136 (O–O)
	5. CNT(5,5)-N-COO^-	2.581851	−0.49302	1.4541 (O–O)
	6. CNT(5,5)-OH-NH_3^+	−0.57704	−0.04804	1.83167 (H–O)

reveal adsorbed configurations with negative binding energies (in −0.1 to −0.6 eV range) excluding adsorbent (5), for which the energy is positive. For both anions on adsorbent (5), the R^{min} distances (Table 21.10) show O-O chemical bonding between oxygen atoms of the anions and functional group –COO^-.

However, significantly positive E_b values (above 2.5 eV) clearly indicate that adsorption on this adsorbent is energetically unfavorable. Adsorption of $HCrO_4^-$ on adsorbent (3) and adsorption of $Cr_2O_7^{2-}$ on adsorbent (4) do not lead to creation of chemical bonds between the anions and functional groups, whereas the absolute values of binding energies in these two cases are low (fall between −0.1 and −0.2 eV). So evidently, the physisorption mechanism is realized in both cases.

For the rest of configurations presented in Table 21.10, the O-H bonds between the anions and functional groups are created (even two O-H bonds are observed for ammonia-containing adsorbent (6)). Such results indicate that chemisorption mechanism is realized in all these cases.

So, our calculations show that $Cr_2O_7^{2-}$ and $HCrO_4^-$ anions can be efficiently adsorbed by the OSG and ammonia-functionalized carbon nanostructures in water.

Our results can explain the experimentally observed dependencies of Cr(VI) uptake by the OSG-functionalized CNT-based materials on pH level of water solution, which were presented in, for example [35]. The Cr(VI) uptake reaches the highest values when pH < 2, it decreases when 2 < pH < 6, and the Cr(VI) compounds are practically not adsorbed when pH > 6 [36]. It is known that at pH < 6 compounds of Cr(VI) exist predominantly as $Cr_2O_7^{2-}$ and $HCrO_4^-$, whereas at pH > 6 they exist as CrO_4^{2-} [35, 36]. Our results show that OSG-functionalized carbon nanostructures are good adsorbents of $Cr_2O_7^{2-}$ and $HCrO_4^-$ in water, while they poorly adsorb CrO_4^{2-}. So, the observed dependence of Cr(VI) uptake on pH level can be explained by this particular selectivity of the adsorbents with respect to the anions.

The above presented computational results and their analysis allow formulation of recommendations for functionalization of the CNT-based materials to enhance their adsorption capability with respect to Cr(VI) compounds in water. Functionalization of the materials both with OSG and ammonia-containing groups is feasible at low pH levels, whereas at high pH (>6), only functionalization by ammonia-containing groups will make sense. Undoped carbon nanostructures are poor adsorbents of Cr(VI) compounds in water, and aliovalent doping with B or N atoms does not improve the situation.

21.6 Conclusions

The results of the study of the system "HX molecule (X = F, Cl, Br), adsorbed on the surface of undoped, B-, and N-doped CNT(3,3), CNT(5,5) and graphene" clusters allow the following conclusions. The calculated binding energies and charges on adsorbates reveal the mechanism of physisorption of HX molecules on undoped graphene and undoped CNTs and on N-doped materials. Therefore, undoped, B-,

and N-doped carbon nanotubes are less attractive to elaboration of sensors of hydrogen halide gases. Materials based on the B-doped CNTs are perspective for sensing of HCl and HBr hydrogen halides as the molecules are chemisorbed on the nanotube surfaces.

The DFT-based electronic structure calculations predict that the CNT-based materials can efficiently adsorb $M^{VI}O_4^{2-}$ (M^{VI} = Cr, Mo, W), $Cr_2O_7^{2-}$, and $HCrO_4^-$ anions in gaseous surrounding. Doping of carbon nanostructures with nitrogen provides additional adsorption sites for the anions, so such kind of doping can enhance adsorption capability of the materials with respect to $M^{VI}O_4^{2-}$, $Cr_2O_7^{2-}$, and $HCrO_4^-$ anions.

Calculations predict that neither pristine nor B- or N-doped CNTs can be efficient adsorbents of $M^{VI}O_4^{2-}$ (M^{VI} = Cr, Mo, W), $Cr_2O_7^{2-}$, and $HCrO_4^-$ anions in water. Functionalization of CNTs by the ammonia-containing functional groups enhances their adsorption capability with respect to CrO_4^{2-}, $Cr_2O_7^{2-}$, and $HCrO_4^-$ anions in water, so such functionalization can enhance removal of Cr(VI) compounds from wastewaters by CNT-based materials. Functionalization of CNTs by the oxygen-containing functional groups does not enhance their adsorption capability in water with respect to CrO_4^{2-}; however it enhances adsorption of $Cr_2O_7^{2-}$ and $HCrO_4^-$ anions.

Acknowledgments The calculations were performed using Bem supercomputer of Wroclaw Center for Networking and Supercomputing (grant no. 300).

References

1. Anjum M, Miandad R, Waqas M, Gehany F, Barakat MA (2016) Remediation of wastewater using various nano-materials. Arab J Chem. https://doi.org/10.1016/j.arabjc.2016.10.004
2. Gupta VK et al (2016) Study on the removal of heavy metal ions from industry waste by carbon nanotubes: effect of the surface modification: a review. Crit Rev Environ Sci Technol 46:93–118
3. Mohmood I et al (2013) Nanoscale materials and their use in water contaminants removal—a review. Environ Sci Pollut Res 20:1239–1260
4. Ren X, Chen C, Nagatsu M, Wang X (2011) Carbon nanotubes as adsorbents in environmental pollution management: a review. Chem Eng J 170:395–410
5. Rao GP, Lu C, Su F (2007) Sorption of divalent metal ions from aqueous solution by carbon nanotubes: a review. Sep Purif Technol 58:224–231
6. Mendoza F et al (2014) Room temperature gas sensor based on tin dioxide-carbon nanotubes composite films. Sensors Actuators B Chem 190:227–233
7. Fam DWH, Palaniappan A, Tok AIY, Liedberg B, Moochhala SM (2011) A review on technological aspects influencing commercialization of carbon nanotube sensors – ScienceDirect. Sensors Actuators B Chem 157(1):1–7
8. Wang Y, Yeow JTW (2009) A review of carbon nanotubes-based gas sensors. J Sensors. https://doi.org/10.1155/2009/493904
9. Mittal M, Kumar A (2014) Carbon nanotube (CNT) gas sensors for emissions from fossil fuel burning. Sensors Actuators B Chem 203:349–362
10. Lee K et al (2013) Highly sensitive, transparent, and flexible gas sensors based on gold nanoparticle decorated carbon nanotubes. Sensors Actuators B Chem 188:571–575

11. Ueda T, Katsuki S, Takahashi K, Narges HA, Ikegami T, Mitsugi F (2008) Fabrication and characterization of carbon nanotube based high sensitive gas sensors operable at room temperature. Diam Relat Mater 17(7–10):1586–1589
12. Kauffman DR, Star A (2008) Carbon nanotube gas and vapor sensors. Angew Chem Int Ed 47(35):6550–6570
13. Cazorla C (2015) The role of density functional theory methods in the prediction of nanostructured gas-adsorbent materials. Coord Chem Rev 300:142–163
14. Bai L, Zhou Z (2007) Computational study of B- or N-doped single-walled carbon nanotubes as NH3 and NO2 sensors. Carbon 45:2105–2110
15. Zhou Z, Gao X, Yan J, Song D (2006) Doping effects of B and N on hydrogen adsorption in single-walled carbon nanotubes through density functional calculations. Carbon 44:939–947
16. Villalpando-Páez F et al (2004) Fabrication of vapor and gas sensors using films of aligned CNx nanotubes. Chem Phys Lett 386:137–143
17. Wang R, Zhang D, Zhang Y, Liu C (2006) Boron-doped carbon nanotubes serving as a novel chemical sensor for formaldehyde. J Phys Chem B 110:18267–18271
18. Adjizian J-J et al (2014) Boron- and nitrogen-doped multi-wall carbon nanotubes for gas detection. Carbon 66:662–673
19. An W, Turner CH (2009) Electronic structure calculations of gas adsorption on boron-doped carbon nanotubes sensitized with tungsten. Chem Phys Lett 482:274–280
20. Talla JA (2012) Ab initio simulations of doped single-walled carbon nanotube sensors. Chem Phys 392:71–77
21. Vikramaditya T, Sumithra K (2014) Effect of substitutionally boron-doped single-walled semiconducting zigzag carbon nanotubes on ammonia adsorption. J Comput Chem 35:586–594
22. Anderson B et al (2005) Encyclopedia of toxicology, four-volume set: encyclopedia of toxicology, 2nd edn. Academic Press, Oxford, p 2000
23. Aylón E et al (2007) Emissions from the combustion of gas-phase products at tyre pyrolysis. J Anal Appl Pyrolysis 79:210–214
24. Hall WJ, Williams PT (2006) Pyrolysis of brominated feedstock plastic in a fluidised bed reactor. J Anal Appl Pyrolysis 77:75–82
25. Barontini F, Cozzani V (2006) Formation of hydrogen bromide and organobrominated compounds in the thermal degradation of electronic boards. J Anal Appl Pyrolysis 77:41–55
26. Karama JPB et al (2013) Modeling the emission of hydrogen chloride and free chlorine from the thermal treatment of polyvinyl chloride- (PVC-) based plastic materials. J Anal Appl Pyrolysis 101:209–214
27. Stavert DM, Archuleta DC, Behr MJ, Lehnert BE (1991) Relative acute toxicities of hydrogen fluoride, hydrogen chloride, and hydrogen bromide in nose- and pseudo-mouth-breathing rats. Fundam Appl Toxicol 16:636–655
28. https://www.sierramonitor.com/electrochemical-toxic-gas-sensor-module-5100-xx-it
29. Datta S, Vero SE, Hettiarachchi GM, Johannesson K (2017) Tungsten contamination of soils and sediments: current state of science. Current Pollution Rep 3:55–64
30. Halmi MIE, Ahmad SA (2014) Chemistry, biochemistry, toxicity and pollution of molybdenum: a mini review. J Biochem Microbiol Biotechnol 2:1–6
31. Wang C-W, Liang C, Yeh H-J (2016) Aquatic acute toxicity assessments of molybdenum (+VI) to *Daphnia magna*. Chemosphere 147:82–87
32. Jung C et al (2013) Hexavalent chromium removal by various adsorbents: powdered activated carbon, chitosan, and single/multi-walled carbon nanotubes. Sep Purif Technol 106:63–71
33. Tarutani N, Tokudome Y, Fukui M, Nakanishi K, Takahashi M (2015) Fabrication of hierarchically porous monolithic layered double hydroxide composites with tunable microcages for effective oxyanion adsorption. RSC Adv 5:57187–57192
34. Xu Y, Arrigo R, Liu X, Su DS (2011) Characterization and use of functionalized carbon nanotubes for the adsorption of heavy metal anions. New Carbon Mater 26:57–62

35. Hu J, Chen C, Zhu X, Wang X (2009) Removal of chromium from aqueous solution by using oxidized multiwalled carbon nanotubes. J Hazard Mater 162:1542–1550
36. Ihsanullah FA et al (2016) Effect of acid modification on adsorption of hexavalent chromium (Cr(VI)) from aqueous solution by activated carbon and carbon nanotubes. Desalin Water Treat 57:7232–7244
37. Pillay K, Cukrowska EM, Coville NJ (2009) Multi-walled carbon nanotubes as adsorbents for the removal of parts per billion levels of hexavalent chromium from aqueous solution. J Hazard Mater 166:1067–1075
38. Verdugo EM, Xie Y, Baltrusaitis J, Cwiertny DM (2016) Hematite decorated multi-walled carbon nanotubes (α-Fe_2O_3/MWCNTs) as sorbents for Cu(II) and Cr(VI): comparison of hybrid sorbent performance to its nanomaterial building blocks. RSC Adv 6:99997–100007
39. Ihsanullah FA et al (2016) Heavy metal removal from aqueous solution by advanced carbon nanotubes: critical review of adsorption applications. Sep Purif Technol 157:141–161
40. Emsley J (2011) Nature's building blocks: an A-Z guide to the elements. Oxford University Press, Oxford
41. Tytłak A, Oleszczuk P, Dobrowolski R (2015) Sorption and desorption of Cr(VI) ions from water by biochars in different environmental conditions. Environ Sci Pollut Res 22:5985–5994
42. Palmer CD, Wittbrodt PR (1991) Processes affecting the remediation of chromium-contaminated sites. Environ Health Perspect 92:25–40
43. Opperman DJ, Heerden E v (2007) Aerobic Cr(VI) reduction by Thermus scotoductus strain SA-01. J Appl Microbiol 103:1907–1913
44. Shouman MA, Fathy NA, Khedr SA, Attia AA (2013) Comparative biosorption studies of hexavalent chromium ion onto raw and modified palm branches. Adv Phys Chem. https://doi.org/10.1155/2013/159712
45. Dakiky M, Khamis M, Manassra A, Mer'eb M (2002) Selective adsorption of chromium(VI) in industrial wastewater using low-cost abundantly available adsorbents. Adv Environ Res 6:533–540
46. Romero-González J, Peralta-Videa JR, Rodríguez E, Ramirez SL, Gardea-Torresdey JL (2005) Determination of thermodynamic parameters of Cr(VI) adsorption from aqueous solution onto *Agave lechuguilla* biomass. J Chem Thermodyn 37:343–347
47. Kotaś J, Stasicka Z (2000) Chromium occurrence in the environment and methods of its speciation. Environ Pollut 107:263–283
48. Boulding JR (1996) EPA environmental assessment sourcebook. CRC Press, Boca Raton, Florida, USA
49. Iijima S (1991) Helical microtubules of graphitic carbon. Nature 354:56–58
50. Oberlin A, Endo M, Koyama T (1976) Filamentous growth of carbon through benzene decomposition. J Cryst Growth 32:335–349
51. Tennent HG (1987) Carbon fibrils, method for producing same and compositions containing same. *U.S. Patent No. 4,663,230*. Washington, DC: U.S. Patent and Trademark Office.
52. Iijima S, Ichihashi T (1993) Single-shell carbon nanotubes of 1-nm diameter. Nature 363:603–605
53. Saito R (1998) Raman spectra of carbon nanotubes. In: Physical properties of carbon nanotubes. Published by Imperial College Press and distributed by World Scientific Publishing Co., pp. 183–206. https://doi.org/10.1142/9781860943799_0010
54. Ajayan PM et al (1993) Opening carbon nanotubes with oxygen and implications for filling. Nature 362:522–525
55. Charlier J-C, Blase X, Roche S (2007) Electronic and transport properties of nanotubes. Rev Mod Phys 79:677–732
56. Charlier JC (1991) First-principles study of the electronic properties of graphite. Phys Rev B 43:4579. Available at: https://journals.aps.org/prb/abstract/10.1103/PhysRevB.43.4579. Accessed 1 Dec 2018

57. Reich S, Thomsen C, Maultzsch J (2008) Carbon nanotubes: basic concepts and physical properties. Wiley, Hoboken, New Jersey, USA
58. Bertoni G, Calmels L (2006) First-principles calculation of the electronic structure and energy loss near edge spectra of chiral carbon nanotubes. Micron 37:486–491
59. Borštnik U, Hodošček M, Janežič D, Lukovits I (2005) Electronic structure properties of carbon nanotubes obtained by density functional calculations. Chem Phys Lett 411:384–388
60. Ito A, Natsume Y, Ohmori S, Tanaka K (2002) Electronic structures of very thin carbon nanotubes: are they still π-electronic materials? Nano Lett 2:629–633
61. Boutko VG, Gusev AA, Shevtsova TN, Pashkevich YG (2011) Structural and electronic properties of single-wall carbon nanotubes with various nitrogen content. Low Temp Phys 37:1021–1025
62. Wang K, Shi C, Zhao N, Du X, Li J (2009) First-principles study of the B- or N-doping effects on chemical bonding characteristics between magnesium and single-walled carbon nanotubes. Chem Phys Lett 469:145–148
63. Buonocore F (2007) Doping effects on metallic and semiconductor single-wall carbon nanotubes. Philos Mag 87:1097–1105
64. D'yachkov PN, Kutlubaev DZ, Makaev DV (2010) Linear augmented cylindrical wave Green's function method for electronic structure of nanotubes with substitutional impurities. Phys Rev B 82:035426
65. Esrafili MD (2013) Nitrogen-doped (6,0) carbon nanotubes: a comparative DFT study based on surface reactivity descriptors. Comput Theor Chem 1015:1–7
66. Zhang L, Xia Z (2011) Mechanisms of oxygen reduction reaction on nitrogen-doped graphene for fuel cells. J Phys Chem C 115:11170–11176
67. Fazio G, Ferrighi L, Di Valentin C (2014) Boron-doped graphene as active electrocatalyst for oxygen reduction reaction at a fuel-cell cathode. J Catal 318:203–210
68. Talla JA (2012) First principles modeling of boron-doped carbon nanotube sensors. Phys B Condens Matter 407:966–970
69. Ghasemi AS (2013) A DFT computation for comparison of NQR of O_2, N_2 and CO over the surface of Single-Walled Carbon Nanotubes Res. J Appl Sci Eng Tech 5:1892
70. Hong G, Chen Y, Li P, Zhang J (2012) Controlling the growth of single-walled carbon nanotubes on surfaces using metal and non-metal catalysts. Carbon 50:2067–2082
71. Sanchez-Valencia JR et al (2014) Controlled synthesis of single-chirality carbon nanotubes. Nature 512:61–64
72. Valentini L et al (2003) Sensors for sub-ppm NO2 gas detection based on carbon nanotube thin films. Appl Phys Lett 82:961–963
73. Hizhnyi Y, Nedilko S, Borysiuk V, Shyichuk A (2018) Removal of oxoanions of MVI (MVI=Cr, Mo, W) metals by carbon nanostructures: insights into mechanisms from DFT calculations. Int J Quantum Chem 118:e25715
74. Hizhnyi Y, Nedilko S, Borysiuk V, Shyichuk A (2017) Ab initio computational study of chromate molecular anion adsorption on the surfaces of pristine and B- or N-doped carbon nanotubes and graphene. Nanoscale Res Lett 12:71
75. Hizhnyi Y, Nedilko SG, Borysiuk V, Gubanov VA (2015) Computational studies of boron- and nitrogen-doped single-walled carbon nanotubes as potential sensor materials of hydrogen halide molecules HX (X = F, Cl, Br). Int J Quantum Chem 115:1475–1482
76. Galano A (2006) On the influence of diameter and length on the properties of armchair single-walled carbon nanotubes: a theoretical chemistry approach. Chem Phys 327:159–170
77. Petrushenko IK, Ivanov NA (2013) Structural and electronic properties of finite-length single-walled carbon and silicon carbide nanotubes: DFT study. Mod Phys Lett B 27:1350210
78. Vasiliev I, del Puerto ML, Jain M, Lugo-Solis A, Chelikowsky JR (2009) Application of time-dependent density-functional theory to molecules and nanostructures. J Mol Struct THEOCHEM 914:115–129
79. Frisch MJ, Trucks GW, Schlegel HB, Scuseria GE, Robb MA, Cheeseman JR, Scalmani G, Barone V, Mennucci B, Petersson GA, Nakatsuji H, Caricato M, Li X, Hratchian HP, Izmaylov AF, Bloino J, Zheng G, Sonnenberg JL, Hada M, Ehara M, Toyota K, Fukuda R,

Hasegawa J, Ishida M, Nakajima T, Honda Y, Kitao O, Nakai H, Vreven T, Montgomery JA Jr, Peralta JE, Ogliaro F, Bearpark M, Heyd JJ, Brothers E, Kudin KN, Staroverov VN, Kobayashi R, Normand J, Raghavachari K, Rendell A, Burant JC, Iyengar SS, Tomasi J, Cossi M, Rega N, Millam JM, Klene M, Knox JE, Cross JB, Bakken V, Adamo C, Jaramillo J, Gomperts R, Stratmann RE, Yazyev O, Austin AJ, Cammi R, Pomelli C, Ochterski JW, Martin RL, Morokuma K, Zakrzewski VG, Voth GA, Salvador P, Dannenberg JJ, Dapprich S, Daniels AD, Farkas O, Foresman JB, Ortiz JV, Cioslowski J, Fox DJ (2009) Gaussian 09, Revision E.01. Gaussian, Inc., Wallingford

80. Becke AD (1993) A new mixing of Hartree-Fock and local density-functional theories. J Chem Phys 98:1372–1377
81. Lee C, Yang W, Parr RG (1988) Development of the Colle-Salvetti correlation-energy formula into a functional of the electron density. Phys Rev B 37:785–789
82. Dunning TH (1989) Gaussian basis sets for use in correlated molecular calculations. I. The atoms boron through neon and hydrogen. J Chem Phys 90:1007–1023
83. Peterson KA, Figgen D, Dolg M, Stoll H (2007) Energy-consistent relativistic pseudopotentials and correlation consistent basis sets for the 4d elements Y–Pd. J Chem Phys 126:124101
84. Figgen D, Peterson KA, Dolg M, Stoll H (2009) Energy-consistent pseudopotentials and correlation consistent basis sets for the 5d elements Hf–Pt. J Chem Phys 130:164108
85. Kumari I, Gupta S, Goel N (2016) A DFT based investigation of NO oxidation by (CrO3)3 cluster. Comput Theor Chem 1091:107–114
86. Zhai H-J, Li S, Dixon DA, Wang L-S (2008) Probing the electronic and structural properties of chromium oxide clusters (CrO3)n− and (CrO3)n (n = 1–5): photoelectron spectroscopy and density functional calculations. J Am Chem Soc 130:5167–5177
87. Boys SF, Bernardi F (1970) The calculation of small molecular interactions by the differences of separate total energies. Some procedures with reduced errors. Mol Phys 19:553–566
88. Dapprich S, Komáromi I, Byun KS, Morokuma K, Frisch MJ (1999) A new ONIOM implementation in Gaussian98. Part I. The calculation of energies, gradients, vibrational frequencies and electric field derivatives (Dedicated to Professor Keiji Morokuma in celebration of his 65th birthday). J Mol Struct THEOCHEM 461–462:1–21
89. Chung LW et al (2015) The ONIOM method and its applications. https://doi.org/10.1021/cr5004419
90. Seidu I, Krykunov M, Ziegler T (2015) Applications of time-dependent and time-independent density functional theory to electronic transitions in tetrahedral d0 metal oxides. J Chem Theory Comput 11:4041–4053
91. Minkin VI (1999) Glossary of terms used in theoretical organic chemistry. Pure Appl Chem 71:1919–1981
92. Israelachvili JN (1991) Intermolecular and surface forces, 2nd edn. Academic Press, London
93. Owen S, Hoeben P, Headlee M (2014) Chemistry for the IB diploma coursebook with free online material. Cambridge University Press, Cambridge, England, UK
94. Haynes WM (ed) (2014) CRC handbook of chemistry and physics. CRC Press, Boca Raton
95. Johnson LW, McGlynn SP (1970) The electronic absorption spectrum of chromate ion. Chem Phys Lett 7:618–620
96. Mercuri F, Baldoni M, Sgamellotti A (2012) Towards nano-organic chemistry: perspectives for a bottom-up approach to the synthesis of low-dimensional carbon nanostructures. Nanoscale 4:369–379
97. Ewels CP, Glerup M (2005) Nitrogen Doping in Carbon Nanotubes. J Nanosci Nanotechnol 5:1345–1363
98. Lee C-G, Kim S-B (2016) Cr(VI) adsorption to magnetic iron oxide nanoparticle-multi-walled carbon nanotube adsorbents. Water Environ Res 88(11):2111–2120. https://doi.org/10.2175/106143016X14733681695401
99. Bhaumik M, Agarwal S, Gupta VK, Maity A (2016) Enhanced removal of Cr(VI) from aqueous solutions using polypyrrole wrapped oxidized MWCNTs nanocomposites adsorbent. J Colloid Interface Sci 470:257–267

100. Dehghani MH et al (2015) Removal of noxious Cr (VI) ions using single-walled carbon nanotubes and multi-walled carbon nanotubes. Chem Eng J 279:344–352
101. Georgakilas V et al (2002) Amino acid functionalisation of water soluble carbon nanotubes. Chem Commun 0:3050–3051

Chapter 22
Single-Molecule Conductance Theory Using Different Orbitals for Different Spins: Applications to π-Electrons in Graphene Molecules

Anatoliy V. Luzanov

Abbreviations

AO	Atomic orbital
DODS	Different orbitals for different spins
EHF	Extended Hartree-Fock
FCI	Full configuration interaction
GF	Green's function
GQD	Graphene quantum dot
HPHF	Half-projected Hartree-Fock
MO	Molecular orbital
MSE	Molecular-scale electronics
QCLRI	Quasi-correlated long-range interaction
QCTB	Quasi-correlated tight-binding (model)
RHF	Restricted Hartree-Fock
TB	Tight-binding (model)
UHF	Unrestricted Hartree-Fock
WBL	Wide-band limit

22.1 Introduction

The emergence of molecular-scale electronics (MSE) opened a remarkable vista for quantum science and nanoscale devices. Over the past two decades the various mechanisms of molecular conductance have been proposed and studied from many

A. V. Luzanov (✉)
SSI "Institute of Single Crystals", NAS of Ukraine, Kharkiv, Ukraine

© Springer Nature Switzerland AG 2019

O. Fesenko, L. Yatsenko (eds.), *Nanophotonics, Nanooptics, Nanobiotechnology, and Their Applications*, Springer Proceedings in Physics 222,
https://doi.org/10.1007/978-3-030-17755-3_22

angles at the experimental and theoretical levels [1–6]. However, some vital issues remain to be fully clarified, and the influence of many-body effects is one of them. Indeed, much theoretical work was done, seemingly successfully, on simple range models, like one-electron tight-binding (TB) approximation (see, e.g., Refs. [6–12].). At the same time, many studies have been reported on the use of more reliable approaches which include electron correlation effects (Refs. [13–19]. and many others). However, high-level many-electron models are too demanding, especially for the MSE applications, so that even simple TB theories retain their certain usefulness.

In this paper we give the new results of using the modified approach of TB type which quite recently was applied in the MSE context [20]. This is the quasi-correlated tight-binding (QCTB) approximation developed in Refs. [21–23]. Actually QCTB is closely related to one old model first discussed in Ref. [24] for spin-doublet alternant π-radicals. Really, QCTB is but a simplest implementation of the different orbitals for different spins (DODS) approach. Nevertheless, in case of alternant π-conjugated hydrocarbons, or bipartites (in graph theoretic terms), QCTB can mimic, more or less crudely, π-electron correlation effects, particularly electron unpairing in molecular closed shells [22, 23]. Interestingly, QCTB was also adopted in Ref. [25] for analyzing fine effects of "spin repulsion" in bipartite networks.

One of the aims of the present paper is to check the predictions of TB and QCTB against the "exact" π-electron results of the full configuration interaction (FCI) method for small π-systems. For moderate-size conjugated structures, such as graphene nanoflakes (for which FCI cannot be undertaken), we additionally propose to use the more advanced DODS model due to Smeyers [26], that is, the half-projected Hartree-Fock (HPHF) method. The latter is the well-known and well-elaborated electron-correlation model (see, e.g., Refs. [26–30].), but it has not been employed previously for MSE problems. On this account, a number of formal points, e.g., the GF method for HPHF, required clarification. In the paper the abovementioned issues are discussed in detail.

The layout of the present work is as follows. The next section contains the main definitions and prerequisite facts about one-electron theory of molecular conductance. Section 22.3 addresses the QCTB machinery and derivation of the working equations for the corresponding one-electron Green's function (GF). Section 22.4, along with Appendix A, develops the basic expressions of HPHF approach as they are related to the problem. In Sect. 22.5, we study electron conductance in various graphene structures, and in the last section we summarize the results, outlining perspectives for future work. Several supporting topics and details are addressed in Appendices.

22.2 Simple One-Electron Schemes

Let us begin with the main definitions and notations which are typical for the single-molecule electron transport theory. As in most current computations of molecular conductance, we will assume a ballistic (without scattering) electron transport. We consider, in a conventionally simplified manner, the coherent transport

through a conjugated molecule sandwiched between two leads (contacts). The leads which are attached to atoms a and b of the given molecule are characterized by phenomenological broadening parameters Γ_a and Γ_b. Such a contact pair will be named the (a,b) connection. Then within the wide-band limit (WBL) approximation (see [31] and references therein) a working formula for the corresponding molecular conductance, g_{ab}, is

$$g_{ab}/g_0 = \Gamma_a\ \Gamma_b |G_{ab}|^2. \tag{22.1}$$

Here g_0 is the quantum conductance unit (in atomic units, $g_0 = \pi^{-1}$); G_{ab} symbolize a relevant matrix elements of the effective retarded one-electron GF, G, for the molecule under study. In general, G depends on real-energy argument E (an incoming electron energy). Moreover, G must take into account effects of coupling between molecular wire and leads.

In one-electron (mean-field) approximation, G can be taken as a resolvent of the appropriate effective Hamiltonian h. If we ignore broadening of molecular energy levels due to their interaction with the leads, then we can set $G(E) = R(E)$ where the standard resolvent matrix R is of the form

$$R(E) = \left(E + i0^+ - h\right)^{-1}. \tag{22.2}$$

Here and throughout the paper, any number in matrix expression is understood as a scalar diagonal matrix; e.g., $E \equiv E\,I$, with I being the identity matrix of respective size. We will also often omit E in $R(E)$ and $G(E)$; e.g., $G \equiv G(E)$. Generally, G as an effective molecular GF differs from R owing to the abovementioned coupling effects with the leads.

We start with the conventional π-electron TB approximation, i.e., we will work now with the Hückel method and its extensions. The Hückel Hamiltonian matrix is well known, and in the next section we will discuss it for bipartites in greater detail. The essential part of the currently used molecular conductance theories is an explicit inclusion of the broadening effect in the effective G. If the WBL prescription is applied, then instead of Eq. (22.2), we can express GF in one-electron approximation as follows:

$$G(E) = \left(E + i\ \Gamma^{[a,b]} - h\right)^{-1}, \tag{22.3}$$

with $\Gamma^{[a,b]}$ being a broadening matrix. The latter is predominately localized on atoms a and b coupled with the leads, so within π-electron schemes we have explicitly

$$\Gamma^{[a,b]} = (\ \Gamma_a\ |a\rangle\ \langle a| + \Gamma_b\ |b\rangle\ \langle b|\ )\ /2, \tag{22.4}$$

where Dirac kets $|a\rangle$ and $|b\rangle$ are the $2p\pi$ atomic orbitals (AOs) of the carbon atoms involved into the studied (a,b) connection (e.g., see, Ref. [32]).

22.3 QCTB Model for Effective Green's Functions

Before applying QCTB scheme to MSE problems, we recall first the customary TB π-electron model. The TB Hamiltonian will be denoted by h^0. From now on we consider only plane bipartite carbon-containing networks—they must not possess odd-membered cycles (König's theorem). In reality, such systems make up a vast majority of the conjugated hydrocarbons of the MSE interest. Let us recall a common structural property of these bipartites. All sites in them can be always divided into two nonintersecting sets of starred (*) and unstarred (∘) sites (in Coulson's terms), and the starred sites are chemically interbonded with the unstarred ones only. Then in the standard π-AO basis set the h^0 matrix allows the known block skew-diagonal representation:

$$h^0 = -\begin{pmatrix} 0 & B \\ B^{\mathrm{T}} & 0 \end{pmatrix}, \tag{22.5}$$

where block $B \equiv (h^0)_{*\circ}$ describes interactions between starred and unstarred sites; superscript T denotes matrix transposition. Apart from a scaling factor $|\beta_0|$ (β_0 is a resonance integral), this B is but the adjacency matrix composed of ones for connected sites; rest elements of B are zero by definition (TB approximation). Evidently, using $h = h^0$ for GF in Eq. (22.2) is straightforward. For the given (a,b) connection, the corresponding GF will be signified by G^{TB}. Then, as in Eq. (22.3) we have.

$$G^{\mathrm{TB}} = \left(E + i\,\Gamma^{[a,b]} - h^0\right)^{-1}. \tag{22.6}$$

Now we turn to QCTB [21, 22], which is the main object of the study here. As to precursors of QCTB, see, besides the first paper [24], also Refs. [33–35]. where the simplified schemes were formulated by invoking DODS and the Hubbard Hamiltonian. In QCTB [21–23] we also make using a spin-splitting description, starting with two effective TB-like Hamiltonians h^α and h^β. Thus, we define

$$h^\alpha = -\begin{pmatrix} \delta & B \\ B^{\mathrm{T}} & -\delta \end{pmatrix}, \quad h^\beta = -\begin{pmatrix} -\delta & B \\ B^{\mathrm{T}} & \delta \end{pmatrix}, \tag{22.7}$$

and associate these Hamiltonians with subsystems of α-electrons (with spin up) and β-electrons (with spin down), respectively. In Eq. (22.7) by parameter δ we bring in a spin polarization, thus mimicking electron correlation effects. Below δ is a fixed number.

Having now at our disposal Hamiltonians h^α and h^β we shall generate two auxiliary resolvents:

$$R^\alpha = \left(E + i0^+ - h^\alpha\right)^{-1}, \quad R^\beta = \left(E + i0^+ - h^\beta\right)^{-1}. \tag{22.8}$$

For spin-singlet states, a symmetrized combination should be used instead, thus giving the QCTB "resolvent" matrix, R^{QCTB}, of the form:

$$R^{\mathrm{QCTB}} = \left(R^{\alpha} + R^{\beta}\right)/2. \tag{22.9}$$

Clearly, this type of GFs pays no attention to the abovementioned energy-level broadening. The more consistent should be the effective Green's function G^{QCTB} of the form

$$G^{\mathrm{QCTB}} = \left(I/R^{\mathrm{QCTB}} + i\ \Gamma^{[\mathrm{a,b}]}\right)^{-1}, \tag{22.10}$$

which is based on a rather general expression, Eq. (27), in Ref. [14]. Evidently, $G^{\mathrm{QCTB}} = R^{\mathrm{QCTB}}$ if $\Gamma^{[a,b]} = 0$. For the given (*a*,*b*) connection, the thus constructed G^{QCTB} will serve as a basic approximation which provides us with a simplistic but reasonable way to describe π-electron correlation effects relevant to MSE problems. Note that in Ref. [20] we have made preliminary applications to demonstrate the possibilities of QCTB for computing molecular conductance in oligomer structures. In the cited paper, the energy-level broadening was handled using a too simplistic (scalar) approach.

22.4 Use of the Half-Projected Hartree-Fock π-Model

As we saw previously in Ref. [20], QCTB provides rather semiquantitative and frequently only qualitative results due to neglecting long-range interactions effects. In other words, in QCTB the systematic errors are incurred by using topological in their essence Hamiltonians, Eq. (22.7). On this account we must adopt more general DODS models for π-electrons. The best variational DODS model is Löwdin's extended Hartree-Fock (EHF) method [36]. However, GF is too tricky to be calculated consistently at the EHF level; at least, no results in this direction are known at present. In this situation, the well-known HPHF model of Smeyers [26], as a simplified version of EHF, seems to be a reasonable alternative choice. Below, we elaborate the GF computational technique at the HPHF level.

Firstly, we briefly recall the basic points, following closely the presentation of HPHF from Refs. [26, 28]. Only singlet molecular ground states will be considered in the present paper, so we will deal with even-numbered *N*-electron systems where $N = 2n$ and *n* is an integer. Recall that for all DODS approaches, the starting point is the wave function $|\,\Phi^{\alpha,\beta}\rangle$ of unrestricted Hartree-Fock (UHF) type. We take this in the spin-free form:

$$\left|\,\Phi^{\alpha,\beta}\right\rangle = \left|\Phi^{\alpha}\right\rangle \otimes \left|\,\Phi^{\beta}\right\rangle, \tag{22.11}$$

where vectors $|\Phi^{\alpha}\rangle$ and $|\Phi^{\beta}\rangle$ are spin-free determinants. The latter are built up from the given spin-free MOs,

$$\left\{\left|\phi_i^{\alpha}\right\rangle\right\}_{1\le i\le n}, \quad \left\{\left|\phi_i^{\beta}\right\rangle\right\}_{1\le i\le n} \tag{22.12}$$

for spin-up and spin-down electrons, respectively. Of course, Eq. (22.11) is equivalent to the usual unrestricted Slater determinant; the above spin-free representation is merely more convenient for manipulations and corresponds to the classical Waller-Hartree double-determinant method [37].

As is well known, generally the UHF wavefunction $|\Phi^{\alpha,\beta}\rangle$ is a non-spin-pure-state. In order to recover a spin-pure or nearly spin-pure state, an appropriate spin projection should be performed. The simplest symmetrization of spin-up and spin-down electrons is such an approximate projection procedure for spin-singlet states. This is precisely used in HPHF, thus giving the improved wave function

$$\left|\Psi^{\mathrm{HPHF}}\right\rangle = \left|\Phi^{\alpha,\beta}\right\rangle + \left|\Phi^{\beta,\alpha}\right\rangle. \tag{22.13}$$

The variational HPHF equations for MO sets, Eq. (22.12), related to state vector (22.13) are not so difficult to derive [26–28], and hence we omit them for brevity.

Now turn to ionized states which are needed for constructing GF. Following Ref. [28], we consider $(2n–1)$-electron state vector $\left|\Psi_+^{\mathrm{HPHF}}\right\rangle$. It is obtained from $|\Psi^{\mathrm{HPHF}}\rangle$ by removing one electron described by own MO $|\phi\rangle$ which we must determine variationally. Namely, let us introduce two $(n–1)$-electron states, $\left|\Phi_+^{\alpha}\right\rangle$ and $\left|\Phi_+^{\beta}\right\rangle$, where explicitly $\left|\Phi_+^{\alpha}\right\rangle = \sqrt{n}\langle\phi(n)|\Phi^{\alpha}\rangle_{(n)}$ and likewise for $\left|\Phi_+^{\beta}\right\rangle$. These states correspond to electron annihilation in $|\Phi^{\alpha}\rangle$ and $|\Phi^{\beta}\rangle$, respectively. Then, the approximate spin-doublet state vector is

$$\left|\Psi_+^{\mathrm{HPHF}}\right\rangle = \left|\Phi_+^{\alpha}\right\rangle \otimes \left|\Phi^{\beta}\right\rangle + \left|\Phi^{\alpha}\right\rangle \otimes \left|\Phi_+^{\beta}\right\rangle. \tag{22.14}$$

The variational equation for $|\phi\rangle$ that optimizes the energy of this ionized state is presented in Ref. [28]. Based on it, we have derived in Appendix A the relations required for R^{HPHF} (GF without broadening effects). Once having computed R^{HPHF} from Eqs. (22.A2), (22.A8), and (22.A9), we evaluate the full GF matrix, G^{HPHF}, by adding broadening effects in the same manner as in Eq. (22.10):

$$G^{\mathrm{HPHF}} = \left(I/R^{\mathrm{HPHF}} + i\ \Gamma^{[a,b]}\right)^{-1}. \tag{22.15}$$

The quality of this HPHF model for GF is estimated for aromatic structures in Appendix B. In the latter we show that for the small cyclic molecules treated by the standard π-electron theory, the HPHF results for GF (at $E = E_{\mathrm{F}}$ where E_{F} is the Fermi energy) are close to FCI quality (Table 22.3). In the same table, QCTB demonstrates a reasonable behavior, but not as good as HPHF. Nevertheless, QCTB

is systematically better than TB, and it is in agreement with our previous study of polyenic systems [20].

One deficient feature of HPHF is a lack of size-consistency (for a general consideration of this and related issues see review [38]). We discuss the issue for GF in detail in Appendix B, and show that in practice this deficiency is not too severe for small and middle-size systems. It allows us, for the similar systems, to consider the obtained HPHF results as giving realistic estimations of GF matrix elements. At least, the HPHF data are much more favorable than other ones which are produced for graphene molecules by TB and even the restricted Hartree-Fock (RHF) method. In fact, we will employ HPHF as a tool for the quality assessment of low-level models (QCTB and TB) in middle-size graphene molecules.

22.5 Applications to Graphene Molecules

22.5.1 Small Graphene Molecules

The graphene networks are often regarded as promising candidates for designing MSE materials. In this context a variety of approximations was made to estimate electronic and conductance properties of nanographene molecules (Refs. [8, 39–45]. and others). The π-electronic structure of several relatively small graphene quantum dots (GQDs) is also investigated in Refs. [46, 47].

In the present calculations of the effective GF and conductance spectra, we employ broadening parameter $\Gamma = \Gamma_a = \Gamma_b = 0.1$ eV taken from Ref. [18]. In all the plots we show conductance (in the g_0 units) as a function of electron energy E. In the abscissa, E is in eV, and E_F, is shifted to 0 for convenience. Moreover, we make use of the logarithmic ordinate. The conductance spectra are plotted for the various π-models in this way: HPHF in red, QCTB in green, and TB in black dashed. We will also signify by R_0 the GF matrix elements at $E = E_F$.

We start our investigation with studying two small graphene molecules shown on Fig. 22.1. The first one is GQD-56 (in our notations here) which is the 56 carbon-atom circumpentacene molecule. It has been examined in a number of works [8, 39, 40] as an interesting example of the graph-theoretic (within TB) conductance theory. The second is GQD-62, that is a 62 carbon-atom structure as a particular example of an armchair graphene nanoflake studied in Ref. [44]. In Table 22.1 we

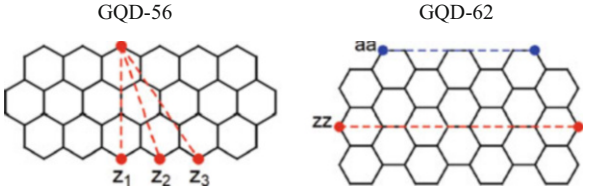

Fig. 22.1 Structure of GQD-56 and GQD-62 and the studied connections. The sites (colored disks) which are attached to electrodes are connected each other by conditional dashed lines

Table 22.1 GF matrix elements R_0 ($E = E_F$) for contact pairs $\mathbf{z_1}$, $\mathbf{z_2}$, and $\mathbf{z_3}$ in GQD-56, and for pairs **aa** and **zz** in GQD-62, accordingly to Fig. 22.1

Contact pair	R_0^{HPHF}	R_0^{QCTB}	R_0^{RHF}	R_0^{TB}
$\mathbf{z_1}$	−0.246	−0.281	−0.719	$-67/42 \cong -1.595$
$\mathbf{z_2}$	0.131	0.132	0.579	$50/21 \cong 2.381$
$\mathbf{z_3}$	−0.036	−0.013	−0.337	$-55/21 \cong -2.619$
aa	0.020	0.042	0.012	$16/2037 \cong 0.008$
zz	−0.155	−0.108	−0.175	$-625/679 \cong -0.921$

give a small piece of information related to the selected connections in GQD-56 and GQD-62 (for GQD-56, the same contact pairs are studied in Refs. [8, 39, 40].).

As seen from Table 22.1, TB predicts, too large GF elements in GQD-56, particularly for relatively distant connections in zigzag-type contact pairs (denoted by $\mathbf{z}_j$ and shown by red dashed lines in the table). More than that, within TB, the matrix elements G_{ab} become spuriously larger with increasing distance between atoms a and b of the contact pair. At the same time, in the GQD-56 example as well as in many other ones, such long-distance atomic pairs have small values of usual π-bond orders (nondiagonal density matrix elements in AO basis). These bond orders, as a rule, qualitatively correlate with the corresponding G values. Such a natural fact argues additionally in favor of HPHF and QCTB but not in favor of TB. Overall, we can conclude that even small graphene molecules with zigzag edge topology require more refined tools than that based on Eq. (22.5) for the simple TB scheme.

The case of GQD-62 seems somewhat different. Here we consider the GF π-electron elements for two types of long-distance connections: the zigzag connection, **zz**, involving both sites on zigzag-type edges (red dashed line on the picture in Fig. 22.1), and the armchair connection, **aa**, involving both sites on armchair-type edges (blue dashed line in Table 22.2). We see from Table 22.1 that in GQD-62 **zz** connection is of the same behavior as in GQD-56, but **aa** connection is much weaker, and this connection is less influenced by electron correlation effects, so that even TB provides a reasonable value of the corresponding GF element at E_F. These peculiarities of armchair-type connections are rather typical (see the next subsection).

On the basis of Table 22.1, we can state that the QCTB results are in a semiquantitative agreement with the more reliable HPHF data. For larger graphene molecules QCTB works less well, as will be seen from the subsequent discussion. As for the RHF model, it works only slightly better than TB. Moreover, in large conjugated π-systems, RHF suffers from the so-called Hartree-Fock instabilities (it was demonstrated in Ref. [47] for moderate-size graphene molecules). Hence, RHF can come to inappropriate broken-symmetry solutions, and for this reason we will refrain from further use of RHF for graphenes.

Consider now conductance spectra for our GQDs. In Fig. 22.2 we present them for the most efficient zigzag contact $\mathbf{z_1}$ in GQD-56 and for the armchair contact **aa** in GQD-62. It is seen that even far from the Fermi level, QCTB gives satisfactory results, at least at a qualitative level, but TB does not. It means that a possible

Table 22.2 GQD-130: Comparison of GF matrix elements R_0 ($E = E_F$) for contact pairs, $\mathbf{a}_j$, and $\mathbf{z}_j$ at the HPHF, QCTB, and TB levels

GQD-130 with contact pairs	Pair	R_0^{HPHF}	R_0^{QCTB}	R_0^{TB}
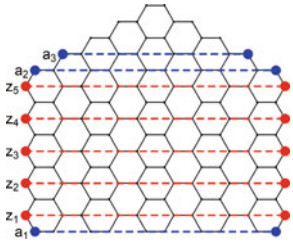	$\mathbf{z_1}$	−0.015	−0.030	−1.784
	$\mathbf{z_2}$	−0.016	−0.032	−3.945
	$\mathbf{z_3}$	−0.011	−0.025	−3.193
	$\mathbf{z_4}$	−0.014	−0.025	−1.147
	$\mathbf{z_5}$	−0.007	−0.010	−0.129
	$\mathbf{a_1}$	0.003	0.003	0.001
	$\mathbf{a_2}$	0.005	0.010	0.001
	$\mathbf{a_3}$	0.030	0.072	0.030

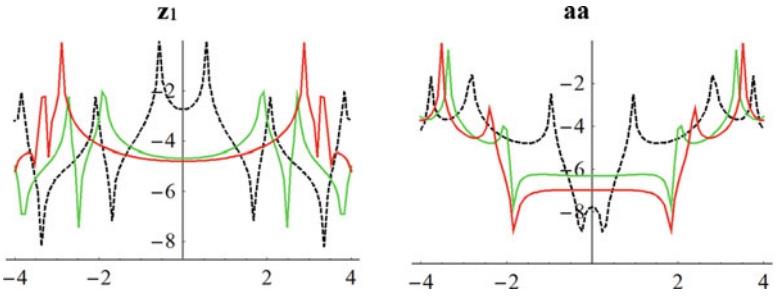

Fig. 22.2 Conductance spectra for connection $\mathbf{z_1}$ in GQD-56 and connection **aa** in GQD-62 (see Fig. 22.1) within the HPHF (in red), QCTB (in green), and TB (in black dashed)

agreement between selected GF values of TB and more advanced models (as in the case of GF at $E = E_F$ for contacts in GQD-62) may be misleading as to a real accuracy of the low-level approach in whole.

22.5.2 *Graphene Quantum Dot C_{130}*

We turn to a more extended graphene structure C_{130}, further named as GQD-130, which is displayed in Table 22.2. This GQD was synthesized in Ref. [48]. The intrinsic π-electron properties of GQD-130 were considered recently in Refs. [47]. Again, we examine the GF π-electron elements of GQD-130 for two types of long-distance connections: zigzag connections, $\mathbf{z}_j$, and armchair connections,

$\mathbf{a}_j$ (respectively, red and blue dashed lines on the molecule image in Table 22.2). We see from the table that there is the same, as in GQD-62, significant difference between these two types of the connections: the zigzag connections give a much greater conductance at $E = E_F$ than the armchair connections for all the models used. At the quantitative level, the calculations on zigzag channels also display a sharp difference between the non-correlated model (TB) and the correlated models (HPHF and QCTB). In GQD-130, the long-distant zigzag GF elements, being small in HPHF and QCTB, behave quite correctly—in a striking contrast to TB.

It is interesting to compare these results with those for short-distance contact pairs in the same system. For instance, a maximum absolute value, G_{max}, of the GF matrix elements at the Fermi energy is attained on the borders—for the strongest C-C π-bonds formed by the two nearest neighbor atoms in $\mathbf{z_5}$ and $\mathbf{a_2}$. By using HPHF, QCTB, and TB we find the corresponding G_{max} to be equal to 0.75, 0.70, and 0.98, respectively. Thus, in all the models we obtain a reasonable value of order 1 for the GF elements of strong π-bonds, as in the ethylene molecule where $\left(R_0^{TB}\right)_{1,2} = 1$. We find that in this case, and in many other sufficiently large systems with strong electron correlation, TB gives sensible results only for too closely situated leads, whereas QCTB widely agrees with HPHF, but mainly in qualitative terms, if including all long-distance connections.

For completeness, in Fig. 22.3 we plotted the conductance spectra for the most interesting long-distance connections in GQD-130. Restricting to a small energy domain (say, to the interval [−2 eV, 2 eV] in the abscissa), we observe that indeed QCTB is fairly good for the more efficient zigzag-type channel, but QCTB is only semiquantitatively acceptable for the weak armchair-type channel. As expected, for the same nanographene problem, the TB plots turn out to be entirely wrong quantitatively as well as qualitatively. At last, our experience with HPHF and QCTB tells that the conductance spectra of other graphene-like molecules with large zigzag edges are fairly similar to that of GQD-130.

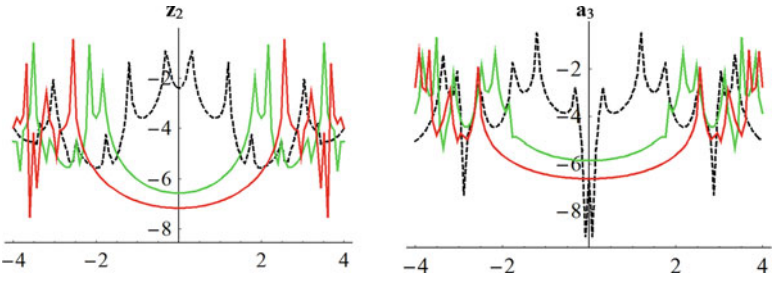

Fig. 22.3 Conductance spectra of GQD-130 for connections $\mathbf{z_2}$ (left panel) and $\mathbf{a_3}$ (right panel) within HPHF (red), QCTB (green), and TB (black dashed)

22.6 Conclusion

A large part of current theoretical studies of single-molecule conductance suggests a soundness of simple tight-binding (TB) π-schemes (at least in qualitative terms). However, as could be expected, the TB approach is too crude for MSE. Hence, it was practically important to scrutinize TB more rigorously and determine its actual validity for computing π-electron Green's functions. In this context, particularly important is the appropriate analysis of nanostructural classes, such as graphene-like molecules. Here we examined some representative graphenic molecules, thus continuing preliminary investigations in Ref. [20]. In the cited work, TB for GF was improved in an unsophisticated manner by invoking QCTB model [21, 22]. In turn, this has caused the need to examine QCTB per se, especially for sufficiently large systems. For this aim we have now brought into play a helpful HPHF model allowing study of extended systems at an affordable cost.

Specific computations on nanographenes corroborate the qualitative (but rarely quantitative) usefulness of QCTB and its ability to provide us with a more adequate physical picture than TB does. More than that, dealing with conductance spectra at the TB level turns out to be meaningless, particularly, for long-distant contact pairs in nanographenes, and it seems to apply to any extended conjugated π-system. Yet, the fact that simple TB schemes are not adequate to treat MSE for large π-structures even qualitatively, was not generally recognized, and we believe that the results reported here will help to draw a serious attention to a more realistic assessment of the TB model.

As usual, many unresolved issues remain. Specifically, there is a nontrivial problem how to improve HPHF by constructing a not too complicated scheme with a better account for electron correlation in large-scale systems. In this issue, McWeeny's generalized product functions [49] can be used for a modeled molecular composite derived from the system in question by dividing it into weakly interacting (localized) fragments. We believe that the McWeeny approach may be able to alleviate the size-inconsistency problem in HPHF. At the same time it seems sensible to explore in detail another our DODS-like approach proposed here in Appendix B as a quasi-correlated long-range interaction (QCLRI) model. There are encouraging features of this π-model: first, for small systems it is good almost as HPHF, and, independently of the molecular size, it is simple as QCTB; second, QCLRI possesses size-consistency. Evidently, these features are indispensable for large-scale systems. Moreover, π-electron radicals and polyradicals, and related spintronics problems are attractive as well for studying by DODS, but they cannot well be handled in a too simple way. However, the ground triplet states may be easily treated approximately by the proposed HPHF methodology, and we hope to address this and other mentioned problems in a near future.

Appendices

Appendix A: Construction of HPHF Green's Function

Before treating in detail GF for HPHF, it is sensible to consider a standard general expression of GF. Let us first rewrite Eq. (22.2) in an appropriate spectral form:

$$R = \sum_i \frac{|\phi_i\rangle\langle\phi_i|}{E + i0^+ - \varepsilon_i} + \sum_a \frac{|\phi_a\rangle\langle\phi_a|}{E + i0^+ - \varepsilon_a}, \tag{22.A1}$$

where ε_i and ε_a are Koopmans orbital energies, that is eigenvalues of h; $|\phi_i\rangle$ and $|\phi_a\rangle$ are corresponding occupied and virtual MOs (eigenkets of h), respectively. In fact, the structure of Eq. (22.A1) remains valid in a more general setting (as in Eq. (5.76) from Ref. [1]). In doing so, $|\phi_i\rangle$ and $|\phi_a\rangle$ should be replaced by the so-called Dyson orbital $\left|d_i^+\right\rangle$ for electron detachment, and by Dyson orbital $\left|d_a^-\right\rangle$ for electron attachment; they may be nonorthogonal to each other and even be linear dependent [50]. In addition, ε_i and ε_a are replaced with transition energies ΔE_i^+ and ΔE_a^-, respectively. Explicitly, $\Delta E_i^+ = E^N - E_i^{N-1}$ (negative ionization potential), and $\Delta E_a^- = E_a^{N+1} - E^N$ (electron affinity). It gives the most general (Lehmann type) spectral representation of GF for N-electron system:

$$R = \sum_i \frac{\left|d_i^+\right\rangle\left\langle d_i^+\right|}{E + i0^+ - \Delta E_i^+} + \sum_a \frac{\left|d_a^-\right\rangle\left\langle d_a^-\right|}{E + i0^+ - \Delta E_a^-}. \tag{22.A2}$$

Now we turn to the HPHF model for which the variational Koopmans-like orbitals were constructed in Ref. [28]. We will need the standard (Hermitian) matrix projectors onto the occupied spin-up and spin-down MOs, that is

$$\rho^\alpha = \sum_{i=1}^n \left|\phi_i^\alpha\right\rangle\left\langle\phi_i^\alpha\right|, \quad \rho^\beta = \sum_{i=1}^n \left|\phi_i^\beta\right\rangle\left\langle\phi_i^\beta\right|, \tag{22.A3}$$

along with a non-Hermitian matrix projector U which is generated by overlapping of ρ^α and ρ^β:

$$U = \rho^\alpha\left(\rho^\beta\rho^\alpha\right)^{-1}\rho^\beta. \tag{22.A4}$$

Matrix inversion here should be understood as the Moore-Penrose pseudoinverse (see, e.g., Ref. [51]). The next are the Fockian matrices, f_α and f_β, associated with the above projectors:

$$f_\alpha = h + J\left(\rho^\alpha + \rho^\beta\right) - K\left(\rho^\alpha\right), \quad f_\beta = h + J\left(\rho^\alpha + \rho^\beta\right) - K\left(\rho^\beta\right) \tag{22.A5}$$

$$f_U = h + J\left(U + U^+\right) - K(U), \tag{22.A6}$$

with J and K being, respectively, standard Coulomb and exchange (super)operators due to Roothaan. In above, h is a core Hamiltonian which includes not only h^0 but electron-nuclear attraction terms.

Then we can derive the HPHF variational equation for $\left|d_i^+\right\rangle$, based on Eqs. (35) and (36) from Ref. [28]. We first define the (nonnormalized) charge density matrix, D, at the HPHF level:

$$D = \rho^\alpha + \rho^\beta + \xi \ \left(U + U^+ \right), \tag{22.A7}$$

where ξ is a pseudodeterminant of $\rho^\alpha \rho^\beta$ (i.e., the last nonnull (nth) coefficient of its characteristic polynomial). This D serves as an auxiliary matrix in the generalized eigenvalue problem of the form:

$$\Theta D^{-1} \left|d_i^+\right\rangle = \left(E_{\mathrm{HPHF}} - \Delta E_i^+\right) \left|d_i^+\right\rangle, \tag{22.A8}$$

where

$$\Theta = \rho^\alpha \left(E_\rho - f_\alpha\right) \rho^\alpha + \rho^\beta \left(E_\rho - f_\beta\right) \rho^\beta + \xi \ \left[U \left(E_U - f_U\right) U + \mathrm{h.c.}\right], \tag{22.A9}$$

and $E_\rho$and E_U are usual UHF-like energies for projectors ρ^α, ρ^β and U, U^+, respectively. Moreover, E_{HPHF} (i.e., E_N needed for ΔE_i^+) is known beforehand: $E_{\mathrm{HPHF}} = (E_\rho + \xi E_U)/(1 + \xi)$. The eigenvalue problem for $\left|d_a^-\right\rangle$and ΔE_a^- is formulated likewise. Namely, the relevant eigenvalue problem for ΔE_a^- can be obtained from Eqs. (22.A5), (22.A6), (22.A7), (22.A8), and (22.A9) by replacing all projectors by their "vacant" counterparts ($\rho^\alpha \rightarrow I - \rho^\alpha$,$U \rightarrow I - U$ etc.), but leaving all the Fockians, Eqs. (22.A5) and (22.A6), unchanged. At last, in order to get the resulting R^{HPHF} from the eigensolutions of Eq. (22.A8) and their counterparts for ΔE_a^-, we directly apply Eq. (22.A2).

We now shortly discuss the selection rules for matrix R_0, i.e., for GF matrix elements at $E = E_{\mathrm{F}}$, neglecting energy broadening effects. The main rule is that for any correct bipartite-symmetry description we have the same block skew-diagonal structure of R_0 as in the underlying TB Hamiltonian, Eq. (22.5). Thus,

$$R_0 = \begin{pmatrix} 0 & R_{*\circ} \\ R_{\circ *} & 0 \end{pmatrix}. \tag{22.A10}$$

This equation for TB is trivial because $R_0^{\mathrm{TB}} = -\left(h^0\right)^{-1}$. Eq. (22.A10) is indeed the selection rule since it states that there are no nonzero elements of GF for (a,b) connections with a and b belonging simultaneously to the same atomic set, either the starred or unstarred set. Far less trivial is the fact that Eq. (22.A10) holds true for GF at the π-FCI level, as was stated rigorously in the important theorem obtained in Ref. [18]. Therefore, Eq. (22.A10) as originating from the bipartite symmetry, should be valid for any consistent π-approximation not violating a topological symmetry. The

same selection is exactly fulfilled for QCTB [20], and it is not so difficult to prove the same rule at the HPHF level as well.

Appendix B: Approximate Versus "Exact" π-Electron Results for Small Aromatics

In order to estimate reliability of the results obtained by various approximate π-models, we consider briefly the formally exact π-electron theory based on the well-known FCI method (e.g., see [52]). In our computations, we will follow the previously proposed FCI matrix algorithm; for additional references see Ref. [53] where a suitable FCI approach to calculating Dyson orbitals is given. As to the MSE problems, the first important results at the π-FCI level were given only recently in Ref. [18]. In what follows, the FCI results we present here will be taken as the benchmark data against which all the others must be compared.

One special point concerns the actual Fermi energy E_F that should be used to ensure Eq. (22.A10) for bipartites. In Ref. [18] the E_F value is not given explicitly. At the same time, for bipartites the remarkable Hush and Pople theorem is valid at the π-electron Hartree-Fock level [54], as well as at the FCI level [55]. From this theorem it follows that $E_F = W_C + \gamma_C/2$, where W_C is the standard effective ionization potential, and γ_C is the π-electron one-center Coulomb repulsion integral for the carbon atom. Just this choice of E_F ensures the validity of Eq. (22.A10) and other properties of GF for bipartites.

In our specific π-electron computations, we use standard π-electron parameters (in eV): resonance integral of the aromatic π-bond $\beta_0 = -2.4$; $W_C = 0$, $\gamma_C = 11.13$, and two-center repulsion integrals due to Ohno. For QCTB computations, we adopt $\delta = 7/24$ and $E_F = 0$. The idealized regular geometry was taken for the carbon backbone in all studies of conjugated π-structures (1.4 Å for CC bond lengths, etc.).

Now, let us say few words about the supplementary rescaling of the GF matrix elements for RHF, HPHF, and FCI, following the procedure from Ref. [20]. This was proposed in order to avoid an inevitably large gap between different approaches. When multiplying RHF, HPHF, and FCI matrix elements of GF by the scaling factor $\beta_0/(\beta_0 - \gamma_{12}/2)$ we make them comparable with their TB and QCTB counterparts. In particular, in the ethylene molecule the respective (1,2) elements, $\left(R_0^{\mathrm{TB}}\right)_{1,2}$ and $\left(R_0^{\mathrm{RHF}}\right)_{1,2}$ for the CC π bond, become identical and equal to 1.

Now we describe the results of comparison between π-FCI (the most rigorous π-approach) and main approximations (HPHF, RHF, QCTB, and TB). In addition, we tentatively and preliminary propose an improvement of QCTB in order to include long-range interactions not incorporated in the topological schemes. We simply do the first iteration of an usual self-consistent RHF procedure based on the TB (Hückel) density matrix as a start. It gives us a modified one-electron Hamiltonian of the correct block structure as in Eq. (22.5) for h^0. Then, expressions of the same

Table 23.3 GF matrix elements R_0 ($E = E_F$) for small aromatic molecules at the various levels of the theory

Structure	R_0^{FCI}	R_0^{HPHF}	R_0^{QCLRI}	R_0^{RHF}	R_0^{QCTB}	R_0^{TB}
	−0.447	−0.458	−0.439	−0.496	−0.451	−0.500
	−0.328	−0.374	−0.357	−0.497	−0.603	−1.000
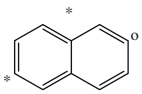	0.236	0.245	0.232	0.270	0.275	0.333
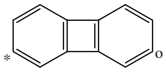	−0.138	−0.139	−0.133	−0.150	−0.215	−0.333
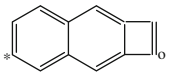	−0.156	−0.157	−0.164	−0.170	−0.271	−0.5

The used (*, ○) connections are shown on the structural formulas

type as in Eqs. (22.7), (22.8), (22.9), and (22.10) are applied in order to compute an approximated GF. This approach will be termed the quasi-correlated long-range interaction (QCLRI) model, and the respective GF will be denoted by G^{QCLRI}. More detail will be given elsewhere.

Let us examine the numerical results presented in Table 22.3. The specific connections (*,○) are shown in Table 22.3 by stars and cycles. We see that HPHF provides the best (in respect to FCI) results whereas there are marked quantitative deviations of QCTB from FCI. Especially large deviations from FCI occur for TB. It is worth paying attention to a good quality of the RHF results for the considered small aromatic molecules. In fact, RHF provides here better results than TB and even QCTB. However, RHF calls for much more computational efforts, but more essential is that RHF is not appropriate for computing GF in extended π-systems (see Sect. 22.5). It is important for future applications to observe that QCLRI, i.e., the above-proposed simple π-scheme, surprisingly works almost as well as HPHF, at least for the considered molecules. It is noteworthy that, unlike QCTB, the QCLRI method possesses the size-consistency discussed in the last paragraph of Sect. 22.4).

It is pertinent to understand now how significant in practice can be errors caused by lacking size-consistency in HPHF. A direct way to estimate actual inaccuracy due to the size inconsistency is to compute GF matrix elements in non-covalent intermolecular dimers of the chosen systems. Indeed, GF should be an additive-type size-consistent quantity (as closely related to the one-electron density matrix), and the same follows also from definition (22.A2). It means that the GF matrix of any noncovalent intermolecular dimer or complex, say, complex AB, must take the form of a direct sum when an average intermolecular distance goes to infinity. For example, in a dissociated dimer AB we have at the FCI level,

$R^{\mathrm{FCI}}[AB] = R^{\mathrm{FCI}}[A] \oplus R^{\mathrm{FCI}}[B]$, and likewise for other size-consistent models, such as RHF, QCLRI, QCTB, and TB. Unfortunately, this is not the case of HPHF and related spin-projected Hartree-Fock models.

Let us examine the selected GF elements of the dimerized systems for the molecules studied in Table 22.3. For each dissociated dimer, its constituent monomeric parts A and B were situated at the intermolecular distance equal to 100 Å. Of course, FCI, QCLRI, RHF, QCTB, and TB obey the size-consistent requirement, so that the corresponding GF matrix elements in the initial monomer molecule and in the related parts of the dimer are exactly the same, and we do not repeat these data. At the same time, in the case of HPHF we obtain slightly different results for the monomer and the respective dimer subunits. We find the following HPHF values for GF elements under dissociation of the benzene, butalene, naphthalene, diphenylene, and naphtha[b]cyclobutadiene dimers:

$$-0.475, -0.407, 0.255, -0.142, -0.157$$

These values should be compared with the respective values in the third column of Table 22.3. We see that in the dissociated dimers the deviation of GF elements from the ones obtained for the monomer are around of order 5%.

References

1. Cuevas JC, Scheer E (2017) Molecular electronics: an introduction to theory and experiment, 2nd edn. World Scientific, Singapore
2. Solomon GC, Herrmann C, Ratner MA (2012) Molecular electronic junction transport: some pathways and some ideas. Top Curr Chem 313:1–38
3. Metzger RM (2015) Unimolecular electronics. Chem Rev 115:5056–5115
4. Moth-Poulsen K (ed) (2016) Handbook of single-molecule electronics. Pan Stanford Publishing Pte Ltd, Singapore
5. Xiang D, Wang X, Jia C, Lee T, Guo X (2016) Molecular-scale electronics: from concept to function. Chem Rev 116:4318–4440
6. Tsuji Y, Estrada E, Movassagh R, Hoffmann R (2018) Quantum interference, graphs, walks, and polynomials. Chem Rev 118:4887–4911
7. Ernzerhof M, Bahmann H, Goyer F, Zhuang M, Rocheleau P (2006) Electron transmission through aromatic molecules. J Chem Theory Comput 2:1291–1297
8. Fowler PW, Pickup BT, Todorova TZ, Myrvold W (2009) Conduction in graphenes. J Chem Phys 131:244110-1-8
9. Markussen T, Stadler R, Thygesen KS (2010) The relation between structure and quantum interference in single molecule junctions. Nano Lett 10:4260–4265
10. Pedersen KGL, Borges A, Hedegård P, Solomon GC, Strange M (2015) Illusory connection between cross-conjugation and quantum interference. J Phys Chem C 119:26919–26924
11. Tsuji Y, Hoffmann R, Movassagh R, Datta S (2014) Quantum interference in polyenes. J Chem Phys 141:224311-1-13
12. Markussen T, Stadler R, Thygesen KS (2011) Graphical prediction of quantum interference-induced transmission nodes in functionalized organic molecules. Phys Chem Chem Phys 13:14311–14317

13. Wang X, Spataru CD, Hybertsen MS, Millis AJ (2008) Electronic correlation in nanoscale junctions: comparison of the GW approximation to a numerically exact solution of the single-impurity Anderson model. Phys Rev B 77:045119-1-10
14. Bergfield JP, Stafford CA (2009) Many-body theory of electronic transport in single-molecule heterojunctions. Phys Rev B **79**:245125-1-10
15. Yeriskin I, McDermott S, Bartlett RJ, Fagas G, Greer JC (2010) Electronegativity and electron currents in molecular tunnel junctions. J Phys Chem C 114:20564–20568
16. Bergfield JP, Solomon GC, Stafford CA, Ratner MA (2011) Novel quantum interference effects in transport through molecular radicals. Nano Lett 11:2759–2764
17. Goyer F, Ernzerhof M (2011) Correlation effects in molecular conductors. J Chem Phys 134:174101-1-10
18. Pedersen KGL, Strange M, Leijnse M, Hedegard P, Solomon GC, Paaske J (2014) Quantum interference in off-resonant transport through single molecules. Phys Rev B 90:125413-1-11
19. Hoy EP, Mazziotti DA, Seideman T (2017) Development and application of a 2-electron reduced density matrix approach to electron transport via molecular junctions. J Chem Phys 147:184110-1-8
20. Luzanov AV (2019) Single-molecule electronic materials: conductance of π-conjugated oligomers within quasi-correlated tight-binding model. Funct. Mater 26:152–163
21. Luzanov AV (2014) Effectively unpaired electrons in bipartite lattices within the generalized tight-binding approximation: application to graphene nanoflakes. Funct Mater 21:437–447
22. Luzanov AV (2016) Effectively unpaired electrons for singlet states: from diatomics to graphene nanoclusters. In: Leszczynski J, Shukla MK (eds) Practical aspects of computational chemistry IV. Springer, Boston, pp 151–206
23. Luzanov AV, Plasser F, Das A, Lischka H (2017) Evaluation of the quasi correlated tight-binding (QCTB) model for describing polyradical character in polycyclic hydrocarbons. J Chem Phys 146:064106-1-12
24. Davison SG, Amos AT (1965) Spin polarized orbitals for localized states in crystals. J Chem Phys 43:2223–2233
25. Estrada E (2018) The electron density function of the Hückel (tight-binding) model. Proc R Soc A474:20170721-1-18
26. Smeyers YG, Doreste-Suarez L (1973) Half-projected and projected Hartree-Fock calculations for singlet ground states. I. Four-electron atomic systems. Int J Quantum Chem 7:687–698
27. Cox PA, Wood MN (1976) The half-projected Hartree-Fock method. I. Eigenvalue formulation and simple application. Theor Chim Acta 41:269–278
28. Luzanov AV (1985) The spin-symmetrized Hartree-Fock method. J Struct Chem 25:837–844
29. Bone RGA, Pulay P (1992) Half-projected Hartree-Fock natural orbitals for defining CAS–SCF active spaces. Int J Quant Chem 45:133–166
30. Smeyers YG (2000) The half projected Hartree-Fock model for determining singlet excited states. Adv Quant Chem 36:253–270
31. Verzijl CJO, Seldenthuis JS, Thijssen JM (2013) Applicability of the wide-band limit in DFT-based molecular transport calculations. J Chem Phys 138:094102-1-10
32. Jhan S-M, Jin B-Y (2017) A simple molecular orbital treatment of current distributions in quantum transport through molecular junctions. J Chem Phys 147:194106-1-10
33. Langer W, Plischke M, Mattis D (1969) Existence of two phase transitions in Hubbard model. Phys Rev Lett 23:1448–1452
34. Langer W, Mattis D (1971) Ground state energy of Hubbard model. Phys Lett A3:139–140
35. Tyutyulkov N (1975) A generalized formula for the energies of alternant molecular orbitals. I. Homonuclear molecules. I J Quantum Chem 9:683–68936
36. Löwdin P-O (1955) Quantum theory of many-particle systems. III. Extension of the Hartree-Fock scheme to include degenerate systems and correlation effects. Phys Rev 97:1505–1520
37. Waller I, Hartree DR (1929) On the intensity of total scattering of X-rays. Proc R Soc London A124:119–142
38. Lyakh DI, Musiał M, Lotrich VF, Bartlett RJ (2011) Multireference nature of chemistry: the coupled-cluster view. Chem Rev 112:182–243

39. Tada T, Yoshizawa K (2002) Quantum transport effects in nanosized graphite sheets. Chem Phys Chem 3:1035–1037
40. Morikawa T, Narita S, Klein DJ (2005) Molecular electric conductance and long-bond structure counting for conjugated-carbon nano-structures. Chem Phys Lett 402:554–558
41. Schomerus H (2007) Effective contact model for transport through weakly-doped graphene. Phys Rev B 76:045433-1-7
42. Cuansing E, Wang JS (2009) Quantum transport in honeycomb lattice ribbons with armchair and zigzag edges coupled to semi-infinite linear chain leads. Euro Phys J B69:505–513
43. Nelson T, Zhang B, Prezhdo OV (2010) Detection of Nucleic Acids with Graphene Nanopores: Ab Initio Characterization of a Novel Sequencing Device. Nano Lett 10:3237–3242
44. Rangel NL, Leon-Plata PA, Seminario JM (2012) Computational Molecular Engineering for Nanodevices and Nanosystems. In: Leszczynski J, Shukla MK (eds) Practical aspects of computational chemistry I. Springer, Heidelberg, pp 347–383
45. Qiu W, Skafidas E (2013) Quantum conductance of armchair graphene nanopores with edge impurities. J Chem Phys: 114: 073703–073701–8
46. Güçlü AD, Potasz P, Korkusinski M, Hawrylak P (2014) Graphene Quantum Dots. Springer, Berlin/Heidelberg/New York
47. Luzanov A (2018) Graphene Quantum Dots in Various Many-Electron π-Models. In: Fesenko O, Yatsenko L (eds) Nanophysics, nanophotonics, and applications. Springer proceedings in physics, vol 210. Springer, Cham, pp 161–174
48. Peng J, Gao W, Gupta BK, Liu Z, Romero-Aburto R, Ge L, Song L, Alemany LB, Zhan X, Gao G, Vithayathil SA, Kaipparettu BA, Marti AA, Hayashi T, Zhu JJ, Ajayan PM (2012) Graphene quantum dots derived from carbon fibers. Nano Lett 12:844–849
49. McWeeny R (1992) Methods of molecular quantum mechanics. Academic Press, London
50. Goscinski O, Lindner P (2003) Natural spin-orbitals and generalized overlap amplitudes. J Math Phys 11:1313–1317
51. Albert AE (1972) Regression and the Moore-Penrose pseudoinverse. Academic Press, New York
52. Amos AT, Woodward M (1969) Configuration-interaction wavefunctions for small pi systems. J Chem Phys 50:119–123
53. Luzanov AV, Ivanov VV, Boichenko IV (1996) Semiempirical determination of Dyson's states in conjugated systems within a full-CI π-electron scheme. J Mol Struct (THEOCHEM) 360:167–174
54. Pople JA, Hush NS (1955) Ionization potentials and electron affinities of conjugated hydrocarbon molecules and radicals. Trans Faraday Soc 51:600–605
55. McLachlan AD (1959) The pairing of electronic states in alternant hydrocarbons. Mol Phys 2:271–284

Chapter 23
Nanostructure Complexes in Water from the Position of SPE-Effect and from the Theory of Water, Created by J. Preparata

Ludmila Stepanovna Martseniuk and Aleksandr Stepanovich Martseniuk

23.1 Introduction

Water is the most important element for all life, and it is widely used in different technological cycles of modern industry.

In connection with the wide development of nanophysics and nanotechnologies, the understanding and forecasting of the phenomena of water interactions with nanotechnology products in various industries, including food technology, medical practice, etc., is needed.

A breakthrough in the understanding of the properties of water has been carried out by creation of the new theory of water by the outstanding Italian physicist — theorist J. Preparata — based on the laws of the quantum theory of fields published in 1995 [1]. This work, for the first time, shows that the quantum system behavior of water and superfluid He^4, unlike other liquids, can be described by the laws of quantum mechanics.

The theory of J. Preparata, for the first time, has adequately described all unusual, from a position of traditional conceptions, properties of water and has given a new impulse to the understanding of many phenomena in living organisms.

The positions of this theory must be taken into account while designing various nanotechnology devices because the nanostructures created by these technologies are quantum systems, and their interactions with the nanostructure complexes of water take place on a quantum level.

L. S. Martseniuk (✉)
Institute of Nuclear Researches NAS Ukraine, Kiev, Ukraine

A. S. Martseniuk
National University of Food Technology, Kiev, Ukraine

© Springer Nature Switzerland AG 2019

O. Fesenko, L. Yatsenko (eds.), *Nanophotonics, Nanooptics, Nanobiotechnology, and Their Applications*, Springer Proceedings in Physics 222,
https://doi.org/10.1007/978-3-030-17755-3_23

23.2 Water — Quantum System

The properties of water substantially depend on a number of factors, such as the admixture composition and the presence of nanostructure complexes, the influence of external fields, the contact with various surfaces, the temperature conditions, etc. The simplified model of Bernard–Fowler, constructed on the assumption of a one-phase structure of water, was not able to interpret a number of experimentally observable effects, especially the SPE-effect, the effect of M. Zhadin, the phenomena of cavitations, the effect of RNA-interference, and many others, showing insolvency of traditional theories and requiring their cardinal revision.

We will touch briefly on the basic positions of the theory of J. Preparata.

For construction of the theory [1], J. Preparata used the Hamiltonian for which the influence of electromagnetic fields, radiated moving particles of a substance, on all complexes of these particles has been discounted.

Such influence was not considered earlier because these effects were thought to be extremely weak.

J. Preparata investigated such an approximation in detail, deducing and deciding a complex system of the equations using a method of the Feynman's "Path Integral".

In a simplified description, the positions of this theory for water [1] are possible to present as follows.

Let's assume that in some volume there are identical two-level water molecules. If from vacuum the photon with length of a wave λ in area V within the bounds of volume $V = \lambda^3$ fluctuated, *all molecules* (we shall assume, that their number is equal N) *will be in a field of interaction with this virtual photon*.

The photon, fluctuated from vacuum with a wavelength of $\lambda = \hbar c/\delta E$, $\delta E = E_k - E_0$, is capable of transferring a molecule from the basic state to the excited state.

Let's assume that the probability P of excitation is on the order (according to the estimates based on the Lamb-shift) of 10^{-4}–10^{-5}. The excited molecule can pass to a ground state having emitted a photon (during an interval corresponding to time of decay), which can excite other molecules or be absorbed by vacuum.

The relative probability of these two events will depend on the densities of molecules $n = N/\lambda^3$ present within the volume. When a density will be exceeded by a critical level, a photon will never be returned in a vacuum. A condition must be executed for this purpose:

$$P_{\text{crit}} = P \cdot N = P \cdot (N/V) \cdot \lambda^3 \tag{23.1}$$

where: P_{crit} is the probability that the photon, fluctuated from a vacuum, will be captured by a molecule and a molecule will pass to the excited state. This process will proceed until many photons get trapped and a sizeable electromagnetic field is built in this region. This field:

1. Will create an attraction among the molecules oscillating with the same resonant frequency as the photon;

2. Will give the beginning of the oscillations of captured molecules with common phase for all area designated in [2, 3] as a coherent domain (CD).
3. Will give rise to the sharp (exponential) transition of the system from an initial state in which there is no tuning on the existing electromagnetic field to formation of areas of coherence — to coherent domains (CD).

As pointed out in [4], transition of the system to the state described by Eq. (23.1): "starts the "runaway" of the system from the perturbative ground state, in which matter and quantum fluctuations are uncoupled and no tuning electromagnetic field exists, to a coherent state in which, within a CD, a coherent electromagnetic field oscillated in phase with matter determining a macroscopic quantum state in which atoms and molecules lose their individuality to become part of a whole electromagnetic field + matter entangled system".

Thus, within a CD all particles stay between it and the common field in the entangled state and behave as a single whole; processes in such an environment take place with a single phase, determined by the frequency of the common field.

At a normal temperature T the destructive dynamics of thermal collisions counteracts the electrodynamics attraction that results in the molecules pushing out from the state of coherency. It leads to the appearance of two fractions: coherent $F_c(T)$ and non-coherent $F_{nc}(T)$.

The two fractions are connected, in water as well as in the case of superfluid helium, by a ratio:

$$F_c(T) + F_{nc}(T) = 1 \tag{23.2}$$

where $F_c(T)$ and $F_{nc}(T)$ are shares of coherent and non-coherent fractions.

The equation is determined by the common number of molecules for every phase at a certain temperature, but every molecule passes between these two stages continuously in time.

This phenomenon makes the flickering picture in time that can be fixed only in the case when the measuring device has shorter resolving time than the typical time of processes of transition between the states. The general homogeneous structure of water is fixed in the usual case only.

For water containing impurities and nanostructure complexes, the situation cardinally changes because the time of CD existence, bound by an attraction to such complexes, increases substantially. It is exactly the presence of such nanostructure complexes that determines the different characteristics of water, especially near-surface water and water of living organisms.

The sizes of CDs are determined by the length of the wave corresponding to energy of transition between the basic and excited states of water molecules, where pure water has the CD size of 0.1 μm, and for the domains attracted to nanostructure complexes or molecular complexes of living organisms, it can correspond to the sizes of these structures.

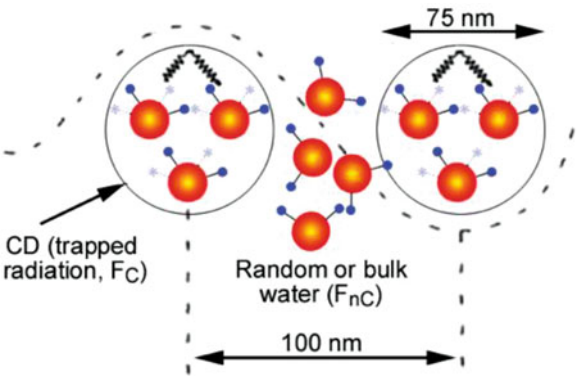

Fig. 23.1 The schematic picture of the structure of usual water under normal conditions according to data of [5]

The CDs are disposed throughout the entire volume of the water environment, being separated by the layers of non-coherent water. At room temperature, the total volume of such CDs is about 40% from the total amount of water.

Within a CD there is a decrease in the basic quantum energy level in comparison with the basic energy level of non-coherent water that provides stability of water CDs in relation to fluctuations of energy. The stability of a CD is pretty great, and the energy of connection between molecules of water inside a CD far exceeds the energy of thermal noise. In Fig. 23.1, the structure of water is schematically presented from the position of theory, created on the basis of the quantum theory of fields.

23.3 SPE-Effect from the Position of Theory of Water Created by J. Preparata

The supposition that water is a quantum system was put forward by different researchers, including the authors of the SPE-effect [6].

The authors in [6] considered the dynamics of occurrence of a liquid water phase as a process of the fusion of ice at heating at which the separate molecules of water and the fragments of the ice that have not melted under the influence of temperature fluctuations are formed. The quantitative ratio between the molecules that are in the ice-like phase and the single molecules of water depends on temperature. At an increase in the temperature, the total amount of the ice-like phases will decrease.

Such theory differs from the homogeneous theory of water where individual molecules are connected among themselves by the short-range forces having the nature of hydrogen bonding. Hydrogen bonds are short lived, and using only the presence of such connections to describe all the experimentally found regularities of a water phase is difficult.

The theory of a homogeneous structure of a liquid phase (« standard model ») is usually applied to the description of liquids with standard behavior. However, water has many anomalies that are not interpreted by the standard theories.

First of all, *the temperature range* in which water exists as a liquid phase *is non-standard*.

The theory of J. Preparata reveals an analogy of the structure and properties of usual water to the properties of superfluid liquid helium He II.

As is known, quantum liquids of superfluid helium can be formed by isotopes ^{4}He and ^{3}He. It is accepted to call such liquids, in which quantum effects prevail, quantum liquids. These effects hinder passing of liquid helium to the solid phase at ordinary pressure up to the temperature of absolute zero. Other liquids, where quantum effects are not so strong and usual forces of an internuclear attraction are more essential, pass to the solid state at normal pressure and enough low temperatures.

He I and He II are distinguishable. At temperature 2.19 K, designated as the $\lambda-$ point, the isotope ^{4}He undergoes the second order phase transition and passes to a superfluid state. In this state, the liquid helium is called He II. The ^{4}He atoms have no spin and submit to Bose–Einstein's statistics, and the ^{3}He atoms have the half-integer spin and correspond to Fermi–Dirac statistics.

The Fermi-liquid ^{3}He passes to the superfluid state at temperature ~2.6 mK and under pressure ~34 atm.

^{4}He and ^{3}He have boiling points at temperatures 4.21 K and 3.19 K accordingly and before transition into a superfluid state behave as usual liquids.

In 1938, L. Tissa [7] offered the first description of He II properties as the two-liquid model that was the basic core in disclosing the essence of the phenomenon of superfluidity.

L. Landau, who also offered the two-liquid model, first developed the theory of superfluidity of liquid helium (in 1941), which included the macroscopical hydrodynamics of a superfluid liquid on the basis of his submitted microscopic theory [8]. According to this model, the water environment can be presented as a mix of two liquids. One of them is named a normal liquid and has normal viscosity. The other liquid, which is named the superfluid component, is able to flow without friction and to penetrate without friction through narrow channels.

The phase diagram of ^{4}He is given in Fig. 23.2.

The normal and superfluid components are not divisible because they are made from the same molecules. Therefore, it is necessary to believe that [9]:

« below T_λ liquid He II can simultaneously perform two various movements. Each movement has its own local speed: v_n for normal and v_s for a superfluid liquid, similarly for each liquid there is an effective density of mass ρ_n and ρ_s. The full density ρ for He II is therefore defined as:

$$\rho = \rho_n + \rho_s, \tag{23.3}$$

and the full flux density is:

$$J = \rho_n v_n + \rho_s v_s. \tag{23.4}$$

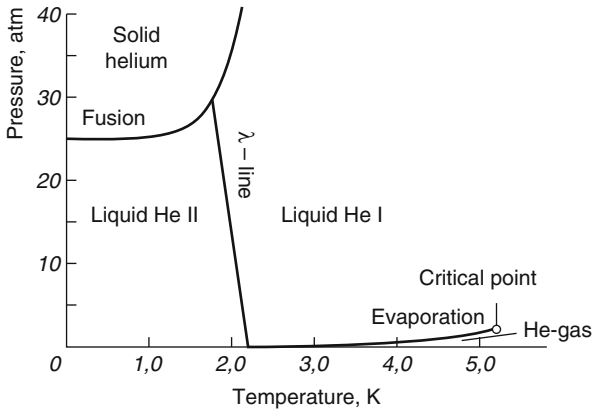

Fig. 23.2 The phase diagram of ^{4}He [9]

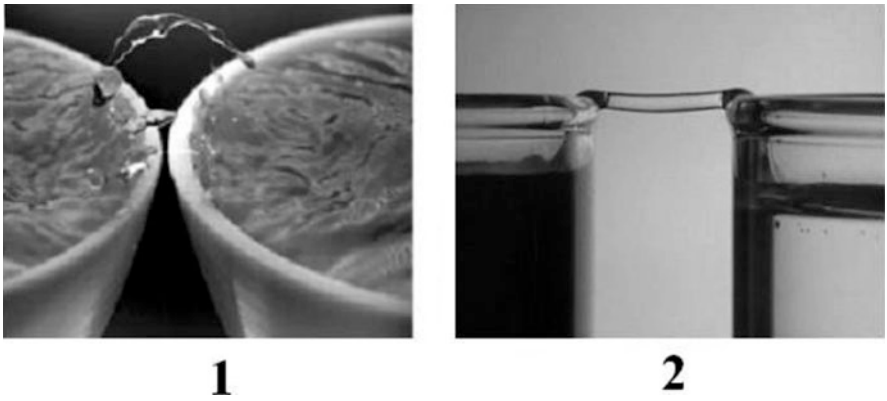

Fig. 23.3 The scheme of formation of the floating water bridge (1) an initial stage; (2) a stationary picture [11]

Such an approach, when both parts of a liquid are considered independent, is especially convenient at small speeds.

E. Del Guidice in [10] indicates a similarity of the water theory, which has been put forward by J. Preparata, with the two-liquid model of He II. Equation (23.2) for water corresponds to Eq. (23.3) for He II and also means that the number of molecules belonging to coherent and non-coherent fractions for the fixed temperature remains constant; however, as specified in [10]: « each molecule passes between these two stages continuously in time».

Another similarity in the properties of water and superfluid He II also indicates their behavior as found by researching the following phenomena: formations of a floating water bridge (Fig. 23.3) [11] and spouting of superfluid helium (Fig. 23.4) [9].

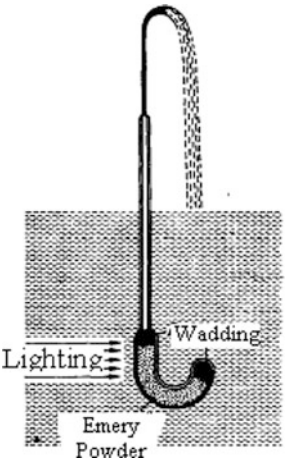

Fig. 23.4 The scheme of spouting of superfluid helium He II [9]

In 1893, a floating water bridge was observed for the first time by Lord W. Armstrong (1871–1916) [11], and the interpretation of this phenomenon was absent for more than 100 years before creation of the theory of water by J. Preparata.

A floating water bridge appears between two vessels filled with water when a voltage of ~15 KV is supplied between two platinum electrodes, inserted in the first and second vessels.

In the beginning, when the voltage is supplied, an unstable picture arises accompanied by the ejection of water near the electrodes (Fig. 23.3(1)) and then a water bridge appears between vessels. For further stabilization of the water environment, a bridge saves the form by increasing the distance between vessels by 10–12 mm (Fig. 23.3(2)), [11]).

The spouting of a superfluid component of liquid helium takes place by lighting a capillary tube with emery powder, situated at the bottom of the tube (as shown in a Fig. 23.4), using a flashlight.

The occurrence of "spouting" of a liquid at the supply of energy from outside is common for these two cases.

From here it follows that water, at the inputting of external energy (such as supply of a voltage), shows quantum characteristics similar to liquid helium. The dynamics of the occurrence of a floating water bridge is described in detail in [11].

J. Preparata, at creation of the theory of water, applied the postulates of quantum field theory. Subsequently, he, together with collaborators, successfully applied the same approach to the description of superfluidity in ^{4}He and ^{3}He [12, 13].

Though J. Preparata constructed the theory only for water, he assumed that basic positions of the theory can be fair for other substances at their condensation to a solid and liquid state. The magnitudes of the parameters of water predicted in this theory, some features of its properties, and also the *dynamics of phase transition of water molecules from vapor to liquid state* well correlate with known experimental data.

At the same time, as specified earlier, the behavior of usual liquids is quite well described by standard theories. Even liquid helium at temperature above T_λ behaves as a usual liquid.

In [8], the characteristics for the description of properties of liquid helium are: the density of a normal liquid ρ_n, the density of a superfluid liquid ρ_s and «the full, true density of a liquid» for which the relation (23.2) is carried out.

In [8], taking into account that for normal and superfluid components the relation (23.3) should be satisfied, it is marked that at absolute zero the ratio of ρ/ρ_n is equal to zero, i.e., a superfluid component is present only. With the increase of temperature, the share of a normal component grows, until at temperature T_λ the full disappearance of the coherent faction will not happen, i.e., ρ/ρ_n becomes equal to unit and He II will transform into He I. Thus, [8]: «a phase transition in liquid helium is connected with a disappearance of a superfluid part in a liquid».

This means that the share of superfluid fraction depends on processes competing among themselves, in which the thermal collisions destroying coherence have the leading part.

For standard liquids with normal behavior, from the position of the generally accepted theories for the basic mechanism of condensation, there is molecular attraction at close distances caused by the presence of short-ranged forces of various origins, mainly van der Waals forces.

In connection with the foregoing, it is possible to draw the ***following conclusion [129]: the basic feature of water consists in that: the phenomenon of condensation of water molecules from gas into liquid state is carried out by another mechanism than in standard liquids*** and determined by the predominance of quantum effects [8] above the classical, the essence of which is explained by the theory of J. Preparata [1]. Exactly by this is conditioned a non-standard temperature interval in which molecules of water are in a liquid phase (Table 23.1).

Properties of the hydrides of elements located in vertical columns of Mendeleev's table should vary monotonously with the increase of weight, as corresponds to the data submitted in Table 23.1.

If such tendency was kept for water, it would be a liquid only in a range from −95 °C up to −80 °C, and at higher temperatures would be a gas.

Let's note that the share of coherent fraction of water depends on temperature and at the temperature approaching a boiling point decreases up to zero [10]. Contrary to water, a full disappearance of coherent fraction for He II already occurs at T_λ.

Table 23.1 The dependence of the freezing temperature and boiling temperature of some hydrogen compounds on molecular weight

The hydrogen compound	Molecular weight	Freezing temperature	Boiling temperature
H_2Te	130	−51	−4
H_2Se	81	−64	−42
H_2S	34	−82	−61
H_2O	18	0	+100

Thus, it is necessary *to draw* **the** *conclusion* that *the beginning of condensation of water molecules in a liquid state, contrary to usual liquids, occurs owing to the occurrence of interaction of molecules with the vacuum virtual photons* under condition, determined by Eq. (23.1). This process is described by the theory created by J. Preparata [1].

It is necessary to believe ***that other unusual properties of water are also caused by the same reasons.***

The existing opinion that all non-standard properties of water follow from the presence of the hydrogen bonds connecting the separate molecules of water by a united net is not correct. Indeed, as follows from J. Preparata's theory of water, the presence of hydrogen bonds is the consequence of the existence of electron coherent fluctuations between the ground and excited states of water molecules in CDs [10].

One of the most essential pieces of evidence of the unusualness of water's behavior, and its cardinal difference from other liquids, is the SPE-effect.

The essence of the SPE-effect, by definition of the authors in [6], is that an irradiation of the water environment by electromagnetic radiation of a mm-range (1 ... 10 mm) at ultralow capacity of a flux < 10 mW/sm^2 (MM EMI) arises the resonant excitations of wave processes in the water environment on the frequencies, coinciding with frequencies of its own molecular fluctuations and accompanied by a partial dissipation. The authors in [6] called these frequencies «resonant».

The authors of the SPE-effect used the standard models of water for its interpretation and have been compelled, instead of receiving the answer to the questions, to add still new questions, to which the standard approaches could not give satisfactory answers.

The resonant spectra of the water, registered from a surface of the irradiated water environment at an irradiation of it by MM EMI, have a number of features and substantially differ on good quality and other characteristics from the usual water spectra registered by other methods (Fig. 23.5).

Briefly, we will enumerate some features fixed experimentally by the method of the SPE-effect on which there was the greatest number of questions.

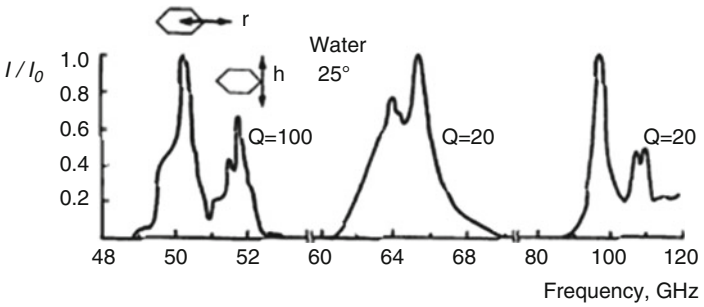

Fig. 23.5 The resonant spectra of distilled water [6]

1. A very high number of good quality peaks of resonant interaction that directly indicates the presence:
   (a) of more than one phase in water;
   (b) of a coherence of one of the phases and its relative stability.
2. Nonthermal, but information character of interaction.

This testifies that the spectra are registered at extremely low levels of irradiation (at the threshold level of 1–10 mkW/см^2) and in the interval of the used flux of powers (1–10 mkW/см^2) do not depend on the power of irradiation.

With increasing of the levels of powers of irradiation, there are the processes that reduce the destruction of coherence, which is expressed in passing of spectra to the chaotic kind. It is possible to assume that at extremely low levels of resonance, influencing of EHF-radiation can take place in some processes, similar to those which arise at the use of *the quantum undestroying measurements* method [14], which allows conducting the quantum measurements without the origin of decoherence of the quantum states. Such interpretation differs from that offered by the authors of work [15].

3. The transparency for frequencies of resonances at extremely low levels of excitation.

Water is a strong absorber of waves of mm-range and does not skip the radiation of this range on a thickness ~1 mm.

It is not clear, in the opinion of the authors in [6], if there is also a mechanism of synchronization of the water environment. The authors mark that passing to the resonance state is a transition of the second type for which entropy is minimum, and, consequently, the maximum of information of the system there corresponds to it. Such a state is metastable; additional expenses of energy are necessary for its maintenance, which can be explainable for the water environment of living organisms but not for usual water.

4. An appearance of dissipation in molecular structures at extremely low intensities of influence of MM EMI. Indeed, although the irradiation of the water environment was conducted by electromagnetic waves of mm-range, spectra were registered in the range of decimeter.
5. The existence of own resonant frequencies and a water memory on the EHF-irradiation, owing to which, and the long resonant afterglow are found.
6. The doubling character of resonant peaks and the dependence of location of these peaks from a nature of interaction with impurity and an environment. Nonresonant spectral bands that appear in more long-wave range are not duplicates.

According to the interpretation of the authors in [16], resonant lines near frequencies of 50 and 60 GHz should be counted as basic vibrations and the others as their harmonics related to fluctuations of electric and magnetic dipoles of water molecules that enter into the composition of hexagonal fragments of water.

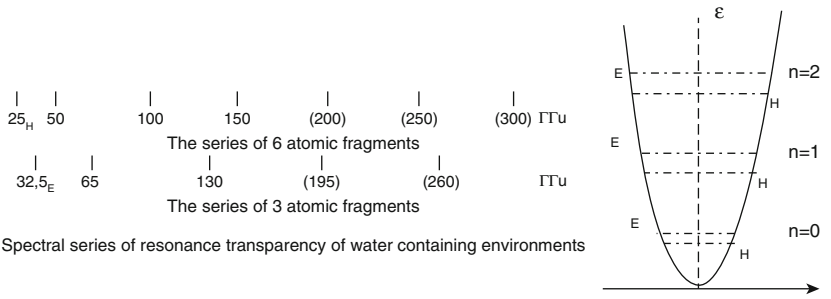

Fig. 23.6 Resonant spectra of water and the energy levels of quantum oscillator [16]

The authors point out the presence of the next frequencies of resonance near 25, 32.5, 50, 65, 100, 130, and 150 GHz and herewith notice that these numbers are limited by the research apparatus possibilities.

It has been shown that the frequencies of resonant peaks correlate among themselves as frequencies of quantum harmonious oscillators: $\varepsilon_n = h\nu_0(1/2 + n)$, where $n = 0, 1, 2, 3 \ldots$. The authors note that the formula for frequency of a harmonious oscillator is possible to convert thus: $\varepsilon_n/h = \nu_0/2, \quad \nu_0, \quad 2\nu_0, \quad 3\nu_0, \ldots$ If in this formula we put the basic frequencies: $\nu_0 = 50$ GHz and 65 GHz, we shall receive the distribution shown in Fig. 23.6, where the position of spectral lines of water corresponding to the distribution of lines of harmonious oscillator is submitted. Thus, work [16] states that in spectra of EHF-resonance interaction with water, the characteristic frequencies of water as a quantum system are shown.

Thus, the authors in [16] on the basis of the results analysis of the experimental research of the SPE-effect have received one more acknowledgement that water is a quantum system.

Let's show that within the framework of the quantum theory of water, developed from a position of the quantum theory of fields by J. Preparata, some of the extraordinary properties of water included in items 1–6 can be satisfactorily interpreted.

Moreover, the extensive experimental material received by the authors of the SPE-effect *is also a direct acknowledgement of theoretical previsions and [1] is its experimental illustration*.

First of all, we will appeal to a question about the nature of resonant spectra.

According to positions of the quantum theory of water [1], usual water includes the areas of coherence — a CD in which all processes occur with a united phase of coherent fluctuations and at the frequency determined by frequency of a united captured coherent field. All molecules in a CD are in a state of entanglement among themselves and a united field. A non-coherent fraction is submitted by the individual molecules of water placed between coherent domains.

Usual water in real conditions always has the nano-heterogeneities in its composition; therefore, it is important to investigate the processes exactly in such water.

As shown in [3], the presence of such nano- and micro-*heterogeneities* is an important factor for the special organization of the water environment. Coherent domains in such a water environment can cooperate among themselves and pass to a state of entanglement (to self-synchronizing) and water gets the additional properties of coherency. Especially, it is of concern to the water environment of living organisms.

For such water and, especially, for natural water, near-surface waters, and waters of living organisms, *the time of existence of CD can be rather large* (about several weeks and more). The water environment of CD, adjoining to walls of surfaces of nano-heterogeneity, receives additional protection against the destroying influence of thermal collisions [17]. This means that in spectra of NHR-interaction the exact phenomena in CD, formed on heterogeneity, are fixed.

Consequently, in such water systems should be registered both very narrow peaks responsible for processes in the coherent fraction and wide strips whose nature is related to processes in the non-coherent fraction, which answers the real experimental information.

An energy barrier with energy E_{Gap} serves as a factor preventing the destruction of coherence in CD. As underlined in [15], the energy of gap (E_{Gap}) is the difference in energy between a coherent state in CD and non-coherent state of all components before an establishment of coherence. The energy barrier protects the coherent system from external perturbations and stabilizes the system.

In addition, near a surface, the water molecules can be attracted to the surface, and an energy of attraction is added to energy of gap E_{Gap}, producible by coherent dynamics [15, 17].

Let's note that if at room temperature the energy of gap E_{Gap} is about 0.26 eV, the energy of temperature fluctuations of all $KT \approx 0.025$ эВ. Exactly these factors provide stability to the properties of ordinary water.

Water CDs, due to an exchange with an environment, can reserve a huge amount of energy, and their energy spectrum thus will be shifted in the short-wave side.

In [10] the process giving rise to the excited states is described as follows.

In a CD every molecule of water oscillates between the basic and excited states; thus, the excited level corresponds to energy 12.06 eV, while the energy of ionization of a water molecule is 12.60 eV. Oscillation with energy of 12.06 eV corresponds to the size of CD ~0.1 μm. Coherent oscillations lead to the occurrence of quasi free electrons, which are easily excited. Each excitation corresponds *to a cold whirlwind* of quasi free electrons.

Actually, every quasi free electron belongs to a coherent state; therefore, the external perturbation, smaller than the energy of a gap, cannot be transferred to any other individual molecule, and is kept in the CD, giving rise to the collective excited state, which is still coherent.

The excited states in water cannot disintegrate in the thermal way because movement of cold whirlwinds of quasi free electrons occurs without friction, just like in superconductors.

There is a huge number of excited states (characterized by angular moment L) with energy of some tens KHz.

Individual excitation of quasi free electrons are added up; therefore, a CD can reserve a huge amount of energy and the time of existence in the excited state is determined by the time of existence of the CD. The spectrum of the excited states on each molecule in CD is limited from above by energy of gap (equal 0.26 eV/molecule); since in a CD there are about six million molecules, it appears that the spectrum of isolated water practically has no limit [10].

In [11] it is underlined that spatial division between levels in a spectrum of coherent domains is in a range of mm-waves.

In work [18] the calculation value of fundamental frequency of electromagnetic field $\nu_{\text{fundamental}}$ of a coherent domain, located as a coaxial tube along a protein, is given. According to [18], for possible values of $\nu_{\text{fundamental}}$, the interval of 0.5–2.5 GHz is specified, namely a range of EHF-waves.

We will remark that these estimations are near those predicted by H. Frelich [19] (the Frelich frequency ~10^{11}–10^{12} s) for the coherent states of living organisms, and the same frequencies are registered in the EHF-spectra of resonance interaction of GHz-waves with water and water environments of living organisms [6].

Thus, it is possible to make ***the assumption*** [20] that the narrow peaks found by the authors in [6] *correspond to fundamental frequencies of water; however, they do not belong to the ice-like phase* as the authors in [6] considered *but instead to CDs.*

In that case, the new prospect is opened directly for researchers to study the coherent phenomena in the entangled macrosystems that are the CDs of water, through studying the effects of resonant interaction of MM EMI with water systems.

It is especially useful for biosystems because the sizes of coherent domains of water are determined by the sizes of nanostructures of living organism and exist much longer than in pure water.

On the basis of experimental material [6], taking into account the supposition done, it is possible to postulate about the properties of CDs.

First of all, a CD is not an ice-like phase of water as the authors in [6] supposed, but a system consisting of molecules being in a certain ordered state. The basic difference is that the molecules in CD are bonded among themselves not by hydrogen bonds, as in crystal ice, but by the forces *of exchange* character owing to an entangling of molecules with a united for all domain electromagnetic field. Indeed, for ice the narrow peaks of NHR-resonant interaction with water, which indicates a coherency of this structure, are not found.

It is possible to assume that some «crystal-like» structure is saved in CD, although it is not «ice-like formations», as the authors supposed in [6].

On the presence of some structural orderliness, the «crystal-like» of CDs indicates that in spectra of NHR-resonant interaction with water environments the doubling of resonant peaks are fixed; this confirms the assumption made above.

The authors in [6] considered that radial and transversal vibrations of the «ice-like» hexagonal structures are responsible for the origin of peaks at frequency 50.3 and 51.8 GHz. (Fig. 23.4).

As specified in [21], quantum correlations are stronger than classical.

They can determine the presence of nonlocal quantum interactions that have not been restricted by speed of interaction. Apparently, the effects of resonant excitation,

resonant transparency, and memory, mentioned earlier, are related exactly to the display of such *nonlocal* interactions.

In the water environment of living organisms there can be an entangling of coherent domains between itself that gives rise to "supercoherence" [10]. It is typical, to a lesser degree, for natural water where introduction of some impurity (for example NaCl) can lead to reduction of a share of coherent fraction that, in turn, influences the temperature of freezing of water solutions. The entangling of the system means that its elements are not independent among themselves and at a change of state of one of them the state of the other elements of the system is changed.

Apparently, the effects of dissipation of energy that have not found satisfactory treatment within the framework of usual representations can be explained from a position of existence of an entangling between elements of water systems.

It is also necessary to note that the coherent water environment has its own resonant frequencies. They are defined by its fundamental parameters, energy of the excited states, interaction with an environment, the temperature parameters determining a share of coherent fraction, etc.

All these features are fixed and in spectra of EHF-resonance interaction of low-intensity radiations with the water environments submitted in [6].

It can be noted that *not ice-like formations* [6] *but instead the coherent domains* are stabilized in water systems owing to structuralization of water. Such structuralization is *caused by the presence of internal* ***nano-heterogeneity*** chemical and energetic interactions with an environment.

The nonthermal (information) character of interaction of the EHF-radiation with the water environment, noted above in item 2 (at SPE-effect revealed by the authors in [6]) can be explained on the basis of the following reasoning, conducted in [15].

The coherent system becomes able to oscillate well with a certain phase only when the number of components becomes uncertain; thus, it is an open system, and it is able to add its fluctuations to the fluctuations of an environment.

Such a coherent system (similarly to biological system) is able "to feel" an environment through the electromagnetic potential created by its phase dynamics.

In this case, the information can spread by means of some agent, the phase, but any actual transmission of energy does not occur. The energy required for a current, according to this circuit, is provided exclusively by the presence of energy in the local scale.

If in some place of the coherent system there is a supply of energy, this energy induces a change of phase and an electromagnetic potential arises that, with a speed faster than the speed of light, reaches a distant area [15] where the phase is accordingly changed and leads to change of the local molecular dynamics. The real moving of energy or matter does not occur.

Interaction between elements of a coherent system of an organism through electromagnetic potential can explain the seeming paradox of obtainment of the big effects caused by the application of very weak electromagnetic fields, as in the case of action by EHF-radiation of low intensity [22] on the chosen magnitudes of resonant frequency. The authors in [15] specify that above a very tiny threshold,

the effect does not depend on the intensity, provided that the intensity is lower than the value where thermal effects begin to be essential. It is not the thermal effect of radiation that concerns the seeming paradox of the disproportionate effects as to the sum of spent energy, which could be understood to assume that «the effective messenger of interaction — not a field, but the potential».

23.4 Results and Conclusions

1. An extensive analysis of the properties of usual water as the composite complex of a highly organized quantum system from a position of the theory of water created on the basis of the quantum theory of fields by J. Preparata is carried out. This first-of-its-kind analysis is made on the basis of the experimental results obtained from research on the effect of the resonant interaction of EHF-radiation with the water environment (SPE-effect) [20, 23].
2. For the first time, it is shown that the statements of the theory of J. Preparata are *fully confirmed by the experimental results, which are obtained by means of the SPE-effect method.*
3. For the first time, *an explanation is given for the paradox of an unusual temperature interval existing for water in the liquid state* which does not correspond to predictions of traditional theories, and it is shown that such discrepancy means that water is not an ordinary liquid, the properties of which it is possible to interpret from the position of traditional presentations.
4. The interpretation of some phenomena, which are found by researching the resonant interaction of MM EMI with the water environment, such as a high number of good quality resonant peaks, nonthermal character of interaction, effects of dissipation of mm-waves, the doubling of resonant peaks, and other phenomena, has been carried out from the position of the theory of J. Preparata [1].
5. *For the first time, a new interpretation of the nature of occurrence of resonant peaks in spectra of the EHF-resonance interaction with water (SPE-effect) is made: as a display of resonant transitions between the excited states in CD.*
6. *For the first time, it is shown that it is necessary to consider the «ice-like» formations, which exist in the opinion of the authors in* [6]*, found in resonant spectra of EHF-resonance interaction, as a sign of the presence of coherent domains in water (which occurs under normal conditions of* ***nanostructures*** *heterogeneities), stable against external influence.*
7. Coherent domains of usual water, whose existence, for the first time, has been theoretically proven by the theory of J. Preparata, can be interpreted as quantum macrostructures (macromolecule); the occurrence of the analogues of which is possible in different liquids, solutions, in micro- and macro-objects, and they can be responsible for the display of various phenomena in substances of living and nonliving matter.

References

1. Preparata J (1995) QED coherence in condensed water. World Scientific, Singapore, p 236
2. Arani R, Bono I, Del Giudice E, Preparata J (1995) QED coherence and the thermodynamics of water. Int J Mod Phys B 9:1813–1841
3. Bono I, Del Giudice E, Gamberale L, Henry M (2012) Emergence of the coherent structure of liquid water. Water 4:510–553
4. Caligiuri L, Musha T (2015) Superradiant coherent photons and hypercomputation in brain microtubules considered as metamaterials. Int J Circ Syst Sign process 9:192–204
5. Madl P, Del Giudice E, Voeikov V et al (2013) Evidence of coherent dynamics in water droplets of waterfalls. Water 5:57–68
6. Sinitsin NI, Petrosjan VI, Elkin VA et al (1999) The special role of system: "millimetric waves—the water environment in the nature". Biomed Radio Electron 1:3–21. (in Russian)
7. Tisza L (1938) Transport phenomena in helium II. Nature 141:913; Tisza L (1947) The theory of liquid helium. Phys Rev 72(9):838–854
8. Landau L (1941) Theory of superfluidity of helium II. J Theor Exp Phys 11(6):592. (in Russian)
9. Tilly DP, Tilly D (1970) Superconductivity and superfluidity. Red. Ginzburg VM, «World», p 304. (in Russian)
10. Del Giudice E, Spinetti P, Tedeschi A (2010) Water dynamics at the root of metamorphosis in living organisms. Water 2:566–586
11. Del Giudice E, Vitiello G (2011) Influence of gravity on the collective molecular dynamics of liquid water: the case of the floating water bridge. Water 2:133–141
12. Del Giudice E, Mele R, Muggia A, Preparata J (1993) Quantum-electrodynamical coherence and superfluidity in ^{3}He. Il Nuovo Cimento 15(10):1279
13. Del Giudice E, Giuffrid M, Mele R, Preparata G (1991) Superfluidity of ^{4}He. Phys Rev B Condens Matter 43(7):5381–5388
14. Menskiy MB (1998) The phenomenon of decoherency and the theory of uninterrupted quantum measuring. Success Phys Sci 168(9):1017–1035. (in Russian)
15. Bischof M, Del Giudice E (2013) Communication and the emergence of collective behavior in living organisms: a quantum approach (review). Mol Biol Int 2013:19, Hindawi Publishing Corporation, Article. ID 987549
16. Gulyaev UV, Sinitsin NI, Petrosjan VI et al (2001) Effects of the resonance-wave state of environments of waters and biological's department of Institute of the Radio Engineering and Electronics. RAS. Saratov. p 6. (in Russian)
17. Del Giudice E, Tedeschi A, Vitiello G, Voeikov V (2013) Coherent structures in liquid water close to hydrophilic surfaces. J Phys Conf Ser 442:012028
18. Del Giudice E, De Ninno A, Fleischmann M et al (2005) Coherent quantum electrodynamics in livin matter. Electromagn Biol Med 24:199–210
19. Fröhlich H (1968) Long-range coherence and energy storage in biological systems. Int J Quantum Chem 2(5):641–649
20. Martseniuk LS (2017) The effects of interaction of coherent water systems with low intensive electromagnetic radiation. Materials of 12th international conference "Interaction of radiation with solids", Sept 19–22. Minsk. p 25–27
21. Misochko OV (2013) Nonclassical states of excitations of crystalline grate: compressed and entangled fonons. Success Phys Sci 183(9):917–933. (in Russian)
22. Devyatkov ND (1973) Influence of millimeter-band electromagnetic radiation on biological objects. Success Phys Sci 110:453–454. (in Russian)
23. Martseniuk LS (2018) Water – the quantum system. XXV Annual scientific conference of Institute of nuclear researches. NAS of Ukraine. Thesis of lectures. p 135. Kyiv. Institute of Nuclear Researches. p 242. (in Ukrain)

Chapter 24
Nanocomposite Hydrogels Containing Silver Nanoparticles as Materials for Wound Dressings

O. Nadtoka, N. Kutsevol, O. Linnik, and M. Nikiforov

24.1 Introduction

The design of consumer products with antimicrobial properties is critically needed in the present living conditions. An ideal wound dressing or infection regulating products must have certain essential properties. They should perform basic functions such as provision and maintenance of moist environment, protection from secondary infections, absorption of wound fluids, macroporous environment for air exchange, painless with contact, and easily removable [1, 2]. For these applications hydrogel films containing silver nanoparticles are developed.

Hydrogel nanocomposites are cross-linked hydrophilic polymers loaded with nanoparticles having capacity to absorb, swell, and retain large amount of water in their cross-linked networks. In particular, the hydrogel nanocomposites in which the hydrogel matrix is combined with inorganic nanoparticles have much attention during the past few years [3]. It is known that silver nanoparticles (AgNPs) have demonstrated significant antimicrobial effect against infection and diseases [4]. They have been applied to a wide range of healthcare products such as burn dressings, scaffold, skin donor and recipient sites, water purification systems, and medical devices [5–7].

O. Nadtoka (✉) · N. Kutsevol
Taras Shevchenko National University of Kyiv, Kyiv, Ukraine

O. Linnik
Chuiko Institute of Surface Chemistry, National Academy of Science of Ukraine, Kyiv, Ukraine

M. Nikiforov
Military Institute of Taras Shevchenko National University of Kyiv, Kyiv, Ukraine

© Springer Nature Switzerland AG 2019

O. Fesenko, L. Yatsenko (eds.), *Nanophotonics, Nanooptics, Nanobiotechnology, and Their Applications*, Springer Proceedings in Physics 222,
https://doi.org/10.1007/978-3-030-17755-3_24

Metal nanoparticles in hydrogel are prepared and stabilized by physical and chemical methods. The chemical approach including chemical reduction, electrochemical techniques, and photochemical reduction is most widely used [8–11].

The size and shape of the inorganic nanoparticles can be controlled by the hydrogel internal network structures [12]. The hydrogel network structures are mainly regulated by the composition of various comonomers, polymers, and cross-linkers that are employed in the synthesis of hydrogels [13, 14]. In their swollen stage, hydrogels offer large free space within the cross-linked network that can act as a nanoreactor and thus contribute synthesis of nanoparticles by providing sufficient space for nucleation and growth of nanoparticles. Inside the hydrogel matrix, silver ions make favorable interactions with the functional moieties present in the polymeric chain and, thus, form a uniform distribution inside the whole network [15]. Upon reduction, uniformly distributed silver nanoparticles of controlled size may be achieved which would subsequently immobilize within the polymeric matrix.

To achieve novel and better antibacterial products, hydrogel-silver nanocomposites are developed in the present investigation. For obtaining these products, dextran-graft-polyacrylamide copolymer (D-g-PAA) hydrogels are synthesized using a bifunctional cross-linker *N*,*N*′-methylene-*bis*-acrylamide (MBA). Our previous research has shown that starlike dextran-graft-polyacrylamide copolymers (D-g-PAA) have advantages in comparison with linear polyacrylamide because of their internal structure which can be regulated in the synthesis process. Dextran can also influence the hydrogel networks and decides the nanoparticle structures. Another factor that influences the size and distribution of silver nanoparticles in a hydrogel is the method of their synthesis. In this paper, we discuss the synthesis of AgNPs using chemical and physical methods.

Taking into consideration all the above factors, the present work involves the development of dextran-graft-polyacrylamide silver nanoparticle (D-g-PAA-AgNPs) hydrogel composites for antibacterial and wound dressing applications.

24.2 Experimental

24.2.1 Materials

Acrylamide (AA), silver nitrate ($AgNO_3$), dextran (D), sodium borohydride ($NaBH_4$), cerium(IV) ammonium nitrate (CAN), and *N*,*N*′-methylene-*bis*-acrylamide (MBA) are purchased from Aldrich Chemical Company and were of analytical grade. Distilled water was used throughout the experiments and as polymerization medium during hydrogel formation.

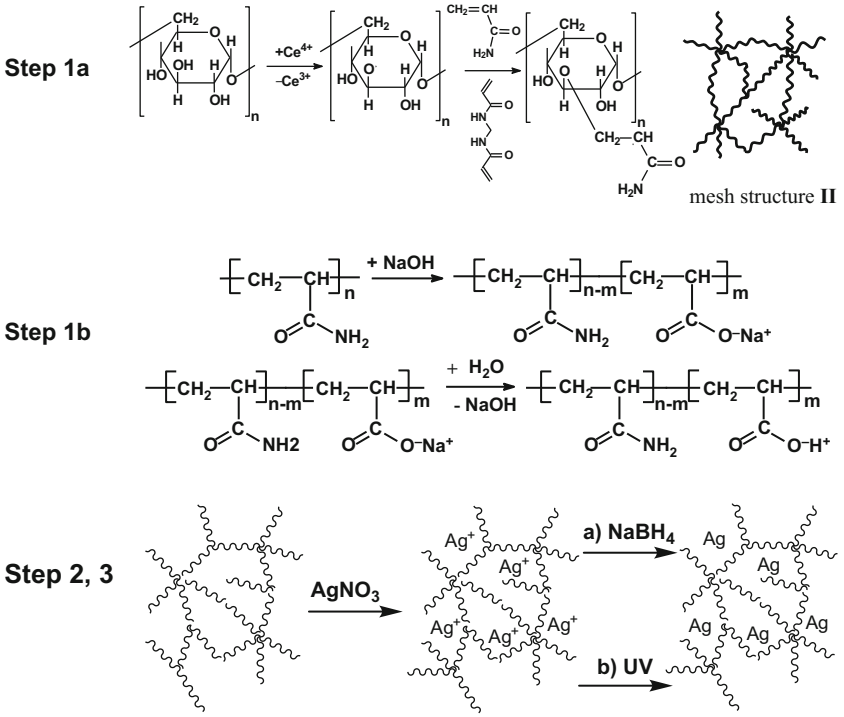

Fig. 24.1 Synthesis of AgNPs-loaded hydrogels

24.2.2 Preparation of Silver Nanoparticles Loaded with Hydrogels

The preparation of the hydrogel nanocomposites involves three steps as shown in Fig. 24.1. These steps include the following: (1) synthesis of hydrogel, (2) silver ion incorporation, and (3) reduction of silver ions into silver nanoparticles.

Hydrogels dextran-graft-polyacrylamide (D-g-PAA) are prepared by solution free radical polymerization in a 50 mL beaker following the procedure reported earlier [16] (Fig. 24.1). The dextran (0.1 g, 0.005 mM) is dissolved in 25 mL of distilled water at ambient temperature (25°C). This solution was purged by argon bubbling for 25 min, and cerium (IV) ammonium nitrate (0.01644 g, 0.03 mmol mL^{-1}) is added as a reaction initiator. After 2 min acrylamide 0.05 mol and *N*,*N*′-methylene-*bis*-acrylamide 0.4% (w/ monomer) are added. Thereafter, argon was passed for 2 min and reaction mixture was left overnight. The formed hydrogel sample is taken out from the beaker, washed with distilled water, and placed in a 400 mL beaker containing 200 mL distilled water (refilled fresh water for every 12 h for 2 days) to remove unreacted monomer from the hydrogel. Finally, the gels are dried at ambient temperature (Fig. 24.1, Step 1a).

Alkaline hydrolysis of synthesized cross-linked hydrogel samples was carried out as follows: 3.6 g of cross-linked hydrogels were dissolved in 200 mL of distilled water. Swollen sample was placed into 20 mL 5 M NaOH at 58 °C. After 10, 15, 20, and 25 min, the hydrolyzed samples were obtained in the salt form. They were immersed in distilled water at room temperature for 48 h, and the water was renewed several times in order to remove NaOH. As result the polyelectrolytes dextran-*graft*-(polyacrylamide-co-polyacrylic acid) (D-g-(PAA-co-PAAc)) were obtained. All samples were dried and kept under vacuum (Fig. 24.1, Step 1b).

Dried hydrogels (~30 mg) are placed to a beaker containing 25 mL of 0.1 M silver nitrate aqueous solution for 48 h to reach equilibrium swelling. During this stage the silver ions are being exchanged from solution to the hydrogel network (Fig. 24.1, Step 2).

Synthesis of AgNPs by chemical methods. In situ reduction of silver ions inside the hydrogel network was done using sodium borohydride as reducing agent (Fig. 24.1, Step 3a). The Ag^+ ions-loaded hydrogels were immersed in sodium borohydride solution (0.1 M) for 30 min. After complete reduction, the hydrogels were rinsed using distilled water, lyophilized, and kept for further characterization. The schematic representation of silver nanoparticle formation inside the hydrogel network is shown as below.

Synthesis of AgNPs by physical methods. The Ag^+ ions-loaded hydrogels were placed under UV light. Photochemical reactions were carried out under irradiation by 1000 W middle-pressure mercury lamp for 5 min. The distance lamp reactor was set at 90 cm. Finally, the obtained silver nanoparticle-loaded hydrogels are dried at ambient temperature (Fig. 24.1, Step 3b).

24.2.3 Swelling Studies

The swelling characteristic of the hydrogels provides information of network integrity before and after loading of silver salt, precipitation of silver nanoparticles inside the networks.

Hydrogel membrane was cut into 10-mm circular discs and dried under vacuum for 72 h to determine their dry weight (w_0). Water content was measured by immersing the D-g-PAA hydrogel membrane in distilled water at 25°C. The wet weight (w_t) was determined by wiping off the surface water with a piece of filter paper. The data provided is an average value of three samples reading. The absorbed water content was then calculated by determining the water content in term of the swelling ratio (S %) using Eq. 24.1:

$$S_t\% = \frac{w_t - w_0}{w_o} \times 100\% \tag{24.1}$$

24.2.4 Characterization of Hydrogel Composites

The Fourier transform infrared (FTIR) spectra of pure and silver-loaded D-g-PAA were recorded with an FTIR spectrophotometer (MAGNA 550, Nicolet Instruments Corporation, USA) using KBr pellet.

UV–visible spectra of the silver nanoparticles from the nanocomposite hydrogel were recorded using Lambda 35 UV–Vis spectrophotometer (PerkinElmer, CA) in the absorbance mode (range 200–1000 nm).

The morphology of hydrogel membrane was observed by SEM mod. Stereoscan 440 (LEO), Cambridge, UK instrument. The cryogenically fractured film in liquid nitrogen was mounted vertically on the SEM stub by silver adhesive paste. The specimens were sputter coated with gold to avoid electrostatic charges and to improve image resolution before being examined by the electron microscopy.

24.3 Results and Discussion

24.3.1 In Situ Formation of Silver Nanoparticles in the Hydrogel

Due to the importance of the hydrogel nanocomposites in antimicrobial wound dressing applications, D-g-PAA hydrogels were developed to act as a nanoreactor and subsequently as an immobilizing matrix for the synthesized nanoparticles [17, 18].

It is reported that change in concentration of the cross-linking agent may affect the free space between the polymeric networks and may affect the size, shape, or distribution of the silver nanoparticles within the hydrogel. A highly dense hydrogel network is desired which favors the intra-/intermolecular interactions between the silver ions and the gel network, resulting in the formation of small-sized silver nanoparticles.

In contrast, a hydrogel with high porosity provides large surface area for silver nuclei generation and, thus, produces a large number of silver nanoparticles with its potential to limit their aggregation. The porosity affords an opportunity for the rapid diffusion of water molecules in and out of the polymers, and this property may be important for antibacterial applications. Therefore, the mesh size of hydrogels appears to be a key factor for in situ formation and immobilization of silver nanoparticles inside the hydrogel.

High water diffusion in hydrogels can be achieved by converting PAA into polyelectrolyte. In the present study, the synthesized hydrogels were subjected to alkaline hydrolysis, and samples with different degrees of hydrolysis were obtained depending on the time of the reaction (D-g-(PAA-co-PAAc)).

A uniform distribution of silver nanoparticles inside the hydrogel could be achieved due to its tendency to form complex and/or non-covalent interactions with

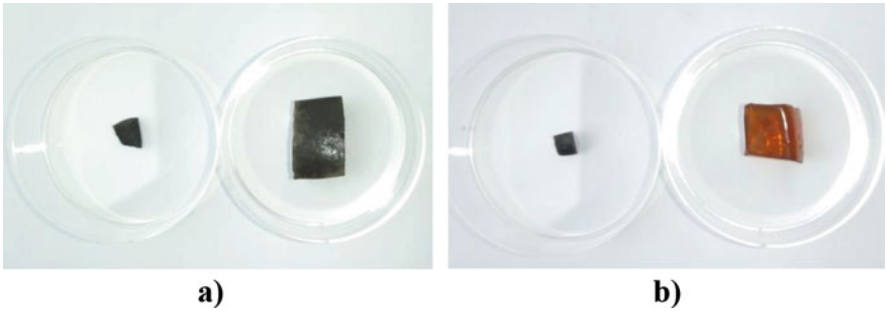

Fig. 24.2 Dry and swollen AgNPs-loaded hydrogel photographs: (**a**) AgNPs reduced in situ with $NaBH_4$ and (**b**) AgNPs reduced in situ with UV irradiation

silver ions and the functional moieties present in the hydrogel network such as –OH, $–NH_2$, and –C=O [19]. The addition of the fully swollen or dry hydrogel to silver nitrate solution causes silver ions to get trapped in the free spaces between the cross-linked polymeric networks and adsorbed with the functional groups via ion-exchange mechanism. Thus, reduction of silver ions using any reducing method results in the formation of silver nanoparticles in the free spaces between the polymeric chains.

In the present approach, AgNPs-loaded hydrogel networks were prepared by several routes such as in situ synthesis of the nanoparticles within a hydrogel with $NaBH_4$ (Fig. 24.1, Step 3a) or under the UV irradiation (Fig. 24.1, Step 3b).

Since sodium borohydride is a strong reducing agent, the color of the hydrogel changed to deep yellow within 10 s. which indicated the formation of silver nuclei. However, color of the discs changed gradually from yellow to light brown and finally to deep brown over time (30 min) which indicated the formation of silver nanoparticles, as shown in Fig. 24.2a.

In our study we also used novel and convenient way for the preparation of hydrogel stabilized silver nanoparticles by an ultraviolet irradiation technique. D-g-PAA generates free radicals in the presence of UV irradiation and acts as the reducing agent toward the silver ion. The advantages of physical methods are speed, radiation used as reducing agents, and no hazardous chemicals involved [20, 21]. Photographs of dry and swollen AgNPs-loaded hydrogels are presented for samples obtained with UV irradiation in Fig. 24.2b.

24.3.2 Swelling Studies

One important property of a wound dressing materials is good hydration capacity which facilitates rapid wound healing, thereby improving the reepithelialization process. Therefore, evaluation of swelling capacity of hydrogels is an important requirement.

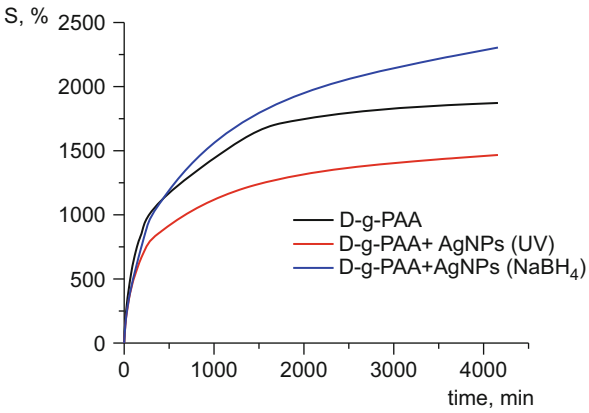

Fig. 24.3 Swelling behaviors of hydrogels: black, pure D-g-PAA; red, hydrogel with AgNPs reduced in situ under the UV irradiation (D-g-PAA + AgNPs(UV)); and blue, hydrogel with AgNPs reduced in situ with $NaBH_4$ (D-g-PAA + AgNPs($NaBH_4$))

The swelling behavior of pure hydrogels and AgNPs-loaded hydrogels in distilled water at room temperature is studied. Figure 24.2 displays dry and swollen hydrogels loaded with silver nanoparticles which are reduced by chemical and physical methods.

The impact of silver nanoparticle incorporation in the D-g-PAA hydrogel and hydrolysis degree on the swelling behavior was evaluated as shown in Fig. 24.3. For hydrogels there was a gradual increase in the swelling ratio up to 1440 min (24 h) after which no significant change was observed. Swelling ratio at this stage was termed as the equilibrium swelling ratio S_{eq}%, whose values were 1700, 1837, and 1263% for D-g-PAA, D-g-PAA + AgNPs($NaBH_4$), and D-g-PAA + AgNPs(UV) hydrogels, respectively.

The results showed that for pure hydrogel maximum value of swelling ratios is 1890%, while for hydrogel with AgNPs reduced in situ under the UV irradiation and with $NaBH_4$, it decreased to 1460% and increased to 2280%, respectively.

Decreasing of swelling in sample containing AgNPs can be explained on the basis of additional cross-links between AgNPs and the electron-rich O and N atoms present in the polymeric chains which restrained the water penetration ability of the hydrogel and decreased the overall swelling behavior [22]. In another study [23], it was established that formation of silver nanoparticles inside the polymeric matrix enhanced the flexibility of the hydrogel network due to stronger interactions between Ag and the hydrophilic moieties present in the polymer. The resulting decrease in hydrophilicity of the composite hydrogel reduced the swelling behavior.

It was noticed that increasing of swelling in sample was obtained in hydrogel where Ag^+ ions were converted into Ag nanoparticles treated with $NaBH_4$ (reducing agent) solutions. In this case the small pores were formed inside the polymer network caused by active gassing of hydrogen. As a result, the hydrogel matrices have absorbed more water.

In addition, the order of swelling capacity also depends on hydrolysis degree of hydrogels (Fig. 24.4). This is due to the fact that the ionic strength of the medium influences the swelling capacity of ionic gels. In the present investigation, the

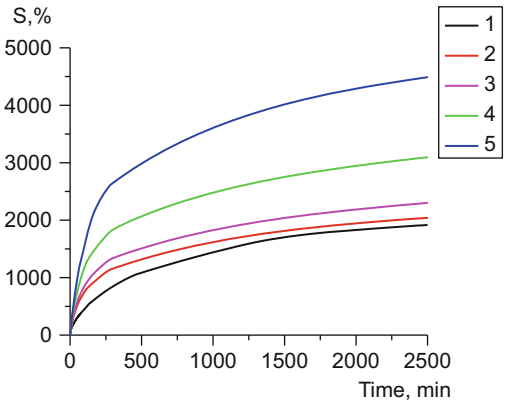

Fig. 24.4 Swelling behaviors of D-g-PAA (1) and hydrogels D-g-(PAA-co-PAAc) obtained by alkaline hydrolysis at 10 (2), 15 (3), 20 (4), and 25 (5) min

samples of D-g-PAA hydrogels were subjected to alkaline hydrolysis for 10, 15, 20, and 25 min to achieve different conversion degrees of gel. It allows to load various amounts of Ag^+ into the hydrogel mesh and influence in situ silver nanoparticle formation.

24.3.3 Characterization of Hydrogels

To further confirm the in situ formation of silver nanoparticles, FTIR, UV–vis spectra, and scanning electron microscopy (SEM) studies are performed.

24.3.3.1 FTIR Studies

To evaluate the effect of oxidation–reduction in Ag^+-loaded networks on the polymer structure, FTIR spectral analysis is performed (Fig. 24.5).

FTIR spectrum of hydrogel has shown characteristic peaks of PAA between 3150 and 3250 cm^{-1} (stretching vibrations of –OH/NH_2 of PAA), 2900–2950 cm^{-1} (symmetric and asymmetric stretching peaks of –CH_2 of PAA), and 1680–1630 cm^{-1} (stretching vibration of –C=O of PAA).

The presence of free –OH moieties of D-g-PAA hydrogels represents ideal sites for the anchoring of silver ions, contributing later to the silver nanoparticle immobilization. Interestingly, the absorption peaks were observed at 2900–2950 cm^{-1} in both pristine and AgNPs-loaded hydrogels, which originate from CH_2 asymmetric stretching and C–H bond of PAA and dextran chains, respectively. However, their intensity was decreased in AgNPs-loaded hydrogel obtained with $NaBH_4$, which confirms that such method of silver reduction causes cracking of the polymeric backbone chain, resulting in an increase in the swelling of the hydrogel.

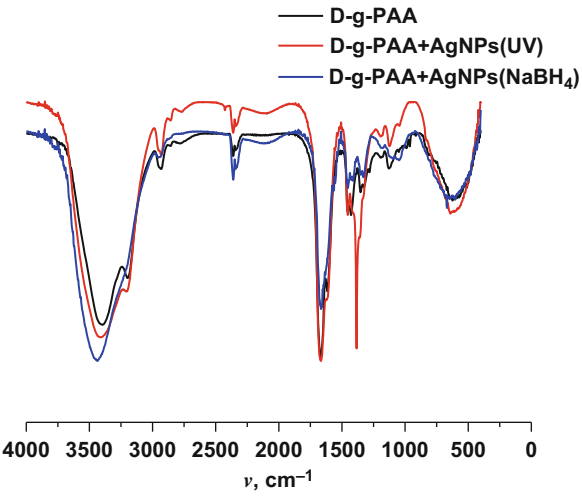

Fig. 24.5 FTIR spectra of hydrogels: black, pure D-g-PAA; red, hydrogel with AgNPs reduced in situ under the UV irradiation (D-g-PAA + AgNPs(UV)); and blue, hydrogel with AgNPs reduced in situ with $NaBH_4$ (D-g-PAA + AgNPs($NaBH_4$))

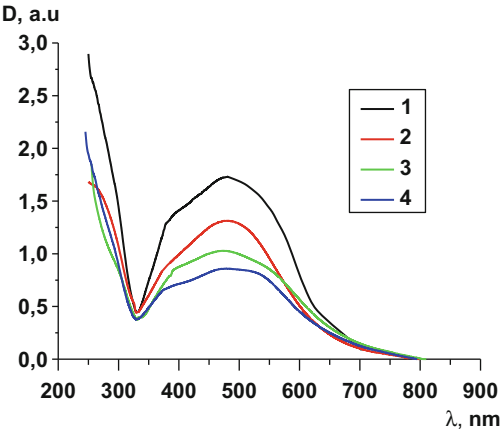

Fig. 24.6 UV–vis spectral curves of AgNPs-loaded hydrogels of various hydrolysis degrees: hydrogels were earlier subjected to alkaline hydrolysis for 0 (1), 10 (2), 20 (3), and 25 (4) min

24.3.3.2 UV–Vis Spectroscopy

Synthesis of silver nanoparticles under UV irradiation inside the hydrogel networks was analyzed by UV–vis spectroscopy as shown in Fig. 24.6.

Metal nanoclusters are optically transparent and act as dipoles. Conduction and valence bands of metal nanoclusters lay closely and electron movement occurs quite freely. The potential applications of these systems are mainly associated with the unusual dependence of the optical and electronic properties on the particle size [24, 25]. Silver particles having 5–50 nm sizes show a sharp absorption band in the 410–420 nm region [26]. As the particles grow bigger, the absorption band broadens [26].

AgNPs-loaded hydrogels with different degrees of hydrolysis have shown an absorption peak around 400–550 nm in the UV–vis spectra (Fig. 24.6), which is

due to the localized surface plasmon resonance of silver nanoparticles. The spectra of the hydrogel showed a relatively broad band which was rather unexpected.

It could be indicative of a distribution of silver nanoparticles with larger particle size range. Another probable reason could be the immobilization of silver nanoparticle deep within the hydrogel film which may cause their spectral behavior to differ from those of isolated nanoparticles.

Interestingly, nanoparticles obtained in non-hydrolyzed hydrogel displayed an additional peak at 370 nm which confirmed the presence of small-sized nanoparticles. However, in all spectra several absorption peaks in the range 350–580 nm were observed which indicated the presence of any AgNPs aggregates and silver clusters within the hydrogel [23].

It should be noted, that AgNPs-loaded hydrogel where silver was reduced in situ with $NaBH_4$ (D-g-PAA + AgNPs($NaBH_4$)) turned out to be nontransparent; therefore it was not possible to use UV–vis spectroscopy for their characteristics.

24.3.3.3 SEM Studies

The cross-sectional morphology of the hydrogels was observed to evaluate in situ formation of silver nanoparticles with UV method inside the hydrogel networks. As shown in Fig. 24.7a, b, pristine hydrogel did not show any particles in the SEM image. Loading of silver nanoparticles inside the hydrogel did not affect its morphology and structural integrity. Figure 24.7c showed that silver nanoparticles were evenly distributed between the polymeric chain networks.

As shown by the SEM results, the main advantage of the current UV technique is that it provided a controlled and uniform distribution of nanoparticles within the hydrogel network without addition of any other stabilizer [27]. It was expected that a homogeneous distribution of silver nanoparticles would be achieved throughout the hydrogel networks due to controlled reduction of the silver ions into the silver nanoparticles under UV irradiation.

24.4 Conclusion

A porous, chemically cross-linked D-g-PAA hydrogel was prepared by radical polymerization for promising antibacterial application. The hydrogel is an ideal candidate for the successful in situ synthesis of silver nanoparticles within the polymeric networks. Hydrogel nanocomposites were prepared by several routes such as in situ synthesis of the nanoparticles within a hydrogel with $NaBH_4$ or under the UV irradiation. Morphology studies indicate that AgNPs are located on the surface as well as interior of the hydrogel. Swelling studies and FTIR indicate influence of Ag-reducing method on polymeric networks of hydrogel nanocomposites. As it turned out the convenient way for the preparation of hydrogel stabilized silver nanoparticles is an ultraviolet irradiation technique. AgNPs-loaded hydrogels

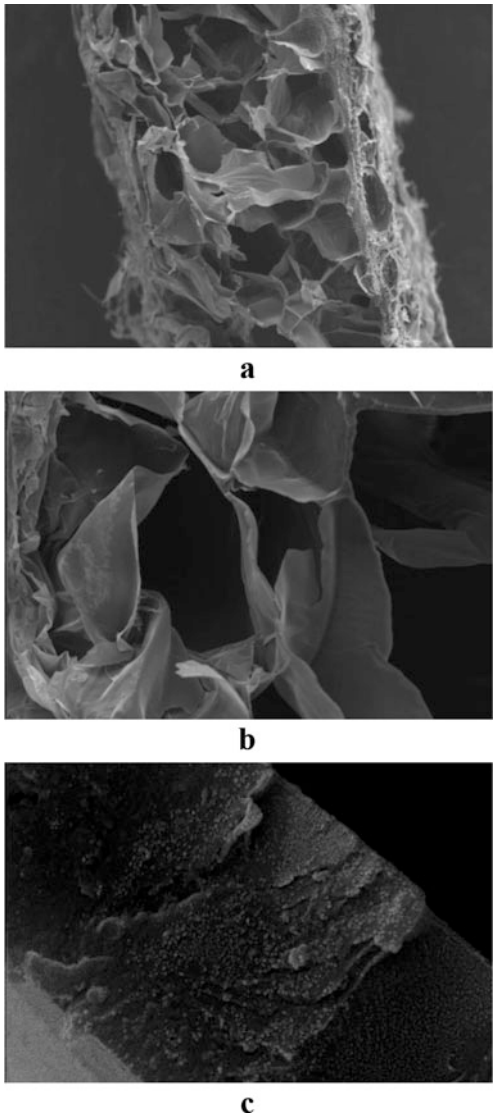

Fig. 24.7 SEM images of cross-linked D-g-PAA hydrogels at (**a**) ×500 and (**b**) ×7000 magnification. (**c**) Demonstrated AgNPs-loaded D-g-PAA hydrogel at ×20,000 magnification

with different degrees of hydrolysis have shown an absorption peak around 400–550 nm in the UV–vis spectra that indicate a distribution of silver nanoparticles with large particle size range. Furthermore, the current work demonstrates that combining hydrogel and nanotechnology promises development of novel materials with potential application in wound dressing or burn wounds.

Acknowledgment With the support of the Military and Research Directorate of the General Staff of the Armed Forces of Ukraine.

References

1. Purna SK, Babu M (2000) Collagen based dressings: a review. Burns 26:54–62
2. Choate CS (1994) Wound dressings. A comparison of classes and their principles of use. J Am Podiatr Med Assoc 84(9):463–469
3. Ma D, Zhang L-M (2008) Fabrication and modulation of magnetically supramolecular hydrogels. J Phys Chem B 112(20):6315–6321
4. Shrivastava S, Bera T, Roy A, Singh G, Ramachandrarao P, Dash D (2007) Characterization of enhanced antibacterial effects of novel silver nanoparticles. Nanotechnology 18(22):225103
5. Jain P, Pradeep T (2005) Potential of silver nanoparticle-coated polyurethane foam as an antibacterial water filter. Biotechnol Bioeng 90(1):59–63
6. Bosetti M, Masse A, Tobin E, Cannas M (2002) Silver coated materials for external fixation devices: in vitro biocompatibility and genotoxicity. Biomaterials 23(3):887–892
7. Hillyer JF, Alrecht RM (2001) Gastrointestinal persorption and tissue distribution of differently sized colloidal gold nanoparticle. J Pharm Sci 90(12):1927–1936
8. Bajpai SK, Murali Mohan Y, Bajpai M, Rasika T, Varsha T (2007) Synthesis of polymer stabilized silver and gold nanostructures. J Nanosci Nanotechnol 7(9):2994–3010
9. Tan Y, Jiang L, Li Y, Zhu D (2002) One dimensional aggregates of silver nanoparticles induced by the stabilizer 2-mercaptobenzimidazole. J Phys Chem B 106(12):3131–3138
10. Tanori J, Pileni MP (1997) Control of the shape of copper metallic particles by using a colloidal system as template. Langmuir 13(4):639–646
11. Lu Y, Mei Y, Schrinner M, Ballauff M, Möller MW, Breu J (2007) In situ formation of Ag nanoparticles in spherical polyacrylic acid brushes by UV irradiation. J Phys Chem 111(21):7676–7681
12. Morones JR, Frey W (2007) Environmentally sensitive silver nanoparticles of controlled size synthesized with PNIPAM as a nucleating and capping agent. Langmuir 23(15):8180–8186
13. Biffis A, Orlandi N, Corain B (2003) Microgel-stabilized metal nanoclusters: size control by microgel nanomorphology. Adv Mater 15(18):1551–1555
14. Saravanan P, Raju MP, Alam S (2007) A study on synthesis and properties of Ag nanoparticles immobilized polyacrylamide hydrogel composites. Mater Chem Phys 103(2–3):278–282
15. Murthy PSK, Mohan YM, Varaprasad K, Sreedhar B, Raju KM (2008) First successful design of semi-IPN hydrogel-silver nanocomposites: a facile approach for antibacterial application. J Colloid Interface Sci 318(2):217–224
16. Nadtoka O, Kutsevol N (2018) Thermal analysis of cross-linked hydrogels based on PVA and D-g-PAA obtained by various methods. Mol Cryst Liq Cryst 661(1):52–57
17. Lu Y, Mei Y, Schrinner M, Ballauff M, Möller MW, Breu J (2007) In situ formation of Ag nanoparticles in spherical polyacrylic acid brushes by UV irradiation. J Phys Chem C 111(21):7676–7681
18. Bardajee GR, Hooshyar Z, Rezanezhad H (2012) A novel and green biomaterial based silver nanocomposite hydrogel: synthesis, characterization and antibacterial effect. J Inorg Biochem 117:367–373
19. Mohan YM, Vimala K, Thomas V, Varaprasad K, Sreedhar B, Bajpai SK, Raju KM (2010) Controlling of silver nanoparticles structure by hydrogel networks. J Colloid Interface Sci 342:73–82
20. Shameli K, Ahmad MB, Yunus WM, Rustaiyan A, Ibrahim NA, Zargar M, Abdollahi Y (2010) Green synthesis of silver/montmorillonite/chitosan bionanocomposites using the UV irradiation method and evaluation of antibacterial activity. Int J Nanomedicine 5:875–887
21. Mallick K, Witcomb MJ, Scurrell MS (2004) Polymer stabilized silver nanoparticles: a photochemical synthesis route. J Mater Sci 39:4459–4463
22. Vimala K, Mohan YM, Varaprasad K, Redd NN, Ravindra S, Naidu NS, Raju KM (2011) Fabrication of curcumin encapsulated Chitosan–PVA silver nanocomposite films for improved antimicrobial activity. J Biomater Nanobiotechnol 2:55–64

23. Ma YQ, Yi JZ, Zhang LM (2009) A facile approach to incorporate silver nanoparticles into dextran-based hydrogels for antibacterial and catalytical application. J Macromol Sci A Pure Appl Chem 46(6):643–648
24. Henglein A (1995) Electronics of colloidal nanometer particles. Ber Bunsenges Phys Chem 99(7):903–913
25. Kreibig U, Vollmer M (1995) Optical properties of metal clusters. Springer, Berlin
26. Pradhan N, Jana NR, Mallick K, Pal T (2000) Seed mediated growth: a convenient way for size control in nanoparticle synthesis. Surf Sci Technol 16:188–195
27. Agnihotri S, Mukherji S, Mukherji S (2012) Antimicrobial chitosan-PVA hydrogel as nanoreactor and immobilizing matrix for silver nanoparticles. Appl Nanosci 2:179–188

Chapter 25
Green Synthesis of Magnetic Spinel Nanoparticles

Mariia Liaskovska, Tetiana Tatarchuk, Mohamed Bououdina, and Ivan Mironyuk

25.1 Introduction

Spinel nanoparticles possess unique and interesting properties. Nanoparticles can be synthesized by chemical and physical approaches, including hydrothermal [1], co-precipitation [2, 3], sol–gel [4–8], solid-state reactions [9], microemulsion [10, 11], mechanical activation [12], and electrochemical synthesis [13]. However, these methods can cause some threats to the environment, and sustainable routes for the synthesis of nanoparticles are being implemented. Moreover, the nanoparticles obtained by green synthesis [14] are very attractive alternative to chemical synthesis because of their wider utilization in many fields due to the use of eco-friendly secondary metabolites from plants with low toxicity as reducing and capping agents [15].

M. Liaskovska
Department of Chemistry, Vasyl Stefanyk Precarpathian National University, Ivano-Frankivsk, Ukraine

Department of Biological and Medical Chemistry named after academician Babenko H.O., Ivano-Frankivsk National Medical University, Ivano-Frankivsk, Ukraine

T. Tatarchuk (✉)
Department of Chemistry, Vasyl Stefanyk Precarpathian National University, Ivano-Frankivsk, Ukraine

Educational and Scientific Center of Materials Science and Nanotechnology, Vasyl Stefanyk Precarpathian National University, Ivano-Frankivsk, Ukraine

M. Bououdina
Department of Physics, College of Science, University of Bahrain, Zallaq, Kingdom of Bahrain

I. Mironyuk
Department of Chemistry, Vasyl Stefanyk Precarpathian National University, Ivano-Frankivsk, Ukraine

© Springer Nature Switzerland AG 2019

O. Fesenko, L. Yatsenko (eds.), *Nanophotonics, Nanooptics, Nanobiotechnology, and Their Applications*, Springer Proceedings in Physics 222,
https://doi.org/10.1007/978-3-030-17755-3_25

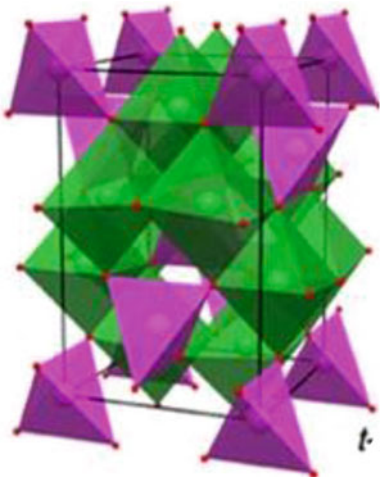

Fig. 25.1 Spinel structure with the formula AB_2O_4 (where A—ions in tetrahedral sites and B—ions in octahedral sites) [22]

It is known that spinel structure (Fig. 25.1) has interesting magnetic [16–21], optical, electrical, and catalytic [16, 21] properties favoring their application in data storages, electronics, biotechnology, etc. [19]. These properties have been found to be largely dependent on their precise crystal structure and composition.

It is known, that spinel nanoparticles have been widely used as catalysts [23, 24], water remediation [25], lithium-ion batteries [26], magnetic storage media [27], and biomedical applications [28].

Green methods are among the main techniques applied for nanoparticle synthesis. Many researchers have focused on the green methods due to the nontoxic nature and low cost of plants, which have been usually used as sources of reducing agents.

25.2 Green Synthesis

In comparison with the conventional chemical and physical methods, green synthesis offers many advantages: simple and facile manufacturing process, fast, economic, and less waste production. The simple process of nanoparticles green synthesis is shown in Fig. 25.2, where precursors are usually metal salt and reducing agent as plant extract. Various parameters such as the concentration of metal salt, amount of reducing agent, time, temperature, and pH can be controlled during the synthesis in order to obtain the desired structure, particle morphology and size, and the corresponding properties.

In this review, green synthesis of magnetic spinel nanoparticles will be described. Figure 25.3 illustrates the eco-friendly materials (seeds, leafs, fruits, etc.) that have been used by different researchers during the synthesis of NPs with spinel structure.

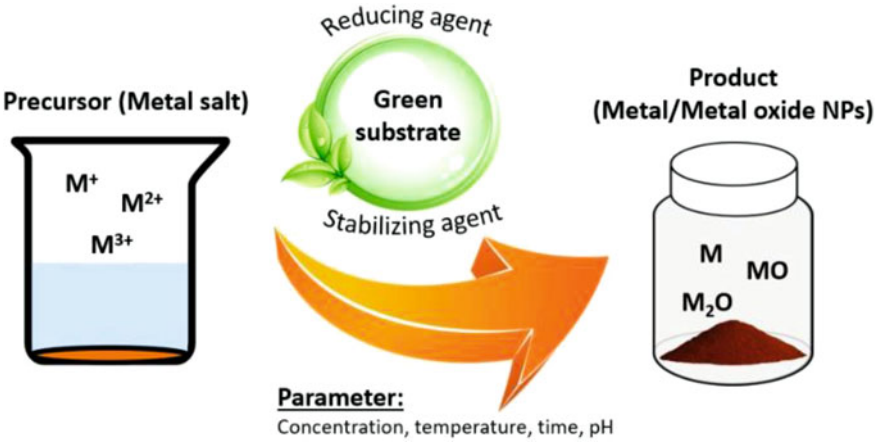

Fig. 25.2 Nanoparticle synthesis process [29]

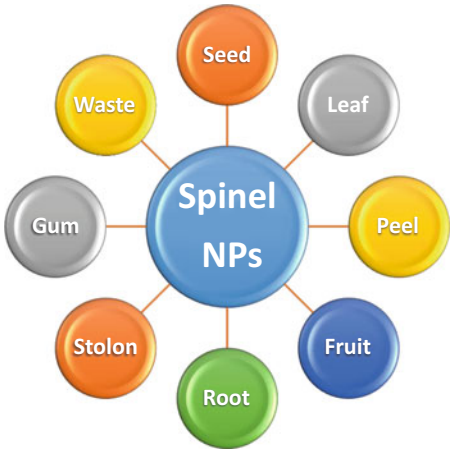

Fig. 25.3 Eco-friendly reducing agents of green NP synthesis

25.2.1 Green Synthesis of Magnetic Spinel NPs

The green-synthesized NPs have been obtained through different techniques that are nontoxic, cost-effective, ecofriendly, and resulting in the formation of NPs with different morphologies and sizes (Table 25.1). From Table 25.1, it can be noticed that the saturation magnetization is dependent from particle shape and size, and decreases with increasing the size of particles. The agglomeration of particles taking place due to their magnetic nature occurs so often, which has a detrimental effect on catalysis as it reduces the effective bulk surface area.

Table 25.1 The synthesis of magnetic spinel NPs using different part of plants

NPs	Green reducing agent	Synthesis method	Morphology	Average size (nm)	Magnetization (emu/g)	References
$CoFe_2O_4$	Okra plant	Conventional heating	Uniformly distributed	445	65.77 emu/g	[30]
		Microwave heating	Aggregated	12	65.31 emu/g	[30]
	Hibiscus flower	Self-combustion process	Agglomerates	10	10.24 emu/g	[31]
		Wet ferritization reaction	Agglomerates	18	15.99 emu/g	[31]
	Hibiscus leaf	Self-combustion process	Agglomerates	18.8	4.86 emu/g	[31]
		Wet ferritization reaction	Agglomerates	20	19.51 emu/g	[31]
	Ginger root	Self-combustion	Porous agglomerates	12.3	–	[32]
	Cardamom seeds	Self-combustion	Grained agglomerates	14.6	–	[32]
$NiFe_2O_4$	Aloe vera	Sol–gel	Agglomerates	15.3–26	6.7–25 emu/g	[33]
	Hydrangea paniculata flower	Sedimentation	Agglomerates	30–50	20 emu/g	[34]
	Walnut green hull	Self-combustion	Agglomerates	27	33 emu/g	[35]
$CuFe_2O_4$	Aloe vera	Sol–gel	Agglomerates	21.7–66.2	5.8–24.2 emu/g	[33]
	Jatropha oil	Combustion	Agglomerates	16	–	[36]
	Tea extract	Biogenic synthesis	Spherical	8.78	–	[37]
	Saffron extract	Hydrothermal	Agglomerates	36	17.3 emu/g	[38]
	Turmeric extract	Hydrothermal	Agglomerates	36	13.3 emu/g	[38]
	Cucumber extract	Hydrothermal	Agglomerates	36	12.2 emu/g	[38]
$FeFe_2O_4(Fe_3O_4)$	Tea residue	Co-precipitation	Cuboid/pyramid	5–25	6.9 emu/g.	[39]
	Granatum rind extract	Co-precipitation	Rod (D = 40 nm and L = 200 nm)	40	22.7 emu/g	[40]
	Lemon juice	Co-precipitation	Spherical	14–17	31.4–61.8 emu/g	[41]
	Mimosa pudica	Co-precipitation	Rough spherical agglomerates	60–80	55.4 emu/g	[42]

25.2.2 Green Synthesis of $CoFe_2O_4$ NPs

The cobalt ferrite NPs with different sizes and magnetic properties can be synthesized using different eco-friendly extracts, which will affect their physical characteristics.

K. Kombaiah et al. synthesized $CoFe_2O_4$ using Okra plant extract as reducing agent by both conventional (sample 1) and microwave (sample 2) heating methods [30]. The used precursors were the solutions of Co^{+2} and Fe^{+3} nitrates as oxidizing agents. XRD analysis determined crystallite size of cobalt ferrite NPs were 47 and 55 nm, accordingly. The samples 1 and 2 were tested for their antibacterial activity, and it was shown that $CoFe_2O_4$ synthesized by microwave heating method showed better structural, optical, and magnetic properties and antimicrobial activities than NPs synthesized by conventional heating method [30].

Dana Gingasu et al. studied the $CoFe_2O_4$ synthesized by using hibiscus flower and leaf extracts from a solution containing nitrates by self-combustion process and wet ferritization reaction [9, 10]. In this study, hibiscus flower/leaf extracts have been used as gelling and reducing agents. The $CoFe_2O_4$ NPs synthesized by self-combustion process were found to possess porous complex shaped agglomerates with nano-grained structure and with crystallite size in the range from 10 to 18 nm. Meanwhile, the average crystallite size of $CoFe_2O_4$ NPs synthesized by wet ferritization reaction was equal to 18.8 nm [31].

Dana Gingasu et al. [32] synthesized cobalt ferrite NPs through self-combustion method, and aqueous extracts of ginger root and cardamom seeds were used as green fuel and reducing agents. The mixture of nitrates and plant extracts behaved similarly to conventional oxidants and fuels. The average crystallite size was as 12.4 and 14.7 nm, respectively. The Mössbauer spectra for both samples exhibit magnetic hyperfine sextets.

25.2.3 Green Synthesis of $NiFe_2O_4$ and $CuFe_2O_4$ NPs

Plants can be utilized also to synthesize magnetic nickel and cobalt ferrite NPs. The plant extracts contain phytochemicals such as terpenoids, steroids, saponins, alkaloids, quinone, glycosides, and flavonoids, which can convert oxidant precursors into NPs.

Laokul et al. prepared magnetic MFe_2O_4 NPs by the modified sol–gel method using Fe^{+3} and M^{+2} (Ni^{+2}, Zn^{+2}, Cu^{+2}) nitrate solution and *aloe vera* extract at different temperatures in the range of 600–900 °C. The average crystallite size was in the range of 15.3–66.2 nm. The magnetic parameters of $NiFe_2O_4$ and $CuFe_2O_4$ are shown in Table 25.2 [33].

From Table 25.1, it can be observed that the saturation magnetization increases due to particle size while the coercivity decreases by increasing the particle size for $NiFe_2O_4$. The particles are able to form clusters due to their magnetic nature [33].

Gopalu Karunakaran et al. investigated the use of *Hydrangea paniculata* flower extract to synthesize $NiFe_2O_4$ from nitrate solution. A volume of 50 mL of

Table 25.2 Parameters of magnetic NPs calcined at different temperatures [33]

Spinel NPs	Temperature (°C)	Crystallite size (nm)	Coercivity, H_c (Oe)	Magnetization, M_s (emu/g)
$NiFe_2O_4$	600	21.7	458	6.7
	700	29.5	447	12.7
	800	39.3	397	17.0
	900	66.2	289	22.5
$CuFe_2O_4$	600	15.3	133	5.8
	700	15.4	250	7.0
	800	19.8	932	22.6
	900	26.0	763	24.2

freshly prepared flower extract was continuously stirred with simultaneous addition dropwise of 100 mL 0.1 M precursor solution. The mixture was kept around 24 h in the dark to achieve complete reaction. The pellet fabricated from the powdered samples was subjected to calcination at 300 °C to obtain NPs. The saturation magnetization of NPs was found to be 20 emu/g [34].

A green method for the synthesis of $NiFe_2O_4/Fe_2O_3/CeO_2$ nanocomposite using Ni^{+2}, Fe^{+3} chlorides, and Ce^{+2} nitrate solutions and different concentrations of walnut green hull extract (50, 100, 150 mL) with 2 mL aminoethanol was explored by Mohammad Reza et al. The size of NPs was fund around 27–51 nm. It was shown that the sample prepared from 150 mL of extract favors the formation of smaller particles (21 nm) with suitable magnetic properties. For all samples, the saturation magnetization increases with decreasing the particle size (20–35 emu/g) [35].

Surendra [36] prepared $CuFe_2O_4$ NPs by using $Cu(NO_3)_2{\cdot}3H_2O$, $Fe(NO_3)_3{\cdot}9H_2O$, and extract Jatropha oil as a green fuel through assisted combustion method. All components were mixed thoroughly to attain homogeneous solution that was dried and subjected to annealing at 450 °C. The probable mechanism of NPs formation is formation of chelate complex with extract components. The estimated average crystallite size is ~16 nm. SEM micrographs show a microstructure formed from porous flakes and agglomeration of particles [36].

Chutia et al. [37] studied the biogenic synthesis of $CuFe_2O_4$ NPs by using solution of $FeCl_3$ in $Cu(CH_3COOH)_2$, with the addition of tea extract of *Camellia*. 5 mL of 0.1 M NaOH solution was added to the solution and stirred for 1 h at room temperature. The precipitate was centrifuged, washed with ethanol, and subjected to annealing at 200 °C for 2 h, which led to the formation of $CuFe_2O_4$ NPs. The average diameter of NPs was found to be 8.78 nm. The as-prepared MNPs have been used as catalyst for acetylation reactions of various alcohols, phenols, and amines (20 acetylated products) at room temperature under solvent-free conditions [37].

Naghikhani et al. [38] investigated the production of $CuFe_2O_4$ using green reduction agents. In their study, the nitrate solutions of Fe and Cu (2:1) were dissolved in distilled water, mixed with extracts (such as turmeric, saffron, and cucumber) and then slowly added to 1 M solution of NaOH (pH of solution and was fixed to 10). The as-obtained solution was transferred into Teflon-lined stainless autoclave and kept at 180°C for 2–10 h to obtain black precipitate of $CuFe_2O_4$ with

a mean crystallite size of about 36 nm. It was shown that the superparamagnetic ferrites were synthesized by using saffron and turmeric extracts with a saturation magnetization of 17.3 emu/g and 13.33 emu/g, respectively, while magnetization-field (M-H) curve of $CuFe_2O_4$ NPs obtained from cucumber extract showed superparamagnetic behavior with lower saturation magnetization of 12.2 emu/g. The photocatalytic behavior of the as-prepared magnetic NPs was investigated using the degradation of dyes under visible light irradiation [38].

25.2.4 Green Synthesis of Fe_3O_4 Spinel NPs

Lunge et al. [39] used tea residue for obtaining magnetite NPs. 15 g of $FeCl_3 \cdot 6H_2O$ were dissolved in 150 mL distilled water, and 30 g of dry tea residue was added and the obtained solution mixture was stirred for 4 h and then kept overnight. Tea residue was then separated by filtration and dried in an oven. $FeCl_3$-treated tea residue was heated in a muffle furnace at 450 °C for 6 h, washed, and dried. The size of particles was estimated to be 5–25 nm. Magnetic NPs were tested as sorbents for removal of As(III) and As(V) from aqueous solutions. The adsorption isotherms are described by the Langmuir model and possessed high adsorption capacities of 188.69 mg/g for arsenic (III) and 153.8 mg/g for arsenic (V) [39].

Venkateswarlu et al. synthesized Fe_3O_4 NPs through an easy and eco-friendly route using $FeCl_3$ and sodium acetate [40]. The precursors were dissolved in freshly prepared *Punica granatum* rind extract solution, and then the mixture was stirred vigorously and heated up, and the resulting solution turned into a homogeneous black color. The obtained black precipitate was separated by magnet, having a mean diameter of 40 nm and a relatively low saturation magnetization of 22.7 emu/g, as shown in Table 25.1.

Bahadur et al. [41] reported about magnetite NPs prepared by modified co-precipitation technique using $FeCl_3.6H_2O$ and $FeCl_2.4H_2O$ salt solution in basic solution. The reaction started with the addition of sodium hydroxide and elicited the oxidation of lemon juice in alkaline medium [41]. The obtained spherical NPs possessed narrow size diameter distribution (14–17 nm) with broad variation in saturation magnetization (31.4–61.4 emu/g).

Niraimathee et al. [42] studied the mechanism of Fe_3O_4 NPs formation using *Mimosa pudica* root extract and ferrous sulfate solution. The magnetic properties of Fe_3O_4 NPs were enhanced by controlling the pH of the solution to 9 with the addition of sodium hydroxide. The spherically shaped NPs of quite larger diameter (60–80 nm) exhibited higher values of saturation magnetization of 55.40 nm [42].

25.3 Conclusions

In this review, simple green and eco-friendly methods adopted for the synthesis of magnetic spinel nanoparticles have been presented. MNPs can be synthesized by conventional method, microwave heating, co-precipitation, and sol–gel methods

while using eco-friendly reducing agents obtained from nature. The obtained NPs prepared by green synthesis method can effectively be applied directly in biomedical-related applications without any modification, for instance, targeted drug delivery. The morphology, particle size, and size distribution as well as magnetic properties of the synthesized NPs are found to be strongly dependent upon the sources of green materials (extracts of plant leaves, plant roots, fruits, seeds, etc.). These NPs offer many advantages, such as low toxicity and biocompatibility, and can be used in pharmaceutical and biomedical applications.

Acknowledgments The authors are grateful to the Ministry of Education and Science of Ukraine (Project Numbers 0118U000258 and 0117U002408) for their financial support.

References

1. Koseoglu Y et al (2012) Low temperature hydrothermal synthesis and characterization of Mn doped cobalt ferrite nanoparticles. Ceram Int 38:3625–3634
2. Tatarchuk T et al (2017) Structural characterization and antistructure modeling of cobalt-substituted zinc ferrites. J Alloys Compd 694:777–791
3. Tatarchuk TR et al (2018) Effect of cobalt substitution on structural, elastic, magnetic and optical properties of zinc ferrite nanoparticles. J Alloys Compd 731:1256–1266. https://doi.org/10.1016/j.jallcom.2017.10.103
4. Kanagesan S (2013) Sol-gel auto-combustion synthesis of cobalt ferrite and it's cytotoxicity properties. Dig J Nanomater Biostruct 8:1601–1610
5. Tatarchuk T et al (2018) Green synthesis of cobalt ferrite nanoparticles using *Cydonia oblonga* extract: structural and mossbauer studies. Mol Cryst Liq Cryst. https://doi.org/10.1080/15421406.2018.1542107
6. Raghuvanshi P et al (2019) Dual control on structure and magnetic properties of Mg ferrite: role of swift heavy ion irradiation. J Magn Magn Mater 471:521–528. https://doi.org/10.1016/j.jmmm.2018.10.004
7. Kane SN et al (2018) Synthesis, characterization and antistructure modeling of Ni nano ferrite. AIP Conf Proc 1953:030089. https://doi.org/10.1063/1.5032424
8. Rajesh Babu B, Tatarchuk T (2018) Elastic properties and antistructural modeling for nickel-zinc ferrite-aluminates. Mater Chem Phys 207:534–541. https://doi.org/10.1016/j.matchemphys.2017.12.084
9. Moayyer HA, Ataie A (2014) Investigation on phase evolution in the processing of nano-crystalline cobalt ferrite by solid-state reaction route. Adv Mater Res 829:767–771
10. Saha M et al (2016) Microstructure, optical and magnetic properties of inverse spinel CoFe2O4 synthesized by microemulsion process assisted by CTAB and AOT. Aust Ceram Soc 52:150–162
11. El-Fadl A et al (2019) Synthesis and magnetic properties of spinel $Zn_{1-x}NixFe_2O_4$ ($0.0 \leq x \leq 1.0$) nanoparticles synthesized by microwave combustion method. Magn Magn Mater 471:192–199. https://doi.org/10.1016/j.jmmm.2018.09.074
12. Rashidi S, Ataie A (2014) One-step synthesis of $CoFe_2O_4$ nano-particles by mechanical alloying. Adv Mater Res 829:747–751
13. Mazarío E et al (2012) Synthesis and characterization of $CoFe_2O_4$ ferrite nanoparticles obtained by an electrochemical method. Nanotechnology 23:355–708
14. Vaseghi Z et al (2017) Green methods for the synthesis of metal nanoparticles using biogenic reducing agents: a review. https://doi.org/10.1515/revce-2017-0005

15. Nadeem M et al (2018) The current trends in the green syntheses of titanium oxide nanoparticles and their applications. Green Chem Lett Rev 11:492–502
16. Liang Y et al (2012) Covalent hybrid of spinel manganese–cobalt oxide and graphene as advanced oxygen reduction electrocatalysts. J Am Chem Soc 134:3517–3523
17. Lavela P et al (2007) Sol-gel preparation of cobalt manganese mixed oxides for their use as electrode materials in lithium cells. Electrochimia 52:7986–7995
18. Zhou L et al (2012) Double-shelled $CoMn_2O_4$ hollow microcubes as high-capacity anodes for lithium-ion batteries. Adv Mater 24:745–748
19. Rios E et al (1998) Mixed valency spinel oxides of transition metals and electrocatalysis: case of the $Mn_xCo_{3/x}O_4$ system. Electrochim Acta 44:1491–1497
20. Habjanic J et al (2014) A 3D oxalate-based network as a precursor for the $CoMn_2O_4$ spinel: synthesis and structural and magnetic studies. Inorg Chem 53:9633–9643
21. Maiyalagan T et al (2014) Spinel-type lithium cobalt oxide as a bifunctional electrocatalyst for the oxygen evolution and oxygen reduction reactions. Nat Commun 5:3949
22. Li C et al (2015) Phase and composition controllable synthesis of cobalt manganese spinel nanoparticles towards efficient oxygen electrocatalysis. Nat Res 6:7345. https://doi.org/10.1038/ncomms8345
23. Azarifar D et al (2016) Silica-modified magnetite Fe_3O_4 nanoparticles grafted with sulfamic acid functional groups: an efficient heterogeneous catalyst for the synthesis of 3,4-dihydropyrimidin-2(1H)-one and tetrahydrobenzo[b]pyran derivatives. J Sulfur Chem 37:656–673
24. Gawande MB et al (2013) Nano-magnetite (Fe_3O_4) as a support for recyclable catalysts in the development of sustainable methodologies. Chem Soc Rev 42:3371–3393
25. Hardani K et al (2015) Removal of toxic mercury (II) from water via Fe_3O_4 /hydroxyapatite nanoadsorbent: an efficient, economic and rapid approach. Amer Assoc Sci Tech J Nanosci 1:11–18
26. Liu M et al (2017) One-pot synthesis of in-situ carbon-coated Fe_3O_4 as a long-life lithium-ion battery anode. Nanotechnology 28:1–9
27. El Ghandoor H et al (2012) Synthesis and some physical properties of magnetite (Fe_3O_4) nanoparticles. Int J Electrochem Sci 7:5734–5745
28. Karimzadeh et al (2017) Superparamagnetic iron oxide (Fe_3O_4) nanoparticles coated with PEG/PEI for biomedical applications: a facile and scalable preparation route based on the cathodic electrochemical deposition method. Adv Phys Chem 2017:9437487
29. Pin Yew Y et al (2018) Green biosynthesis of superparamagnetic magnetite Fe_3O_4 nanoparticles and biomedical applications in targeted anticancer drug delivery system. Arab J Chem. https://doi.org/10.1016/j.arabjc.2018.04.013
30. Kombaiah K et al (2018) Okra extract-assisted green synthesis of $CoFe_2O_4$ nanoparticles and their optical, magnetic, and antimicrobial properties. Mater Chem Phys 204:410–419
31. Gingasu D et al (2016) Green synthesis methods of $CoFe_2O_4$ and Ag-$CoFe_2O_4$ nanoparticles using hibiscus extracts and their antimicrobial potential. J Nanomater 2016:2106756. Hindawi
32. Gingasu D et al (2017) Green synthesis of cobalt ferrite nanoparticles using plant extracts. Rev Roum Chim 62:645–653
33. Laokul P et al (2011) Characterization and magnetic properties of nanocrystalline $CuFe_2O_4$, $NiFe_2O_4$, $ZnFe_2O_4$ powders prepared by the *Aloe vera* extract solution. Curr Appl Phys 11:101–108
34. Karunakaran G et al (2018) Green synthesis of $NiFe_2O_4$ spinel-structured nanoparticles using *Hydrangea paniculata* flower extract with excellent magnetic property. Miner Met Mater Soc 70:1337–1343
35. Reza M et al (2016) Green synthesis of NiFe2O4/Fe2O3/CeO2 nanocomposite in a walnut green hulls extract medium: magnetic properties and characterization. Curr Nanosci 12:1. https://doi.org/10.2174/1573413712666160513124809
36. Surendra BS (2018) Green engineered synthesis of Ag-doped $CuFe_2O_4$: characterization, cyclic voltammetry and photocatalytic studies. J Sci: Adv Mater Dev 3:44–50. https://doi.org/10.1016/j.jsamd.2018.01.005

37. Chutia R, Chetia B (2018) Biogenic $CuFe_2O_4$ magnetic nanoparticles as a green, reusable and excellent nanocatalyst for acetylation reactions under solvent-free conditions. New J Chem 42(18):15200–15206. https://doi.org/10.1039/c8nj02685h
38. Naghikhani R et al (2017) Simple and green synthesis of $CuFe_2O_4$–CuO nanocomposite using some natural extracts: photo-degradation and magnetic study of nanoparticles. Mater Electron 29:4689–4703. https://doi.org/10.1007/s10854-017-8421-1
39. Lunge S et al (2014) Magnetic iron oxide (Fe_3O_4) nanoparticles from tea waste for arsenic removal. J Magn Magn Mater 356:21–31. https://doi.org/10.1016/j.jmmm.2013.12.008
40. Venkateswarlu S et al (2014) A novel green synthesis of Fe_3O_4 magnetic nanorods using *Punica Granatum* rind extract and its application for removal of Pb(II) from aqueous environment. Arab J Chem. https://doi.org/10.1016/j.arabjc.2014.09.006
41. Bahadur A et al (2017) Eco-friendly synthesis of magnetite (Fe_3O_4) nanoparticles with tunable size: dielectric, magnetic, thermal and optical studies. Mater Chem Phys 198:229–235
42. Niraimathee VA et al (2016) Green synthesis of iron oxide nanoparticles from Mimosa pudica root extract. Environ Sust Dev 15:227. https://doi.org/10.1504/ijesd.2016.077370

Chapter 26
Properties of Ultrathin Lipid Layers Surrounding Boron Nitride Nanotube: Computer Simulation Study

Przemyslaw Raczynski

26.1 Introduction

The cholesterol, an organic molecule, is a principal sterol, and each animal cell is capable of synthesizing it. Despite the fact that excessive level of cholesterol may have harmful effect on human physiology [1], it is indispensable in the body. For example, it is essential for the proper functioning of cell membranes [2, 3] and in animals it is manufactured for this and other uses. Another vital component of cell membrane is phospholipid, a molecule composed of two hydrophobic fatty acid "tails" and a hydrophilic "head." These two components of the molecule are joined together by a glycerol. Phospholipid, together with cholesterol, creates an important part of biological membranes—phospholipid bilayer because of their amphiphilic nature. The bilayer is a structure which protects the interior of cell from outside environment [4, 5]. In the past decade, the increasing numbers of attempts to use carbon nanotubes in medicine are observed. A few years ago, we conducted studies on the carbon nanotube (CNT)–cholesterol or silicon carbide (SiCNT)–cholesterol/phospholipid interactions [6–8].

Currently, our examinations were extended into investigation of properties of cholesterol or phospholipid layers surrounding boron nitride nanotube (BNNT), which, structurally, is similar to the CNT. BNNT is more polar compared to CNT or SiCNT which may lead to differences in behavior of lipids surrounding them. Because toxicological investigations show that BNNTs exhibit greater biocompatibility, their use in the biomedical field was suggested [9, 10]. If nanostructures are

P. Raczynski (✉)
Institute of Physics, University of Silesia, Katowice, Poland

Silesian Centre of Education & Interdisciplinary Research, Chorzów, Poland
e-mail: przemyslaw.raczynski@us.edu.pl

© Springer Nature Switzerland AG 2019

O. Fesenko, L. Yatsenko (eds.), *Nanophotonics, Nanooptics, Nanobiotechnology, and Their Applications*, Springer Proceedings in Physics 222,
https://doi.org/10.1007/978-3-030-17755-3_26

to be exploited as delivery or indentation systems, it is of interest to recognize the interaction between them and biomembrane components.

As in the previous researches [6–8, 11–13], we used MD technique. The BNNT nanotube was surrounded by thin films of cholesterol or POPC molecules. All studied systems were examined in a wide range of temperatures, including physiological one. The dynamical and structural observables were calculated and qualitatively investigated the behavior of cholesterol and phospholipid molecules in the layers.

26.2 Materials and Methods

All molecular dynamics (MD) simulations were performed using the NAMD 2.8 software [14, 15]. The time step was equal to 0.5 fs for all simulations reported in this study. The initial configurations for the systems were obtained from the series of NVT and NPT simulations. During the preparation process, the systems were heated to $T = 330$ K, next equilibrated in this temperature by $1*10^7$ steps, and then slowly cooled to the lowest temperature studied (260 K), with cooling rate equal to 0.005 K/step. Finally, the main simulations were started for five temperatures ($T = 260$, 285, 310, 335, and 360 K). Main simulations for each temperature were performed for $1*10^7$ steps. Between the temperatures, the systems were, first, slowly heated and, next, simulated for $2*10^6$ steps, before we started the main simulations. Systems with water were additionally equilibrated in NPT ensemble for $2*10^6$ simulation steps to relax the pressure effects introduced by system heating.

The systems were examined in perpendicular simulation box (PBC) [16, 17]. The initial simulation box was set to $60 \times 60 \times 57$ Å. The z-axis size of simulation box allows us to treat BNNT as infinite rod as it was associated with the nanotube length.

BNNT was covered by $n = 15$ and 30 cholesterol molecules or 18 phospholipids. Thirty cholesterol or 18 phospholipid molecules form a continuous, full layer surrounding the (10, 10) boron nitride nanotube.

The force field parameters and partial charges for boron nitride nanotube were taken from [18, 19]. All other elements of the system modeled using CHARMM27 parameter were set [20]. Atomic charges on cholesterol molecule were taken from [21]. POPC was chosen as representative phospholipid occurring in eukaryotic cell membrane. The TIP3P CHARMM adapted water model [22] was used in our simulations. To visualize and inspect the systems, VMD 1.9.2 [23, 24] program was utilized.

26.3 Results

Figure 26.1 presents the snapshots of instantaneous configurations for the systems without water (Fig. 26.1a) and with it (Fig. 26.1b). The presented systems consist of $n = 15$ cholesterol molecules at temperature $T = 310$ K.

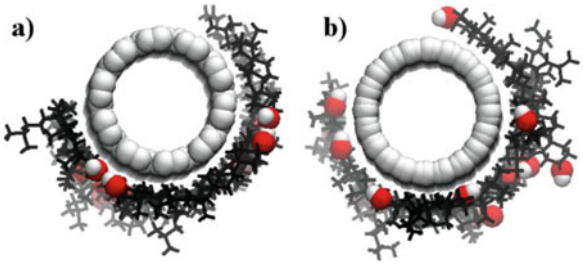

Fig. 26.1 The snapshots of instantaneous configurations of the system composed of $n = 15$ cholesterols surrounding BNNT at $T = 310$ K; (**a**) system without water, (**b**) system with water (water not shown); front view. OH groups are additionally marked

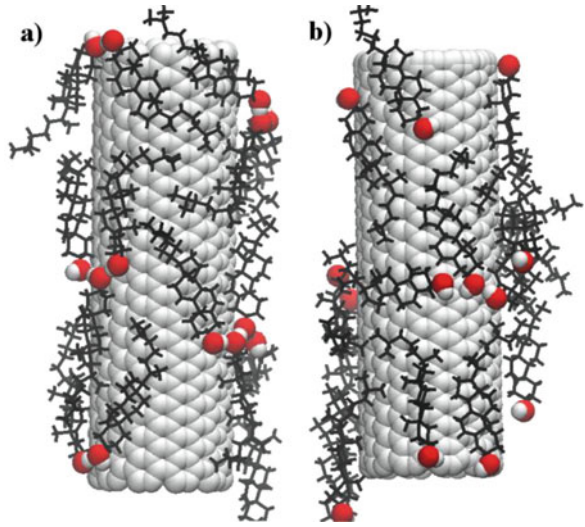

Fig. 26.2 The snapshots of instantaneous configurations of the system composed of $n = 15$ cholesterols surrounding BNNT at $T = 310$ K; (**a**) system without water, (**b**) system with water; side view. OH groups are additionally marked

In both systems cholesterols form a thin layer surrounding BNNT. They tend to aggregate together and as a result a part of nanotube is covered by cholesterols and another part is not. It can be observed that in system with water, the distribution of the cholesterols in layer covering BNNT is slightly larger (the uncovered part of BNNT is smaller), compared to the system without it. In case of systems with $n = 30$ cholesterols and phospholipids, BNNT is fully surrounded by molecules and they form thin, single layer covering it.

Larger differences in arrangement of cholesterols covering BNNT are visible in Fig. 26.2, where the same systems are presented as in Fig. 26.1 but perpendicularly to the nanotube surface.

Configurations in Fig. 26.2 show that, without water, the cholesterols OH groups prefer orientation toward other polar groups. In water, however, the cholesterols mesh their hydrophobic chains, because of their amphiphilic nature. In both systems cholesterols prefer orientation along the nanotube main axis.

An example of the mean square displacement $\left\langle \left| \Delta \vec{r}\,(t) \right|^2 \right\rangle$ of the center mass of cholesterols, where $\Delta \vec{r}\,(t) = \vec{r}\,(t) - \vec{r}\,(0)$ and $\vec{r}$ is the position of a single molecule mass center, is shown in Fig. 26.3. The system without water consisting of

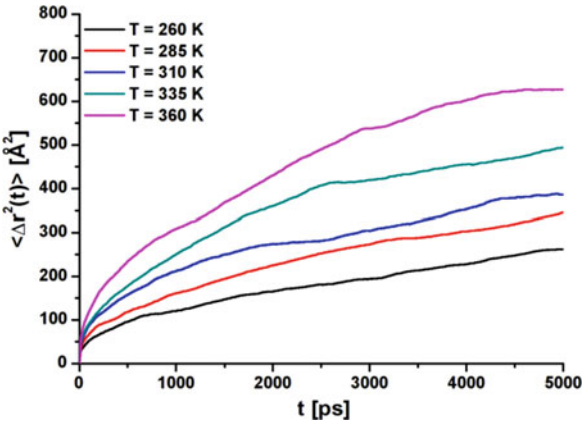

Fig. 26.3 An example of the mean square displacement of the center of cholesterol mass; temperature dependence for the system composed of $n = 15$ molecules without water

$n = 15$ cholesterols covering BNNT was chosen. The mobility of the molecules in the presented system grows with an increasing of the temperature. The dynamics of molecules in all systems studied exhibits similar temperature dependency, although it should be noted that in aqueous systems lipid mobility is significantly decreased.

$\left\langle \left| \Delta \overrightarrow{r}(t) \right|^2 \right\rangle$ and the translational diffusion coefficient D are related via the Einstein relation: $\left\langle \left| \Delta \overrightarrow{r}(t) \right|^2 \right\rangle \approx 6Dt$. Nonzero slope of the $\left\langle \left| \Delta \overrightarrow{r}(t) \right|^2 \right\rangle$ is an indicator of a mobility of molecules. The obtained values of D were estimated from the linear part of $\left\langle \left| \Delta \overrightarrow{r}(t) \right|^2 \right\rangle$.

In Fig. 26.4a, comparison of D between larger and smaller systems, without water, is shown. The cholesterol molecules in smaller system have noticeably higher mobility. The larger average BNNT surface area per single molecule (for $n = 15$ molecules) corresponds with increased mobility and fewer restrictions for movement. However, in water the mobility of molecules is different and the cholesterols in systems with $n = 30$ molecules do not exhibit reduced mobility (Fig. 26.4b). This behavior can be explained by hydrophobic nature of cholesterol molecule. In Fig. 26.1, it is shown that the molecules keep together. In smaller system, with water, the nanotube is surrounded not only by cholesterol, but also by water. The water molecules for systems with lower number of lipid molecules are as effective in blocking cholesterol movements as other cholesterols within uniform layer. This phenomenon can be associated with the wettability of polarized BNNT surface. Water molecules can be physisorbed on the nanotube surface, effectively blocking the movement of cholesterols.

In Fig. 26.4c the comparison of translational diffusion coefficient between system with water and without it is shown. Cholesterols in the system with water have noticeably smaller mobility (even one order of magnitude for low temperatures). The smaller mobility can be explained by polar environment surrounding hydrophobic cholesterol layer. In water cholesterols mesh with each other their nonpolar tails, and it additionally limits their mobility. For the smaller systems consisted of 15

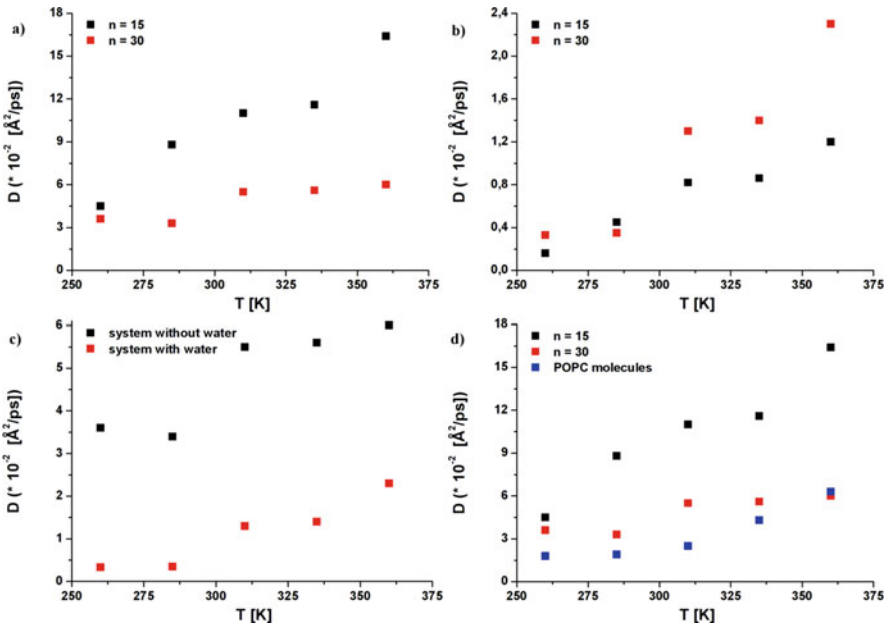

Fig. 26.4 Obtained values of translational diffusion coefficient D: (**a**) comparison of cholesterol molecules and for systems without water; (**b**) comparison of cholesterol molecules and for systems with water; (**c**) comparison for cholesterol molecules in systems composed of $n = 30$ molecules and BNNT; (**d**) comparison of cholesterol and POPC molecules and for systems without water

cholesterols and for the systems with POPC molecules, the behavior of molecules in water environment and without water is similar.

Comparison between mobility of cholesterol molecules and POPC molecules surrounding BNNT is shown in Fig. 26.4d. In both systems, without water (presented here) and with it, mobility of POPC molecules is the smallest. The mobility of cholesterol molecules in larger system and POPC molecules is similar because in these systems molecules form thin layer covering the nanotube, whereas cholesterols in smaller system, as it was mentioned above, have larger accessible area to move even if they keep together on the BNNT surface.

Figure 26.5 presents Lindemann index. As an example, systems consisting of $n = 30$ cholesterol were chosen. In the figure the comparison between systems with water and without it is shown, and the values obtained for system without water are higher.

Lindemann index can be indicator of the phase transition if large discontinuity occurs. However, no significant discontinuity appeared in any of the studied systems. It is possible that system with water is in amorphous solid- or glass-like phase, because the values of the δ_L are below 0.1 for all temperatures studied.

Figure 26.6 shows the radial distribution function of the center of the molecule mass, with respect to the nanotube longitudinal axis $g_A(r)$ and at $T = 310$ K. In

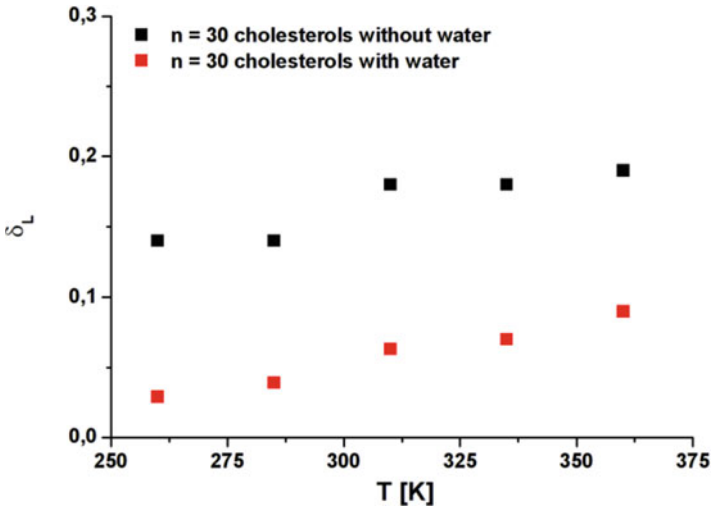

Fig. 26.5 Comparison between obtained values of Lindemann index for system with water and without it

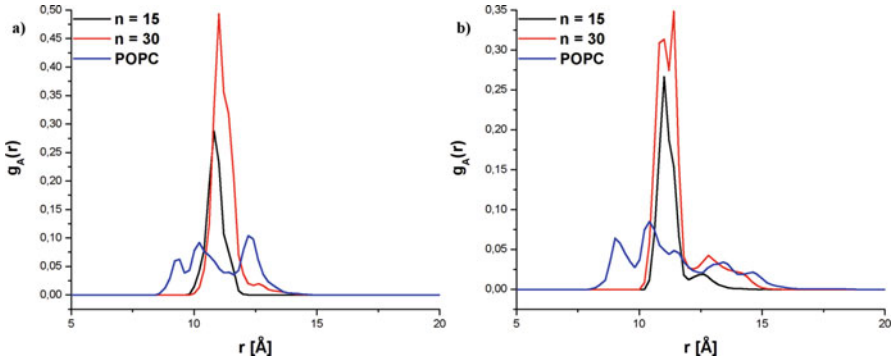

Fig. 26.6 The radial distribution function of the center of molecule mass, with respect to the main axis and $T = 310$ K: (**a**) comparison between systems without water; (**b**) comparison between systems with water

the systems without water (Fig. 26.6a), single, clearly defined peaks suggest that cholesterol molecules form single, continuous layer, while POPC phospholipids form more complicated structure. Some additional structure ordering is present in the layer composed of $n = 30$ cholesterols in the system with water (Fig. 26.6b). It can be associated with the orientation of cholesterol methyl groups toward the BNNT surface.

Figure 26.7 shows the temperature dependence of the radial distribution function $g(r)$ of the center of mass of cholesterol molecule and for the system consisted of $n = 30$ molecules. For better clarity, only three temperatures are shown.

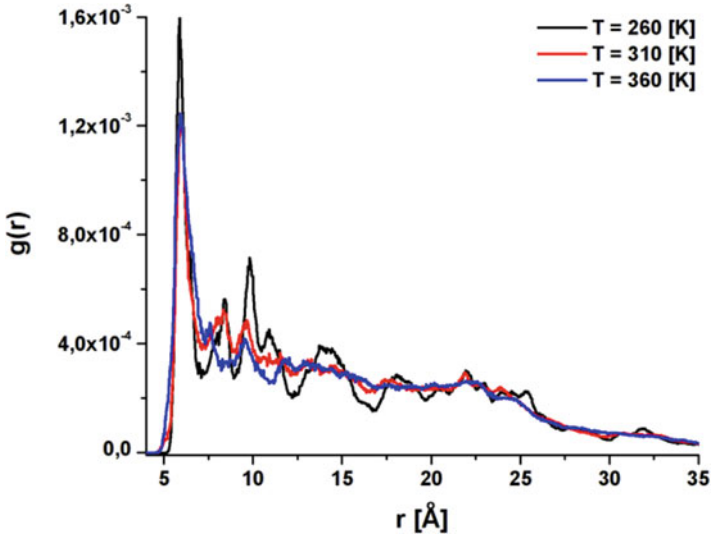

Fig. 26.7 Temperature dependence of radial distribution function of the center of cholesterol mass for aqueous system consisted of $n = 30$ molecules

At the smallest temperature studied peaks, connected with the distance to the nearest (first peak) and next neighbors are clearly visible. With an increase in the temperature, only the first peak remains clearly visible, whereas the next vanishes. This suggests that only local, short-range ordering appears and reorientation of cholesterol molecules in the layer is easier.

Figure 26.8 presents differences in behavior of cholesterol and POPC phospholipid molecules surrounding different nanotubes. In Fig. 26.8a, comparison of translational diffusion coefficient is shown for cholesterol molecules. In case of SiCNT, a larger number of cholesterol molecules were taken because in case of longer C–Si bonds, the diameter of the nanotube of the same chirality is higher, compared to CNT or BNNT. This approach ensures similar number of cholesterols per unit of external surface area for each nanotube.

The dynamics of cholesterol molecules surrounding various nanotubes differs. Definitely, the molecules surrounding SiCNT exhibit the smallest mobility. Cholesterols covering CNT surface have larger mobility, whereas mobility of cholesterol molecules is the highest in layer surrounding BNNT. It is clearly visible especially for the higher temperatures studied. Boron nitride nanotube is the most polar (compared to CNT or SiCNT), and it has an impact on the mobility of not only cholesterols but also POPC molecules (Fig. 26.8b).

As in case of cholesterol molecules, also the number of phospholipids surrounding SiCNT is larger due to larger dimensions of SiCNT. The differences, shown in case of cholesterol layer, are highlighted. POPC molecules surrounding BNNT have

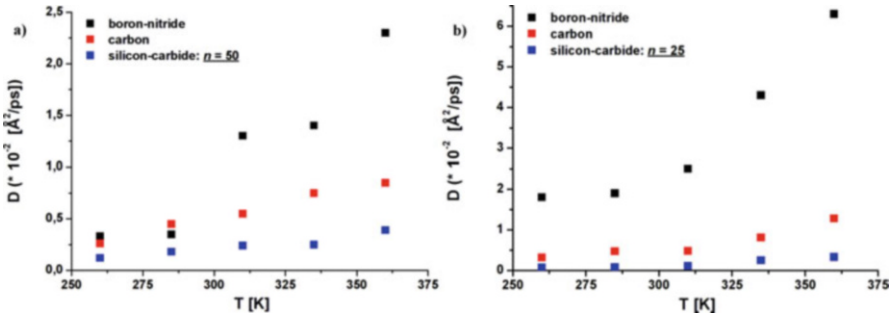

Fig. 26.8 Obtained values of translational diffusion coefficient *D* for different nanotubes: (**a**) comparison of *D* for cholesterol molecules (water environment); (**b**) comparison of D for POPC phospholipid molecules (systems without water)

even one order of magnitude higher mobility than these covering SiCNT or CNT. The dynamics of phospholipids in layer surrounding CNT is similar to mobility of these surrounding SiCNT but mobility of the latter is smaller for each temperature studied.

26.4 Conclusions

The behavior of cholesterol and POPC molecules surrounding different nanotubes was studied. All systems were examined in five temperatures, including physiological one.

The obtained results show that mobility and ability to reorient of the lipid molecules increase with heating of the system. Different orientation of molecules in systems with water (tails of cholesterols mesh) and without it (polar groups of lipids oriented toward other polar groups) is visible. Differences in dynamics between systems with water and without it also occur because in systems with water molecules have noticeably smaller mobility. When comparing different nanotubes, the molecules surrounding BNNT exhibit the highest mobility, whereas mobility of molecules surrounding SiCNT is the smallest. Obtained Lindemann indexes do not indicate any form of phase or structural transition.

The presented results can provide some insight into interaction between lipids forming phospholipid membrane and nanotubes. In the context of using nanotubes as drug nanocontainers, penetrating cell membrane knowledge about mutual interactions is desired.

Acknowledgments This research was supported in part by PAAD Infrastructure cofinanced by Operational Programme Innovative Economy, Objective 2.3.

References

1. Lusis AJ (2000) Atherosclerosis. Nature 407:233–241. https://doi.org/10.1038/35025203
2. Scott HL (2002) Modeling the lipid component of membranes. Curr Opin Struct Biol 12:495–502. https://doi.org/10.1016/S0959-440X(02)00353-6
3. Feller SE (2000) Molecular dynamics simulations of lipid bilayers. Curr Opin Colloid Interface Sci 5:217–223. https://doi.org/10.1016/S1359-0294(00)00058-3
4. Alberts B (2008) Molecular biology of the cell. Garland Science, New York. [etc.]
5. Sperelakis N (2012) Cell physiology sourcebook essentials of membrane biophysics. Elsevier/AP, Amsterdam/Boston
6. Raczynski P, Gorny K, Samios J, Gburski Z (2014) Interaction between silicon-carbide nanotube and cholesterol domain. A molecular dynamics simulation study. J Phys Chem C 118:30115–30119. https://doi.org/10.1021/jp505532f
7. Raczynski P, Raczynska V, Gorny K, Gburski Z (2015) Properties of ultrathin cholesterol and phospholipid layers surrounding silicon-carbide nanotube: MD simulations. Arch Biochem Biophys 580:22–30. https://doi.org/10.1016/j.abb.2015.06.008
8. Raczynski P, Dawid A, Pietek A, Gburski Z (2006) Reorienatational dynamics of cholesterol molecules in thin film surrounded carbon nanotube: molecular dynamics simulations. J Mol Struct 792–793:216–220. https://doi.org/10.1016/j.molstruc.2006.01.064
9. Zhong J, Dai LC (2012) Targeting liposomal nanomedicine to Cancer therapy. Technol Cancer Res Treat 11:475–481. https://doi.org/10.7785/tcrt.2012.500259
10. Ciofani G, Danti S, Genchi GG, Mazzolai B, Mattoli V (2013) Boron nitride nanotubes: biocompatibility and potential spill-over in nanomedicine. Small 9:1672–1685. https://doi.org/10.1002/smll.201201315
11. Gorny K, Dendzik Z, Raczynski P, Gburski Z (2012) Dynamic properties of propylene glycol confined in ZSM-5 zeolite matrix-A computer simulation study. Solid State Commun 152:8–12. https://doi.org/10.1016/j.ssc.2011.10.020
12. Raczynski P, Dawid A, Dendzik Z, Gburski Z (2005) Dielectric relaxation in water-cholesterol mixture cluster: molecular dynamics simulation. J Mol Struct 750:18–21. https://doi.org/10.1016/j.molstruc.2005.03.036
13. Dawid A, Raczynski P, Gburski Z (2014) Depolarised Rayleigh light scattering in argon layer confined between graphite plains: MD simulation. Mol Phys 112:1645–1650. https://doi.org/10.1080/00268976.2013.853111
14. Kale L, Skeel R, Bhandarkar M, Brunner R, Gursoy A, Krawetz N, Phillips J, Shinozaki A, Varadarajan K, Schulten K (1999) NAMD2: greater scalability for parallel molecular dynamics. J Comput Phys 151:283–312. https://doi.org/10.1006/jcph.1999.6201
15. Phillips JC, Braun R, Wang W, Gumbart J, Tajkhorshid E, Villa E, Chipot C, Skeel RD, Kalé L, Schulten K (2005) Scalable molecular dynamics with NAMD. J Comput Chem 26:1781–1802. https://doi.org/10.1002/jcc.20289
16. Allen MP, Tildesley DJ (1989) Computer simulation of liquids. Clarendon Press/Oxford University Press, Oxford [England]/New York
17. Rapaport DC (2004) The art of molecular dynamics simulation. Cambridge University Press, Cambridge
18. Won CY, Aluru NR (2007) Water permeation through a subnanometer boron nitride nanotube. J Am Chem Soc 129:2748–274+. https://doi.org/10.1021/ja0687318
19. Won CY, Aluru NR (2008) Structure and dynamics of water confined in a boron nitride nanotube. J Phys Chem C 112:1812–1818. https://doi.org/10.1021/jp076747u
20. Feller SE, MacKerell AD (2000) An improved empirical potential energy function for molecular simulations of phospholipids. J Phys Chem B 104:7510–7515. https://doi.org/10.1021/jp0007843
21. Henin J, Chipot C (2006) Hydrogen-bonding patterns of cholesterol in lipid membranes. Chem Phys Lett 425:329–335. https://doi.org/10.1016/j.cplett.2006.04.115

22. Jorgensen WL, Chandrasekhar J, Madura JD, Impey RW, Klein ML (1983) Comparison of simple potential functions for simulating liquid water. J Chem Phys 79:926. https://doi.org/10.1063/1.445869
23. Humphrey W, Dalke A, Schulten K (1996) VMD – Visual Molecular Dynamics. J Mol Graph 14:33–38
24. Humphrey W, Dalke A, Schulten K (1996) VMD: visual molecular dynamics. J Mol Graph Model 14:33–38. https://doi.org/10.1016/0263-7855(96)00018-5

Chapter 27
Properties of n-Cyanobiphenyl Nematogene Phases Formed Between Carbon Nanotube Arrays: Computer Simulation Study

Violetta Raczyńska, Krzysztof Górny, Przemyslaw Raczynski, and Zbigniew Dendzik

27.1 Introduction

Properties of molecular systems physisorbed on 2D materials are of interest not only from fundamental point of view but also because of wide potential applications ranging from novel optoelectronic devices to temperature measurements and molecular sensing [1–3]. Ordering and stability of mesogen phases anchored on a variety of substrates strongly depend on the specific properties of these substrates. Carbon nanotubes are among the most promising substrates which are considered to this end [4–5]. Aromatic nature of carbon nanotube surface and the presence of two benzene rings in 5-cyanobiphenyls (5CB) structures lead to the formation of planar alignment of anchored mesogen molecules which form layered structures, where structural and dynamical properties depend on the number of C atoms in the aliphatic tail of the mesogens as well as on the distance between the carbon nanotube arrays.

In this work we apply molecular dynamics computer simulation method to study the process of formation of n-cyanobiphenyl phases between the arrays of carbon nanotubes, stability of these phases, effects of distance between the arrays, surface density of the mesogen layers, and mobility of mesogen molecules.

V. Raczyńska
Institute of Physics, University of Silesia, Chorzów, Poland

K. Górny · Z. Dendzik
Institute of Physics, University of Silesia, Chorzów, Poland

Silesian Center for Education and Interdisciplinary Research, University of Silesia, Chorzów, Poland

P. Raczynski (✉)
Institute of Physics, University of Silesia, Katowice, Poland

Silesian Centre of Education & Interdisciplinary Research, Chorzów, Poland
e-mail: przemyslaw.raczynski@us.edu.pl

© Springer Nature Switzerland AG 2019

O. Fesenko, L. Yatsenko (eds.), *Nanophotonics, Nanooptics, Nanobiotechnology, and Their Applications*, Springer Proceedings in Physics 222,
https://doi.org/10.1007/978-3-030-17755-3_27

27.2 Simulation Details

The simulated system was composed of 126 molecules of 5CB nematogens located between two arrays of carbon nanotubes. The distance between the main axes of the respective nanotubes of both layers was set to $d = 26$, 31, and 36 A, which corresponds to the smallest distance between the opposite nanotube array of $l = 15$, 20, and 25 A, respectively. Periodic boundary conditions (PBC) were applied. The dimensions of the simulation cell were $75.0 \times 71.2 \times 100.0$ Å. The value of z-component was large enough to sufficiently reduce the self-interaction component of long-range electrostatic interaction between the system and its PBC image.

All simulations were performed using NAMD 2.11 simulation code [6]. Visualization was performed using VMD [7]. All interactions were modeled with CHARMM-type force field adapted by Tiberio et al. [8] with time step set to 1 fs. The carbon nanotubes of both arrays have been treated as rigid. Nonbonding interactions between the 5CB atoms have been described using electrostatic potential and van der Waals term modeled with Lennard-Jones 12–6 potential with Lorentz−Berthelot mixing rules and cutoff of 12 Å. Interactions between the nanotube arrays and 5CB molecules have been described with a model that accounts only for van der Waals interactions. Long-range interactions were calculated using particle mesh Ewald (PME) summation technique with grid spacing of 1.5 Å. Equations of motion were integrated for 10 ns, using the Brunger–Brooks–Karplus (BBK) scheme. The simulation was performed in NVT ensemble, for temperatures $T = 270$, 290, 310, 330, and 350 K, controlled with Langevin thermostat with damping coefficient $\gamma = 1.0$ ps $- 1$. For each temperature, the first 2 ns were treated as equilibration and excluded from calculation of structural and dynamical properties.

The instantaneous configuration of the simulated system for $l = 20$ A at temperature $T = 310$ K is shown in Fig. 27.1.

27.3 Results and Discussion

In order to test the impact of the free volume accessible for 5CB molecules on the ordering characteristic of the sample, we performed simulations with different values of the distance between the nanotube arrays. To assess the distribution of the mesogen molecules, we calculated the density profiles along z-axis of the Cartesian frame, perpendicular to the direction to the substrate planes [9]. Figure 27.2 shows the obtained results for different values of the distance between the nanotube arrays and for different temperatures.

Density profiles suggest that the mesogen molecules tend to occupy the cavities between the nanotubes in arrays. In each system, at least two distinct layers can be identified. In the case of the systems with the smallest value of the distance l, the third, incomplete, layer starts to form. This onset of formation of additional layer can be attributed to frustration. In the larger systems, it is more energetically favorable

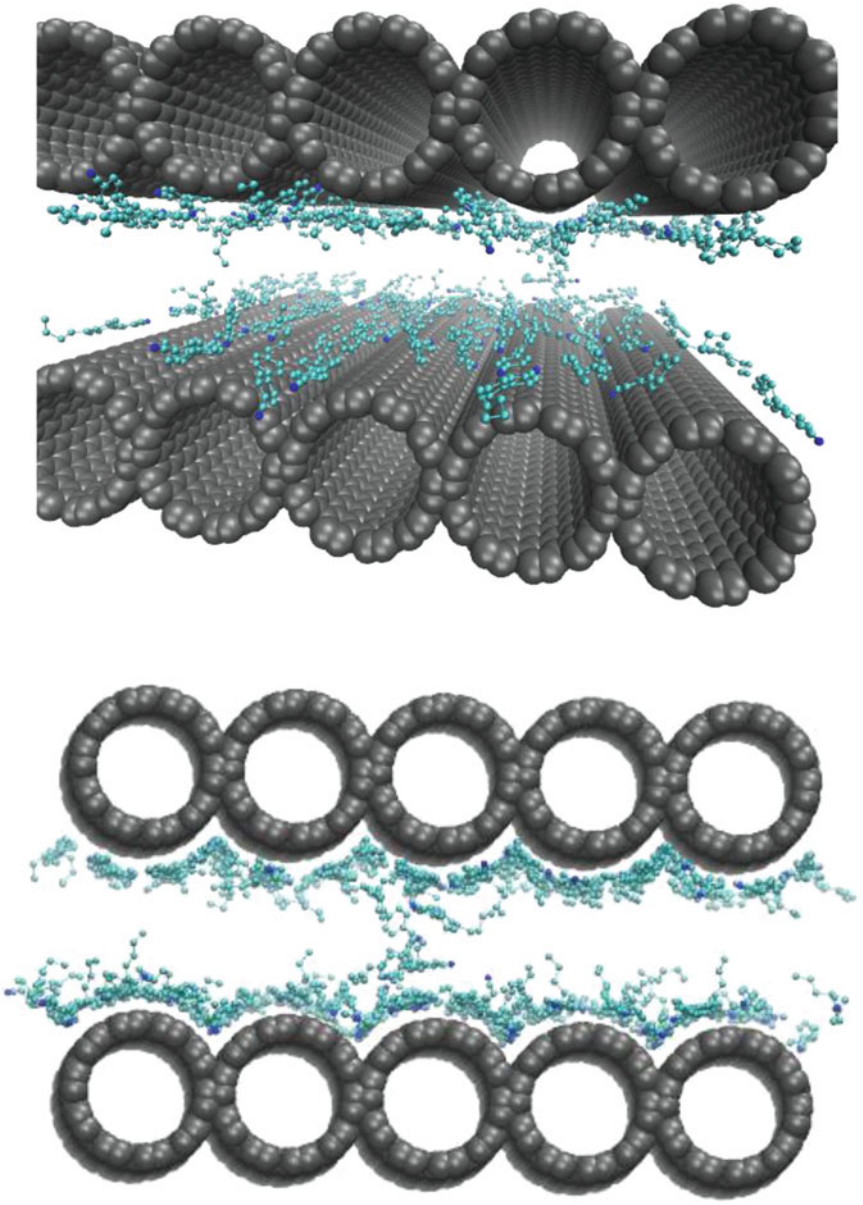

Fig. 27.1 The snapshot of the simulated system – instantaneous configuration of 5CB mesogen phase between two carbon nanotube arrays at the distance $l = 20$ A (perspective and orthogonal view)

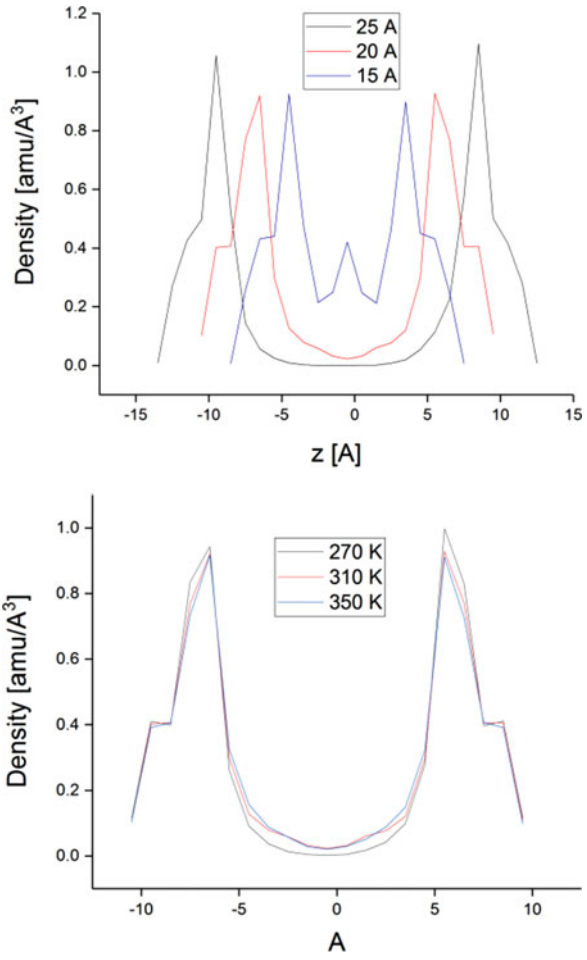

Fig. 27.2 Density profiles of 5CB mesogens between the carbon nanotube arrays, calculated along z-axis, for different distances between the arrays $l = 15$, 20, and 25 A at temperature $T = 310$ K (top panel) and for $l = 20$ and temperatures $T = 270$, 310, and 350 (bottom panel)

to settle on one of the layers closest to the substrate arrays. For the system with $l = 20$ A and $l = 25$ A, the increase of temperature leads to partial desorption caused by either desorption of soft alkyl chains or even entire molecules, although the latter case has been relatively rarely observed in visual inspection of the simulation trajectories.

The ordering of nematic samples is usually measured in terms of the second rank nematic order parameter P_2, defined as

$$P_2 = < \frac{3}{2}\cos^2\beta - \frac{1}{2} >, \tag{27.1}$$

where β is the angle between molecule selected axis and the global director of the sample and <> denotes the average over time and ensemble. The value of the

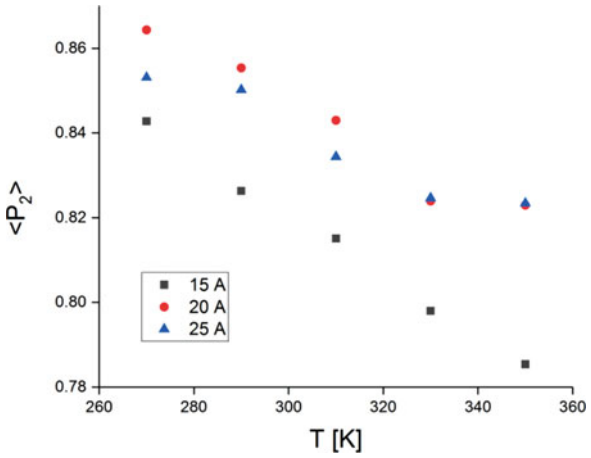

Fig. 27.3 Mean value of the second rank nematic order parameter determined for 5CB phases between the nanotube arrays for different values of the distance l

director of the sample can be calculated as the eigenvector corresponding to the largest eigenvalue of the order matrix Q [5].

Figure 27.3 presents the values of P_2 averaged over all accessible simulation time frames. The high values of P_2 indicate that the system is in the nematic phase in all studied cases. Lower values of P_2 in the case of the distance $l = 15$ A can be attributed to the presence of the incomplete, frustrated layers of mesogens which forms between the main two layers closest to the surface of the substrates. The molecules in that layer possess considerably larger accessible-free volume, which effectively leads to their higher mobility and lower degree of ordering. The decrease of the order parameter with increasing temperature for the systems with distance $l = 20$ A and $l = 25$ A is mitigated by strong adsorption of the mesogens in the grooves between nanotubes. The molecules are not able to rotate freely or totally desorb from the array surface, effectively stabilizing the system, while reaching the threshold of $P_2 = 0.82$.

In contradiction to conventional 2D materials, like graphene or hexagonal boron nitride sheets, in the case of the substrate composed of carbon nanotube array, the nanotubes' main axes introduced distinguished direction on the plane. In order to study whether this feature impacts on the ordering characteristic of this system, we calculated the components of the Cartesian coordinates of the director of the sample. The time evolution of these coordinates is presented in Fig. 27.4.

It can be clearly seen that the director of the sample is aligned along the distinguished direction imposed by the nanotubes' axes. This feature contributes to the increased stability of the nematic 5CB phase between such defined carbon nanotube array substrates. As for the applied 5CB mesogen model, the nematic–isotropic phase transition in bulk sample occurs at temperature $T_{NI} = 310$ K [8]; the nematic 5CB phase between the nanotube array substrate remains stable even up to $T = 350$ K.

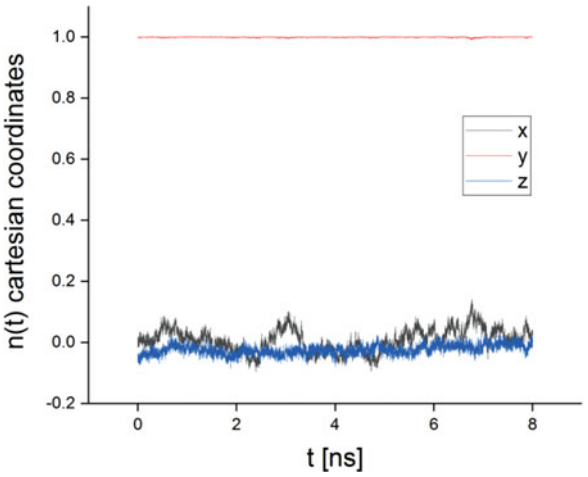

Fig. 27.4 The time evolution of the components of the Cartesian coordinates of the director of the sample

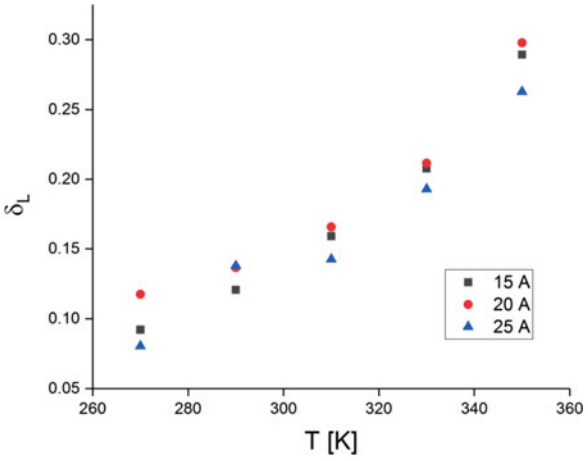

Fig. 27.5 Temperature characteristics of the Lindemann index of the 5CB mesogens between nanotube arrays, for different values of the distance between them

To get insight into the dynamics of 5CB phase between nanotube arrays, we have also determined its Lindemann index defined as

$$\delta_L = \frac{2}{N\,(N-1)} \sum_{i<j}^{N} \frac{\left(\langle r_{ij}{}^2\rangle - \langle r_{ij}\rangle^2\right)^{\frac{1}{2}}}{\langle r_{ij}\rangle}, \tag{27.2}$$

where r_{ij} is the distance between the center of mass of ith and jth molecules [10].

Figure 27.5 shows the values of δ_L plotted against temperature. There are no discontinuities which may indicate phase transitions in the systems in the studied temperature range. The system with the distance $l = 20$ A exhibits the highest mobility. If the accessible-free volume was the only factor, the highest mobility would be observed in the case of $l = 25$ A. The obtained results suggest that

the dynamics of the system can be treated as an outcome of the counterbalance between the amount of the free volume available for the mesogen molecules and the physisorption of the mesogens to the substrate and subsequent restriction on the reorientational degrees of freedom.

27.4 Conclusions

The distinguished direction introduced by the carbon nanotube array morphology contributes to the improved thermal stability of embedded 5CB nematic phase compared to bulk sample. The director of the sample is always aligned with the nanotubes' main axes. This improved stability is however accompanied by reduced orientational degree of freedom and mobility. In the case of larger distance between the nanotube arrays, strong physisorption dominates over the increase of the free volume accessible to the mesogen molecules.

References

1. Roscioni OM, Muccioli L, Zannoni C (2017) Predicting the conditions for homeotropic anchoring of liquid crystals at a soft surface. 4-*n*-Pentyl-4′-cyanobiphenyl on alkylsilane self-assembled monolayers. ACS Appl Mater Interfaces 9:11993–12002. https://doi.org/10.1021/acsami.6b16438
2. Raczyńska V, Górny K, Raczyński P, Dendzik Z (2018) Percolation threshold of 5-Cyanobiphenyl mesogene phases between graphene planes: computer simulation study. In: Fesenko O, Yatsenko L (eds) Nanochemistry, biotechnology, nanomaterials, and their applications. NANO 2017. Springer proceedings in physics, vol 214. Springer. https://doi.org/10.1007/978-3-319-92567-7_17
3. Skrzypek M, Dendzik Z, Brol P, Gburski Z (2004) Cluster and layers of fullerene molecules between graphite planes. J Mol Struct 704:287–290. https://doi.org/10.1016/j.molstruc.2004.02.045
4. Rahman M, Lee W (2009) J Phys D Appl Phys 42:063001–063013. https://doi.org/10.1088/0022-3727/42/6/0630013
5. Górny K, Raczyński P, Dendzik Z, Gburski Z (2015) Odd−even effects in the dynamics of liquid crystalline thin films on the surface of single walled carbon and silicon carbide nanotubes: computer simulation study. J Phys Chem C 119:19266–19271. https://doi.org/10.1021/acs.jpcc.5b05961
6. Phillips JC, Braun R, Wang W, Gumbart J, Tajkhorshid E, Villa E, Chipot C, Skeel RD, Kalé L, Schulten K (2005) Scalable molecular dynamics with NAMD. J Comput Chem 26:1781–1802. https://doi.org/10.1002/jcc.20289
7. Humphrey W, Dalke A, Schulten K (1996) VMD - visual molecular dynamics. J Mol Graph 14:33–38. https://doi.org/10.1016/0263-7855(96)00018-5
8. Tiberio G, Muccioli L, Berardi R, Zannoni C (2009) Towards in silico liquid crystals. Realistic transition temperatures and physical properties for n-Cyanobiphenyls via molecular dynamics simulations. Chemphyschem 10:125–136. https://doi.org/10.1002/cphc.200800231
9. Giorgino T (2014) Computing 1-D atomic densities in macromolecular simulations: the density profile tool for VMD. Comput Phys Commun 185:317–322. https://doi.org/10.1016/j.cpc.2013.08.022
10. Allen MP, Tildesley DJ (1989) Computer simulation of liquids. Clarendon Press/Oxford University Press, Oxford, UK/New York

Chapter 28
Tryptophan-Stabilized Plasmonic Fe_3O_4/Ag Nanoparticles

Ie. V. Pylypchuk, Iu. P. Mukha, N. V. Vityuk, K. Szczepanowicz, L. P. Storozhuk, A. M. Eremenko, P. Warszyński, and P. P. Gorbyk

28.1 Introduction

Among known nanomaterials, magnetic nanoparticles especially with the biogenic magnetite structure are of particular interest for biomedicine/biotechnology. Such nanocomposites based on magnetite (Fe_3O_4) possess favorable biodegradability [1], low toxicity, and predictable surface chemistry [2–3]. They are widely used for magnetic resonance imaging [4–6] and targeted drug delivery [4, 7]. Importantly, such magnetic nanoparticles have been already reported to be effective against some kinds of tumors [8–9], and their clinical applications for hyperthermia were described in [7, 10].

Silver NPs belong to the nanomaterials class with well-described properties, especially for application in biomedicine. Ag NPs can be used for creation target biosensors for DNA [11], for the surface-enhanced Raman scattering (SERS) [12], molecular imaging of cancer cells, and treatment of dermatitis [13]. Deposited on graphene oxide, Ag NPs were used for enhanced X-ray contrast, as well as an effective agent for photothermal ablation of tumors [14]. In addition, the antimicrobial properties of silver have been also extensively studied, for instance, Ag NPs' application as a component against *Escherichia coli* in cotton fibers [15–18]. Zinc oxide modified with Ag NPs revealed good antibacterial activity against *Staphylococcus aureus* and *Escherichia coli* [19]. Colloidal solutions of 10-nm-size

I. V. Pylypchuk (✉) · I. P. Mukha · N. V. Vityuk · L. P. Storozhuk · A. M. Eremenko · P. P. Gorbyk
Chuiko Institute of Surface Chemistry, NAS of Ukraine, Kyiv, Ukraine

K. Szczepanowicz · P. Warszyński
Jerzy Haber Institute of Catalysis and Surface Chemistry, Polish Academy of Sciences, Krakow, Poland

© Springer Nature Switzerland AG 2019

O. Fesenko, L. Yatsenko (eds.), *Nanophotonics, Nanooptics, Nanobiotechnology, and Their Applications*, Springer Proceedings in Physics 222,
https://doi.org/10.1007/978-3-030-17755-3_28

nanosilver showed a high bactericidal activity against strains of *Staphylococcus aureus*, *Escherichia coli*, and *Pseudomonas aeruginosa* and fungicidal activity against *Candida albicans* [20].

It is obvious that the development of core–shell particles combining superparamagnetic core and plasmonic shell is attractive and opens a broad area of potential applications. In the case of Fe_3O_4/Ag nanoparticles, a number of methods for their synthesis have been extensively studied. Such composites were applied in the catalytic reduction of 4-nitrophenol [21] and ultrasensitive detection in RNA extract from cancer cells [22] and as SERS substrate for the detection of trace amount of furazolidone and other prohibited or restricted antibiotics [23] and have potent antibacterial activity against *Escherichia coli* (gram-negative bacteria), *Staphylococcus epidermidis* (gram-positive bacteria), and *Bacillus subtilis* (spore bacteria) [24].

The main disadvantage of Fe_3O_4/Ag nanoparticles reported in the literature is the fact that their synthesis methods are hazardous to the environment and living organisms and surfactants and reducing agents are involved. In some cases, microwave irradiation [25], organic solvents [24], and other harmful conditions and substances are being used. Only few articles report green methods for Fe_3O_4 core Ag shell nanoparticle preparation. For example, the waste material of *Vitis vinifera* (grape) stem extract as the green solvent and reducing and capping agent in the synthesis of Fe_3O_4–Ag core–shell nanoparticles is proposed [26]. In [21] the authors reported a facile method to generate core–shell-structured $Fe_3O_4@SiO_2$–Ag magnetic nanocomposite by an in situ wet chemistry route with the use of polyvinylpyrrolidone as both a reductant and stabilizer.

Our previous works have shown that by using amino acid tryptophan both as a "green" and nontoxic reducing agent and a particle stabilizer, we can increase the effectiveness of noble metal nanoparticles as chemotherapeutic agents during their in vivo application [27]. The reduction of NPs' toxicity is due to the essential amino acid, which is transformed in such systems through the kynurenine pathway alike in the human body [28–29]. The developed synthetic procedure allows obtaining stable colloids of metal NPs in aqueous solutions that possess anticancer effect [30].

Thus, we hypothesized and successfully showed that application of tryptophan leads to more effective and "green" synthetic route for the noble metal shell deposition on the surface of Fe_3O_4 NPs.

28.2 Experimental Details

28.2.1 Materials

The following reagents were used in the present study: silver nitrate ($AgNO_3$) and iron (II) and iron (III) chlorides ($FeCl_2$ and $FeCl_3$) (Merck, Germany); tryptophan, SC12-20120713, China; sodium oleate (Sigma Aldrich); and ammonia solution

(NH_4OH, 25% in water). All reagents were of analytical grade and used without further purification. Distilled water was used for the preparation of all sample solutions.

28.2.2 Preparation of NPs

Magnetite synthesis 24 g of ferrous chloride and 48 g of ferric chloride solution were dissolved in 1 L of distilled water. This solution was added dropwise to 250 ml of ammonia solution (NH_4OH, 25% in water). Black precipitate was collected and washed several times by distilled water and maintained at pH = 7. The synthesis of magnetite was carried out by the co-precipitation of iron salts according to the reaction:

$$Fe^{2+} + 2Fe^{3+} + 8NH_4OH \rightarrow Fe_3O_4 + 4H_2O + 8NH_4{}^{+}.$$

Preparation of colloidal solution of Fe3O4 NPs 15 g of sodium oleate was added to obtained magnetite, and the suspension was kept on water bath (80 °C) for 1 hour with stirring. The obtained magnetic fluid with magnetite concentration of 50 mg/ml was used as initial solution for further experiments (sample indicated as "1 - Fe_3O_4").

Ag and Fe3O4 core Ag shell nanoparticle synthesis Colloidal solutions of silver nanoparticles were obtained via chemical reduction of silver nitrate with amino acid tryptophan. Initial solution of Trp was adjusted to high pH as described in [21, 22]. Silver nitrate was added to the solution of amino acid, previously heated to boiling, stirred, and heated continuously. Here the components' molar ratio was $\nu(\text{Trp}):\nu(M) = 3:1$. The colloid of nanocomposite containing iron oxide core and silver shell $Fe_3O_{4\,\text{core}}\,Ag_{\text{shell}}$ was synthesized in the same way but with magnetite injection right before silver was added. Magnetite was used twice in less molar amount compared to Ag (samples indicated as "2 - Ag NPs" and "3 - $Fe_3O_{4\,\text{core}}\,Ag_{\text{shell}}$").

NPs purification Magnetic $Fe_3O_{4\,\text{core}}\,Ag_{\text{shell}}$ nanoparticles were purified in the following way. NPs were collected in a test tube by magnet for 2 days. After changing supernatant, the precipitate of magnetic NPs was re-dispersed in water. The supernatant changing procedure was repeated three times (sample indicated as "4 - $Fe_3O_{4\,\text{core}}\,Ag_{\text{shell}}$ purified").

Additionally, control solutions of magnetite with tryptophan, silver nitrate, and silver nanoparticles were prepared (samples indicated as "5 - control Fe_3O_4 + Trp", "6 - control Fe_3O_4 + $AgNO_3$", and "7 - control Fe_3O_4 + Ag NPs").

28.2.3 Characterization of NPs

Particle size analysis The size (hydrodynamic diameter) of synthesized nanoparticles was determined by DLS using Zetasizer Nano series from Malvern Instruments. All measurements were performed at 25 °C. Each value was obtained as average from three runs with at least 10 measurements.

Zeta potential measurements The zeta potential of nanoparticle solution was measured in 1 ml of water (not less than 5.97 * 10^8 particles/ml) at 25 °C by the microelectrophoretic method using Malvern Zetasizer Nano ZS apparatus. Each value was obtained as an average from three subsequent runs of the instrument with at least 20 measurements.

Transmission electron microscopy (TEM) was performed using Transmission Electron Microscope JEOL 2010.

Scanning electron microscopy (SEM) Morphology of nanoparticles was observed by JEOL JSM-7500F, field emission scanning electron microscope, at an operation voltage of 15 keV. Samples were prepared by immersing copper cylinder in nanocapsule suspension and drying overnight.

UV–Vis The absorption spectra of colloidal solutions of nanoparticles were recorded in the UV–Visible region with a spectrophotometer Lambda 35 (PerkinElmer), in 1 cm quartz cells.

In vitro MTT tests In order to evaluate the cytotoxicity of $Fe_3O_{4\,core}\,Ag_{shell}$ and purified $Fe_3O_{4\,core}\,Ag_{shell}$ nanocomposites, the viability of human skin fibroblast line BT5ta was assessed using alamarBlue (alamarBlue®, Invitrogen). The BT5ta cells were previously seeded at density of 2 × 104 cells per well on 96-well tissue-culture-treated polystyrene plate (Nunc). For the cytotoxicity assessment, 100 μl of the obtained samples were placed in contact with the cells and were incubated at 37 °C in a humidified atmosphere of 5% CO_2 for 24 h. After that time, the cells were examined for signs of toxicity using an alamarBlue assay kit. A sample in the DMEM buffer subjected to the same conditions was used as a negative control. Resazurin, the active blue ingredient of AlamarBlue reagent, is a nontoxic, cell-permeable compound that, once in a viable cell, is reduced to red-colored resorufin. alamarBlue® reagent was diluted in culture medium (1:10) and added to a 96-well plate after aspirating the culture medium containing the samples in contact with cells. The samples were diluted 2, 4, 8, 16, and 64 times. After 4 h of incubation at 37 °C, the absorbance at 570 nm was measured in a microplate reader, using 600 nm as a fpr normalization. The quantity of resorufin formed was directly proportional to the number of viable cells. The error bars for each data point were the standard deviation of three independent measurements.

28.3 Results and Discussion

As was mentioned before, $Fe_3O_{4\,core}$ Ag_{shell} colloid was obtained by the reduction of silver ions on the magnetite surface using tryptophan. In general, silver shell was formed around the core of magnetic nanoparticle, stabilized with amino acid. The average size of Fe_3O_4 NPs stabilized with sodium oleate in the initial colloidal solution was in the range of 7–20 nm in diameter according to TEM and SEM images (Fig. 28.1) as was shown previously and 32–50 nm according to the dynamic light scattering measurements (Fig. 28.2a). It should be noted that the size of NPs obtained by DLS method corresponds to their hydrodynamic diameter. Hydrodynamic diameter of Fe_3O_4/sodium oleate NPs measured by DLS method (Fig. 28.2a) can be attributed to aggregation of initial iron oxide NPs after precipitation.

Zeta potential of initial Fe_3O_4 NPs was −24.6 mV (Fig. 28.2b). The negative zeta potential of the coated nanoparticles can be attributed to the negatively charged carboxylate groups present in the sodium oleate. Zeta potential values near −30 mV indicate that in addition to stabilization by steric repulsion, the sodium oleate can also stabilize the particles by electrostatic repulsion mechanisms. Particles with low zeta potential values tend to aggregate due to interparticles' attractive interactions. It is generally accepted that nanoparticles with the value of zeta potential greater than +25 mV or less than −25 mV have high degree of kinetic stability.

In order to understand the impact of the components presented in system control, solutions were also investigated. The sample list and summarized physicochemical characteristics of obtained samples are given in Table 28.1.

Zeta potential and size distribution Addition of Trp as well as $AgNO_3$ to Fe_3O_4 NPs caused the change of zeta potential of obtained system to more negative and subsequently made them more stable. The average hydrodynamic radius of obtained

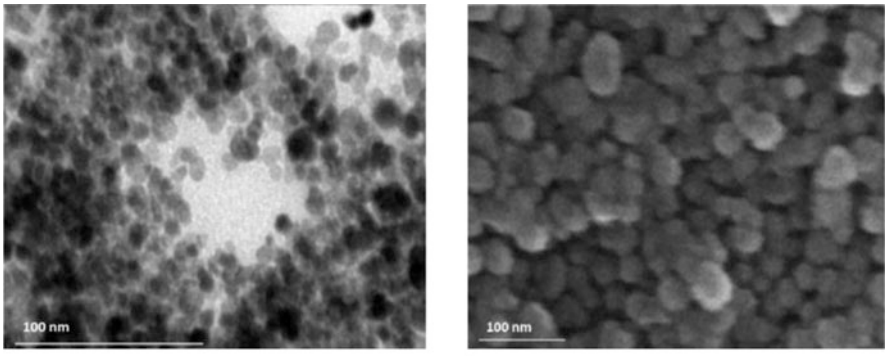

Fig. 28.1 TEM (**a**) and SEM (**b**) images of magnetite/sodium oleate nanoparticles in initial solution

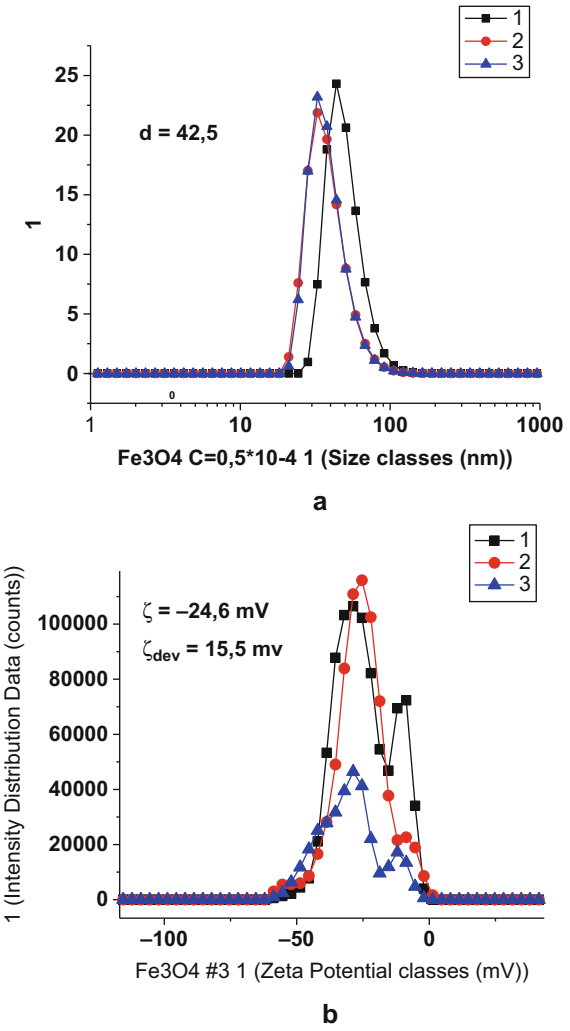

Fig. 28.2 Size distribution (**a**) and zeta potential of Fe_3O_4/sodium oleate NPs (**b**)

Table 28.1 Physicochemical characteristics of obtained colloids

	Sample	Size (*d*, nm)	Zeta potential (mV)	UV–Vis, max (nm)
1	Fe_3O_4	32–50	−25	–
2	Ag NPs	20–30	−30	429 nm
3	Fe_3O_4 $_{core}$ Ag_{shell}	4–6	−11	422 nm
4	Fe_3O_4 $_{core}$ Ag_{shell} purified	43–58	−15	424 nm
5	Control Fe_3O_4 + $AgNO_3$	28–32	−50	413 nm(after 8 months)
6	Control Fe_3O_4 + Trp	32–50	−41	–
7	Control Fe_3O_4 + Ag NPs	7–9	−27	429 nm

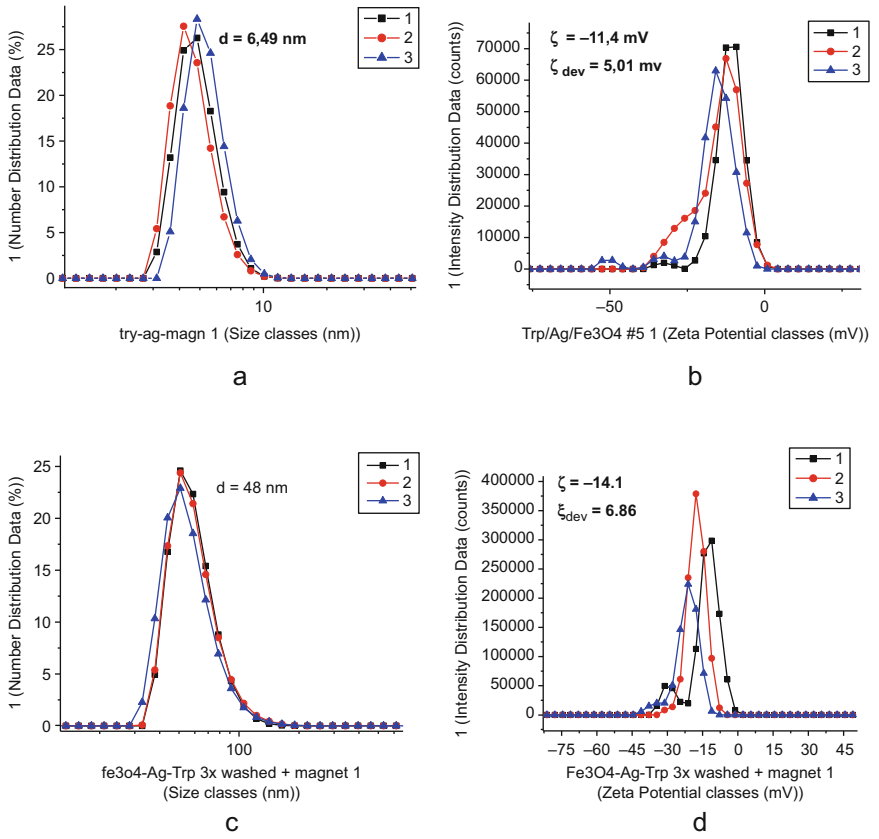

Fig. 28.3 Size distribution by number (**a**) and zeta potential (**b**) of initial colloid of Fe_3O_4 core Ag shell nanoparticles (sample 3)

Fe_3O_4 core Ag_{shell} NPs suspension (sample 3) was around 7 nm (Fig. 28.3a) with zeta potential of −11 mV (Fig. 28.3b). Previously, in [29], it has been shown that in the case of silver, two fractions of nanoparticles are formed—small particles up to 10 nm and NPs with the average size of 25 nm. Decrease of the average size of obtained complex core–shell nanosized system can be explained by the formation of individual small Ag nanoparticles simultaneously with the silver shell growth around magnetite NPs. As the size in DLS data reflects statistical value based on the number of NPs in solution, a large number of small Ag NPs lead to lowering of the average size of particles in the system. Thus, for the separation and purification of Fe_3O_4 core Ag_{shell} NPs, magnetic field was applied followed by washing**.** In this case, only magnetic NPs were collected. The effect of magnetic field application on size distribution can be seen in Fig. 28.3c. After purification by magnetic separation, the average particle size increased to 43–58 nm. Taking into account the change of NPs size (unwashed NPs −7 nm; purified NPs −48 nm), we can conclude that small

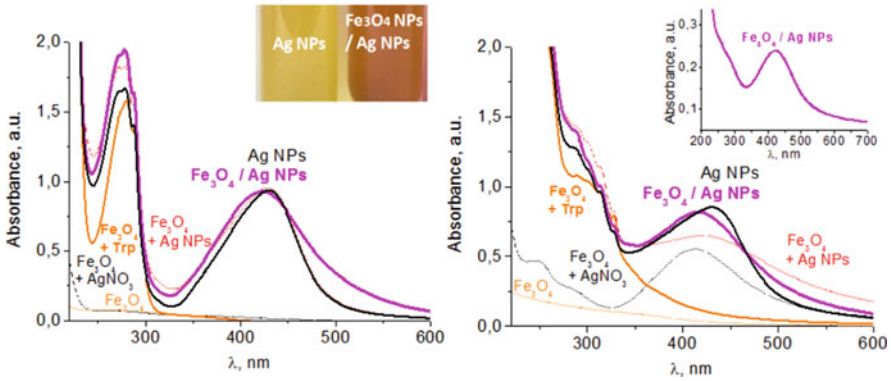

Fig. 28.4 Optical spectra of nanoparticles and control solutions after 1 week (**a**) and 8 months (**b**) after preparation. Insets show the color of obtained colloids (**a**) and optical spectrum of washed sample of $Fe_3O_{4\ core}\ Ag_{shell}$ (**b**) (top) and $Fe_3O_{4\ core}\ Ag_{shell}$ nanoparticles purified with a magnet (sample 4)

Ag NPs, which contributed to a low measured size, were removed. $Fe_3O_{4\ core}\ Ag_{shell}$ NPs (sample 4, Fig. 28.3d) after that separation were moderately stable, having zeta potential $= -15$ mV.

Optical spectra One week after preparation, colloidal solutions of Ag NPs had bright yellow color that was reflected in absorption spectra as broad and intensive band of localized surface plasmon resonance (LSPR) of silver (Fig. 28.4a). Its maximum was located at 429 nm. The same LSPR band position was characteristic for the mixture of magnetite and silver nanoparticle colloids (control Fe3O4 + Ag NPs), whereas the LSPR maximum of Fe_3O_4 core Ag shell before silver NPs separation was blue shifted to 422 nm. The band was broader indicating higher level of polydispersity in colloidal solution.

For all colloidal systems containing silver nanoparticles (individual Ag NPs, the mixture of magnetite and individual Ag NPs, and complex nanosized core–shell system), absorption bands of tryptophan at 270–290 were slightly modified 1 week after synthesis. They all had vibrational structure with maxima at 271, 278, and 287 nm compared to the control solution of amino acid with a short wavelength shoulder and maxima at 280 and 288 nm.

After 8 months of storage at room temperature and daylight, LSPR bands of individual silver NPs and complex nanosized core–shell system of silver and magnetite were broadened, but they retained 90% of their intensity (Fig. 28.4b). The changes occurred because of aging of colloids. Also the loss of band symmetry was due to the absorption of products of tryptophan oxidation. The maxima of such bands were located at 314 and 328 nm with an intensive shoulder near 288 nm.

Control solution of "$Fe_3O_4 + AgNO_3$" system after mixing had no maxima in both absorption regions characteristic for metal and amino acid. But after 8 months, we observed the yellowing of solution and the appearance of new broadband in UV–

Vis spectrum with a maximum at 413 nm that belongs to LSPR of silver. Thus, in the presence of a solubilizer, namely, the stabilizer of Fe3O4 NPs—sodium oleate—the reduction of Ag + ions can occur resulting in Ag NPs formation.

After purification of $Fe_3O_{4\ core}$ Ag_{shell} NPs with magnetic field, small silver particles were eliminated (Fig. 28.4b), while plasmon resonance absorption band maximum remained at max = 424 nm (Fig. 28.4 inset). Thus, complex nanosized core–shell system had a stable silver shell leading to the appearance of LSPR absorption.

Scanning electron microscopy was applied in order to investigate NPs morphology. On SEM images of the mixture of Fe_3O_4 + Ag NPs (Fig. 28.5a), nanoparticles of triangular, oval, and irregular shapes can be observed.

Triangular particles with a size about 100 nm can be identified as individual silver NPs as they were not presented on the SEM images of the same sample, but

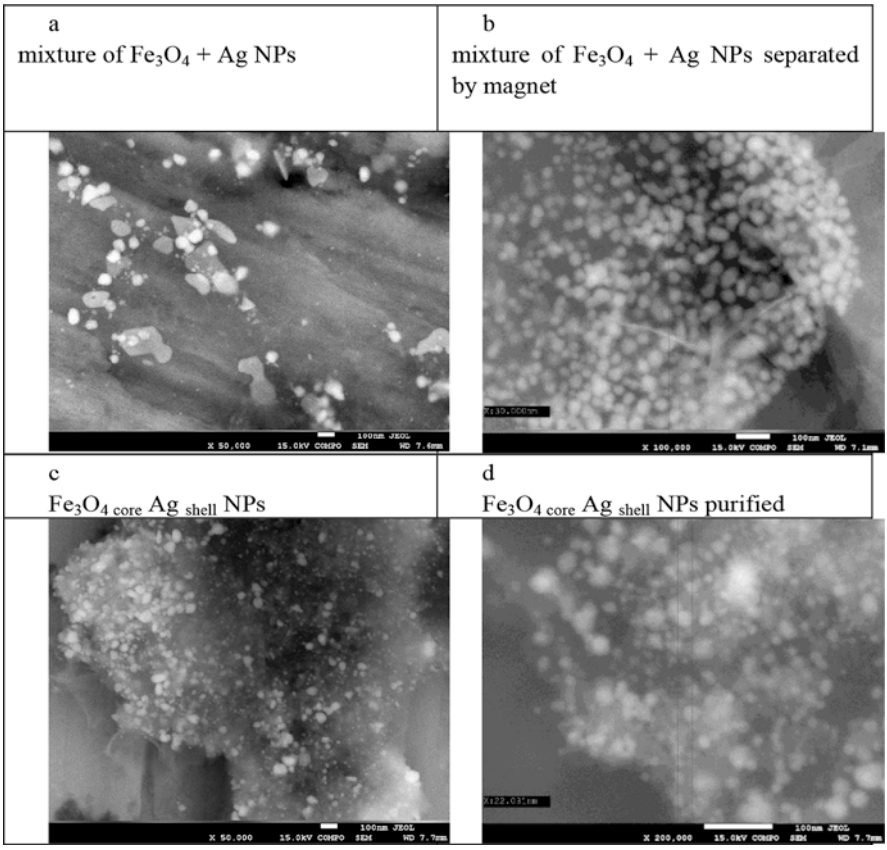

Fig. 28.5 SEM images of the mixture of individual magnetite and silver nanoparticles (**a**, **b**) and complex $Fe_3O_{4\ core}$ Ag_{shell} system (**c**, **d**) investigated before (on the left **a**, **c**) and after (on the right **b**, **d**) purification with a magnet

magnetically separated (Fig. 28.5b). Particles of oval and irregular shapes can be attributed to both magnetite and silver NPs. As it can be observed, after separation NPs are mainly of spherical shape. We can assume that predominantly magnetite NPs remained in suspension.

SEM images of $Fe_3O_{4\ core}\ Ag_{shell}$ NPs before and after magnetic separation are presented in Figs. 28.5c, d, respectively. Particles in $Fe_3O_{4\ core}\ Ag_{shell}$ colloid before separation were of irregular shape and had wide size distribution. After separation with magnetic field, the shape of $Fe_3O_{4\ core}\ Ag_{shell}$ particles becomes more regular, close to spherical or oval (Fig. 28.5d).

In addition, after separation the intensity of Fe signal in EDS spectra of $Fe_3O_{4\ core}\ Ag_{shell}$ system increased, compared to the suspension after synthesis.

Apparently during Ag^+ reduction by Trp, the mixture of nanoparticles is formed. Such mixture consists of magnetite NPs, individual silver NPs, and tailored complex system of core–shell type (Fig. 28.6).

The cytotoxicity study of composites based on nanosized silver and magnetite ($Fe_3O_{4\ core}\ Ag_{shell}$ and $Fe_3O_{4\ core}\ Ag_{shell}$ after magnetic separation) was carried out on BT5ta cell line for suspension as received after synthesis and at various dilutions. At the same time, tryptophan alone, Ag NPs, and magnetite samples were used to evaluate cytotoxicity of separate components. Experimental data were presented as means ± standard deviation. One-way analyses of variance were performed for evaluation of the results. The differences were considered significant only if $p < 0.05$. The results of cytotoxicity analysis evaluated against the negative control are collected in Figs. 28.7 and 28.8.

According to the data obtained by MTT assay, more than 70% of BT5ta cells were found to be viable relative to the control, during 24 h of incubation with NPs. There is no significant difference in viability of BT5ta cells between all studied samples, as is shown in the diagram in Fig. 28.7.

The studied colloids were diluted 2, 4, 8, 16, and 64 times with distilled water. The diagram in Fig. 28.8 shows that with decreasing concentration of NPs, the percent of cell viability increased. In the samples $Fe_3O_{4\ core}\ Ag_{shell}$ and purified $Fe_3O_{4\ core}\ Ag_{shell}$ diluted in 2 times (indicated as dilution 1), the percent of viability of cells was 65% and 68%, respectively. Further dilution in 4, 8, 16, and 64 times did not cause the statistically significant difference in the percent of cell viability

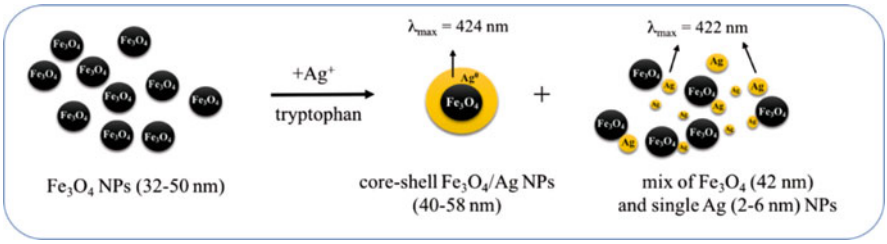

Fig. 28.6 Formation of NPs mixture during Ag^+ reduction

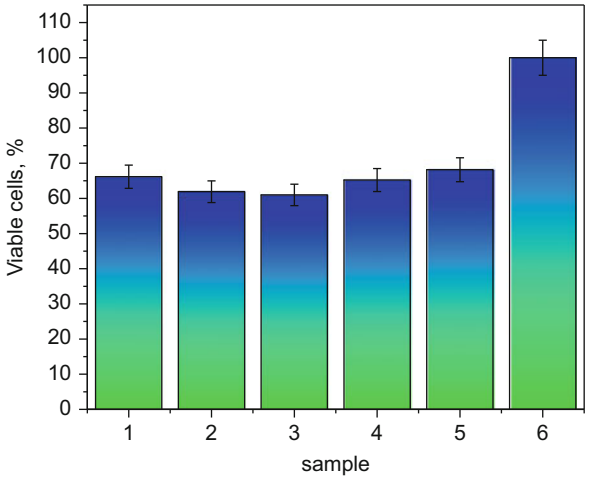

Fig. 28.7 Viability of BT5ta cell line in contact with initial solutions of 1, tryptophan; 2, Ag NPs; 3, Fe_3O_4; 4, $Fe_3O_{4\ core}\ Ag_{shell}$; and 5, purified $Fe_3O_{4\ core}\ Ag_{shell}$ and 6, control

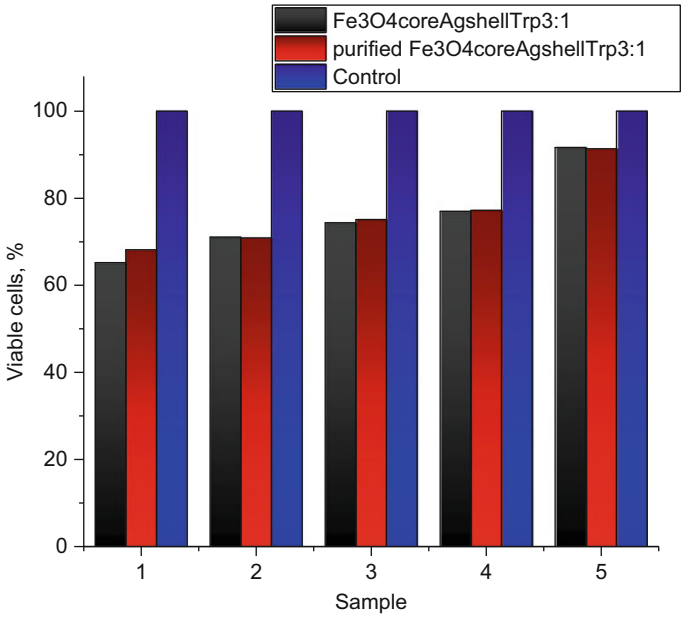

Fig. 28.8 Viability of BT5ta cell line in contact with $Fe_3O_{4\ core}\ Ag_{shell}$ (**a**) and purified $Fe_3O_{4\ core}\ Ag_{shell}$ (**b**) samples compared to control (**c**). 1, 2, 3, 4, and 5 refer to the dilution of initial colloid suspension in 2, 4, 8, 16, and 64 times

for both samples, namely, for initial and purified nanocomposite values 71 and 71% (dilution 2), 74 and 75% (dilution 3), 77% (dilution 4), and 91% (dilution 5) were obtained, respectively.

The result shows that $Fe_3O_{4\ core}\ Ag_{shell}$ nanoparticles have low cytotoxic effect toward BT5ta cells and can be used for medical purposes

28.4 Conclusions

The use of tryptophan as a reducing agent and co-stabilizer for nanosized silver allows to obtain magnetic particles bearing plasmonic absorption band in a visible range with max = 424 nm with the average size of ~ 50 nm. According to in vitro cytotoxicity tests, particles are biocompatible and do not significantly suppress BT5ta cells. Thus, the reduction of silver ions by tryptophan in the presence of previously formed magnetite nanoparticles can be applied for creation of highly biocompatible magnetic nanocomposite particles.

Acknowledgments This work is supported in the framework of grants of the National Academy of Sciences of Ukraine for the research laboratory/group of young scientists of NASU for conducting investigations in priority directions of science and technology development in 2018 (no. 29/2018).

References

1. Sun CR, Du K, Fang C, Bhattarai N, Veiseh O, Kievit F, Stephen Z, Lee DH, Ellenbogen RG, Ratner B, Zhang MQ (2010) PEG-mediated synthesis of highly dispersive multifunctional superparamagnetic nanoparticles: their physicochemical properties and function in vivo. ACS Nano 4(4):2402–2410
2. Kołodyńska D, Gęca M, Pylypchuk IV, Hubicki Z (2016) Development of new effective sorbents based on nanomagnetite. Nanoscale Res Lett 11(1):152
3. Pylypchuk IV, Kołodyńska D, Gorbyk P (2017) Gd (III) adsorption on the DTPA-functionalized chitosan/magnetite nanocomposites. Sep Sci Technol 53:1–11
4. Sun C, Lee JS, Zhang M (2008) Magnetic nanoparticles in MR imaging and drug delivery. Adv Drug Deliv Rev 60(11):1252–1265
5. Senpan A, Caruthers SD, Rhee I, Mauro NA, Pan D, Hu G, Scott MJ, Fuhrhop RW, Gaffney PJ, Wickline SA (2009) Conquering the dark side: colloidal iron oxide nanoparticles. ACS Nano 3(12):3917–3926
6. Di Marco M, Sadun C, Port M, Guilbert I, Couvreur P, Dubernet C (2007) Physicochemical characterization of Ultrasmall Superparamagnetic Iron Oxide Particles (USPIO) for biomedical application as MRI contrast agents. Int J Nanomedicine 2(4):609
7. Kumar CS, Mohammad F (2011) Magnetic nanomaterials for hyperthermia-based therapy and controlled drug delivery. Adv Drug Deliv Rev 63(9):789–808
8. Li Y-W, Chen Z-G, Zhao Z-S, Li H-L, Wang J-C, Zhang Z-M (2015) Preparation of magnetic resonance probes using one-pot method for detection of hepatocellular carcinoma. World J Gastroenterol: WJG 21(14):4275
9. Ferrari M (2005) Cancer nanotechnology: opportunities and challenges. Nat Rev Cancer 5(3):161

10. Thiesen B, Jordan A (2008) Clinical applications of magnetic nanoparticles for hyperthermia. Int J Hyperth 24(6):467–474
11. Farkhari N, Abbasian S, Moshaii A, Nikkhah M (2016) Mechanism of adsorption of single and double stranded DNA on gold and silver nanoparticles: investigating some important parameters in bio-sensing applications. Colloids Surf B: Biointerfaces 148:657–664
12. Li S, Li D, Zhang Q-Y, Tang X (2016) Surface enhanced Raman scattering substrate with high-density hotspots fabricated by depositing Ag film on TiO2-catalyzed Ag nanoparticles. J Alloys Compd 689:439–445
13. Iravani S, Korbekandi H, Mirmohammadi S, Zolfaghari B (2014) Synthesis of silver nanoparticles: chemical, physical and biological methods. Res Pharm Sci 9(6):385
14. Shi J, Wang L, Zhang J, Ma R, Gao J, Liu Y, Zhang C, Zhang Z (2014) A tumor-targeting near-infrared laser-triggered drug delivery system based on GO@ Ag nanoparticles for chemo-photothermal therapy and X-ray imaging. Biomaterials 35(22):5847–5861
15. Yeo SY, Lee HJ, Jeong SH (2003) Preparation of nanocomposite fibers for permanent antibacterial effect. J Mater Sci 38(10):2143–2147
16. Durán N, Marcato PD, De Souza GI, Alves OL, Esposito E (2007) Antibacterial effect of silver nanoparticles produced by fungal process on textile fabrics and their effluent treatment. J Biomed Nanotechnol 3(2):203–208
17. Chen C-Y, Chiang C-L (2008) Preparation of cotton fibers with antibacterial silver nanoparticles. Mater Lett 62(21-22):3607–3609
18. Yuan Z, Zhao Y, Yang W, Hu Y, Cai K, Liu P, Ding H (2016) Fabrication of antibacterial surface via UV-inducing dopamine polymerization combined with co-deposition Ag nanoparticles. Mater Lett 183:85–89
19. Zaharia A, Muşat V, Ghisman VP, Baroiu N (2016) Antimicrobial hybrid biocompatible materials based on acrylic copolymers modified with (Ag) ZnO/chitosan composite nanoparticles. Eur Polym J 84:550–564
20. Mukha IP, Eremenko A, Smirnova N, Mikhienkova A, Korchak G, Gorchev V, Chunikhin AY (2013) Antimicrobial activity of stable silver nanoparticles of a certain size. Appl Biochem Microbiol 49(2):199–206
21. Chi Y, Yuan Q, Li Y, Tu J, Zhao L, Li N, Li X (2012) Synthesis of Fe3O4@ SiO2–Ag magnetic nanocomposite based on small-sized and highly dispersed silver nanoparticles for catalytic reduction of 4-nitrophenol. J Colloid Interface Sci 383(1):96–102
22. Pang Y, Wang C, Wang J, Sun Z, Xiao R, Wang S (2016) Fe3O4@ Ag magnetic nanoparticles for microRNA capture and duplex-specific nuclease signal amplification based SERS detection in cancer cells. Biosens Bioelectron 79:574–580
23. Yu W, Huang Y, Pei L, Fan Y, Wang X, Lai K (2014) Magnetic Fe_3 O_4/Ag hybrid nanoparticles as surface-enhanced Raman scattering substrate for trace analysis of furazolidone in fish feeds. J Nanomater 2014:103
24. Gong P, Li H, He X, Wang K, Hu J, Tan W, Zhang S, Yang X (2007) Preparation and antibacterial activity of Fe3O4@ Ag nanoparticles. Nanotechnology 18(28):285604
25. Zheng B, Zhang M, Xiao D, Jin Y, Choi MM (2010) Fast microwave synthesis of Fe_3 O_4 and Fe_3 O_4/Ag magnetic nanoparticles using Fe_2+ as precursor. Inorg Mater 46(10):1106–1111
26. Venkateswarlu S, Kumar BN, Prathima B, Anitha K, Jyothi N (2015) A novel green synthesis of Fe_3O_4-Ag core shell recyclable nanoparticles using *Vitis vinifera* stem extract and its enhanced antibacterial performance. Phys B Condens Matter 457:30–35
27. Shmarakov IO, Mukha IP, Karavan VV, Chunikhin OY, Marchenko MM, Smirnova NP, Eremenko AM (2014) Tryptophan-assisted synthesis reduces bimetallic gold/silver nanoparticle cytotoxicity and improves biological activity. Nano 1:6
28. Mukha I, Vityuk N, Severynovska O, Eremenko A, Smirnova N (2016) The pH-dependent stucture and properties of Au and Ag nanoparticles produced by tryptophan reduction. Nanoscale Res Lett 11(1):101

29. Mukha I, Vityuk N, Grodzyuk G, Shcherbakov S, Lyberopoulou A, Efstathopoulos EP, Gazouli M (2017) Anticancer effect of Ag, Au, and Ag/Au bimetallic nanoparticles prepared in the presence of tryptophan. J Nanosci Nanotechnol 17(12):8987–8994
30. Shmarakov I, Mukha I, Vityuk N, Borschovetska V, Zhyshchynska N, Grodzyuk G, Eremenko A (2017) Antitumor activity of alloy and core-shell-type bimetallic AgAu nanoparticles. Nanoscale Res Lett 12(1):333

Chapter 29
Influence of Mg Content on Structural and Magnetic Properties of Green-Synthesized $Li_{0.5-0.5x}Mg_xFe_{2.5-0.5x}O_4$ ($0.0 \leq x \leq 0.8$) Nanoferrites

P. Tiwari, S. N. Kane, R. Verma, T. Tatarchuk, and F. Mazaleyrat

29.1 Introduction

Spinel ferrites are insulating magnetic oxides that display low eddy current, dielectric losses, high electrical resistivity, high saturation magnetization, and high permeability and would be of use in various applications, e. g., in high-frequency devices, microwave devices, bioscience (hyperthermia, MRI), switching devices, gas sensing, multilayer chip inductor, etc. [1–4]. Spinel ferrites exhibit face-centered cubic (FCC) structure that belongs to Fd3m space group with two inter-penetrating sub-lattices: tetrahedral (A) and B octahedral (B). The presence of metal ions on A and B sites affects both structural and magnetic properties, is a multifaceted process, and strongly depends on composition, a specific synthesis procedure, post-preparation thermal treatments, etc. In spinel ferrites, to understand their structural and magnetic properties, and the correlation between them, it is important to get precise information about cationic distribution on A and B sites. For the same, X-ray

P. Tiwari
Magnetic Materials Laboratory, School of Physics, D. A. University, Indore, India

Department of Physics, Prestige Institute of Engineering Management and Research, Indore, India

S. N. Kane · R. Verma
Magnetic Materials Laboratory, School of Physics, D. A. University, Indore, India

T. Tatarchuk (✉)
Department of Chemistry, Vasyl Stefanyk Precarpathian National University, Ivano-Frankivsk, Ukraine

Educational and Scientific Center of Materials Sciences and Nanotechnology, Vasyl Stefanyk Precarpathian National University, Ivano-Frankivsk, Ukraine

F. Mazaleyrat
SATIE, ENS Cachan, CNRS 8029, Universite Paris-Saclay, Cachan, France

© Springer Nature Switzerland AG 2019

O. Fesenko, L. Yatsenko (eds.), *Nanophotonics, Nanooptics, Nanobiotechnology, and Their Applications*, Springer Proceedings in Physics 222,
https://doi.org/10.1007/978-3-030-17755-3_29

diffraction (XRD) is accepted as one of the most appropriate and successful tools for the accurate determination of cation distribution on sites A and B [5–7]. It is worth noting that the success of XRD is rather limited by the similar scattering factors of some of the cations present in the spinel ferrites.

Presently, there is a need to investigate simple, cost-effective, eco-friendly techniques to synthesize nanocrystalline spinel ferrites, where tunability of their properties can be realized. Literature shows various synthesis techniques including biosynthetic protocols making use of plant extracts, microorganisms, etc. which have come out as moderately easy and practicable alternative to physical procedures and chemical synthetic methods. Published work also documents the use of simple synthesis route utilizing efficient green precursors, e.g., honey, neem (*Azadirachta indica*) leaves, ginger, banana peel, garlic, *aloe vera* plant extract, cardamom seeds, etc., giving superior yield of nanoferrites, displaying appropriate magnetic properties [8]. It is worth noting that phenols, amino acids, carbohydrates, polysaccharides, flavonoids, terpenoids, etc. present in plant extracts act as capping agents, stabilizing agents, as well as chelating agents [9], desirable for the synthesis of ferrite nanoparticles via sol–gel auto-combustion method. In addition, when nanoparticles are synthesized via green synthesis, the toxicity can be reduced via green synthesis, making them attractive for diverse biomedical applications, due to better biocompatibility [10].

Li ferrite has inverse spinel structure with Li ion preferring to occupy B site and Fe^{3+} ions being distributed on both A and B sites. Owing to high Curie temperature and high saturation magnetization and squareness in their hysteresis loop in Li ferrites, they are used in many electronic devices such as inductors, converters or electromagnetic wave absorbers, phase-shifters, radar, etc. in the radio frequency range. Literature reports study of Li–Zn [11], Li–Cd [12, 13], Li–Co [14], and Li–Mg [15] ferrites, where properties of Li ferrites were tailored by doping various ions. Substitution of ions enhances the squareness ratio of hysteresis loops of Li ferrite and also leads to increase of coercivity (H_c). It is known that sintering is needed not only for the formation of spinel phase but it also improves crystallinity and helps in achieving equilibrium cationic distribution. A constraint with Li-based ferrites is that due to low melting point of Li (~180 °C), sintering at high temperature cannot be used due to evaporation of Li, affecting the stoichiometry. To overcome the limitation, an appropriate synthesis method needs to be used, where either lower sintering temperature or even no sintering can facilitate the formation of spinel phase. Here, sol–gel auto-combustion synthesis route is of significant relevance, where synthesis is done at relatively lower temperature ~110 °C, which also has the advantage of energy-efficient synthesis. In order to meet the aforementioned prerequisite during synthesis, sol–gel auto-combustion technique is of use to facilitate the formation of the spinel phase and also has the advantage of energy-efficient synthesis. Although literature reports Li-based ferrites, nevertheless green synthesis utilizing sol–gel auto-combustion method is less explored in the literature.

So the present work reports on the synthesis of $Li_{0.5-0.5x}Mg_xFe_{2.5-0.5x}O_4$ ($x = 0.0$–0.8) ferrite, utilizing honey green synthesis via sol–gel auto-combustion

method, and their structural, magnetic characterization and antistructure modeling to explain the nature of the surface defects.

29.2 Experimental Details and Data Analysis

$Li_{0.5-0.5x}Mg_xFe_{2.5-0.5x}O_4$ ($x = 0.0$–0.8) spinel ferrites were synthesized by sol–gel auto-combustion method, as described in [1, 14]. Samples were prepared using AR grade nitrate precursors and were dissolved in 10 ml deionized water in stoichiometric ratio. Green fuel (*Honey)* was used in the synthesis, maintaining metal salt-to-fuel ratio as 1:1, without adjusting pH of the solution (*measured pH of the solution was 2*). In the synthesis process, honey acts as a i) chelating agent and ii) fuel, to ease the combustion. Resultant solution was heated at ~110 °C to obtain a fluffy powder called as *dry gel* and was thermally treated at 450 °C for 3 hours. Bruker D8 diffractometer (*θ – 2θ configuration*) utilizing CuK_α radiation (*wavelength 0.15406 nm*), operating at room temperature, was used to get X-ray diffraction (XRD) measurements. Room temperature hysteresis loops were measured by vibrating sample magnetometer (VSM) (Lakeshore Model 7410) by applying a maximum field of $H_{max} \approx \pm 1.9$ T, which was used to obtain coercivity (H_c), saturation magnetization (M_s), and magnetic losses. MAUD (*material analysis using diffraction*) software [16] was used to obtain Rietveld refinement of XRD patterns, to calculate the experimental lattice parameter (a_{exp}).

Cation distribution of all the studied samples was estimated using Bertaut method [17–19] making use of XRD intensity ratio, in which pair(s) of reflections are selected and intensities for reflection (hkl) are calculated. It is worth noting that XRD peak intensities depend on the position of atoms in the spinel unit cell, whereas XRD peak position(s) depend on the size and shape of the unit cell. In this work, we use (220) (422) (400) (440) planes that were used for computing cation distribution, as these planes are responsive to cationic distribution on tetrahedral *A* and octahedral *B* sites of the spinel lattice.

Observed and calculated intensity ratios were compared for numerous combinations of cation distribution at A and B sites using expression, $\frac{I^{obs}_{hkl}}{I^{obs}_{h'k'l'}} = \frac{I^{cal}_{hkl}}{I^{cal}_{h'k'l'}}$, where I^{obs}_{hkl} and I^{cal}_{hkl} are the observed and calculated intensities for the reflection (hkl) [11, 12]. Best cationic distribution for tetrahedral and octahedral sites for which theoretical and experimental intensities' ratios agree noticeably is taken to be the correct one. The theoretical lattice parameter (a_{th}) and Néel magnetic moment or theoretical magnetization at 0 K "$M_{s(t)}$" are calculated using formula, $n_N = M_B - M_A$, where M_A is the magnetic moment of *A* site and M_B is the magnetic moment of *B* site. Oxygen positional parameter ($\boldsymbol{u}^{\bar{4}\mathbf{3m}}$), bond angles ($\theta_1$, θ_2, θ_3, θ_4, θ_5), theoretical lattice constant (a_{th}), oxygen parameter ($\boldsymbol{u}^{\bar{4}\mathbf{3m}}$), inversion parameter ($\delta$), canting angle ($\alpha_{y\text{-}k}$), ionic radii of A site (r_A) and B site (r_B), shared tetrahedral edge ($d_{A\times E}$), and shared octahedral edge ($d_{B\times E}$) were calculated via cationic distribution. Specific surface area (*S*) was calculated using

the expression, $S = [6/(D_s \times \rho_{XRD})]$, where D_s is Scherrer's grain size and ρ_{XRD} is the X-ray density. Dislocation density was calculated using the relation, dislocation density $= 1/D_s{}^2$ (lines/m^2) [20], where D_s is the grain diameter.

29.3 Results and Discussions

Figure 29.1a depicts the XRD patterns of the studied samples, whereas the inset shows enlarged view of (311) reflection, showing changes in the lattice parameter. The presence of important peaks corresponding to (220), (311), (222), (400),

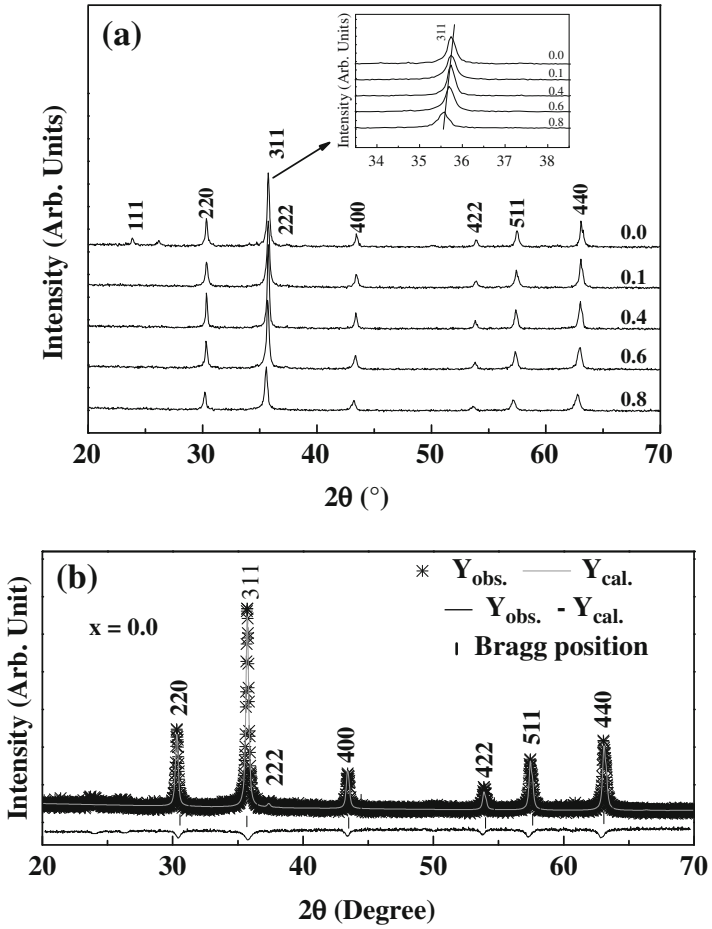

Fig. 29.1 (**a**) XRD patterns of the studied $Li_{0.5-0.5x}$ $Mg_xFe_{2.5-0.5x}$ O_4 ferrites, (**b**) Rietveld refinement for sample $x = 0.0$

Table 29.1 Variation of lattice parameter (a_{exp}), grain diameter (D), cell volume (V), X-ray density (ρ_{xrd}), surface area (S), and dislocation density of $Li_{0.5-0.5x}$ $Mg_xFe_{2.5-0.5x}O_4$ with Mg content (x)

X	D (nm)	V (nm^3)	ρ_{xrd} (kg/m^3)	S (m^2/g)	Dislocation density (lines/m^2)
0.0	26.3	0.5769	4767.4	47.9	14.5×10^{14}
0.1	23.9	0.5772	4748.8	52.6	19.1×10^{14}
0.4	27.9	0.5774	4698.3	45.6	12.8×10^{14}
0.6	24.2	0.5791	4651.7	53.2	17.1×10^{14}
0.8	23.4	0.5860	4565.3	56.3	18.3×10^{14}

(422), (511), (440) planes confirms the formation of face-centered cubic structure. Representative Rietveld refined XRD plot for sample $x = 0.0$ is shown in Fig. 29.1b. Formation of single-phase nanocrystalline spinel phase (*with Scherrer's grain diameter varying between 23.4 and 27.9 nm, as shown in* Table 29.1) is validated by XRD data.

Table 29.1 depicts the variation of grain diameter (D_s), cell volume (V), X-ray density (ρ_{XRD}), specific surface area (S), and dislocation density for the studied samples. Observed changes in V, ρ_{XRD}, and S are ascribable to the incorporation of Mg^{2+} ion (ionic radius of Mg = 0.072 nm) with a little higher ionic radius and depleting Li^{1+} ion (ionic radius of Li^{1+} ion = 0.071 nm) in the spinel lattice. The specific surface area of the studied samples also varies with Mg^{2+} ion incorporation. There is an inverse relationship between particle size and density with surface area, as also seen in the present studies. High specific surface area of particles is useful for catalytic processes. With increasing Mg^{2+} content, dislocation density gets affected. It should be noted that the presence of dislocations in the spinel lattice would act as pinning centers, hindering the domain wall movement, and will have effect on H_c.

Cationic distribution on A and B sites, inversion parameter (δ), values of experimental lattice parameter (a_{exp}), theoretical lattice parameter (a_{th}), and oxygen positional parameter ($\boldsymbol{u}^{\bar{4}3m}$) with Mg^{2+} content are depicted in Table 29.2. Observed variation of a_{exp} with increasing Mg content is ascribable to the addition of an ion (Mg^{2+}) with slightly higher ionic radius, for an ion which has a bit lower ionic radius (Li^{1+} ion), causing expansion of the unit cell. Closer values of a_{exp} and a_{th} suggest that the estimated cation distribution is in reasonable agreement with the real distribution, as was also observed earlier [18]. Obtained variation of oxygen positional parameter $\boldsymbol{u}^{\bar{4}3m}$ (range between 0.3835 and 0.3959) is higher than its ideal value u_{ideal} – 0.375 and shows oxygen displacement, due to incorporation of Mg^{2+} ions in the spinel lattice, resulting in the expansion of the unit cell, shown by changes in $\boldsymbol{u}^{\bar{4}3m}$. Inversion parameter ($\delta$) values estimated from cation distribution range between 0.50 and 0.75 demonstrate the mixed spinel character of samples. Obtained cation distribution shows that Li^{1+} and Mg^{2+} ion are located on both A and B sites. With increasing Mg^{2+} ion in the studied samples, population of Fe^{3+} ions on B site is also altered and would influence magnetic properties.

Table 29.2 Cation distribution (*for A and B sites*), delta parameter, experimental, theoretical lattice parameter, and oxygen position parameter (u) of $Li_{0.5-0.5x}$ $Mg_xFe_{2.5-0.5x}$ O_4 with Mg content

x	Cation distributions	δ	a_{exp} (nm)	a_{Th} (nm)	$u^{\bar{4}3m}$
0.0	$(Li^{+}_{0.25}Fe^{3+}_{0.75})^{A}[Li^{+}_{0.25}Fe^{3+}_{1.75}]^{B}$	0.75	0.8324	0.8385	0.3835
0.1	$(Li^{+}_{0.25}$ $Mg^{2+}_{0.05}$ $Fe^{3+}_{0.70})^{A}[Li^{+}_{0.20}$ $Mg^{2+}_{0.05}$ $Fe^{3+}_{1.75}]^{B}$	0.70	0.8326	0.8403	0.3842
0.4	$(Li^{+}_{0.15}$ $Mg^{2+}_{0.20}$ $Fe^{3+}_{0.65})^{A}[Li^{+}_{0.15}$ $Mg^{2+}_{0.20}$ $Fe^{3+}_{1.65}]^{B}$	0.65	0.8327	0.8433	0.3851
0.6	$(Li^{+}_{0.10}$ $Mg^{2+}_{0.40}$ $Fe^{3+}_{0.50})^{A}[Li^{+}_{0.10}$ $Mg^{2+}_{0.20}$ $Fe^{3+}_{1.70}]^{B}$	0.50	0.8335	0.8577	0.3959
0.8	$(Li^{+}_{0.05}$ $Mg^{2+}_{0.30}$ $Fe^{3+}_{0.65})^{A}[Li^{+}_{0.05}$ $Mg^{2+}_{0.50}$ $Fe^{3+}_{1.45}]^{B}$	0.65	0.8368	0.8456	0.3845

Table 29.3 Variation in ionic radii of A site (r_A) and B site (r_B), shared tetrahedral edge ($d_{A\times E}$), and shared octahedral edge ($d_{B\times E}$) for $Li_{0.5-0.5x}$ $Mg_xFe_{2.5-0.5x}$ O_4 as a function of Mg content (x)

x	r_A (nm)	r_B (nm)	d_{AxE} (nm)	d_{BxE} (nm)
0.0	0.0545	0.06531	0.3143	0.2742
0.1	0.0556	0.0655	0.3162	0.2725
0.4	0.0577	0.0655	03182	0.2705
0.6	0.0572	0.0620	0.3180	0.2715
0.8	0.0579	0.0665	0.3184	0.2732

Table 29.3 depicts the ionic radii of A site (r_A) and B site (r_B), shared tetrahedral edge ($d_{A\times E}$), and shared octahedral edge ($d_{B\times E}$) for the studied samples. Experiential variation of r_A, d_{AE}, and r_B, d_{BE}, with Mg^{2+} content is ascribable to the migration of cations from A to B site or vice versa, as shown in Table 29.3, and is expected to alter magnetic properties noticeably, displaying a strong correlation between structural and magnetic properties.

Figure 29.2 shows Mg content dependence of bond angles θ_1, θ_2, θ_3, θ_4, θ_5. It is worth noting that the strength of the magnetic interactions (*A–O–B*, *B–O–B*, and *A–O–A*) is directly proportional to the bond angle. The bond angles θ_1 and θ_2 represent the angles between A–O–B, θ_3 and θ_4 represent the angles between B–O–B, and θ_5 represents the angles between A–O–A. The observed trend of bond angles θ_1, θ_2, θ_3, θ_4, and θ_5, for x up to ~0.4, indicates strengthening of B–B interaction and weakening of A–B, A–A interaction. For x values beyond ~0.4, obtained tendency of bond angles θ_1, θ_2, θ_3, θ_4, and θ_5 depicts weakening of A–B and A–A interaction, whereas strength of B–B interaction hardly changes, as a result lowering of "$M_{s(exp)}$" is observed, as can be seen in Table 29.4.

Table 29.4 gives coercivity (H_c), experimental saturation magnetization (M_s), magnetization at 0 K ($M_{s\,(0K)}$), magnetic losses (static), and magneto-crystalline anisotropy (K_1) for the studied samples. Table 29.3 visibly shows the Mg^{2+} ion content-dependent magnetic properties of the studied samples (*also seen by changes in cationic distribution, shown in* Table 29.2), as can be seen in Fig. 29.3a–c. Figure 29.3a depicts hysteresis loops of the studied samples, whereas inset shows linear dependence of H_c and M_s on anisotropy. It should be noted that both

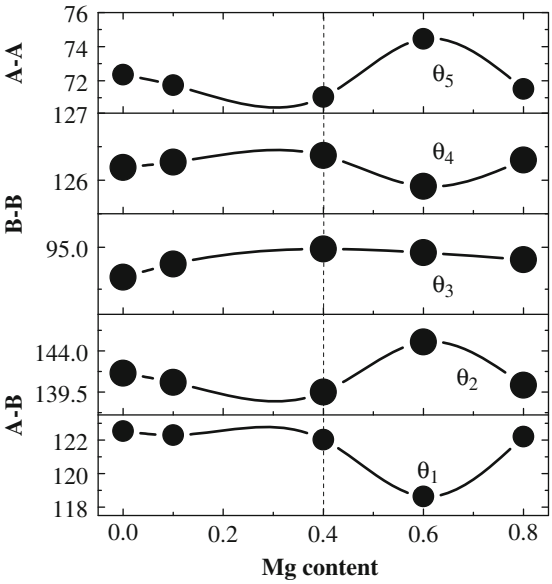

Fig. 29.2 Compositional dependence of bond angles

Table 29.4 Coercivity (H_c), experimental saturation magnetization (M_s), magnetization at 0 K ($M_{s\,(0K)}$), static magnetic losses, magneto-crystalline anisotropy (K_1), and Yafet–Kittel angle ($\alpha_{y\text{-}k}$) (*obtained from cation distribution*) for $Li_{0.5-0.5x}\ Mg_xFe_{2.5-0.5x}\ O_4$ ferrite as a function Mg

x	H_c (O_e)	$M_{s(exp)}$ (Am^2/kg)	$M_{s(0k)}$ (Am^2/kg)	Losses (J/kg)	$K_1 \times 10^4$ (erg/cc)	$\alpha_{y\text{-}k}$ (°)
0.0	126.70	54.3	134.8	1.50	3.3	48.92
0.1	114.00	48.0	132.3	1.81	2.6	54.76
0.4	102.30	42.6	124.6	1.23	2.0	53.84
0.6	93.30	33.1	123.9	0.81	1.4	53.13
0.8	90.30	28.9	110.9	0.74	1.2	54.54

H_c and M_s are connected with anisotropy via the following expression [21], $K_1 = [(H_c \times M_s)/0.98]$, which shows direct proportionality between H_c, M_s, and K_1, as is clearly shown in the inset of Fig. 29.3a (*by means of linear variation of* H_c, M_s *with* K_1). Figure 29.3b shows the linear variation of saturation magnetization at 300 K "$M_{s(exp)}$" and theoretical magnetic moment at 0 K –"$M_s(t)$ 0 K" (*obtained from cationic distribution*) with Mg^{2+} ion content in the samples. Observed changes in the population of Fe^{3+} ions on B site (shown in Table 29.2) and the corresponding variation of "M_s 300 K" (*shown in* Table 29.3*, obtained by VSM measurements*) clearly demonstrate the role of cationic distribution in determining magnetic properties. It can be seen in Fig. 29.3b, for the studied samples, that "$M_{s(t)}$0 K" values are higher than "M_s 300 K" values. Discrepancy between the experimental and calculated M_s values suggests that the magnetic arrangement of spins in our ferrite samples is not governed by a perfectly collinear antiparallel alignment, as proposed by Néel's model, but rather could be affected by a spin canting on the B site with respect to the direction of spins on A site resulting in a noncollinear

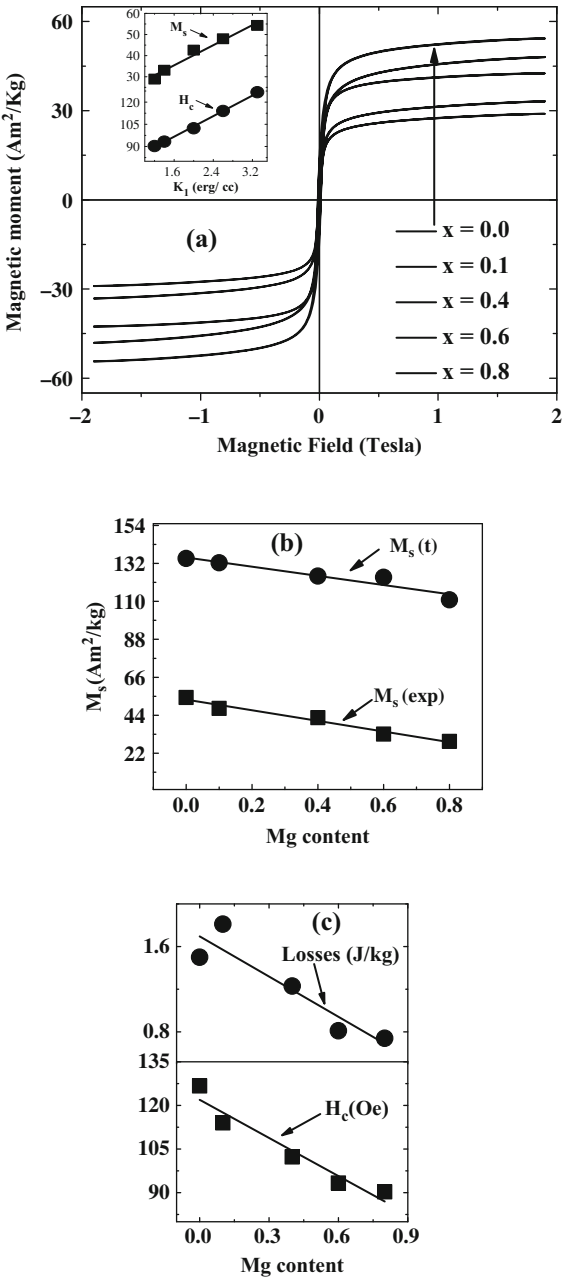

Fig. 29.3 (**a**) Hysteresis loops of the studied samples. Inset: Mg^{2+} dependence of H_c and M_s. (**b**)Variation of experimental $M_{s\,(exp.)}$, $M_{s\,(t)}$ with Mg^{2+} content. (**c**) Variation of H_c and losses with Mg content. Continuous lines are linear fit to the data

arrangement in the two sub-lattices. This spin canting effect, evidenced by finite Y-K angle ($\alpha_{y\text{-}k}$) values in all the studied samples, can be explained by the three-lattice model suggested by Yafet and Kittel [22] (as shown in Table 29.4). Perusal of Table 29.4 shows that with increasing Mg content H_c continuously decreases

(*range between 90.3 Oe and 126.7 Oe*). For the studied samples, observed variation of H_c with grain diameter D_s (H_c *and grain diameter* D_s *are shown, respectively, in* Tables 29.1 and 29.4) suggests that the studied samples fall in the overlap between single-domain and multi-domain structures as mentioned elsewhere [23]. Perusal of Fig. 29.3c shows reduction of both H_c and static losses with increasing Mg content, which very clearly shows magnetic softening of the studied samples (*with increasing Mg content*).

Antistructural modeling [24–26] was used in the current research which can show the active centers on the ferrite surfaces. The spinel antistructure $V_A''\left[V_2'''\right]_B(V_4^{\bullet\bullet})_O$ is a basis of this theory, where V_A'' is an A-vacancy with negative charge, V_B''' is a B-vacancy with negative charge, and $V_O^{\bullet\bullet}$ is the oxygen vacancy with positive charge. The superposition of each A-cation with A-vacancy V_A'', each B-cation with B-vacancy V_B''', and oxygen anion with O-vacancy $V_O^{\bullet\bullet}$gives us the information about the active centers. Antistructural modeling was also used in our previous works as an approach for describing defects in the different systems [27–30].

The superposition of cations and anions with spinel vacancies can be written as follows:

$$Me_A^{+} + V_A'' \rightarrow Me'_A \qquad Me_B^{+} + V_B''' \rightarrow Me''_B$$
$$Me_A^{2+} + V_A'' \rightarrow Me_A^{\times} \qquad Me_B^{2+} + V_B''' \rightarrow Me'_B$$
$$Me_A^{3+} + V_A'' \rightarrow Me_A^{\bullet} \qquad Me_B^{3+} + V_B''' \rightarrow Me_B^{\times}$$
$$O^{2-} + V_O^{\bullet\bullet} \rightarrow O_O^{\times}$$

where $\times$ is an effective zero charge. Taking into account that the positive charges must be balanced by negative charges, the antistructural modeling for Li-doped Mg ferrites can be written as follows:

$$\left(\mathrm{Li}_a^{+}\mathrm{Mg}_b^{2+}\mathrm{Fe}_{1-a-b}^{3+}\right)_A\left[\mathrm{Li}_c^{+}\mathrm{Mg}_d^{2+}\mathrm{Fe}_{2-c-d}^{3+}\right]_B\left(\mathrm{O}_4^{2-}\right)_O + \underbrace{V_A''\left[V_2'''\right]_B(V_4^{\bullet\bullet})_O}_{\text{spinel antistructure}} \rightarrow$$
$$\rightarrow \underbrace{\left(\mathrm{Li}'_a\mathrm{Mg}_b^{\times}\mathrm{Fe}_{1-a-b}^{\bullet}\right)_A\left[\mathrm{Li}''_c\mathrm{Mg}'_d\mathrm{Fe}_{2-c-d}^{\times}\right]_B\left(\mathrm{O}_4^{\times}\right)_O}_{\text{lithium-magnesium ferrite}}$$

where a, b, c, and d are the mole fraction of cations obtained from XRD data. Thus, the superposition of spinel antistructure with crystallochemical formulae of

Table 29.5 Antistructure modeling for $Li_{0.5-0.5x}$ $Mg_xFe_{2.5-0.5x}$ O_4 samples

x (Mg^{2+})	Chemical formulae	Crystal quasichemical composition
0.0	$Li_{0,50}Fe_{2,50}O_4$	$\left(\mathrm{Li}'_{0.25}\mathrm{Fe}_{0.75}^{\bullet}\right)_A\left[\mathrm{Li}''_{0.25}\mathrm{Fe}_{1.75}^{\times}\right]_B\left(\mathrm{O}_4^{\times}\right)_O$
0.1	$Li_{0,45}Mg_{0,10}Fe_{2,45}O_4$	$\left(\mathrm{Li}'_{0.25}\mathrm{Mg}_{0.05}^{\times}\mathrm{Fe}_{0.70}^{\bullet}\right)_A\left[\mathrm{Li}''_{0.20}\mathrm{Mg}'_{0.05}\mathrm{Fe}_{1.75}^{\times}\right]_B\left(\mathrm{O}_4^{\times}\right)_O$
0.4	$Li_{0,30}Mg_{0,40}Fe_{2,30}O_4$	$\left(\mathrm{Li}'_{0.15}\mathrm{Mg}_{0.20}^{\times}\mathrm{Fe}_{0.65}^{\bullet}\right)_A\left[\mathrm{Li}''_{0.15}\mathrm{Mg}'_{0.20}\mathrm{Fe}_{1.65}^{\times}\right]_B\left(\mathrm{O}_4^{\times}\right)_O$
0.6	$Li_{0,20}Mg_{0,60}Fe_{2,20}O_4$	$\left(\mathrm{Li}'_{0.10}\mathrm{Mg}_{0.40}^{\times}\mathrm{Fe}_{0.50}^{\bullet}\right)_A\left[\mathrm{Li}''_{0.10}\mathrm{Mg}'_{0.20}\mathrm{Fe}_{1.70}^{\times}\right]_B\left(\mathrm{O}_4^{\times}\right)_O$
0.8	$Li_{0,10}Mg_{0,80}Fe_{2,10}O_4$	$\left(\mathrm{Li}'_{0.05}\mathrm{Mg}_{0.30}^{\times}\mathrm{Fe}_{0.65}^{\bullet}\right)_A\left[\mathrm{Li}''_{0.05}\mathrm{Mg}'_{0.50}\mathrm{Fe}_{1.45}^{\times}\right]_B\left(\mathrm{O}_4^{\times}\right)_O$

ferrites shows us the surface-active centers (Table 29.5). It can be seen that the concentration of positively charged ferric ions $Fe_A^{\bullet}$ in A site versus magnesium ion content decreases and the concentration of Li'_A and Li''_B decreases, while the Mg'_B increases with the Mg content. Antistructural modeling provides us new information about surface-active centers (Table 29.5): $Fe_A{}^{3+}$, $Li_A{}^{+}$, $Mg_B{}^{2+}$, and $Li_B{}^{+}$ will be active centers in chemical reactions, while $Mg_A{}^{2+}$ and $Fe_B{}^{3+}$ cations will not be active centers due to their effective zero charge in the crystal lattice.

29.4 Conclusions

Single-phase $Li_{0.5-0.5x}Mg_xFe_{2.5-0.5x}O_4$ ($x = 0.0$–0.8) nanoferrites were synthesized via honey green synthesis protocol. XRD confirms the formation of single-phase $Li_{0.5-0.5x}Mg_xFe_{2.5-0.5x}O_4$ nanoferrites. Studied samples show mixed spinel nature. Mg addition in the studied samples leads to cationic redistribution, displaying changes in $M_{s(exp)}$, H_c, K_1, showing improved soft magnetic nature. Magnetism of the studied samples is governed by Yafet-Kittel three sub-lattice model, rather than Néel's model. An antistructural modeling was used for describing active surface centers, and the changes in concentration of donor's and acceptor's active centers were explained.

Acknowledgments The authors thank Dr. M. Gupta, UGC-DAE CSR, Indore, for XRD data. SNK gratefully acknowledges 1-month invited professor stay at ENS Universite Paris-Saclay, Cachan (France), during June 2018. This work is partially supported by UGC-DAE CSR, Indore, in the form of a research project. T. Tatarchuk is grateful to the Ministry of Education and Science of Ukraine (Project Numbers 0118U000258 and 0117U002408) for their financial support.

References

1. Raghuvanshi S, Mazaleyrat F, Kane SN (2017) Time evolution of structural and magnetic properties of Ni-Zn nano ferrite: an opinion. JOJ Mater Sci 1(2). https://doi.org/10.19080/JOJMS.MS.ID.555561
2. Wang ZL, Liu Y, Zhang Z (2002) Handbook of nanophase and nanostructured materials, vol 3. Kluwer Academic/Plenum Publishers, New York
3. An K, Hyeon T (2009) Synthesis and biomedical applications of hollow nanostructures. Nano Today 4:359–373
4. Guido B, Elisabetta F, Vincenzo L, Marcella T, Rossinib SA (1996) IR study of alkene allylic activation on magnesium ferrite and alumina catalysts. J Chem Soc 92(23):4687–4693
5. Gastaldi L, Lapiccirella A (1979) Three different methods of determining the cation distribution in spinels: a comparison. J Solid State Chem 30:223–229
6. Birgani AN, Mohammad N, Hasanpou A (2015) Study of cation distribution of spinel zinc nano-ferrite by X-ray. J Magn Magn Mater 374:179–181
7. Kurmude DV, Barkule RS, Raut AV, Shengule DR, Jadhav KM (2013) X-Ray diffraction and cation distribution studiesin zinc-substituted nickel ferrite nanoparticles. J Supercond Nov Magn. https://doi.org/10.1007/s10948-013-2305-2

8. Yadav RS, Kuřitka I, Vilcakova J, Havlica J, Masilko J, Kalina L, Tkacz J, Švec J, Enev V, Hajdúchová M (2017) Impact of grain size and structural changes on magnetic, dielectric, electrical, impedance and modulus spectroscopic characteristics of $CoFe_2O_4$ nanoparticles synthesized by honey mediated sol-gel combustion method. Adv Nat Sci Nanosci Nanotechnol 8:045002
9. Gingasu D, Mindru L, Preda S, Calderonmoreno JM, Culita DC, Patron L, Diamandescu L (2017) Green synthesis of cobalt ferrite nanoparticles using plant extracts. Rev Roum Chim 62:645–653
10. Al-Qubaisi MS, Rasedee A, Flaifel MH, Ahmad SHJ, Hussein-Al-Ali S, Hussein MZ, Eid EEM, Zainal Z, Saeed M, Ilowefah M, Fakurazi S, Isa NM, Zowalaty MEE (2013) Cytotoxicity of nickel zinc ferrite nanoparticles on cancer cells of epithelial origin. Int J Nanomedicine 8:2497–2508
11. Watawe SC, Keluskar S, Gonbare T (2006) Preparation and magnetic properties of cadmium substituted lithium ferrite using microwave-induced combustion. Thin Solid Films 505:168–172
12. Akhter S, Hakim MA (2010) Magnetic properties of cadmium substituted lithium ferrites. Mater Chem Phys 120:399–403
13. Vijaya Bhasker Reddy P, Ramesh B, Reddy Ch G (2010) Electrical conductivity and dielectric properties of zinc substituted lithium ferrites prepared by sol–gel method. Physica B 405:1852–1856
14. Panchal S, Raghuvanshi S, Gahlot K, Mazaleyrat F, Kane SN (2016) Cationic distribution assisted tuning of magnetic properties of $Li_{0.5-x/2}Zn_xFe_{2.5-x/2}O_4$. AIP Adv 6:055930–055936
15. Shobana MK (2012) Electrical and structural studies of lithium doped cobalt ferrite. J Phys Chem Solids 73:1040–1043
16. Lutterotti L, Scardi P (1990) Simultaneous structure and size-strain refinement by the Rietveld method. J Appl Crystallogr 23:246–252
17. Bertaut EF (1950) C R Acad Sci 230:213
18. Verma R, Kane SN, Raghuvanshi S, Satalkar M, Modak SS, Mazaleyrat F (2018) Synthesis, structural and magnetic properties of $Mg_{0.6}Zn_{0.4}Cr_xFe_{2-x}O_4$ ($0.0 \leq x \leq 2.0$) nano ferrite. AIP Conf Proc 1953:030135–1–030135–4
19. Raghuvanshi S, Mazaleyrat F, Kane SN (2018) $Mg_{1-x}Zn_xFe_2O_4$ nanoparticles: interplay between cation distribution and magnetic properties. AIP Adv 8:047804–1-047804-11
20. Revathi V, Karthik K (2018) Microwave assisted CdO–ZnO–MgO nanocomposite and its photocatalytic and antibacterial studies. J Mater Sci: Mater El 29(21):18519–18530. https://doi.org/10.1007/s10854-018-9968-1
21. Patange SM, Shirsath SE, Jadhav SS, Jadhav KM (2012) Cation distribution study of nanocrystalline $NiFe_{2-x}Cr_xO_4$ ferrite by XRD, magnetization and Mössbauer spectroscopy. Phys Status Solidi A 209(2):347–352
22. Murthy NSS, Natera MG, Youssef SI, Begum RJ, Srivastava CM (1969) Yafet-kittel angles in zinc-nickel ferrites. Phys Rev 181:969–977. https://doi.org/10.1103/PhysRev.181.969
23. Kolhatkar AG, Jamison AC, Litvinov D, Willson RC, Lee T (2013) Tuning the magnetic properties of nanoparticles. Int J Mol Sci 14(8):15977–16009
24. Tatarchuk TR, Bououdina M, Paliychuk ND, Yaremiy IP, Moklyak VV (2017) Structural characterization and antistructure modeling of cobalt-substituted zinc ferrites. J Alloys Compd 694:777–791. https://doi.org/10.1016/j.jallcom.2016.10.067
25. Babu RB, Tatarchuk T (2018) Elastic properties and antistructural modeling for nickel-zinc ferrite-aluminates. Mater Chem Phys 207:534. https://doi.org/10.1016/j.matchemphys.2017.12.084
26. Kane SN, Raghuvanshi S, Satalkar M, Reddy VR, Deshpande UP, Tatarchuk TR, Mazaleyrat F (2018) Synthesis, characterization and antistructure modeling of Ni nano ferrite. AIP Conf Proc 1953:030089. https://doi.org/10.1063/1.5032424
27. Prabukanthan P, Lakshmi R, Harichandran G, Tatarchuk T (2018) Photovoltaic device performance of pure, manganese (Mn^{2+}) doped and irradiated $CuInSe_2$ thin films. New J Chem 42:11642. https://doi.org/10.1039/C8NJ01056K

28. Rajesh Kumar T, Prabukanthan P, Harichandran G, Theerthagiri J, Tatarchuk T, Maiyalagan T, Maia G, Bououdina M (2018) Physicochemical and electrochemical properties of Gd^{3+}-doped ZnSe thin films fabricated by single-step electrochemical deposition process. J Solid State Electrochem 22:1197. https://doi.org/10.1007/s10008-017-3865-z
29. Ahmed MA, Hassan HE, Eltabey MM, Latka K, Tatarchuk T (2018) Mössbauer spectroscopy of $Mg_xCu_{0.5-x}Zn_{0.5}Fe_2O_4$ (x = 0.0, 0.2 and 0.5) ferrites system irradiated by γ-rays. Phys B Condens Matter 530:195. https://doi.org/10.1016/j.physb.2017.10.125
30. Raghuvanshi S, Tiwari P, Kane SN, Avasthi DK, Mazaleyrat F, Tatarchuk T, Mironyuk I (2019) Dual control on structure and magnetic properties of mg ferrite: role of swift heavy ion irradiation. J Magn Magn Mater 471:521. https://doi.org/10.1016/j.jmmm.2018.10.004

Chapter 30
Current State of Fuel Cell Research

Iryna Ivanenko, Yurii Fedenko, Anastasiia Ruda, and Mitchenko Tetiana

30.1 Current State of the Problem

Today, one of the most important scientific and practical tasks of modern energy is the development of highly efficient and environmentally friendly alternative energy sources to reduce the harmful effects on the environment. Fuel cells are widely used as such sources of energy.

Fuel cell (FC) is a device in which the chemical energy of a fuel (reducing agent) and an oxidizer, continuously and separately brought to the electrodes, is directly converted into electrical energy [1]. The efficiency of such a system is high (from 50%) due to the absence of the stage of conversion of thermal energy into mechanical and then mechanical to electric (as in the case of solid fuel combustion). The difference in fuel cells from primary (batteries) and secondary (accumulators) current sources is that both the fuel and the oxidant are not part of the element but are constantly supplied from the outside, which makes it possible to use the FCs indefinitely in time. In addition, the fuel here is hydrogen, which means that the main exhaust of such systems is simply a water vapor [2]. Air is usually used as the oxidizer, and the operating time of the fuel cell at a given power is directly proportional to the fuel reserve.

In oxygen-hydrogen FC with alkaline electrolyte (solution KOH) in general, the anode undergoes an oxidation reaction of hydrogen:

$$2H_{ads} \rightarrow 2H^{+} + 2e^{-} \tag{30.1}$$

I. Ivanenko (✉) · Y. Fedenko · A. Ruda · M. Tetiana
Department of Inorganic Substances Technology, Water Treatment and General Chemical Engineering of National Technical University of Ukraine "Igor Sikorsky Kyiv Polytechnic Institute", Kyiv, Ukraine

© Springer Nature Switzerland AG 2019

O. Fesenko, L. Yatsenko (eds.), *Nanophotonics, Nanooptics, Nanobiotechnology, and Their Applications*, Springer Proceedings in Physics 222,
https://doi.org/10.1007/978-3-030-17755-3_30

Electric oxygen reduction carried out on a cathode:

$$\frac{1}{2}O_2 + 2H^+ + 2e^- \rightarrow H_2O \tag{30.2}$$

The total reaction:

$$H_2 + \frac{1}{2}O_2 \rightarrow H_2O. \tag{30.3}$$

Reactions (30.1, 30.2, and 30.3) reflect the total process of electrochemical oxygen reduction (ORR) [3].

However, a catalyst is required for the reactions to occur on the electrodes. The oxygen reaction catalyst (ORR) is critical for fuel cells. Its main purpose is to provide the required rate of electrochemical reaction at the boundary of the phase separation.

Platinum, deposited on fine carbon materials, is acquired widespread as a catalyst in fuel cells. But it has a number of shortcomings. First, the cost of platinum is quite high, and its resources are limited. Therefore, the price of electrodes with platinum exceeds 70% of the cost of the entire fuel cell. Second, platinum catalysts are easily and irreversibly poisoned with carbon monoxide and hydrogen sulfide, which inevitably are present as impurities on an industrial scale. Third, existing platinum catalysts have low selectivity in catalytic processes, both cathode and anode [4].

Therefore, fuel cells with platinum catalysts cannot be considered as the only prospect for the widespread use of energy in the future. And, consequently, the preparation of highly efficient and inexpensive electrocatalysts without platinum or with reduced content is an actual task in modern energy.

30.2 The Classification and Principles of Working of Fuel Cells

Fuel cells are an autonomous source of energy independent of fossil fuels. In addition, the lack of combustion of fuel at high temperatures means the environmental purity of such devices. In addition to high productivity and efficiency, the process of producing electricity in a fuel cell is accompanied by a minimal impact on the environment, which is especially important in view of the serious deterioration of the overall environmental situation in the modern world.

Other advantages of fuel cells can be attributed to the following [5]:

- These are noiseless energy sources (the fuel cell itself does not have moving parts).
- The possibility of using different types of fuel.
- A wide range of capacities (from 1 to 10,000 kW).
- Rapid response to load variables.

- High reliability and safety of low-temperature devices.
- Modular design, which allows relatively easily to increase the capacity of already existing power plants with FC.

Most often, FC is classified by the type of electrolyte as a medium for the internal transport of ions. The nature of the electrolyte determines the operating temperature of the FC, from which, in turn, the choice of catalyst and auxiliary materials depends. There are five main types of FC [6], which are discussed below.

In solid-polymeric fuel cells (SPFCs), electrolyte is a proton-exchange polymer membrane. Currently, there are several different types of polymer membranes – fluorine-containing polymer, based on sulfonic acids polymers, membranes based on aromatic polymers (polyether ketones, polysulfones, polyether sulfones), and membranes based on polyimides and polyvinyl alcohols. Nafion perfluorinated electrolyte membranes (Du Pont Company) became the most widely used. An important property of such membranes is high proton conductivity in an oiled state, and therefore, for the effective operation of FC, it is necessary to select and adhere to the regime of optimal distribution of moisture (water management). The operating temperature is not higher than 100 °C, and the fuel is hydrogen, without CO contamination, to prevent poisoning of Pt catalyst. A solid fuel cell electrolyte is much easier to use than a liquid analogue. A thin platinum catalyst chemically activates the reaction on the electrodes. In the past, these devices were very expensive through platinum, but new technologies significantly reduced the thickness of the platinum layer, which allowed, accordingly, reducing the price.

In alkaline fuel cells (AFCs), a concentrated KOH solution immobilized in an asbestos matrix is used as an electrolyte. Depending on the alkali content, such FC can operate in the temperature range from 65 °C (35–50% by weight KOH) to 250 °C (~85% by weight KOH). The catalyst can be noble metals, Ni, or complex oxides. Alkaline FC must be protected from the influence of CO and CO_2; the first, as in the previous case, is a catalytic poison, and the second interacts with the electrolyte, changing its composition. Algal fuel cells are widely used in spacecraft. They were developed by NASA for use in the Gemini project and further used on Space Shuttle. AFCs are very effective, release only pure water after the reaction. However, these devices require the purest of hydrogen and oxygen and an electrolyte with KOH, which is very expensive.

In phosphoric acid fuel cells (PAFCs), the transfer of protons from the anode to the cathode is carried out in a concentrated solution of phosphoric acid (85–100% v/v), fixed on a carrier with SiC. The operating temperature of 150–220 °C provides high conductivity of the electrolyte. The catalyst is platinum. This kind of FC is commercially available, since 1992; PAFC has the potential for use in small, stationary power generation systems. They are known for their reliability, perfect work, and high efficiency. They can work on contaminated water spills. The world's largest phosphorus power plant works in Tokyo; its power is 11 MW.

In carbonate-fusible fuel cells (CFFCs), the electrolyte is a melt of a mixture of alkali metal carbonates in a ceramic matrix with $LiAlO_2$. At a temperature of about 600–700 °C, this melt is a good conductor of CO_3^{2-} ions. A fairly high working

temperature allows the use of fuel in the CFFC directly without any additional preparation and nickel – as a catalyst. Since CFFCs operate at a temperature of 650 °C, it is more expedient to use them on large stationary installations. They are especially useful in hospitals or in such buildings where there is a constant need for electric and thermal energy (heating or cooling).

In solid oxide fuel cells (SOFCs), electrolyte is a dense ceramic membrane with ZrO_2. For the appearance of sufficient oxygen-ion conductivity in this phase, it is necessary to heat up to temperatures of 600–1000 °C. Oxidation of fuel (H_2, CO, CH_4) occurs at the anode, which is a metal-ceramic composite Ni/ZrO_2 or Co/ZrO_2; complex oxides, which have an electron ($La_{1-x}Sr_xMnO_{3-\delta}$) or a mixed ($La_{1-x}Sr_xCoO_{3-\delta}$) conductivity, are used as a cathode. These fuel cells are most suitable for large stationary electric generators that can supply a factory or city with electricity.

The main performance characteristics of FC of different types are summarized in Table 30.1.

The greatest successes have been achieved in the field of membrane fuel cells (MFCs). Currently, one of the most promising fuel cells for wide application is solid polymers (SPFC), which have a high density of power and have reached the highest technological readiness. The main obstacle to their widespread use is still high cost compared to traditional energy-generating devices.

The main components of the fuel cell are anode, cathode, and electrolyte. Anode provides fuel in the form of combustible gas (hydrogen, hydrocarbon compounds, CO, etc.), where the catalyst dissociates fuel molecules into cations. At the same time, an oxidizing gas (oxygen, air) is fed to the cathode. At the cathode is the reaction of oxygen recovery, while it is ionized. Anions of oxygen pass through a dense ceramic electrolyte to the anode. At an anode, there is a reaction of oxidation of fuel, which involves cations of fuel and oxygen anions. As a result of the reaction, electrons and heat energy are released. Also, the reaction products are water vapor (using pure hydrogen) or water vapor and carbon dioxide (with hydrocarbon fuels) [8] (Fig. 30.1).

The catalytic layer is one of the main components of fuel cells. It is a thin (5–20 μm) gas-permeable layer containing a fine-dispersed catalyst with a developed surface. On the one hand, the catalytic layer adjoins the proton conductive membrane and on the other hand, to the gas diffusion layer.

Platinum and metals of platinum group (MPGs) are commonly used to catalyze the oxidation of hydrogen, as well as the recovery of oxygen occurring in fuel cells.

The high cost and scarcity of metals make, however, the use of pure metal catalysts unprofitable and require a reduction in their number with the maximum effectiveness of their use. This is achieved by the use and development of new catalysts on carriers. The carrier should be cheap and have electrical conductivity and sufficient chemical and electrochemical stability. In addition, the catalytic bed should have good gas permeability and provide good contact with the proton-exchange membrane. The specified requirements are satisfied with carbon materials.

Table 30.1 The main performance characteristics of FC of different types [7]

FC type	SPFC	L	PAFC	CFFC	SOFC
Temperature, °C	80–100	65–250	150–220	600–1000	600–1000
Material of anode	Pt/C, Pt-Ru/C	Pt/C, Pt-Co/C	Pt/C, Pt-Ru/C	Ni-Al, Ni-Cr	Ni, NiO
Material of cathode	Pt/C	Pd/C Ni (Pt)	Pt/C, Pt-WO_3/C	NiO, $LiFeO_2$	$LaSrMnO_3$
Electrolyte	Polymer membrane (ionomer)	KOH/NaOH on the career	H_3PO_4 on the career	$LiKCO_3$, $LiNaCO_3$ on the career	ZrO_2, CeO_2, Y_2O_3
The range of optimal capacities, kW	0.01–100 kW	~ 100 kW	~ 100 kW	≥1 MW	≥1 MW
Resource, h	$\leq 2 \cdot 10^4$	$\leq 10^4$	$\leq 5 \cdot 10^4$	$\leq 2 \cdot 10^4$	$\leq 6 \cdot 10^4$

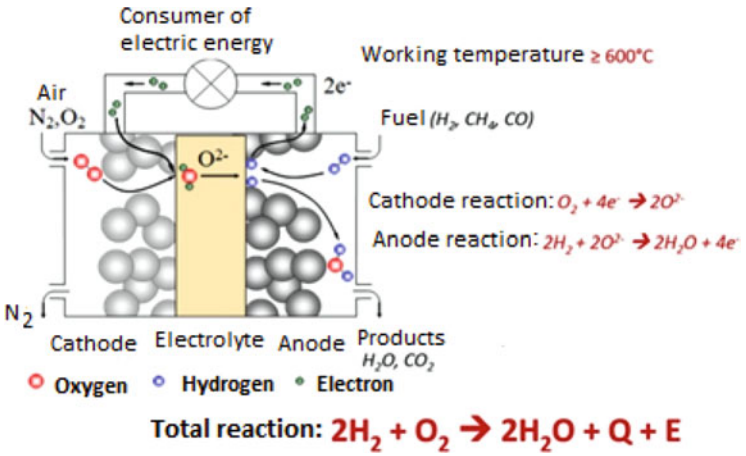

Fig. 30.1 The principle of work on the example of a ceramic fuel cell [8]

30.2.1 Generators of Hydrogen Based on Sodium Borohydride

The usage of hydrogen generators allows you to obtain H_2 directly at the site of its use, eliminating the problems of its storage, and transportation. Physical methods of hydrogen storage in the form of cryogenic liquid or compressed gas in most cases are ineffective (low volume density, high energy consumption, the ability to evaporate), and also insufficiently comfortable and safe (explosive gas under high pressure); therefore, the storage of hydrogen in the state of chemical compounds (hydrocarbons, water, hydrides) is an interesting and promising alternative [9].

In the creation of such sources of hydrogen for mobile power installations on the basis of fuel elements in recent times, special attention is paid to binary and complex hydrides as a compact form of storage of hydrogen [10, 11].

The reasons for the use of hydrides as a hydrogen source are the high volume density of hydrogen in hydrides and the relative ease of its production from these compounds. Among hydrides, sodium borohydride ($NaBH_4$) has a special place due to the high content of H_2 (10.8% by weight), an acceptable price, and stability of its alkaline solutions. The process of catalytic hydrolysis of sodium borohydride is a promising way of obtaining high-purity hydrogen, with half of hydrogen released from water [12, 13]:

$$NaBH_4 + 2H_2O \overset{kat}{\rightarrow} NaBO_2 + 4H_2. \tag{30.4}$$

The usage of catalysts ensures hydrogen production in the temperature range from – 40 °C to +85 °C, accelerates the process of generation of H_2, prevents the formation of by-products, and also makes it easy to control the process of hydrogen generation, stop it, and start it at the consumer's request.

At present, an important task is to create new catalytically active materials for use in portable hydrogen generators based on sodium borohydride. In the proposed generators, expensive catalysts based on platinum group metals are used [14–17]. For this reason, the most relevant are studies aimed at reducing their content in catalysts or replacements for transition metals.

According to the literature, the most promising are catalysts based on amorphous cobalt borides [18, 19]. However, because of the applied nature of most works, the results obtained are not systematized, and the reasons for most of the revealed patterns remain unpublished. The results obtained by different authors are incorrectly compared because of the difference in the conditions of experiments.

Therefore, there is an active search for catalysts of the hydrolysis process of sodium borohydride. The catalytic activity of acids [20] and noble [21, 22] and transition metals [22, 23] is shown.

30.3 Hydrogen Peroxide as the Oxidizer for FC

Fuel cells designed for use in non-atmospheric air, for example, in space or at the bottom of reservoirs, require liquid or compressed O_2 as a cathode oxidizer.

The O_2 transport tank significantly reduces oxygen density and safety standards for fuel cell systems. As these indicators are critical for fuel cells used as space or underwater energy sources, alternative oxidants other than O_2, such as H_2O_2, have been investigated.

Several types of fuel cells using H_2O_2 as an oxidizer have been developed in recent years, including methanol fuel cells with hydrogen peroxide [24–26], hydrogen peroxide and borohydride fuel elements [27–29], and fuel cells with transition metals and hydrogen peroxide [30–35].

The productivity of the cathode essentially depends on the nature of the cathode catalysts. Several types of catalysts for the H_2O_2 electrical conducting reaction include noble metals (Pt, Pd, Ir, Au, Ag, and a combination of these metals) [27–31, 36], macrocyclic complexes of transition metals (complexes of porphyrin Fe and Co, complexes of Cu triazine) [37], and other types such as $PbSO_4$ and Co_3O_4 [35, 38]. Among these types of electrical catalysts are the most active and stable catalysts of noble metals. However, precious metals, other than expensive, also catalyze the chemical decomposition of H_2O_2 to O_2. Therefore, it is necessary to look for electrical catalysts with low cost and greater resistance to the decomposition of H_2O_2.

A preliminary literature review [35] shows that Co_3O_4 nanoparticles have good activity and resistance to electro-catalytic reduction of H_2O_2 in alkaline solution.

30.3.1 Electrical Catalytic Activity of Cobalt-Containing Catalysts

Texas specialists suggest the use of platinum alloy with cobalt and copper. The new catalyst is an alloy of particles, the metal content of which varies from surface to nucleus: the surface of particles is enriched with platinum, and the core consists predominantly of copper and cobalt. The first tests of this catalyst showed an efficiency that exceeds a similar indicator of modern catalysts for fuel cells in 4–5 times. In addition, the nanocatalyst was significantly cheaper [39].

For the production of a catalyst, deposited on a graphite electrode, metal particles were placed in an acid solution and subjected to cyclic effects of alternating voltage. Less noble metals, especially copper, dissolved from the surface, leaving it enriched with platinum. The core had the same composition as the original alloy.

Moreover, formed as a result of electrochemical etching of copper and cobalt, voids on the surface of the particles resulted not only in the enrichment of the surface with platinum but also in a significant increase in the surface area of the catalyst. However, the increase of the catalyst's efficiency by 4–5 times compared to pure platinum catalyst, according to Strasser, cannot be explained solely by an increase in surface area.

Computer calculations have shown that the distance between the platinum atoms in the enriched shell is shorter compared with the same distance in pure platinum. Such "compressed" state is fixed with the help of enriched cobalt and copper core. The shortened interatomic distance platinum promotes a more readily adsorption of oxygen. This, apparently, changes the electronic structure of the shell so that the process of transferring an electron to the formation of a negatively charged molecule of oxygen becomes much simplified [39].

A new material based on graphene has been developed at Brown University (Rhode Island), which is capable of serving as an almost effective catalyst of the oxygen-reducing reaction, as well as platinum, but at the same time it is more stable. This material is a graphene sheet coated with cobalt nanoparticles and its oxide [40].

A number of scientists have succeeded in reducing the content of platinum in catalysts, but at the very least to abandon its use has still not succeeded.

The cobalt catalyst described in the article for the online edition of Angewandte Chemie was the first alternative solution that does not contain precious metals. Cobalt is a fairly widespread metal and costs many times cheaper than platinum.

Laboratory tests have shown that the new catalyst is slightly inferior to platinum at the initiation rate of the reaction, but during its course it restores oxygen at a faster pace than platinum. Graphene-cobalt material has also shown better resistance to degradation. After 17 h of operation, it retained 70% of initial efficiency, compared with 60% for platinum over the same period of time.

Scientists have used the self-assembly method to produce material, which provides the best control of the size, shape, and location of nanoparticles. To do this, they prepared two separate solutions for cobalt and graphene nanoparticles, and then carefully mixed them with the use of sound waves. Graphene material with

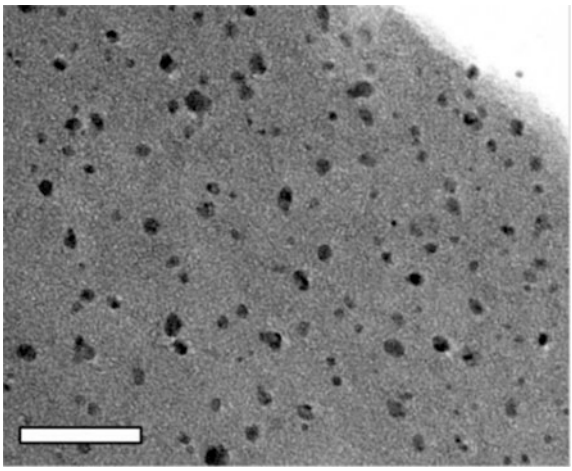

Fig. 30.2 Graphene with inlaid metal cobalt [40]

uniform cobalt inlaid was deposited from a solution in a centrifuge and dried. In the open atmosphere, the outer layers of atomic cobalt are oxidized, forming on each nanoparticle a shell protecting the cobalt core (see Fig. 30.2) [40].

The thickness of the shell was controlled by varying the residence time of the material in a state heated to 70 °C. Experimentally, it was found that in the best way the catalytic properties of the material are detected with a shell thickness of 1 nm [40].

The catalyst that was created in this way brought out fuel cells from the laboratory phase in their widespread commercial distribution.

30.3.2 Usage of Cobalt as Electrical Catalyst of FC

Cathodes containing cobalt and used in solid oxide fuel cells (SOFCs) are known for their ability to operate at high temperatures.

The cathode oxygen reaction (ORR) is important for a microbial fuel cell (MFC). A carbon-based catalyst, doped with nitrogen and cobalt (CoNC), was synthesized to initiate ORR in MFC. CoNC, prepared at 900 °C (CoNC-900), demonstrated high catalytic activity and excellent resistance (5.5% reduction after 10,000 cycles). Long-term performance tests have shown that the CoNC-900 MFC is very stable [41].

A platinum-free catalyst for oxygen reaction (ORR) and hydrogen oxidation reactions (HORs) was developed for a fuel cell with a proton-exchange membrane (PEMFC). The synthesized catalyst is two-functional and consists of cobalt with palladium and nitrogen. Palladium-cobalt nanoparticles of bimetallic alloy are scattered over graphite carbon nitride (Pd-Co/gCN), and they serve as an effective anode and cathode catalyst in a fuel cell with a proton-exchange membrane. The

inclusion of cobalt with palladium in the material changes the bond strength of the palladium-hydrogen (Pd-H) complex and promotes the initiation of HOR, which leads to a significant improvement in the super-potential at the anode, while cobalt, coordinated with nitrogen, mainly increases the activity of the ORR on the cathode in an acidic medium [42].

Another type of catalyst – a catalyst for cobalt hydroxide oxide (CoOOH-PPy-BP), modified polypyrrole – was obtained by chemical impregnation and used as a cathode catalyst in hydrocarbon fuel cells. CoOH surface oxygen vacancies provide favorable sites for O_2 uptake, accelerating the activation of O_2. And electronic holes created due to vacancies of oxygen on CoOOH capture electrons from the anode, forming excited cationic states [$Co^{3+}+e^-$] [43].

The efficiency of the fuel element with borohydride (DBFC) depends both on the activity of the anode catalyst and on the hydrolysis of borohydride. Anode Co_3O_4 catalysts from different sources of cobalt were investigated, and it was shown that the catalytic activity of Co_3O_4 was related to its microstructure, which was based on the precursor. The maximum power was 40, 62, and 28 $mW{\cdot}cm^{-2}$ DBFC with an anode of $CoCl_2$ and a Co_3O_4 catalyst (denoted DBFC-A), Co $(NO_3)_2$ (denoted DBFC-B), and $Co(CH_3COO)_2$ (denoted DBFC-C), respectively. DBFC-A showed good voltage stability with a specific capacity of 720 $mA{\cdot}g^{-1}$ and the highest amount of electron transfer [44].

A new three-dimensional (3D) porous nickel-cobalt film (Ni-Co) is successfully applied to nickel foam and is further used as an effective anode for a fuel cell containing urea and hydrogen peroxide (DUHPFC). Schematic principle of this fuel cell is shown in Fig. 30.3. By changing the ratio of moles of cobalt/nickel, an anode of polypropylene Ni-Co/Ni was obtained with a ratio of 80% in terms of the best efficiency [45].

Electrodeposition of cobalt on ferrite stainless steel plays an important role in reducing chromium poisoning on the cathode side of solid oxide fuel cells (SOFCs). The electrochemical activity between $La_{0.6}Sr_{0.4}Co_{0.8}Fe_{0.2}O_3$ (LSCF) and stainless steel with cobalt coating in the atmosphere at 700 °C was investigated. Thus, the formed Co_3O_4 layer blocks the chromium migration [46].

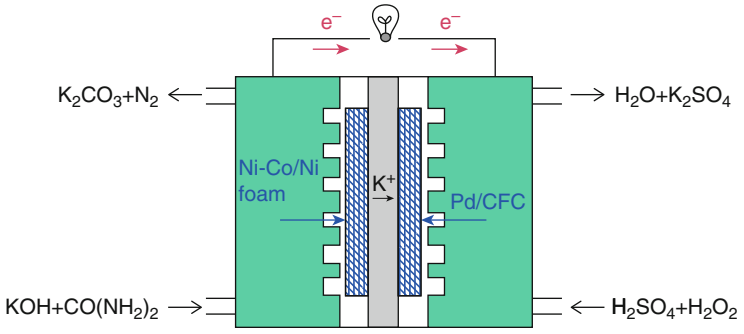

Fig. 30.3 Schematic representation of the fuel cell [45]

30.3.3 Investigation of Co as Anode for Li-Ion Batteries

The main cathode material of lithium-ion batteries is lithium cobalt oxide (or lithium cobaltate), lithium manganese oxide (also known as spinel or lithium manganate), lithium phosphate lithium, and lithium nickel manganese cobalt (NMC) and lithium nickel cobalt alumina (NCA) [47]. Various materials, including silicon-based alloys, are also used as anode. Nanostructured lithium titanate, as an anode additive, shows a promising life cycle, excellent low temperature characteristics, and excellent safety [47].

In order for the battery voltage to be sufficiently large, Japanese researchers used as active material a positive electrode of cobalt oxides. Cobalt oxide has a potential of about 4 V relative to the lithium electrode, so the operating voltage of the Li-ion battery has a characteristic value of 3 V and above [48].

Lithium-ion battery design with high energy storage and high efficiency is a subject of enhanced research interest, which is of key importance for large-scale applications and further commercialization.

Conventional lithium-ion batteries are expensive and have stability problems that restrict their practical use. In search of cheaper and more secure Li-ion batteries, the concentration gradient method is used to obtain $LiNi_{0.9}Co_{0.1-x}Ti_xO_2$ ($0.02 \leq x \leq 0.05$) cathode materials enriched on the surface of Co and Ti, which demonstrate a decrease in oxygen loss and improvement of structural stability. The material with the best characteristics ($x = 0.04$) shows a discharge capacity of 214 $mAh{\cdot}h^{-1}$ in the range of charge voltage/discharge 3.0–4.3 V (versus Li/Li^+) and perfectly stores up to 98.7% capacities after 50 cycles [49].

Organic-inorganic hybrids increase the choice of materials for Li-ion batteries due to the versatility of organic ligands. As an alternative to carboxylate-based ligands, Fe and Co methylenediphosphonate were successfully synthesized and tested as negative electrodes based on diphosphonates for Li-ion batteries [50].

Highly active Co/Mn-1,4,5,8-naphthalene tetracarboxylate (Co-NTC or Mn-NTC) was synthesized using a simple rheological phase method with NTCDA. This complex of Co-NTC or Mn-NTC can be spontaneously burned in ambient air to produce nanosized metal oxide. The cyclic leveling of the charge showed that the Co-NTC or Mn-NTC combustion product (used as anode for lithium ion batteries) provides high discharge and charge output power and provides excellent battery stability [51].

A promising anode material for high-performance lithium-ion batteries (LIBs) may also be silicon (Si), but it is rapidly erased due to strong volumetric expansion during the introduction/removal of Li. To mitigate structural deterioration, Si was doped with various metal sources, but the resulting materials showed low electrical conductivity. To solve this contradictory problem, a new nanocomposite of graphene oxide (rGO) Si/Co-$CoSi_2$/rGO has been developed by mechanical mixing of Si nanoparticles, Co_3O_4 microparticles, and rGO nanowires with subsequent carbon-forming restoration. The proposed nanocomposites demonstrated a high specific

capacity of 952 $mAh \cdot h^{-1}$ with a preservation of 79.3% of the capacity after 80 cycles of charge/discharge at a current density of 100 $mA \cdot g^{-1}$ [52].

The analysis of literary sources shows that progress in the development of electrochemical energy is largely determined by the successes in the development of active and stable nanomaterials for cathodes and anodes of fuel cells. However, the high cost and scarcity of metals make the use of pure metal catalysts unprofitable and require a reduction in their number with the maximum effectiveness of their use. This is achieved by the use and development of new catalysts on carriers.

Consequently, the necessity to create inexpensive, stable, and efficient electrocatalysts is an urgent task of today, the solution of which will be of considerable interest in the theoretical and practical aspects.

References

1. Chang Y et al (2018) Humidification strategy for polymer electrolyte membrane fuel cells – a review. Appl Energy 230:643
2. Majlan E et al (2018) Electrode for proton exchange membrane fuel cells: a review. Renew Sustain Energy Rev 89:117
3. Archer SA et al (2018) Systematic analysis of biomass derived fuels for fuel cells. Intern J Hydrogen Energy 230:643
4. Dafalla A et al (2018) Stresses and their impacts on proton exchange membrane fuel cells: a review. International J Hydr Energy 43:2327
5. Priya K et al (2018) A comprehensive review on parameter estimation techniques for proton exchange membrane fuel cell modelling. Renew Sustain Energy Reviews 93:121
6. Santoro C et al (2018) Microbial fuel cells: from fundamentals to applications. A review. J Pow Sours 356:225
7. Ying Y et al (2018) Silica-related membranes in fuel cell applications: an overview. International J of Hydrn Energy 43:16068
8. Tarasov BP (2006) Problemy i perspektivy sozdaniya materialov dlya hraneniya vodoroda v svyazannom sostoyanii. Al'ternativnaya ehnergetika i ehkologiya 2:11. (in Russian)
9. Orimo S et al (2007) Complex hydrides for hydrogen. Chem Rev 107:4111
10. Tarasov BP et al (2005) Metody hraneniya vodoroda i vozmozhnosti ispol'zovaniya metallogidridov. Al'ternativnaya ehnergetika i ehkologiy 12:14
11. Schlesinger H et al (2003) Sodium borohydride, its hydrolysis and its use as a reduction agent and in the generation of hydrogen. J Am Chem Soc 75:215
12. Galli S et al (2010) Development of a compact hydrogen generator from sodium borohydride. Int J Hydrog Energy 35:7344
13. Gervasio D et al (2005) Room temperature micro-hydrogen-generator. J Power Sources 149:15
14. Kojima Y et al (2004) Development of 10 kW-scale hydrogen generator using chemical hydride. J Power Sources 125:22
15. Hirscher M (2010) New materials for future energy storage / M. Hirscher. In: Handbook of hydrogen storage. – 2010. – P, pp 126–128
16. Demirci U et al (2010) Cobalt in $NaBH_4$ hydrolysis. Phys Chem Chem Phys 12:14651
17. Muir S et al (2011) Progress in sodium borohydride as a hydrogen storage material: development of hydrolysis catalysts and reaction system. Int J Hydrogen Energy10 36:5983
18. Chandra M (2006) Dissociation and hydrolysis of ammonia-borane with solid acids and carbon dioxide: an efficient hydrogen generation system. J Power Sources 159:855

19. Xu Q et al (2007) Room temperature hydrogen generation from aqueous ammonia-borane using noble metal nano-clusters as highly active catalysts. J Power Sources 168:135
20. Umegaki T et al (2009) Boron-and nitrogen-based chemical hydrogen storage materials. Int J Hydrog Energy 34:2303
21. Patel N et al (2010) Nanoparticle-assembled Co-B thin film for the hydrolysis of ammonia borane: a highly active catalyst for hydrogen production. Appl Catal 95:137
22. Tong D et al (2010) Magnetically recyclable hollow Co-B nanospindles as catalysts for hydrogen generation from ammonia borane. J Mater Sci 45:862
23. Prater D et al (2003) Energy density of a methanol/hydrogen-peroxide fuel cell. Appl Energy 74:135
24. Bewer T et al (2004) Novel method for investigation of two-phase flow in liquid feed direct methanol fuel cells using an aqueous H_2O_2 solution. J Pow Sources 125:1
25. Sung W et al (2007) Membraneless microscale fuel cell using non-noble catalysts in alkaline solution. J Pow Sources 172:198
26. Gu L et al (2007) Cathode electrocatalyst selection and deposition for a direct borohydride/hydrogen peroxide fuel cell. J Pow Sources 73:77
27. Miley G et al (2007) Direct $NaBH_4/H_2O_2$ fuel cells. J Pow Sources 165:509
28. Raman R et al (2004) High output voltage direct borohydride fuel cell. Electrochem Sol Lett 7:488
29. Yang W et al (2006) Nanostructured palladium-silver coated nickel foam cathode for magnesium–hydrogen peroxide fuel cells. Electrochim Acta 52:9
30. Yang W et al (2006) Nanostructured silver catalyzed nickel foam cathode for an aluminum–hydrogen peroxide fuel cell. Electrochim Acta 160:1420
31. Medeiros M et al (2004) Magnesium-solution phase catholyte semi-fuel cell for undersea vehicles. J Pow Sources 136:226
32. Brodrecht D et al (2003) Aluminum-hydrogen peroxide fuel-cell studies. Appl Energy 74:113
33. Hasvold O et al (2006) Power sources for autonomous underwater vehicles. J Pow Sources 162:935
34. Cao D et al (2008) Catalytic behavior of Co_3O_4 in electroreduction of H_2O_2. J Pow Sources 179:87
35. Medeiros M et al (2010) Optimization of the magnesium-solution phase catholyte semi-fuel cell for long duration testing. J Pow Sources 96:236
36. Liu H et al (2006) Electrocatalytic reduction of O_2 and H_2O_2 by adsorbed cobalt tetramethoxyphenyl porphyrin and its application for fuel cell cathodes. J Pow Sources 161:743
37. Raman R et al (2015) Electro-reduction of hydrogen peroxide on iron tetramethoxy phenyl porphyrin and lead sulfate electrodes with application in direct borohydride fuel cells. J Appl Electrochem 35:1157
38. https://www.gazeta.ru/science/2007/10/25_a_2263849.shtml
39. http://ko.com.ua/kobalt_s_grafenom_mozhet_vytesnit_iz_toplivnyh_jelementov_doroguyu_platinu_67429
40. Tang X et al (2017) Cobalt and nitrogen-doped carbon catalysts for enhanced oxygen reduction and power production in microbial fuel cells. Electrochim Acta 247:193
41. Ghosh A et al (2017) Palladium-nitrogen coordinated cobalt alloy towards hydrogen oxidation and oxygen reduction reactions with high catalytic activity in renewable energy generations of proton exchange membrane fuel cell. Appl Energy 208:37
42. Wang J et al (2017) Vacancy-assisted oxygen reduction reaction on cobalt-based catalysts in direct borohydride fuel cell revealed by in-situ XAFS and XRD. Electrochim Acta 254:72
43. Ma J et al (2017) Effect of cobalt precursors on Co_3O_4 anodic catalyst for a membrane-free direct borohydride fuel cell. J Alloys Compounds 724:474
44. Gokuladeepan P et al (2018) Effect of annealing temperature on oxygen reduction reaction of reduced graphene oxide incorporated cobalt oxide nanocomposites for fuel cell applications. Appl Surf Scie 449:705

45. Garcia E et al (2013) The electrochemical behavior of cobalt electrodeposits on 430 stainless steel as solid oxide fuel cell interconnect. Surf Coat Technol 235:10
46. http://keeppower.com.ua/li-ion-article
47. Osamah Siddiqui O et al (2018) A review and comparative assessment of direct ammonia fuel cells. Therm Scie Engine Progr 5:568
48. Ko H et al (2017) Co/Ti co-substituted layered $LiNiO_2$ prepared using a concentration gradient method as an effective cathode material for Li-ion batteries. J Power Sour 372:107
49. Bizon B et al (2018) Real-time strategies to optimize the fueling of the fuel cell hybrid power source: a review of issues, challenges and a new approach. Renew Sustain Energy Revi 91:1089
50. Schmidt S (2017) Fe and Co methylene diphosphonates as conversion materials for Li-ion batteries. J Power Sour 342:879
51. Han X et al (2017) Preparation of highly activated Co/Mn-1,4,5,8-naphthalenetetracarboxylate and its combustion product as anodes for Li-ion batteries. J Electroan Chem 802:89
52. Park A et al (2017) Si/Co-$CoSi_2$/reduced graphene oxide ternary nanocomposite anodes for Li-Ion batteries with enhanced capacity and cycling stability. J Alloys Comp 724:1134

Chapter 31
Synthesis and Study of Methacrylic Monomers and Polymers on the Basis of Aurones

Nataliia Iukhymenko, Anton Martynes-Harsiia, Oksana Kharchenko, Vitaliy Smokal, Oksana Krupka, and Aleksiy Kolendo

31.1 Introduction

The constant expansion of the areas of use of polymer materials, increase of requirements to their operational characteristics, and efficiency and ecological harmlessness raise the task of increasing their resistance to the action of external factors: high temperatures, oxygen, light, ozone, radiation, and others. The question of thermostability of polymers and the search for ways to increase it are always possible, because they arise at each stage of the existence of polymeric materials—in their production and storage and in the processing of products and further use. Research on the aging and stabilization of polymers, in particular, polystyrene (PS), which is widely used in various industries, is an urgent task and has a practical focus on finding new efficient and relatively inexpensive stabilizers [1–4].

There are many methods of polymer stabilization, the traditional method of mechanical mixing and methods of covalent adding of the application, which methodically simplifies the input of the stabilizer and eliminates such undesirable phenomena as effervescence or volatility of the stabilizer [5].

It was proved that the molecular structure of the antioxidant first of all has to ensure its high reactivity in the presence of mutual peroxidation of ROO• and high stability of the formed radicals. The effectiveness of phenolic antioxidants increases with the introduction of substituents into the phenol molecule, which reduce the

N. Iukhymenko (✉)
Department of Chemistry, Taras Shevchenko National University of Kyiv, Kyiv, Ukraine

Faculty of Chemistry, Macromolecular Chemistry Department, Taras Shevchenko National University of Kyiv, Kyiv, Ukraine

A. Martynes-Harsiia · O. Kharchenko · V. Smokal · O. Krupka · A. Kolendo
Department of Chemistry, Taras Shevchenko National University of Kyiv, Kyiv, Ukraine

© Springer Nature Switzerland AG 2019

O. Fesenko, L. Yatsenko (eds.), *Nanophotonics, Nanooptics, Nanobiotechnology, and Their Applications*, Springer Proceedings in Physics 222,
https://doi.org/10.1007/978-3-030-17755-3_31

polarity of the OH bond, reduce the ability to form hydrogen bonds, or increase the stability of the phenoxyl radical. The inhibitory activity of amines is influenced by substituents in the para position, but the inhibitory activity still depends on the effect of σ-π conjugation in the molecule, namely, during its growth, the mobility of hydrogen atoms increases, and the effectiveness of the stabilizing action of amines increases. For thermal stabilization of PS in the industry most often used diamines; with mechanical mixing of PS with small quantities.

Interest in aurones is versatile, on the one hand, the production of new synthetic derivatives possessing pharmaceutical properties and, on the other hand, as inhibitors of the degradation process for PS.

In the works [6–9], the stabilizing effect of some applications based on amino derivatives, with their covalent introduction on the destruction of special-purpose vinyl polymers, is shown. In this paper, we will verify that aurones have properties that inhibit the process of PS destruction.

The destruction of polymeric materials can be significantly slowed down by introducing appropriate stabilizers, which do not significantly affect the technological regimes of polymer synthesis and the specific properties of polymeric materials.

31.2 Experimental

^{1}H NMR (400 MHz) spectra were recorded on a Mercury (Varian) 400 spectrometer. Chemical shift is in ppm from the internal standard tetramethylsilane.

The thermal behavior of the obtained polymeric samples was investigated by dynamic thermogravimetric analysis on the TA Q 600 STD (TA Instruments) thermal analyzer and by the differential scanning calorimetry method on the Thermal Analyzer 1090 (DuPont) equipped with the DTA/DSC-910 (DuPont) module in the temperature range of 20–600 °C at a heating rate of 10 deg./min in the air atmosphere. Intakes of samples were 5–10 mg.

Standard distillation procedures were performed for triethylamine and THF just prior to use. All other reagents and solvents were commercially available and used as received.

The standard synthesis of aurone hydroxylation involves the condensation of the corresponding substituted 3-(2H)-benzofuranone (1), with arylaldehydes (2) in hot alcoholic acid or basic conditions (Scheme 31.1).

The reaction above leads to a high yield and rapid formation (10–15 min) of aurones in mild conditions. In the condensation of active methylene groups with carbonyl compounds on a solid substrate, the reaction proceeds very well, even on ordinary neutral aluminum oxide. A number of new compounds with different functional groups were synthesized according to the scheme.

(2Z)-2-(4-hydroxybenzylidene)-1-benzofuran-3(2H)-one. The yellow and orange crystals were obtained, m.p. 247 °C, yield 80%.

1H NMR (400 MHz, DMSO-d6), δ, ppm: 6.9 (1H, s), 7.3 (2H, t, H-3′, 5′), 7.6 (2H, m, H-5, 7), 7.8 (2H, m, H-4, 6), 8.2 (2H, m, H-2′, 6′), 10.9 (1H, s).

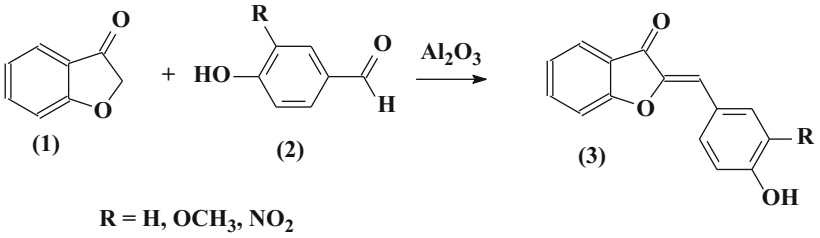

Scheme 31.1 Synthesis of hydroxylated auron

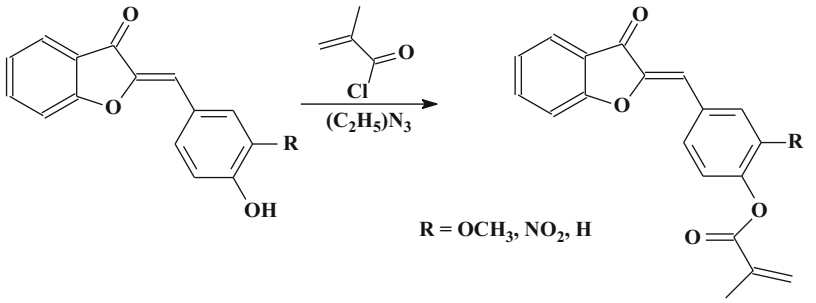

Scheme 31.2 Synthesis of aurones methacrylate monomers

(2Z)-2-(4-hydroxy-3-nitrobenzylidene)-1-benzofuran-3(2H)-one. The yellow-orange crystals were obtained, m.p. 183 °C, yield 86%.

1H NMR (400 MHz, DMSO-d6), δ, ppm: 7.0 (1H, s), 7.25 (1H, t, H-5), 7.3 (1H, t, H-7), 7.5 (1H, d, H-5′), 7.8 (2H, t, H-4, 6), 8.2 (1H, d, H-6′), 8.5 (1H, t, H-2′), 11.7 (1H, s).

(2Z)-2-(4-hydroxy-3-methoxybenzylidene)-1-benzofuran-3(2H)-one. The yellow-orange crystals were obtained, m.p. 195 °C, yield 86%.

1H NMR (400 MHz, DMSO-d6), δ, ppm: 3.85 (3H, s, OCH_3), 6.9 (1H, s), 7.0 (1H, t, H- 7), 7.3 (1H, t, H-5), 7.6 (3H, m, H-2′, 5′, 6′), 7.8 (2H, t, H-4, 6), 9.9 (1H, s).

(2Z)-2-(3-hydroxybenzylidene)-1-benzofuran-3(2H)-one. The yellow crystals were obtained, m.p. 187 °C, yield 39%.

1H NMR (400 MHz, DMSO-d6), δ, ppm: 6.9 (1H, s), 7.3 (2H, m, H-5, 7), 7.6 (2H, t, H-4′, 5′), 7.8 (2H, m, H-2′, 6′), 7.95 (2H, m, H-4, 6), 9.8 (1H, s).

General procedure for synthesis of 4′-methacryloxyaurones [10–12]. 3′-Hydroxyaurone (1 mol) was dissolved in 10 ml DMF and triethylamine (1 mol) was added to the solution (Scheme 31.2). The reaction mixture was kept in an ice water bath at 0 °C with stirring. Methacryloyl chloride (1.5 mol) was added drop wise. The reaction mixture was stirred for 4 h at 0 °C. After stirring the reaction mixture was precipitated in ice. Precipitate was filtered, washed with water, and dried. Solid precipitate was crystallized from mixture toluene-hexane (1:2).

4-[(Z)-(3-oxo-1-benzofuran-2(3H)-ylidene)methyl]phenyl 2-methylacrylate m.p. 91 °C, yield 76%.

1H NMR (400 MHz, DMSO-d6), δ, ppm: 2.0 (3H, s, CH_3), 5.9 (s, -C=CH (cis)), 6.3 (s, -C=CH (trans)), 7.0 (1H, s), 7.35 (3H, m, H-3′, 5′, 7), 7.6 (1H, m, H-5), 7.8 (2H, m, H-4, 6), 8.1 (2H, t, H-2′, 6′).

2-nitro-4-[(Z)-(3-oxo-1-benzofuran-2(3H)-ylidene)methyl]phenyl 2-methylacrylate m.p. 183 °C, yield 86%.

1H NMR (400 MHz, DMSO-d6), δ, ppm: 2.1 (3H, s, CH_3), 6.0 (s, -C=CH (cis)), 6.35 (s, -C=CH (trans)), 7.1 (1H, s), 7.45 (2H, m, H-5, 7), 7.7 (1H, t, H-5), 7.8 (2H, t, H-4, 6), 8.75 (1H, t, H- 6′), 8.6 (1H, t, H-2′).

2-methoxy-4-[(*Z*)-(3-oxo-1-benzofuran-2(3*H*)-ylidene)methyl]phenyl 2-methylacrylate m.p. 105 °C, yield 79%.

1H NMR (400 MHz, DMSO-d6), δ, ppm: 2.15 (3H, s, CH_3), 3.85 (3H, s, OCH_3), 5.85 (s, -C=CH (cis)), 6.4 (s, -C=CH (trans)), 6.95 (1H, s), 7.35 (2H, m, H-5,7), 7.7 (3H, m, H-2′, 5′, 6′), 7.8 (2H, t, H-4, 6).

3-[(Z)-(3-oxo-1-benzofuran-2(3H)-ylidene)methyl]phenyl 2-methylacrylate m.p. 110 °C, yield 61%.

1H NMR (400 MHz, DMSO-d6), δ, ppm: 2.0 (3H, s, CH_3), 5.9 (s, -C=CH (cis)), 6.35 (s, -C=CH (trans)), 6.95 (1H, s), 7.1 (1H, d, H-4′), 7.15 (1H, m, H-7), 7.55 (1H, d, H- H-5′), 7.75 (2H, m, H- 2′, 6′), 7.9 (2H, m, H-4, 6).

In order to study the polymerization capacity of new monomers, we investigated the kinetics of radical thermo-initiated homopolymerization of new monomers by dilatometric method in 10% solutions in DMF at 80 °C and in the presence of 1% AIBN from the mass of the monomer in argon.

On the basis of kinetic data, growth rates, reduced velocity, and total polymerization rate constants are calculated, as shown in Table 31.1. As shown in Fig. 31.1 and Table 31.1, all new monomers are polymerized in solution at initiation of AIBN at a higher rate than the unsubstituted phenylmethacrylate (PhMA), in addition to compound IIb (the nitro group inhibits the polymerization process). The m-isomer (Ib), in which there is no conjugation with the auronic fragment, polymerizes at a higher rate than the p-isomer. The monomer IIIb, which has a donor substituent in the m-position to the auronic fragment, has the fastest velocity of polymerization.

From Table 31.1, it is seen that all new methacrylates are more active in polymerization than unsubstituted phenyl methacrylate, except for the nitride-containing derivative, which, possibly, acts as a moderator of the process of radical polymerization under these conditions. m-Methacrylate polymerizes at a faster rate than the p-isomer due to the lack of conjugation with the aurono fragment, and the most active is the p-methacrylate with a methoxyl substituent in the m- position to the auronic fragment.

Table 31.1 Kinetic parameters of thermo-initiated radical polymerization of monomers Ib–IVb and phenylmethacrylate (80 °C, 10% solution in DMF, 1% AIBN, argon)

The code of the monomer	Monomer	Conversion, %, (225 min)	Mr	$V_{re} \times 10^4$, s^{-1}	$V_g \times 10^5$, mol/l × s^{-1}	$K_\Sigma \times 10^4$, mol/l × s^{-1}
Ib	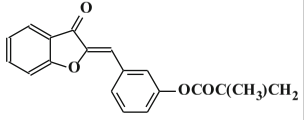	63	306	3.49	1.14	4.17
IVb	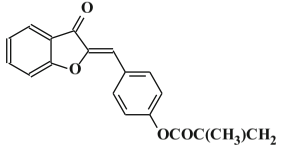	61	306	3.12	1.02	3.73
IIb	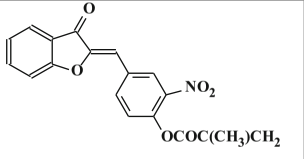	48	351	0.6	0.17	0.72
IIIb	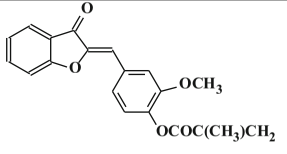	71	336	4.08	1.22	4.87
PhMA			162	0.61	0.37	1.1

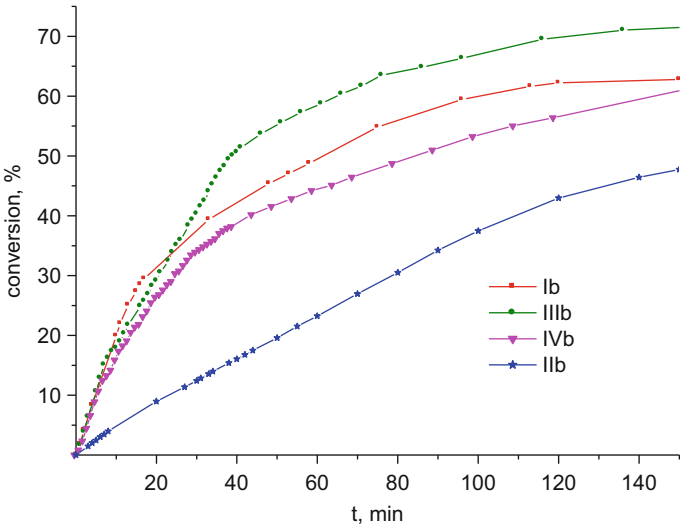

Fig. 31.1 Kinetic curves of radical homopolymerization of 10% monomers Ib–IVb solutions in DMF at 80 °C and 1% of AIBN (argon)

31.2.1 Polymerization

Polystyrene and modified samples were synthesized by free-radical polymerization according to well-known method [9–11]. The polymerization was carried out in 10 wt% DMF solution of monomers and was conducted using azobis (isobutyronitrile) (AIBN) as a free-radical initiator (1 wt% of monomer) at 78 °C for 16 h in a solution of ethyl acetate, in an argon atmosphere (Scheme 31.3). The purification of the yield polymers was carried out by double reprecipitation from ethyl acetate to isopropanol followed by drying to constant weight in vacuum.

31.3 Results and Discussion

Destruction of modified polystyrene was studied using drainage measurements. The figure shows thermogravimetric (TG) and DTG radical polystyrene degradation curves are obtained by copolymerization of polystyrene and polystyrene with the introduction of 3% auronium methacrylates at a heating rate of 10 deg./min [13–15].

It can be seen (see Fig. 31.2a and b) that the thermo-oxidative destruction of PS and its modified samples occurs in two stages: stage I at 250–430 °C and stage II at higher temperatures (370–550 °C). Stage I of thermal oxidative destruction of PS is accompanied by oxidation of the polymer and its depolymerization.

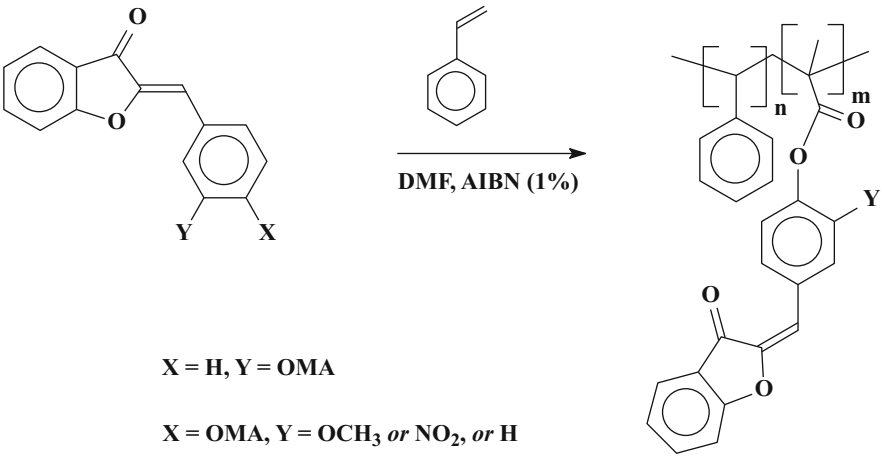

Scheme 31.3 Synthesis of aurones methacrylate copolymers

There are no special differences in the character of the TGA curves for PS and its modified samples, but the latter are more resistant to thermal oxidative degradation by reducing its intensity in the temperature range from 300 to 400 degrees (see curves TG and DTG) and increasing the temperature of the maximum decomposition rate on these stages at 13–48 degrees (DTG curves).

As can be seen from Fig. 31.2, the additions of methacrylates I–IV used do not change the nature of thermal oxidative degradation of PS, but they have different effects on the characteristic temperatures of the process: temperatures of 10%, 20%, and 40% of the mass loss—$T_{10\%}$, $T_{20\%}$, and $T_{40\%}$—and the temperature of the maximum speed of the process of destruction, T_{max} (see Table 31.1). The destruction of all samples begins at the same temperature, but modified first, it occurs somewhat slower. After losing 20% of the mass, the rate of destruction of a sample modified by application II becomes slightly less than for others (the value of ΔT increases from $T_{10\%}$ to $T_{40\%}$), and for other modified samples remain close to unmodified.

As can be seen from Fig. 31.2b, the temperature of the maximum decomposition rate of sample I in the first stage of the stage is the smallest (360 °C), sample II is slightly higher (363 °C), and sample III is even higher (373 °C). The highest temperature of the maximum rate of destruction is observed for sample IV, and is 382 °C. Interestingly, this sequence is antibatic to the rates of radical homopolymerization of the corresponding monomers (see Table 31.1).

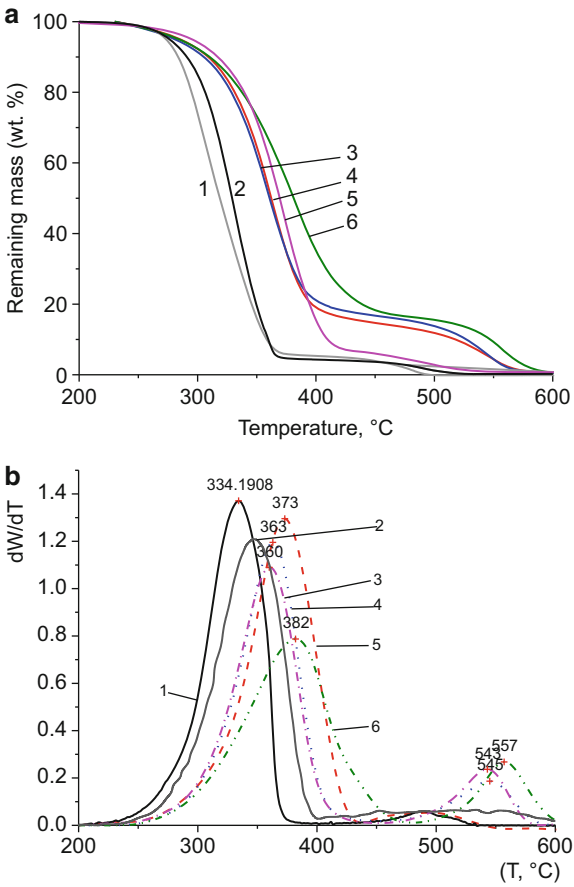

Fig. 31.2 Fragments of TG (**a**) and DTG (**b**) degradation curves in the atmosphere air of the PS (1), industrial polystyrene Styron (Switzerland) (2), PS-IIIb (3), PS-Ib (4), PS-IVb (5), and PS-IIb (6), when you enter 3% of the mole of the application

In general, modified polystyrene with the additions I–IV turned out to be more thermostable than the laboratory unmodified and industrial model PS of the STYRON brand. So, $T_{10\%}$ of the modified samples exceeds the suitable for STYRON PS by 22–34 degrees, and the application with the methacryl group in the n-position to the auronic fragment and with the nitro group turned out to be the most effective. That is, the latter can be offered for practical use in creating thermostabilized PS (Table 31.2).

Table 31.2 Characteristic temperatures for destruction of polystyrene samples

Sample	$T_{10\%}$, °C	$\Delta T_{10\%}$[a], °C	$T_{20\%}$, °C	$\Delta T_{20\%}$[a],°C	$T_{40\%}$, °C	$\Delta T_{40\%}$[a],°C	T_{max}, °C	ΔT_{max}[a],°C
PS - Styron	283	–	295	–	311	–	347	–
PS	291	0	307	0	323	0	334	0
m-isomer	305	14	329	22	352	29	363	29
O-CH_3	309	18	331	24	354	31	360	26
NO_2	310	19	337	30	369	46	382	48
p-isomer	317	26	340	33	362	39	373	39

[a]The difference between the values of the corresponding characteristic temperatures for the samples containing the application and the unmodified FP

31.4 Conclusions

By condensation of benzofuran-3-one with hydroxybenzaldehydes synthesized hydroxyaurones, by acylation of which with methacrylic acid chloride, new methacrylic monomers were obtained. The kinetics of radical thermo-initiated homopolymerization of new monomers by dilatometric method in 10% solutions in DMF was investigated. It is shown that all new methacrylates are more active in radical homopolymerization than unsubstituted phenyl methacrylate, except for the nitride-containing derivative, which, possibly, acts as a moderator of the process of radical polymerization under these conditions.

It was determined that the investigated additives, when covalently introduced into polystyrene, inhibit the process of its destruction. An antibate relationship has been revealed between the values of the effective rate constants of the radical homopolymerization of new monomers and the temperature of the maximum rate of destruction of polystyrene samples modified by these monomers.

It was shown that the most effective for thermal stabilization of polystyrene were applications with a methacryl group in the n-position to the auronic fragment and with the nitro group introduced into the last methacrylate in the m-position to the auronic fragment. That is, the latter can be offered for practical use in creating thermostabilized PS.

References

1. Nestorak I et al (2011) Investigation of inhibiting action mechanism of succinimidophenyl-methacrylate derivatives prepared by the Diels-Alder reaction on polystyrene decomposition. Mol Cryst Liq Cryst 536:208–214. https://doi.org/10.1080/15421406.2011.538609
2. Schwetlick K et al (2002) Antioxidant action mechanisms of hindered amine stabilizers. Polym Degrad Stab 78(1):35–40
3. Smoliak LY et al (2003) Estimation of parameters that correlate molecular structure of hindered amines with their stabilizing efficiency. Polym Degrad Stab 82(2):169–172
4. Boersma A (2006) Predicting the efficiency of antioxidants in polymers. Polym Degrad Stab 91(3):472–478
5. Ebdon JR et al (2000) Thermal degradation and flame retardance in copolymers of methyl methacrylate with diethyl(methacryloyloxymethyl)phosphonate. Polym Degrad Stab 70(3):425–436
6. Kolendo AYu et al (2009) Ukr. P. 41029. Promyslova Vlastnist', 8. (in Ukrainian)
7. Karabets Y et al (2014) Brominating of oxyphenylimides for enhancement of stabilizing processes Mol. Cryst Liq Cryst 590:90–96. https://doi.org/10.1080/15421406.2013.873852
8. Karabets Y et al (2017) Synthesis and investigation of bromine containing oxy- and Propionoxyphenylimides for polymers thermostabilization Mol. Cryst Liq Cryst 640:54–57. https://doi.org/10.1080/15421406.2016.1255512
9. Nestorak I et al (2008) Thermal stabilizing properties of maleimidophenylmethacrylates derivatives with substitutes of various molecular arhitectures in imide cycle. Mol Cryst Liq Cryst 497:299–306. https://doi.org/10.1080/15421400801921991

10. Kharchenko O et al (2016) Design, synthesis, and photochemistry of styrylquinoline-containing polymers. Mol Cryst Liq Cryst 640:71–77. https://doi.org/10.1080/15421406.2016.1255516
11. Smokal V et al (2018) Synthesis and photophysical properties of new styrylquinoline-containing polymers. Mol Cryst Liq Cryst 661(1):38–44. https://doi.org/10.1080/15421406.2018.1460236
12. Kharchenko O et al (2018) Reactivity and polymerisation ability of styrilquinaline containing metacrylic monomers. Chem Chem Technol 12(1):47–52. https://doi.org/10.23939/chcht12.01.047
13. Derkowska-Zielinska B et al (2018) Functionalized polymers with strong push-pull azo chromophores in side chain for optical application. Opt Mater 85:391–398. https://doi.org/10.1016/j.optmat.2018.09.008
14. Guichaoua D et al (2018) Functionalized methacrylic thiazolidinone polymer for optical applications. ICTON 8473860. https://doi.org/10.1109/ICTON.2018.8473860
15. Bourbigot S et al (2004) Kinetic analysis of the thermal degradation of polystyrene–montmorillonite nanocomposite. Polym Degrad Stab 84(3):483–492

Index

A
Acetaminophen (paracetamol), 263–269
Acrylic acid, 226, 227, 229
Acrylamide (AA), 226, 227, 229–232, 376, 377
Acrylonitrile (AN), 226, 229, 231, 232
Adsorption, 122, 209–215, 218–221, 226, 242, 244, 245, 249, 255, 305–335, 395, 413, 450
Adsorptive multilayer systems, 74, 75, 96, 431
Ageing, 257
Ag nanoparticles, 381, 417–428
7-Amino-Actinomycin (7AAD), 275, 278–280
Ammonium nitrate, 376, 377
Amorphous phases, 89, 241
Annealing, 31, 32, 88, 123, 394
Annexin, 275, 278–280
Anode material, 453
Apoptosis, 278–280
Atherosclerosis, 263

B
Band gap, 21, 22, 37–39, 41, 46, 89, 90, 92, 180, 182, 191
Band structure, 20, 24, 36–41, 310
Barriers, 9, 89, 173, 174, 177, 182, 247, 370
Binding energy, 173, 174, 177, 179–181, 189, 190, 192, 264, 265, 318, 319, 321
Biochar, 209–222
Bismuth, 20, 22–26, 28–45
Borides, 449
Boron-nitride nanotube, 325

C
Carbides, 399
Carbon nanotubes (CNT), 95–101, 145–162, 287, 290, 305–335, 399, 409–415
Catalyst, 64, 121, 127, 147, 148, 290, 390, 444–452, 454
Catalytic activity, 449–452
Cavitation erosion damage, 96, 360
Cementitious composites, 286–288, 291, 292, 294–297
Ceramics, 31, 58, 122, 222, 445, 446, 448
Chemical heat treatment, 31
Chemical sedimentation, 392
Chloride-fluoride melts, 31, 132, 133, 200, 229, 286, 394, 418, 459, 466
Cholesterol, 263–269, 399–406
Cobalt, 393, 449–453
Cobalt oxide, 453
Coherent domains (CD), 361, 362, 369–373
Coherent system, 372
Composite and nanostructure, 3–15, 88, 121, 190, 287, 288, 293, 307, 317, 322, 325, 326, 331–335, 359–373, 453
Composite's transparency, 95, 101
Composition, 20, 21, 23, 28, 36, 80, 84, 121, 122, 127, 132, 135, 136, 146, 149, 152, 161, 209, 239, 279, 290, 360, 368, 369, 376, 390, 437, 439, 450
Computer simulations, 399–406, 409
Condensation from gas phase, 28, 132, 211, 244, 365–367, 458, 466
Conductance spectra, 347–351

© Springer Nature Switzerland AG 2019

O. Fesenko, L. Yatsenko (eds.), *Nanophotonics, Nanooptics, Nanobiotechnology, and Their Applications*, Springer Proceedings in Physics 222,
https://doi.org/10.1007/978-3-030-17755-3

Conductivity, 9, 69, 146, 147, 155, 157–159, 162, 182, 238, 242–249, 310, 445, 446, 453
Contact interactions, 161, 227, 297, 307, 360
Co-precipitation, 28, 29, 31, 32, 389, 392, 395, 419
Core-shell nanoparticles, 287, 418, 423–426
Corrosion of steel, 14, 15
Corrosion resistance, 14, 15
Corrosion resistance catalytic activity, 14, 15
Coulomb and polarization interaction, 158, 176, 177, 190, 327, 328, 353, 354
Crystal growth, 28
Crystallization process, 3, 28, 31, 287
Crystal structure, 20, 21, 23, 28, 32–37, 73–85, 147, 390
Current density, 454
Currentless deposition, 3, 4, 8–12, 15, 83, 240, 295, 418

D
Degradation, 14, 121, 122, 127, 159, 273, 289, 395, 450, 462–464
Dendrites, 3, 4, 8, 11–15
Density functional theory (DFT), 37, 263–269, 306, 307, 310–316, 335
Desorption, 211, 214, 226–232, 242, 412
Dextran-graft-polyacrylamide, 64, 376, 377
DFT calculations, 315, 316
Dielectric loss, 431
Different orbitals for different spins, 341–356
Diffusion of Titanium, 12, 15, 67, 243, 296, 379, 402, 403, 405, 406, 446
Digital holographic microscopy, 168, 170
Dirac quasi-electron, 343, 363
Dispersion, 109, 117, 189, 255, 264, 265, 287, 291, 292, 294, 296, 311
Dispersion relation, 294

E
Effective mass, 174, 175, 177, 178
EHF, *see* Extended Hartree-Fock (EHF)
Elastic layered structures, 5, 104, 107–109, 119, 146, 239
Electrochemistry, 3, 4, 8, 9, 15, 213, 220, 221, 250, 306, 389, 444, 446, 450, 452, 454
Electrode capacitance, 213
Electrodeposition, 4, 8, 9, 12, 452
Electromagnetic potential, 372
Electron correlation, 342, 344, 345, 348, 350, 351
Electronic structure, 20, 21, 27, 37, 38, 161, 306, 310–320, 335, 347, 450
Electron microscopy, 4, 65, 211, 236, 379, 382, 420, 425
Entangled states, 361
Ethanol, 30, 394
Exchange interaction, 37, 219, 236–239, 371
Exciton states, 173–193
Extended Hartree-Fock (EHF)
  interaction, 345, 368–373
  radiation, 368, 372, 373

F
Fe_3O_4/Ag, 417–428
Fuel cells (FCs), 249, 443–454
Functionalization, 146, 148, 155, 159, 161, 162, 291, 292, 327, 329–331, 334, 335
Fundamental constants, 103, 104, 107, 114, 119

G
Glass, 13, 14, 28, 53, 66, 79–82, 84, 85, 100, 109, 110, 113, 114, 173, 174, 403
Gold nanoparticles, 64–65, 274
Graphene, 210, 287, 305, 308–313, 315–317, 320, 322, 323, 325, 331, 332, 334, 341–356, 413, 417, 450, 451, 453
Graphene quantum dot (GQD), 349–350
Graphite supporter, 210
Green chemistry, 418
Green's function (GF), 342–356
Growth constant, 286
Guided-mode resonance, 73

H
Hamiltonian, 175–178, 316, 343–345, 353, 354, 360
High temperature, 19, 28, 31–34, 36, 46, 88, 155, 211, 218, 432, 451, 457
High temperature electrochemical synthesis, 4
Holographic interferometry technique, 3–64
Humidity-sensitivity, 19, 73, 74, 78, 111, 112, 248, 249, 275, 286, 305
Hydrogels, 225–232, 375–385
Hydrogen binding, 264, 266, 316–320
Hydrogen generator, 448, 449
Hydrogen halide, 306, 311, 312, 316–320, 335
Hydroxide, 287, 395, 452

I
Ice, 211, 362, 371–373, 459
Inorganic nanoparticles, 74, 79, 375, 376
Interband and intraband absorption spectra, 189
Interface scattering, 31, 75, 80, 146, 242, 295
In vitro, 255–261, 420
In vitro cultivation, 255–261
Ion etching, 73
Ionic conduction, 25, 92
Ionic implantation, 122, 123, 127
Ionic melts, 28, 445
Ion track technology, 4, 15
Ion transport, 235–250
IR and Raman spectra, 264, 265
Iron, 198, 201, 203, 278, 287, 418, 419, 421, 428
Irradiation, 4, 5, 7, 8, 15, 63, 66, 122–127, 137–142, 145–162, 200, 290, 367, 368, 378, 380, 383, 384, 395, 418
IR-spectroscopy, 149, 216–218, 221

K
Kinetics, 23, 26, 27, 63, 132–134, 175, 182, 200–202, 204, 292, 293, 296, 460–462

L
Light reflection, 103, 112
Light-transmission factor, 96
Lipoproteins, 263
Liquid crystals, 132
Luminescence, 13, 19–46, 87, 174

M
Magnetic nanoparticles, 197–200, 204, 417, 421
Magnetic properties, 198, 393–396, 431–440
Magnetic relaxation, 199
Magnetite, 198, 287, 395, 417, 419, 421, 423–426
Mechanical properties, 106, 146
Mechanical-pulse treatment, 54
Membranes, 107, 108, 110–112, 114, 115, 205, 221, 222, 235–246, 248, 260, 273, 276, 279, 289, 378, 379, 399, 400, 406, 445–447
Mesenchymal stem cells (MSCs), 273–281
Microbiological evaluation, 209, 285–298
Mitochondria, 30, 203–206, 279–281
Mixed oxide system, 26, 28, 31, 33, 38, 230, 394, 435
mm-waves, 371, 373
Modification, 34–37, 40, 63, 95, 117, 131, 165, 221, 236, 241, 243–247, 249, 263, 287, 290, 291, 296, 396
Molar gas constant, 103, 106
Molecular anions, 26, 312, 315, 320–334
Molecular dynamics (MD), 372, 400, 409
Morphology, 3, 4, 8–10, 12, 15, 19–46, 124, 379, 384, 390, 392, 415, 420
Multilayer, 74, 75, 96, 431
Multiwall carbon nanotubes, 147–162, 308, 311, 313–314, 325, 331

N
Nanocoatings, 291
Nanocomposite(s), 74, 78–84, 96, 146, 225, 255–261, 287, 298, 375–385, 394, 419, 428, 453
Nanocomposite Material, 79, 80, 96, 287, 298, 375, 377, 379, 453
Nanocrystalline structure, 27, 32, 432, 435
Nanocrystals, 3, 29, 31, 32, 41, 89
Nanofertilizer, 225–232
Nanograins, 25, 27, 393, 434
Nano-heterogeneity, 369, 370, 372
Nanoindentation, 400
Nanomaterials, 27, 235, 255–258, 260, 261, 285–298, 305, 320–334, 417, 454
Nanoparticles (NPs), 27, 31–33, 42, 61, 62, 67, 69, 73–85, 198, 200, 204, 210, 225, 229, 235–250, 255, 256, 260, 273–281, 286–288, 290–293, 296–298, 375–385, 389–396, 417–428, 432, 449–451, 453
Nanopores, 218, 221, 235, 237
Nanoporous structure, 221
Nanopowder, 19–46
Nano-relief study, 5, 54, 73
Nanoscale layers, 37, 64, 87–92, 121–128, 214–216, 222, 274, 287, 292
Nanosized cluster, 237
Nanosized films, 92
Nanosized organic molecules, 209, 221, 227, 232
Nanostructured thin films, 90, 92
Nanostructures, 3–15, 88, 121, 288, 293, 296, 305, 307, 313, 317, 322–326, 332–335, 351, 359–373, 453
Nanotubes, 95–101, 145–162, 287, 289, 305–335, 399–406, 409–415
Near-surface water, 370
Necrosis, 278, 279, 281
Nematic phase, 413, 415
Nickel, 147, 148, 393, 446, 452, 453

NMR spin-lattice relaxation, 132, 135, 241, 458–460
Numerical simulations, 5, 77–78, 89, 90

O
Object recognition, 169
Oocyte-cumulus complexes (OCCs), 256, 257, 261
Ooxidation, 14, 15, 88, 126, 201, 203, 294, 382, 395, 424, 443, 446, 451
Optical absorption, 88, 90, 191323
Optical devices, 87, 103–109, 115, 118
Optical nonlinearity, 74
Optical phenomena, 87–92
Organic-inorganic nanocomposites, 79
Ovaries, 257, 260
Oxidation resistance, 451

P
Pattern formation, 10, 11, 26, 36, 63, 74, 79, 80, 82, 108, 111, 112, 147, 148, 309, 433, 434
Percolation, 146, 159, 160, 248
Percolation probability, 146, 159, 160, 248
Permittivity, 73–75, 174–178
Phase, 4, 9, 11, 12, 15, 25, 28–32, 34–36, 38, 40–42, 62, 74, 77, 89, 122, 146, 166–170, 189, 230, 231, 237, 239, 360–366, 368, 371, 372, 403, 406, 409–415, 432, 435, 440, 446, 453
Phase layers, 9, 35, 89, 362, 403, 406, 409, 413
Phase transformation of bentonite, 32, 42, 44
Phase transition, 230, 363, 366, 403, 413
Phosphate, 19–46, 210, 227, 244, 297, 453
Phospholipid bilayer, 399
Photocatalysis, 20, 121–127, 290, 295, 395
Photodynamic anticancer therapy, 204
Photoluminescence, 19, 20, 22, 33, 41, 87, 88, 91
Photonic crystals, 73–85, 106–111
Photo-sensitive polymer-based nanocomposites, 74
Photothermal therapy, 63, 417
pH-sensitive acrylic hydrogels, 225–232
Physicochemical geomechanics, 19, 103–119, 255, 421, 422
Plant extract, 390, 393, 432
Plasmonic nanostructures, 13–14
Plasmon resonances, 74, 384, 424, 425
Polyacrylamide (PAAG), 64, 69, 226, 229, 231, 232, 376–378
Polyethylene MWCNT, 147–157, 160–162, 313–315
Polymer based sensors, 73
Polymer composite, 145, 146
Polytetrafluoroethylene (PTFE), 95–100, 146, 213
Pore model, 5, 238, 242
Praseodymium, 43, 45, 46
Precise pressure measurement, 106
Pressure, 31, 34, 35, 103–119, 123, 148, 159, 210, 236–239, 244, 246, 249, 286, 363, 400, 448
Pulse current, 53, 54
Pulsed laser radiation, 65

Q
Quantum dots, 173–193
Quantum electrodynamics, 361
Quantum theory, 359, 362, 369, 373
Quasi-stationary states, 177–182, 191–193

R
Rapid hologram processing, 53–59, 165–170
Redox cycling, 64, 198, 203–205, 220
Reduction, 3, 64, 65, 97, 140, 146, 161, 244–247, 274, 287, 376–378, 382, 384, 418, 419, 425, 426, 439, 444, 446, 449, 454
Reflection, 40, 73, 75, 77, 78, 84, 88, 90–92, 103, 104, 106, 108–117, 148, 433, 434
RE^{3+} ions, 27, 33, 42–44
Reservoir filtration decreasing, 105, 106, 116, 449
Resistance, 4, 122, 146, 155, 157, 159–162, 198, 203, 242, 295, 449–451, 457
Resistivity, 19, 146, 149, 154–162, 431
Rheological anomaly, 453

S
Scanning electron microscopy (SEM), 6, 7, 9, 10, 12, 13, 15, 33, 34, 37, 122, 123, 125, 236, 379, 382, 384, 385, 420, 421, 425, 426
Silica gel, 28, 210, 243, 248, 287, 297
Silver nanoparticles, 273, 375–385, 419, 424, 425
Single wall carbon nanotubes, 148, 157, 308, 310
Sodium borohydride, 65, 376, 380, 448–449

Sol-gel, 31, 88, 239, 389, 392, 393, 395, 432, 433
Surface-enhanced Raman scattering (SERS), 3, 4, 14, 15, 417, 418
Solid matrix, 445
Solid oxide fuel cell (SOFC), 446, 447, 451, 452
Sorption, 211, 218, 225–232, 255, 295
Spectrophotometric analysis, 88, 96, 226, 379, 420
SPE-effect, 359–373
Spermatozoa, 256–258
Spin dynamics, 79–81, 84, 198–200, 203–206, 342, 344–346, 352, 363, 438
Spinel, 389–396, 431–433, 435, 439, 440, 453
Spinel ferrite, 431–433
Spouting of superfluid helium, 364, 365
Stainless steel foil, 121–127
Star-like copolymer, 69
Strengthened layer, 77, 121, 122, 199, 227, 232, 286, 325, 326, 381, 436, 452
Structural relaxation, 27, 44, 46
Structural transformations, 36
Structure, 3, 8–13, 15, 19–46, 69, 73–85, 104, 109–112, 121, 147, 150, 154, 159–162, 211, 214–216, 235–239, 241–242, 244–249, 289, 306, 308–316, 320–335, 347, 349, 352–354, 360–364, 376, 382, 390, 393, 399, 404, 417, 431, 432, 435, 457
Substrate, 3–5, 8, 9, 12–15, 53, 54, 75, 79–85, 88, 111, 227, 229, 241, 409, 410, 412, 413, 418, 458
Superfluid liquid helium, 363
Surface engineering, 3, 296
Surface morphology, 124
Surface treatment, 31, 79, 84, 123, 126, 127, 145, 161, 218, 221
Suspension, 200, 256, 287, 419, 420, 423, 426, 427
Swelling, 225–227, 229–232, 236–239, 244, 246, 247, 249, 378–382, 384
Synergistic mixtures, 286, 295
Synthesis methods, 27–33, 221, 239, 240, 392, 396, 418, 432

T
Technological equipment, 221, 307
Temperature, 4, 19, 23–28, 31–36, 41, 42, 46, 54, 56, 58, 87, 88, 104–108, 119, 122–127, 146, 149, 155–160, 174, 189, 199, 202, 210, 211, 218, 236, 239, 240, 248, 249, 274, 284, 286, 304, 360–364, 366, 372, 373, 378, 381, 393, 394, 400, 402, 404–406, 409, 410, 412–414, 424, 432–433, 445–448, 457, 458, 463–466
Template synthesis, 4
Ternary alloys, 121, 450, 451, 453
Thick films, 79–84, 88, 92
Thin film anodization, 5, 79, 90, 92, 400
Thin films, 5, 79, 90, 92, 400
Tight-binding (TB) model, 342–344, 347–351, 353–356
Tin dioxide (SiO_2), 87–92
Titania, 121–127, 287, 297
Topography, 83–84, 345, 348, 353, 354
Topological insulators, 345, 353, 354
Toxicity, 280, 289–293, 296–298, 389, 396, 417, 418, 420, 432
Transmission coefficient, 97–99
Transmission electron microscopy (TEM), 4, 5, 9–11, 15, 65, 211, 215, 236, 241, 420, 421
Transparent conductive layers (TCLs), 54
Tungsten, 122

U
Ultrafine-grained structure, 255
Ultra violet (UV) irradiation, 80, 83, 154, 159

V
Vacuum, 25, 112, 113, 115, 122, 133, 173, 174, 178, 179, 181, 182, 190, 242, 330, 360, 370, 378, 462
Velocity, 53, 80, 104, 105, 114, 460

W
Water
  bridge, 364, 365
  clusters, 238
  phases, 362
  properties, 27, 29–32, 54, 147, 148, 151
Water-salt solutions, 395
Waveguide photonic crystal structures, 73–85
Wear resistance, 286
Wide-band limit (WBL), 343
Wound dressing, 375–385

X
X-ray diffraction (XRD), 36, 122, 123, 147, 148, 393, 431–435, 439, 440

Z
Zirconium, 20, 240